UNIVERSITY OF ŽILINA

TRANSCOM PROCEEDINGS 2015

11-th EUROPEAN CONFERENCE OF YOUNG RESEARCHERS AND SCIENTISTS

under the auspices of

Tatiana Čorejová
Rector of the University of Žilina

SECTION 5

MATERIAL ENGINEERING MECHANICAL ENGINEERING TECHNOLOGIES

ŽILINA June 22 - 24, 2015
SLOVAK REPUBLIC

Edited by Vladimír Bulej, Michal Mokryš

ISBN: 978-80-554-1047-0
ISSN of Transcom Proceedings CD-Rom version: 1339-9799
ISSN of Transcom Proceedings online version: 1339-9829
(http://www.transcom-conference.com/transcom-archive)

TRANSCOM 2015
11th European conference of young researchers and scientists

TRANSCOM 2015, the 11th international conference of young European scientists, postgraduate students and their tutors, aims to establish and expand international contacts and co-operation. The main purpose of the conference is to provide young scientists with an encouraging and stimulating environment in which they present results of their research to the scientific community. TRANSCOM has been organised regularly every other year since 1995. Between 160 and 400 young researchers and scientists participate regularly in the event. The conference is organised for postgraduate students and young scientists up to the age of 35 and their tutors. Young workers are expected to present the results they had achieved.

The conference is organised by the University of Žilina. It is the university with about 13 000 graduate and postgraduate students. The university offers Bachelor, Master and PhD programmes in the fields of transport, telecommunications, forensic engineering, management operations, information systems, in mechanical, civil, electrical, special engineering and in social sciences incl. natural sciences.

SECTIONS AND SCIENTIFIC COMMITTEE

1. TRANSPORT AND COMMUNICATIONS TECHNOLOGY.

Scientific committee: Adamko Norbert (SK), Bugaj Martin (SK), Buzna Ľuboš (SK), Drozdziel Paweł (PL), Jánošíková Ľudmila (SK), Madleňák Radovan (SK), Rievaj Vladimír (SK), Teichmann Dušan (CZ)

2. ECONOMICS AND MANAGEMENT.

Scientific committee: Blašková Martina (SK), Hittmár Štefan (SK), Borkowski Stanisław (PL), Gregor Milan (SK), Kucharčíková Alžbeta (SK), Matuszek Józef (PL), Mičieta Branislav (SK), Rostášová Mária (SK), Sroka Włodzimierz (PL), Tomová Anna (SK), Zhivitskaya Helena (BLR)

3. INFORMATION AND COMMUNICATION TECHNOLOGIES.

Scientific committee: Dado Milan (SK), Hudec Róbert (SK), Kharchenko Vyacheslav (UKR), Klimo Martin (SK), Kršák Emil (SK), Matiaško Karol (SK), Pancerz Krzysztof (PL), Spalek Juraj (SK), Švadlenka Libor (CZ), Vaculík Juraj (SK), Vašinek Vladimír (CZ), Vrček Neven (HR)

4. ELECTRIC POWER SYSTEMS. ELECTRICAL AND ELECTRONIC ENGINEERING.

Scientific committee: Altus Juraj (SK), Brandštetter Pavel (CZ), Bury Peter (SK), Cacciato Mario (I), Čápová Klára (SK), Dobrucký Branislav (SK), Chernoyarov Oleg Vyacheslavovich (RU), Janoušek Ladislav (SK), Luft Mirosław (PL), Szychta Elżbieta (PL), Špánik Pavol (SK), Vittek Ján (SK)

5. MATERIAL ENGINEERING. MECHANICAL ENGINEERING TECHNOLOGIES.
Scientific committee: Adamczak Stanisław (PL), Guagliano Mario (I), Konečná Radomila (SK), Kunz Ludvík (CZ), Kuric Ivan (SK), Meško Jozef (SK), Neslušan Miroslav (SK), Takács János (H), Ungureanu Nicolae Stelian (RO)

6. MACHINES AND EQUIPMENT. TRANSPORT MEANS. APPLIED MECHANICS.
Scientific committee: Gerlici Juraj (SK), Chudzikiewicz Andrzej (PL), Malcho Milan (SK), Medvecký Štefan (SK), Zapoměl Jaroslav (CZ), Žmindák Milan (SK)

7. CIVIL ENGINEERING.
Scientific committee: Bujňák Ján (SK), Ižvolt Libor (SK), Segalini Andrea (I)

8. NATURAL SCIENCES (APPLIED MATHEMATICS). SOCIAL SCIENCES.
Scientific committee: Dopita Miroslav (CZ), Dzhalladova Irrada (UKR), Grecmanová Helena (SK), Katuščák Dušan (SK), Marčoková Mariana (SK), Růžičková Miroslava (SK), Šindelářová Jaromíra (CZ)

9. SECURITY ENGINEERING. FORENSIC ENGINEERING.
Scientific committee: Kasanický Gustáv (SK), Kohút Pavol (SK), Navrátil Leoš (CZ), Řehák David (CZ), Sventeková Eva (SK), Šimák Ladislav (SK), Zagorecki Adam (UK), Zamiar Zenon (PL)

ORGANIZING COMMITTEE

CHAIRPERSONS Čelko Ján, Bokůvka Otakar

EXECUTIVE SECRETARY Vráblová Helena

MEMBERS Bašťovanský Ronald, Belan Juraj, Bendík Ján, Brída Peter, Brůna Marek, Bulej Vladimír, Číba Jakub, Čičmancová Silvia, Dulina Ľuboslav, Ďurovec Martin, Florková Zuzana, Gašová Zuzana, Grajcaríková Petra, Grejták Marek, Herda Miloš, Hőger Marek, Hrbček Jozef, Hruboš Marián, Hudák Martin, Koman Gabriel, Kutaj Milan, Kuzmová Mária, Kvet Michal, Magdolen Marián, Malichová Eva, Maňurová Mária, Masárová Gabriela, Metruk Rastislav, Murgašová Veronika, Nosek Radovan, Odrobiňák Jaroslav, Olešnaníková Veronika, Oriešková Veronika, Palkechová Marcela, Porubiaková Andrea, Pšenáková Zuzana, Račko Ján, Rusinková Jana, Rypáková Martina, Semanová Štefánia, Stankovičová Zuzana, Šarafín Peter, Šimková Ivana, Šušlik Ľuboš, Vaško Alan, Vincúrová Gabriela.

SECTION 5 MATERIAL ENGINEERING MECHANICAL ENGINEERING TECHNOLOGIES

REVIEWERS:

Belan Juraj
Bokůvka Otakar
Bolibruchová Dana
Bronček Jozef
Brůna Marek
Bulej Vladimír
Císar Miroslav
Czán Andrej
Čilliková Mária
Čuboňová Nadežda
Donič Tibor
Drbúl Mário
Ďurčanský Peter
Fabian Peter
Hrček Slavomír
Hurtalová Lenka
Konečná Radomila
Koňár Radoslav
Kopas Peter
Kuba Jozef
Kumičáková Darina
Kuric Ivan
Liptáková Tatiana
Markovičová Lenka
Meško Jozef
Mičian Miloš
Mičietová Anna
Moravec Ján
Neslušan Miroslav
Nový František
Palček Peter
Pastirčák Richard
Pilát Peter
Pilc Jozef
Sládek Augustín
Stančeková Danka
Šajgalík Michal
Tillová Eva
Trško Libor
Uhríčik Milan
Uríček Juraj
Vaško Alan
Vaško Milan
Zatkalíková Viera

Note:

Author/s are responsible for language contents of their papers

CONTENTS

BAČA, ADRIÁN – KONEČNÁ, RADOMILA – NICOLETTO, GIANNI, Žilina, Slovak Republic: Microstructural and Mechanical Properties of Ti6Al4V Alloy Produced by SLM and EBM 9

BANAK, RAFAŁ – ZOWCZAK, WŁODZIMIERZ – MOŚCICKI, TOMASZ, Kielce, Poland: Theoretical Model of the Laser Welding Process 13

BAŃKOWSKI, DAMIAN – KRAJCARZ, DANIEL – MŁYNARCZYK, PIOTR, Kielce, Poland: Review of Machines for Finishing Processes with Smoothing Vibratory Media 19

BEK, MARKO – GONZALEZ-GUTIERREZ, JOAMIN – EMRI, IGOR, Ljubljana, Slovenia: Granular Flow Apparatus for Flowability Measurements of Granular Materials 25

BELKA, RADOSŁAW – KOWALSKI, SZYMON – ŻÓRAWSKI, WOJCIECH – SUCHAŃSKA, MAŁGORZATA, Kielce, Poland: A Study of Plasma Sprayed Hap Coatings Using the EDX and Raman Methods 31

BÍREŠOVÁ, JANA – HOCKICKO, PETER, Žilina, Slovak Republic: Investigation of Behavior of Metaphosphate Glass for the $Ba(PO_3)_2$ Composition by Means of Dielectric Relaxation Spectroscopy 37

BOLANOWSKI, PAWEŁ, Kielce, Poland: The Microstructure According to the Welding TTT Curve in Comparison with the Microstructure of the Real Welded Joint by Using the Example of Welded 900A Steel 43

BUCKI, TOMASZ – MOLA, RENATA – DZIADOŃ, ANDRZEJ, Kielce, Poland: Surface Alloying of Magnesium by GTAW Using AlMg4.5Mn Wire 49

ČIERNY, JAROSLAV – PATSCH, MAREK – MALCHO, MILAN, Žilina, Slovak Republic: Long-Term Operation and Measurement Parameters of Working Stirling Engine Type Gamma 53

DANIELEWSKI, HUBERT – SKRZYPCZYK, ANDRZEJ, Kielce, Poland: Impact of Bifocal Welding Head Angle Orientation on Welding Shape of TP347HFG High-temperature Steel 58

DEBNÁROVÁ, LENKA – KURIC, IVAN, Žilina, Slovak Republic: Methodology of Group Technology and Classification for Technical Production Planning 63

DOPJERA, DANJEL – MIČIAN, MILOŠ, Žilina, Slovak Republic: The Ultrasonic Testing of Welded Joint According to Standard STN EN 12732+A1 69

DRESSLEROVÁ, ZUZANA – PALČEK, PETER – CHALUPOVÁ, MÁRIA – UHRÍČIK, MILAN, Žilina, Slovak Republic: Effect of Cyclic Loading on the Internal Damping of AZ31 and AZ91 Magnesium Alloys 73

DURSTOVÁ, ZUZANA – NESLUŠAN, MIROSLAV, Žilina, Slovak Republic: Influence of Tool Wear and Sample Hardness on Barkhausen Noise after Hard Turning 78

DZIOBA, IHOR – FURMAŃCZYK, P., Kielce, Poland: Determining the Critical Value of Fracture Toughness Using the Measurement of the Stretch Zone Width 82

DZIOBA, IHOR – LIPIEC, SEBASTIAN, Kielce, Poland: Calculation the Stress Distribution σ_{22} in front of the Crack in Ductile Iron ADI 86

FATURÍK, MARTIN, Žilina, Slovak Republic: Ultrasonic Testing of Plastic Material 90

GÓRAL, ANNA – SOKOŁOWSKI, KRZYSZTOF – ŻÓRAWSKI, WOJCIECH – MAKRENEK, MEDARD, Krakow, Poland: Microstructure of Plasma Sprayed ZrO_2-$8Y_2O_3$ Coatings 95

GORYCKI, ŁUKASZ, Kielce, Poland: Analysis of the Impact of the Cage Type on the Frictional Moment Ball Bearings. 100

HOLUBJÁK, JOZEF – CZÁN, ANDREJ – ŠAJGALÍK, MICHAL – DRBÚL, MÁRIO – PIEŠOVÁ, MARIANNA – KUZDÁK, VIKTOR, Žilina, Slovak Republic: Deformation Zones Verification of Nickel Alloys by Implementation of Multi-parametric Measuring System 104

HRABOVSKÝ, TOMÁŠ – BLAŽEK, DALIBOR – NESLUŠAN, MIROSLAV, Žilina, Slovak Republic: Evaluation of Magnetically Oriented Surface after Hard Milling Cycles 110

JANKEJECH, PETER – FABIAN, PETER – RENGEVIČ, ALEXANDER, Žilina, Slovak Republic: Influence of Time during Isothermal Quenching 116

JANUS, URSZULA, Kielce, Poland: Energy Analysis in Ultra-High Strength Steel. Microscopic Observations 121

KAPUSŇÁK, MICHAL – PETZOVÁ, JANA – KUPČA, ĽUDOVÍT – BŘEZINA, MARTIN, Trnava, Slovak Republic: Evaluation of Initial Mechanical Properties of Surveillance Specimens for Mochovce Nuclear Power Plant Units 3 and 4 125

KMIECIK-SOŁTYSIAK, URSZULA – ADAMCZAK, STANISLAV, Kielce, Poland: The Application of Optical Methods for Measuring Roundness Profiles 130

KORDÍK, MAREK – ČILLIKOVÁ, MÁRIA, Kielce, Poland: Comparison of the Properties of Coatings and Coating Methods 134

KOWALCZYK, JAKUB – ULBRICH DARIUSZ – SAWCZUK WOJCIECH, Poznan, Poland: Testing of Welded Joints of Thin Metal Sheets Used in the Automotive Industry 138

KOZIOR, TOMASZ, Kielce, Poland: Stress Relaxation in SLS Additive Technology 142

KRAJCARZ, DANIEL, Kielce, Poland: Influence of Selected Water-jet Cutting Parameters on Surface Quality Aluminum Alloy 148

KRANJEC, MATEJ – KUNC, ROBERT – PREBIL, IVAN, Ljubljana, Slovenia: Finite Element Stress-Strain Numerical Analysis of Response of the Achilles Tendon 154

KULPA, JAKUB – WITKOWSKI, GRZEGORZ, Kielce, Poland: Multisensensory Measurements in Modern Production Techniques 160

KURP, PIOTR, Kielce, Poland: Compare of Sliding Tribilogical Properties for Laser Padded Coatings Deposited onto C45 Steel Substrate 164

LAGO, JÁN – BOKŮVKA, OTAKAR – NOVÝ, FRANTIŠEK – JANČOVIČ, PETER, Žilina, Slovak Republic: Possibilities of Laser Beam Using for Increasing the Fatigue Life of Welded Domex® Steel by Remelting the Weld Toe 168

LAZIĆ, VUKIĆ – ARSIĆ, DUŠAN – NIKOLIĆ, RUŽICA – ALEKSANDROVIĆ, SRBISLAV – DJORDJEVIĆ, MILAN –HADZIMA, BRANISLAV, Kragujevac, Serbia: Optimization of Welding of the Truck's Rear Axle Semi-housing 172

LOVÍŠEK, MARTIN – LIPTÁKOVÁ, TATIANA, Žilina, Slovak Republic: Electrochemical Characteristics of Aluminum Brass 178

MAJ, PIOTR – MIKO, EDWARD, Kielce, Poland: Review of Factors Affecting on the Accuracy Dimensionally-contoured Manufactured Items on Numerically Controlled Milling Machines 182

MAKIEŁA, WŁODZIMIERZ – GOGOLEWSKI, DAMIAN, Kielce, Poland: The Comparison of Surface Stereometry Using Hotelling T2 Test 186

MAKRENEK, MEDARD – PAJDO, MILENA – ŻÓRAWSKI, WOJCIECH – BELKA, RADOSŁAW – GÓRAL, ANNA, Kielce, Poland: The Properties of the Materials Used in the Process of Plasma Spraying of Optical Coatings 191

MARTIKÁŇ, ANTON – SORDI, VITOR LUIZ – PETRU, JANA – CZÁN, ANDREJ – ŠAJGALÍK, MICHAL – STRÚHARŇANSKÝ, JOZEF, Žilina, Slovak Republic: Analyze of Surface Integrity of Ausgaging Construction Parts from Nuclear Reactor Austenitic Steel 196

MAZUR, MAGDALENA – ULEWICZ, ROBERT – SZATANIAK, PAWEŁ, Częstochowa, Poland: Fractographic Analysis of Research in the Field of High-Cycle Fatigue Regime..... 202

MELO, BORISLAV – MORAVEC, JÁN, Žilina, Slovak Republic: Impact on PVD Coating TiCN Increase the Opening Life of Active Parts of Cold-moulding Tools from Steel Vanadis 4 Extra... 206

NOVOSAD, MILAN – KURIC, IVAN, Žilina, Slovak Republic: Machine Tool Verification 210

OBLAK, PAVEL – GONZALEZ-GUTIERREZ, JOAMIN – ZUPANČIČ, BARBARA – AULOVA, ALEXANDRA – EMRI, IGOR, Ljubljana, Slovenia: Effect of Extensive Recycling on High Density Polyethylene (HDPE) Mechanical Properties 214

OMASTA, MIROSLAV – HADZIMA, BRANISLAV, Žilina, Slovak Republic: Electrochemical Characteristics of Elektron 21 Magnesium Alloy with Octacalcium Phosphate (OCP) Coating.... 220

ORAVCOVÁ, MONIKA – PALČEK, PETER – ZATKALÍKOVÁ, VIERA – CHALUPOVÁ, MÁRIA, Žilina, Slovak Republic: The Effect of Heat Treatment on Structure Stability of AISI 316Ti 224

ORMAN, ŁUKASZ J. – KAPJOR, ANDREJ – HUŽVÁR, JOZEF, Kielce, Poland: Analysis of Boiling Heat Transfer on the Isothermal Surface Covered with a Single Copper Mesh 229

PATEK, MAREK – MIČIAN, MILOŠ – SLÁDEK, AUGUSTÍN, Žilina, Slovak Republic: Analysis of Weld Joints of the Split Sleeve for Branch Connections Repairs 233

PATSCH, MAREK – ČIERNY, JAROSLAV, Žilina, Slovak Republic: Operation and Measuring the Emissions of the Fuel Cell 239

PIOTR, THOMAS, Kielce, Poland: Influence of Relative Strain Values on Pressure Forces in Combined Extrusion of Parts Made of ENAW-1050A Alloy 243

PIOTR, THOMAS, Kielce, Poland: Determining the Values of Forces in Nut Hook Bending..... 247

PLISZKA, IZABELA – RADEK, NORBERT – RADZISZEWSKI, LESZEK, Kielce, Poland: The Geometric Structure of the Electro-Spark Deposited WC-Cu Coatings Modified by Laser Treatment 251

RENGEVIČ, ALEXANDER – KUMIČÁKOVÁ, DARINA, Žilina, Slovak Republic: Safety Cooperation between Human and Robot 257

RICHTÁRECH, LUKÁŠ – BOLIBRUCHOVÁ, DANA, Žilina, Slovak Republic: Elimination of Iron Secondary Al-Si Alloy 263

SÁSIK, RÓBERT – MADAJ, RUDOLF – HOČ, MICHAL – SPIŠÁK, PETER, Žilina, Slovak Republic: Chemical Analysis of Produced Prototype by Selective Laser Melting (SLM) Method Using Rapid Prototyping Technology..... 267

SKARBEK-ŻABKIN, ANNA – SZCZEPANEK, MARCIN, Warszawa, Poland: Energy Parameters of Waste Generated while Vehicle Disassembly 273

SKRZYNIARZ, MICHAŁ – MIKO, EDWARD – NOWAKOWSKI, ŁUKASZ, Kielce, Poland: Determination of Minimum Uncut Chip Thickness in Turning 278

SOVIAROVÁ, ANDREA – TROJANOVÁ, ZUZANKA – PALČEK, PETER – CHALUPOVÁ, MÁRIA – KNAPEK, MICHAL, Žilina, Slovak Republic: Monitoring of Microstructural Changes in AZ91 Magnesium Alloy by Internal Damping Measurement 282

SPIŠÁK, PETER – MADAJ, RUDOLF – SÁSIK, RÓBERT, Žilina, Slovak Republic: Implementation of the Model Trucks FTS Using 3D Printing 288

STANČEK, JÁN – URÍČEK, JURAJ – BULEJ, VLADIMÍR, Žilina, Slovak Republic: Possibilities of Renewal Energy Sources for Electric Vehicles 293

STRĄK, EWELINA – PASTUSZKO, ROBERT – KŁOSOWIAK, ROBERT – URBANIAK, RAFAŁ, Kielce, Poland: FC-72 and Novec^{TM} 649 Boiling on a Mini-Fin Surface Coated with Carbon Nanotubes 297

STRUHARŇANSKÝ, JOZEF – PIEŠOVÁ, MARIANNA, Žilina, Slovak Republic: Evaluation of Stress Conditions in Turning with Rotating Tool 303

SZATANIAK, PAWEŁ – NOVÝ, FRANTIŠEK – ULEWICZ, ROBERT, Wieluń, Poland: Fatigue Properties and Application Options of the Fine-Grained Steel of DOMEX Type 309

SZWED, BARTŁOMIEJ – KONIECZNY, MAREK, Kielce, Poland: Characterization of Solid-state Diffusion Joints between Titanium and Stainless Steel Using Nickel Interlayer 315

ŠVECOVÁ, IVANA – TILLOVÁ, EVA – BORKO, KAMIL – CHALUPOVÁ, MÁRIA, Žilina, Slovak Republic: Effect of Modifying Process on Si-Morphology and Mechanical Properties in Secondary AlSi10MgMn Cast Alloy 319

ULBRICH, DARIUSZ – KOWALCZYK, JAKUB – SAWCZUK, WOJCIECH, Poznan, Poland: Assessment of the Possibilities of Using Ultrasonic Method for Testing the Quality of Adhesive Joints Type Metal – Metal 323

VAJDOVÁ, ALENA – MIČIETOVÁ, ANNA, Žilina, Slovak Republic: Machinability of Steel S690 after Laser and Plasma Beam Cutting 327

VRZGULA, PETER – BUCHACO, MIROSLAV – MIČIAN, MILOŠ, Žilina, Slovak Republic: Alternative Uses of NDT-leak Testing Method of Pressure Changes in the Gas Industry 333

WRÓBLEWSKI, EMIL – ISKRA, ANTONI – BABIAK, MACIEJ, Poznan, Poland: The Impact of Supplementing Motor Oil with Carbon Nanotubes on Improving the Tribological Piston – Cylinder System's Performance 338

ZMARZŁY, PAWEŁ – GOGOLEWSKI, DAMIAN, Kielce, Poland: The Adaptation of Unconventional Manufacturing Technology in Casting 344

ZMARZŁY, PAWEŁ, Kielce, Poland: Computer Analysis of Three-point References Method Parameters to Waviness Measurement of Cylindrical Surfaces 349

ZRAK, ANDREJ – MEŠKO, JOZEF, Žilina, Slovak Republic: Heat Transfer Analysis by Using Finite Element Method 355

ŽIHALOVÁ, MÁRIA – BOLIBRUCHOVÁ, DANA, Žilina, Slovak Republic: Vanadium and Combined Vanadium and Chromium Influence to Mechanical Properties of AlSi10MgMn Alloy with Elevated Iron Level 359

TRANSCOM 2015, 22-24 June 2015
University of Žilina, Žilina, Slovak Republic

Microstructural and Mechanical Properties of Ti6Al4V Alloy Produced by SLM and EBM

[*]Adrián Bača, [*]Radomila Konečná, [**]Gianni Nicoletto
[*]University of Žilina, Faculty of Mechanical Engineering, Department of Material Engineering, Univerzitná 8215/1, 01026 Žilina, Slovakia, {adrian.baca, radomila.konecna}@fstroj.uniza.sk
[**]University of Parma, Department of Industrial Engineering, Parco Area della Scienze 181/A, 43124 Parma, Italy, {gianni.nicoletto}@unipr.it

Abstract. This contribution deals with the study of Ti6Al4V titanium alloy fabricated by powder bed additive manufacturing (AM) process. Most promising AM technologies for the production of titanium alloys are selective laser melting (SLM) and electron beam melting (EBM). Both of these methods achieve full melting of the metal powder and final products exhibits comparable mechanical properties to the conventionally produced alloys. Therefore, it is very important to fully understanding of the relationship between the process parameters, microstructure and mechanical properties of the material produced by these non-conventional technologies. The mechanical properties of as-built and HIP tensile specimens produced with reference to specific building axes were investigated. It was found that the build orientation and microstructure affects the tensile properties, and in particular the elongation of the specimens.

Keywords: Ti6Al4V alloy, selective laser melting, electron beam melting, additive manufacturing

1. Introduction

Titanium alloys, have a wide range of applications, thanks to their high specific strength to density ratio, good corrosion resistance and excellent mechanical properties (even at high temperature) [1]. Additive manufacturing (AM) technology has been successfully applied in the manufacturing of titanium components for the aerospace, automotive, chemical and medical industries with equivalent or better mechanical properties as parts fabricated via more traditional casting and machining methods [2, 3].

Metal powder bed technologies such as SLM and EBM share a similar basic working principle. The process begins with part design use computer-based methods. This 3D computer designed model is sliced into thin layers before it is fed to the AM machine. Thin layer of metal powder is spread on the process table and high intensity energy source (laser/electron beam) scans and liquid phase melts the desired area of the powder bed based on the sliced data from the file. On completion of a scan, the process table lowers by single layer thickness and new powder is spread. The beam scans the powder bed and process continues until a complete part is build [4, 5].

Mechanical properties of Ti6Al4V (typical α+β) alloy are strongly influenced by the production route, which can determine meaningful differences in the resulting microstructure. In principle, a lamellar microstructure improves the resistance to fatigue crack propagation, to creep and to oxidation, whilst a globular one is favorable to strength and elongation [6]. The important parameters for a lamellar structure with respect to mechanical properties are the β-grain size, size of the colonies of α-phase lamellae, thickness of the α-lamellae and the nature of the interlamellar interface (β-phase). Slow and intermediate cooling rates lead to a diffusion controlled nucleation and growth process of α-lamellae into the β-grains. A high cooling rates result in a martensitic transformation of the β-phase. This structural process requiring further study [7-9].

This study investigates the influence of microstructure after EBM and SLM process followed by a hot isostatic pressing (HIP) treatment on mechanical properties of Ti6Al4V alloy.

2. Material and experimental methods

Titanium Ti6Al4V alloy produced by SLM (Renishaw AM 250) and EBM (Arcam Q10) form of atomized powder was used as an experimental material. Each equipment manufacturer specifies a metal powder that is allowed to build components when the equipment is used. The nominal chemical compositions of each powder are listed in Tab. 1.

Process	Al	V	Fe	O	C	N	H	Ti
SLM	5.50 ÷ 6.50	3.50 ÷ 4.50	<0.25	<0.13	<0.08	<0.03	<0.010	Balance
EBM	5.50 ÷ 6.75	3.50 ÷ 4.50	<0.30	<0.20	<0.10	<0.05	<0.015	Balance

Tab. 1. Nominal chemical composition of the Ti6Al4V powder used for SLM and EBM system.

The laser melting machine from Renishaw (Fig. 1a) uses an ytterbium fiber laser with a wavelength of 1075 nm and laser power of 200 W to fuse metallic powder into 3D objects. The spherical alloy powder (ASTM Grade 23) with the granulometry in the 15 and 45 µm was used. The Arcram machine (Fig. 1b), using Ti6Al4V (Grade 5) powder with the average particle size between 45 and 100 µm that is melted by a powerful (up to 3000 W) electron beam.

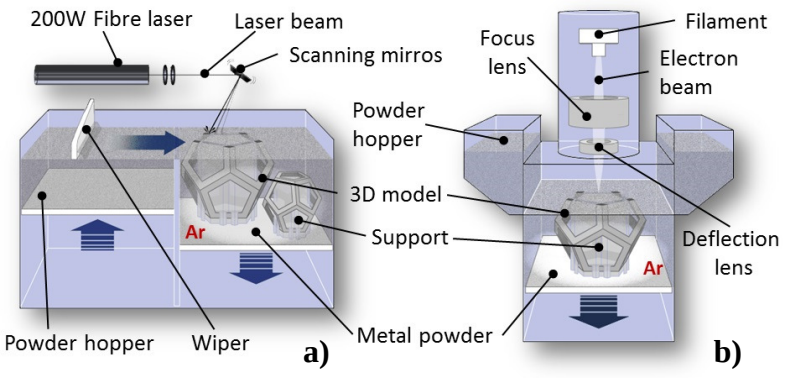

Fig. 1. Scheme of the SLM (a) and EBM system (b) [5].

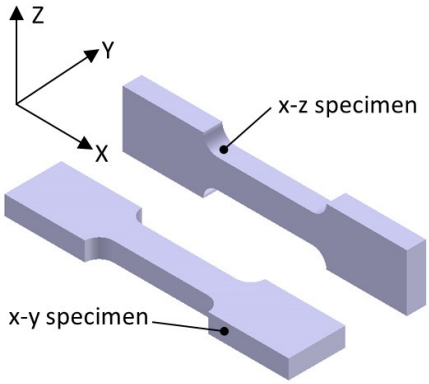

Fig. 2. Specimens build orientation.

Tensile specimens were fabricated according to two orientations (Fig. 2) using different grade of powder for each corresponding equipment. HIP process at 930 °C and 100 MPa argon pressure for one hour was performed to increase quality and density of the SLM parts. The objective is the closure of all existing discontinuities associated to the additive manufacturing fabrication process.

Tensile tests were performed according to ASTM 8/E 8M-08, using a MTS 810 servo hydraulic machine equipped with a 25 mm MTS extensometer. The tests were conducted at room temperature in displacement control mode (rate 0.01 mm/s). Broken specimens were metallographically polished and etched using 10% HF. Metallographic sections were prepared according to transverse direction of the specimens. The microstructure characterization after melting process was determined by light microscope (LM) Neophot 32 [9].

The Vickers hardness was determined using a HPO-250K/AQ tester with a 100 N force for 10 s and micro-hardness using micro-hardness tester Zwick/Roel ZHVµ-A with a 5 N for 10.5 s.

3. Results and discussion

3.1. Structure characterization

The microstructure of SLM + HIP specimens consists of a lamellar structure of α+β phases which are stabilized by alloying elements (Fig. 3). During the manufacturing process α´- martensite was formed and the subsequent HIP process converted the original structure into a lamellar α+β [5, 8]. The structure of α+β phases may take the form of colonies (1) where parallel α-phase lamellae (light) in the elongated primary β-phase grain are created during cooling from the high

temperature of the HIP process. On the boundaries of the colonies the typical Widmanstätten microstructure was observed (2) and some of elongated β-grains show a coarsening of α-phase (3). These areas with coarse α-grains may be responsible for lower elongation of x-y compared to x-z specimen. The thickness of α-lamellae and colony size has the most significant influence on mechanical properties. Thin lamellas contribute to the higher strength as reported in [9].

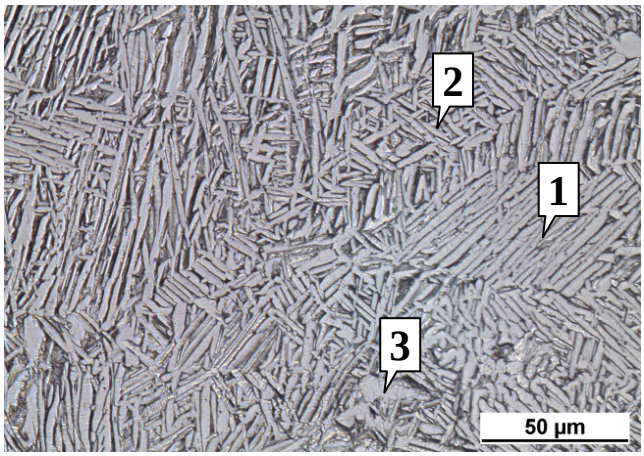

Fig. 3. Lamellar structure of α+β phases (SLM + HIP), LM

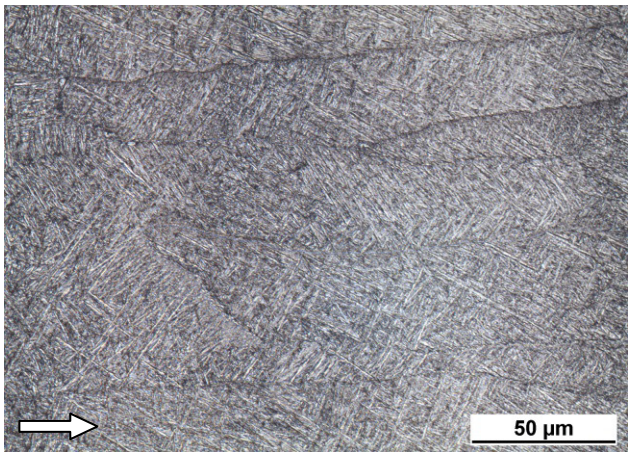

Fig. 4. Needless α´- martensite structure (EBM), LM

Fig. 4 shows optical micrograph of α´- martensite needless in the structure of EBM specimen. The needless obtained by EBM technology are thinner [7, 10] compared to the conventionally produced alloys. The elongated primary β-phase grains are parallel to the build direction (white arrow, Fig. 4). The size of these grains directly affects the resulting mechanical properties such as tensile strength and hardness [6].

3.2 Mechanical properties

Fig. 5 compares the yield strength, tensile strength and elongation of Ti6Al4V alloy specimens produced by non-conventional and conventional manufacturing methods. The mechanical properties for the cast and wrought specimens were obtained from manufacturer's data sheet [5, 9, 10].

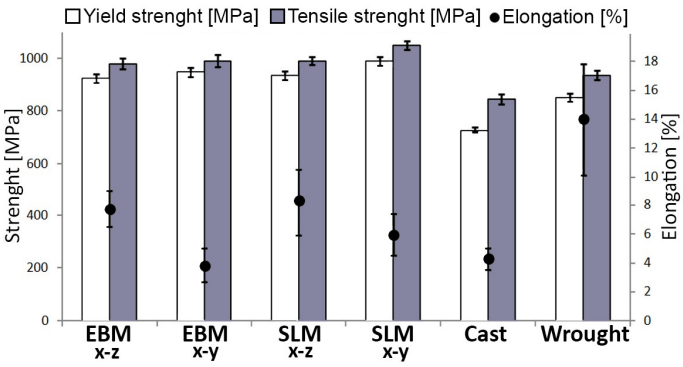

Fig. 5. Mechanical properties of Ti6Al4V alloys.

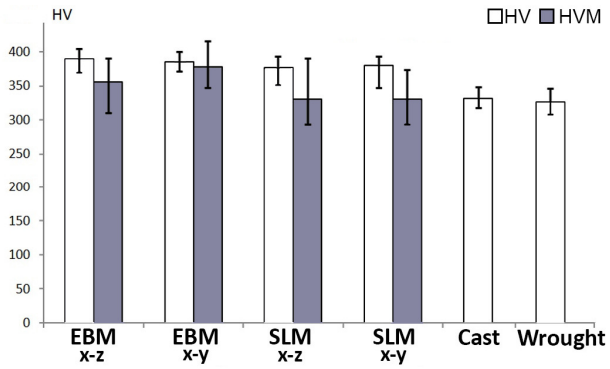

Fig. 6. Hardness of Ti6Al4V alloys.

The yield strength and tensile strength of the SLM + HIP and EBM specimens with x-y orientation were slightly higher than the x-z orientation. Otherwise the lower elongation to rupture than the x-z specimens was found. That demonstrates the effect of different specimen orientations with respect to the build direction on the mechanical properties [7-9]. The tensile and yield strength of both the SLM + HIP and EBM specimens was similar and roughly 10 - 15 % higher than that of the cast and wrought alloys. The elongation of the SLM + HIP and EBM specimens is lower than wrought specimens but it is higher than 2 % reported earlier by Koike et al. [10].

Fig. 6 shows the measured hardness values for different production of specimens. The hardness of both the SLM + HIP and EBM specimens was similar (in the range 380 - 390 HV) and higher than that of the cast (332 HV) and wrought (326 HV) specimens. The average micro-hardness values of the SLM + HIP specimens are similar, but lower than EBM specimens. The microstructure of the EBM specimens was characterized by fine needless of α'- martensite showing the higher micro-hardness compared to the two-phase lamellar microstructure (α + β) obtained by SLM + HIP process.

4. Conclusion

The main conclusions are as follows:

- During the SLM and EBM manufacturing process α´- martensite was formed.
- The HIP process applied after SLM increased the content of closed pores and converted the original α´- martensite into the lamellar α+β structure.
- The x-y orientation of the SLM + HIP and EBM specimens were characterized by lower elongation and higher strength compared to the specimens with x-z orientation.
- The specimens produced by SLM + HIP and EBM were characterized by higher strength, hardness and lower elongation when compared to the wrought and cast specimens.
- The micro-hardness of EBM specimens was higher than SLM + HIP specimens because of different microstructure.

Acknowledgement

The authors wish to acknowledge the company Protoservice srl., Fornovo Taro, Italy for providing the Ti6Al4V tensile specimens produced by SLM and EBM. The research was supported by project VEGA grant No. 1/0685/2015.

References

[1] BANERJEE, D., WILLIAMS, J. C. *Perspectives on titanium science and technology*. Acta materialia, 61(3): 844-879, 2013.

[2] WILLIAMS, J. C, STARKE, JR. E. A. *Progress in structural materials for aerospace systems*. Acta materialia. 51(19): 5775-5799, 2003.

[3] LUTJERING, G., WILLIAMS, J. C. *Titanium.* Springer-Verlag, 2007.

[4] VORA, P., MUMTAZ, K. A., HOPKINSON, N., TODD, I., DERGUTI, F. *Investigating a semi-solid processing technique using metal powder bed additive manufacturing processes*. Proceedings solid freeform fabrication symposium (24) 454, 2013.

[5] MURR, L.E., QUINONES, S.A., GAYTAN, S.M., LOPEZ, M.I., RODELA, A., MARTINEZ, E.Y., HERNANDEZ, D.H., MARTINEZ, E., MEDINA F., WICKER, R.B. *Microstructure and mechanical behavior of Ti-6Al-4V produced by rapid-layer manufacturing, for biomedical applications.* J. Mech. behav. biomed. mater., *2*, 20-32, 2009.

[6] LEYENS, C., PETERS, M. *Titanium and titanium alloys*, Wiley-Vch, 2003.

[7] PETERS, M., LUTJERING, G. *Proceedings of the Titanium'80: Science and Technology*, TMS, 925–935, 1990.

[8] LUTJERING, G., ALBRECHT, J., IVASISHIN, O.M. *Proceedings of the titanium'95: Science and technology*, TMS, 1163–1170, 1995.

[9] KONEČNÁ, R., NICOLETTO, G., KUNZ, L., FINTOVÁ, S. *Texture and tensile properties of Ti6Al4V produced by selective laser melting*. Materials science, Vol 20, No 4, 2014.

[10] KOIKE, M., GREER, P., OWEN, K., LILLY, G., MURR, L.E., GAYTAN S.M., MARTINEZ, E., OKABE, T. *Evaluation of titanium alloys fabricated using rapid prototyping technologies-electron beam melting and laser beam melting.* Materials 4(10), 1776-1792, 2011.

TRANSCOM 2015, 22-24 June 2015
University of Žilina, Žilina, Slovak Republic

Theoretical Model of the Laser Welding Process

[*]Rafał Banak, [*]Włodzimierz Zowczak, [**]Tomasz Mościcki
[*]Kielce University of Technology, Faculty of Mechatronics and Mechanical Engineering, Laser Processing Research Centre, al. Tysiąclecia Państwa Polskiego 7, 25-314 Kielce, Poland, {rbanak, wzowczak}@tu.kielce.pl
[**] Institute of Fundamental Technological Research Polish Academy of Sciences, Pawińskiego 5B, 02-106 Warsaw, Poland, tmosc@ippt.pan.pl

Abstract. To determine the distribution of the temperature field and the shape of the melting zone during the laser welding process of 304 stainless steel a three-dimensional numerical model was built and numerical simulation was performed. In order to improve the accuracy of the calculations temperature dependent material properties, heat loos due to the vaporization and heat exchange with surrounding medium due to the convection and radiation was considered.

Keywords: Computational Fluid Dynamics, Laser welding simulation, Finite Volume Method

1. Introduction

Nowadays laser beam is one of the highest power density sources available to industry [1]. Lasers are used to cut as well as to weld metals. In industrial applications CO_2 and solid state laser systems are most dominating [2]. There are two main types of laser welding: conduction mode and keyhole welding. Keyhole or deep penetration welding is commonly used to join thick elements. Due to the high power density joined metals begin to evaporate which leads to the formation of the plasma. Keyhole welding process is relatively unstable – welds often contains pores and spatters. Conduction mode welding occurs when power density does not excess 10^{10} W/m^2. That process is more stable than keyhole mode but on the other hand depth of welding is usually limited to hundreds μm.

Laser welding have many advantages over arc or gas metal arc welding process. Narrow heat affected zone and low distortions combined with precise laser beam delivery gives possibility to weld heat sensitive components and electronic parts. Often there are requirements imposed on the weld dimensions and maximum temperature – like for dissimilar materials welding where mixing zone size should allow materials to mix but at the same time the process temperature cannot exceed the boiling point of the component. One can predict laser welding process parameters basing on previously conducted experiments but this approach often requires many attempts and money consuming investigations.

A convenient alternative to relatively expensive destructive tests seems to be analytical [4][3] and numerical models. Since analytical approach has many limitations arising from unsteady nature of welding process, complex geometries and changing material properties numerical simulations are now major topic in most papers describing welding. Currently there are some software suits which are designed to perform numerical analysis of welding process. They are usually designed for industry use and offers ready solutions for common welding processes. On the other hand multiphysics suits offer the ability to create own heat sources and taking into account additional effects associated with welding like evaporation or turbulent flow in weld pool. In this paper for computation of temperature distribution and weld pool geometry commercial CFD software Ansys Fluent was used.

2. Mathematical model

Mathematical model used in numerical simulation describing interaction of the laser beam with the work piece consists of Fourier-Kirchoff and Navier-Stoke differential equations. For incompressible flow system of equation consists of [5]:

$$\frac{\partial \rho}{\partial t} + \nabla \cdot (\rho \vec{v}) = 0 \tag{1}$$

$$\frac{\partial \rho}{\partial t}(\rho \vec{v}) + \nabla \cdot (\rho \vec{v}\vec{v}) = -\nabla \rho + \nabla \cdot \left(\overline{\overline{\tau}}\right) + \rho \vec{g} + \vec{F} \tag{2}$$

where p is the static pressure, ρ, g and F are the gravitational body force and external body forces and stress tensor $\overline{\overline{\tau}}$ is given by [5]:

$$\overline{\overline{\tau}} = \mu \left[\left(\nabla \vec{v} + \vec{v}^{T} \right) - \frac{2}{3} \cdot \vec{v} I \right] \tag{3}$$

where μ is the molecular viscosity and I is the unit tensor. Second right hand side of equation is the effect of volume dilation.

The turbulence kinetic energy, k , and its rate of dissipation ε, are obtained from the following transport equations [6]:

$$\frac{\partial}{\partial t}(\rho k) + \frac{\partial}{\partial x_i}(\rho k u_i) = \frac{\partial}{\partial x_j}\left[\left(\mu + \frac{\mu_t}{\sigma_k} \right) \frac{\partial k}{\partial x_j} \right] + G_k + G_b - \rho \varepsilon - Y_M + S_k$$

$$\frac{\partial}{\partial t}(\rho \varepsilon) + \frac{\partial}{\partial x_i}(\rho \varepsilon u_i) = \frac{\partial}{\partial x_j}\left[\left(\mu + \frac{\mu_t}{\sigma_\varepsilon} \right) \frac{\partial \varepsilon}{\partial x_j} \right] + C_{1\varepsilon} \frac{\varepsilon}{k}(G_k + C_{3\varepsilon} G_B) \tag{4}$$

$$- C_{2\varepsilon} \rho \frac{\varepsilon^2}{k} + S_\varepsilon$$

where G_k is generation of turbulence kinetic energy due to the mean velocity gradients, G_b – generation of turbulence kinetic energy due to buoyancy, Y_M is contribution of the fluctuating dilatation in compressible turbulence to the overall dissipation rate, $C_{1\text{-}3\varepsilon}$ – are the constants, σ_k and σ_ε – turbulent Prandtl numbers for k and ε (1.0 and 1.3 respectively) [7]. Due to the incompressible nature of welding process some elements of (4) are equal zero.

Laser heat source was built and included into computations in the following form [8]:

$$-k_{eff} \frac{\partial T_s}{\partial \vec{n}} = I_L \cdot A - \alpha (T - T_\infty) - \sigma \varepsilon_p \left(T^4 - T_\infty^4 \right) - \rho u(t) L_v \tag{5}$$

where L_v is heat of vaporization, $\vec{n}$ is the unit vector, α is external heat transfer coefficient, ε_p is emissivity of the external wall surface and σ is Stefan-Boltzman constant. Velocity of the evaporation front u is determined from the Hertz-Knudsen equation [9]:

$$u(T_s) = \frac{(1-\beta)}{\rho} \left(\frac{m}{2\pi k T_s} \right)^2 p_b \exp\left[\frac{L}{k} \left(\frac{1}{T_b} - \frac{1}{T_s} \right) \right] \tag{6}$$

where L is the heat of evaporation, T_b is the boiling point at pressure p_b=10^5 Pa and T_s is the surface temperature.

Boundary conditions at the surfaces which are not affected by the laser beam were included as follow:

$$-k_{eff} \frac{\partial T_s}{\partial \vec{n}} = \alpha (T - T_\infty) + \sigma \varepsilon_p \left(T^4 - T_\infty^4 \right) \tag{7}$$

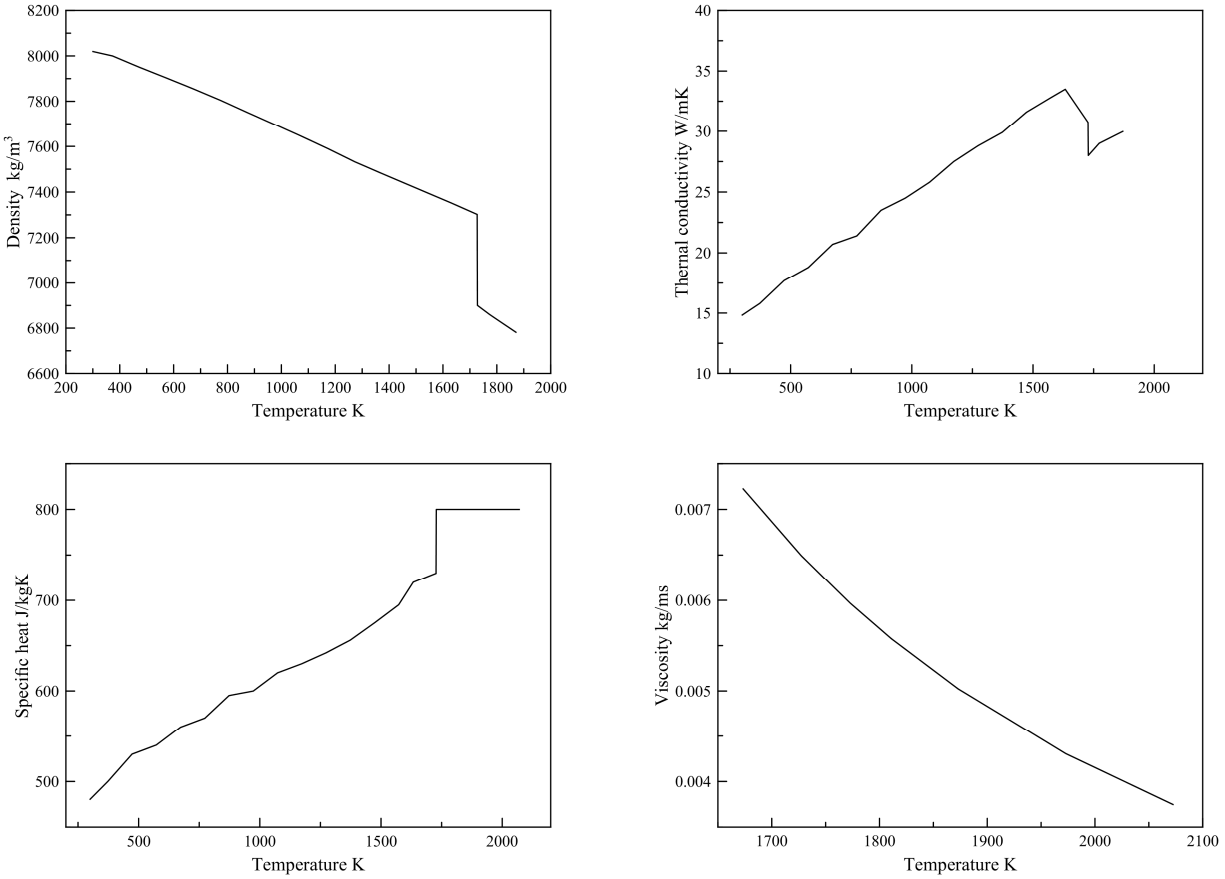

Fig. 1. Temperature dependent material parameters of 304 stainless steel [10].

As mentioned in melting and solidification process calculations it is important to take into account the temperature dependent material properties which are shown in Fig. 1. Assumed constant values are shown in Tab. 1.

Constant	**Value**
Melting heat	10^3 *J/kg*
Gas constant	8314.3 *J/kg mol K*
Liquidus temperature	1723 *K*
Solidus temperature	1658 *K*
Vaporization temperature	3135 *K*
Reference temperature	300 *K*
Reference pressure	$1.013*10^5$ *Pa*
Mole mass	55.8 *g/mol*
Stefan-Boltzman constant	$5.67*10^{-8}$ *W/m^{2}T^4*
Heat of vaporization	$6.09*10^6$ *J/kg*
Emissivity	0.4

Tab. 1. Constant values used in computations.

Due to the large temperature gradients denser mesh was created along laser path and close to the surface affected by laser beam. Rectangular computational domain, shown in Fig. 2, with 4x4x2 mm with 850000 cells was created. To compromise between the accuracy and duration of calculations, the time step between the iteration was set to $2.5 \cdot 10^{-5}$ s.

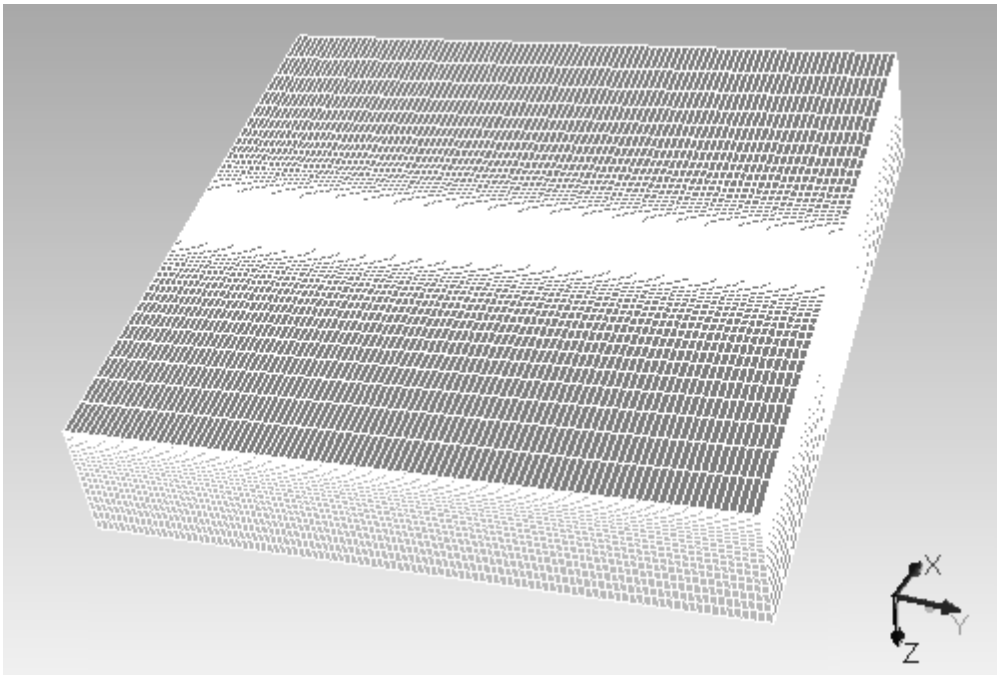

Fig. 2. Computational domain created for finite volume method calculations.

3. Numerical simulation results

For the calculations laser power P = 4000 W, laser spot diameter d = 0.5 mm, absorption coefficient κ = 0.05 and welding speed V = 2 m/min in Y direction were assumed. Surface tension phenomenon has a major influence on weld pool geometry – especially in the case of conduction mode welding. Presented model takes into account the Marangoni stress phenomenon with surface tension coefficient equal to 0.00049 N/m·K [11]. Negative surface tension coefficient values turns the motion of liquid steel in the weld poll inward to outward.

Fig. 3 shows molten pool geometry and temperature distribution in cross-section parallel to welding direction at time = 0.062 s and at center point X = 0.002 m Y = 0.002 m. Plots are focused on laser beam affected area. Fractional values on liquid fraction plot indicates existence of so called mushy zone. It's the area where iron is partially melted.

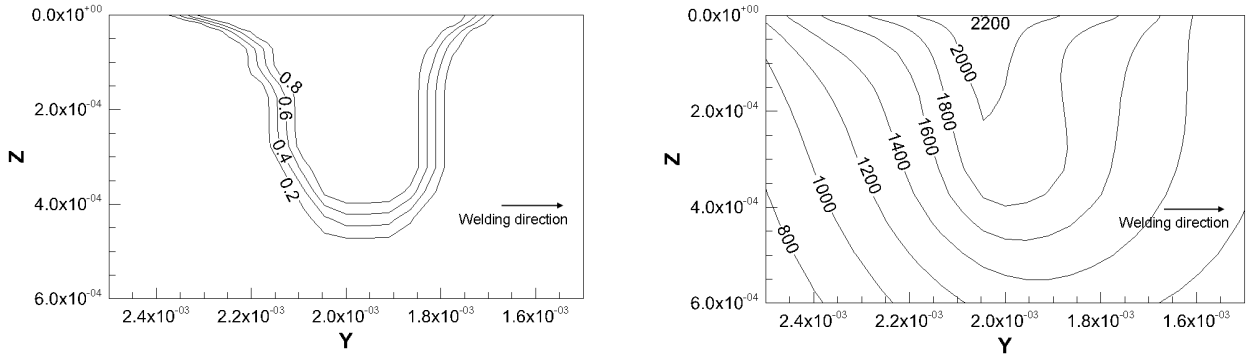

Fig. 3. Liquid fraction of molten iron (left) and temperature distribution (right) in cross-section parallel to welding direction.

Fig. 4 shows molten pool geometry and temperature distribution in cross-section plane perpendicular to the welding direction in same point as in Fig. 3. Maximum penetration depth for given parameters is equal to 420 µm while face of the weld has 525 µm width.

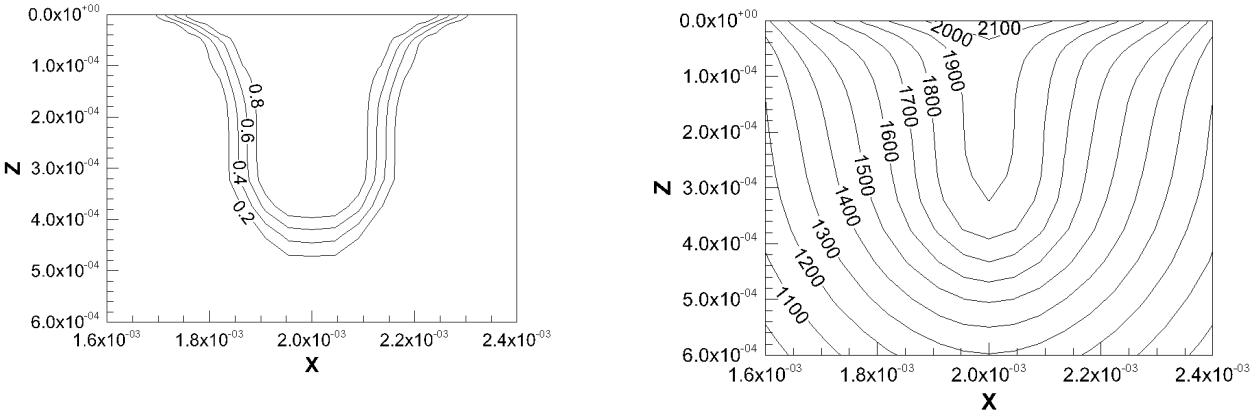

Fig. 4. Liquid fraction of molten iron (left) and temperature distribution (right) in cross-section perpendicular to welding direction.

Fig. 5 shows temperature distribution along laser beam path. Maximum temperature obtained from calculation was ~2200 K which is much lower value than vaporization temperature of stainless steel 304. This is important due to the fact that the exceeding of the boiling and evaporation temperature of the material usually results in a transition in to keyhole welding.

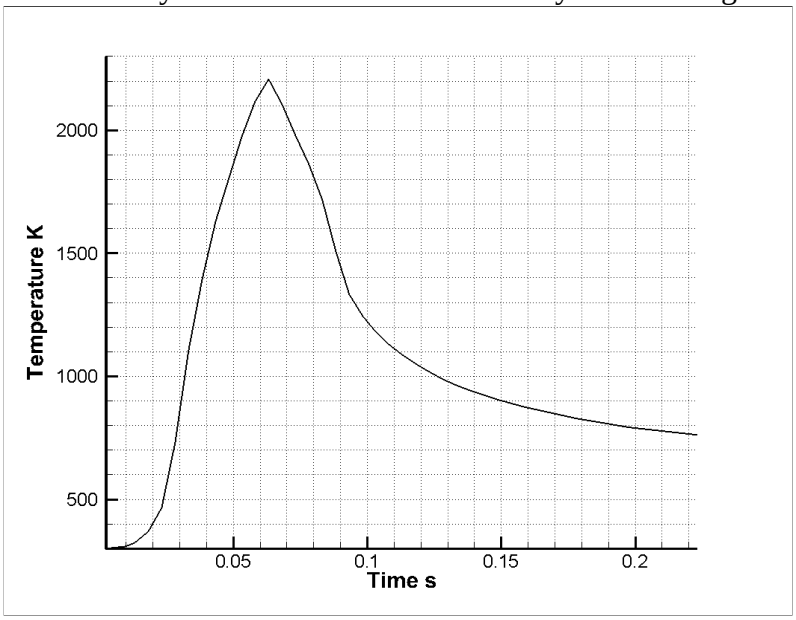

Fig. 5. Temperature distribution with respect to time at point X = 0.002 m Y = 0.002 m.

4. Conclusion

Due to the complexity of laser welding process the Ansys Fluent software has been utilized. The objective of the study was to build numerical model by means of which temperature distribution and welding pool geometry can be determined. In non-linear, transient heat and mass transfer analysis a three-dimensional model with a moving heat source was considered. Phase change phenomenon has been connected with a non-linear temperature-dependent material properties, metal evaporation heat loos model and heat exchange with surrounding medium in order to get results as close to the real as possible. User defined functions has been written to ensure more comprehensive control over laser spot size and power density.

Although described case need experimental verification it's in good agreement with similar already carried out joints. It seems that the numerical simulation is a convenient tool for prediction of laser beam welding. It can be successful employed in cases where the combined materials are expensive to reduce costs of determination of optimal process parameters. Proposed model can be easily adapted to different materials or heat sources (different lasers or welding methods).

Acknowledgement

This research was supported in part by PL-Grid Infrastructure. This work was supported by National Centre for Research and Development (NCBiR) contract number PBS1/B5/13/2012

References

[1] W. M. Steen and J. Mazumder, *Laser Material Processing*. 2010.

[2] M. Turňa, B. Taraba, P. Ambrož, and M. Sahul, "Contribution to Numerical Simulation of Laser Welding," *Phys. Procedia*, vol. 12, pp. 638–645, 2011.

[3] W. Zowczak, "Uproszczone pole temperatury dla analizy procesu spawania laserowego," *Przegląd Elektrotechniczny*, vol. 07, p. 76, 2011.

[4] B. Grabas and E. Mazur, "Obliczenia teoretyczne kształtu laserowej spoiny punktowej," *Przegląd Elektrotechniczny*, vol. R. 84, nr , pp. 126–128, 2008.

[5] Ansys, "ANSYS FLUENT theory guide," 2009.

[6] N. Chakraborty, "The effects of turbulence on molten pool transport during melting and solidification processes in continuous conduction mode laser welding of copper–nickel dissimilar couple," *Appl. Therm. Eng.*, vol. 29, no. 17–18, pp. 3618–3631, Dec. 2009.

[7] B. E. Launder and D. B. Spalding, *Lectures in Mathematical Models of Turbulence*. London: Academic Press, 1972.

[8] T. Mościcki and J. Radziejewska, "Numerical simulation and experimental analysis of simultaneous melting and burnishing of 304 stainless steel with oscillatory laser heat source," *Kov. Mater.*, vol. 51, no. 1, pp. 37 – 44, 2013.

[9] A. V Bulgakov and N. M. Bulgakova, "Thermal model of pulsed laser ablation under the conditions of formation and heating of a radiation-absorbing plasma," *Quantum Electron.*, vol. 29, no. 5, pp. 433–437, May 1999.

[10] K. C. Mills, *Recommended values of thermophysical properties for selected commercial alloys*. Cambridge: Woodhead Publishing, 2002.

[11] T. Matsumoto, T. Misono, H. Fujii, and K. Nogi, "Surface tension of molten stainless steels under plasma conditions," *J. Mater. Sci.*, vol. 40, no. 9–10, pp. 2197–2200, May 2005.

TRANSCOM 2015, 22-24 June 2015
University of Žilina, Žilina, Slovak Republic

Review of Machines for Finishing Processes with Smoothing Vibratory Media

[*]Bańkowski Damian, [*]Krajcarz Daniel, [*]Piotr Młynarczyk,
* Kielce University of Technology, Kielce, Poland, EU, damianbankowski1@gmail.com
Kielce University of Technology, Kielce, Poland, EU, dkracarz@wp.pl
Kielce University of Technology, Kielce, Poland, EU, mlynarczykpeter@gmail.com

Abstract. The paper presents the available machines for finishing process with using of loose material impact on the workpieces. Loose media treatments can be used in different variations of the kinematic example, for example: vibro-abrasive machining (also referred to as a vibration machining), tumbling.. In the nomenclature of English are also used to determine rotofinish or tumbling. This type of treatment leads to a relative reduction in surface roughness and consequently to improve reflectivity. One of the most commonly used methods is shotblasting. Other hand, becomes more and more widely used vibro-abrasive machining. The advantages of this method is the wide spectrum types, shapes and dimensions of the media and the ability to assist the machining process machining fluids. There are devices with very low volume of 5 liters for polishers used in jewelry to industrial equipment for large workpieces with a capacity of 1000 liters.

Keywords: Fine machining, vibration machining, vibro-abrasive, rotofinish, tumbling.

1. Introduction

You can find many definitions of abrasive machining. Of these, two were selected to sufficiently explain the concept in question. The first definition states that the abrasive treatment is to remove the small allowances material by abrasive tools or loose smoothing media. Grain orientation with respect to the main directions of kinematic at the time of contact with the material is a random. According to the second definition, the term treatment is meant abrasive machining methods, in which the process of removing the fixed volume of material shaped blades are made of particles of hard materials, of indefinite shape and an indefinite number of closely [2] form, which are supplied into contact with the workpiece. Abrasive treatments the can be divided into three groups: bonded abrasive machining, loose abrasive machining and electrochemical machining additional abrasive material are separated using mechanical energy, and eroding treatment. Which is based on the separation material by the action of electrical energy, chemical, and thermal. The abrasive machining is a kind of machining, side chip forming [10].

Considering the interactions that occur during the process of vibration treatment should remember about interactions between all components of the system, ie .: Media machining - media machining, media - workpieces, the media - the container wall, details - details, details - the walls of the container. However, due to the ratio of the number of pieces of media and the media surface active machining surfaces of the container walls are the most important interactions smoothing media abrasive machined details. Therefore important to choose the appropriate kind of smoothing media abrasive used, and therefore the type of material from which made the media machining. The size and type of the abrasive grains, their intensity packing and type of binding medium [13]. Undoubtedly very important to the final result is also the shape and dimensions of the smoothing abrasive media.

2. Type of Vibro-abrasive Machining Equipment

From a variety manufacturers equipment, we can distinguish such devices for the treatment of Vibratory finishing as: [3,6,14]

- Rotary vibrators (vibration polisher):
  - Without sieve separation (flat bottom)
  - With sieve separation (flat bottom)
  - With sieve separation (bottom ascending)
- Trough Vibrators
- Vibrator Circular -Long Radius
- Rotomatic Continuous Flow Installations
- Plunge Grinding Machine
- High Energy Disc System
- Surf Finisher
- Machines Sanding And Blasting
- Separators
- Electromagnetic Separator
- Vibrating Separator
- Equipment For The Treatment Of Waste Water Treatments Roto-Vibrational
- Vibrating Dryers
- Rotary Dryers

3. Parameters and Machining Capabilities with Loose Smoothing Media

The differences between the types of devices mainly amount to a kind of movement of the media for machining workpieces. It is connected directly to the machine kinematics, eg. Rotation, vibration, a combination of vibration and rotational motion, or linear motion in long units gutter[14]. In addition, the details may be mounted on special racks and then immersed in tumbler or may be freely movable therein along with the charge. Another difference is running dry processes or by using fluid processing aids and abrasive pastes. In each of the processes can freely control the time of treatment. Minimum time required depends on the type of material workpiece, the type of media, and the final results we want to achieve. In addition, depending on the device you can control the rotation speed and frequency of vibration or flow rate of the media.

4. Machine Overeview

To be able to compare of similarities, differences, or the mode of action individual machines to finishing it need to refer to the machines on the market. Each machine have a common for the processing characteristics, such as equipment and machinery in a suitable container, the use of a vibratory drive, we recommend fittings, etc. But also, these characteristics are elements that can be individually addressed for the machine. So it is necessary to briefly illustrate the most common vibrating machinery.

Among the machines for loose abrasive media finishing we can distinguished rotary such as: drum rotary, planetary, cascading rotary and vibratory. Drum rotary tumbler (Figure 1) makes rotational motion, causing lifted the media rotating of the drum walls. Media by movement of the drum is lifted to the chute line. After exceeding this line, we can observe fall of media particles onto the lower part of the drum. Subside chute layer is raised up again. This process is repeated cyclically [8]. Treatment of objects contained in the drum only takes place when there is a media chute.

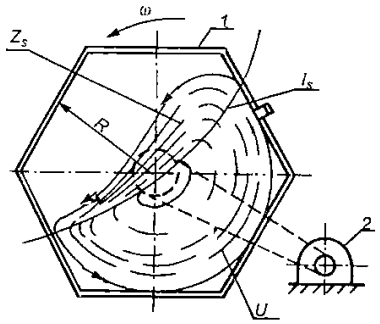

Fig. 1. Diagram and operation of a rotary drum:. 1 container, 2 driving assembly, l_s - chute line, U-lifted zone, R radius of the container, Zs- chute zone, ω- angular velocity [2]

Rotary vibratory can be divided into two groups depending on the oscillating motion in the plane or space. Rotary vibratory fitted with motion in the plane media, makes planar vibration in elliptical orbit. Rotary vibratory can be divided into two groups depending on the oscillating motion in the plane or space.[11] Rotary vibratory fitted with motion in the plane media, vibration doing planar elliptical orbit. The second group rotary makes a spiral movement of the spatial vibration. Diagram of rotary vibratory with planar vibrating and space vibrating are shown in Figure 2

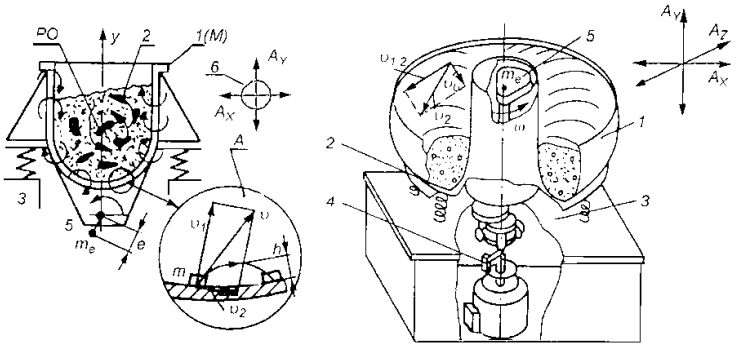

Fig. 2. Diagram of rotary kinematic vibration. 1- container, 2 batch, 3- housing, 4- power unit assembly, 5 - inertial vibrator [2].

Vibratory Tumbler is integrated to a driving unit vibrating container. Because of the way of induce vibrations we can distinguished different types of vibration tumblers: [4]

• an eccentric - Tumbler bowl is mounted eccentrically on the axis of a high speed motor;

• eccentric inertial - Tumbler bowl is rigidly connected to the motor, whose axis is eccentrically mounted member selected inertia, respectively;

• Electromagnetic - Tumbler bowl is rigidly connected to a ferromagnetic element located within the two electromagnets (sometimes three, in the case of a three-phase power or application invertor).

Rotary tumbler - Rotary drum polisher are similar like its design laboratory ball mills but differ from them essentially rotation speed of the drum and used for the processing of the charge. The ball mill speed is so high that heavy balls were lifted as high as possible by centrifugal force, and grew in a maximum potential energy necessary for an effective fragmentation of the material being ground. In tumbler polishing occurs due to the friction of small abrasive elements of the cleaned items and the speed should be chosen so as to ensure that only intensive mixing. Used in the appliance industry like construction of large size called rotary drum mixers. Experimental design for optimal rotation of the drum with a diameter of less than one meter [4]:

$$N = -0{,}08 \cdot D_{cm} + \frac{230}{D_{cm}} + 20 \quad . \tag{1}$$

where:

D_{cm} - diameter of the drum in centimeters.

For the most common drum with a diameter of between 15 cm and 30 cm is sufficiently accurate approximate formula [4]:

$$N = 40 - 0{,}5 \cdot D_{cm.} \quad (2)$$

To finishing parts with complex shapes (remove burrs, reducing roughness, rounded edges) and to clean the surface of various pollutants generated during the operation and after previous treatments (reduction of stress in the surface layer) is used to treat the Abrasive Flow Machining – AFM. Cutting efficacy is dependent on the physical and geometrical properties of the workpiece, the instrumentation used, and the processing time. AFM as compared to polishing or honing is faster in execution. It is designed for finishing surfaces, difficult to access.
This treatment consists of (Figure 3) by high pressure to cyclic pressing abrasive material (alumina, silicon carbide, boron carbide) along the surface of the workpiece in a unidirectional or bidirectional system. The recesses of edges and corners of the abrasive grains in the material vary from 1 to 3 mm resulting in plastic deformation, and thus formed by abrasive flow machining surface layer increases the fatigue strength of the treated section [9].

A complex direction of movement of the abrasive medium reflects the texture direction stereometric preferred surface of the workpiece. The effects of treatment significantly influenced the properties of pastes, which are produced on a matrix viscoelastic polymer type of poliborosiloxan [5].

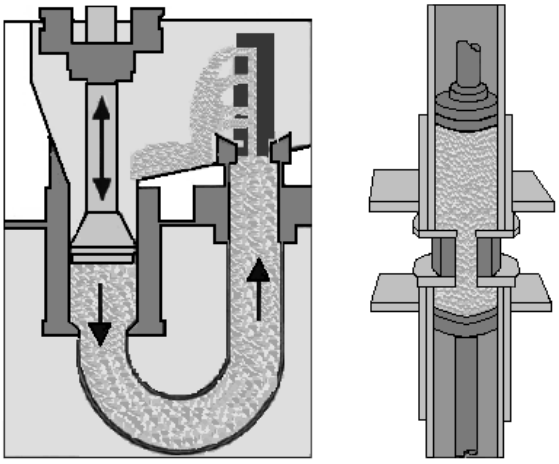

Fig. 3. Diagram of the AFM [17]

A variation of rotary tumblers are rotary inertia tumblers. This device is an assembly of two tumblers embedded perpendicular to the arm at the ends of the rotating beam. By centrifugal force increases the pressure abrasive on workpieces, which also allows several times to increase the rotation of the drum. Use of inertial tumbler can reduce the processing time of 20-50 times.

5. Example of Vibro-abrasive Machining.

Vibro-abrasive machining in Rotary container has been analyzed for samples made of chrome - nickel. This steel has high strength, durability and lack of susceptibility to chemical substances. Steel X5CrNi18-10 have a large resistance to radically changing the temperature, so there is no distortion under high temperature changes.[7]

Samples were prepared for treatment with chromium - nickel tube which had been cut into discs chainsaw with a diameter of 31mm and a width of 3 mm.

The study used a rotary vibratory machine SMR-D-25 to finishing, with a capacity of 25 liters. Parameters of the process was 2500 Hz frequency oscillation Tumbler, the use of ceramic CB 20T Series medium(22kg) and the addition of 250 ml of demineralized water. The duration of the process was 20, 40, 60, 80, 100 minutes.

Studies on the geometric structure of the surface treated vibro-abrasive samples were carried out using the device and Taylor Hobson Surtronic 25. The method of measuring the surface roughness of the device is a contact profilometry. Machine settings were as follows: measuring length was 4 mm, and cut -off filter (Gaussian filter) was 0.8 mm.

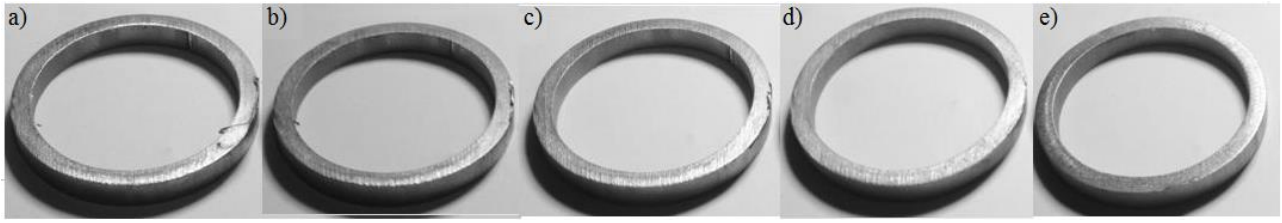

Fig. 4. Rings after vibratory finishing: a) 20 minutes, b) 40 min., C) 60 min., D) 80 min, e) 100 min.

In Table 2 are shown the results of measurement of roughness parameters depending on the treatment time [12]. For the analysis included three parameters: Ra - arithmetic average deviation profile Rz - surface roughness for 10 points [1], Rp - the height of the highest peak of the roughness profile.

	0 min	20 min	40 min	60 min	80 min	100 min
Ra, µm	7,62	7,81	7,47	7,02	5,98	5,34
Rz, µm	37,5	33,8	36,1	29,8	31,6	29,7
Rp, µm	19,3	14,1	16,4	14,9	15,3	12,8

Tab. 1. Results of measurements of Ra, Rz, Rp depending on the length of treatment vibratory

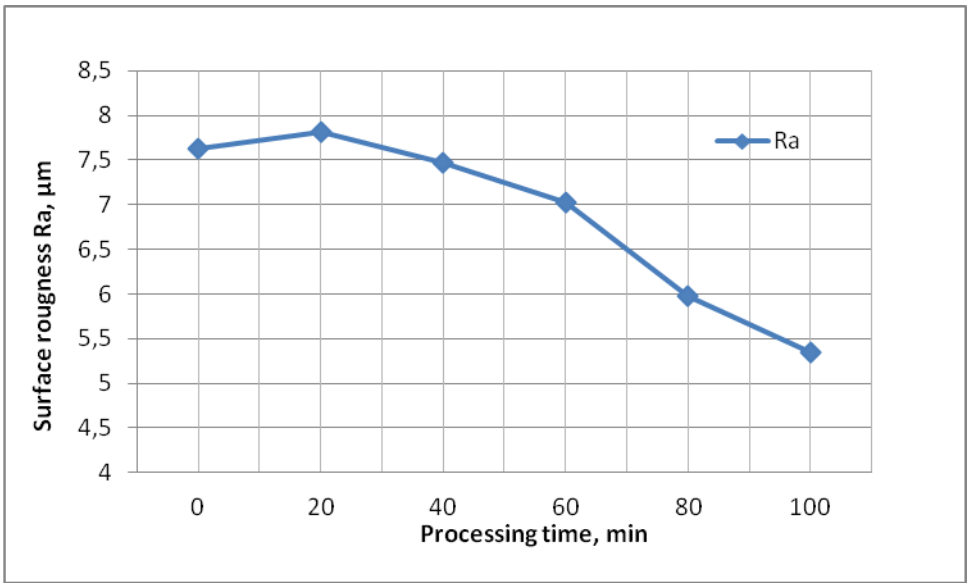

Fig. 5 Graph of average roughness Ra of the treatment time.

After the smoothing process and the measurement of surface roughness allows for the creation of Table 1. Figure 5 allows us to determine a beneficial effect on reducing the vibration treatment of the surface roughness. The samples at baseline had a mean roughness Ra of 7.62 .microns. With the increase in the duration of the treatment roughness decreases to 5.43 microns for the treatment time 100minut. In addition to the 100 minutes of treatment we have to improve parameter Rz by 30% from 7.62 microns to 5.34 microns.

6. Conclusion

To sum up treatment in rotating containers, vibrating or other are perfectly suited to machining complex parts. This allows for a significant reduction in the execution time detail and cost.

The use of processing small fittings in containers allows to remove burrs which was visible for the test discs.

To conclude vibro-abrasive machining have positive effect on the surface roughness. We achieve improve parameter Ra from 7,62 to 5,34 after 100 minutes finishing. In the case of higher requirements posed finishing surfaces be used longer machining times polishing.

Technology of rotary machining is good solution refinishing process conditions and high volume production. Rotary machining methods are an effective method and can fully replace the finish processes small details carried out by conventional methods of files, tape polishing and polishing.

References

[1] Adamczak S., Miko E., Cus Franc; Strojniski Vestnik, *A model of surface roughness constitution in the metal cutting process applying tools with defined stereometry*; -Journal of Mechanical Engineering; 2009, No 55

[2] Filipowski R., Marcinak M.: *Techniki obróbki mechanicznej i erozyjnej*, Oficyna Wydawnicza Politechniki Warszawskiej, Warszawa 2000

[3] http://marbad.pl/content/view/77/72/

[4] http://pl.wikipedia.org/wiki/Tumbler_%28obr%C3%B3bka_wibro%C5%9Bcierna%29

[5] http://www.designnews.pl

[6] http://www.rosler.com/products/vibratory-finishing/rotary-vibrators

[7] Konieczny M., Microstructural characterisation and mechanical response of laminated Ni-intermetallic composites synthesised using Ni sheets and Al foils, Materials Characterization 2012 Tom: 70, str. 117-124

[8] Nowicki B., Stefko A., Szulc S., „*Obróbka powierzchniowa*", Warszawa, PWN, 1970

[9] Oczoś Kazimierz, *Doskonalenie procesów obróbki ściernej*, „Mechanik" 2010, nr 10.

[10] Oryński F., Synajewski R., Bechciński G.,: *Fizyczny model szlifowania wibracyjnego płaszczyzn w kierunku poprzecznym*. Mechanik, 1,30-34, 2013.

[11] Rodziewicz M.: *Wygładzanie luźnym ścierniwem w pojemnikach*, Wyd. WNT, Warszawa 1968

[12] Spadło S. Dudek D., Młynarczyk P.: *Badania wygładzania wibrościernego powierzchni tulei mosiężnych*, IZTW, Kraków 2012. s. 285-293

[13]Spadło S., Pierzynowski R.,: *Zastosowanie obróbki wibrościernej do polerowania powierzchni elementów amunicji*. Machine Engineering Vol. 12 No 1, Electrical Machining Technology. Copyright Wydawnictwo Wrocławskiej Rady FSNT NOT Wrocław 2009. pp. 70-77

[14]Vibro Dry Experience PL, Rollwasch Italiana S.p.a

TRANSCOM 2015, 22-24 June 2015
University of Žilina, Žilina, Slovak Republic

Granular Flow Apparatus for Flowability Measurements of Granular Materials

[*]Marko Bek, [**]Joamin Gonzalez-Gutierrez, [**,***]Igor Emri
[*]Gorenje gospodinjski aparati, d.d., Velenje, Slovenia, marko.bek@fs.uni-lj.si
[**]University of Ljubljana, Faculty of Mechanical Engineering, Center for Experimental Mechanics, Ljubljana, Slovenia
[***]Institute for Sustainable Innovative Technologies, Ljubljana, Slovenia

Abstract. Flow of granular materials is a complex process, however, it is important to measure, because the flow of granular material during processing, handling and transportation strongly influences the quality of the final product and its cost. Flowability of granular materials depends on the characteristics of the material and on the conditions at which flow is occurring. Existing methods of measuring flowability of powders are described in this paper. A new methodology is introduced to measure flow of granular materials under pressure: Granular Flow Analyzer (GFA).

The concept of the GFA was tested by measuring five different materials with different average particle sizes. It was observed that as the particle size decreases so does its flowability. This is in agreement with powder literature. Therefore, it can be concluded that in general the GFA method can be a useful tool to measure flowability of powders under pressure. However further improvements are required to increase its sensitivity and accuracy.

Keywords: Flowability, GFA index, Granular materials, Granular flow, Metal powders.

1. Introduction

Granular materials are present in our everyday life whether as raw materials, intermediate or final products. For instance, we find them in the food industry from cereal grains to dehydrated milk; in the pharmaceutical industry different powders are blended and compressed to produce tablets; metal, polymeric or ceramic parts can be produced through different sintering techniques; moreover, granular materials are present in nature as sand and rocks. In all these examples, the flow of powder during processing, handling and transportation strongly influences the quality of the product and its cost.

A granular material is defined as a collection of discrete solid particles that are filled with an interstitial fluid, usually air. From this definition, one can notice that they cannot be classified either as solids or liquids leading to a complex behavior difficult to understand and predict [1]. In the literature, several terms are used interchangeably to describe granular materials, such as bulk solids, particulate solids and powder.

Within the world of granular materials, metal powders constitute an important part of the industry. In this context, one important topic of research nowadays is to study the flowability of powders in powder metallurgy because an increase in flowability represents an increase in the productivity of the overall process and a reduction in the cost of transportation of powders.

Flowability is defined as the ability of a powder to flow and results from the combination of material physical properties, which along with the equipment used for handling or processing governs how easy a granular material can flow. There are several techniques used for measuring flowability. Some of them require simple apparatuses while others use sophisticated setups. Simple traditional apparatuses as Hall-flowmeters and angle of repose devices provide a comparative analysis of which particular powder flows better with respect to another under certain conditions of

measurement [2, 3]. On the other hand, more sophisticated setups as shear cells and powder rheometers can provide more quantitative information as cohesion and angle of friction that influence the flowability of powders [4, 5]. Nevertheless since flowability changes according to the conditions in which flow is occurring, measuring devices more or less should resemble the handling or processing equipment in which the powder will be used [6]. Since most of the measuring techniques available in the market work under gravitational and shear flows, the present paper aims to introduce a new method of characterization where the driving force for granular flow is high pressure.

2. Granular Flow Analyzer

The Granular Flow Analyzer (GFA) is a novel apparatus to measure flowability of granular materials; it was developed at the Center for Experimental Mechanics (CEM), Faculty of Mechanical Engineering, University of Ljubljana.

Figure 1 shows schematically the main parts of the apparatus. The GFA is composed of a hollow cylinder that is loaded with granular material. Once the cylinder is filled with particles, a force is applied by means of a piston (Figure 1a); such force will induce a pressure inside the cylinder that at the same time induces elastic deformations in the axial and tangential directions of the external wall of the cylinder. The strain in the external face of the cylinder can be measured experimentally by means of a strain gages setup (Figure 1b). Finally Figure 1c shows the dimensions of the cylinder. One can notice that the powder inside the cylinder is subjected to a confined compression, Ma and Ravi-Chandar [7] developed an apparatus that works under the same principle, however such compression was applied to solid materials and their goal was to characterize the stress state of the inserted solid material.

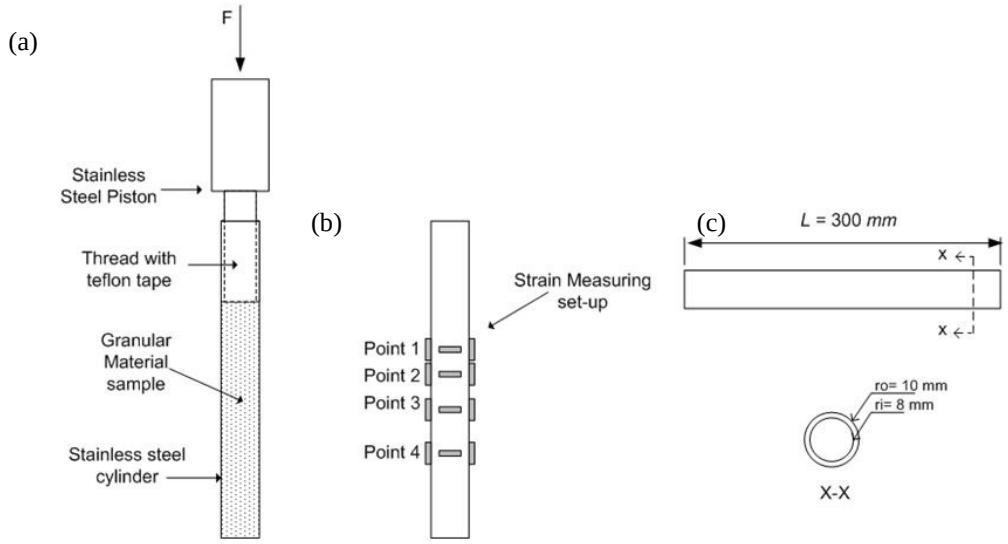

Fig. 1. Schematic of the GFA: a) cylinder filled with the granular material subjected to a compressive load, b) strain sages setup that is used in the apparatus to measure strain evolution along the length of the cylinder and c) dimensions of the cylinder

The goal of the GFA is to obtain the pressure profile along the length of the cylinder and to relate such profile with the flowability of granular materials. The concept of the GFA is valid because flowability is controlled by the transmission of forces through the granular material and the pressure distribution along the length of the cylinder is a measure of how force is transmitted from the piston to the powder and from the powder to the cylinder. In this context, one expects that depending on the flow properties of the powder, the pressure will be transmitted in a different way along the cylinder, thus allowing us to obtain a method of a steady-state flowability

characterization. By applying force with different rate GFA may be used for studying flowability of granular materials in dynamic-equilibrium as well.

2.1 Working principle of GFA

Even though pressure distribution in axial direction is the final result that we seek from the apparatus, what it is being measured experimentally are strains in the tangential (ε_θ) and axial (ε_z) directions at 4 points along the length of the cylinder. Figure 2 shows schematically the expected results for the strain evolution in a fluid, and in a granular material, respectively. In the case of the fluid (Figure 2a), it is known that the hydrostatic pressure is constant along the length of the cylinder and it is proportional to the tangential strain, whereas the axial strain occurs just due to Poison effect. In the case of the granular material (Figure 2b), it is expected that the pressure is maximum close to the piston where the force is applied, followed by a pressure drop. The pressure drop occurs because the force is distributed through layers of particles and formation of force chains that attenuate the pressure along the cylinder and increase the friction force between particles and inner wall of the cylinder [8, 9]. In this case, the tangential strain is maximum at the position where the force is applied and drops in the same way as pressure does, whilst the axial strain increases as the tangential decreases because the force is been transmitted to the wall as an axial load due to friction.

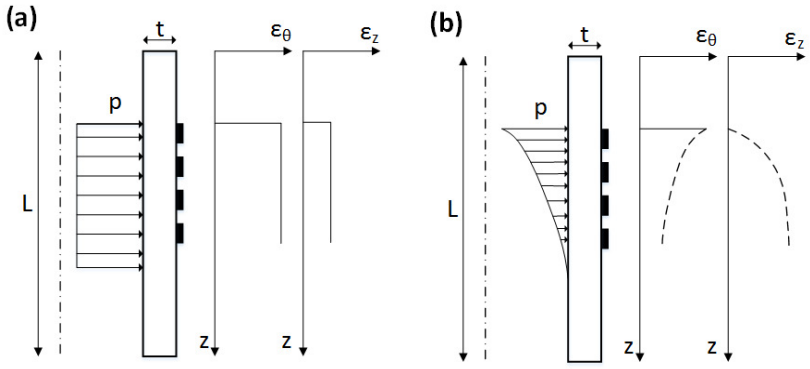

Fig. 2. Expected results for tangential and axial strain along the length of the cylinder of the GFA a) for a fluid and b) for a granular material

Figure 3 shows the measuring capabilities of the GFA, i.e. evolution of pressure along the cylinder at a fixed force. The apparatus allows us to apply forces from 50 to 6000 N.

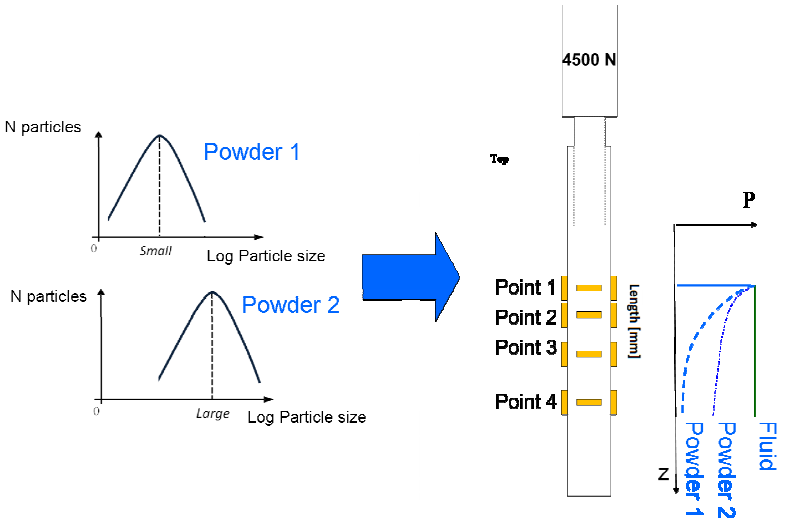

Fig 3. Measuring capabilities of the GFA apparatus

Figure 3 illustrates how one can compare the flowability of two granular materials in the GFA, taking as reference the pressure profile of a fluid which is constant along the length of the cylinder,

one can determine if certain powder has better or worse flowability by analyzing how steep is the pressure drop along the length of the cylinder, i.e. a granular material with less pressure drop will present better flowability (behavior closer to liquid) than another with very rapid pressure drop. Based on the literature, it is expected that powders with a smaller average particle size will have less flowability; for this reason Powder 1 in Figure 3 has a much faster pressure drop than Powder 2.

3. Experimental verification of the GFA apparatus

For the purpose of GFA apparatus demonstration five different materials provided by BASF (Germany) were analyzed: 4 stainless steel powders (Fraction I - 41,7µm; Fraction II – 20 µm; Fraction III - 23,7 µm; Fraction IV - 6,8 µm) and 1 type of polyoxymethylene (POM) pellets with average particle size 4000 µm.

3.1 Methodology of experiments

Before performing any test, one has to determine the right amount of sample to be used during the experiments, this is done by performing preliminary experiments that follow the same steps described, but with the only difference that the amount of powder is changed until satisfying the condition that the position of the piston after applying the desired load is 17 mm above the first measuring point (11 cm from the top of the cylinder). This distance of 17 mm was chosen in order to avoid the instability zone (where tangential strain overshoots as consequence of the close ends of the cylinder) that occurs close to the final position of the piston according to the FE analysis that was performed. However this distance can be deliberately changed by the operator in order to artificially increase the number of measuring points along the length of the cylinder, this is done for instance by putting together two curves (with three measuring points) measured at different distances from the piston in order to get the pressure profile curve composed of 6 points instead of 3. All materials were tested 10 times at two different positions (7 and 17 mm from the final position of the piston). The pressure profile of each test was obtained in three points. The two sets of tests at different piston distances that were performed per fraction were combined to form a pressure profile with 6 points along the length of the cylinder taking as reference point the position of the piston (7, 17, 28, 38, 58 and 68 mm from the position of the piston). The force that was applied during the tests was 4428 ± 25 N corresponding to a maximum pressure Po = 22.025 ± 0.125 MPa.

With the aim of obtaining quantitative information from the pressure profile a new parameter called "GFA index" was introduced. The "GFA index" is simply the area of the pressure profile of the granular material ($A_{granular}$) divided by the area of the pressure profile corresponding to a theoretical fluid (A_{fluid}):

$$GFA_{index} = \frac{A_{granular}}{A_{fluid}} \tag{13}$$

The area of the curves is calculated by the trapezoidal rule; this is shown in Figure 8 where the total area of the curve corresponds to the sum of 6 trapezoids that are formed from the number of measuring points used to calculate the pressure profile. By increasing the number of measured points determination of the GFA index will be improved.

5. Results and discussion

Following the methodology described in section 3, the pressure profiles of all powders were measured. Pressure was normalized by dividing the absolute value of pressure over the maximum pressure in the system, which corresponds to the force recorded in the load cell over the cross section area of the cylinder. The maximum pressure varied slightly from test to test in the range of 21.9 to 22.2 MPa. Therefore the calculated pressure was normalized by the applied pressure to take into account the small deviation seen from one measurement to the next.

Figure 9a shows the "GFA index" for five granular materials relating it to the average particle size. Figure 9b shows the "GFA index" for four (metal) granular materials. As mentioned, experiments for particular granular materials were repeated 10 times from where average values as well as standard deviation of normalized pressure were calculated for each distance as shown in figure 8. Using trapezoidal rule average area of granular material and average area corresponding to standard deviations obtained from the previous step, were calculated. In final step GFA index was calculated for all particle sizes and results are presented in figure 9.

From the results one can observe that fraction IV presents the lowest "GFA index" which indicates that it has the lowest flowability, this agrees with [8] and [9] that state that as particle size decreases cohesion increases and thus flowability is reduced. Fractions III and II present almost the same GFA index and fraction I has the highest "GFA index" indicating the best flowability among the metal powders. Despite the big error bars in POM, the results evidence that POM has much better flowability with respect to metal powders because of the lower friction between the POM pellets.

We can observe that the value of the "GFA index" of POM is approximately 3 times higher than the value of the "GFA index" in the metal powders, however, it is important to notice that the difference in average particle size is of about 4 orders of magnitude (Table 2).

In short, one can say that a trend of decreasing flowability as particle size decreases is observed. However, the results between the flowability of metal powders are not significantly different from one another. This indicates that even though the expected trend is achieved further improvements are needed in the apparatus and the measuring procedure.

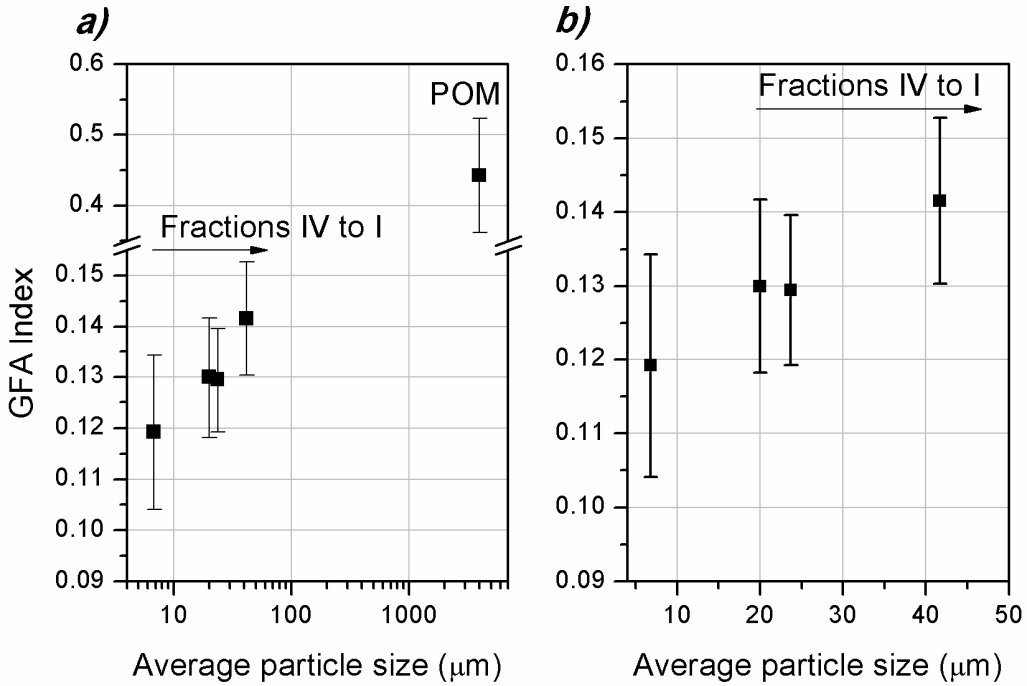

Fig. 9. a) GFA index for metal powders and POM, b) GFA index for metal powders (close up look)

6. Conclusions

A new apparatus to assess the flowability of granular materials under pressure is presented here: the GFA. It consists of a hollow cylinder where granular materials can be pressurized by means of a piston; the pressure drop inside the cylinder is estimated by measuring the strain along the length of the cylinder. A new parameter, GFA-index, used to assess the flowability of different granular materials has also been introduced, which is the ratio of the area under the measured pressure profile along the length of the cylinder over the area of the theoretical hydrostatic pressure along the length of the cylinder.

The GFA prototype was utilized to test five fractions of stainless steel 316LW and granules of polyoxymethylene of different average particle size in order to demonstrate the concept and capabilities of the apparatus. Using the GFA, it was observed that as the particle size increases, the flowability measured as the GFA index also increases. This observation is in line with flowabilty measurements provided in the literature. However, for metal powders the results were not significantly different, which suggests that further work is required to improve the accuracy of the GFA.

Important recommendations towards the accuracy improvement of the GFA include: the standardization of conditions during sample preparation (such as powder filling and tapping of the cylinder); the implementation of a sensor to control the displacement of the piston during the test; and measure the strain at the outer face with another approach that allows us to obtain the complete pressure profile along the cylinder instead of just in three positions or four position, a potential alternative is to use an optical method, such as speckle interferometry.

References

[1] JAEGER, H. M., and NAGEL, S. R. (1992). Physics of the granular state. *Sciencemag* , 1523-1531, Vol. 255.

[2] VLACHOS, N., & CHANG, I. T. (2010). Investigation of flow properties of metal powders from narrow particle size distribution to polydisperse mixtures through an improved Hall-flowmeter. *Powder Technology 205* , 71-80.

[3] GELDART, D., ABDULAH, E. C., HASSANPOUR, A., NWOKE, L. C., & WOUTERS, I. (2006). Characterization of powder flowability using measurement of angle of repose. *China Particuology 4* , 104-107

[4] SHINOHARA, K., & GOLMAN, B. (2002). Dynamic shear properties of particle mixture by rotational shear test. *Powder Technology 122* , 255-258.

[5] FREEMAN, R. (2007). Measuring the flow properties of consolidated, conditioned and aetated powders - A comparative study using a powder rheometer and a rotational shear cell. *Powder Technology 174* , 25-33

[6] PRESCOTT, J. K., and BARNUM, R. A. (2000). On Powder Flowability. *Pharmaceutical Technology* , 60-86.

[7] MA, Z., and RAVI-CHANDAR, K. (2000). Confined Compression: A Stable Homogeneous Deformation for Constitutive Characterization. *Experimental Mechanics* Vol. 40, No. 1 , 39-45.

[8] CAMPBELL, C. S. (2005). Granular material flows - An overview. *Powder Technology* 162, 209-229.

[9] RAO, K. K., and NOTT, P. R. (2008). An Introduction to Granular Flow. New York: Cambridge University Press.

TRANSCOM 2015, 22-24 June 2015
University of Žilina, Žilina, Slovak Republic

A Study of Plasma Sprayed Hap Coatings Using the EDX and Raman Methods

[*]Radosław Belka, [**]Szymon Kowalski, [**]Wojciech Żórawski, [*]Małgorzata Suchańska
[*] The Faculty of Electrical Engineering, Automatic Control and Computer Science, [**]The Faculty of Mechatronics and Mechanical Engineering, Department of Terotechnology, Kielce University of Technology, al. Tysiąclecia Państwa Polskiego 7, 25-314 Kielce, Poland,
r.belka@tu.kielce.pl, skowalski@tu.kielce.pl, ktrwz@tu.kielce.pl, m.suchanska@tu.kielce.pl

Abstract. In this paper the EDX and Raman studies of plasma-sprayed HAp coatings are presented. Parameters of characteristic vibrational bands of phosphate and hydroxyl functional group have been compared for powder feedstock and final coatings. Based on the EDX and Raman studies degenerative effects of the deposition process for the presence hydroxyl function group and symmetry of phosphate groups has been discussed.

Keywords: hydroxyapatite, plasma spraying, coatings, EDX, Raman spectroscopy.

1. Introduction

Hydroxyapatite (HAp) is a nonorganic material of the bones of the vertebrate responsible for their mechanical durability. In human bones it occupies 60-80 % of the volume depending on a number of factors. Synthetic HAp is valued in bone endoprosthetic to its high biocompatibility. It is widely used to fill cavities of bone and as the coating of bone implants to increase their biocompatibility and adhesion to bone surface [1-4].

HAp occurring in bones is continuously absorbed by osteoclasts cells and excreted by osteoblasts. This process is called resorptin. Synthetic HAp can also be resorbed if certain conditions are satisfied. This means the HAp is not biocompatible only but also bioactive material.

This paper presents basic information about HAp and its crystallographic and molecular structure. The sample of plasma sprayed HAp on Ti6A4V was also prepared and analyzed by EDX and Raman methods.

2. HAp - general information

The general formula of HAp is usually written as $Ca_{10}(PO_4)_6(OH)_2$ [4], rarely $3Ca_3(PO_4)_2 \cdot Ca(OH)_2$) or $Ca_5(PO_4)_3 \cdot OH$ [5-6]. Hydroxyapatite has a hexagonal crystal structure with the space group $P6_3/m$, and a unit cell of 44 atoms. The main dimensions of the cell are a = 9.41 Å and c = 6.88 Å; [3]. The tetrahedral phosphate anion (PO_4^{3-}) has a strong covalent character and acts as a robust group in the interaction with the surroundings. Ca^{2+} cations occupy two distinct crystal sites, Ca(I) and Ca(II): thus the formula unit can be rewritten as $Ca(I)_4Ca(II)_6(PO_4)_6(OH)_2$. Ca(I) is 9-fold coordinated to oxygen ions from six neighboring phosphate groups, while Ca(II) is 7-fold coordinated with oxygen ions, six from phosphate groups and one from an OH. Ca(I) lies along the columns parallel to the crystal c-axis, with two Ca(I) ions in each column. Ca(II) cations are distributed in two triangular bases, twisted 60° relative to each other with hydroxyl O in the center, forming a hexagonal channel with the OH array located in the center and parallel to the channel (also the lattice c-axis).

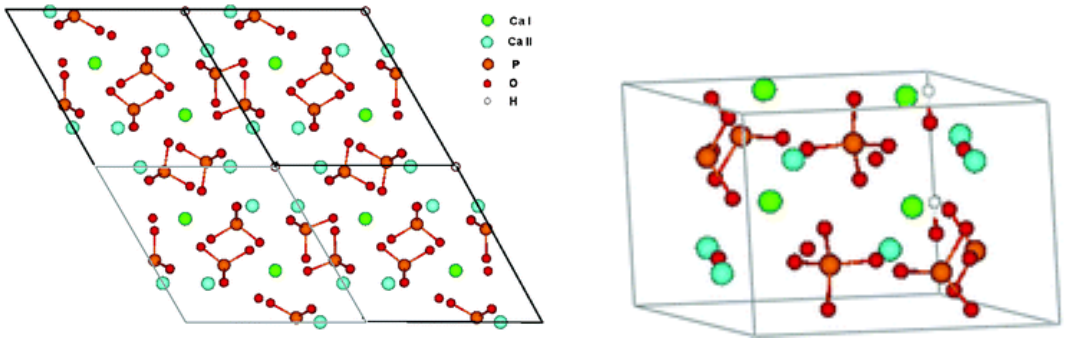

Fig. 1. Structure of hydroxyapatite seen in top view along the *c*-axis (left) and looking along *a* and *b*-axis (right) [3].

In table 1 the Raman vibrational modes of PO_4 tetrahedra of HAp and the other calcium phosphate salts (OCP and TCP) are presented.

Mode	Symmetry	Observed bands [cm^{-1}]		
		HAp	OCP	TCP
ν_1	A_1	961 (vs)	958 (vs)	970 (vs)
ν_2	E	447 (m), 433 (w)	449 (m), 429 (m)	460 (w), 439 (m)
ν_3	T_2	1076 (w), 1054 (w) 1046 (m), 1030 (w)	1080 (w), 1049 (vw)	1074 (w), 1046 (m)
ν_4	T_2	610 (w), 594 (m), 582 (w)	610 (m), 593 (m), 582 (m)	624 (w), 612 (m), 599 (w), 578 (w)

vs:very strong, m: medium, w: weak, vw: very weak

Table 1. Raman shifts observed and assigned to HAp and the other calcium phosphate salts [4].

3. Experimental

The coatings were deposited on flat Ti6A4V (6% Al, 4% V) samples with dimensions of 15 mm x 15mm x 1 mm. Before plasma spraying all of the samples were degreased and grit blasted with electrocorundum EB-12 at a pressure of 0.5 MPa.

Sulzer Metco XPT-D-703 hydroxyapatite powder feedstock was applied in this study. Plasma spraying was performed by means of a Plancer PN-120 plasma spraying system with a Thermal Miller 1264 powder feeder. The plasma spraying parameters were set as following: current - 600 A, voltage - 60 V, plasma gas pressure - 0.7 MPa, spraying distance - 100 mm, powder feeding rate - 60 g/min were applied to deposit coatings [10]. After the deposition thickness of the coatings was around 0.3 mm.

The HAp powder (I) and the HAp coating (II) deposited on the Ti alloy substrate by plasma spraying [5] were studied using the EDX (Energy-dispersive X-ray spectroscopy - Jaol SEM microscope) and Raman spectroscopy methods. The Raman studies was performed using an automated micro-Raman Nicolet Almega XR spectrometer (Thermo Scientific) with the 532nm excitation. The spectra were obtained in the micro mode in the low (200 - 4000cm^{-1} range, 6 cm^{-1} resolution) and the high (range 200 – 1200cm^{-1}, 2cm^{-1} resolution) resolution modes. The obtained spectra were processed using Nicolet Omnic 8 software to remove the luminescent background.

4. Results and Discussion

4.1. SEM and EDX study

Figure 2 presents an EDX spectrum and SEM images of the deposited HAp coating (II). The identification of chemical compounds and stoichiometric ratio were done based on energy dispersive X-ray microanalysis – Table 2.

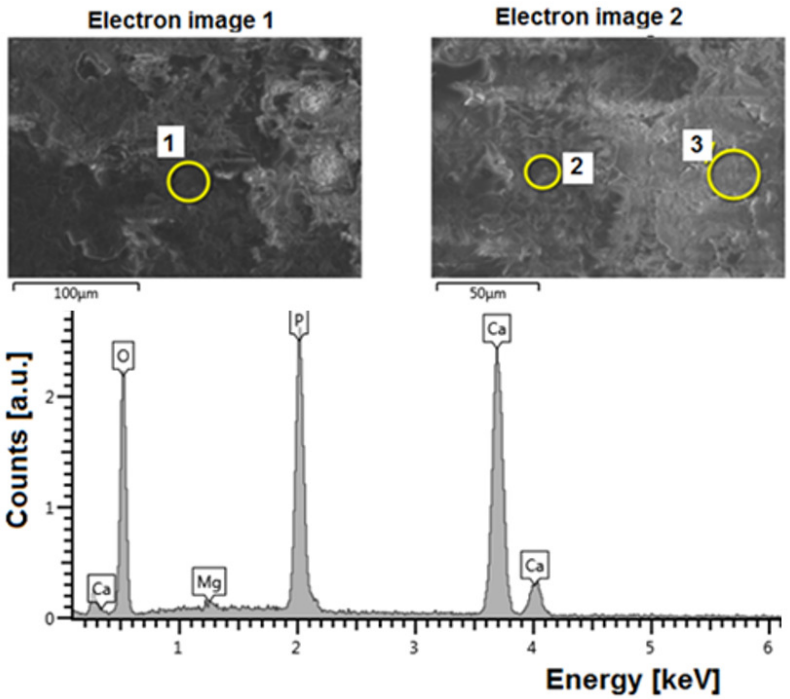

Fig.2. EDX spectrum (1) of HAp coating (II) deposited on Ti6A4V substrate

Spectrum Label	Atomic percentage			Ca/P ratio
	Mg	P	Ca	
Spectrum 1	0.33	11.06	17.06	1.542
Spectrum 2	0.26	9.24	16.66	1.803
Spectrum 3	0.19	9.67	16.68	1.725
Average	-	-	-	1.690
Theoretical	0	-	-	1.667

Table 2. Atomic percentage in investigated HAp coating (II).

The X-ray microanalysis shows that the molar Ca/P ratio is clearly not uniform (fluctuations of approx. 1.54-1.8), but the average value is close to the theoretical value for HAp. The presence of calcium phosphate $Ca_3(PO_4)_2$ (tricalcium phosphate - TCP) [2] cannot be excluded. It is not possible to determinate without additional research if structure of HAp is stoichiometric. However results indicate that the structure is close to non-stoichiometric due to big fluctuation Ca/P ratio which is characteristic of ns-HAp (1.5-2.0) [9].

Small fractions (1-2%) of Mg suggest the presence of magnesium phosphate [7]. The Mg admixture probably leads to a decrease in the grain size, which on the other hand causes a reduction of the anisotropic properties. While spraying Ca^{2+} ions can be substituted by Mg^{2+} [9].

4.2. Raman study

In figure 3 the Raman spectra of HAp powder (I) and plasma-spraying deposited HAp coating (II) were presented. The four characteristic modes for PO_4 tetrahedron [4] are clearly observed.

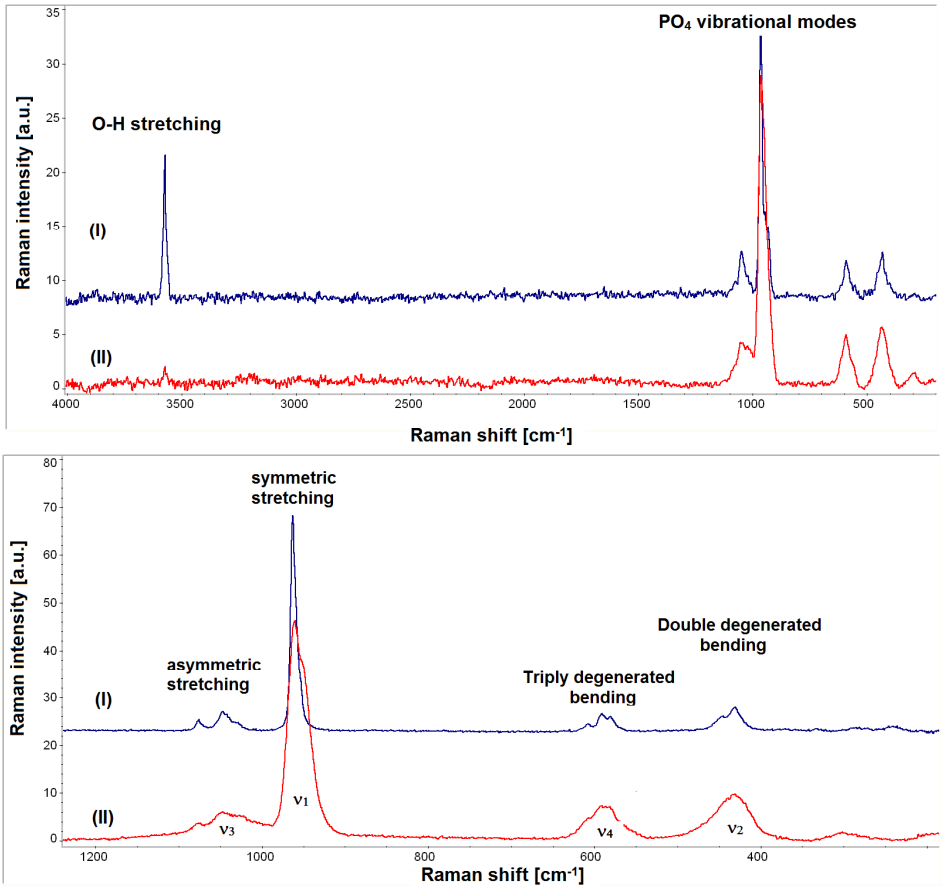

Fig 3. Raman spectra of HAp powder (I) and plasma-spraying deposited layer (II) in low (top) and high (bottom) resolution modes

In Raman spectra of HAp powder (I) the four basic vibrational modes of PO_4 group (denoted as $\nu_{1\text{-}4}$) were observed in region of 400 – 1100cm^{-1} and also strong O-H vibrational mode exists at 3573cm^{-1}. In deposited coating (II) O-H mode are distinctly attenuated and $\nu_{1\text{-}4}$ modes are broadened. It is connected, probably, in disordering of crystalline structure of HAp during deposition process to non-stoichiometric.

mod	Band no	Powder (I)			Deposited coating (II)		
		Pos [cm^{-1}]	Int	FWHM	Pos [cm^{-1}]	Int	FWHM
ν1	Band 1	958.7	18.27	11.20	949.5	29.72	23.32
	Band 2	963.2	33.62	5.60	963.1	30.93	15.45
ν3	Band 3	1030.2	1.44	9.50	1021.7	3.12	27.23
	Band 4	1041.6	2.06	9.41	1039.2	1.90	14.31
	Band 5	1049.0	3.26	10.48	1052.0	3.49	19.07
	Band 6	1076.0	2.09	9.01	1076.7	1.88	13.80
ν2	Band 7	430.3	4.58	17.31	429.0	9.01	43.10
	Band 8	448.2	2.18	17.87	454.3	2.26	42.81
ν4	Band 9	580.2	2.81	12.61	565.5	1.69	27.04
	Band 10	591.4	3.00	9.57	587.3	5.93	26.33
	Band 11	607.8	1.41	11.49	609.9	3.40	29.86

Table 3. Comparison of Raman band parameters of HAp powder (I) and deposited coating (II).

In the deconvolution process of the spectra the 2 component functions to approximate a non-degenerated ν_1 mode were used as a result of the presence of band shoulder and 4 functions to approximate ν_3 module. In results, total of 11 bands were isolated for both powder HAp (I) and

HAp coating (II). This demonstrates the breaking of ideal T_d symmetry of phosphate groups both in powder and deposited HAp.

In table 3 values of Raman band parameters of HAp powder (I) and deposited coating (II) are presented. There was a distinct widening (2-3 times) of bandwidths in HAp coating (II) as compared with the powder (I) - it may indicate an increase of structure disordering (amorphization). The ν_1 mode was approximated by two basis functions. As a result, the position of the band no 2, was located at position approx. 963cm^{-1} (both the powder and the layer), so it was approx. 2 cm^{-1} higher than in the literature [4]. However, the average position of maximum of the mode were exactly at 961cm^{-1}, which is characteristic for HAp, no other form of calcium phosphate.

In the case of HAp powder, band 1 can be treated as shoulder (differing positions less than 5 cm^{-1}). However, in the case of HAp layer positions of the 1 and 2 bands differ at approx. 14 cm^{-1}. Band 1 will may be characteristic of calcium phosphate (TCP).

5. Conclusion

The averaged Ca/P ratio and positions of vibration modes of $(PO_4)^{3-}$ phosphate group in the Raman indicate the hydroxyapatite (HAp) as material deposited on the substrate during a plasma-spraying process. Nevertheless, some parameters (FWHM and intensities) of characteristic bands in Raman spectra of powder and deposited HAp have been clear different. It can be concluded, deposition process influents on crystal disordering and homogeneity of HAp.

Spatial heterogeneity of Ca/P ratio and the attenuation (absence) of OH bending mode in Raman spectra may indicate formation of other molecules, e.g. calcium phosphate (TCP, $Ca_3(PO_4)_2$). We can suppose that structure is non-stoichiometric or partially anisotropic.

We found that hydroxyapatite was modified by magnesium. It is justified by dust destination.

Acknowledgement

This research was performed using equipment co-founded by the European Regional Development Fund within the Innovative Economy Operational Programme 2007-2013 (No POIG 02.02.00-26-023/08-00).

References

[1] SCHNETTLER R., KNÖSS PD, HEISS C, STAHL JP, MEYER C, KILIAN O, WENISCH S, ALT V., *Enhancement of bone formation in hydroxyapatite implants by rhBMP-2 coating* J Biomed Mater Res B Appl Biomater., 2009 90(1):75.

[2] LIAO S. L., KAO S. C. S., TSENG J.H.S. L-K LIN L., *Surgical coverage of exposed hydroxyapatite implant with retroauricular myoperiosteal graft*, Br J Ophthalmol.; 2005 89(1): 92–95.

[3] YIN SH., ELLIS D.E., *First-principles investigations of Ti-substituted hydroxyapatite electronic structure*, Phys. Chem. Chem. Phys. 2010 12: 156.

[4] KOUTSOPOULOS S., *Synthesis and characterization of hydroxyapatite crystals: A review study on the analytical methods*, J Biomed Mater Res. 2002 62(4):600.

[5] SHAMRAI V., KARPIKHIN A., SIROTINKIN V., KALITA V., KOMLEV D., *Enhanced Adhesion Properties, Structure and Sintering Mechanism of Hydroxyapatite Coatings Obtained by Plasma Jet Deposition*, Plasma Chemistry And Plasma Processing, 2014 35 (1)

[6] JONDO Y., HYUNGWON S., EKAVIANTY P., YOUNG-HWAN H., SUKYOUNG K., BYUNG-NAM K., *Characterisation of transparent hydroxyapatite nanoceramics prepared by spark plasma sintering*, Advances in Applied Ceramics: Structural, Functional & Bioceramics. 2014, 113 (2): 67-72.

[7] FROST R.L., LÓPEZ A., XI Y., GRANJA A., SCHOLZ R., FERNANDES LIMA R.M., *Vibrational spectroscopy of the phosphate mineral kovdorskite – $Mg_2PO_4(OH)\cdot 3H_2O$*, Spectrochimica Acta Part A: Molecular and Biomolecular Spectroscopy 2013 114:309

[8] TSUI Y.C., DOYLE C., CLYNE T.W., *Plasma sprayed hydroxyapatite coatings on titanium substrates Part 1: Mechanical properties and residual stress levels*, Biomaterials Nov 1998; 19 (22): 2015

[9] ZIMA A., *Wpływ dodatków modyfikujących na właściwości hydroksyapatytowych wielofunkcyjnych tworzyw implantacyjnych przeznaczonych nanośniki leków.* Rozprawa doktorska, Akademia Górniczo-Hutnicza, Kraków 2007.

[10] ADAMCZAK S., JANECKI D., STĘPIEŃ K., Measurement, 2011 44 (1): 164.

[11] BĄKOWSKI A., RADZISZEWSKI L., *Evaluation of the uncertainty of selected parameters that characterise diesel engine work,* Applied Mechanics and Materials Vol. 712 (2015) pp 69-74,

TRANSCOM 2015, 22-24 June 2015
University of Žilina, Žilina, Slovak Republic

Investigation of Behavior of Metaphosphate Glass for the $Ba(PO_3)_2$ Composition by Means of Dielectric Relaxation Spectroscopy

[*]Jana Bírešová, [*]Peter Hockicko
[*]University of Žilina, Faculty of Electrical Engineering, Department of Physics, Univerzitná 1, 01026 Žilina, Slovakia
biresova@fyzika.uniza.sk, hockicko@fyzika.uniza.sk

Abstract. The sample of metaphosphate glass $Ba(PO_3)_2$ was investigated using the electrical conductivity measurements in the range of frequency 10 Hz- 2 MHz and over range of temperatures 652K -750K. The aim of this work is investigation of properties as dielectric loss and complex permittivity, which allow us study of the fundamental properties and relaxation mechanism of the investigated material. Dielectric relaxation is explored through real and imaginary impedance measurements. Also, the Arrhenius activation energy calculated from dc measurements and loss tangent is found, characterize hopping processes and transport mechanism of this ion conducting glass.

Keywords: metaphosphate glass, dielectric constant, loss tangent, electrical conductivity

1. Introduction

Presently, phosphate glasses have been extensively investigated due to their diverse properties, which predicted them for using in many kind of application. Phosphate glasses have high transparency for UV light because of the thermo-optical constants are close to zero, the refractive index is nearly independent on temperature and they have the low dispersion that determines them for using in optical application as optical system, lasers, molded optical elements [1-5, 12-15].

In a development of low-temperature melting and high-expansion phosphate glasses can be used as low temperature elements, anticorrosive pigments, materials for immobilization of nuclear waste, dispersant for clay processing and sequestering agent for hard water treatments. Also, phosphate glasses are demanded for devices like solid electrolyte, fuel cells, rechargeable Li-ion batteries and batteries in hearth pacemaker [2-10].

In spite of their advantages, in manufacturing process is still the lack of industrial application for the phosphate glasses [13] due to their low chemical durability. Considering of all the pros and cons, the phosphate glasses are still in the interest of researchers, who try to improve their chemical properties with an addition of modifier and better understand their structural properties.

The basic unit of phosphate glass networks are the phosphate anion tetrahedra that cause from the formation of sp^3 hybrid orbital by the phosphorus outer electrons. The phosphate anion tetrahedral anions are named according to a Q^i scheme, where i denotes the number of bridging oxygen in a PO_4 unit. In vitreous phosphorus pentoxide, the network is formed by PO_4 unit that are three-fold linked by bridging oxygen atoms and one terminal oxygen is double-bounded with the P atom. The result of addition of metal oxide into the PO_4 network is depolymerisation by converting bridging oxygen atoms to non-bridging oxygen atoms. The bound between P-O-P is broken and is created Q^2 groups.

This paper deals with $Ba(PO_3)_2$ which is the species within group of investigated metaphosphate glasses. In metaphosphate composition is ratio of O/P = 3, the structure is formed of infinity long chains and with/without rings by Q^2 units [6, 8, 12].

The electrical properties of phosphate glasses have been widely studied [8, 10, 11, 15]. In this paper we are aiming for dielectric properties of the $Ba(PO_3)_2$ metaphosphate glass, as dc

conductivity, dielectric constant, loss factor *tg(δ)* and the complex permittivity $\varepsilon^* = \varepsilon'(\omega) - j\varepsilon''(\omega)$ where ε' is real component and ε'' is imaginary component. These electrical parameters provide information about the structural properties of materials and also reveal the transport and relaxation processes.

2. Experimental

The sample of metaphosphate glass of the alkaline earth with composition 50MO.50 P_2O_5 (M = Ba) was prepared using the material $BaCO_3$ and (NH_4) $2HPO_4$ (Merck, 99%), and the components were mixed to temperature 450 °C in an electric furnace, then melted and mixed in the propane atmosphere for 2 h at the temperature ranging from 900 °C to 1200 °C. The sample was prepared within the series of metaphosphate glasses at Department Ceramics and Glass Institute in Spain.

The electrical conductivity measurements were done using LCR Meter OT 7600 Plus at frequencies in the range 10 Hz to 2 MHz (200 measurements for each of the range of temperature in steady state) and over range of temperatures 652K -750K. We were performed measurements of chosen temperatures (with time per measurements: 5 min and time per stabilization of measured system: 20 min).

The prepared sample has the parameters: thickness h = 2.47 mm and diameter d = 7.1 mm. End of faces were polished to be flat and parallel.

3. Theoretical description

In the presence of electrical field, a conductivity material is as a proof an increase in electrical conductivity with rising temperature. The dc conductivity varies as a function of temperature in accordance with the Arrhenius equation

$$\sigma_{DC} = \sigma_0 \exp\left(\frac{-E_a^{DC}}{k_B T}\right). \quad (1)$$

The activation energy of the conduction process can be determined from experimental measurements from Nyquist plot (imaginary part of complex impedance Z" versus real part Z'). The complex impedance of material is given by equation

$$Z^* = Z' - jZ''. \quad (2)$$

The dependence of imaginary part and real part of complex impedance allow us calculating electrical conductivities of investigated materials according following relation

$$\sigma = \frac{h}{RS}, \quad (3)$$

where *h* is thickness of sample, *S* is area of sample, *R* value of resistance (the value is marked in Fig. 1).

By insertion of the dielectric medium between the plates of capacitor the increase in charge storing capacity is observed, that is represented by dielectric constant. In many engineering applications, the dielectric constant gives a characteristic of the given material [4, 7, 10], is regarded as a material constant.

After applied electric field the some relaxation time occurs that is reciprocal value to relaxation frequency. The dipole cannot keep shifting orientation direction when the frequency of the applied field exceeds its relaxation frequency and, therefore, it will not make a contribution to the dielectric constant. The dielectric constant is virtually frequency independent (in range Hz - MHz), these

provide an indication of this frequency dependence at low end of the frequency spectrum. Separation into imaginary and real part allows us study of the fundamental properties of the investigated material:

$$\varepsilon^{*}(\omega) = \varepsilon^{'}(\omega) - j\varepsilon^{''}(\omega). \quad (4)$$

Dielectric loss characterizes the absorption of the electric energy by a dielectric material that is subjected to an alternating electric field. This loss may be important at electric field frequencies in the vicinity of the relaxation frequency for specification of material.

The loss tangent is defined by relation:

$$\tan\delta(\omega) = \frac{\varepsilon^{''}(\omega)}{\varepsilon^{'}(\omega)}. \quad (5)$$

The activation energy can be estimated from the plots of *log f* vs. *1000/T* where f_{max} can be found using the isochronal peaks of *tan δ(ω,T)*.

These plots are straight lines in accordance with Arrhenius equation:

$$f = f_0 \exp(-E_a^{tg\delta(\omega)}/(k_B T_{\max})). \quad (6)$$

Where *f* is the frequency of the applied electrical field, f_0 is the pre-exponential factor and $E_a^{tg\delta(\omega)}$ is the activation energy associated to the dielectric loss.

4. Results and discussion

In this paper we deal with electrical properties of the $Ba(PO_3)_2$ methaphosphate glass, which we obtain as response of dielectric to an electric field, and they are characterized according previous theoretical principles.

From Nyquist plot in Fig. 1, is taken the value of resistance and according (3) is calculating electrical conductivities of investigated materials for range of selected temperatures. Fig. 2 is shown the obtained data of conductivities using for the linear fit in accordance with (1). From Fig. 2 is estimated the value of activation energy for the conduction process, E_{a1}=1.05 eV.

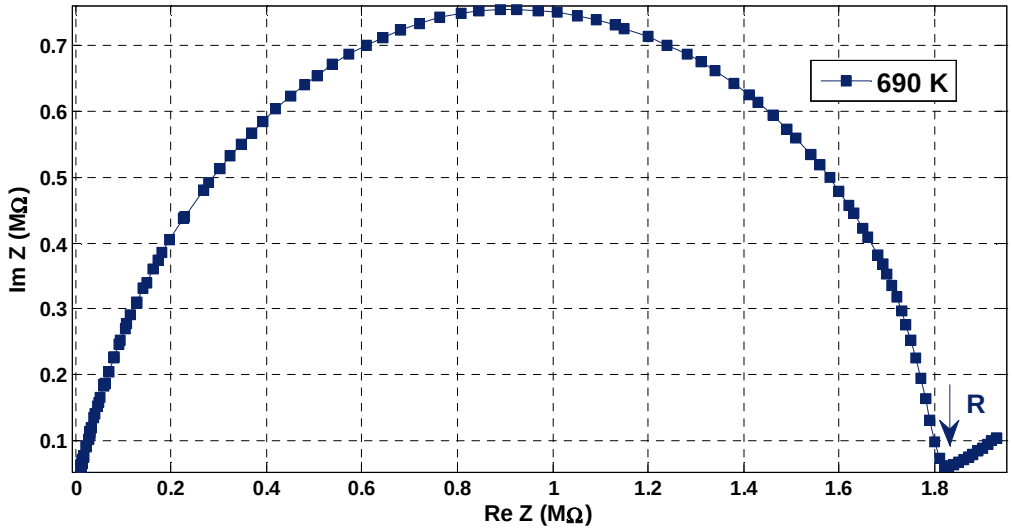

Fig. 1 Nyquist plot, the dependence of real and imaginary measurements for $Ba(PO_3)_2$ at selected temperature 690K.

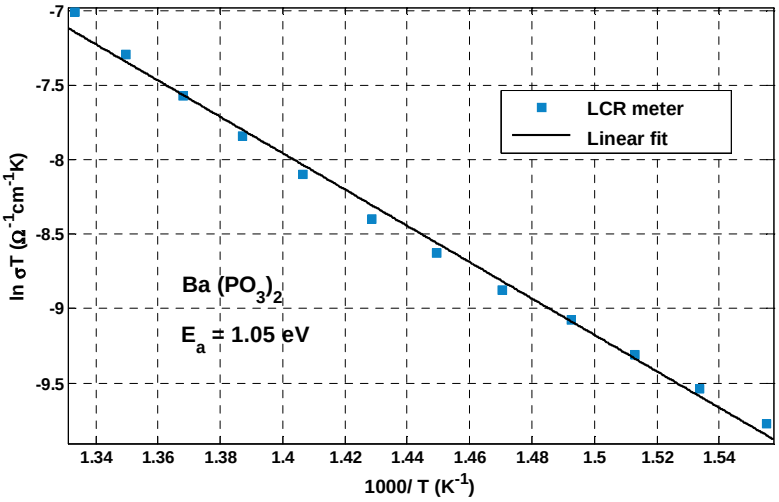

Fig. 2. The temperature dependences of dc conductivity calculated from Nyquist diagrams (Fig. 1), straight line correspond to the fit of the Arrhenius equation (1) to the experimental data.

In Fig. 3 is shown similar tendency of dielectric permittivity like authors are mentioned in [4]. The frequency dependence of the real part of the complex permittivity for $Ba(PO_3)_2$ is shown in Fig. 3a). The frequency rises, the immobile and mobile ions cannot oscillate as quickly as the applied field, dispersion takes place and ε_r declines to a constant value $\varepsilon_{r\infty}$, which probably results from polarization process. Also, the high value of ε_r in low frequency reached, that is explain [4] like result to a net polarization of the ionic medium.

The part b) in Fig. 3 shows the frequency dependence of the imaginary part of the complex permittivity for $Ba(PO_3)_2$ glass, the dependence is associated with damping effect [4].

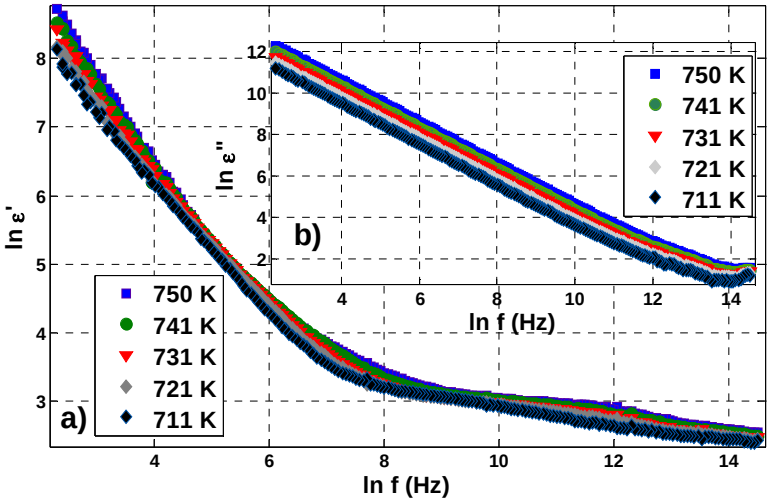

Fig. 3. a) The frequency dependence of the real part on the complex permittivity for $Ba(PO_3)_2$ b) the frequency dependence of the imaginary part on the complex permittivity for investigated sample $Ba(PO_3)_2$.

Overall, the dielectric losses at high frequencies are much lower than those appearing at low frequencies. In Fig. 4 is shown the frequency dependence of loss tangent, which characterize losses by conduction. Thus, the values of loss tangent are higher for glasses with higher electronic conduction. The calculation of activation energy associated with the absorption coefficient $\tan\delta(\omega)$ that notices us on the basic relaxation processes of mobile ions. From Fig. 4, is taken the value of f_{max} and is using for the linear fit in accordance with (6). From Fig. 5 is estimated the value of activation energy associated to the dielectric loss, $E_{a2} = 0.69$ eV.

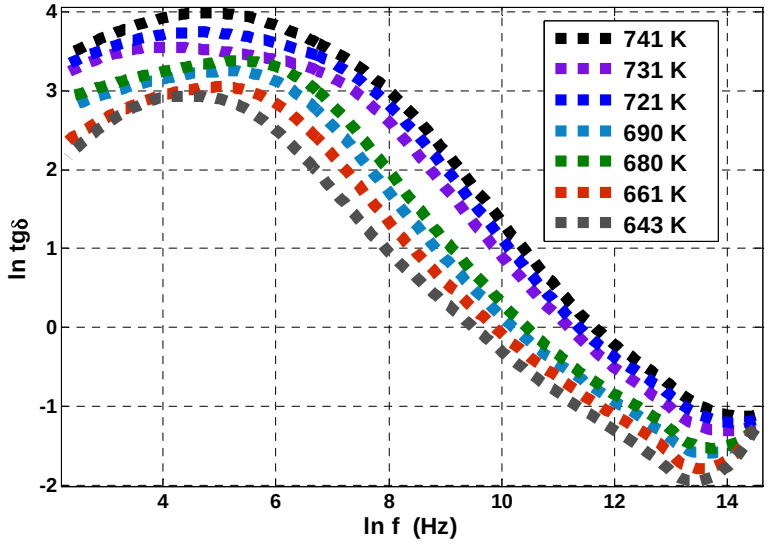

Fig. 4. Frequency dependent the loss tangent of $Ba(PO_3)_2$ at selected temperatures below T_g.

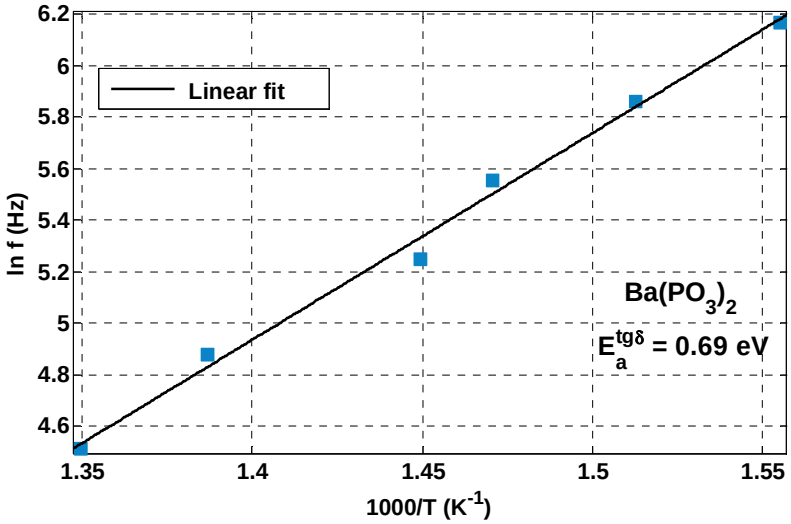

Fig. 5. Arrhenius plot (6), the dependence of maxima of dielectric loss tangent and values of reduce temperature.

The different values of activation energy E_{a1} and E_{a2} can be a case of different process within investigated metaphosphate glass, the activation energy will be compared with results from the acoustic attenuation measurements and they could also contribute to understand structure of ion conducting glass.

5. Conclusion

After thermal excitation in range of temperatures below T_g, we were investigated changes of the dc conductivity for the sample $Ba(PO_3)_2$. The values of dc conductivities were using for calculation of the activation energy for the conduction. Also, we have been investigated dielectric properties of the $Ba(PO_3)_2$ glass, which allow us characterize of the fundamental properties and damping effect. The value of the activation energy was also found from isochronal peak of loss tangent.

Acknowledgement

The authors would like to thank to Francisco Muñoz and Laura Muñoz-Senovilla from Ceramics and Glass Institute (CSIC), Madrid for preparing and providing the investigated samples and F. Černobila for technical assistance. This study was supported by projects VEGA No. 1/0853/13 and ITMS: 26210120021 co-funded from EU sources and European Regional Development Fund.

References

[1] STRIEPE, S., DEUBENER, J. Viscosity and kinetic fragility of alkaline earth zinc phosphate glasses. In *Journal of Non-Crystalline Solids*. 2012, vol. 358, pp. 1480–1485.

[2] EHRT, D., EBELING, P., NATURA, U. UV Transition and radiation – induced defects in phosphate and fluoride-phospate glasses. In *Journal of Non-Crystalline Solids*. March 2000, vol. 263-264, pp. 240-250.

[3] ČERVINKA, L., BERGEROVÁ, J., TROJAN, M. An X-ray study of phosphate glasses of the composition $[M(PO_3)_2]_n$(M=Zn, Cu, Mn, Ca and Mg) . In *Journal of Non-Crystalline Solids*. December 1995, vol. 192-193, pp. 121-124.

[4] SHASH, N., AHMED, I. Structure and electrical properties of ZnO doped barium-metaphosphate glasses. In *Materials Chemistry and Physics*. January 2013, vol. 137, iss. 3, pp. 734-741.

[5] SINOUH, H., BIH, L., BOUARI, A., AZROUR, M., MANOUN, P., LAZOR, P. BaO effect on the thermal properties of the phosphate glasses inside Na_2O-SrO-TiO_2-B_2O_3-P_2O_5 system. In *Journal of Non-Crystalline Solids.* July 2014, vol. 405, pp. 33-38.

[6] WALTER, G., GOERIGK, G., RUSSEL, C.The structure of phosphate glass evidenced by small angle X-ray scattering. In *Journal of Non-Crystalline Solids*. October 2006, vol. 352, iss. 38-39, pp. 4051-4061.

[7] HOCKICKO, P., BURY, P., MUÑOZ, F. Investigation of relaxation and transport processes in LIPO(N) glasses. In *Journal of Non-Crystalline Solids*. 2013, vol. 363, pp. 140-146.

[8] HOCKICKO, P., BÍREŠOVÁ, J. Acoustic investigation of phosphate-based glasses by means of theoretical models. In *Akustika*. March 2015, vol. 23, pp. 18-21

[9] NEYRET, L., LENOIR, M., GRANDJEAN, A., MASSONI, N., PENELON, B., MASSONI, N., MALKI, M. Ionic transport of alkali in borosilicate glass. Role of alkali nature on glass structure and on ionic conductivity at the glassy state. In *Journal of Non-Crystalline Solids*. December 2015, vol. 410, pp. 74-81.

[10] PRADHAN, K. D., KARAN, N. K., THOMAS, R., KATIYAR, R. S. Coupling of conductivity to the relaxation process in polymer electrolytes. In *Materials Chemistry and Physics*. July 2014, vol.147, pp. 1016-1021.

[11] MANDANICI, A., RAIMONDO, A., FADERICO, M., CUTRONI, M., MUSTARELLI, P., ARMELLINI, C., ROCCA, F. Ionic conductivity, electric modulus and mechanical relaxations in silver iodide-silver molybdate glasses. In *Journal of Non-Crystalline Solids*. January 2014, vol. 401, pp.254-257.

[12] BROW, K. R. Review: the structure of simple phosphate glasses. In *Journal of Non-Crystalline Solids*. 2000, vol. 263-264, pp. 1-28.

[13] MUÑOZ-SENOVILLA, L., MUÑOZ, F. Behavior of viscosity in metaphosphate glasses. In *Journal of Non-Crystalline Solid.* 2014, vol. 385, pp. 9-16.

[14] TOYODA, S., FUJINO, S., MORINAGA, K. Density, viscosity and surface tension of 50RO–50P2O5 (R: Mg, Ca, Sr, Ba, and Zn) glass melts. In *Journal of Non-Crystalline Solids*. February 2003, vol. 321, pp. 169-174.

[15] SHELBY, E. J. Properties of alkali-alkaline earth metaphosphate glasses. In *Journal of Non-Crystalline Solids*. 2000, vol.263-264, pp. 271-276.

TRANSCOM 2015, 22-24 June 2015
University of Žilina, Žilina, Slovak Republic

The Microstructure According to the Welding TTT Curve in Comparison with the Microstructure of the Real Welded Joint by Using the Example of Welded 900A Steel

[*]Paweł Bolanowski
[*]Kielce University of Technology, Department of Applied Computer Science and Armament Engineering, Faculty of Mechatronics and Machine Design, Al. Tysiąclecia Państwa Polskiego 7, 25-314 Kielce, Poland, pawelbolan@wp.pl

Abstract. The microstructure and consequently the mechanical properties of welded joint can be determined theoretically on the basis of the type of material, parameters of welding, thickness of material etc. The aim of this paper is to show differences between the microstructure according to the theoretical analysis (based on the welding TTT-curve) and the microstructure observed in the real welded joint by using example of welded 900A steel.

Keywords: Welded joint, microstructure, mechanical properties, welding TTT curve

1. Introduction

The term „welded joint" includes: base material, a joint and a heat affected zone.

The heat affected zone is a part of base material with its microstructure changed by the heat source. Width of the heat affected zone depends on welding method, heat input of welding, velocity of welding and thickness of welded elements. During welding processes various temperatures can be observed in the heat affected zone – from values close to the temperature of metal melting to the distinctly lower temperatures. Thermal-metallurgical processes are responsible for the exact configuration of microstructure.

It is impossible to keep the chemical and microstructural homogeneity of the material in the heat affected zone. The types of microstructural changes in the heat affected zone depend on: the maximum temperature of the material during welding and the time of cooling down from 800˚C to 500˚C, which is called $\tau_{800-500}$.

$\tau_{800-500}$ is described by the following formula:

$$\tau_{800-500} = \frac{K \cdot E^n}{\beta(\bar{t}-t_0)^2 \cdot \left[1+\frac{2}{\pi}\cdot arctg(\frac{g-g_0}{\alpha})\right]} \quad (1)$$

E - heat input of welding [J/cm]

t_o - temperature of material just before welding

g – thickness of material

Other parameters for shielded metal arc welding obtain values shown in Tab. 1.

K	n	g_o	α	$\bar{t}$	β
1,35	1,5	14,6	6	600	1

Tab. 1. The values of other parameters needed to calculate $\tau_{800-500}$ for shielded metal arc welding

Nomograph shown on Fig. 1 was created on the basis of the (1).

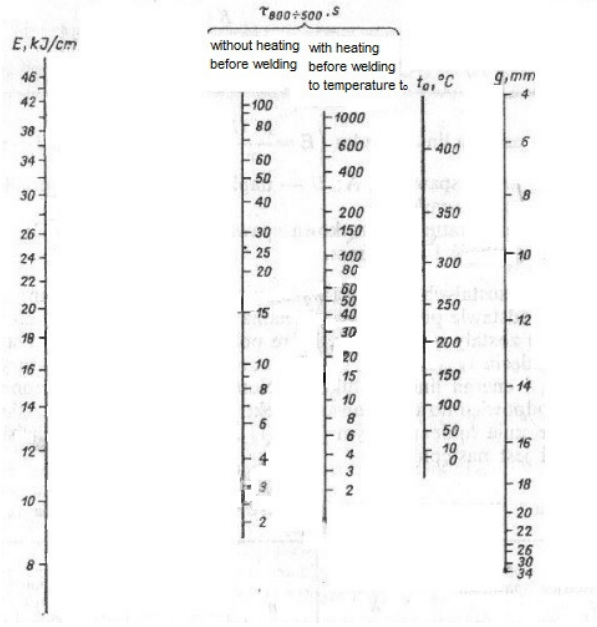

Fig. 1. The nomograph for defining $\tau_{800-500}$

The method of using the nomograph shown above is as follows: draw the interval from the axis signed as E to the axis marked as g. The value of welding heat input on the axis E and the thickness of welded material are the source and the end of interval respectively. The point of intersection of the mentioned interval with the axis marked as: "without heating before welding" is the source of the new interval. The end of the new interval is the value of heating before welding. The point of intersection of the second interval with the axis marked as: "with heating before welding to temperature t_0" is the value of $\tau_{800-500}$.

Using the welding TTT curve (welding time-temperature-transformation curve) requires the calculation of the time $\tau_{800-500}$. Due to the welding TTT curve it is possible to predict the configuration of the microstructure in the heat affected zone.

The aim of this paper is to compare the microstructure in the heat affected zone observed after real process of welding with the microstructure predicted on the basis of welding TTT curve, by using the example of the welded rail made of 900A steel.

2. Material

Two segments of rail from 900A steel have been welded. The thickness of web of rail is 34 mm. The chemical composition and the mechanical properties of 900A are shown in Tab. 2.

Rail	Chemical composition [%]					Mechanical properties	
	C	Mn	Si	P	S	Rm [Mpa]	A5 [%]
900A	0.72	1.06	0.33	0.15	0.15	940	11.8

Tab. 2. The chemical composition and the mechanical properties of 900A steel

Covered electrodes EB150 were used for welding. The chemical composition and mechanical properties of deposited metal are shown in Tab. 2.

Electrode	Chemical composition [%]			Mechanical properties			
	C	Mn	Si	Rm [Mpa]	Re [Mpa]	A5 [%]	KV [J]
E 42 4 B 42	0.08	1.1	0.4				

Tab. 3. The chemical composition and the mechanical properties of EB150

3. Process of welding

WPS was written during the period of preparing to welding. The selected parameters of welding are shown in Tab. 4.

Bead	Method	Diameter of electrode ϕ[mm]	Current intensity [A]	Napięcie [V]	Rodzaj prądu Biegunowość	Prędkość spawania [cm/s]
TW	111	3.25	100-120	24-25	= (+)	0.2 -0.4
1 – 6	111	3.25	100-120	24-25	= (+)	0.27-0.33
7 – 9	111	4.0	140-150	26-27	= (+)	0.27-0.33
10 – n	111	5.0	180-190	27-28	= (+)	0.27-0.33

Tab. 4. The selected parametrs of welding

The ends of rails were preheated by oxy-acetylene blowpipe to the temperature of 330 °C. The interpass temperature during welding was in range 300 – 330 °C.

The ready welded rail is shown on the Fig. 2.

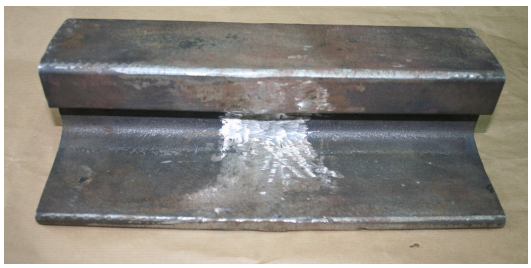

Fig. 2. Experimental welded joint of bridge rail

4. Methodology

4.1. Microstructure and macrostructure examination.

The specimen was cut in the depth 10 mm from the face of weld. The scheme of the specimen is shown on the Fig. 3.

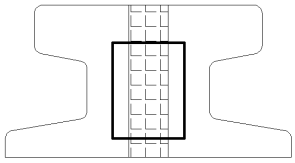

Fig. 3. The scheme of specimen for macroscoping and micropscoping examination

Cut specimen was machined and prepared for the metallographic examination in the grinder-polisher produced by Struers.

The 97 cm^3 of ethyl alcohol and 3 cm^3 of nitric acid were ingredients of etching reagent used for revealing the microstructure of 900A steel. The microstructure was observed using an MA-200 microscope.

4.2. Hardness examination

Hardness was measured along the lines formed by points 1-5 and a-c (shown on Fig. 8) and on the extensions of this lines. Hardness tester HPO – 10 produced by VEB Werkstoffprüfmaschinen was used to hardness examination. Specimen was carried out in Vickers scale (HV5).

5. Results

The macrostructure of the welded joint is shown on the figure. The microstructure was observed in the points 1÷5 and a÷c. Fig. 3. presents the specimen for microstructure examination. The microstructure were observed in points 1÷5, A÷B and a÷c.

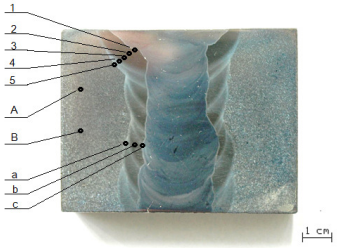

Fig. 4. Macrostructure of welded joint of bridge rail

The microstructure observed in points A and B is shown on Fig. 5, in points 1÷ 5 on Fig. 6 and in points a÷c on Fig. 7.

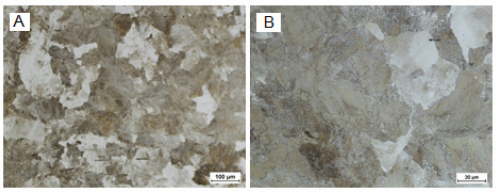

Fig. 5. The microstructure of the base material in different enlargements (points A and B shown in figure 5)

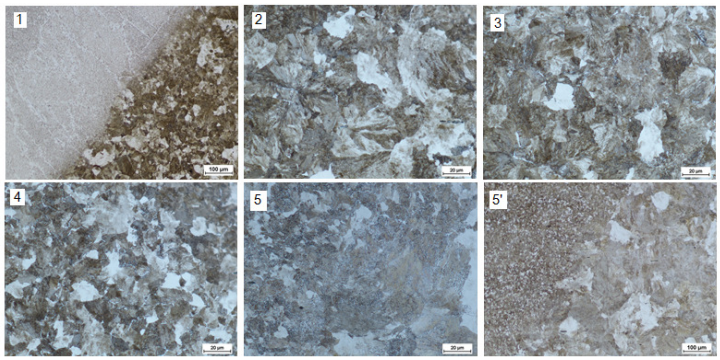

Fig. 6. The microstructure in points 1-5 frm figure 5 (1 – the line of fusion, 2 – coarse grain zone, 3 - Zone of half-normalization, 4 - Zone of normalization, 5 and 5' - Contrast between the base material and the heat-affected zone (different enlargements)

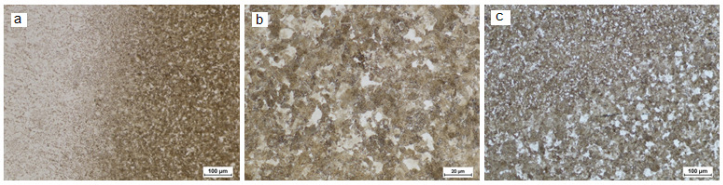

Fig. 7. The microstructure in points a-c (a – line of fusion, b – coarse grain zone, c – contrast between the base material and the heat affected zone)

The type of microstructure can be determined by microscopic observation but the hardness examination can be done in order to confirm the truthfulness of assumption, because hardness of every microstructure (like perlite, ferrite, martensite etc.) in the same steel is different.

The graphs of hardness along the lines 1÷5 and a÷c and their extensions are shown on Fig. 8. It shows the hardness of microstructure depending on the distance from the first measurement.

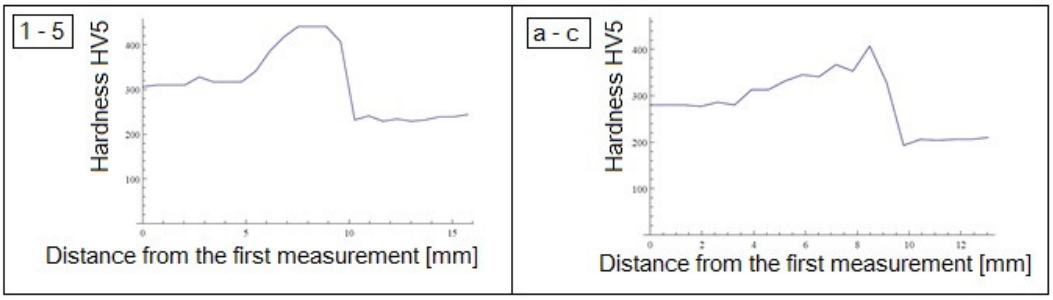

Fig. 8. The hardness of microstructure along the lines 1-5 and a-c and on their extensions

6. Discussion

The average heat input of welding can be calculated by (2).

$$E = \frac{I \cdot U}{v} \tag{2}$$

I – the average current intensity [A]
U – the average arc voltage [V]
v – the average velocity of welding [cm/s]

The value of the average heat input of welding is 12.5 kJ/cm.

The carbon equivalent of 900A steel can be calculated on the basis of the chemical composition of this steel by (3).

$$C_{eq} = C + \frac{Mn}{6} + \frac{Cr + Mo + V}{5} + \frac{Ni + Cu}{15} \tag{3}$$

The value of the carbon equivalent of 900A steel is 0,9%.

In case of the material thickness 34 mm and the heat input of welding 12.5kJ, the value of $\tau_{800-500}$ is 15 seconds. This information was obtained on the basis of nomograph shown on Fig. 9.

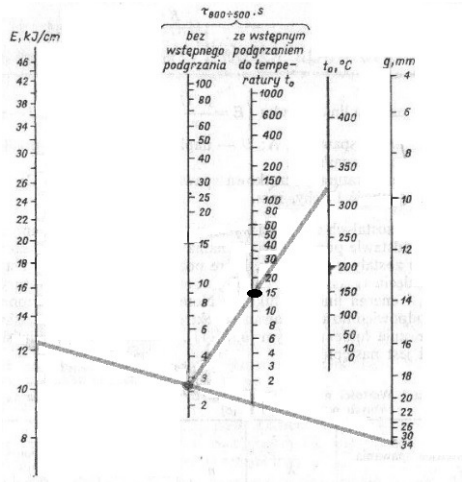

Fig. 9. Determination of $\tau_{800-500}$

The TTT-curve for steel with approximate value of carbon equivalent is presented on Fig. 10.

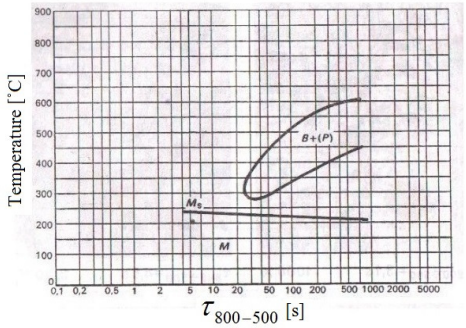

Fig. 10. The welding TTT curve of steel with carbon equivalent equal to 0.9%

According to the graph shown on Fig. 10 the martensitic microstructure should be formed in material for $\tau_{800-500}$ equal 15 seconds but observed microstructure is perlitic-ferritic. Hardness examination shows that the maximum value of hardness in the heat affected zone is 441 HV5 (45 HRC) which is not specific for martensitic microstructure in steel with carbon equivalent equal 0,9%. In accordance with the graph shown on Fig. 11 the characteristic value of hardness of martensite is 55 HRC (596 HV5).

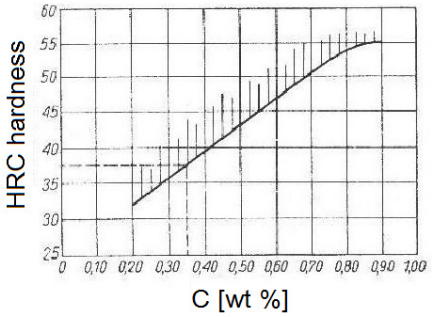

Fig. 11. The relationship between the carbon content in steel and the hardness of the martensite

7. Conclusions

The differences between the microstructure predicted on the grounds of the welding TTT curve and the microstructure of the real welded joint was studied in case of 900A steel. Martesitic microstructure should be observed in the heat affected zone in accordance with the welding TTT curve. It was the perlitic-ferritic microstructure what was really observed. The occurrence of this microstructure was confirmed by hardness examination. It was found that theoretical methods cannot constitute the base to predict the properties of the welded joint. It is advised to weld the experimental joints and examine it before specification and qualification of welding procedures in the presence of a supervisor from the notified body. The best properties in the heat affected zone (in the weakest zone of the welded joint) and high quality of manufacture can be achieved due to experimental selection of parameters of welding. Theoretical methods can only be used to roughly predict of the most adequate parameters.

References

[1] MIZERSKI J. *Spawanie, wiadomości podstawowe*, publ. REA, Warsaw 2007.
[2] *Poradnik inżyniera – spawalnictwo*, joint study publ. Wydawnictwa Naukowo-Techniczne, Warsaw 2003.
[3] BRÓZDA J., PILARCZYK J., ZEMAN M. *Spawalnicze wykresy przemian austenitu CTPc-S*, publ.Śląsk, Katowice 1983.
[4] PRZYBYŁOWICZ K. *Metaloznawstwo* publ. Wydawnictwa Naukowo-Techniczne, Warsaw 1999.
[5] BOLANOWSKI P. *Properties of welded joint of bridge rail welded by 111 method*, journal Przegląd, Spawalnictwa 7/2014

TRANSCOM 2015, 22-24 June 2015
University of Žilina, Žilina, Slovak Republic

Surface Alloying of Magnesium by GTAW Using AlMg4.5Mn Wire

[*]Tomasz Bucki, [*]Renata Mola, [*]Andrzej Dziadoń
[*]Kielce University of Technology, Faculty of Mechatronics and Mechanical Engineering, Department of Applied Computer Science and Armament Engineering, al. Tysiąclecia Państwa Polskiego 7, 25-314 Kielce, Poland, tbucki@tu.kielce.pl, rmola@tu.kielce.pl, adziadon@tu.kielce.pl

Abstract. Surface alloying of magnesium was performed by GTAW (Gas tungsten arc welding**)** method using AlMg4.5Mn wire as the alloying material. Microstructure of the resulting surface layer consisted of dendrites of the solid solution of aluminum in magnesium and eutectic located in the interdendritic areas. The eutectic was composed of $Mg_{17}Al_{12}$ intermetallic phase and solid solution of aluminium in magnesium. Between the magnesium substrate and the alloyed layer, a thin zone of the solid solution of aluminium in magnesium was observed. The microhardness of alloyed surface was higher as that of the substrate more than twice.

Keywords: magnesium, alloying, welding method, GTAW

1. Introduction

Magnesium and its alloys are used commonly in many fields, such as automotive and aerospace industries. The popularity of magnesium alloys is caused by their low density, high specific strength, good castability and machinability. Despite these attractive properties, a relatively poor resistance to wear and corrosion is a serious impediment against wider applications of magnesium. A way to eliminate these disadvantages is the surface treatment of magnesium. As shown in review works many methods of the surface engineering are applied, ie. electrochemical plating, deposition of conversion films, laser surface treatment, PVD and CVD [1-3]. One of the effective ways to improve surface properties of magnesium substrate is fabrication alloyed surface layer by laser surface alloying or alloying using welding methods [4-8].

The aim of presented work was to improve surface properties of magnesium substrate. The magnesium surface was enriched in aluminium by GTAW method using AlMg4.5Mn wire. The microstructure and microhardness of the Al-enriched layer were investigated.

2. Experimental details

Pure magnesium (99.9% Mg) was used as the substrate material. Samples with dimensions 60x40x15 mm were cut from the ingot. The surfaces were grinded with 800-abrasive paper and finally cleaned in ethanol. Surface alloying was made using a Lorch T220 AC/DC inverter arc welder. The weld parameter adopted in the experiment were as follows: alternating current of 37A, frequency 150 Hz, balance 67 % positive part of current. The tungsten electrode was 1,6 mm diameter. Argon with a purity of 99.995% and a flow rate 10 l/min was used as shielding gas. The alloying material (AlMg4.5Mn, 2.5 mm diameter wire) was dipped by hand into the arc. Next, the samples were sectioned and prepared for microscopic observations following standard metallographic methods.

The microstructure analysis of the aluminized specimens was conducted using Nikon ECLIPSE MA 200 optical microscope and a JEOL JSM - 7100F scanning electron microscope equipped with an X-ray spectrometer (EDS). The microhardness was measured using Vickers microhardness tester at a load of 100 g.

3. Results and discussion

Microstructure of alloyed magnesium is shown in Fig.1a. The overall thickness of the alloyed layer was about 2 mm. Layer consists of outer zone and inner zone adjacent to the magnesium substrate. In the outer zone locally occurred pores.

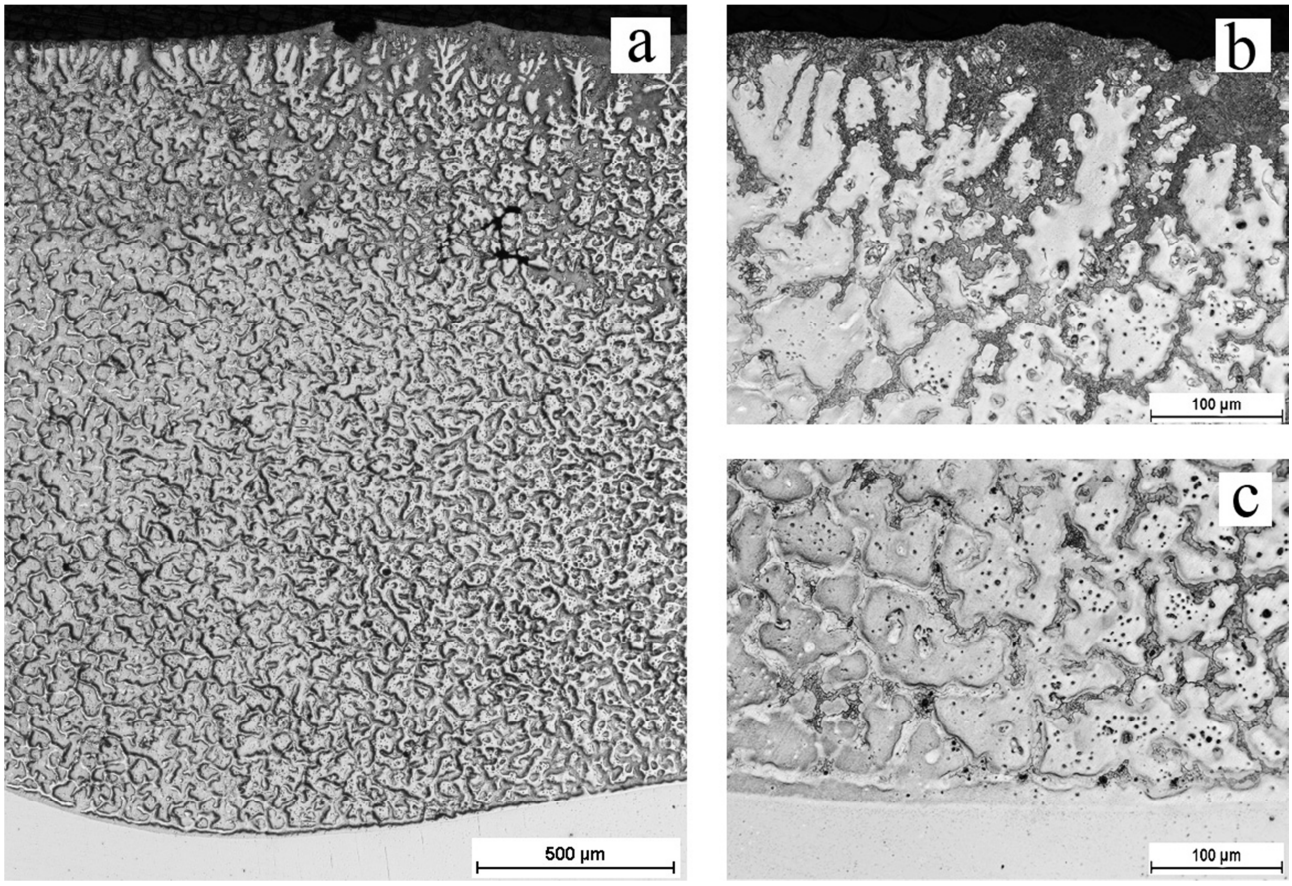

Fig. 1. Microstructure of a magnesium sample after surface alloying with Aluminium by GTAW method observed with an optical microscope (a) cross-section of surface layer (b) outer zone and (c) inner zone observed at a higher magnification

In outer zone (Fig. 1b.) and inner zone (Fig. 1c.) the lighter dendrites and darker areas distributed in interdendritic spaces were observed. Between the layer and the substrate, there was a thin transition zone with a thickness about 20 µm (Fig. 1c). Based on the microscopic observation, it was found that in outer zone there is a larger content of the eutectic areas than in inner zone.

A high magnification SEM image of the alloyed layer is presented in Fig. 2. The EDS quantitative analysis was carried out at points marked in this figure. The chemical composition of the dendrites marked 1 (89.88 at% Mg, 10.12 at% Al) indicates, according to the phase equilibrium system Al-Mg [9], solid solution of aluminium in magnesium. The content of magnesium and aluminium in region 2: 71.01 at% Mg and 28.99 at% Al suggest eutectic composed of $Mg_{17}Al_{12}$ intermetallic phase and solid solution of aluminium in magnesium. The aluminium content in thin zone adjacent to magnesium substrate was about 6 at%. This means that between Al-enriched layer and magnesium substrate a zone of solid solution of aluminium in magnesium was formed.

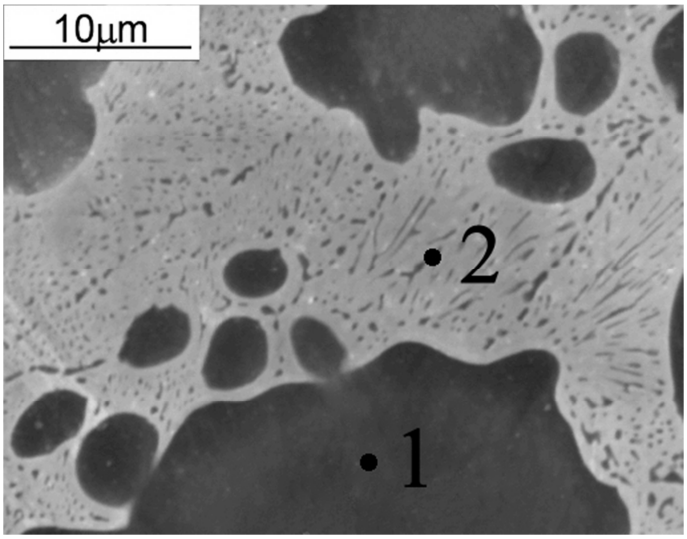

Fig. 2. Details of the microstructure of the alloyed layer observed with an SEM

In the alloyed layer are located white particles, which can be observed at high magnification (Fig. 3a.). Fig. 3b. shows line analysis from this particle. The elements concentration along the index line indicate multicomponent aluminium and manganese Al-Mn-Fe rich phase. Manganese probably originates from AlMg4.5Mn wire.

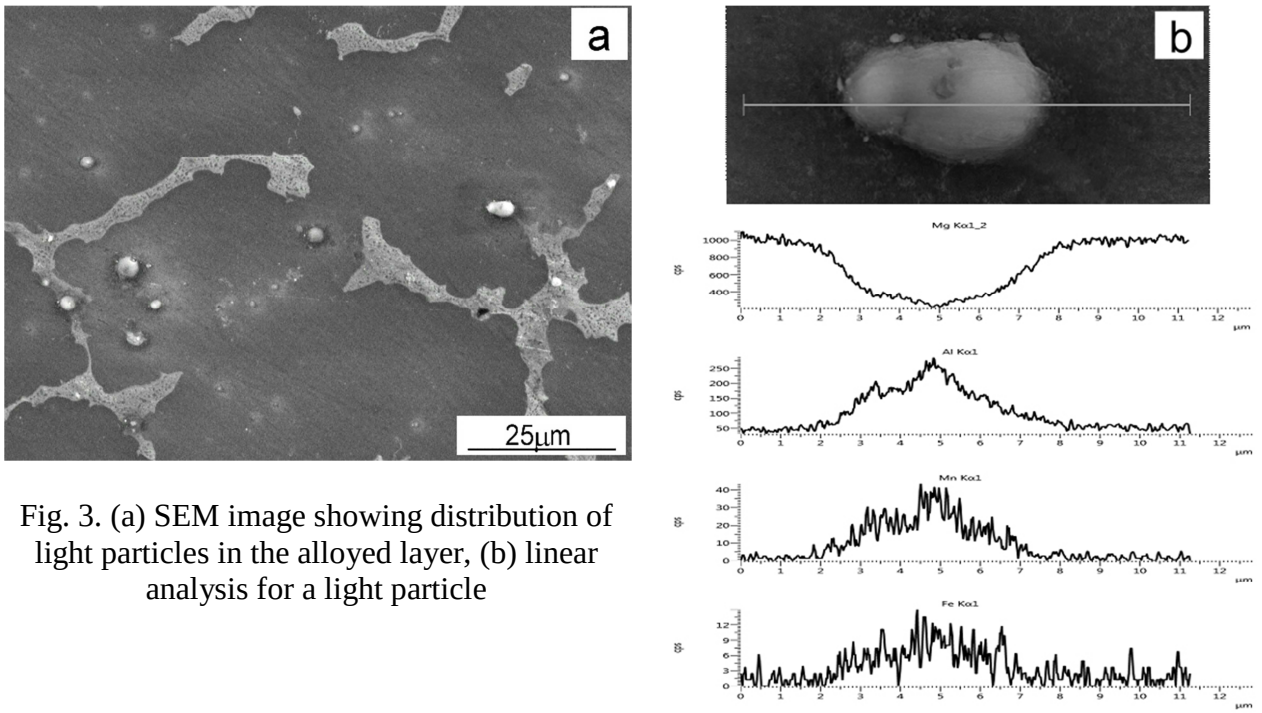

Fig. 3. (a) SEM image showing distribution of light particles in the alloyed layer, (b) linear analysis for a light particle

The Vickers microhardness test was performed (microhardness indentations are shown in Fig. 4.). The microhardness was 69-102 HV0.1 in the aluminium-enriched layer and about 32 HV0.1 in magnesium - substrate. The results of microhardness measurements in outer and inner zone of the alloyed surface layer were slightly different. Hardness in the inner zone was 69-78 HV0.1. In outer zone the hardness was higher about 80-102 HV0.1. This difference is probably due to higher aluminium content in the outer zone and consequently greater amount of eutectic which contains mainly the hard intermetallic phase $Mg_{17}Al_{12}$. As shown in literature [10] this phase has hardness 210-223 HV0.1.

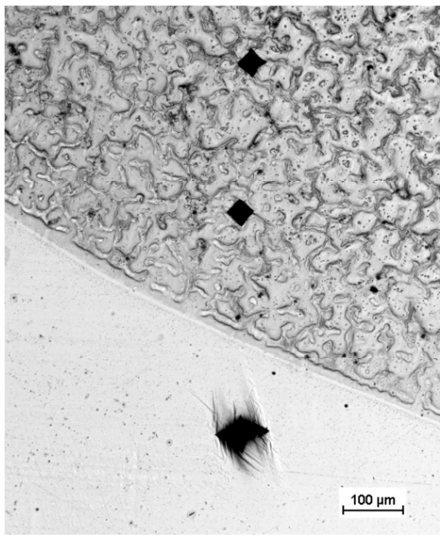

Fig. 4. Microhardness measurement indentations in the alloyed layer and magnesium substrate

4. Conclusions

-The alloyed layer of magnesium that was fabricated by GTAW method, using AlMg4.5Mn wire as alloying material has thickness of about 2 mm.
- The structure of the resulting layer consisted of eutectic and dendrites made of a solid solution of aluminum in magnesium. The eutectic contains mainly $Mg_{17}Al_{12}$ intermetallic phase and solid solution of aluminum in magnesium. Between the layer and the substrate, there was a thin transition zone of solid solution of aluminum in magnesium with overall thickness about 20 µm.
- The microhardness of alloyed layer was in the range 69-102 HV0.1 and was higher about 2-3 times than that of the substrate.

References

[1] GRAY, J. E., LUAN, B., *Protective coatings on magnesium and its alloys – a critical review.* Journal of Alloys and Compounds, 336, 2002.
[2] STANKIEWICZ, A., LASZCZYŃSKA, A., WINIARSKI, J., SZCZYGIEŁ, B., *Wybrane metody wytwarzania powłok ochronnych na magnezie i jego stopach.* Ochrona przed korozją, 53, 2010.
[3] ZHONG, CH., LIU, F., WU, Y., LE, J., LIU, L., HE, M., ZHU, J., HU, W., *Protective diffusion coatings on magnesium alloys. A review of recent developments.* Journal of Alloys and Compounds, 520, 2012.
[4] ELAHI, M. R., SOHI, M. H., SAFAEI, A., *Liquid chase surface alloying of AZ91D magnesium Alloy with Al and Ni powders.* Applied surface Science, 258, 2012.
[5] IGNAT, S., SALLAMAND, P., GREVEY, D., LAMBERTIN, M., *Magnesium alloys laser (Nd:YAG) cladding and alloying with side injection of aluminium powder.* Applied Surface Science, 225, 2004.
[6] PAITAL, S. R., BHATTACHARYA, A., MONCAYO, M., HO, Y., MAHDAK, K., NAG, S., BENERJEE, R., DAHOTRE, N. B., *Improved corrosion and wear resistance of Mg alloys via laser surface modification of Al on AZ31B.* Surface and Coatings Technology, 206, 2012.
[7] DZIADOŃ, A., MOLA, R., *Analiza mikrostruktury warstwy wierzchniej magnezu wzbogaconej w aluminium w wyniku stopowania laserowego.* Rudy i Metale Nieżelazne, nr 5, 2011.
[8] DZIADOŃ, A., MOLA, R., *charakterystyka mikrostruktury warstwy wierzchniej magnezu wzbogaconej w aluminium i krzem za pomocą lasera CO_2.* Rudy i Metale Nieżelazne, nr 10, 2013.
[9] LANDOLT-BÖRNSTEIN, *Crystallographic and Thermodynamic Data of Binary Alloys, New Series, Group IV.* Springer-Verlag, Berlin, 1998.
[10] MOLA, R., JAGIELSKA-WIADEREK, K., *Formation of Al.-enriched surface layers through reaction at the Mg-substrate/ Al-powder interface.* Surface and Interface Analysis, 46, 2014.

TRANSCOM 2015, 22-24 June 2015
University of Žilina, Žilina, Slovak Republic

Long-Term Operation and Measurement Parameters of Working Stirling Engine Type Gamma

[*]Jaroslav Čierny, [*]Marek Patsch, [*]Milan Malcho
[*]University of Žilina, Faculty of Mechnical Engineering, Department of Power Engeneering, Univerzitna 1, 010 26 Žilina, Slovakia, {jaroslav.cierny, marek.patsch, milan.malcho}@fstroj.uniza.sk

Abstract. This article deals with problematics of micro-cogeneration units based on Stirling engine type Gamma. These technologies are not widespread and not available in Slovakia, so our results show their advantages and disadvantages, as well as the possibility of price competition to commercially available sources. At the end of the article is also simulate the behavior of the units in projected house at various heat removal, which we want solve in the near future.

Keywords: natural gas, Stirling engine type gamma, micro-cogeneration, heat demand

1. Introduction

Energy production with the highest efficiency and the lowest production costs, in the current development of technology is increasingly required. One of these technologies which may be new trend of current requirements is CHP - combined production of energy in a single device. This technology combines heat and power generation in one device at a decentralized level with higher overall efficiency, reducing costs and the consumer can use saved money to get a different kind of energy. Since we are talking about micro-CHP, according to European standards (EU 2004/8 / EC) micro-CHP is a unit with an output of electricity power up to 50 kW_e. The most common technologies which are used in micro-CHP are:

- Combustion turbine with combined cycle
- combustion engine,
- microturbines,
- Stirling engine
- fuel cell,
- Rankine cycle and others.

On our department we have installed micro-CHP unit based on Stirling engine type Gamma (fig.1) WhisperGEN EU1, so basis principle and results from long-term operation will be described in next parts of article.

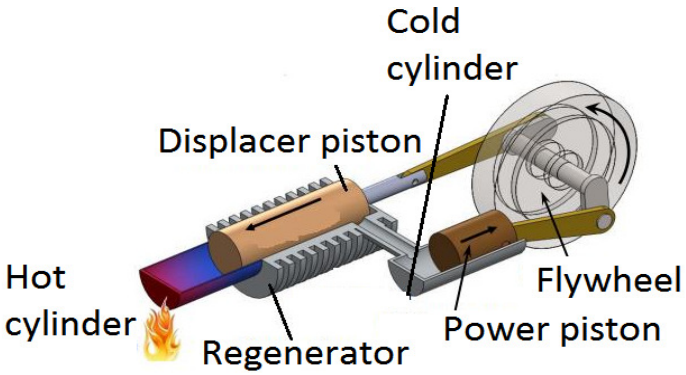

Fig. 1 Stirling engine type Gamma

2. Stirling engine WhisperGen model EU1

Stirling engine for micro-CHP is a piston engine with external combustion, when the heat is supplied from an external source. WhisperGen EU1 works as double-acting four-cylinder stroke Stirling engine with a nominal power output 1 kW of electricity and a heat output range of 5.5 up to 14 kW. The device contains two gas burners, each have nominal heat output of 7 kW, primary burner is the Stirling engine and a second is an auxiliary burner which covers additional heat demand.

Operation principle of the Whispergen EU1 is shown in figure 2. The Stirling engine burns natural gas in the burner, located above the Stirling engine and thereby heating the engine head. The heat transfer through the head to the working gas in the engine (nitrogen with a working pressure up to 20 bar in 70°C). The movement of the pistons is ensured by expansion and compression of the working gas. The working gas expands when is heated by combustion of the fuel in the combustion chamber. Compression occurs when gas is cooled by leaving water which flows through the water jacket inside the base part of the engine.

Vertical movement of the pistons is converted to rotary motion by complex of crank mechanism. The rotary motion is converted into electrical energy 230 V and 50 Hz by cooled four-pole single phase induction generator.

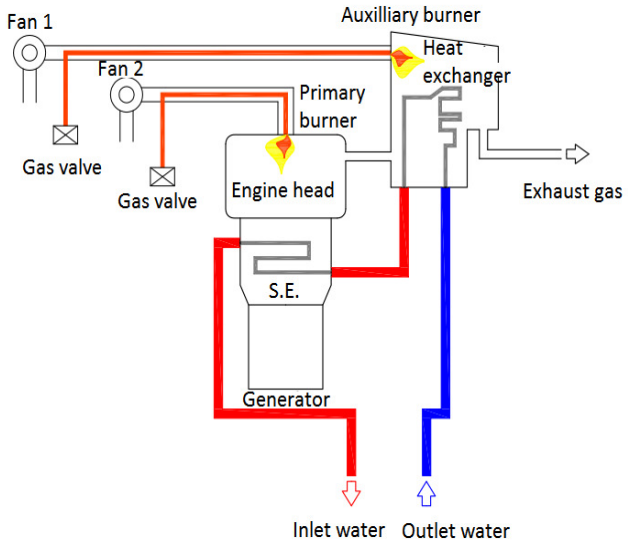

Fig. 2 Operation principle of WhisperGen EU1

In the table 1, we can see the nominal values for a unit specified by the manufacturer.

Output electrical performance (nominal)	< 1000 W
Electrical efficiency	< 11 %
Heat performance (min. – max.) with auxilliary burner	5,5 – 14 kW
Overall efficiency	92 – 94%
Gas consumption	1,55 m^3 per hour

Tab. 1 Values of engines specified by manufacturer

3. Operation of WhisperGen EU1 at the University of Žilina

The operation of micro-CHP WhisperGen EU1 was carried out on land at the University of Žilina see figure 3. The system itself is composed of Stirling engine Whispergen EU1, 800 liters storage tank, expansion tank, pump station, heating valves and measuring elements (Yokogawa flow meter, gas meter with remote reading and more ...).

Fig. 3 Realized micro-CHP unit at the University of Žilina

To get the thermal performance of S.E. we scanned and processed inlet water temperature (by sensor PT100), outlet heating water, the mass flow rate (by mass flowmeter Yokogawa), the pressure (by pressure sensor Ahlborn) and temperature of the storage tank. For quick verification of the condition of the heating system, we had analogue sensors. The heat charging of the storage tank is supplemented by a three-way valve with actuator and the control valve Herz STRÖMAX DN25. By this valve we can regulate flow of heating water and change the temperature gradient.
To determine information about consumed and produced electricity we used two-way wattmeter Rawet with dividers coils.

The heat from the system was used in corridors at the University by heating unit Sahara (25,4 kW by 90/70°C). Electricity produced by S.E. is supplied to the university network and part of the electricity was used to power pumps connected in the system. These pumps regulated S.E. as it needed.

During the operation, we achieve an average electrical efficiency of 4%, representing a significant difference declared by manufacturer value of 11%. Average electrical performance was 280 W and thermal performance was about 5,7 kW. Differences between values were caused by two facts, namely that S.E. did not work alone and was constantly switching only at sufficiently high temperature gradient between the inlet and outlet heating water, but heat transfer to the system was practically constant, controlled by room thermostat and the sensor of storage tank. We could not provide for the operation or we can provided it only when the storage tank was cold.

The second factor was the frequent failure rate of the unit. S.E. was operated around 8760 working hours (figure 4.), but only 5365 hours was fully working (only S.E.). After these the unit was shut down. On closer analyzing we found, there was a leakage (by supply valve) of the working gas (figure 4) and seller does not have sufficient experience with repair of unit so we had to try repair it by own with new supply valve and 40 bar closing valve.

After repairing the unit we would like to provide real operation of engine providing adequate heat transfer and also by simulating the real operation of the designed houses (low energy and common) with 4 members in the program TechCON. Total heat loss of the object was 10.8 kW. Demand of heat energy and preparation of heat water was calculated according to STN 12831 and STN 060 320/15316-3 = 80.72 GJ/ yr. + 33.32 GJ/yr.

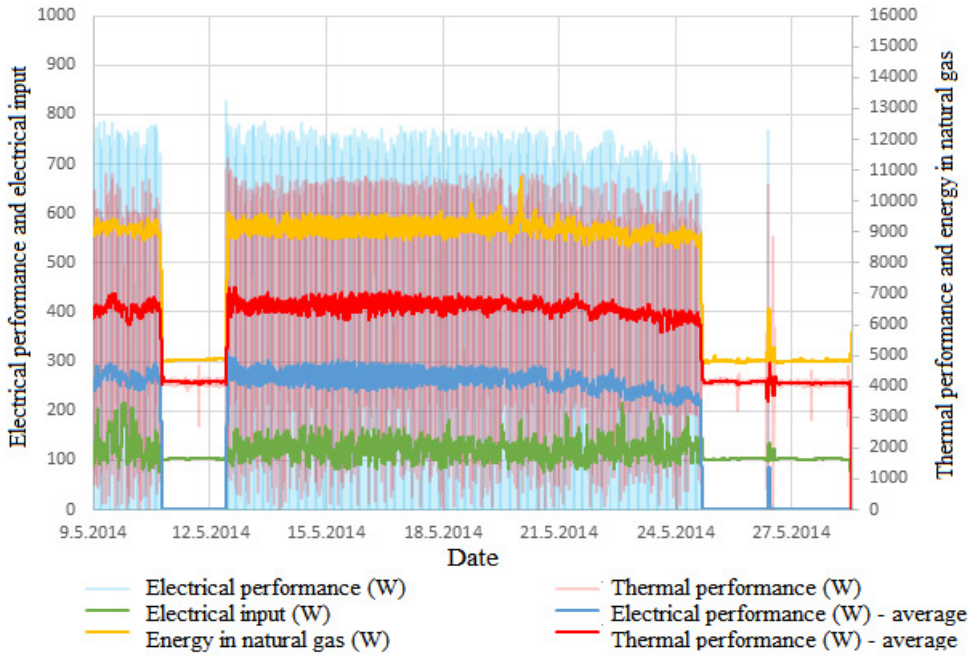

Fig. 4 Selected values of S.E. operation and his failure rate

Fig. 5 Defective supply working gas valve and new system of working gas supply

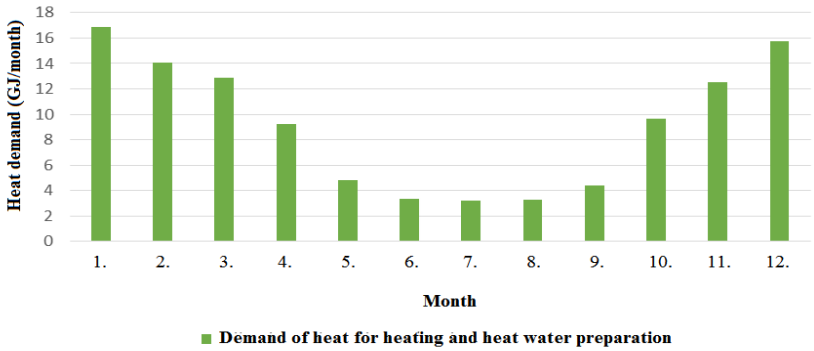

Fig. 6 Demand of heat for designed house in TechCON

4. Conclusion

Micro-cogeneration units are useful in the production of energy, and therefore we want to continue to pay attention of their research, but their high cost (over 15 000€) and low reliability, prevents them to succeed in the Slovak market. Therefore we want to research them and incorporate different types of control valves, heat meter and thus simulate different conditions of energy

consumption in households, followed by comparison with commercially available condensing boiler.

Acknowledgement

Project 567/PG04/2011 "*Energy efficiency comparision of natural gas in micro-cogeneration units on the principle of the fuel cell and Stirling engine"* is realized with the support of non-investment fund EkoFond, which is established by the SPP.

The task is carried out within the project „ Research Center of the University of Žilina" ITMS 26220220183.

References

[1] HOLUBCIK M., HUZVAR J., JANDACKA J.: *Combined production of heat and electricity with use of micro cogeneration* / M. Holubcik, J. Huzvar and J. Jandacka. In: IN-TECH 2011 : proceedings of international conference on innovative technologies : 01.09.2011 to 03.09.2011, Bratislava, Slovakia. - [S.l.]: Jan Kudláček, 2011. - ISBN 978-80-904502-6-4. - S. 200-202.

[2] HOLUBCIK M., HUZVAR J., JANDACKA J.: Copper equipment for heat transfer in the micro cogeneration unit [Medené zariadenie na prenos tepla v mikrokogeneračnej jednotke] / In: ERIN 2011 - education, research, innovation [elektronický zdroj]: proceedings of 5th conference for young researchers and PhD students : 13th-16th April 2011 - Tatranská Kotlina - Vysoké Tatry - Slovakia. - Prešov: Harmony Apeiron, 2011. - ISBN 978-80-89347-05-6. - S. 57-60.

TRANSCOM 2015, 22-24 June 2015
University of Žilina, Žilina, Slovak Republic

Impact of Bifocal Welding Head Angle Orientation on Welding Shape of TP347HFG High-Temperature Steel

[*]Hubert Danielewski, [**]Andrzej Skrzypczyk,
[*]Kielce University of Technology, Faculty of Mechatronics and Machine Engineering, Laser Processing Research Centre, 25-314 Kielce, Poland, hdanielewski@tu.kielce.pl
[**] Kielce University of Technology, Faculty of Mechatronics and Machine Engineering, Department of Applied Computer Science and Armament Engineering, 25-314 Kielce, Poland, tmaask@tu.kielce.pl

Abstract. Manuscript applies an investigation of weld shape, including width and face of weld shape for different focal points orientation of bifocal welding head. Research of weld profile consist five different angle orientation of optical system. Material using in investigation was TP347HFG high-temperature stainless steel using in heating installation. In order to demonstrate effect of different angle orientation of focal system an experiment was carry out in same process parameters expect bifocal welding head angle orientation. Weld was carried out on a TP347HFG pipe parallel to the pipe axis. Welding system was high power CO_2 laser with six-axis machining system.

Keywords: Laser welding. Bifocal welding head system. Head angle orientation.

1. Introduction

Laser welding is unconventional method of joining materials. This quantum device uses a concentrated photon beam to heat and melt edge of joining material. Specificity of laser welding require exact fitting of joining edges. Exact fitting as well as absence of chamfering allow to refer welding of two pieces of material to depth of fusion in uniform material. Welding process due to the lack of adequate fit of joined edges may caused welding defects and inadequate joint penetration. This effect could be reduced by using multifocal welding system. This technique enable to broaden the area of weld by splitting laser beam into few focusing on the surface beams.

Laser welding are much faster process than a conventional welding, for that matter heat affected zone are significant smaller as well as thermal stresses caused welding defects are reduced. Welding by using laser quantum device are highly repetitive process that doesn't require an additional material. This advantages cause that laser welding is used in welding of heating installation [1].

In energy installation significant part perform an alloy and high alloy steels, especially those classified as heatproof steels with nominal working temperature over 400 ^{o}C. The main elements of energy steels are chromium, molybdenum, manganese, vanadium and trace amounts of titanium, niobium and tungsten, these alloy additions increase the resistance to oxidation, creep strength of steel and deformation under long-term operation conditions. These steels are classified as medium or hard welded steels. Using laser welding a good strength characteristics joints without welding defects can be attained.

Width of the weld zone are crucial in thick materials. In the case of welding steels obtained to heating installation thickness are specified in the standards and usually exceed 5mm so are treated as thick materials. Thermo physical material properties such as specific heat, conductivity and diffusivity are results from composition of alloying elements in material and affect on weldability and shape of weld zone [2].

2. Properties and weldability of TP347HFG boiled steel.

2.1. Properties of TP 347 HFG Steel.

TP 347 HFG is a type of austenitic stainless steel using mainly in heating installation. According to standards it's fulfills the requirements of the following specifications:

- 1.4908 (X8CrNi 19 11) according to EN 10216-5, European Standard
- TP347HFG according to ASME SA-213/SA-213M, US Standard
- VdTÜV material data sheet 547 (03.2007), Federal Republic of Germanya.

TP 347 HFG is 18Cr-8Ni stabilised by niobium material from group of high-tamperature steels. This material, with its ability to maintain a fine grain structure even at high temperatures, provides very high steam-side high-temperature corrosion resistance by enhancing chromium diffusion to the surface along the grain boundaries to form a protective Cr_2O_3 layer at higher service temperatures. In addition, high creep resistance is provided at temperatures in the range of 570 °C to 640 °C. TP 347 HFG is material suitable for use at higher steam temperatures (up to 600°C steam) for example in biomass and waste-fired plants [3].

Austenitic stainless steels as TP 347 HFG have adequate strength, steam-side oxidation and fireside corrosion resistance for use as superheaters. Ni-based alloys show good corrosion resistance at higher pressures/temperatures. The niobium carbonitride precipitates occurring during the operation of the installation also influence the material properties, besides causing a finer grain size of the resulting material. The grain size mainly influences the corrosion resistance as well as improves the creep resistance during installations services.

Temperature ^oC	Thermal conductivity W/(m·K)
20	14.1
100	15.4
200	16.9
300	18.3
400	19.7
500	21.2
600	22.6
700	23.8
750	24.6

Tab. 1. Thermal conductivity of TP 347 HFG according to the VdTÜV material data sheet.

Properties of TP 347 HFG in high-temperature exploitation especially content of improving oxidation resistant chromium determine this material to be used in high temperatures operational conditions. With increasing temperature, a more protective Cr_2O_3 layer is formed. Under special conditions, a flat and uniform layer is developed at the metal surface. This effect is assisted by increased pressure. The mixed iron-chromium-nickel spinel is formed above layer. After initial formation of this layer further thickening is very slow, resulting in superior oxidation resistance compared to the coarse-grained variant of another type of stainless steel materials [4].

ASTM/AME A/SA213	Working temperature ^oC	Yield strength MPa	Tensile strength MPa	Elongation %)	Hardness Rockwell HRC
TP347HFG	650	205	550	35	90

Tab. 2. Mechanical properties of TP 347 HFG according to ASTM standards.

Coefficient of Thermal Expansion between 20 Celsius degree and...	
Temperature °C	10-6/K
100	16.3
200	16.9
300	17.3
400	17.8
500	18.2
600	18.5
700	18.7
750	18.8

Tab. 3. Thermal expansion of TP 347 HFG according to the VdTÜV material data sheet.

2.2. Weldability of TP 347 HFG stainless steel.

Weldability is usually characterised by the resistance to hot cracking and the mechanical properties of the welded joints. The selection of filler material becomes an important factor for good properties of the welded component in conventional welding methods. Weld should have a high corrosion resistance and even better mechanical properties than the base material.

Steel TP 347 HFG is characterized as a weldable. Conventional welding techniques using inert shielded gas with welding wires, welding sticks or with cored wire electrodes and metal arc welding with lime alkaline enclosed electrodes can be perform. It is crucial to use great quality filler materials which are also tested at the foreseen application temperature. Preheating and heat treatment after the welding process in the fabrication of TP 347 HFG is not mandatory. However, if the material is sensitized after welding, then a post welding treatment should be perform to restore the properties, mainly to increase the wet corrosion resistance. Generally, austenitic stainless steels have a high susceptibility to hot cracking in the weld.

Laser welding contrary to arc welding methods is characterized as a high speed process which resulting in reduces of heat affected zone. Thermal stress caused by temperature gradients can be reduced by proper selection of laser welding parameters. Thermal gradients can be reduces as well by using multifocal optics that divided beam reducing process intensity. Widening welding zone by using multifocal welding optics reduces requirement of precise fitting of welded edges and affect decreasing defects in weld [5].

Using different angle orientation of focusing in bifocal welding head affects on weld shape, especially width. Investigation on this phenomena was presented in this paper.

3. Impact of bifocal welding head angle orientation on welding profile.

An experimental welding of TP 347 HFG high-temperature stainless steel pipe with bifocal focus pointing system was performed. Thickness of welded pipe was 6mm, with diameter of pipe 50mm. Source of heat was high power CO_2 laser Trumph TruFlow6000. In an experiment to avoid excess of ionizing plasma as a shield gas with flow rate of 12 l/min helium was used [6].

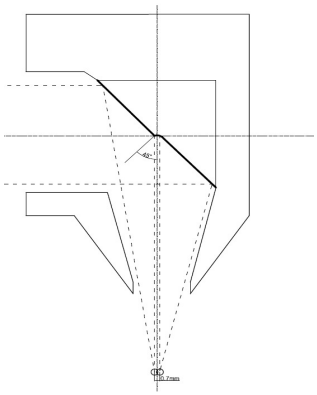

Fig. 1. Bifocal welding optics scheme.

Output laser beam power was set at 6kW with impulse frequency of 50 kHz and welding speed of 1800mm/min. Speed of weld was selected in order to achieve complete weld penetration without excessive root of weld.

In order to achieve reliable results pipe was cooling after each welding. Welding head starting with perpendicularly orientation to the welding direction, and after every weld foci system was rotated by an angel of 22 degree. An experiment was performed for 5 angle orientation: 0, 22, 44, 66 and 90 degrees.

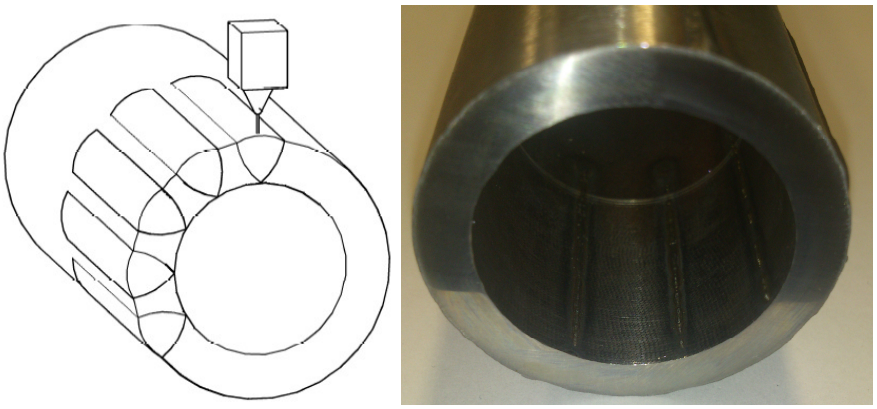

Fig. 2. Flow-sheet of welding process and roots of welded pipe.

Width of weld was measured with optical microscope Olympus SZX 10. To compare results of measurement second measure by confocal digital microscope Hirox KH-8700 was carried out. In second measure width of weld was performed by face of weld surface analyze measuring.

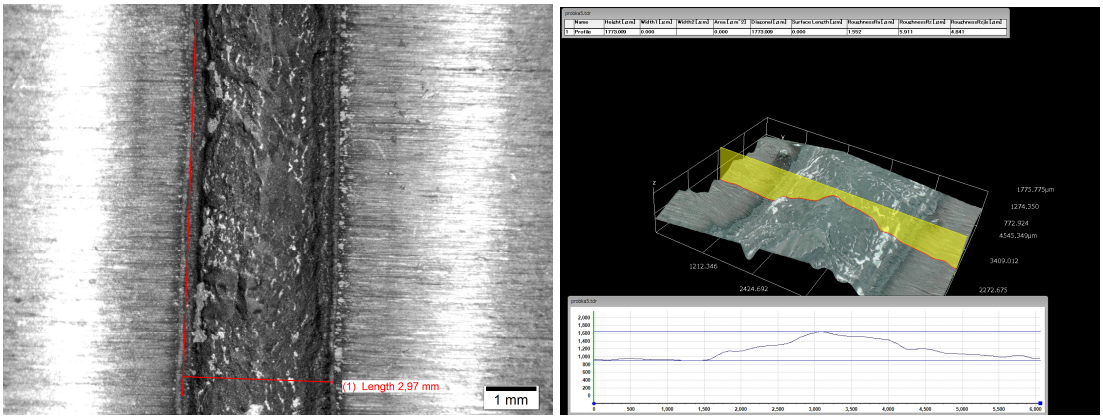

Fig. 3. Width and face of weld profile measurement.

To achieve reliable results measurement for each weld was perform on length of 10mm. Results of measurement by Olympus optical microscope was presented in table 4.

Lp.	Angle of foci orientation deg.	Width of face of weld mm
1	0	2.71
2	22	2.97
3	44	3.4
4	66	3,43
5	90	3.51

Tab. 4. Measured face of weld width.

4. Conclusion

Experimental weld of TP 347 HFG stainless high-temperature steel using bifocal welding head was performed. The main purpose of an experiment was to shown relationship between face of weld width and angle of bifocal welding system orientation. Method presented in paper shown possibility of controlling weld width without changing process parameters that may caused a adverse reactions of thermal effects. Width control could be achieve by defocusing laser beam, that method results reducing in photon radiation density that may affect partial penetration of weld. Using bifocal welding head that affects are reduced. Advantage of bifocal over single focus welding system is reduce temperature gradient and stabilization of the welding process. By using bifocal welding head and proper orientation of foci system intimate contact of welding edge can be reduced. Laser joining using bifocal welding system thanks to advantages described above is perfect for heating installation steels welding.

Acknowledgement

Research was carried out within the project: “Laser welding technologies for the energy and environmental” number PBS1/B5/13/2012

References

[1] ANTOSZEWSKI B., GRADOŃ R., TRELA P., CENDROWICZ E., *A study of laser-beam welding conducted at Centre for Laser Technologies of Metal*, Proceedings of SPIE

[2] STEEN W.M., MAZUMDER J., WATKINS K.G. *Laser Material Processing*, Springer-Verlag, London 2010

[3] VISWANATHAN, R.; SARVER, J.; TANZOSH, J.M.: Boiler materials for ultra-supercritical coal power plants – steamside oxidation. Journal of Materials Engineering and Performance, Vol. 15, (2006), No. 3, p. 255-274

[4] MIURA, M; OGAWA, K.; The Weldability of high corrosion resistant stainless steels. Sumitomo Search, No. 34, (1987), p. 29-38

[5] LAUFER G. Introduction to Optics and Lasers in Engineering. Cambridge University Press (2005).

[6] ZOWCZAK W., *On the modelling of laser subtractive manufacturing, Proceedings of Kielce University of Technology*, Electricity 40, pp. 163-172, 2002

TRANSCOM 2015, 22-24 June 2015
University of Žilina, Žilina, Slovak Republic

Methodology of Group Technology and Classification for Technical Production Planning

[*]Lenka Debnárová [*]Ivan Kuric
[*]University of Zilina, Faculty of Mechanical Engineering, Department of Automation and Production Systems, Univerzitna 2, 01026 Žilina, Slovakia, {Lenka.Debnárová}@fstroj.utc.sk
{Ivan.Kuric}@fstroj.utc.sk

Abstract. There are two major tasks that a company must undertake when it implements group technology. These two tasks represent significant obstacles to the application of GT: identifying the part families and rearranging production machines into machine cells. It is time consuming and costly to plan and accomplish this rearrangement and the machines are not producing during the changeover. The realisation of benefits expected from cellular manufacturing largery depends on how effectively the three phases of design have been performed, namely part/machine grouping, developing the cell layout and cell system layout on the shop floor. This key question of cellular manufacturing has attracted numerous attempts in applying various design methods. The methodology is composed of presentation of definitions such as analysis the products, cell layout, the possibility of classification and coding product and benefits for businesses.

Keywords: Group technology, coding, cellular manufacturing, products analysis, cluster analysis, segmentation, capacity planning.

1. Introduction

Group technology (GT) is a manufacturing philosophy that has attracted a lot of attention because of its positive impacts in the batch-type production. Cellular manufacturing (CM) is one of the applications of GT principles to manufacturing. In the design of a CM system, similar parts are groups into families and associated machines into groups so that one or more part families can be processed within a single machine group. The process of determining part families and machine groups is referred to as the cell formation (CF) problem. CM has been considered as an alternative to conventional batch-type manufacturing where different products are produced intermittently in small lot sizes. For batch manufacturing, the volume of any particular part may not be enough to require a dedicated production line for that part. Alternatively, the total volume for a family of similar parts may be enough to efficiently utilize a ma- chine-cell. It has been reported that employing CM may help over- come major problems of batch-type manufacturing including frequent setups, excessive in-process inventories, long through-put times, complex planning and control functions, and provides the basis for implementation of manufacturing techniques such as just-in-time (JIT) and flexible manufacturing systems (FMS). The typical company makes thousands of different parts, in many different batch sizes, using a variety of different manufacturing operations, processes and technologies. It is beyond the capability of the human mind to comprehend and manipulate such vast amounts of detailed data. People still need to make decisions regarding how to run a manufacturing company and succeed in today‘s competitive environment on home and foreign markets. The pressures on management continue to escalate as global competition drives the need for producing a greater variety of high quality products, in smaller lot sizes and lower costs. These ongoing demands continuously increase the level of complexity present in a manufacturing environment. What is needed is both a strategy and a tool that can be used to achieve such a purpose. Group technology is a manufacturing technique and philosophy to increase production efficiency by exploiting the “underlying sameness” of component shape, dimensions, process route, etc. [2] [3]

Group Technology is the realization that many problems are similar, and that by grouping similar problems, a single solution can be found to a set of problems thus saving time and effort. It is the technique for manufacturing small to medium lot size batches of parts of similar process, geometry, size & shape. The manufacturing efficiencies are generally achieved by arranging the production equipment into machine groups or cells, to facilitate workflow. Grouping the production equipment into machine cells, where each cell specializes in the production of a part family, is called cellular manufacturing. [2]

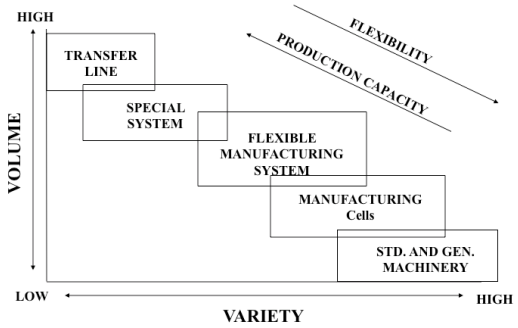

Fig. 1. Manufacturing company and competitive environment on home and foreign markets

2. Part Families Hints

Group Technology is based on general principle that many problems are similar and by grouping similar problem a single solution can be found to a set of problem thus saving time & effort. The group of similar part is known as PART FAMILY and the group of machinery used to process an individual part family is known as MACHINE CELL. A part family is a collection of parts that are similar either because of geometric shape and size or because similar processing steps are required in their manufacturing. A group of parts that possess similarities in geometric shape and size, or in the processing steps used in their manufacture. Part families are a central feature of group technology, there are always differences among parts in a family, but the similarities are close enough that the parts can be grouped into the same family. [1] [2]

Geometric classification of families is normally based on size and shape, while production process classification is based on the type, sequence, and number of operations. The type of operation is determined by such things as the method of processing, the method of holding the part, the tooling. [2]

There are three general methods for solving this problem, which involve the analysis of much data by properly trained personnel.

- Visual inspection - using best judgment to group parts into appropriate families, based on the parts or photos of the parts.
- Production flow analysis - using information contained on route sheets to classify parts.
- Parts classification and coding - identifying similarities and differences among parts and relating them by means of a coding scheme.

Visual inspection

In this method are classified on the basis of visual judgment. It involves arranging the parts into families by visually examining the physical parts or their photographs. It is achieved by photographing parts using scale and sorting into classes by eye. This method is carried out by experts and this is an inexpensive & less Accurate method. [2]

Fig. 2. Manual visual inspection

Production flow analysis (PFA)

Parts that go through common operations are grouped into part families. The machines used to perform these common operations may be grouped as a cell; consequently this technique can be used in facility layout (factory layout). Initially, a machine component chart must be formed. This is an M x N matrix, where

M = number of machines

N = number of parts

x = 1 if part j has an operation on machine i; 0 otherwise.

If the machine component chart is small, parts with similar operations might be grouped together by manually sorting the rows and columns.

Clustering Algorithm is a simple algorithm used to form machine-part groups. We can be divided into following steps:

Step 1: Assign binary weight and calculate a decimal weight for each row.

Step 2: Rank the rows in order of decreasing decimal weight values.

Step 3: Repeat steps 1 and 2 for each column.

Step 4: Continue preceding steps until there is no change in the position of each element in the row and the column. [7]

Classification & Coding

Coding is defined as process of allocating symbol to the parts. The symbol represents design characteristics of parts, manufacturing attributes or both. Classification is the process dividing the set of parts into part family. Coding refers to the process of assigning symbols to the parts. The symbols represent design attributes of parts or manufacturing features of part families. [8]

Although well over 100 classification and coding systems have been developed for group technology applications, all of them can be grouped into three basic types:

- monocode or hierarchical code,
- polycode or attribute,
- hybrid or mixed code.

This is the most time consuming of the three methods. In parts classification and coding, similarities among parts are identified, and these similarities are related in a coding system. Classification and coding systems are devised to include both a part's design attributes and its manufacturing attributes. [8]

Most classification and coding systems are one of the following:

- systems based on part design attributes,
- systems based on part manufacturing attributes,
- systems based on both design and manufacturing attributes,
- PART DESIGN ATTRIBUTES,
- major dimensions,
- basic external shape,
- basic internal shape,
- length/diameter ratio,

- material type,
- part function,
- tolerances,
- surface finish.

Part Manufacturing Attributes:

- major process,
- operation sequence,
- batch size,
- annual production,
- machine tools,
- cutting tools,
- material type.

Design retrieval a designer faced with the task of developing a new part can use a design retrieval system to determine if a similar part already exists. A simple change in an existing part would take much less time than designing a whole new part from scratch.

- Automated process planning. The part code for a new part can be used to search for process plans for existing parts with identical or similar codes.
- Machine cell design. The part codes can be used to design machine cells capable of producing all members of a particular part family, using the composite part concept.

The variations in codes resulting from the way the symbols are assigned can be grouped into three distinct types of codes.

Monocode or hierarchical code

In this type of code, the meaning of each character is dependent on the meaning of the previous character; that is, each character amplifies the information of the previous character. Such a coding system can be depicted using a tree structure. It means the interpretation of each succeeding symbol depends upon the value of the proceeding symbol. Here the first group indicates the major groups such as casted part, machined part, sheet metal parts etc. The second digit may indicates the shape of parts such as rotational, rectangular etc. The main benefit of this type of method is that it provides large information in a short code. [6]

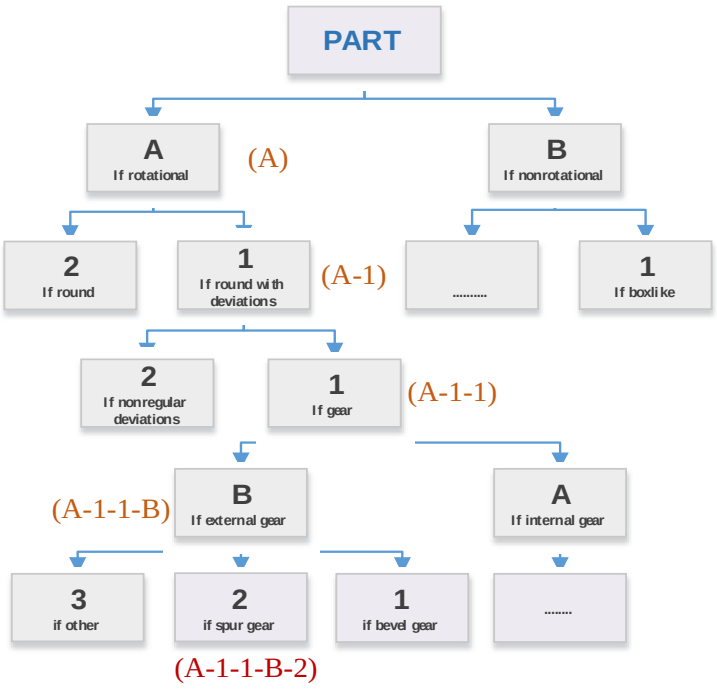

Fig. 1. Monocode Spur gear A-1-1-B-2

It is difficult to capture information on manufacturing sequences in hierarchical manner, so applicability of this code in manufacturing is rather limited.

Polycode (Atribute)

The code symbols are independent of each other. Each digit in specific location of the code describes a unique property of the workpiece. It is easy to learn and useful in manufacturing situations where the manufacturing process have to be described. The length of a polycode may become excessive because of its unlimited combinational features. [6]

The length of a Polycode may become excessive because of its unlimited combinational features. There are differences in information storage capacity between monocode and polycode.

Mixed code (Hybrid code)

In reality, most coding systems use a hybrid (mixed) code so that the advantages of each type of system can be utilized. The first digit for example, might be used to denote the type of part, such as gear. The next five positions might be reserved for a short attribute code that would describe the attribute of the gear. The next digit (7th digit) might be used to designate another subgroup, such as material, followed by another attribute code that would describe the attributes. There are 3 types of part classification & coding systems which are mostly use by organization. [6]

1. Optiz classification system
2. MICLASS system
3. Code system

Digit	Class of feature	Possible value of digits				
		1	2	3	4	---
1	External shape	Cylindrical without deviations	Cylindrical with deviations	Boxlike	---	---
2	Internal shape	None	Center hole	Brind center hole	---	---
3	Number of holes	0	1-2	3-5	---	---
4	Type of holes	Axial	Cross	Axial cross	---	---
5	Gear teeth	Worm	Internal spur	External spur	---	---
---	---	---	---	---	---	---

Fig. 5. Polycode Spur gear 22213

Some of the important systems:

- Opitz classification system – (The University of Aachen in Germany, nonproprietary, Chain type)
- Brisch System – (Brisch-Birn Inc.)
- CODE (Manufacturing Data System, Inc.)
- CUTPLAN (Metcut Associates)
- DCLASS (Brigham Young University)
- MultiClass (OIR: Organization for Industrial Research), hierarchical or decision-tree coding structure
- Part Analog System (Lovelace, Lawrence & Co., Inc.)

For the purpose of selecting or developing your own code, it is important to understand the attributes of classification and coding systems.

3. Group Technology and the Benefits Include

Group technology offers substantial benefits to companies that have the perseverance to implement it. The benefits include:

- GT promotes standardization of tooling, fixturing and setups.
- Material handling is reduced because parts are moved within a machine cell rather than within the entire factory.

- Process planning and production scheduling are simplified.
- Setup times are reduced, resulting in lower manufacturing lead times.
- Work-in-process is reduced.
- Worker satisfaction usually improves when workers collaborate in a GT cell.
- Higher quality work is accomplished using group technology.

4. Application Group Technology in Production

GT is most appropriately applied under the following conditions:

- The plant currently uses traditional batch production and a process type layout and these results in much material handling effort, high in-process inventory, and long manufacturing lead times.
- The parts can be grouped into part families. This is a necessary condition. Each machine cell is designed to produce a given part family or limited collection of part families, so it must be possible to group parts made in the plant into families.

The potential obstacles of GT classification:

Management Resistance to Change

- Unwilling to devote the time and energy.

Extensive Data Requirements

- The proper identification needs detailed item descriptions à extensive purchase records/data.

High Start-Up Cost

- Item characteristics are not available without the aid of automated information storage and retrieval systems which usually incur high expenses until GT is in place.

5. Conclusion

This paper introduces the main concepts we encounter when applied methodology of group technology classification and its benefits. There are many benefits and obstacles toward the use of group technology in an organization. All things considered, GT is viewed as an essential step in the move toward factory automation and necessary step in maintaining a high quality level and profitable production.

References

[1] BOE, W. J., CHENG, CH. H. *A Close Neighbour Algorithm for Designing Cellular Manufacturing Systems.* International Journal of Production Research, No.10/91, pp. 2097-2116.

[2] BURBRIDGE, J. L. *Production Flow Analysis.* Clarendon Press, Oxford, 1989.

[3] KURIC, I. *Form of automated proposal of process plans.* Habilitation work, University of Zilina, 1996.

[4] ASKIN, R. & STANDRIDGE, C. *Modeling and analysis of manufacturing systems.* New York, NY: John Wiley, 1993.

[5] SHAHIM, A., JANATYAN, N. *Group Technology and Lean Production: Conceptual Model for Enhancing Productivity.* International Business Research, October 2010.

[6] HASSAN, M. M. D. *Layout Design in Group Technology Manufacturing*. International Journal of Production Economics, Vol.38 No.2-3/1995, pp.173-188.

[7] HAM, I., HITOMI, K. & YOSHIDA, T. *Group technology application to production management.* Nijhoff, EN: Kluwer, 1985.

[8] WEMMER, L. & HYER, N. *Cellular manufacturing practice.* Manufacturing Engineering, 102(3), 79-82., 1985.

[9] KAČURÁK, M. *Filozofia skupinovej technológie.* Košice : Technická univerzita, Transfer inovácií 5/2002, str. 134-135., 2002.

[10] KOVÁČ, J. *Projektovanie výrobných procesov a systémov.* [online]. Košice : Technická univerzita, Edícia EQUAL, 2006. 125 s. [cit. 2015.01.02] Dostupné na internete: <http://www.sjf.tuke.sk/seminsky/IVS/PVPaS.pdf >. ISBN 80-8073-720-7, 2006.

TRANSCOM 2015, 22-24 June 2015
University of Žilina, Žilina, Slovak Republic

The Ultrasonic Testing of Welded Joint According to Standard STN EN 12732+A1

Daniel Dopjera, Miloš Mičian
University of Žilina, Faculty of Mechanical Engineering, Department of technological engineering,
Univerzitná 1, 010 26 Žilina, Slovakia, {daniel.dopjera, milos.mician}@fstroj.uniza.sk

Abstract. The article describes the ultrasonic testing of girth welded joint according to two reference curves. First curve is DAC Ø2 mm with gain of ultrasonic signal +8dB and second curve is DAC Ø3 mm. The lack of side-wall fusion was artificial made in girth welded joint. The ultrasonic testing was designed in software ESBeamTool 5 from the company Eclipse Scientific, which simulates the geometrical ultrasonic beams spread. The girth welded joint was testing with ultrasonic flaw detector OmniScan MX2 16:64 PA, from the company Olympus NDT. It was used Phased Array probe 5L16-A10 with plexiglas wedge SA10-N55S and gel EchoMIX^{TM}.

Keywords: NDT, Ultrasonic defectoscopy (testing), Phased Array.

1. Introduction

Ultrasonic defectoscopy is nondestructive testing (NDT) of materials able to detect surface and volume cracks. Ultrasound is defined as mechanical oscillation of particles about their equilibrium position in elastic medium with frequency greater than 20 kHz. Ultrasonic waves are created by spreading of biding forces of mechanical oscillation between particles. By mechanical oscillation of particles are divided into longitudinal, transverse and surface waves. Plate waves (symmetric and asymmetric) are created within thin materials.

2. Design and manufacture of sample

It was controlled girth welded joint on the gas pipe DN200 with outside diameter 219.1 mm and thickness ≈ 8 mm (Fig. 1). Material of gas pipe was ferrite steel (S355N).

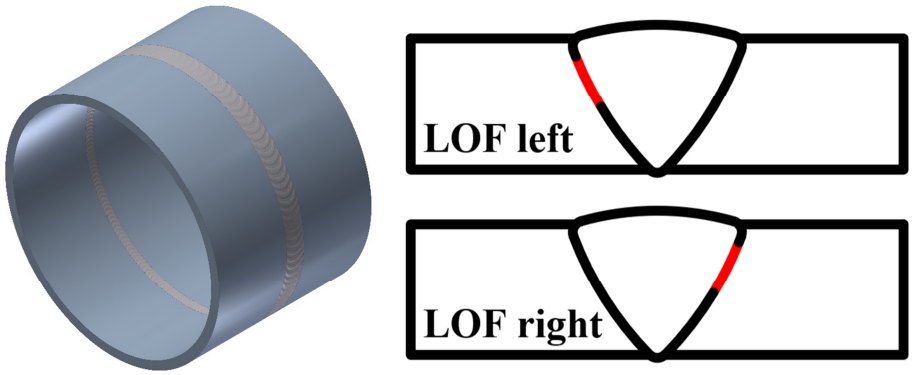

Fig. 1. Gas pipe DN200

In welded joint were artificially made two defects: first lack of side-wall fusion on the left side of welded joint and second lack of side-wall fusion on the right welded joint.

3. Designed of ultrasonic testing

For ultrasonic testing Phased Array was designed ultrasonic Phased Array probe 5L16-A10 (16 linear elements) with frequency 5 MHz and plexiglas wedge SA10-N55S (refracted shear waves in steel 55°). It was designed S-Scan (sectorial scan) from +40° to +70° for both side of welded joint. Index offset was 10 mm and it is distance the ultrasonic probe from the center of welded joint.

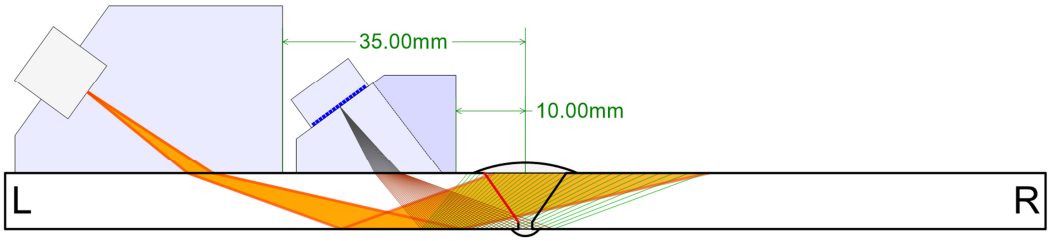

Fig. 2. The lack of side-wall fusion on the left side of welded joint L (A)

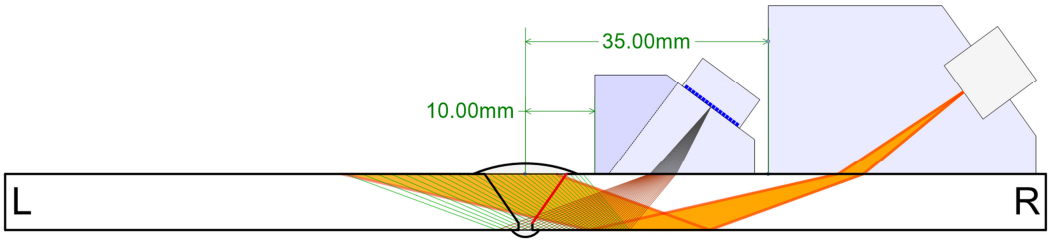

Fig. 3. The lack of side-wall fusion on the right side of welded joint R (B)

For conventional ultrasonic testing was designed ultrasonic probe C551-SM (diameter of element 10 mm) with frequency 5 MHz and plexiglas wedge ABWM-7T (refracted shear waves in steel 70°). Both ultrasonic probes were calibrated on the calibration block K1. It was used gel EchoMIX^{TM}. In the Fig. 2 and Fig. 3 we can see designed of ultrasonic testing.

4. The ultrasonic data

For both ultrasonic testing was used ultrasonic flaw detector OmniScan MX2 with module 16:64 PA (software MXU 4.1R12) and encoder with resolution 12 steeps.mm^{-1}.

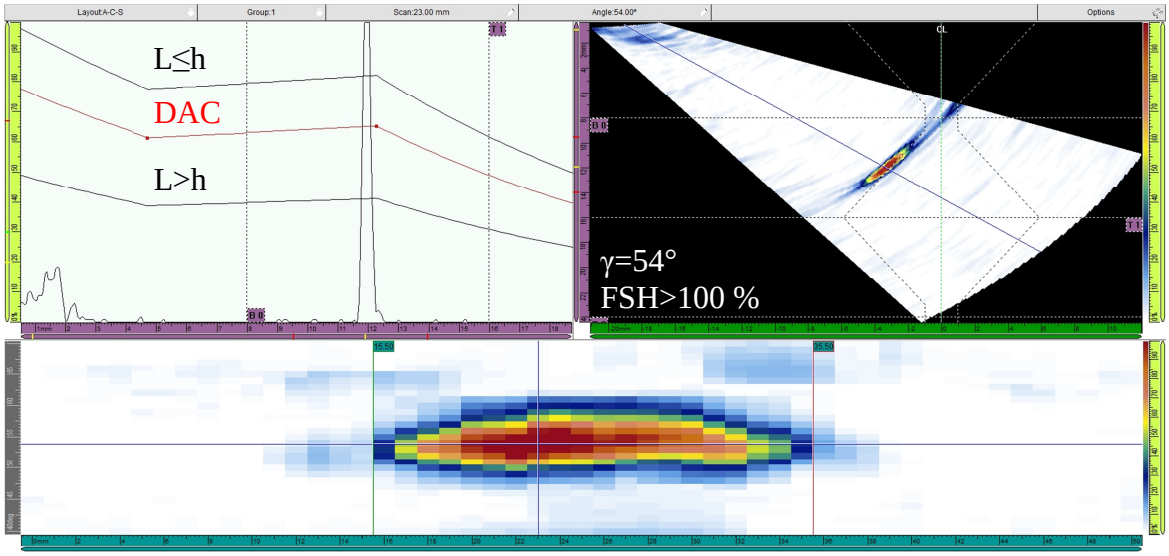

Fig. 4. The lack of side-wall fusion on the left side of welded joint, DAC Ø2 mm +8dB (A)

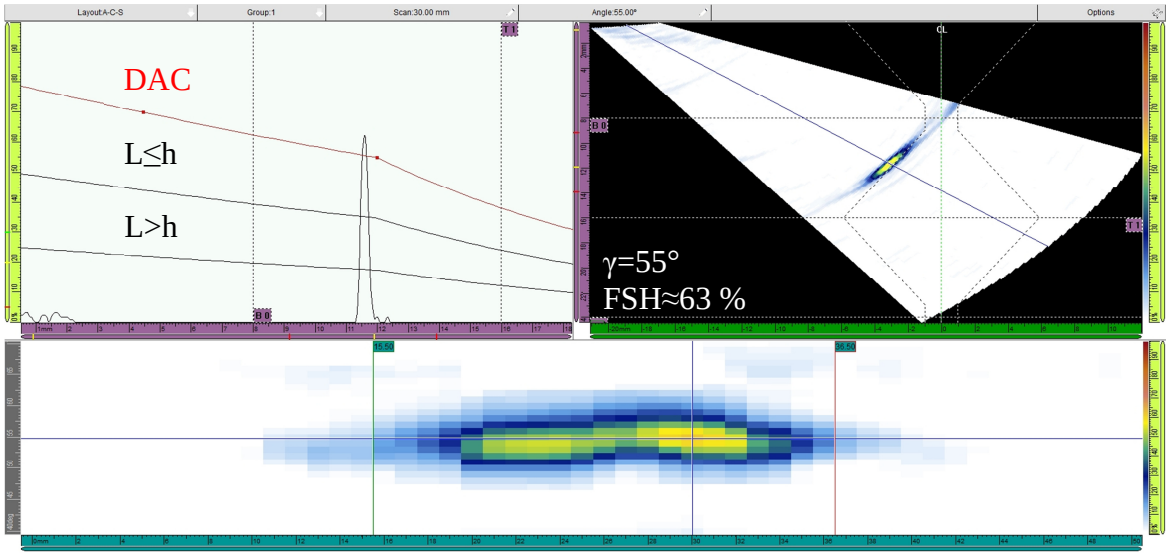

Fig. 5. The lack of side-wall fusion on the left side of welded joint, DAC Ø3 mm (A)

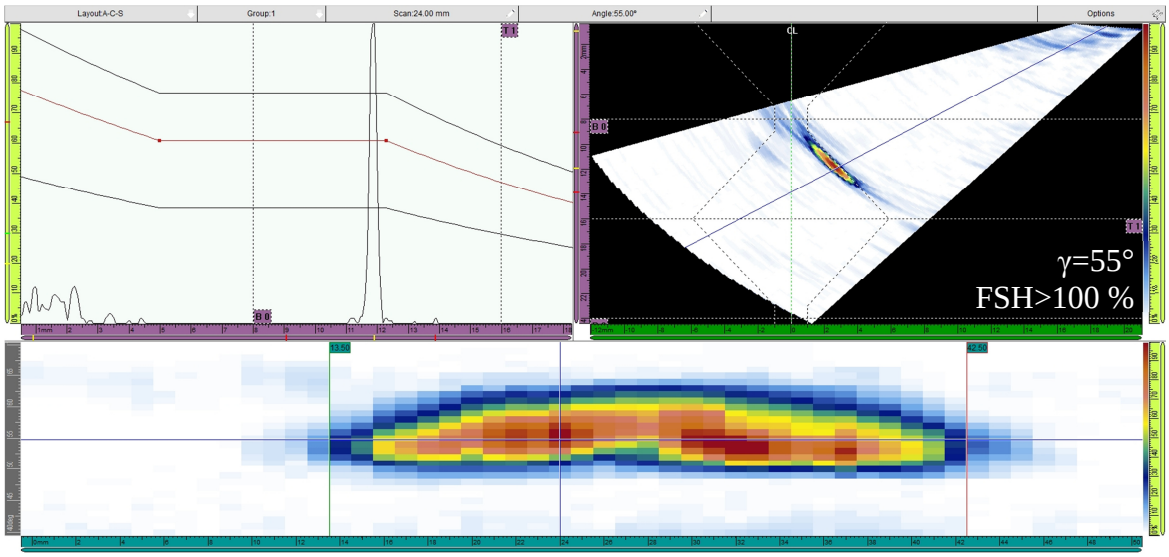

Fig. 6. The lack of side-wall fusion on the right side of welded joint, DAC Ø2 mm +8dB (B)

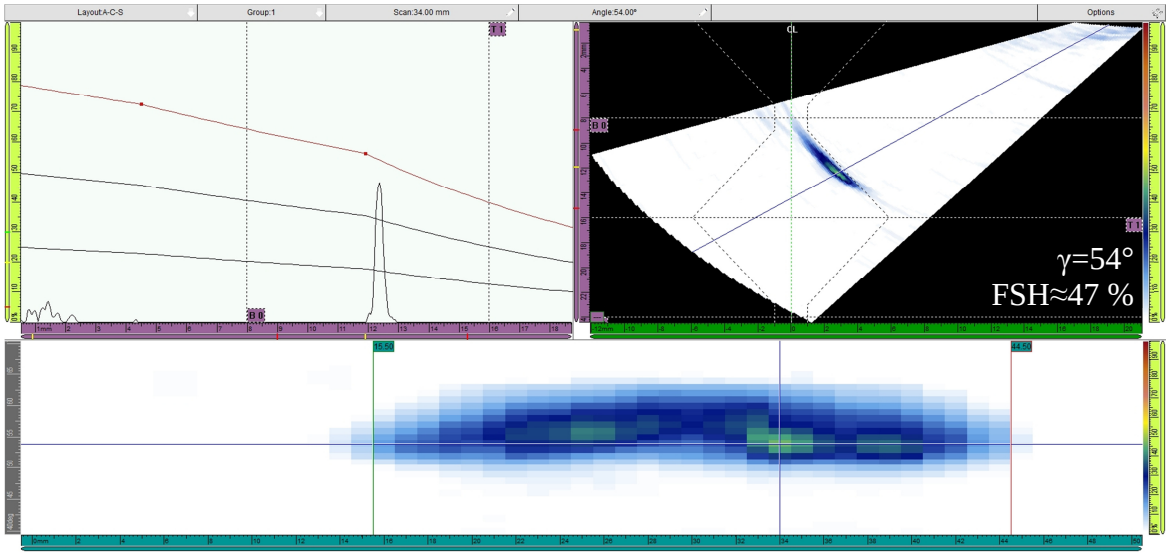

Fig. 7. The lack of side-wall fusion on the right side of welded joint, DAC Ø3 mm (B)

In the Fig. 4 and Fig. 5 we can see ultrasonic data from Phased Array, wherein welded joint was with lack of sidewall fusion on the left side. Phased Array probe detects this lack of sidewall fusion just from the left side of welded joint with reflected ultrasonic beam. From the right side of welded joint it is undetectable. The same is the case when lack of sidewall fusion is on the right side of welded joint (Fig. 6 and Fig. 7).

DAC curve	Level of admissibility 2	
	L≤h	L>h
Ø2 mm +8dB	+2 dB	−4 dB
Ø3 mm	−4 dB	−10 dB

Tab. 1 Level of admissibility 2

The indications were assessed according to curve DAC Ø2 mm with gain of ultrasonic signal +8dB (standard STN EN 12732+A1) and DAC Ø3 mm (standard ČSN EN ISO 17640). Standard STN EN 12732+A1 prescribes level of admissibility 2 (

Tab. **1**). Letter L is length of indication and letter h is thickness of material. Both indications were evaluated as unacceptable (

Tab. **2**).

Indication	DAC Ø2 mm +8 dB		DAC Ø3 mm	
	L [mm]	ČSN EN ISO 11666	L [mm]	ČSN EN ISO 11666
A	20	Unacceptable	21	Unacceptable
B	29		29	

Tab. 2 The evaluation of indications according to level of admissibility 2

Highest echoes were detected at angles 54 and 55°. The length of the indication was determined according to C–Scan. The conventional ultrasonic probe failed to detect both lack of side-wall fusion.

5. Conclusion

The orientation of defects is reason, why Phased Array probe does not detect lack of side-wall fusion on the opposite side. In the welded joint of gas pipelines are the most serious lack of side-wall fusion and they are unacceptable. These results show how must be tested the girth welded joint of pipe DN200 with thickness ≈ 8 mm. Ultrasonic testing must be carried from the both side of girth welded joint with Phased Array probe. Ultrasonic testing with conventional ultrasonic probe is inadequate.

References

[1] ČSN EN ISO 11666. 2011. *Nedestruktivní zkoušení svarů. Zkoušení ultrazvukem. Stupně přípustnosti.*
[2] ČSN EN ISO 16811. 2014. *Nedestruktivní zkoušení. Zkoušení ultrazvukem. Nastavení citlivosti a časové základny.*
[3] ČSN EN ISO 17640. 2011. *Nedestruktivní zkoušení svarů. Zkoušení ultrazvukem. Techniky, třídy zkoušení a hodnocení.*
[4] OLYMPUS. 2007. *Advances in Phased Array Ultrasonic Technology Applications.* Waltham, MA: Olympus NDT, 2007. ISBN 0-9735933-4-2.
[5] STN EN 12732+A1. 2014. *Plynárenská infraštruktúra. Zváranie oceľových potrubí. Funkčné požiadavky.*

TRANSCOM 2015, 22-24 June 2015
University of Žilina, Žilina, Slovak Republic

Effect of Cyclic Loading on the Internal Damping of AZ31 and AZ91 Magnesium Alloys

[*]Zuzana Dresslerová, [*]Peter Palček, [*]Mária Chalupová, [*]Milan Uhríčik
[*]University of Žilina, Faculty of Mechanical Engineering, Department of Material Engineering, Univerzitná 8215/1, 010 26 Žilina, Slovakia, {zuzana.dresslerova, peter.palcek, maria.chalupova, milan.uhricik}@fstroj.uniza.sk

Abstract. The article is focused on the analysis of the internal damping changes depending on the amplitude of the magnesium alloys AZ31 and AZ91 and their comparison. Internal damping reflects the ability of the material irreversibly dissipating mechanical energy oscillations. That means, the material of high internal damping ability is able to significantly reduce the vibration amplitude. Internal damping is generally dependent on many factors (temperature, material purity, grain size, mechanical and thermal processing, etc.) and its value is determined by interactions between various mechanisms dissipation of mechanical energy. In experimental measurements only ultrasonic resonance method was used. This method is based on continuous excitation of oscillations of the specimen, and the entire apparatus vibrates at a frequency which is near to the resonance. Starting resonance frequency for all measurements was about f = 20500 Hz.

Keywords: Magnesium alloy, internal damping, cyclic loading.

1. Introduction

Magnesium alloys are the lightest commercial alloys. Magnesium alloys are very attractive for automotive and electrochemical industry and their good combination of strength and damping make them usable also for other applications. Engineering magnesium alloys are used especially for production of light weight-walled casting, lockers in automotive engines, parts of mobile phones, cameras or notebooks, etc. Magnesium alloys have also good damping properties (belong to the group of the HIDAMETS materials – HIgh DAmping METals) [1, 2].

Effect of gradual storage of mechanical energy in the material causes a change of mechanical and physical characteristics, which can cause degradation of material properties such as: reduction of the machine tools accuracy, initiation of fatigue cracks, generation of noise and vibration in the working environment, changes of material properties, reduction of corrosion resistance, degradation of regulatory devices and sensors, eventually damage of entire device. Measurement of the internal damping allows monitoring the ongoing structural changes and various mechanisms [3, 4].

Dispersion of mechanical energy in the material is just a one of the ways energy transformation, for example conversion of mechanical energy into heat energy. Total internal damping affects a number of different, interacting and functioning factors, such as defects in the crystal structure, the movement of dislocations, plastic deformation, after slide of grain boundaries, elastodynamic and magnetoelastic phenomena. Their research contributes to the understanding and development of new, improved and more accurate technologies for materials according to current needs of different industries [5].

2. Experimental material

For experimental measurements of internal damping magnesium alloys AZ31 and AZ91 were used. Result of the spectrometer chemical analysis is shown in the Tab. 1. The AZ31 and AZ91

magnesium alloys were produced by the squeeze-casting method and were delivered without heat treatment.

Element		Al	Zn	Mn	Ca	Si	Fe	Cu	Mg
Content [wt. %]	AZ31	2.980	0.655	0.202	0.180	0.067	0.007	0.001	balance
	AZ91	7.280	0.554	0.202	0.001	0.007	0.008	0.001	balance

Tab. 1. Chemical composition of magnesium alloys AZ31 and AZ91.

The experimental material was submitted to metallographic analysis before measuring of internal damping, which allows obtaining information about the shape, size, type and quantity of structural components contained in the material, and thereby contributes to understanding of the ongoing processes in the material during cyclic loading.

The microstructure of the magnesium alloy was analyzed in as cast state and after homogenization annealing state. After squeeze casting the microstructure of material was dendritic (Fig. 1). In interdendritic regions was occurred inhomogenities and phase colonies of different type and origins, from which is the most important intermetallic phase $Mg_{17}Al_{12}$ [6, 7].

Heat treatment consisted of a homogenization annealing at 390 °C for 22 hours followed by quenching in the water with the purpose to obtain a solid solution of aluminum and zinc and other elements in the magnesium matrix. Almost all intermetallic particles were dissolved and the microstructure of the alloy was homogenized. The microstructure after annealing is created by polyedric grains and the grain boundaries are clearly visible. The homogenization annealing led to dissolution of intermetallic phases, diffusion equalizing of concentrations of alloying elements in the alloy and created polyedric structure (Fig. 2) [8].

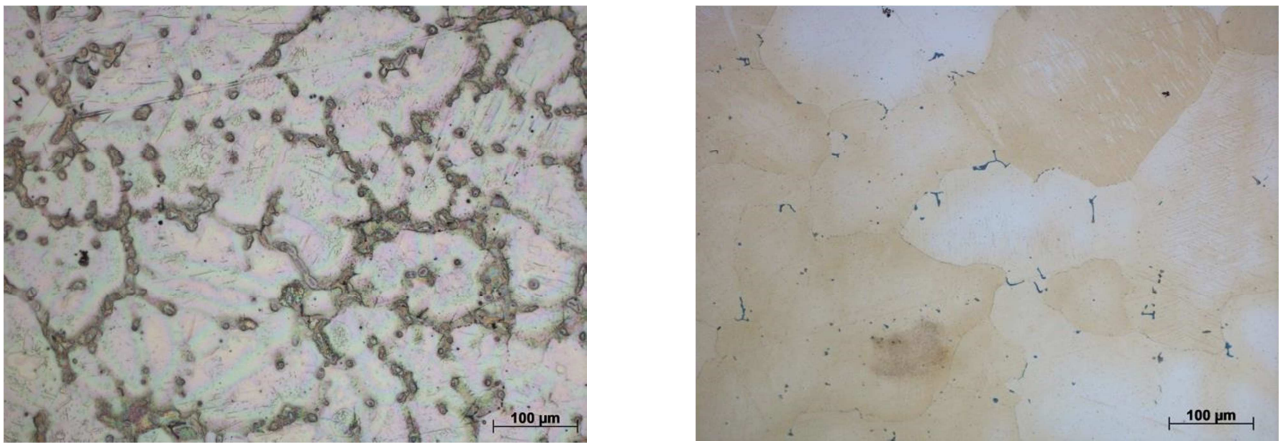

a) as cast state b) after homogenization annealing

Fig. 1. Microstructure of magnesium alloy AZ31, etch. Picral.

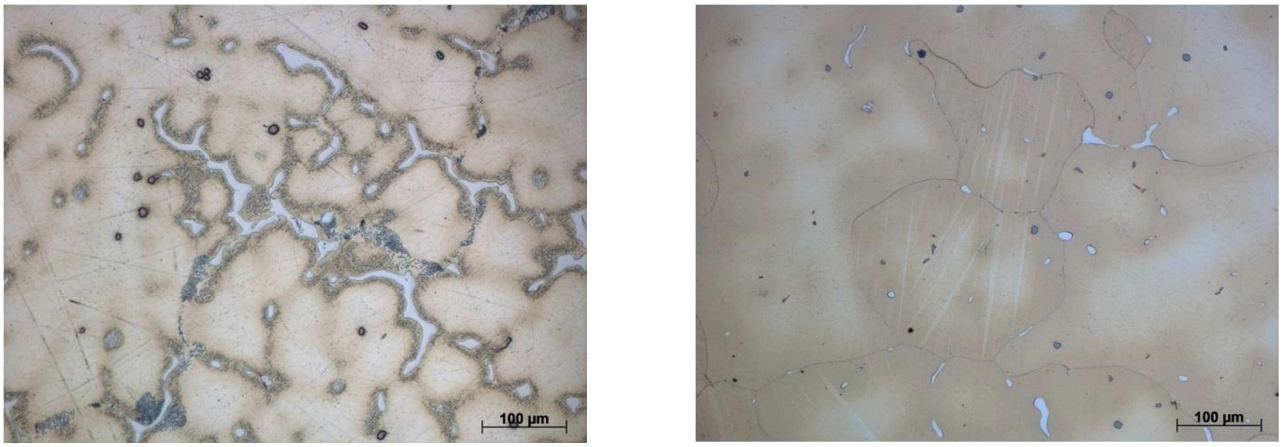

a) as cast state b) after homogenization annealing

Fig. 2. Microstructure of magnesium alloy AZ91, etch. Picral.

3. Experimental equipment and measurement method

The internal damping was measured using indirect ultrasonic method of determining the quality factor resonant system. This method is based on continuous excitation of oscillations of the specimen, and the entire apparatus vibrates at a frequency which is close to the resonance. Quality of the resonance system Q^{-1} is calculated by measuring the resonance peak (Fig. 3) and determining its width for 3 decibel level.

$$Q^{-1} = \frac{\Delta f_{r3dB}}{f_r}. \quad (1)$$

Where f_r is resonant frequency [Hz], $\Delta f_{r3dB} = f_2 - f_1$ is width of resonance curve for 3 decibel level [Hz].

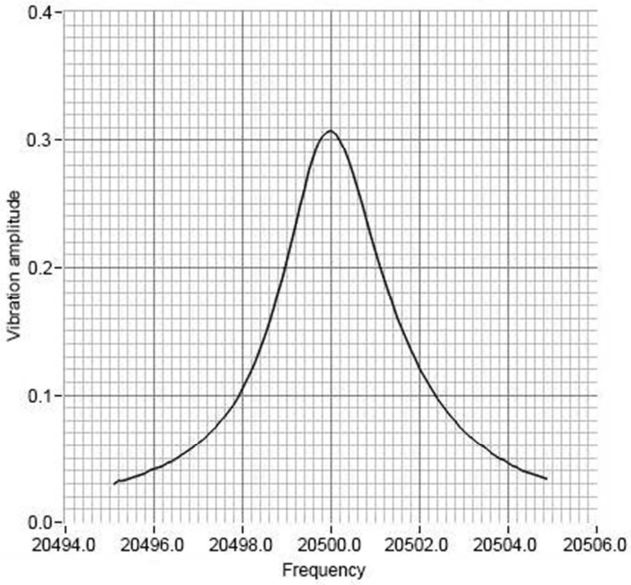

Fig. 3. Characteristic resonance curve.

The original experimental equipment (Fig. 4) consists from electronic and mechanical part. One of the electronic parts is generator which produces a sine wave. The electric signal is then amplified and transformed into a mechanical wave by using the piezoceramic transducer. The ultrasonic wave is amplified in aluminium horn and spreads into the specimen by the titanium rod. After passing through the specimen the wave is reflected at the free end and spreads back through the entire device. The amplitude of resulting oscillations is measured by multimeter.

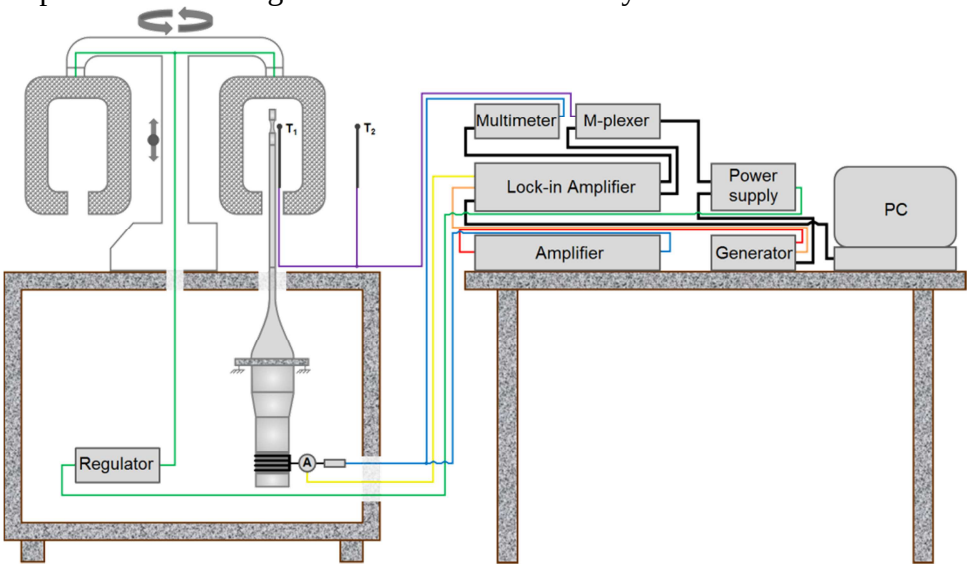

Fig. 4. Ultrasonic resonance device for internal damping measurement.

The mechanical part is the core of the whole apparatus, consists of:

- Transducer is the most difficult part of the mechanical apparatus, which serves like the source and at the same time like the detector of ultrasonic waves.
- Rod, which is made of titanium and has a cylindrical shape with a diameter of 12 mm. Its function is to isolate the heat from the specimen, which is heated in a furnace and the transducer then maintains at a constant room temperature.
- The last part is specimen. Dimensions and shape of the specimen are designed to fulfill the resonance condition that means the natural frequency must be approximately the same like the frequency of the test equipment.

4. Measurement results

Internal damping depending on the vibration amplitude was measured on specimens in as cast state and after homogenization annealing. Vibration amplitude of the input excitation voltage was 100 mV. The measurement was performed at room temperature (20 ° C) in increments of 50 mV to the finally chosen excitation voltage. In the Fig. 5, there are shows the results of measurement of the internal damping depending on the vibration amplitude of the magnesium alloy AZ31 and AZ91 in as cast state and after homogenization annealing. The first measurement was carry out on the specimen in as cast state, then the same specimen was homogenization annealed and the measurement was repeated. Value of internal damping for alloy AZ31 was at the beginning of the measurement $Q^{-1} = 1.85.10^{-4}$ and for alloy AZ91 $Q^{-1} = 1.78.10^{-4}$. With increasing of excitation voltage the internal damping at first decreased and at vibration amplitude 0.28 there was a linear increase of the internal damping in both materials. At the same amplitude oscillations the magnesium alloy AZ31 reached slightly higher values of internal damping. Point of the curve from which there is an increase of internal damping represents the transition from the elastic range behavior of the material to mikroplastic range behavior and it is described as second critical amplitude of deformation.

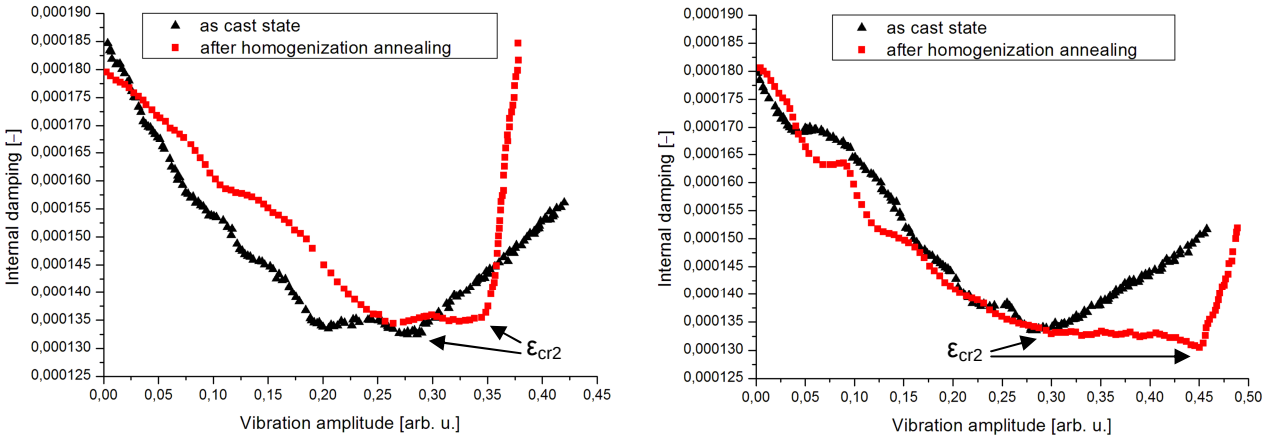

a) AZ31 b) AZ91

Fig. 5. Results of measurement of the internal damping depending on the vibration amplitude of the magnesium alloy.

The initial value of the internal damping after heat treatment was approximately the same as in as cast state. With increasing of excitation voltage, as in the previous case, the internal damping at first had a downward trend, but there was a difference in their growth. By comparing the measurements of the internal damping in as cast state and the measurements after homogenization annealing, we can see that an increase of the internal damping after homogenization annealing was occurred at higher vibration amplitudes and this increase was steeper.

5. Conclusion

Based on experimental results from internal damping measurement of AZ31 and AZ91 magnesium alloys can be stated:

- The value of the first critical amplitude of deformation ε_{cr1} (from which are beginning to amplitude-dependent mechanisms) wasn't recorded during any measurement.
- With increasing of excitation voltage the internal damping in both materials in as cast state and after homogenization annealing at first decreased.
- After reaching a certain vibration amplitude was occurred linear increase of the internal damping, which can be explained that it has reached the second critical amplitude of deformation ε_{cr2}.
- At the same vibration amplitude in as cast state the magnesium alloy AZ31 achieve greater value of internal damping than the magnesium alloy AZ91.
- After heat treatment, the second critical amplitude of deformation ε_{cr2} shifted to higher vibration amplitudes and the increase of the internal damping was steeper than in as cast state.

Acknowledgement

This work has been supported by Scientific Grant Agency of Ministry of Education of Slovak Republic and Slovak Academy of Sciences N°1/0683/15 and by project APVV SK-CZ-2013-0076.

References

[1] SCHALLER, R., FANTOZZI, G., GREMAUD, G. *Mechanical spectroscopy Q^{-1} 2001 with applications to materials science.* Switzerland Trans Tech Publications, 2001, 683p. ISBN 0-87849-876-1.

[2] ZHANG, Z., ZENG, X., DING, W. *The influence of heat treatment on damping response of AZ91D magnesium alloy*. In: Materials Science and Engineering, vol. 392, issues 1 - 2, 2005. p.150 - 155. ISSN 0921-5093.

[3] GRANATO, A. V., LÜCKE, K. *Theory of mechanical damping due to dislocations*. In: Journal of Applied Physics, vol. 27, issue 6, 1956a. s. 583 - 593. ISSN 1089-7550.

[4] PUŠKÁR, A. *Vnútorné tlmenie materiálov*. Žilina: EDIS, 1995, 382p. ISBN 80-7100-260-7 (in Slovak).

[5] BLANTER, M. *Internal Friction in Metallic Materials*. Springer - Verlag: Berlin Heidelberg, 2007, 539p. ISBN 3-540-68757-2.

[6] DRESSLEROVÁ, Z., PALČEK, P. *Temperature Dependence of the Internal Friction Measured at Different Excitation Voltages*. Manufacturing Technology, October 2014, vol. 14, no. 3, p. 287-290. ISSN 1213-2489.

[7] SOVIAROVÁ A., DRESSLEROVÁ Z., PALČEK P., CHALUPOVÁ M. *Influence of precipitation on internal damping of AZ61 alloy*. Advanced manufacturing and repairing technologies in vehicle industry: 30th international colloquium: 22-24 May 2013, Visegrád, Hungary. Budapešť: BME, 2013. p. 153-158. ISBN 978-963-313-079-7.

[8] SOVIAROVÁ A., PALČEK P., BLAŽEK D., CHALUPOVÁ M. *Analysis of Dependence of Internal Friction on temperature of Magnesium Alloy with Aluminium Addition.* Period. Polytech. Transp. Eng. 2014, vol 42, no. 2, p. 139-143. ISSN 1587-3811.

TRANSCOM 2015, 22-24 June 2015
University of Žilina, Žilina, Slovak Republic

Influence of Tool Wear and Sample Hardness on Barkhausen Noise after Hard Turning

[*]Zuzana Durstová, [*]Miroslav Neslušan
[*]University of Žilina,Faculty of Mechanical Engineering, Department ofMachining and Manufacturing Technology, Univerzitná 1, 01026 Žilina, Slovakia, {Zuzana.Durstova, Miroslav.Neslusan}@fstroj.uniza.sk

Abstract. The paper deals with nondestructive evaluation of hard turned surfaces via Barkhausen noise (BN) technique. The paper is focused on investigation of tool wear as well as sample hardness. Surface integrity is expressed in terms of BN features such as effective BN, Peak Position and Full Width at Half Maximum (FWHM). Moreover, BN envelopes extracted from the raw BN signal is also discussed. Results of experiments indicate that surfaces heat treated to hardness 40 HRC exhibit much higher sensitivity of BN features along with progressively developed flank wear VB as opposed to samples of hardness 62 HRC.

Keywords: Tool wear, hard turning, Barkhausen noise.

1. Introduction

Bearing steel components are widely used in heavy mechanical industry e.g. aerospace, automotive, etc. These components are subjected to severe operating conditions such as high loads, high speed, extreme temperatures and hostile environments [1]. Since most mechanical components produced by hard turning and grinding are widely used in rolling contact applications, the fundamental knowledge of fatigue damage mechanism is necessary for understanding manufacturing process effects [2]. Hard turning is a developing technology that offers many potential benefits compared to grinding, which remains the standard finishing process for critical hardened steel surfaces. Some decisive factors leading to this manufacturing trend are: substantial reduction of manufacturing costs, decrease of production time, improved surface integrity, reduction or elimination of environmentally harmful cooling media and part distortion caused by heat treatment [3]. However, hard turning can introduce modifications within the surface layer of a workpiece. These modifications are metallurgical transformations as a result of intense, localized and rapid thermo-mechanical loading. The surface layer can show an extremely different structure from the bulk material due to the white layer formation or featureless in a scanning electron microscope. It is referred to as untempered martensite and characterized by an increase in hardness than the bulk material. The mechanism of white layer formation is attributed to severe plastic deformation, which produces a homogenous structure or one with a very fine grain size, and/or rapid heating and quenching, which results in phase transformation [1].

Hard turning owes its popularity primarily to the capability of generating complex geometric surfaces with better form accuracy and improved tolerances in one single machining pass. Previous decades of manufacturing research on hard turning have focused on finding out the influence of tool geometry, tool wear, cutting temperature, and cutting forces [4]. Moreover, monitoring of hard turned surface is a non destructive manner has not been developed yet as opposed to grinding. BN is a physical phenomenon produced by irreversible and discontinuous Bloch Walls (BW) motion in ferromagnetic materials due to pinning strength of microstructure constituents such as dislocation tangles, carbides or precipitates as well as stress state. The concept in which such technique is adopted in the real industrial application is based on the higher magnitude of BN (produced by over tempered surfaces) due to thermal softening as a result of decreased dislocation density, carbides coarsening and tensile stresses. All these aspects contribute to the higher BN compared with the low

BN of thermally untouched surfaces [5]. Surface state after hard machining is a function mainly of flank wear *VB* and cutting speed. Application of a tool of high *VB* produces relative thick (WL) as well as the corresponding heat affected zone (HAZ) [6]. On the other hand, grinding cycles produces usually WL free surfaces. HAZ of ground surfaces increases magnitude of BN compared to bulk whereas WL in the near-surface region emits poor BN due to existence of higher volume of retained austenite, compressive stresses and very fine grain [7]. Being so, relation BN versus VB for turning cycles is not always monotonous thus making application of BN for hard turned surfaces a debatable issue. This paper very briefly reports about some aspects of hard turned surface from the point of view of BN features (as they develop along with flank wear VB).

2. Experimental Conditions

Experiments were conducted on samples made of steel 100Cr6 of hardness 62 and 40 HRC. Rings of diameter 55 mm and 10 mm in width were hard turned by inserts of variable flank wear VB (in the range 0,05 to 0,8 mm, see Fig. 1). Cutting and other conditions: lathe SUI 40, dry cutting, cutting tool made of CBN DNGA 50408, a_p = 0,25 mm, f = 0,09 mm, v_c = 100 m.min^{-1}.

BN measurement was performed by the use of RollScan 300 and software package MicroScan (mag. frequency 125 Hz, mag. voltage 10 V). Each BN value was determined by averaging of 10 consecutive BN bursts (5 magnetizing cycles). BN values indicated in the paper represent the effective (rms) value of BN signal.

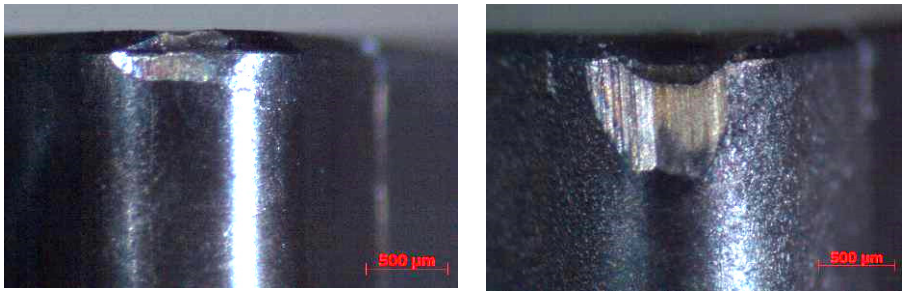

a) VB = 0,2 mm b) VB = 0,8 mm

Fig. 1. Illustration of flank wear.

3. Results of Experiments

Fig. 2 illustrates evolution of BN (effective) values versus progressively developed VB. As it was mentioned above, hard turned surface undergoes severe plastic deformation at elevated temperature. It is well known that as VB increase in size WL also increase in thickness. However poor BN emission of WL is due to high dislocation density, fine grain and compressive stresses WL is compensated BW alignment in direction of cutting speed [8]. Being so, BN values stay nearly untouched versus VB and gentle increase for VB = 0,8 mm is due to transformation of negative geometry (to neutral) and corresponding release of stress field ahead the cutting edge. On the other hand, thermally softened structure represented by samples of hardness 40 HRC is more sensitive to rehardening effect. As Fig. 2 demonstrates, BN values fall down; attain the minimum and gently increase for surfaces produced by insert of more developed VB. Peak Positions, shown in Fig. 3, corresponds with BN values. Higher hardness of samples hardened on 62 HRC corresponds with the higher Peak Positions as that found in Fig. 3. This figure also shows that Peak Position stays nearly untouched along with more developed VB and moderate increase (drop) can be found as soon as tool geometry is altered due to macroscopic tool breakage (for VB = 0,8 mm), see also Figs. 5 and 6. On the other hand, much remarkable increase of FWHM was detected for samples made of 40 HRC, see Fig. 4. This aspect corresponds with more remarkable changes of effective values (for 40 HRC) indicated in Fig. 2.

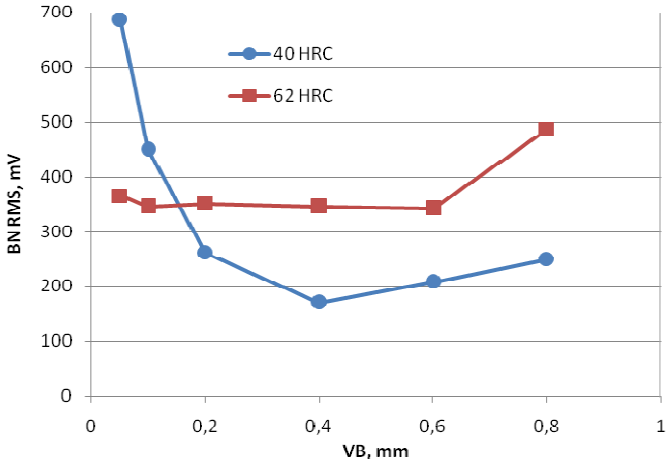

Fig. 2. RMS values of BN versus VB.

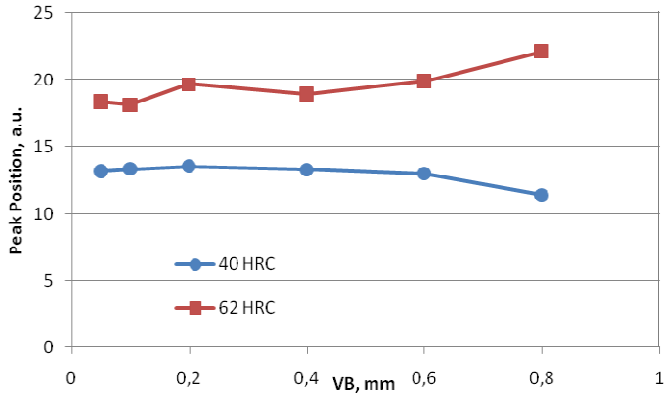

Fig. 3. Peak position of BN versus VB.

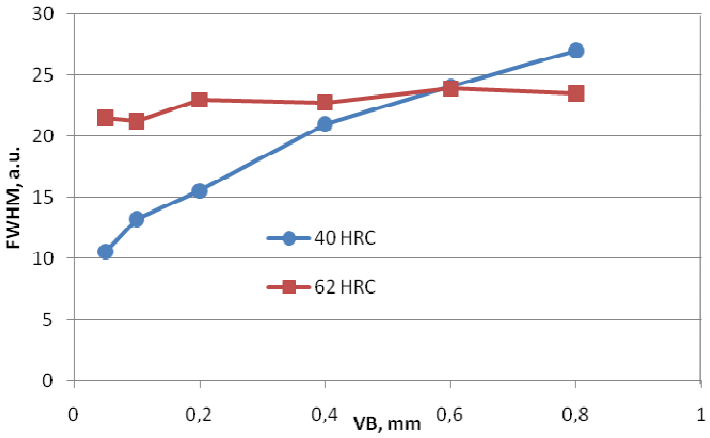

Fig. 4. FWHM values of BN versus VB.

It is well known that machined surface during hard turning undergoes severe plastic deformation. It means that machined process should exhibit specific features typical for strengthened surface. Fig. 4 demonstrates that such effect is minor is the case of surfaces of higher hardness whereas much remarkable increase for samples of hardness 40HRC can be found. FWHM is usually connected with various microstructure features and constituents occurring in the BN sensitive layer as well as the distribution in which they occur (usually corresponds to the normal Gauss distribution). Progressive increase of FWHM for 40 HRC indicates that BN sensitive layer contains near surface rehardened layer, deeper thermally softened as well as untouched structure in deep region. As the thickness of WL and HAZ increase in thickness along with more developed VB FWHM also exhibits remarkable increase due to more steep structure gradient, see Fig. 4.

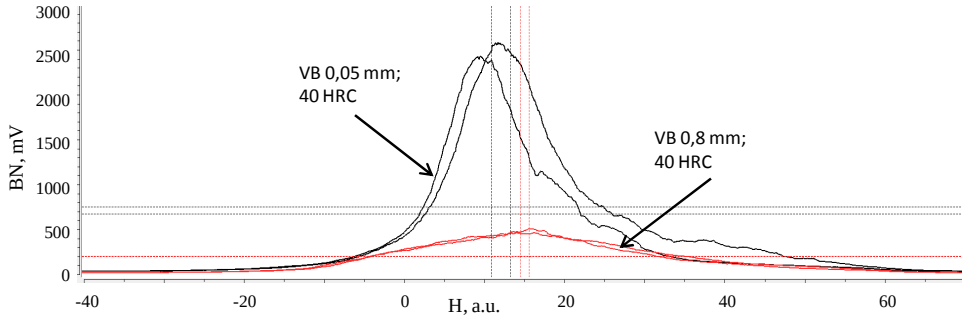

Fig. 5. BN envelopes, 40HRC.

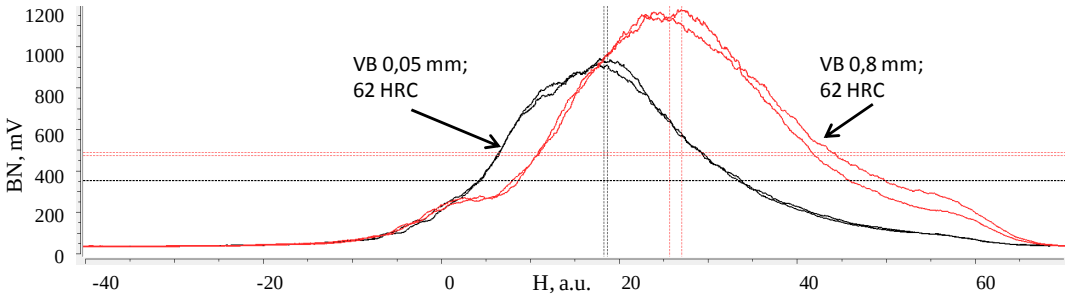

Fig. 6. BN envelopes, 62 HRC.

4. Conclusions

Hard turning operations produce a quite sophisticated state of machined surface as opposed to grinding. Evaluation of hard turned surfaces in nondestructive manner via BN technique is currently very difficult. Due remarkable magnetic and stress anisotropy BN signals after hard turning exhibit specific features. Any reliable concept for monitoring hard turned surface needs further thorough research and understanding of specific mechanism linked with structure features.

Acknowledgement

This project is solved under the financial support of KEGA agency (projects n. 005ŽU and n. 009ŽU - 4/2014).

References

[1] JOUINI, N., REVEL, P., MAZERAN, P. E., BIGERELLE, M. *The ability of precision hard turning to increase rolling contact fatigue life.* Tribology International, 2013.

[2] GUO, Y. B., WARREN, A. W. *The impact of surface integrity by hard turning vs. grinding on fatigue damage mechanisms in rolling contact.* Surface and Coatings Technol., 2008.

[3] BOUACHA, K., YALLESE, M. A., KHAMEL, S., BELHADI, S. *Analysis and optimization of hard turning operation using cubic boron nitride tool.* Internat. J. of Refractory Metals and Hard Materials, 2014.

[4] AGRAWAL, A., GOEL, S., RASHID, W., PRICE, M. *Prediction of surface roughness during hard turning of AlSi 4340 steel (69 HRC).* Applied Soft Computing, 2015.

[5] MIČÚCH, M., ČILLIKOVÁ, M., NESLUŠAN, M., MIČIETOVÁ, A.: *Micromagnetic study of cutting conditions and grinding wheel wear influence on surface integrity.* Manufacturing Technology, 2014.

[6] BRANDT, D.: *Randzonenbeeinflussung beim Hartdrehen*. Dr.-Ing. Dissertation, Universität-Hannover, 1995.

[7] GUO, Y.B., SAHNI, J.: *A comparative study of hard turned and cylindrical ground white layers.* Internat. Journal of Machine Tool & Manufacture, 2004.

[8] NESLUŠAN, M., et. all.: *Magnetic anisotropy in hard turned surfaces.* Acta Physica Polonica, 2014.

TRANSCOM 2015, 22-24 June 2015
University of Žilina, Žilina, Slovak Republic

Determining the Critical Value of Fracture Toughness Using the Measurement of the Stretch Zone Width

*I. Dzioba, **P. Furmańczyk
*Kielce University of Technology, Faculty of Mechatronics and Mechanical Engineering, Department of Machine Design, al. Tysiąclecia Państwa Polskiego 7, 25-314 Kielce, Poland, pkmid@tu.kielce.pl
** Kielce University of Technology, Faculty of Mechatronics and Mechanical Engineering, Department of Applied Computer Science and Armament Engineering, Laboratory of Scanning Electron Microscopy and Energy Dispersive X-Ray Spectroscopy, al. Tysiąclecia Państwa Polskiego 7, 25-314 Kielce, Poland, pfurmanczyk@tu.kielce.pl

Abstract. The paper presents the methods of calculating the value of the integral-J_i, when the crack initiation. Based on measurements of the stretch zone width according to several proposals suggested in the literature. It also identified the most universal method for calculating the integral- J_i.

Keywords: stretch zone width, crack initiation, J-integral

1. Introduction

A lot of attention has been paid in fracture mechanics to the methods for determining critical fracture toughness, i.e., the value at which the crack starts propagating in the elastic plastic material. The methods and standards relating to the determination of the critical fracture toughness value are based on various fracture process parameters: the J integral - J_{IC} [1], crack tip opening displacement, δ_C, [2] and stretch zone width (*SZW*), Δa_{SZWc} [3]. Figure 1 shows the J_R resistance curve with the location of fracture toughness critical parameters marked on it. Each of the fracture toughness parameters can be used to evaluate the fracture process up to the subcritical crack initiation.

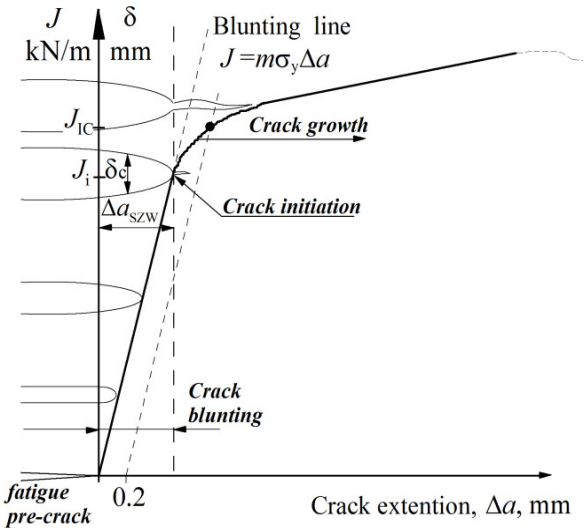

Fig. 1. Plot of crack extension and J_R curve for elastic plastic material [6].

In this segment of the crack extension the crack tip blunting takes place, and the relationships between fracture toughness characteristics are expressed by the formulas [4]

$$\delta = d_{\mathrm{n}} \frac{J}{\sigma_{\mathrm{y}}}, \tag{1}$$

$$\delta = 2 \cdot \Delta a_{\mathrm{SZW}}, \tag{2}$$

which makes it possible to calculate the value of J integral at the moment of crack initiation from the formula

$$J_{\mathrm{i}} = \frac{2\sigma_{\mathrm{y}}}{d_{\mathrm{n}}} \Delta a_{\mathrm{SZW_c}}. \tag{3}$$

In formulas (1) and (2), σ_{y} is the yield point, d_{n} is the function that depends on the yield point and the strengthening coefficient, n, according to Ramberg-Osgood law [4]. In a number of works discussed below, coefficient λ instead of $1/d_{\mathrm{n}}$ was introduced and/or $\sigma_{\mathrm{f}} = 0.5(\sigma_{\mathrm{y}}+\sigma_{\mathrm{u}})$ instead of σ_{y} [5]. The critical value of the J integral, J_{IC}, is determined for the blunting crack gain, $\Delta a = 0.2$ mm [1]. This value is usually higher than that at the moment of initiation, J_{i}. Determining the critical fracture toughness at the moment of initiation, J_{i} using the measurement of the critical width Δa_{SZWc} is laborious and only possible with specialised equipment (high performance scanning or optical microscope) and qualified technicians. For these reasons the method is rarely used even though it is able to evaluate the fracture toughness of a material exclusively based on the analysis of the fracture surface of the element with no tests conducted, which is very important while analysing damaged parts.

This paper presents the overview of methods used to determine the value of J integral – J_{i} at the moment of the crack initiation, and discusses the basic components of the method.

2. Development of the fracture toughness measurement method based on SZW

The stretch zone is the area between the fatigue pre crack zone and the crack extension zone. On the SEM images the stretch zone width appears as a mild transition between the fatigue pre crack zone and the crack extension zone, which in the cross section of the fracture surface resembles an “elongated” undercut (fig.2) [7].

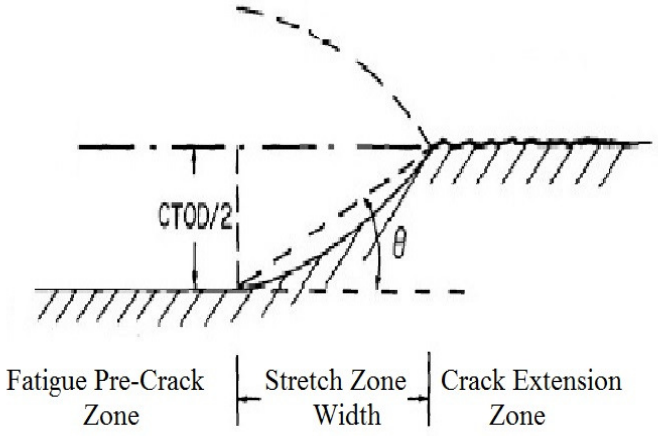

Fig. 2. Graphical representation of the relationship between the CTOD and the SZW [7]

Many researchers have reported that there is a relationship between the width of the stretch zone and the crack tip opening displacement, δ [7]. In the graphical representation of the tip opening displacement model, the stretch zone width (Δa_{SZW}) constitutes half of the crack tip opening displacement, that is

$$CTOD = 2\Delta a_{SZW}\,. \tag{4}$$

The relationship between the J integral, the crack tip opening displacement (CTOD) and the stretch zone width in the general case takes the following form [5]

$$\Delta \bar{a}_{SZW} = \frac{CTOD}{2\tan\theta} = \frac{J}{2\lambda\sigma_f \tan\theta}, \tag{5}$$

where σ_f - the coefficient defined at formula 3, λ - the coefficient defined below, θ – the angle between the stretch zone and the horizontal line.

Calculations made by Japanese researchers [3,5,10] to find the value of the J integral using the measurement of the SZW are based on the plots of the blunting line. The measurement of the crack extension (Δa) is replaced with the measurement (Δa_{SZWc}), conducted in scanning electron microscopes (SEM) with an assumption made that angle θ =45°. The Japan Society of Mechanical Engineers (JSME) has published the procedure of the method [3]. The JSME recommends measuring SZW at three points: 3/8*B*, 4/8*B* and 5/8*B* (*B* – specimen width) [3].

European guidelines published by ESIS and GKKS propose 9 measurement points located along the specimen width, *B*. They do not specify the precise location of those points, recommending the measurements to be made from the cross sectional axis of the specimen or in the vicinity of the axis [8,9].

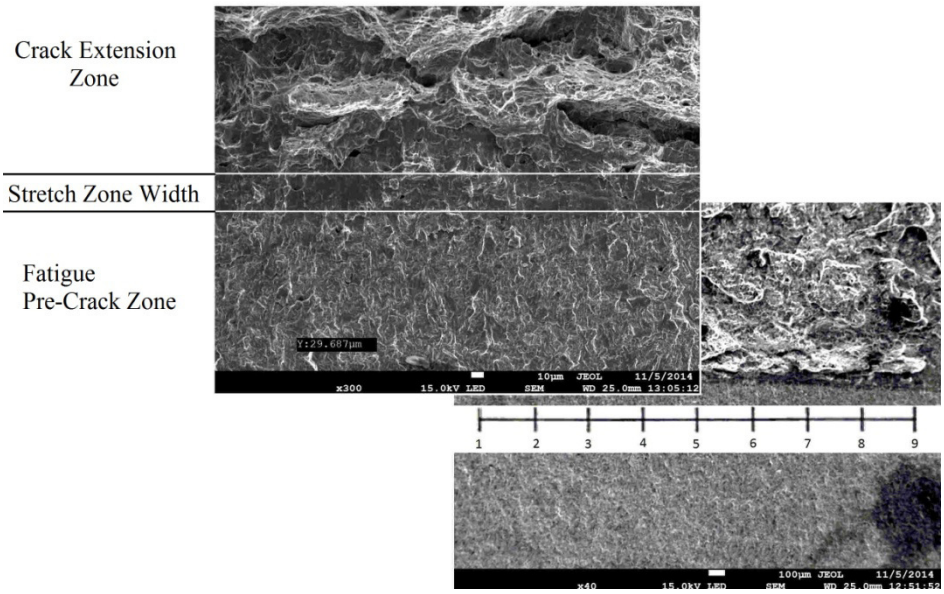

Fig.3. SEM images of the SZW measurement made to GKKS and ESIS.

The SZW measurements have to be averaged in compliance with [3,8,9]:

$$\Delta \bar{a}_{SZW} = \frac{i}{j}\sum_{i=1}^{j} \Delta a_{SZW_j}\,, \tag{6}$$

where j is the number of measurement points.

Calculations of the J integral at the moment of crack initiation J_i, based on the measurement of the stretch zone width can be made in according to several proposed procedures suggested in the literature.

According to the JSME, the value of J_i *is* calculated as follows [3,5,10]

$$J_i = \lambda\sigma_f \Delta \bar{a}_{SZW}\,, \tag{7}$$

where σ_y is the yield point, λ is the experimentally determined coefficient with value in the range 2-4. The value of the λ coefficient depends on the material tested; lower coefficient value corresponds to the higher values of the yield point [10]. Suggestions included taking constant values $\lambda = 4$ (Miyamoto) [11] or $\lambda = 3$ (Chinese Standard GB2038-80) [11].

Based on the experimental studies of the relationship between the SZW and the value of J_i Kobayashi proposed the following formula [12]:

$$J_i = \frac{E}{C}\Delta\bar{a}_{SZW}, \tag{8}$$

where E is Young's modulus, C is the experimentally determined coefficient, with the value in the range from 54.7 to 147, and the recommended value C= 89 [12].

The J_i can also be calculated from the formula derived from the relationship between the J integral and the crack tip opening displacement [13].

$$J_i = \frac{2\sigma_y \Delta\bar{a}_{SZW}}{d_n}, \tag{9}$$

where d_n is the coefficient dependent on the strengthening coefficient n from the Ramberg-Osgood equation and the yield point σ_y [4].

3. Conclusion

This paper describes the method for the measurement of the stretch zone width and the calculation of the J integral at crack initiation, J_i. The literature review indicates that formula (9) is the most universal. This is a result of formula (9) containing coefficient-function d_n, which is not a constant value but depends on the yield point and the strengthening coefficient n of the material tested. The dependence of those parameters on the characteristics of the material makes formula (9) universal, and the other formulas with constant coefficients may then be more suitable for use with materials of particular properties.

References

[1] ASTM E1820-09. Standard Test Method for Measurement of Fracture Toughness. Annual book of ASTM standards, 03,01, 2011 p.1070-1118,
[2] ASTM E1737-96. Standard Test Method for J-Integral Characterization of Fracture Toughness. Philadelphia 1996.
[3] JSME S 001-81. Standard Method of Test for Elastic-Plastic Fracture Toughness J_{IC}. JSME Standard, Japan 1981.
[4] NEIMITZ A. Mechanika Pękania. PWN. Warszawa 1999.
[5] KOBAYASHI H. NAKAMURA H., NAKAZAWA H. Evaluation of Blunting Line and Elastic-Plastic Fracture Toughness. ASTM STP 803. 1983. p. 420-438.
[6] DZIOBA I. Modelowanie i analiza procesu pękania w stalach ferrytycznych. Wydawnictwo Politechniki Świętokrzyskiej. Kielce 2012.
[7] NGUYEN-DUY PHUC. Relationship Between Critical Stretch Zone Width, Crack-Tip Opening Displacement, and Fracture-Energy Criterion: Application to SA-516-70 Steel Plates. Fracture Mechanics. ASTM STP 743. 1981. p. 543-552
[8] ESIS Procedure for Determining the Fracture Behaviour of Materials. ESIS P2-92. Appendix 4. p.A4.1-A4.6, 1992.
[9] SCHWALBE K.-H. LANDES J.D. HEERENS J. Classical Fracture Mechanics Methods. GKSS 2007/14.2007
[10] MIYAMOTO H., KOBAYASHI H., OHTSUKA N. Elastic-Plastic Fracture Toughness J_{IC} Test Method Recommended in Japan.,1985 p.550-558.
[11] ZU-HAN LAI, CHANG-XIANG MA. Comparison of Several Methods of J_{IC} Determination. Engineering Fracture Mechanics Vol. 22. 1985. p. 1117-1119.
[12] CAO W.D., LU X.P. On the Relationship the Geometry of Deformed Crack Tip and Crack Parameters. Application of Fracture Mechanics to Materials and Structures. 1984. p.525-545.
[13] BICEGO V., RINALDI C. Fractographic Study of Toughness Variability In the Transition Region , Mechanical Engineering Publications, 1991. p. 459-475.

TRANSCOM 2015, 22-24 June 2015
University of Žilina, Žilina, Slovak Republic

Calculation the Stress Distribution σ_{22} in Front of the Crack in Ductile Iron ADI

[*]Ihor Dzioba, [*]Sebastian Lipiec,
[*]Kielce University of Technology, Faculty of Mechatronics and Mechanical Engineering, Department of Machine Design, al. Tysiąclecia Państwa Polskiego 7, 25-314 Kielce, Poland, {pkmid, slipiec}@tu.kielce.pl

Abstract. The paper presents an analysis of the stress distribution in front of the crack in ausferritic ductile iron ADI (Austempered Ductile Iron). Mechanical properties of the material in uniaxial tensile test were determined. The characteristics of the fracture toughness of ductile iron ADI evaluated based on critical value of the *J* integral. The stress distribution in front of the crack were obtained analytically by the HRR formulas and by numerical calculations. The *Q* parameter was determined on basis of HRR and numerical calculations.

Keywords: ductile iron, fracture toughness, HRR-stress, *Q* parameter.

1. Introduction

Determination of stress distribution in front of the crack in nonlinear materials is possible through the use of HRR solution developed by Hutchinson and Rice and Rosengren [1,2] (equation1). According to the model proposed by O'Dowd and Shish [3] (equation.2) introduced *Q* parameter, which takes into account the other members of the asymptotic solutions.
These solutions take the form of:

$$\sigma_{ij} = \sigma_0 \left(\frac{J}{\alpha \sigma_0 \varepsilon_0 I_n r} \right)^{\frac{1}{1+n}} \widetilde{\sigma_{ij}}(\theta, n) \tag{1}$$

$$\sigma_{ij} = (\sigma_{ij})_{\mathrm{HRR}} + Q \sigma_0 \widetilde{\sigma_{ij}}(n, \theta) \tag{2}$$

where:
J- *J* integral
σ_0- yield stress
ε_0- strain corresponding to yield stress, $\varepsilon_{0=} \sigma_0/E$
α- material constant
n- hardening coefficient
I_n- function of *n*
r- distance from the front of the crack

An important problem in the specification of the stress distribution in front of the crack to define hardening coefficient *n*, by Ramberg- Osgood law [4]:

$$\frac{\varepsilon}{\varepsilon_0} = \frac{\sigma}{\sigma_0} + \alpha \left(\frac{\sigma}{\sigma_0} \right)^n \tag{3}$$

The value of the hardening coefficient *n* can be determined through the use of approximation by a power law from the true plot points $\sigma_T - \varepsilon_T$, located between the yield stress and tensile strength of the material. It is also possible numerical determination of the value of the hardening coefficient *n* according to the method proposed in the work [5]. Determining scheme exponent hardening coefficient *n* analytical method is shown in Figure 1.

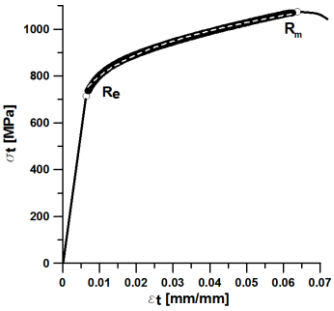

Fig. 1. Scheme of the value of a hardening coefficient *n* determine.

In the description of the stress distribution are taken into account all the members a range of solutions. The *Q* parameter is characterized by a finite value. The critical value of the *J* integral, J_{IC}, is a function of the *Q* parameter. This parameter is closely related to the relative length of the crack *a/W* [4] and other dimensions of a specimen. In order to calculate the *Q* parameter are determined numerically stresses in the material and the *Q* value is calculated from the relationship proposed by [6], at a normalized distances from the crack tip $\gamma = r\sigma_0/J = 2$:

$$Q = \frac{(\sigma_{\theta\theta})_{num} - (\sigma_{\theta\theta})_{HRR}}{\sigma_0} \tag{4}$$

2. Results

2.1. Mechanical properties and fracture toughness of ductile iron ADI

The study analyzed the stress distribution σ_{22} in the ductile iron ADI EN-GJS-1050-6. According to a study carried out in [7], ductile iron ADI has a matrix ausferritic, in which there is separation of spheroidal graphite. Size of particle diameters ranged from 2 to 40 μm. The image of the microstructure is shown in Figure 2. Mechanical properties of material obtained in uniaxial tensile test is presented in Figure 3a and in Table 1.

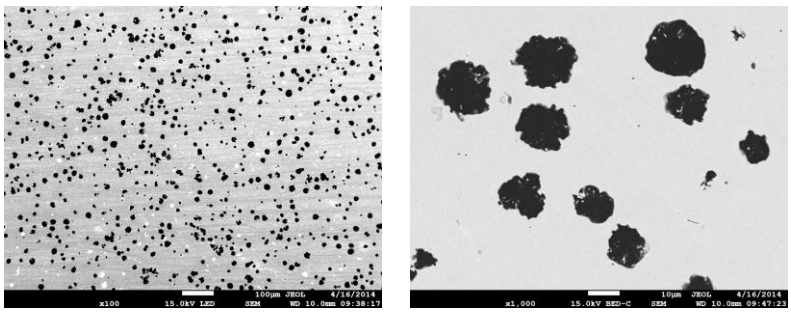

Fig. 2. The microstructure of the ductile iron ADI [7].

a) **b)**

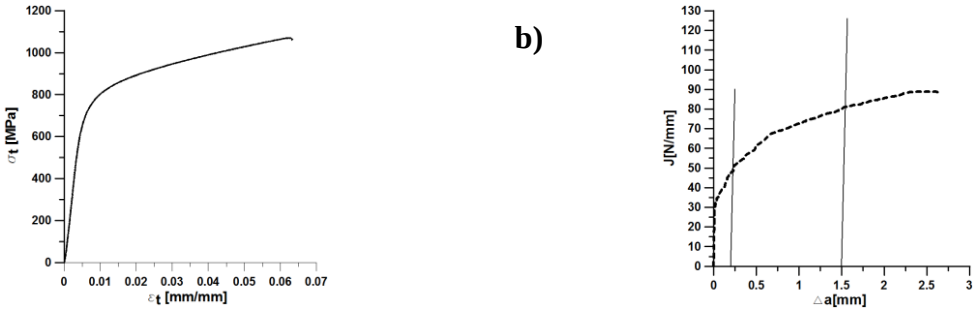

Fig. 3. a) The true stresses and strains plot; b) The J_R curve for the ductile iron ADI.

E **[MPa]**	***R*****e [MPa]**	***R*****m [MPa]**	***n***
149 573,65	744,88	1078,17	6,92

Tab. 1. Mechanical properties of the ductile iron ADI.

The characteristics of the fracture toughness was determined on three-point bending specimens with unilateral notch SENB. Potential drop technique for crack growth was used, according to ASTM [8,9]. Evaluation of fracture toughness of the ductile iron ADI estimated based on the critical value of the *J* integral, J_{IC}. The critical value of the *J* integral for ductile iron ADI was equal 48.72 N/mm. The J_R curve graph and scheme for determine the critical value J_{IC} is shown in Figure 3b.

2.2. Numerical computations

Numerical computations were conducted using Adina, versions 9.0. The calculations assume the existence of the material plane strain state. Stress field was set for the model of acute gap and assuming the occurrence of small strain. The calculated stress field was used to determine the *Q* parameter. Nine-node finite elements were used. The crack in the numerical model was stationary in nature. The model used in the numerical calculations are shown in Figure 4.

a) **b)**

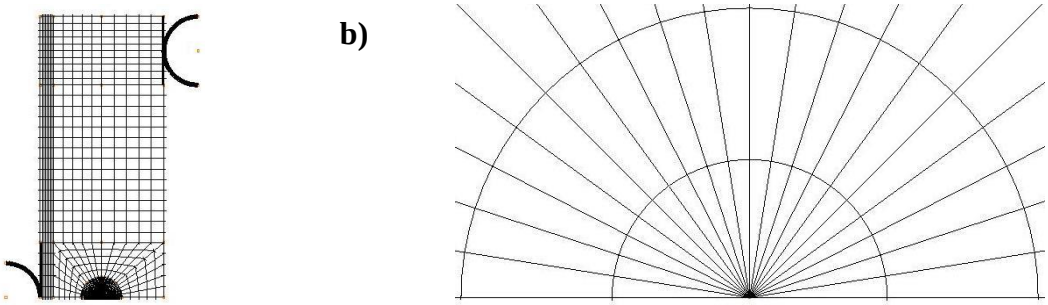

Fig. 4. Numerical model a) full model, b) crack tip zone details [10].

2.3. Comparison of stress distributions of the crack and the value of Q parameter in ductile iron ADI

On the basis of an analysis of the stress distributions in front of the crack in ductile iron ADI. The analysis was performed by equation 1 – HRR solution and by numerical calculation. The stress distributions in front of the crack of two methods are shown in Figure 5.

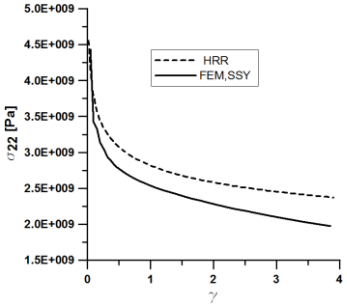

Fig. 5. The stress distributions in front of the crack in ductile iron ADI.

The Q parameter was calculated at a normalized distances from the crack tip $\gamma=r\sigma_0/J=2$, according to equation 4. The value of the Q parameter for analyzed specimen made from ductile iron ADI is equal 0,402.

3. Conclusion

Stress distribution in front of the crack in ductile iron ADI, obtained by analysis of HRR, is somewhat over in relation to the result obtained in the numerical calculations. This may be due to the fact, that a HRR solution take into account only the first member of a series. The numerical analysis result obtained is closer to reality. They taking into account the impact on the 3D stress-strain state in front of the crack for real element.

References

[1] HUTCHINSON J.W. *Singular Behaviour at the End of a Tensile Crack in a Hardening Material.* Journal of the Mechanics and Physics of Solids. 1968, 16, pp.1-12.

[2] RICE J.R., ROSENGREN G.F. *Plane Strain Deformation Near a Crack Tip in a Power-law Hardening Material*. Journal of the Mechanics and Physics of Solids, 1968, 16, pp.1-12.

[3] DOWD O., SHIH C.F. *Family of crack-tip fields characterized by a triaxiality parameter-I Structure of fields.* Journal of the Mechanics and Physics of Solids. Tom 39, 1991, pp.898-1015.

[4] NEIMITZ A. *Mechanika Pękania*. Wydawnictwo Naukowe PWN,1998.

[5] PAŁA R., GAŁKIEWICZ J. *Temperature Influence on σ_0 and n Characteristics in the R-O Relationship for High-Strenght Steel*. Key Engineering Materials. 2014,598,pp.190-194.

[6] NEIMITZ A., PAŁA T., DZIOBA I. *Wpływ temperatury i parametru Q na krytyczną wartość odporności na pękanie dla wysokowytrzymałej stali ferrytycznej hardox-400.* Materiały XXV Sympozjum Zmęczenie i Mechanika Pękania. 2014,115-116.

[7] DZIOBA I., KASIŃSKA J. *Wpływ morfologii grafitu na własności mechaniczne i odporność na pękanie żeliwa ADI.* XLII Szkoła Inżynierii Materiałowej. 2014.

[8] ASTM E1737-96., *Standard Test Method for J-Integral Characterization of Fracture Toughness*, Philadelphia, 1996.

[9] ASTM E1820-09. *Standard Test Method for Measurement of Fracture Toughness. Annual book of ASTM standards*; 03.01; 2011: 1070-1118.

[10] ADINA System 9.0.

TRANSCOM 2015, 22-24 June 2015
University of Žilina, Žilina, Slovak Republic

Ultrasonic Testing of Plastic Materials

Ing. Martin Faturík[1]
[1]Department of mechanical engineering technology, University of Žilina. Univerzitná 1, 010 26 Žilina. Slovakia E-mail: martin.faturik@stroj.uniza.sk

Abstract: Article presents ultrasonic testing of plastic materials using face probe. Because usage of plastic materials is still higher and demands on quality as well, it is suitable/necessary to test these materials similarly as metal materials, to seek for hidden defects and integrity.

Keywords: Plastic materials, NDT

1. Testing of plastic materials using ultrasonic waves

Value of plastic materials as a construction materials is still rising, therefore demands on their testing using every method, ultrasonic too, are rising as well, even if their acoustic properties are not optimal. Their common sign is significantly higher coefficient of dampening than of metals. Especially when dealing with filled plastics, coefficient of dampening is even higher. Ultrasonic frequencies higher than 5 MHz are sparsely usable for testing of plastic materials, filled in particular, because with them, just like with liquids, dampening is growing by absorption with second power of frequency. Dispersion is another factor associated with filled plastic materials, if grains or fibers of filling material have dimensions comparable with wave length. Wave length in plastic materials is approximately half the length in the metals. Filling with grained or fibrous materials and equally the porosity are causing dampening on frequency, matching required resolution, causing ultrasonic testing to be unsuitable for the task. Ultrasonic defectoscopy is being used for detecting cavities, discontinuities, porosity and sometimes it´s used for evaluation of strength based on ultrasound spread velocity. (Obraz, 1989)

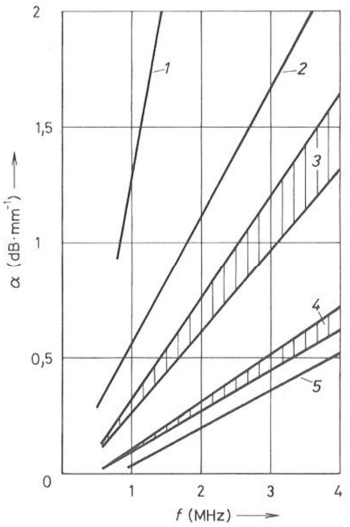

Fig. 1. Frequency dependence of dampening α in soft plastic materials: 1 – softened polyvinyl chloride, 2 – polybutadiene, 3 - polypropylene and polyethylene, 4 – polyamide and hard polyvinyl chloride, 5 - polyethylene

In terms of ultrasonic testing it´s possible sort the plastic materials to soft and hard.. Hard plas-

tics have good acoustic properties, for example acrylic (methyl methacrylate), polystyrene, polyamide and teflon, while soft plastics, like polyethylene, polyvinyl chloride and polyisobutylene have lower velocity of spread and high absorption, therefore are testable with difficulty.(Fig. 1)

Once are hard plastics filled, possibility of their testing depends from the type of filling and sometimes it´s significantly worse. Besides this, dampening of ultrasound is excessively high even for hard plastics., when they are still not hardened. Overall, soft plastics with higher spread velocity of ultrasound have lower dampening. On Fig. 2 is frequency functionality of dampening coefficient α of hard plastics (acrylic and polystyrene) used as a probe wedges. Longitudinal ultrasonic waves spread velocities of selected plastics are in **Chyba! Nenašiel sa žiaden zdroj odkazov.**. Ultrasonic spread velocity depends on temperature and with increasing temperature it decreases (Fig. 3). (Obraz, 1989)

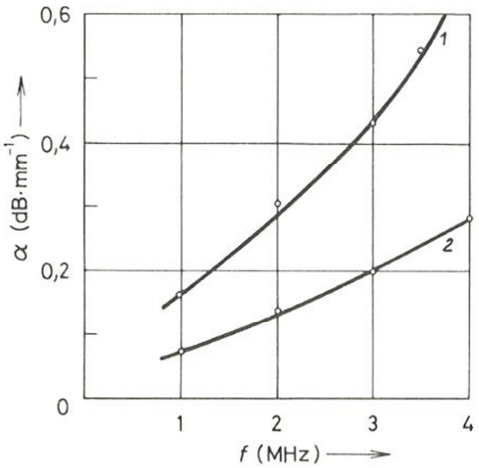

Fig. 2. Measured frequency dependence of dampening coefficient α for hard plastics: 1 – acrylic; 2 – polystyrene

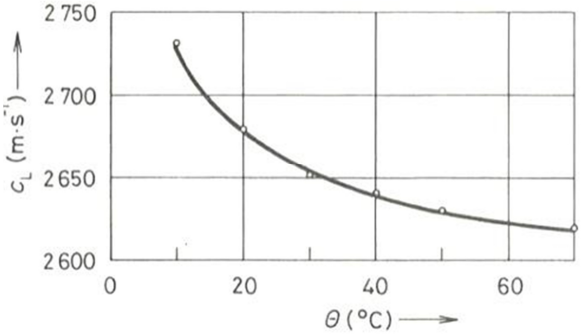

Fig. 3. Spread velocity c_L for acrylic dependent on temperature Θ

Type of plastic	Velocity c_L (m .s ^{1})
Teflon	1350
Polyurethane	1780
Linear polyethylene	1780
Epoxy 1200	2270
Branched polyethylene	2340
Polystyrene	2362
Ebonite	2400
Polyamide 6	2540
Polymethylmetacrylate	2700

Tab. 1. Velocities c_L in selected plastics

Same influence has filling in plastics. Velocity of ultrasound waves spreading decreases, on Fig. 4, where is dependency of longitudinal waves velocity c_L, density ρ and specific acoustic wave resistance ρ*cL*, on mass ratio to tungsten and epoxy resin (Epoxy 2200). Mixture of tungsten powder and epoxy is being used for dampening of piezoceramic convertor for making ultrasound probes. By filling are achieved high values of acoustic wave resistance and dampening (Fig. 5) especially with frequencies higher than 2 MHz.

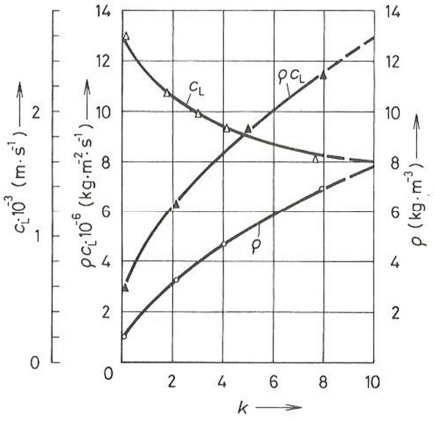

Fig. 4. Dependence of spread velocity c_L, density ρ and acoustic wave resistance ρc_L of epoxy resin filled with tungsten powder with grain size100 µm on their mass ratio k

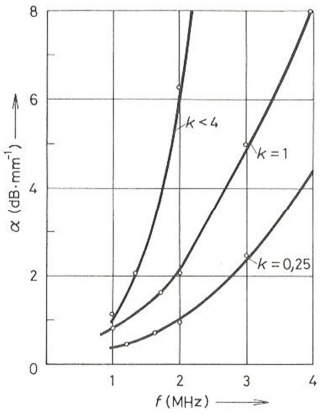

Fig. 5. Frequency dependence of dampening α at different degrees of filling on mass ratio k of tungsten powder and epoxy resin

Ultrasound is used for cavity detection in rods pressed from plastics. Rods with diameter 100 mm are being tested at contact bond using face probes with frequencies 1 to 2 MHz. Besides cavities ultrasound is used for longitudinal cracks and duplicates on axis part. Single or double probes can be used. But if it are defects off-axis or rods have smaller diameter, it is necessary to use double probe (Fig. 6).

Fig. 6. Selection of probes for testing materials

All probe types, especially for frequencies lower than 2 MHz, should have the widest relative width of frequency bandwidth ($\Delta f/f_S$ = 0,8 to 1), to have short dead band area and resolution capabilities even in the vicinity of probe. There are probes specially made for testing of plastics. With this kind of probe it is possible in common conditions detect defects in filled plastics with substitute dimensions of several tenths of millimeter.

Plastics are often tested using immersion technique (Fig. 7). Results are very good, because reflection coefficient on border of plastic and water is less than in metals and equally, loses by refraction on curved surfaces are smaller. Angles of incidence are chosen for defects to be detected by longitudinal wave, although forming of transversal wave cannot be prevented. If small defects are to be detected, it is recommended using beam focusing, just like with metals. (Obraz, 1989)

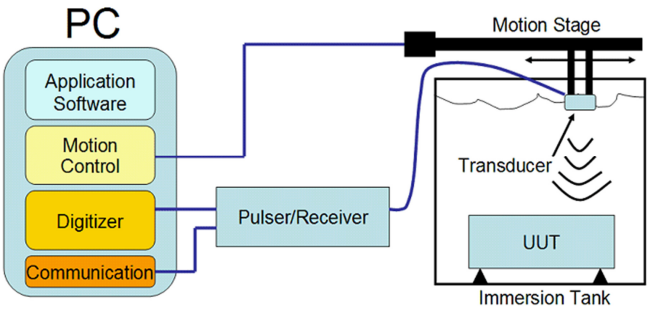

Fig. 7. Example of immersion ultrasonic testing aparature

In addition to plastic bars, plates are also used with thickness of 50 mm and more. In them, duplications may occur. It is possible to look for them just like in metal sheets, whereby according the dampening frequency of 2 or 1 MHz is used. Higher frequencies are suitable for wrought plastics. With high dampening defects have no fault echoes, this is solved by using transition method.. Same goes for layered plastics, used for isolations. These are tested using frequencies of 0,5 MHz.

Pipes made from plastics are being controlled for wall thickness and welded joints on pipelines, for example pipelines made from linear polyethylene. Thicknesses of pipe walls or containers are tested with frequencies 1 to 2 MHz. For accurate measurement of smaller thicknesses from 0,01 to 13 mm a device using frequency up to 20 MHz and with it is possible to measure thickness with resolution of 0,01 mm. Frequencies up to 2 MHz with resolution 1mm are being used for thicker materials.

Longitudinal waves can be used entirely for testing welded joints and test with direct reflection. Suitable probes for thickness up to 30 mm are with angle of refraction 60° and 70° in tested plastic. Probes with angle 45°are being used for testing bigger thicknesses of welds. Angled probes are special and their usage was enabled by wedge from plastic with very small wave spread velocity. Angle values are only approximate, because they depend on longitudinal wave spread velocity. There-

fore, every angled probe for plastic testing has specified spread velocity or angle of impact. Welds on plastics are often very narrow (Fig. 8), it is effective to use tandem probe configuration.

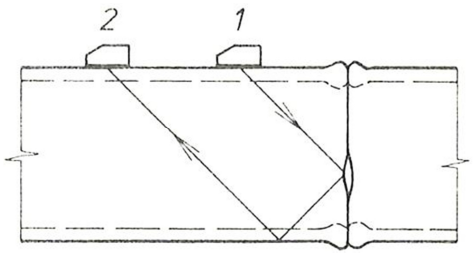

Fig. 8. Weld testing on thin wall pipe from plastic with tandem configuration of probes: 1 – transmitter; 2 - receiver

Plastic reinforced with glass and carbon fibers are tested with ultrasound as well, although sometimes with great difficulty. Irregularities in laminate structure, non-adherent layers, points with reduced strength, where there is no connection or resin didn´t hardened, all of this can be detected. Fiber structure of laminates is causing anisotropy in the direction of fibers. Because of this, acoustic properties of laminate are significantly different in direction along the fibers and perpendicular to them. For testing it, the only direction is perpendicular to fibers. If the dampening of composite is too big, using of transition method is needed, but preferred method is reflective. Often fault echo cannot be expected with delamination. Indicator of delamination is drop of end echo, which is being experimentally established between 2 to 12 dB. Highest frequency must be used for this testing, 6 to 8 MHz. (Obraz, 1989)

2. Conclusion

As it can be seen from facts mentioned above, testing of plastics using ultrasound is not easy and simple and requires complex preparation from testing personal. Ultrasonic testing however allows to lower the count of defective products and lower the overall cost of production through lowering cost necessary for disposal and possible reclamation from customer.

Continuing development in technology of ultrasonic testing and decreasing price of devices for testing are contributing to spread this technology. Plastics are materials, which share of usage still grows, they have properties close to some of metals, therefore it is necessary to ensure their properties to be flawless and that can be achieved through thorough testing.

References

[1] OBRAZ, J. 1989. *Zkoušení materiálu ultrazvukem*. Praha : SNTL Nakladatelství technické literatury, 1989. s. 464. ISBN 80-03-00097-1.

[2] KOVÁČIK, M. 2010. *Skúšanie materiálov ultrazvukom*. Bratislava : s.n., 2010.

[3] LANGENBERG, K.-J., MARKLEIN, R., MAYER, K. 2012. *Ultrasonic nondestructive testing of materials* (Theoretical foundations). Boca Raton : CRC Press, 2012. s. 736. ISBN 978-1-4398-5588-1.

[4] LEITNER, B. 2003. *Nedeštruktívne skúšanie materiálov v plynárenstve*. Žilina : Žilinská univerzita v Žiline, 2003. s. 197. ISBN 80-8070164-4.

[5] NATIONAL INSTRUMENTS. 11/2014. *Ultrasonic Nondestructive Testing - Advanced Concepts and Applications*. 2014. Tutorial in .pdf

TRANSCOM 2015, 22-24 June 2015
University of Žilina, Žilina, Slovak Republic

Microstructure of Plasma Sprayed ZrO_2-$8Y_2O_3$ Coatings

[*]Anna Góral, [**]Krzysztof Sokołowski, [**]Wojciech Żórawski, [***]Medard Makrenek

*Institute of Metallurgy and Materials Science, Polish Academy of Sciences, 25 Reymonta St., 30-059 Krakow,
[**]Kielce University of Technology, The Faculty of Mechatronics and Mechanical Engineering, Department of Terotechnology, av. Tysiąclecia Państwa Polskiego 7, 25-314 Kielce, Poland,
[***]Kielce University of Technology, The Faculty of Management and Computer Modeling, Department of Physics
a.goral@imim.pl, sokolowskik@tu.kielce.pl, ktrwz@tu.kielce.pl, fizmm@tu.kielce.pl,

Abstract. Atmospheric plasma spraying (APS) is an attractive technique to obtain nanostructured coatings due to its versatility, simplicity and relatively low cost. In the present paper morphologies of the ZrO_2-$8Y_2O_3$ powders and as sprayed coatings were analyzed. The grains of YSZ powder observed at high magnification consist of high porous agglomerates sintered from submicron grains. The plasma sprayed YSZ coating possess submicron grains. Parameters of the topography sprayed coating are depended on grain size distribution of started powders.

Keywords: plasma spraying, thermal barrier coating, YSZ, TBC

1. Introduction

Expectations of designers for materials used in the industry are still increasing what makes necessary to conduct research on structural materials, which will have better properties than materials that have been used so far. The group of ceramic materials is developed separately. They were used as the main structural material or to reduce manufacturing costs as coatings on cheaper materials improving surface properties. Development of coatings with different properties than those of the substrate material and improving the currently used is the result. Variety of properties is a result of miscellaneous phase composition of ceramic materials which can take the best properties according to demand. The possible properties, which could be achieved by ceramics, are [1-6]: resistance to corrosion in chemically aggressive environments, resistance to high temperatures, resistance to erosion and friction, high hardness, electrical insulation, low coefficient of thermal conductivity, biotolerance.

Especially important group of ceramic composite coatings which are characterized by good resistance to high temperature and low thermal conductivity are thermal barrier coatings (TBC– Thermal Barrier Coatings). An example of a microstructure of this type of coating is presented in Fig. 1. Very often intermediate thin layer between the TBC coating and substrate, usually consisted of thermally grown oxide (TGO), is also deposited to obtain good adhesion of such coating system. The most commonly used material is zirconia stabilized with yttria (YSZ) due to the lowest thermal conductivity of about 2 W/mK. Elements covered by this material can work at temperatures above their melting point. TBC used on heat resistant alloys reduces substrate material temperature about 170 K compared to the ambient temperature at the surface of the coating [2, 5].

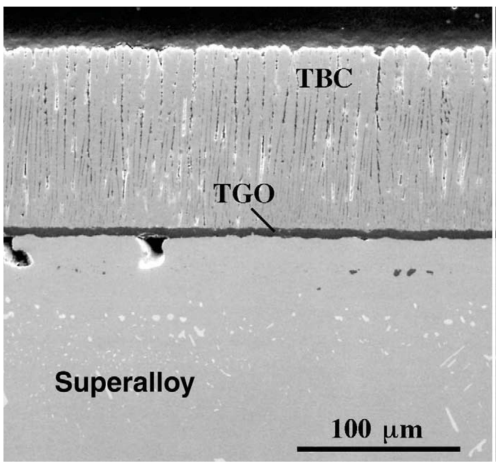

Fig. 1. An example of a cross-section of a thermal barrier coating; TBC - thermal barrier coating, TGO - thermally grown oxide [2]

Taking into account the use of thermal barriers we can distinguish the following benefits arising from their use [2,4,5]: an extended period of use the part or machine; increased efficiency of the machine (e.g. the engine through a rise in temperature in the turbine); reduced flow of coolant; reduced manufacturing costs by using cheaper base material (substrate layer), and through local coverage coatings in highly exposed to friction, temperature; elimination of manufacturing processes such as heat treatment, chrome plating. Requirements for TBC coatings used on components of internal combustion engines and gas turbines are very high [3,4,8]: durability excess of 20,000 hours in hot section of the engine; thermal conductivity less than 2 W / mK at 1270 K; maximum exhaust-gas temperature 1470 K; resistance to contaminants present in heavy fuels; durability in excess of 5000 cycles room temp. 1270 K rate of rise of temperature changes 200 K/min; durability exceeding 2000 cycles room temp. 1470 K.

Rising demands on coating thermal barriers entail the need for research to develop new methods of coating, allowing creation of a more homogeneous structure. Another object is to obtain a material with better properties than the currently used. In the light of the above, the aim of the present study was to characterize the composite ZrO_2-$8Y_2O_3$ (YSZ) powders and to determine the microstructure as well as surface topography of coatings plasma sprayed on a steel substrate.

2. Experimental details

ZrO_2-$8Y_2O_3$ powder feedstock (Metco 204 NS) with a grain size distribution in the range of 125+11μm was applied to produce of YSZ coatings. Plasma spraying was performed by means of Plancer PN-120 plasma spraying system with Thermal Miller 1264 powder feeder. Fundamentals of plasma spraying principles are presented in Fig. 2. Plasma spraying parameters are listed in Table 1.

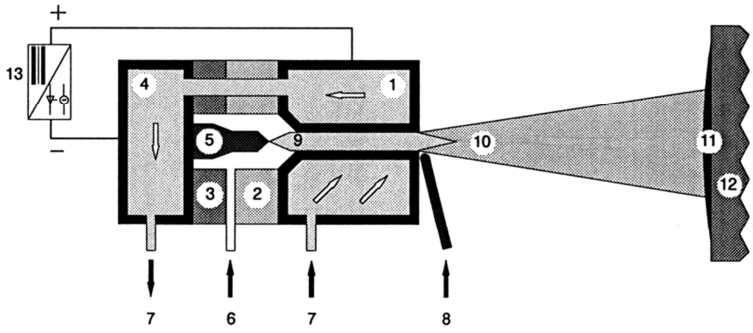

Fig. 2. Fundamental plasma spraying principles: 1-nozzle (anode), 2-insulation, 3-center section, 4-rear section, 5-electrode (cathode), 6-plasma gas, 7-water cooling, 8-powder, 9-electrical arc, 10-plasma jet, 11-coating, 12-workpiece, 13-generator

Parameter	Value
Current, A	600
Voltage, V	60
Plasma gas pressure, MPa	0.7
Spraying distance, mm	100
Powder feeding rate, g/min	45

Table 1. Plasma spraying parameters for YSZ powder

For the metallographic sections and abrasive examination, the coatings were deposited on flat low-carbon steel samples with dimensions of 30 mm x 30 mm x 3 mm. Before plasma spraying, all substrates were degreased and grit blasted with electrocorundum EB-12 at a pressure of 0.5 MPa. After spraying the thickness of the coatings was 0.5 mm. The morphologies of the powders and the obtained coatings were analyzed using the following microscopes: SEM JSM–5400 with an ISIS 300 Oxford (EDS) microprobe, SEM FEI Nova™ NanoSEM 200. The topography of as sprayed coatings were analyzed by means of a Talysurf CCI-Lite non-contact 3D profiler.

3. Results and discussion

3.1. Characterization of YSZ powders

Fig. 3a shows SEM morphology of the nanostructured YSZ-powder. Most grains have a regular spherical shape, only some of them are fractured. Morphology of the grain surface at high magnification in SEM (Fig. 3b) shows that each grain of powder consists of submicron grains which create sintered high porous agglomerates. The slight necking connecting nanograins are a result of manufacturing process which allows to obtain grains in size range of -125+11 μm.

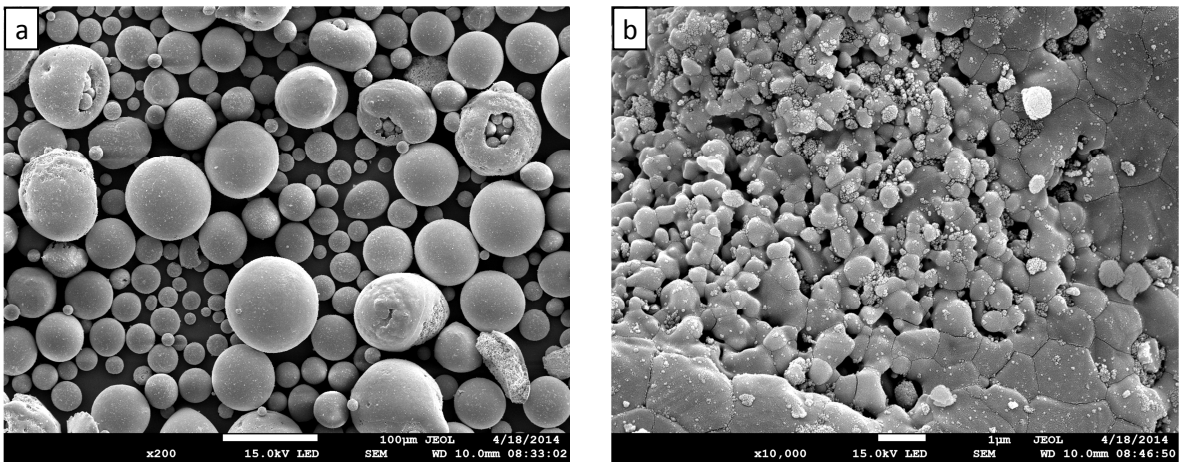

Fig. 3. Morphology of YSZ Metco 204NS powder: a) morphology of grains, b) morphology of surface grain

The microstructures of the cross section and surface of the plasma-sprayed YSZ coating are shown in Fig. 4 and Fig. 5, respectively. The coating presents lamellar microstructure typical for thermal sprayed layers with visible randomly distributed small pores and cracks. Different sizes of zirconia grains were observed at higher magnification of coating (Fig. 4b). Most of grains are deformed but

some of them possess the low level of deformation. Light places in Fig. 4a correspond to pores which are present between lamellae.

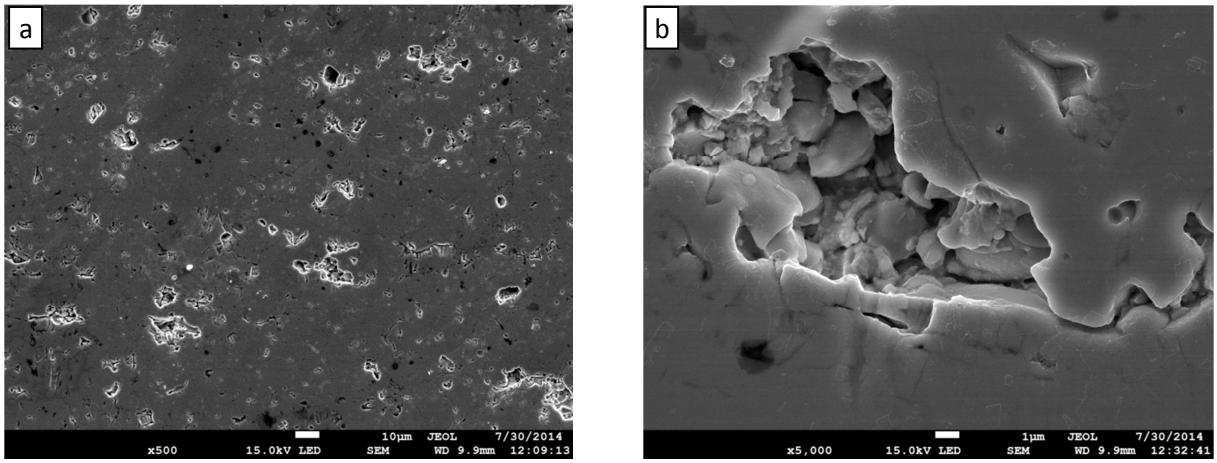

Fig. 4. SEM morphology of the cross section a), b) high magnification of selected area of cross section of the YSZ Metco 204NS coating

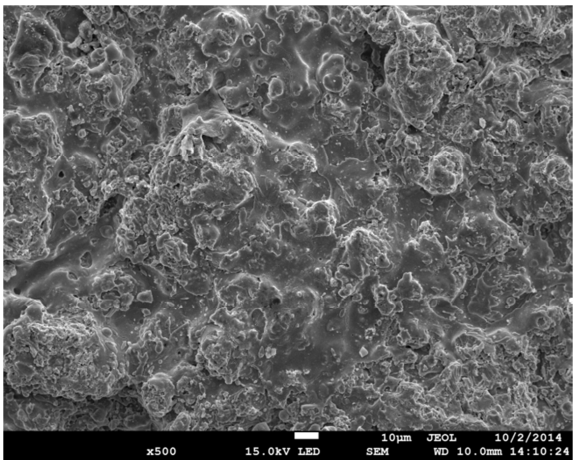

Fig. 5. SEM morphology of the surface of the YSZ Metco 204NS coating

The topography of sprayed surfaces (Fig. 5) was scanned and measured to estimate influence of started coating material (Fig. 6). Results of measurements are reported in Table 2. The highest arithmetic mean of the surface height S_a of as plasma sprayed coating is high because the range of grains of powder was significantly wide. The similar dependency was observed for the mean squared surface height, S_q. Negative value of asymmetry of the surface, S_{sk} indicated that the surfaces was flattened and occurring peaks were rounded. Kurtuosis S_{ku} is responsible for steep irregularities and defects. The value of kurtuosis near 3 indicated that distribution of profile ordinate corresponds to higher concentration around the mean value. Parameters: the maximum peak S_p, the maximum valley S_v are nearly the same in the case of plasma sprayed coating surfaces and almost two times less than the maximum height S_z. It is the result of a participation of finer splat grains in spraying process independent of narrow cut of powder [8, 9].

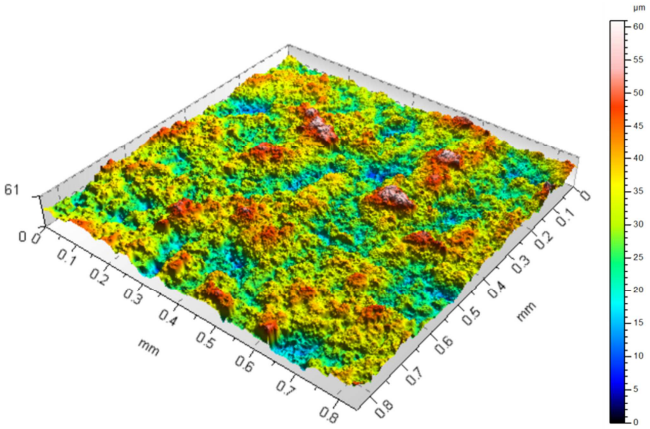

Fig. 6. Surface topography of plasma sprayed YSZ coating

Parameter	Surface of YSZ coating after spraying, µm Standard
S_a,	7.5038
S_q,	9.3202
S_{sk}	-0.0693
S_{ku}	2.7493
S_p,	27.0948
S_v,	23.8610
S_z,	50.9558

Table 2. Surface topography parameters according to ISO 25178

4. Conclusions

1. The grains of YSZ powder observed at high magnification in SEM are in the form of high porous agglomerates sintered from submicron grains.
2. The plasma sprayed YSZ coating possess submicron grains which were present in the sprayed powder.
3. Parameters of the topography of as plasma sprayed YSZ coating are depended on grain size distribution of starting powders.

References

[1] ASHBY MICHAEL F., JOHNES DAVID R.H., *Materiały inżynierskie, Kształtowanie struktury i właściwości, dobór materiałów*, WNT Warszawa 1996. (in polish).
[2] CLARKE D. R., PHILLPOT S. R., *Thermal barrier coating materials*, MaterialsToday, June 2005, ss. 22-29.
[3] GUGEL E., WOETTING G. G., *Materials selection for ceramics components in automobiles, industrial ceramics*, Vol. 19, 1999, p. 196-199.
[4] HEJWOWSKI T., WEROŃSKI A., *The effect of thermal barrier coatings on diesel engine performance.* Vacuum (2002) ss. 427-432.
[5] MOSKAL G., ROZMYSLOWSKA A., GAZDA A., HOMA M., *Wybrane termofizyczne właściwości proszków cyrkonianowych na bazie pierwiastków ziem rzadkich typu Re2Zr2O7 (Re- Gd, La, Sm, Nd) przeznaczonych do natryskiwania cieplnego powłokowych warstw barierowych*, Prace Instytutu Odlewnictwa, Tom XLIX, 2009, Zeszyt 4, ss. 15-26, (in polish).
[6] KINGERY W. D., *Introduction to ceramics*, John Wiley & Sons, Inc., New York 1960.
[7] TOPOLSKA K., *Koncepcja przyspieszonych badań trwałości powłok ceramicznych na elementach silnika spalinowego*, K0NES 2005, (in polish).
[8] ADAMCZAK S., JANECKI D., STĘPIEŃ K., *Measurement*, 44 (1) (2011) 164.
[9] RADZISZEWSKI L., *Intrusive effect of a contact transducer on testing results, Metrology and Measurement Systems* Vol. XI, Nr 1/2004 s.31 – 43 Warszawa 2004.

TRANSCOM 2015, 22-24 June 2015
University of Žilina, Žilina, Slovak Republic

Analysis of the Impact of the Cage Type on the Frictional Moment Ball Bearings

[*]Łukasz Gorycki
[*] Politechnika Świętokrzyska w Kielcach, Katedra Technologii Mechanicznej i Metrologii, Laboratorium Łożysk Tocznych, 25-314 Kielce, al. Tysiąclecia Państwa Polskiego 7, lgorycki@tu.kielce.pl

Abstract. The paper presents the methodology and results of measurement designed to determine the effect of the rolling element separator (cage) at the frictional moment in ball bearings. The measurement was carried out on four groups on bearing with different cages. Measurements were carried out on torque-meter STPM, a device that has been designed and manufactured at Kielce University of Technology. The measurement results showed that the type of cage used in ball bearings has a significant impact on the frictional moment. In addition, the results also confirm that the size of the curvature ratio and the accuracy of the races shape have a significant impact on the frictional moment.

Keywords: Rolling bearing, bearing test, resistive torque, cage.

1. Introduction

In order to maximize the reliability of equipment the manufacturers are forced to systematic improvement their products. The changes apply to the design, manufacturing technology, maintenance and optimization selection of elements. For bearings, this selection mainly depends on the work conditions in which they will be used. After determining the operating conditions the bearing are selected based on design parameters such as: bearing type, size, clearance, type of rolling element separator, lubrication, etc., and taking into account the operational parameters, such as: capacity, speed limits, frictional moment, rotation accuracy, noise, etc. Bearing life and reliability are crucial for the machines operation in which they are used. Premature wear or damage to the bearings, is associated with a time-consuming and costly replacement. This is particularly important in the case of large-size bearings used for supporting large cylindrical elements [1]. One of the most important factors determining the bearing life is the frictional moment. It shows the levels of energy losses. This energy is lost as heat or to the destruction of the lubricant and the bearing cooperating surfaces. This moment dependent on many factors, both those related to the bearing design parameters applied lubricant and working conditions of the bearing. Although the qualitative impact of each factor on the frictional moment is known, their numerical contribution to the final result has not been full examined yet, and not all of these factors are taken into account in the mathematical relationships use. This paper dealt with analysis of the impact of rolling element separator type on the frictional moment.

Rolling elements separator (cage) is a bearing element, that is use to separate the rolling elements (balls, cones, etc.), in order to avoid friction between them, and their even positioning on the periphery of the bearing. During the work of the bearing, the cage may come in contact with the rolling elements and the rings. In places the contact the size of friction that will occurs will depend on the work conditions and the shape and material from which the cage was made. The material used for the manufacture of cage depends mainly on the type of bearings in which it will to be used. The cage may be made from carbon steel, brass, plastic or synthetic resin [2].

Frictional moment is the result of the energy losses in the area of co-operation of the rolling elements with the races and the cage, as well as losses resulting from wading in the means of rolling elements lubricants. The larger the frictional moment of the working bearing is the shorter its life will be. Therefore, users of bearings want to be able to select the most appropriate bearing to

specific conditions. In order to determine the theoretical frictional moment in rolling bearings mainly two mathematical relationships are used, the mathematical relationships are described in formulas (1) and (5).

Frictional moment formula according to Palmgren'a [3]:

$$M = M_0 + M_1 \tag{1}$$

where:
M_0 - torque losses caused by friction and wading in the lubricants, [Nmm] (represented by the formula 2 and 3),
M_1 - torque taking into account the contact size of the rolling elements and the races , resulting from the load and the intensity of the phenomena occurring in these areas [Nmm] (represented by the dependence 4)

n – rotation speed [min^{-1}],
ν – kinematic viscosity [$m^2 \cdot s^{-1}$],
f_0 - coefficient depending on the bearings type and lubricating method,
d_m – bearing pitch diameter [mm],
f_1 - coefficient depending on the type of bearing and the load,
P_1 - coefficient depending on the type of bearing and the load [N].

for $\nu \cdot n \geq 2000$

$$M_0 = 10^{-7} \cdot f_0 \cdot (\nu \cdot n)^{2/3} \cdot d_m^3 \tag{2}$$

for $\nu \cdot n < 2000$

$$M_0 = 1{,}6 \cdot 10^{-5} \cdot f_0 \cdot d_m^3 \tag{3}$$

$$M_1 = f_1 \cdot P_1 \cdot d_m \tag{4}$$

Frictional moment formula according to SKF [4]

$$M = M_{rr} + M_{sl} + M_{seal} + M_{drag} \tag{5}$$

where:

M - total frictional moment [Nmm],
M_{rr} – rolling frictional moment [Nmm],
M_{sl} – sliping frictional moment [Nmm],
M_{seal} – seals frictional moment [Nmm],
M_{drag} - frictional moment resulting from resistance to motion in the oil, grease kneading, splashing etc. [Nmm].

The mathematical relationships take into account many factors which influence the frictional moment but not all of them. In addition to the aforementioned type of cage, these models do not take into account the curvature ratio and the accuracy of the implementation of the races shape (errors shape, waviness and roughness). The results in the article [5] shows curvature ratio in difficult conditions (high load and speed) has a clear effect on the moment resistance of the working bearings.

The frictional moment measurements were performed in 3 series on torque-meter STPM shown in Figure 1.

2. Research Equipment

In order to analyze the impact of the cage at the frictional moment, a series of measurements was performed on torque-meter STPM [6]. The torque-meter was designed at Kielce University of Technology and is a response to the needs of industry for equipment for frictional moment in rolling bearings [7]. It provides the ability to perform frictional moment measurements on small and medium sized roller bearings.

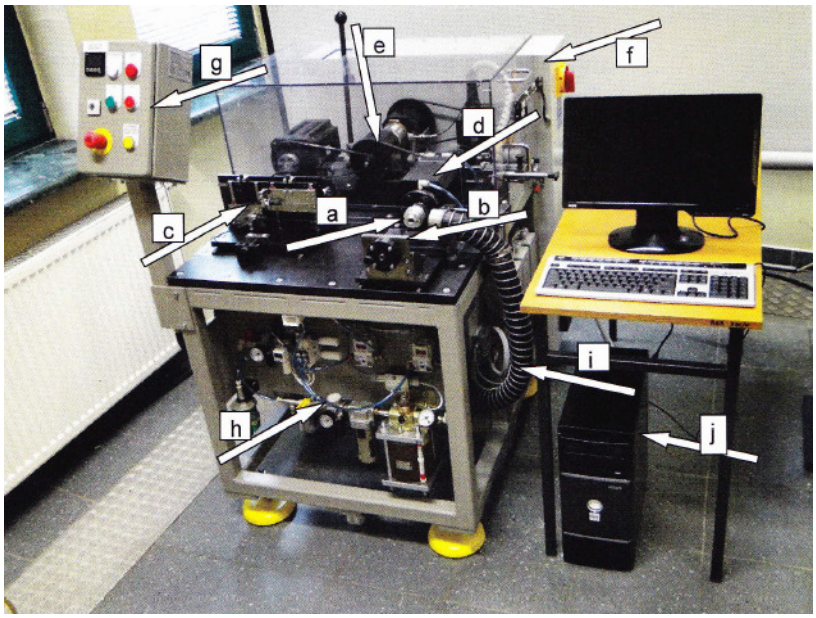

Fig. 1. The torque-meter STPM use in the Rolling Bearing Research Laboratory in Kielce University of Technology. a) probe; b) axial load; c) radial load; d) research spindle; e) driving gear; f) the control box; g) control panel; h) the pneumatic supply unit; i) blow; j) PC.

3. Measurement

The tests were performed on the following four bearing samples:
- Sample A: 6202A8, plastic cage;
- Sample B: 6202A8, metal cage;
- Sample C: 6202A17, plastic cage;
- Sample D: 6202A17 metal cage.

Each bearing sample consists of 10 items. Samples not only have different cages, but also have differed races shape. 6202A8 bearings have a larger radius of the races then the 6202A17 bearings. Each bearing was measured twice, in each measurements the axial load was acting with the same magnitude but in a opposing direction Before each measurement, in order to secure the bearing and minimizing the effect of lubricant on the frictional moment, a same small amount of oil TOTAL Drosera MS 10, was added to the bearings. For each sample, three series of measurements was performed. Each with different values of the axial load, radial and rotational speed. The magnitude of these parameters are shown in Table 1.

	1 Series	**2 Series**	**3 Series**
Axial load [N]	10	180	180
Radial load [N]	0	300	400
Rotation speed min^{-1}	15000	15000	20000

Tab. 1. Parameters for 3 three series of measurements.

The results of frictional moment measurement, measured in three series obtained for four samples of bearings are shown in Table 2.

	1 Series	2 Series	3 Series
Sample A	1,4278	4,8746	8,2011
Sample B	2,6218	10,2713	12,4815
Sample C	2,0660	5,3238	8,1897
Sample D	3,8111	10,8335	13,2098

Tab. 2. Measurement results of frictional moment [Nmm], for the 4 bearing groups in each measurement series.

4. Conclusions

The results of the experiment presented in this paper confirm the significant impact of the material used to make the cage in the ball bearings on the frictional moment. Ball bearings with metal cages generate more frictional moment then the bearings with plastic cages.This is due to differences in the friction coefficients, cage weight or the contact surfaces (plastic baskets have a lower friction coefficient and are much lighter than steel baskets).

The changes of the frictional moment value in the following series of measurements, show a similar behavior of the bearings in relation to the changing research condition: the speed of rotation, radial and axial loads. Only in sample C the characteristics are different than in the other sample (for example in the 3 series the frictional moment measurement result for the sample C should be greater than those obtained for sample A), this suggesting that in addition to the cage type and the curvature ratio, other parameters lick the accuracy of its performance (eg. wave profile or race deviation) could have a significant impact on the results of sample C bearings.

References

[1] NOZDRZYKOWSKI, K. JANECKI D. *Comperative studies of reference measurments of cylindrical surface roundness profiles of large machine components*, Metrology and Measurment Systems. Tom: XXI (2014), Zeszyt: 1, Strony: 67-76.

[2] Motion & Control, NSK, Technical Report, 2005.

[3] Krzemiński-Frede H. *Łożyska toczne.* PWN, Warszawa 1989.

[4] Katalog produkcyjny SKF, 2011.

[5] Gorycki Ł., Domagalski R., Zmarzły P. *Pomiary momentów oporowych łożysk tocznych w aspekcie dokładności kształtowo - wymiarowej elementów współpracujących*. Mechanik nr. 3, 2015. ISSN 0025-6552.

[6] Janecki, D. *Instrukcja obsługi programu do pomiaru statycznego i dynamicznego momentu oporowego w łożyskach „Momentomierz”*. Politechnika Świętokrzyska. Kielce 2014.

[7] Adamczak, S. Domagalski, R. Sender, E. *Metody badań łożysk tocznych w aspekcie współczesnych wymagań wyrobów o wyższych parametrach eksploatacyjnych. Tribologia*, 2011, nr 6, s 11-18.

TRANSCOM 2015, 22-24 June 2015
University of Žilina, Žilina, Slovak Republic

Deformation Zones Verification of Nickel Alloys by Implementation of Multi-parametric Measuring System

[1] Jozef Holubjak, [1]Andrej Czán, [1]Michal Sajgalík, [1]Mario Drbul, [1]Marianna Piesova, [1]Viktor Kuzdák[1]

[1] University of Zilina, Faculty of Mechanical Engineering, Department of Machining and Manufacturing Technology, Univerzitna 1, 01026 Zilina, Slovakia, {jozef.holubjak, andrej.czan, michal.sajgalik, mario.drbul, marrianna.piesova, viktor.kuzdák}@fstroj.uniza.sk

Abstract. The article deals with integration of progressive measuring methods on multi-parametric experimental measuring. During the experiments was performed measuring of temperature and its spread, cutting forces ratio and monitoring of deformation processes using multifunctional measuring system. Outputs of this system provides valuable knowledge about processes in the cutting zone, but most of all it is able to verify these processes during cutting process and availability based on complex measuring and evaluation to determine relationships between examined processes and phenomena.

Keywords: Multi-parametric measuring system, deformations, nickel alloys

1. Introduction

Cutting process analytical modelling allows us to understand the basic principles of the metal cutting phenomena while reducing the dependence on empiricisms by avoiding a large amount of time-consuming experiments. More important is that, it enables the evaluation of the main process factors such as force of cutting and aids in its prediction, which is required for the optimal execution of the machining operation. Many analytical models have been developed to date which can determine the relations between the variables involved in the cutting process. It is generally accepted that the cutting process in the course of metal machining is restricted to the area in front of the tool cutting edge due to intensive local shear deformation of the machined material (1, 2).

Most of the current analytical models describe the cutting process as a simple two-dimensional model named orthogonal cutting. However, most cutting operations are actually three-dimensional and can be properly described using an oblique cutting model, where the cutting edge is inclined at an angle of obliquity, λ, consistent with the primary motion course of the workpiece. Nevertheless, the simplified orthogonal model is generally used as a good demonstration of the oblique model.

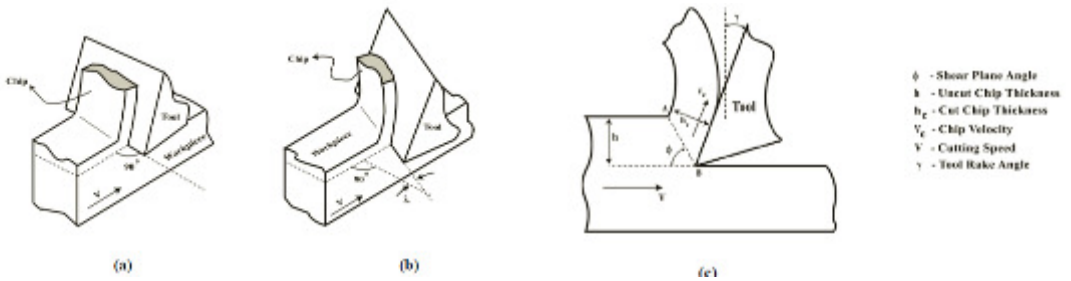

Fig. 1. (a) Orthogonal cutting model (b) Oblique cutting model (c) General 2D representation of the cutting process with the variables of the cutting process (6).

Figure 1 illustrates the orthogonal and oblique cutting models. In Figure 1(c), the workpiece, initially moving at speed *v*, goes through a plastic shearing strain and that leads to a chip streaming at speed v_c after passing a certain shear area exemplified by the shear plane AB. Due to its importance as a measure of the energy efficiency of the cutting process, the shear plane orientation,

φ, is essential to analytical models for the development of the cutting process (3, 4). In addition to the stress at the cutting area, the orientation of the shear plane affects the kinematics of the machining process too. Merchant (5) designed the most simple and widely used model to determine the shear plane angle. He constituted a mathematical concept for describing force relationships in the cutting process.

2. Multifunction Measuring System

The modelling system FEM is an important tool for rationalization of the metal cutting process, allowing industry to make parts faster, better, and at less cost but mainly ensuring the functional characteristics (12, 13). Innovative measurement methods of the process using thermal systems, high-speed scanning of dynamic processes and influence can be used to improve and verify the accuracy of these models. Four goals of manufacturing-related research at the Department of Machining and Manufacturing are: to develop and improve measurement techniques, to develop an understanding of the uncertainties involved with performing such measurements, to compare models of machining with thermal and visible spectrum images to verify the models, and to share this understanding with the machining community (14, 15). Two of the many types of chips are called continuous and segmented. A continuous chip is a long ribbon of relatively uniformly deformed material. By contrast, a segmented chip has alternating zones of low and high shear strain. A zone of low strain in a segmented chip is called a segment. The zones of high strain between the segments are mechanically weak, so the long ribbons of material tend to break into short pieces (18). The shear zone is somewhat stationary when continuous chips are formed, but often travels along with the chips when the chips are segmented. We will call the area surrounding the shear zone the face of the chip. The shear zone has a higher temperature than the face. For segmented chips, the shear zone generally also has a higher emissivity than the face (19).

This multi-axis measuringsystem (Figure 2) was designed for the universal lathe SUI-40, but the construction of the stand guarantees some universality of the measuring system for other types of machines.

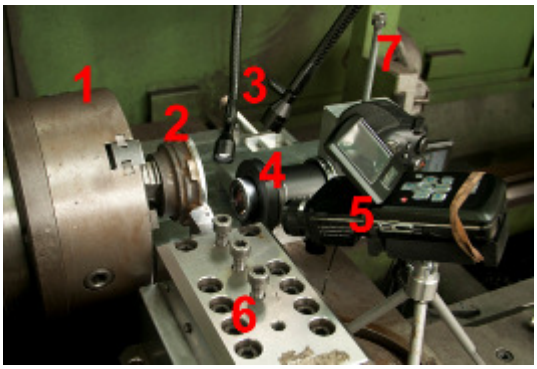

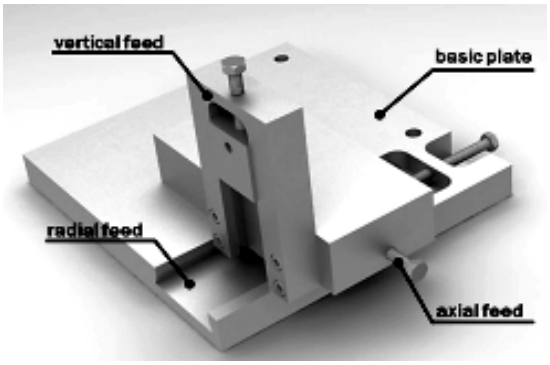

Fig. 2. Multifunction measuring system, 1 – chuck; 2 – sample; 3 – cold light; 4 – high-speed imaging camcorder, 5 – thermo-vision system; 6 – dynamometer with tool; 7 – macro-stand

Fig. 3. Macro-stand with triaxial feed for mounting of high-speed imaging camcorder, which provides simultaneous movement of the cutting tool and camcorder

Dynamical monitoring of the cutting process can be provided by the high-speed imaging camcorder, which ensures high-speed imaging in all experiments, with an imaging frequencyof 1000fps. For detailed study, a super-macro lens Raynox MSN-202 with 20x magnification was used. Based on this optical system, we can capture an area of 4mm x 3mm. The actual heat distribution can be monitored by the thermo-vision system, which captures the thermal field in the cutting zone and heat distribution when machining. This compactcamera allows us to measure temperatures up to 1200°C with a tolerance of ±2°C. Special optics with deflected lens allow us to place the camera outside of the perpendicular on the scanned object (14). The piezoelectric 3-

component dynamometer can capture fast dynamic force relations, measured as cutting forces with high-speed scanning up to $1x10^5$Hz.All the applied measuring devices are integrated on a macro-stand (Figure 3). For correct mounting and manipulation, the macro-stand was designed with mounting on the lathe support, in order to ensure the simultaneous motion of the camera and cutting tool. Nickel alloys are a popular material due theirhigh heat and creep resistance. Due to their specific properties, they are used in the aerospace industry. Due to their mechanical and chemical properties, they are included among the hard-machined materials. Because this material is characterized as having a combination of strength, toughness and hardness, it is necessary to choose specific cutting conditions(17, 18). These were chosen from the real cutting conditions used in practice and they are shown in of Figure 4. All experiments were performed without coolant, because this would prevent the scanning by the high-speed thermo-graphic camera (18). The free cutting approach ensures as much as possible of the area of the cutting zone and also ensuresthat the chips depart in the opposite direction of action from that of the cutting tool (19).

3. Evaluation of the Experiments

Measurements of cutting forces were conducted in various cutting conditions. As we can see, the cutting force Ff increased with the increasing feed and, conversely, cutting force Fc decreased with increasing cutting speed (Figure 4). It can be deduced from the measured data that the behaviour of nickel alloy Monel400 is similar to the machining austenite of steel, but with a higher ratio of cutting forces considering the mechanical properties of this alloy. From monitoring of the dynamic course of the cutting forces, we can say that the cutting process is created by frequent accumulation of material as the built-up edge. The built-up edge has considerable influence for the cutting geometry, which causes the high dynamization of the cutting process.

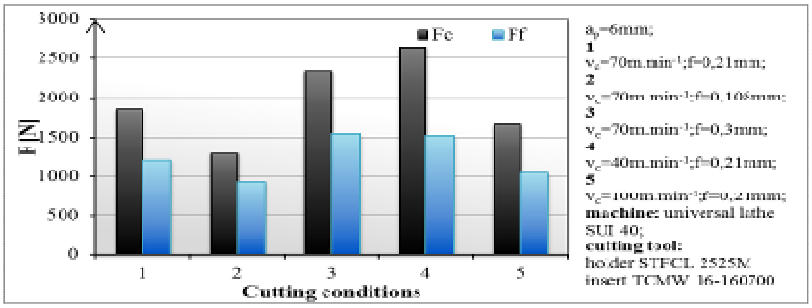

Fig. 4. Static values of cutting forces in various cutting conditions

Methods of examining and monitoring the cutting zone are developing with available technologies that are applicable for the monitoring and capturing of processes during the cutting process (14). The most common possibilities include research of deformation processes based on finished changes after the end of the cutting process, such as examining metallographic samples from the cutting zone, acquired by the immediate interruption of the cutting process, etc. (15). This research reached sufficient and complete conclusions about the processes in the cutting zone, but in a static concept after the finished process. Therefore, it was necessary to find new innovative technologies for idealized physico-mathematical models, as the previous experimental outcomes provide information about finished processes only. It is necessary to record deformation processes in the form of a high-speed video and image sequences from which the creation, shape of chips and deformations in the cutting zone when machining can be evaluated, and these can be made from monitoring of the cutting zone by a high-speed imaging camcorder (17, 18).

In the high-speed video records, it is possible to see the formation of deformation processes depending on the cutting conditions. At low cutting speeds, the formation of elementary chips occurs, giving rise to high dynamic shocks which load and cyclically fatigue the cutting edge up to destruction (Figure 5).

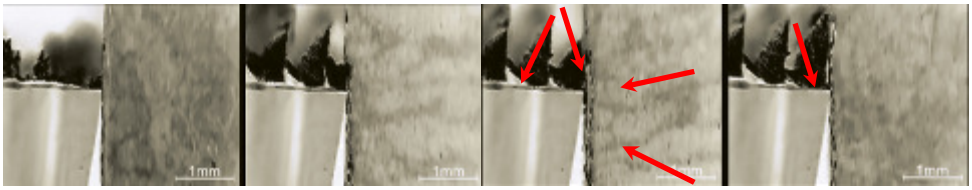

Fig. 5. Cutting process with continuous cut and minimal cutting speed v_c = 40 m.min^{-1} and feed 0.21mm, rise of elementary chip and deformation areas of plastic and elastic deformation

At the higher cutting speeds, the formation of continuous ribbon chip occurs, which has a different character of influence on the cutting edge, where thermal effects outweigh the dynamic shocks and cyclic loadings (Figure 6).

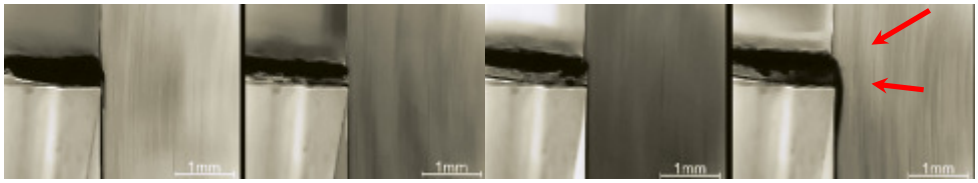

Fig. 6. Cutting process with continuous cut and maximal cutting speed v_c = 100 m.min^{-1} and feed 0.21mm, formation of continuous ribbon chip and deformation areas of plastic and elastic deformation

In the last picture (of Figure 6) of the measuring system, the primary and tertiary area and their influence on the machined surface can be seen. This surface has the effect of pooling the high stress loadings, which act negatively on the functional properties of parts. By application of the notch, there was simulation of discontinuous cut, in which the monitoring of the cutting process before and after tensioning of the technological system was important. Cutting conditions were identical to the conditions of the continuous cut. In this experiment, there is formation of the same chip, which has an identical character to that in the previous experiment. The cutting edge of the cutting tool is exposed to temperature mainly and dynamic shock and cyclic loadings (Figure 7).

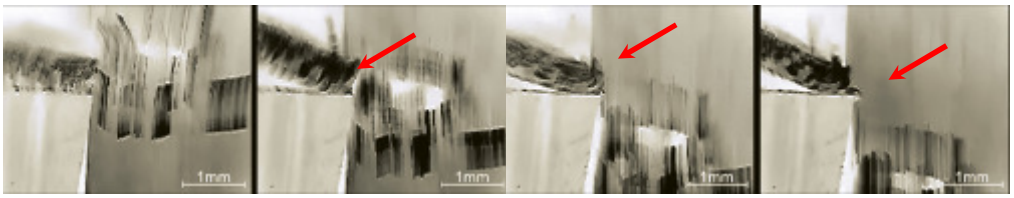

Fig. 7. Cutting process with continuous cut and maximal cutting speed vc = 100 m.min-1 and feed 0.21mm, formation of continuous ribbon chip and deformation areas of plastic and elastic deformation

In each picture of the measuring system, relaxation of the technological system (tool – workpiece) can be seen with the transition to the tensioning of the technological system. These images show the formation of deformation processes, and are thus a suitable basis for new simulation and mathematical models.

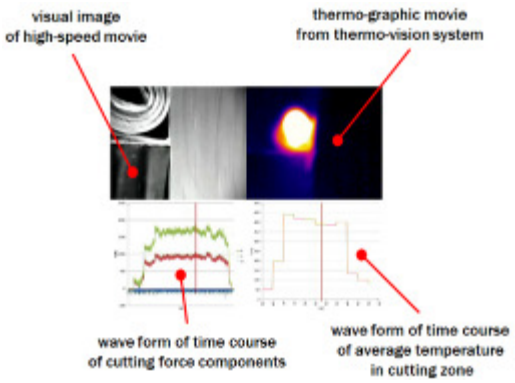

Fig. 8. Deployment of monitored processes in the video output of multifunctional measuring system (11)

The data obtained from the individual processes during the experiments have a direct relationship with each other because they were obtained simultaneously in a single machining process. In this case they provide especially a waveform record of the cutting forces, the time course of temperature field development and visual records of the deformation phenomena during the machining process. The measured data were then processed on a computer into video clips that show how individual phenomena are associated with each other in the cutting zone (Fig 8).

Sequential frames from multi-parametric output are shown schematically: In the upper left corner is a visual record from the high-speed camera. In the top right corner is a thermo-graph – respectively the thermo-graphic time course of the thermo-vision system (this is slowed down for the high-speed camera frame rate). Belowthe video output is the waveform of the components of the cutting force on the left and the graphic time course of the development of the average temperature in the cutting zone. During the turning of the nickel alloy Monel 400, the phenomenon occurs that the the primary contact of the tool and machined material is highly loaded with the pressure of transition from forming to the cutting process. In the first frame (Figure 9), it is possible to see the formation of elementary chips after the intrusion of the cutting tool into the action, and after the stabilization of the cutting process, flat spiral chips were created.

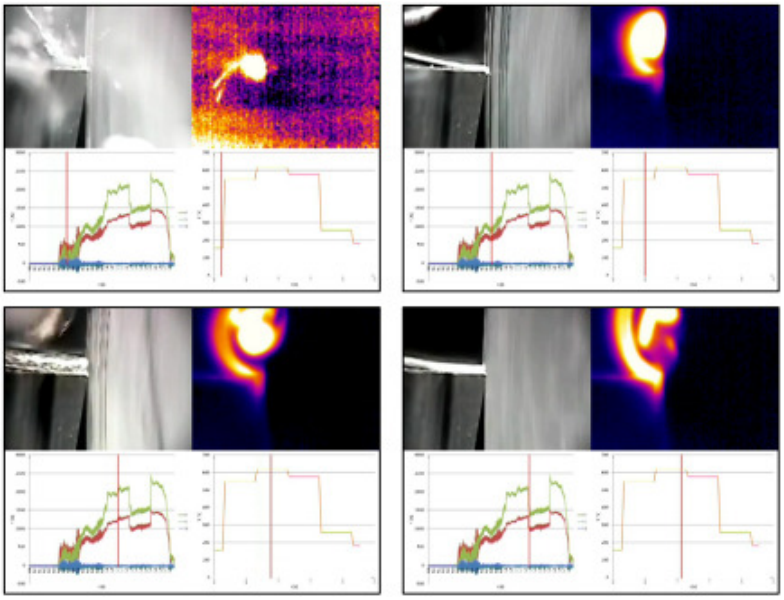

Fig. 9. Selected frames from video output of the multifunction measuring system (continuous cutting; v_c=70m.min^{-1}; f=0,21mm; a_p=6mm; machine: universal lathe SUI-40; cutting tool: holder STFCL 2525M, insert TCMW 16-160700)

The microstructure and mechanical properties of the materials caused a built-up edge to form almost throughout the cutting process. The components of cutting force during the formation of the built-up edge and its subsequent “holding on” to the front face of the cutting tool grew, respectively, very high. After being picked, the cutting forces decreased sharply. With the new creation of a built-up edge, the whole process was repeated. This iterative cycle resulted in a specific shape of waveform of the components of the cutting force. In the third frame of Figure 9 the built-up edge and increased components of the cutting force can be seen. The last frame of Figure 9 capturesthe moment immediately after the built-up edge is picked.

4. Conclusions

The multifunction measuring system designed for the monitoring of processes in the cutting zone allows observation of the deformations, temperature field, forming and shape of chip directly in the course of the cutting process, without interruption. We can evaluate the measured data in the specific dependences which exist between them. The forces which act in the process change depending on the cutting conditions, structure and mechanical properties of the machined material.

The deformation processes which are in the cutting zone during machining take place at high speed. Under normal observation with the naked eye or by microscope only, these processes are not identifiable. Detailed observation is possible using the high-speed imaging camcorder. In this way, we can observe not only the deformation processes but also the creation and formation of chips.

With the multifunction measuring system, we can better intensify the machining process, cutting conditions and so improve the product quality. We can also reduce the cost, because this system allows simultaneous measuring. Based on the observations of the deformation processes in the cutting zone, as well as the creation and formation of chips, we can also optimize the shape of the cutting inserts.

This article was funded by the University of Zilina project OPVaV-2009/2.2/04-SORO number (26220220101) - "Intelligent system for nondestructive technologies on evaluation for the functional properties of components of X-ray diffraction ".

References

[1] CEP, R., OCENASOVA, L., NOVAKOVA, J., et. al.: Interrupted Machining Tests of Ceramic Cutting Tools, TMT 2009 Proc., October 2009, Hammamet, vol. 13, no. 1, pp. 733-736. ISSN 1840-4944.

[2] NOVÁKOVÁ, J., PETŘKOVSKÁ, L., BRYCHTA, J., STANČEKOVÁ, D.: Influence of cutting parameters on integrity surface at high speed cutting. Transactions of the VŠB - Technical University of Ostrava. Mechanical Series, vol. LV., no. 1/2009, Česká Republika. Ostrava: VŠB – TUO, pp. 203-209.

[3] SHAW, M. C.: 2005. Metal Cutting Principles, 2nd Edition, Oxford University Press.

[4] MERCHANT, M. E.: Basic mechanics of the metal cutting process, Journal of Applied Mechanics, vol. 11, 1944.

[5] BOOTHROYD, G., KNIGHT, W. A.: Fundamentals of Machining and Machine Tools, CRC Press, 2006.

[6] LEE, E. H., SHAFFER, B. W.: Theory of plasticity applied to a problem of machining, Journal of Applied Mechanics, vol. 18, 1951, pp. 405-413.

[7] ZOREV, N. N.: Metal Cutting Mechanics, Pergamon Press, 1966.

[8] PALMER, W. B., OXLEY, P. L. B.: Mechanics of Orthogonal Machining, Proceedings of the Institution of Mechanical Engineers, vol. 173, no. 24, 1959, pp. 623-654.

[9] ROTH, R. N., OXLEY, P. L. B.: A slip line field analysis for orthogonal machining based on experimental flow fields, Journal of Mechanical Engineering Science, vol. 14, 1972, pp. 85-97.

[10] CEP, R., JANASEK A., PETRU J., CEPOVA L., CZAN A., VALICEK J.: Hard machinable machining of cobalt-based superalloy. In Manufacturing Technology XIII/13, 2013. UJEP:, pp. 226-231. ISSN 1213-2489.

[11] MOHYLA, P., TOMČÍK, P., BENEŠ, L., HLAVATY, I.: Effect of post-welding heat treatment on secondary hardening of welded joints of Cr-Mo-v steel. Metal Science and Heat Treatment, vol. 53, issue 7-8, 2011, pp. 374-378. ISSN 0026-0673.

[12] CZAN, A., TILLOVA, E., SEMCER, J., PILC, J.: Surface and subsurface residual stresses after machining and their analysis by x-ray diffraction, Communications – Scientific Letters of the University of Zilina, vol. 15, issue 2, 2013, pp. 69-76. ISSN 1335-4205.

[13] WHITENTON, E. P., et al.: High-speed dual spectrum imaging for the measurement of metal cutting temperatures, Manufacturing Engineering Laboratory, NIST, Gaithersburg, 2010.

[14] PILC, J., MIČIETOVÁ, A., SALAJ, J., ČILLIKOVÁ, M.: The influence of selected aspects in planing operations by using auto-rotation tool, Transactions of Famena, vol. 29, issue 2, 2005, pp. 55-60. ISSN 1333-1124.

[15] CEP, R., KOURIL, K., MRKVICA, I., JANASEK, I., PROCHAZKA, J.: Zkoušky nastroju Kyocera v podminkach prerusovaneho rezu, Strojirenska Technologie, vol. XV, 2010/3, pp. 51-58. ISSN 1211-4162.

[16] LITVAJ, I., PONIŠČIAKOVÁ, O., STANČEKOVÁ, D., DRBÚL, M.: Knowledge processes and their implementation in small transport companies, 17th International Conference on Transport Means 2013, Kaunas, Lithuania, 24–25 October 2013, Code 102486, pp. 153-156. ISSN 1822-296X.

[17] HOLESOVSKY, F., NAPRSTKOVA, N., NOVAK, M.: GICS for grinding process optimization. In Manufacturing Technology XII/12. 2012. UJEP: Ústi n. Labem, pp. 22-26. ISSN 1213-2489.

[18] ČEP, R., JANÁSEK, A., ČEPOVÁ, L., PETRŮ, J., HLAVATÝ, I., CAR, Z., HATALA, M.: Eksperimentalno ispitivanje rezne sposobnosti izmjenjivih reznih umetaka | [Experimental testing of exchangeable cutting inserts cutting ability]. In Tehnicki Vjesnik, 20 (1), 2013, pp. 21-26. ISSN 1330-3651.

[19] WHITENTON, E. P., IVESTER, R., et al.: Simultaneous visible and thermal imaging of metals during machining. In Thermosense XXVII. Orlando, International Society for Optical Engineering, 2005.

TRANSCOM 2015, 22-24 June 2015
University of Žilina, Žilina, Slovak Republic

Evaluation of Magnetically Oriented Surface after Hard Milling Cycles

[*]Tomáš Hrabovský, [**] Dalibor Blažek, [*]Miroslav Neslušan
[*]University of Žilina, Faculty of Mechanical Engineering, Department of Machining and Manufacturing Technology, Univerzitná 1, 01026 Žilina, Slovakia, {tomas.hrabovsky, miroslav.neslusan}@fstroj.uniza.sk
[**]Nanotechnology Centre, VŠB-TU Ostrava, 17. listopadu 15, 70833 Ostrava – Poruba, Czech Republic
dalibor.blazek@vsb.cz

Abstract. This paper deals with the specific magnetic state of surface after hard milling operation carried on roll bearing steel 100CrMn6 of hardness 62 HRC. The paper reports about strong magnetic anisotropy of hard milled surface induced by severe plastic deformation at elevated temperatures. The surface undergoing such process produces high magnitude of Barkhausen noise in direction of cutting speed whereas perpendicular direction does not. Due to Bloch walls aligned in direction of cutting speed appearance of hysteresis loops differs from conventional ones. Moreover, appearance of hysteresis loops is sensitive to the thickness of white layers occurring in the near surface region.

Keywords: Hysteresis loop, Kerr rotation, Hard milling

1. Introduction

Hard milling cycles can substitute grinding operation in making a variety of components with possible technical, economy and ecology benefits. On the other hand, mechanism of chip separation significantly differs from grinding. The main distinctions of hard milling can be found follows [1]:

- much higher magnitude of compressive stresses and cutting temperatures over entire tool – workpiece contact,
- much shorter time period during which the surface undergoes severe plastic deformation,
- shorter contact length between cutting edge and workpiece,
- white layers (WL) initiated at quite low flank wear VB.

Grinding cycles are nowadays very often monitored by nondestructive Barkhausen noise (BN) techniques to identify and exclude components of unacceptable surface state. BN is a physical phenomenon produced by irreversible and discontinuous Bloch Walls (BW) motion in ferromagnetic materials due to pinning strength of microstructure constituents such as dislocation tangles, carbides or precipitates as well as stress state [2, 3, 4]. The concept in which such technique is adopted in the real industrial application is based on the higher magnitude of BN (produced by over tempered surfaces) due to thermal softening as a result of decreased dislocation density, carbides coarsening and tensile stresses. All these aspects contribute to the higher BN compared with the low BN of thermally untouched surfaces [5, 6]. It should be noticed that nondestructive monitoring of hard milled surfaces based on BN technique has not found industrial relevance yet due to complicated relations between BN and surface integrity. Surface state after hard machining is a function mainly of flank wear *VB* and cutting speed. Application of a tool of high *VB* produces relative thick (WL) as well as the corresponding heat affected zone (HAZ) [7]. On the other hand, grinding cycles produces usually WL free surfaces. Thickness of HAZ after hard milling is about 1 order lower than that induced by grinding cycle. HAZ increases magnitude of BN compared to bulk whereas WL in the near-surface region emits poor BN due to existence of higher volume of retained austenite, compressive stresses and very fine grain [8]. Being so, relation BN versus *VB* is not always monotonous thus making application of BN for hard milled surfaces a debatable issue.

To develop the suitable concept in which hard milled surfaces could be monitored the detail and thorough investigation of specific character of hard milled surface should be carried out and alternative techniques for their analysis should be established. MOKE is a specific technique based on application of polarized laser beam reflected by investigated surface in the magnetic field. Its penetration depth is limited to the several nm. This method can be employed for evaluation of magnetic properties of nano layers, influence of surface reflexivity, anisotropy, detection of hysteresis loops appearance etc. [9, 10].

3 basic configurations can be found in dependence on magnetic field orientation:

- longitudinal: magnetization of a sample is parallel with the laser beam (Fig. 1a),
- transversal: magnetization of a sample is perpendicular with the laser beam (Fig. 1b),
- polar: magnetization is perpendicular to the sample plane (Fig. 1c).

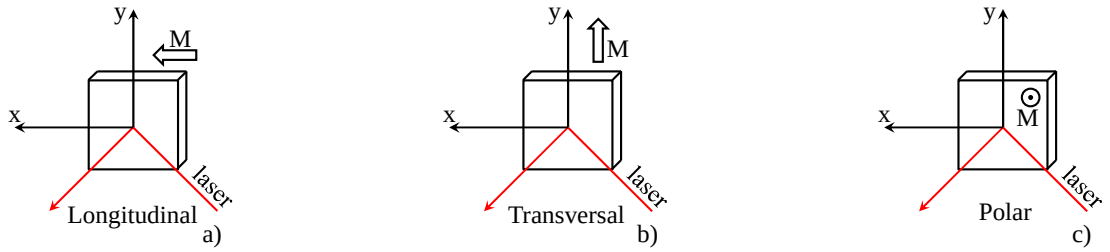

Fig. 1. Three basic configurations during measurement of Kerr rotation

This paper reports about evaluation of hard milled surface via MOKE technique based on Kerr rotation. Hysteresis loops, BN as well as surface microstructures are studied on samples produced by variable VB as a major factor influencing surface integrity of hard milled surfaces.

2. Experimental conditions

Experiments were conducted on samples made of bearing steel 100CrMn$_6$ of hardness 62 HRC. Five samples of dimension 20x20x5 mm were prepared for MOKE study. Cutting process was monitored as a long term test where such aspects as flank wear *VB*, structure alterations and corresponding surface integrity expressed in (BN) were investigated. Cutting and other conditions: milling machine - FA4 AV, dry cutting, cutting tool made of cemented carbides R300-1240E-PM, R300-050Q22 - 12M 262489 of diameter Ø 50mm with 2 inserts of variable flank wear *VB* (in the range 0,05 to 0,74 mm), a_p = 0,25 mm, v_f = 112 mm.min^{-1}, n = 500 min^{-1}. Flank wear was measured for both cutting inserts and *VB* values indicated in the paper represent their average value.

BN measurement was performed by the use of RollScan 300 and software package MiocroScan in the frequency range of 10 to 1000 kHz (mag. frequency 125 Hz, mag. voltage 10 V). Each BN value was determined by averaging of 10 consecutive BN bursts (5 magnetizing cycles). Due to strong surface anisotropy, each surface was measured in two directions - tangential and axial as Figure 2 illustrates. BN values indicated in the paper represent the effective (rms) value of BN signal. To reveal the microstructure transformations induced by milling 10 mm long pieces were sectioned from the samples and routinely prepared for metallographic observations (etched by 5% Nital for 10s).

Brief illustration of MOKE equipment is indicated in Fig. 2 and Fig. 3. Measurement was carried out in longitudinal and transversal (perpendicular) directions with incidence angle of laser beam 45° (the difference between the second harmonic components was measured). Other conditions: λ = 670 nm, f = 50 kHz, I = 10 A, 2000 points per hysteresis loop.

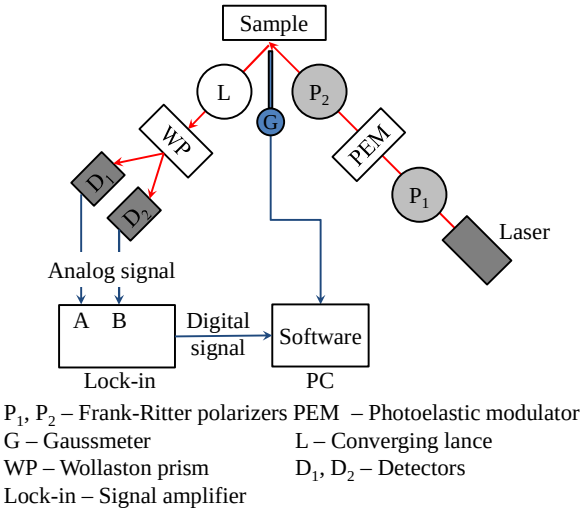

Fig. 2. Brief illustration of MOKE

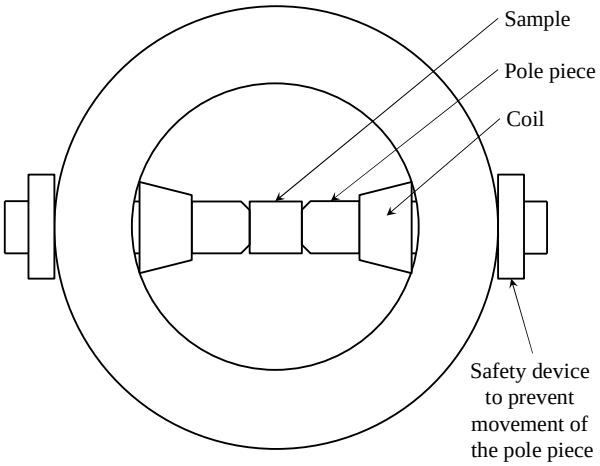

Fig. 3. Position of a sample between poles

3. Experimental Results and their Discussion

Due to cutting temperatures exceeding austenitizing temperature followed by rapid cooling the near surface region usually contains thin WL followed by HAZ in the deeper regions. As VB becomes more developed the thickness of WL (as well as HAZ) also increases in thickness, see Fig. 4. Fig. 5 illustrates the BN obtained for the different directions and VB. Fig. 5 shows that the BN magnitude of surface produced by inserts with VB = 0,05 mm is much higher that that obtained in the transversal direction. Moreover, as VB becomes more developed BN emission is strongly reduced. Such remarkable magnetic anisotropy of the hard machined surfaces was previously reported [11]. As it was claimed [11], the main reason can be viewed in cutting temperature exceeding the Curie temperature needed to disturb domains configuration of ferromagnetic steel. Domain configuration of the near surface during heating is disturbed and the new domain alignment is configured during rapid cooling. Domains are not randomly but preferentially oriented in the direction of the cutting speed (tangential direction). This information implies that the specific domain configuration and the corresponding specific mechanism of BW motion during cyclic magnetization dominate (discussed later).

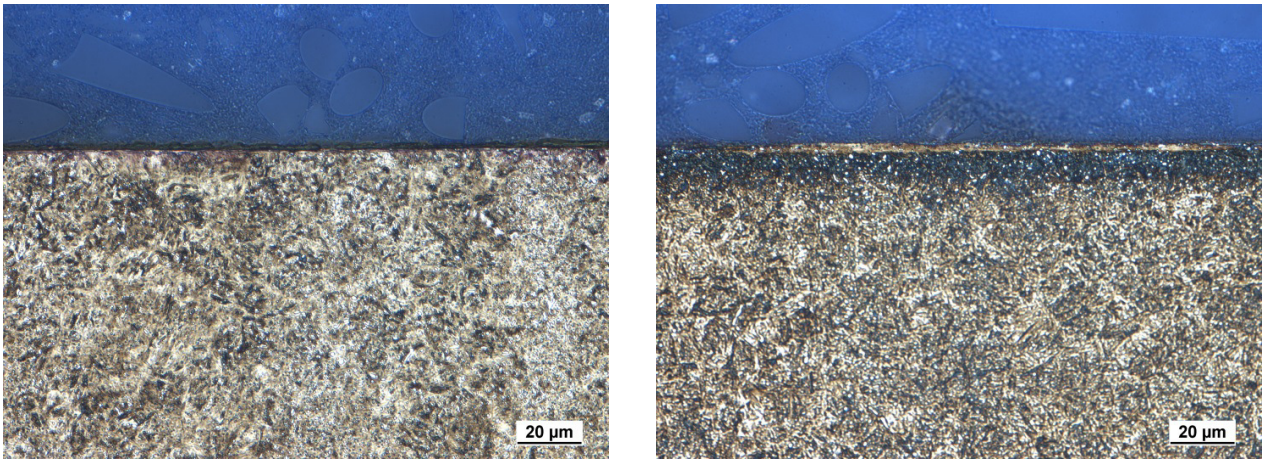

a) VB = 0,05 mm b) VB = 0,74 mm

Fig. 4. Microstructure of hard milled surfaces, Nital 5%, zv. 800x

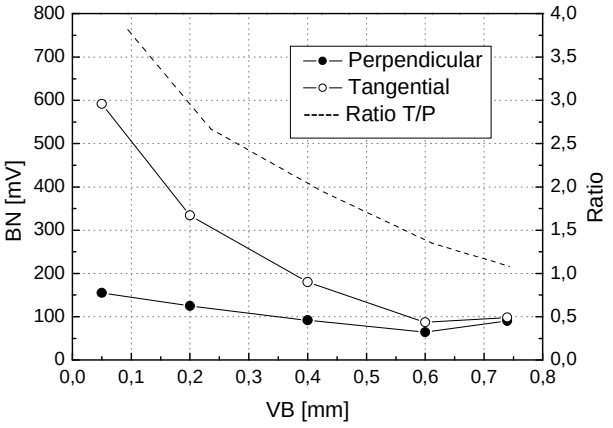

Fig. 5. BN values and degree of anisotropy

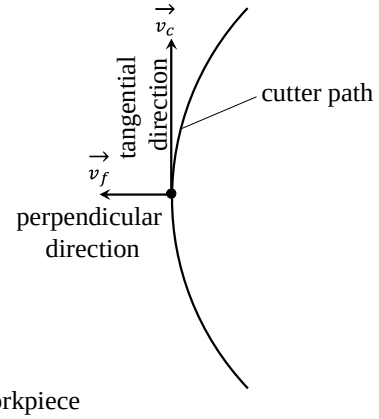

Fig. 6. Illustration of cutter path

Fig. 5 shows that BN drops down along with the progressive developed VB. This effect is linked with structure transformations in the near surface layer as a region mostly contributing to the BN. While HAZ is a region producing richer BN due to reduced hardness (effect of thermal softening), WL after grinding usually emits quite poor BN emission as a result of higher volume of retained austenite, compressive stresses, very fine grain, high dislocation density and carbon in a supersaturated state. WL is a region in which cutting temperature exceeds the austenitizing temperature. Flank wear land represents the path during which the machined surface undergoes the severe plastic deformation at elevated temperatures. More developed VB corresponds with the longer time period within the machined surface undergoes severe plastic deformation at elevated temperatures and temperature in the tool – workpiece interface increases with VB due to increasing normal and shear stresses [12].

Both aspects contribute to the thicker WL (as well as HAZ) along with VB because the austenitizing temperatures penetrate deeper beneath the surface. As it was reported, the near surface region contains WL as a structure constituent emitting poor BN. For these reasons, high hardness and high BN values are controversial and should be discussed. To explain such high BN signal two basic specific aspects of such surfaces should be considered. First one is connected with the above mentioned strong magnetic anisotropy and new domain alignment. Second one is attributed to the limited thickness of affected near surface region and its structure. Due to limited thickness of affected region, preferential orientation of domains and the corresponding BW the mechanism in which domains and BW are switched differs from the conventional concept usually linked with BW motion in structures without strong anisotropy. Isotropic surfaces usually produces hysteresis loop of the typical S-shape as a product of BW interference with the variable pinning sites represented by different microstructure features. Being so, mechanically soft structures containing small volume of pinning sites of low pinning strength gives narrow hysteresis loop of high remanence and low coercive force whereas hard structures gives more thick hysteresis loop of low remanence and high coercive force [13]. Nevertheless, both structures gives S-shape hysteresis loop, see Figure 7, c, d. On the other hand, anisotropic surface produces more angular hysteresis loop as that shown in Fig. 7a. High BN values at low VB are due to low orientation mismatch among the neighboring grains (domains) and low volume of retained austenite. Moreover, carbides pinning strength is strongly reduced because their domain alignment re-configured during heating and rapid cooling are also driven by magnetostriction. Furthermore, carbides are severely stretched in tangential direction. For these reasons, cyclic magnetization produces strong BN because all domains change their orientation during short time period. Such process produces quite different hysteresis loop of typical angular shape as Fig. 7a indicates. This mechanism, together with the specific domain configuration explains high BN values for low VB can be found as well as explain the appearance of the corresponding hysteresis loop depicted in Fig. 7a. The domain configuration, as that illustrated in Fig. 7a, is thickness sensitive and typical for thin ferromagnetic surface layers only. As soon as the

thickness of such layer is gradually increased the mechanism of BW motion is altered. Increasing pinning strength of WL is due to increasing volume of retained austenite as well as carbides retaining in their original shape in deeper regions. This aspect explains why BN drops down and angular shape of hysteresis loop is transformed to the typical S – shape, see Fig. 7b. Moreover, as the hysteresis loop becomes more S-shaped the saturation also drops down due to reduced volume of ferromagnetic structure at the expense of the volume of retained austenite.

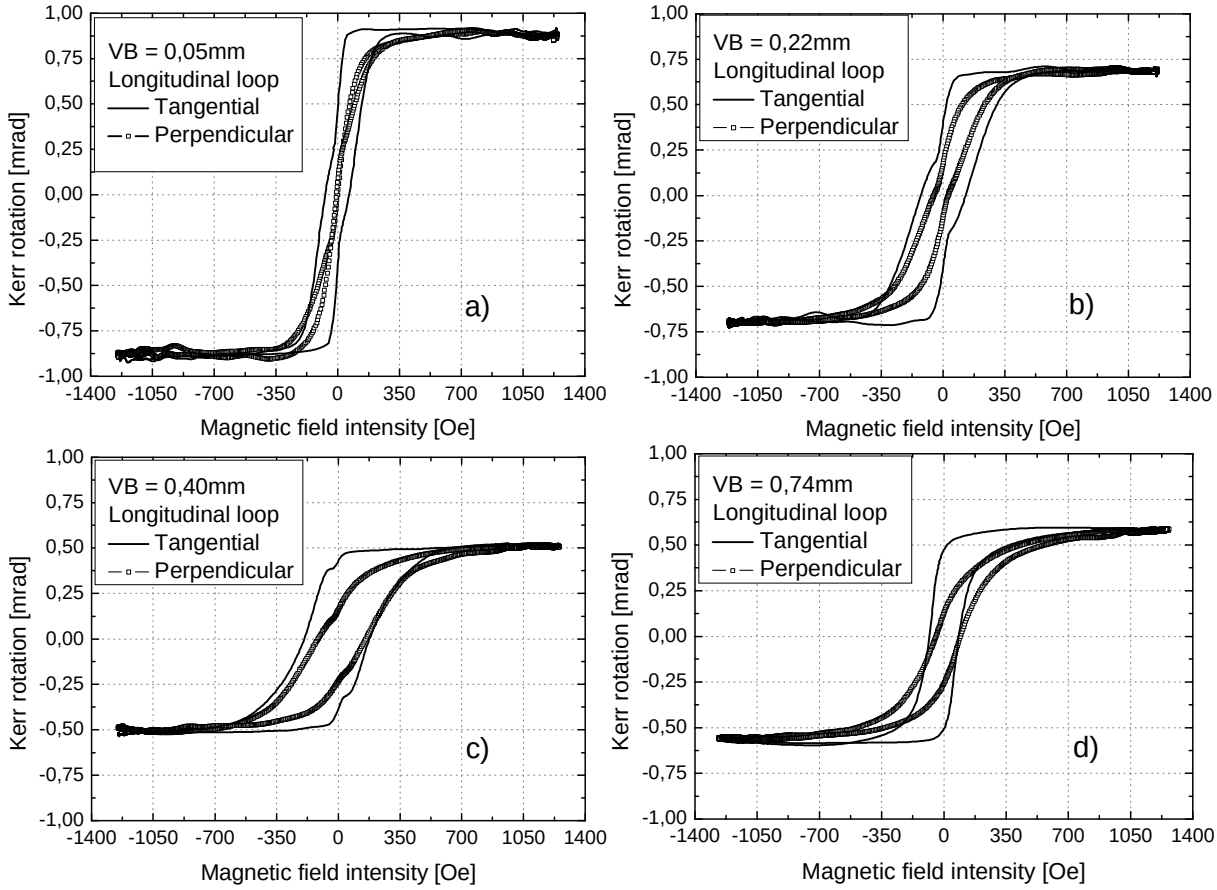

Fig. 7. Hysteresis loops for surface produced of variable VB

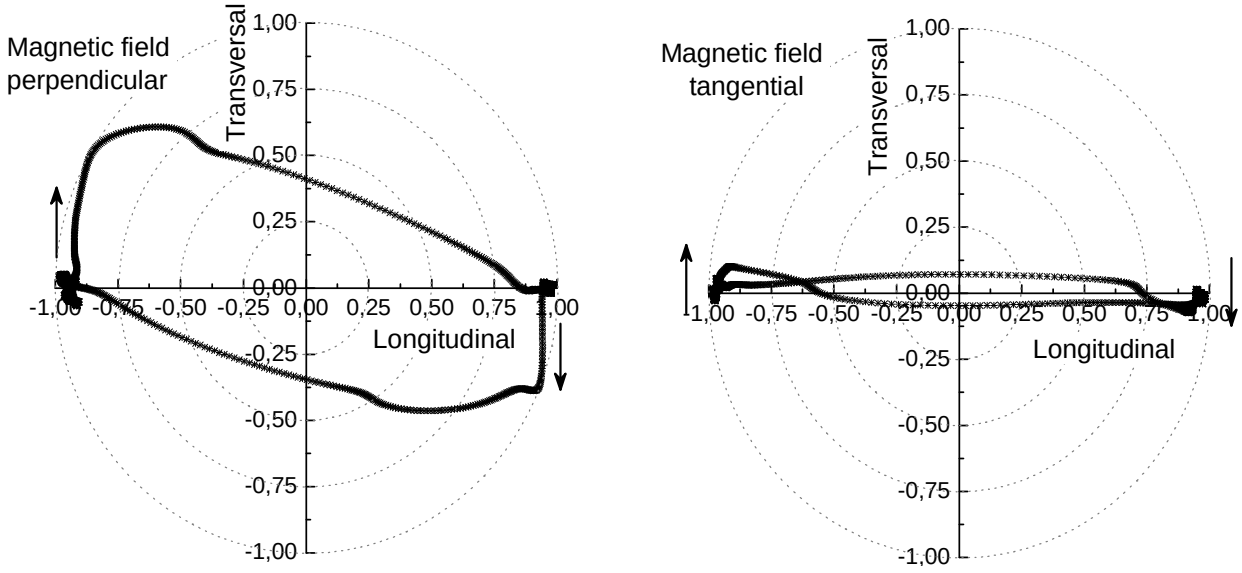

a) Perpendicular direction b) Tangential direction

Fig. 8. Polar plots, VB = 0,4 mm

Specific information about BW motion can be found from polar plots as those indicated in Fig. 8. It is well known that BW rotation can be distinguished from BW irreversible motion. Fig. 8a indicate BW rotation when the sample in magnetized in transversal direction (hard axis of magnetization). Direction of BW follows the gradual rotation of magnetizing field (follow the circle path) due to magnetostriction effect of induced residual stresses (stress anisotropy – stresses in tangential direction dominates). As soon as, the critical value of magnetic direction is attained irreversible 90º BW motion occur (BW position leave the circle path, see Fig. 8a). On the other hand, small changes in magnetization produces quite fast process of irreversible 180º BW motion when the sample is magnetized in longitudinal direction (easy axis of magnetization), see Fig. 8b.

4. Conclusions

Hard milling cycle produces the different state of surface integrity than that after grinding. Its nondestructive evaluation via BN technique is very specific. Due to strong magnetic anisotropy BN signals after hard milling exhibit specific features (not discussed in this paper) at variable magnetizing conditions. A reliable concept for monitoring hard milled surfaces employed in industry via BN technique need thorough research and understanding of specific mechanism linked with structure features.

Acknowledgement

This article was edited under the financial support of KEGA projects n. 005ŽU - 4/2014, 009ŽU - 4/2014 and project New Creative Teams in Priorities of Scientific Research grant CZ1.07/2.3.00/30.0055. The authors would like to thank to Nanotechnological centre on VŠB TU Ostrava for long term tests (MOKE analysis) carried out in its laboratories.

References

[1] GUO,Y.B, Sahni, J. *A comparative study of of hard turned and cyllindrical ground white layers*, International Journal of Machine Tool & Manufacture 44, 2004 , pp. 135 - 145.
[2] KAMEDA, J., RANJAN, R. *Nondestructive evaluation of steels using acoustic and magnetic Barkhausen signals – II. Effect of intergranular impurity segregation*, Acta Metall., vol. 35/7, 1987, pp. 1527-1531.
[3] GATELIER-ROTHEA, C., et all. *Characterization of pure iron and carbon-iron binary alloy by Barkhausen noise measurements: study of the influence of stress and microstructure*, Acta Mater. Vol. 46/14, 1998, pp.4873-4882.
[4] RANJAN, R., JILES, D.C., RASTOGI, P. *Magnetic properties of decarburized steels: An investigation of the effects of grain size and carbon content*, IEEE Trans. Magn., vol. 23/3, 1987, pp.1869-1876.
[5] MIČÚCH, M., ČILLIKOVÁ, M., NESLUŠAN, M., MIČIETOVÁ, A. *Micromagnetic study of cutting conditions and grinding wheel wear influence on surface integrity*, Manufacturing Technology, vol. 14, 2014, pp. 66-71.
[6] ROSIPAL, M.: *Application of Barkhausen noise for study of surface integrity of machined surfaces*, PhD. Dissertation, University of Žilina, 2012.
[7] NESLUŠAN, M., ROSIPAL, M., OCHODEK, V. *Analysis of some aspects of surface integrity after grinding and hard turning trough Barkhausen noise*. Proc. of ICBN 09, Hejnice, 2011.
[8] BRANDT, D. *Randzonenbeeinflussung beim Hartdrehen*, Dr.-Ing. Dissertation, Universität-Hannover, 1995
[9] ŽIVOTSKÝ, O., POSTAVA, K., et. all. Depth-sensitive characterization of surface magnetic properties of as-quenched FeNbB ribbons, Applied surface science 255, 2008.
[10] ŽIVOTSKÝ, O., HENDRYCH, A. *Influence of tensile stress on the surface magneto-optical hysteresis loops in amorphous and (nano)crystalline ribbons*, IEEE Transactions on magnetics, vo. 50, No. 4, April 2014.
[11] NESLUŠAN, M. et. all. *Magnetic anisotropy in hard turned surfaces*. Acta Physica Polonica, 124 (2014), pp. 188 – 189.
[12] WANG, Y., LIU, C. R. *The effect of Tool Flank Wear on the Heat Transfer, Thermal Damage and Cutting Mechanics in Finishing Hard Turning*, CIRP Annals 48 ,1999, pp. 53 – 56.
[13] HAJKO, V., POTOCKÝ, L., ZENTKO, A. *Magnetization processes*, ALFA Bratislava, Slovakia, 1982.

TRANSCOM 2015, 22-24 June 2015
University of Žilina, Žilina, Slovak Republic

Influence of Time During Isothermal Quenching

[*]Peter Jankejech, [*]Peter Fabian, [**]Alexander Rengevič
[*]University of Žilina, Faculty of Mechanical Engineering, Department of Technological Engineering,
[**]University of Žilina, Faculty of Mechanical Engineering, Department of Automation and Production Systems
Univerzitna 2, 01026 Žilina, Slovakia, {peter.jankejech, peter.fabian, alexander.rengevic}@fstroj.uniza.sk

Abstract. This contribution deals with isothermal quenching of steel which is used for bearing industry. The chemical composition of steel is slightly different in comparison with the classic 100Cr6Mn type by the addition of molybdenum which has its specific influence during isothermal quenching. The main purpose is to focus on the influence of time during isothermal quenching in salt bath. The influence will be investigated and evaluated by applying hardness test, impact toughness test and light metallography. The conclusion of this contribution is to improve the knowledge of isothermal quenching by using steels with such chemical composition.

Keywords: Microstructure, molybdenum, quenching, hardness, toughness.

1. Introduction

Bearing components are design to withstand high forces during service. Because of this the requirements on mechanical properties are strict and many times it is a challenge to manufacture such components. The process where the material receives its qualities is heat treatment. Typical method of heat treatment in bearing industry is quenching which is followed by tempering. The quenching process guarantees that the component will obtain its specific hardness and strength. If martensitic quenching is applied the component must be tempered to relax from residual stresses and brittleness. When it comes to quenching of parts with big cross sections the properties from surface to the core may differ. To avoid differences another type of heat treatment is applied. It is called isothermal quenching where the temperature during quenching process is controlled (Fig.1).

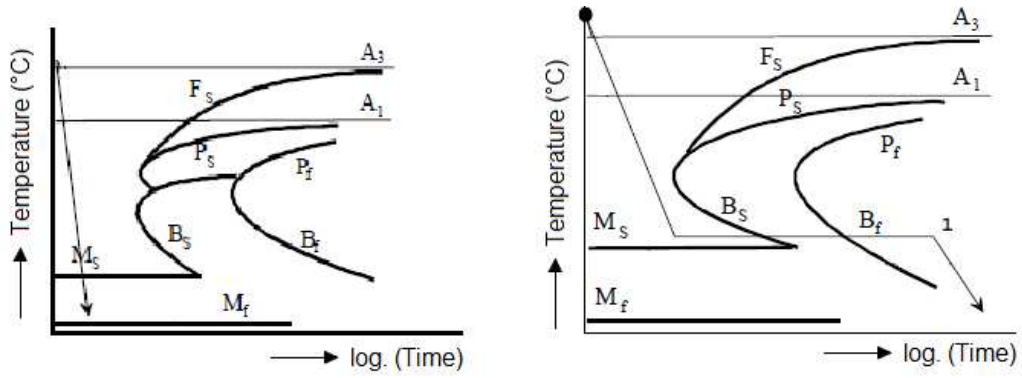

Fig. 1. Difference between martensitic (left) and isothermal (right) quenching (1,2)

After austenitization the material is cooled down by applying a defined cooling rate to the point (temperature) where isothermal transformation from austenite to the desired structure takes place. The transformation is then followed by holding on the reached temperature. (1) This means that the temperature from the surface to the core has enough time to balance before the transformation line is reached. After the transformation is finished the microstructure and properties

are almost the same. (2) Isothermal quenching is realized in salt baths, because this type of environment can hold higher temperatures than other quenching environments. It is optional if the tempering will or will not be applied. By using isothermal quenching the component has lower hardness, higher toughness and less residual stresses (in compare with martensitic quenching). (3,4)

Chemical composition is an essential character of the material that defines what kind of heat treatment should be provided. Considering the chemical composition of conventional 100Cr6 bearing steel, isothermal heat treatment would be very complicated to provide because manganese pushes the lower bainite start line in TTT diagram more to the right (Fig.2) and therefore the time for the austenit to full bainit transformation would be time consuming or better said uneconomic.

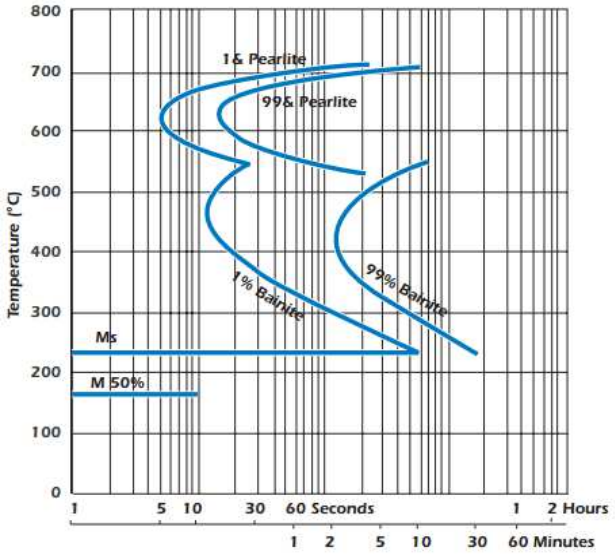

Fig. 2. TTT diagram of 100Cr6Mn steel where one can see that because of manganese the bainite start line is pushed to the right (3)

In this case the examined material contains an addition of molybdenum. Molybdenum is known for its affects of pushing the (in many cases unwanted) pearlite transformation zone to the right and keeping the bainitic transformation zone untouched. The other affect of molybdenum is that it lowers the martenzite start line and finish line also. Material with such chemical composition has the assumption for isothermal quenching purposes. (5,6)

2. Experimental part

The examined steel is designed for bearing industry with the following chemical composition listed in Tab.1.

C	Si	Mn	P	S	Cr	Mo	Cu	Al
0,93-1,05	0,4-0,6	0,8-1,1	max 0,025	max 0,015	1,8-2,05	0,5-0,6	max 0,3	max 0,05

Tab. 1. Chemical composition of examined steel

Received samples are barrel shaped parts used in high diameter bearings. These samples were precut in half as received. Procedure of heat treatment consisted of preheating, austenitizing, holding on the time of austenitization and then cooling down to the critical temperature where transformation from austenite to lower bainit took place. One sample (sample no.1) was cooled down to 185°C and then isothermally hold for 9 hours on this temperature. The second sample (sample no.2) was cooled down to 230°C and isothermally hold for 12 hours. Another difference in heat treating procedure was that sample no.1 was tempered at 250°C for one hour and cooled on air.

The procedure of mechanical testing consisted of hardness and impact toughness testing. Samples for hardness measurement were taken from the top of the cut barrels (Fig.3) and measured on a ROCKWELL RB-1/PC device (19 measurements on each sample). Toughness testing was provided on unnotched samples taken from the received barrels (S – surface, M – middle, C – core) as stated in Fig.4 and measured by using CHARPY hammer. Tensile testing was not possible because of the low force capacity of the testing equipment designed more for aluminum alloys.

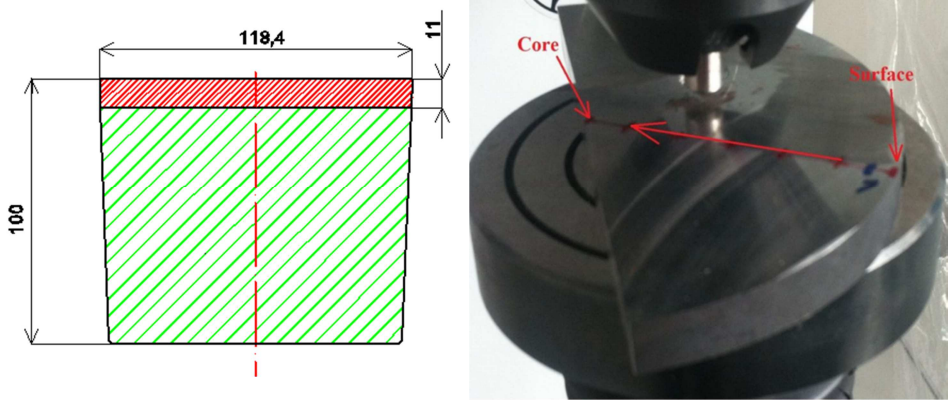

Fig. 3. Drawing of sample location and measurement of hardness

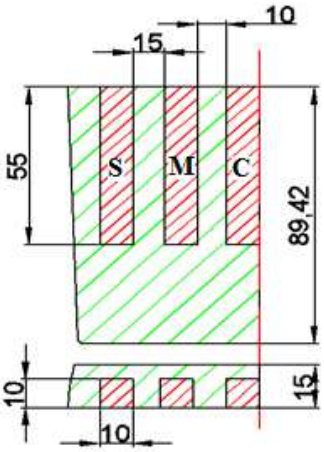

Fig.4 Drawing of dimension and markings of samples for impact toughness

Metallographic procedure consisted of mounting, grinding, polishing and etching (VILLELA BAIN etchant). Etched samples were investigated on a light microscope Zeiss LSM 700.

3. Results

As stated in Fig.5 it is obvious that sample no.1 has higher hardness than sample no.2. It is because the temperature of salt bath environment in which sample no.1 was put was 45°C lower than the environment in which sample no.2 was put. Another thing that influences the hardness of the two samples is the holding time in the salt bath. Holding time of sample no.1 was three hours less than sample no.2.

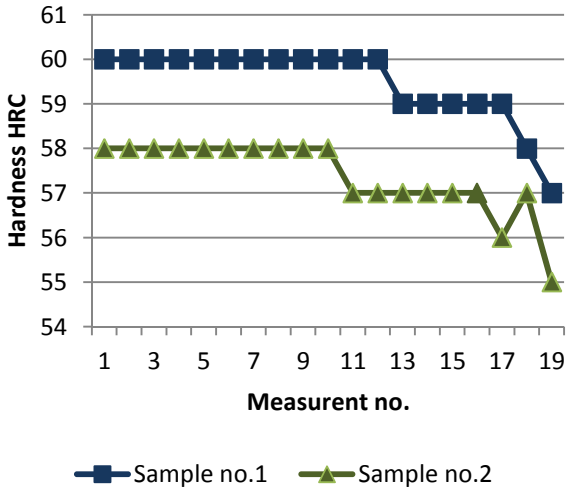

Fig.5 Hardness comparison of two samples (surface to core)

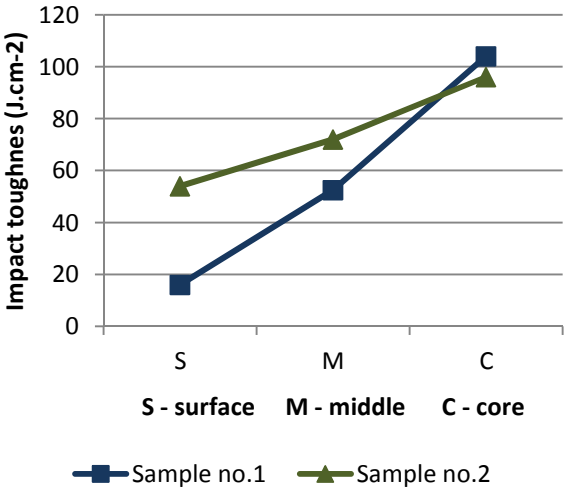

Fig.6 Impact toughness comparison of two samples

From the hardness values it is possible to assume that impact toughness on the surface of sample no.1 will be lower than on sample no.2. Fig.6 demonstrates that the impact toughness on the surface of sample no.1 is really lower than on the surface of sample no.2. Another interesting thing to see in Fig.6 is that the impact toughness in the core of the two samples is approximately the same. This means that due to the nearly same mechanical properties in the core the microstructure of both samples will be approximately the same.

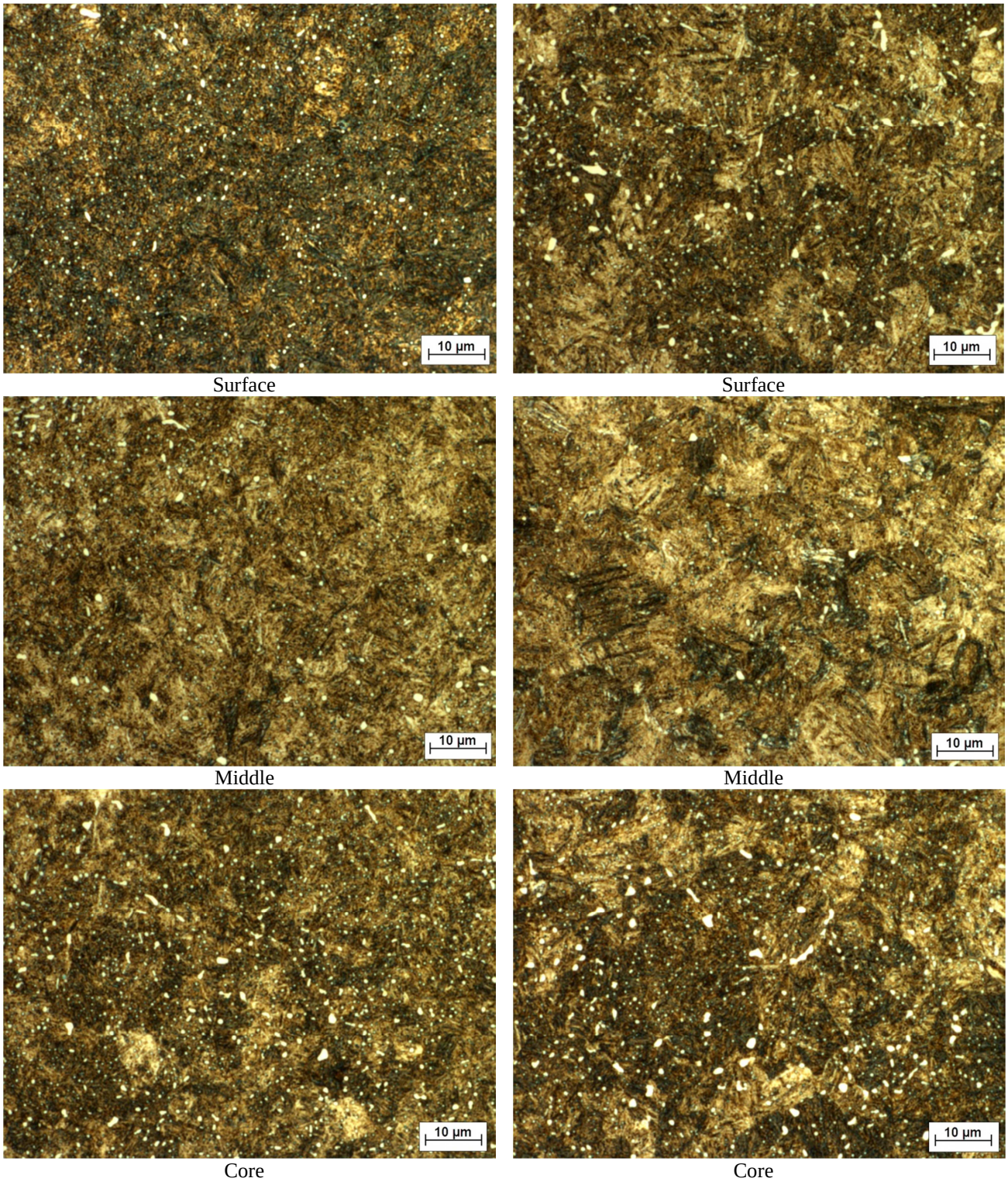

Fig. 7. Microstructural comparison of sample no.1 (left) and sample no.2 (right); magnification 500x, etchant VILLELA BAIN

The microstructure of sample no.1 (Fig.7) consists of a mixture of martensite and lower bainit located on the surface. From the hardness and impact toughness results it is possible to assume that the ratio of martensite from surface to the core of sample no.1 will be decreasing. The core of sample no. 1 will contain only lower bainit. In comparison with sample no.1 the surface of sample no 2 contains higher amount lower bainit. This explains the lower surface hardness on sample no.2 in comparison with sample no.1. Distribution of carbides is more homogenous in sample no.1 due to tempering. Carbides in sample no.2 are bigger on the surface than in sample no.1. In the core the size and distribution of carbides in both samples are approximately the same.

4. Conclusion

According to the results from destructive testing and metallography it is possible to assume that higher holding times at higher temperatures in salt environment during isothermal quenching have positive effect on achieving bainitic microstructure in the full cross section of the component with such chemical composition as listed in Tab.1. Material with this kind of microstructure its self has a good combination of impact toughness, hardness and strength. What is more important is that by using higher holding times at higher temperatures the representation of lower bainit is higher on the surface and that means the area will be exposed mostly to compression stresses than tension. This feature is positive because during grinding process the surface is more immune to cracking.

Acknowledgement

Authors would like to highly appreciated PSL a.s. for material providing and assistance in this contribution.

References

[1] FABIAN, P. - JANKEJECH, P. - KYSELOVA, M. 2014. *Simulation of roundness, hardness and microstructure of bearing rings with thin cross sections by using SYSWELD*. In: Communications., 2014, 124-129 s. ISSN 1335-4205.

[2] FABIAN, P. - JANKEJECH, P. - KYSELOVA, M. 2014. *Application of Barkhausen noise on the surface integrity of bearing components*. In: Wulfenia journal., 2014, Vol. 21, no.4, 503-514 s. ISSN 1561-882X

[3] BREZNICAN M., FABIAN P., MESKO J. 2013. *Modeling of selected parameters of quenched bearing rings* In: Interdisciplinary integration of science in technology, education and economy. - Khmelnytsky National University, 2013. - ISBN 978-617-70-94-07-3. - S. 130-138.

[4] BREZNICAN M., FABIAN P., MESKO J. 2013. *Effect of austenitization conditions on selected properties of bearing steel 100Cr6.*In: Advanced manufacturing and repairing technologies in vehicle industry : 30th international colloquium : 22-24 May 2013, Visegrad, Hungary. - Budapest: BME, 2013. - ISBN 978-963-313-079-7. - S. 99-102.

[5] BREZNICAN, M. – FABIAN, P. – MESKO, J. – DRBUL, M. 2013. *The simulation of influence of quenching temperature on properties of bearing rings* In: Manufacturing technology : journal for science, research and production. - ISSN 1213-2489. - Vol.13, no. 1 (2013), s. 20-25

[6] SLADEK, A. - FABIAN, P. - PASTIRCAK, R. - BREZNICAN, M. 2012. *The roundness and microstructure of thin-wall bearing rings*. In: Manufacturing technology : journal for science, research and production. - ISSN 1213-2489. - Vol.12, No. 13 (2012), s. 237-241.

TRANSCOM 2015, 22-24 June 2015
University of Žilina, Žilina, Slovak Republic

Energy Analysis in Ultra-High Strength Steel. Microscopic Observations.

*Urszula Janus
*Kielce University of Technology, Al. 1000 lecia P.P.7, 25-314 Kielce, Poland

Abstract. The analysis of the ultra-high strength steel fracture is presented. The specimens made of Hardox-400 steel with bainitic structure were investigated. Attention was focused on these cases in which the changes of fracture mechanism from ductile to cleavage were observed. They were observed for different temperatures and specimen geometries. The fracture tests were followed by the fractographic observations and simple computation.
Key words: Cleavage, ductile fracture, ultra-high strength steel, energy release rate.

1. Introduction

In 1920 A. A. Griffith considering fracture of glass went to conclusion that potential energy of the loaded body containing crack has maximum value at an onset of crack growth. During fracture an accumulated energy is released. Griffith introduced a quantity which is called now the energy release rate G (1). It describes the change of the potential energy of the system with fracture due to crack increase by a small amount da.

$$G = \frac{\partial \Pi}{\partial a} = \frac{\partial (W - U)}{\partial a}, \tag{1}$$

where:
W- work of external forces, U- strain energy.
Due to a change of a fracture mechanism from cleavage to ductile crack is temporarily arrested. Observing and recording this process allows for investigations of the amount of energy released on a unite crack surface creation.

2. Experimental research

The mechanical properties of Hardox-400 steel used in the experimental program are listed in Tab.1.

In the experimental program three point bending specimens were used. Width of the specimens was always W = 24 mm and different thicknesses were used B: 1, 2, 4, 8, 12, 16, 20 and 24 mm. In each specimen a fatigue crack was introduced in such a way that the relative crack length a/W was approximately equal to 0.5. The span length of the specimens was equal to S = 96 mm(4W).

Experiments were conducted at a wide range of temperatures from +20 ^{o}C ÷ -100 ^{o}C using the tensile test machine MTS with an environmental chamber.

Temperature, ^{O}C	**E, (MPa)**	**R_e, (MPa)**	**R_m, (MPa)**	**A_5, (%)**
+20	184	953	1197	15.7
0	183	952	1208	14.9
-10	175	944	1203	16.8
-20	187	989	1231	16
-50	181	993	1246	15.8
-100	196	1086	1315	18.4

Tab. 1 Mechanical properties of Hardox-400 steel (average value of all measured values).

The specimens were cut out from 30 mm thick block. The specimens were machined in such a way that small differences in micro-structure at the crack front did not influence the fracture mechanism. In Tab. 2 chemical composition of Hardox-400 is presented.

	C	Si	Mn	P	S	Cr	Ni	Mo	B
Hardox-400	0.12	0.52	1.25	0.01	0.001	0.66	0.04	0.012	0.001

Tab. 2 Chemical composition of Hardox-400 steel (% wt)

Cracks in the specimens extended according to both cleavage and ductile mechanisms (void nucleation, growth and coalescence). Under certain conditions, depending on temperature, and specimen geometry, the fracture mechanism changed during loading. In such a situation the cleavage was manifested as a sudden crack jump. These jumps were observed in force displacement diagrams (Fig. 1). The images of transcrystalline cleavage and ductile fracture surfaces are totally different and they can be easily defined (Fig. 2).

The elastic energy was "stored" in a specimen before the cleavage jump and part of it was released during the jump. It is assumed that a new created area, by the transcrystalline cleavage, is proportional to the amount of elastic energy released. The amount of elastic energy available in a specimen for a crack jump is necessary but not sufficient condition for the crack extension. According to modified Ritchie-Knott-Rice criterion [1], [2], [3], the crack initiation requires that opening stress must exceed the critical value over certain critical area which is a material constant.

Fig.1 presents total energy before and after the cleavage jump (I, II, III and I', II', III') (hatched regions). Using equation (2) the compliances at characteristic points were evaluated. The amounts of elastic energy stored in the specimen were equal to areas of triangles: before the first jump - ABC, before the second jump - DEF, before the third jump - GHI. In turn the triangles: A'B'C', D'E'F' and G'H'I' represent the elastic energy still stored in the specimen after the consecutive jumps.

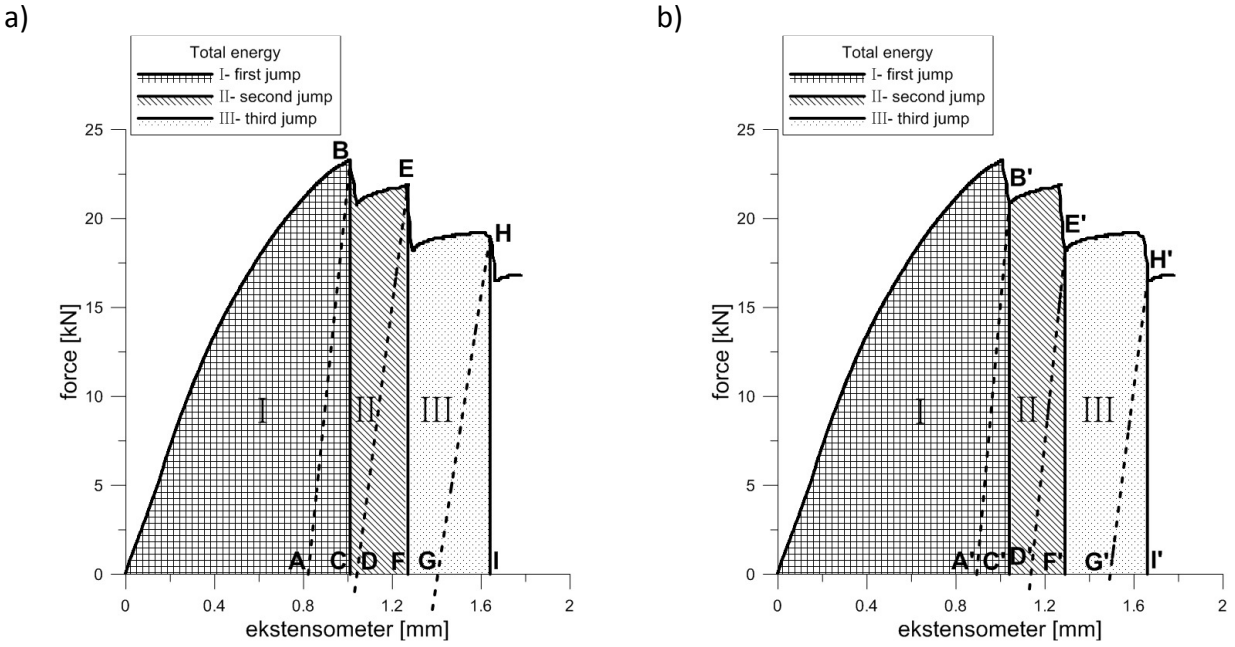

Fig. 1 Total and elastic energy (specimen thickness 12 mm, temperature +20 °C), a) before jump, b) after jump.

The fractographic pictures of the specimens fracture surfaces revealed clear borders of transcrystalline cleavage jumps surfaces. In Fig. 2 the fractured surface of 12mm-thick-specimen tested at the temperature of +20 °C is presented for different levels of magnification.

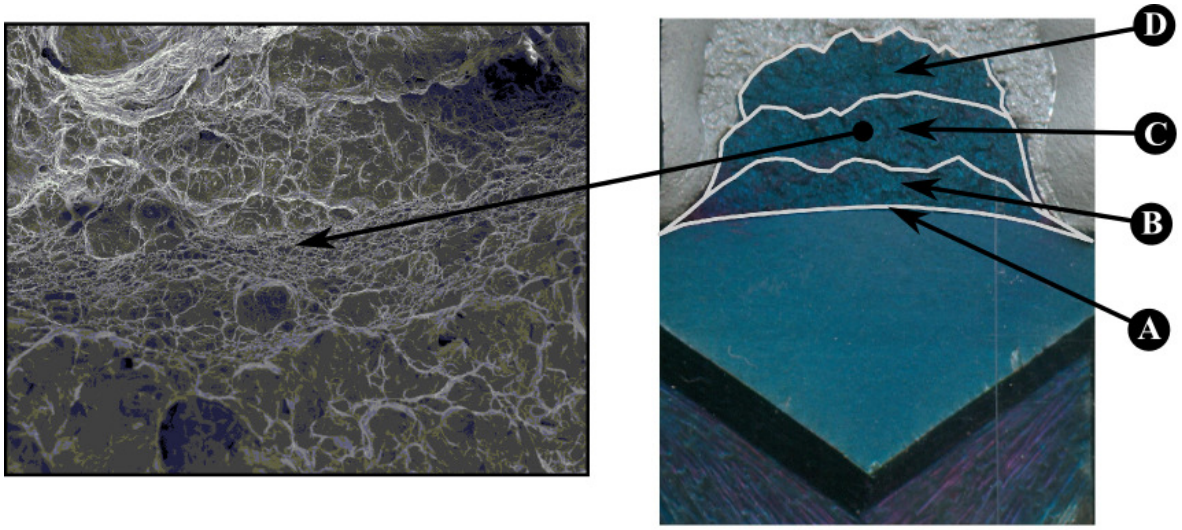

Fig. 2 12mm-thick-specimen, temperature +20 °C: A - fatigue crack, B - first jump, C - second jump, D - third jump.

3. Experimental results

The experimental results were analyzed. The areas I, II and III presented in Fig. 1 signify the total energies evaluated before and after the crack jumps. The total energy consists of elastic energy (which can be released on a crack jump) and plastic energy (consumed by plastic deformations and micro-defect evolution).
The calculations of total and elastic energies were based on formula (2) [4] which requires a specimen compliance and a crack length. To evaluate a released energy the formula (3) was used. Results are presented in Tab.3.

$$C = \frac{16}{EB}\frac{1}{(W-a)^2}, \qquad (2)$$

where E = 184 GPa, W = 24 mm, $\frac{a}{W} \cong 0.5$

$$\Delta E_I = ABC - A'B'C', \ \Delta E_{II} = DEF - D'E'F', \ \Delta E_{III} = GHI - G'H'I'. \qquad (3)$$

Areas of crack increase **ΔS** for each jump were measured directly from cracked surface (Fig. 3) (Tab.4).

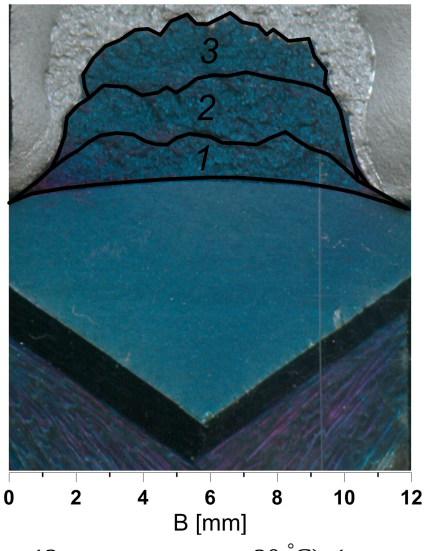

Fig. 3 The fracture surface (specimen of thickness 12 mm, temperature 20 °C), 1- area of the first jump, 2- area of the second jump, 3- area of the third jump.

*E- total energy before the onset of crack jump [J], E_{spr}- elastic energy before the onset of crack jump [J], E_{spr}'- elastic energy after crack jump [J], ΔE- released energy [J]

*	I	II	III
E	14.6	20.2	27.2
E_{spr}	1.86	1.97	1.81
E_{spr}'	1.54	1.46	1.4
ΔE	0.33	0.52	0.4

Tab. 3 Total, elastic and released energy for jump I, II and III.

	1	***2***	***3***
ΔS	10.25	13.15	10.11
G	0.03	0.04	0.04

Tab. 4 Areas of crack increase ΔS for jump 1, 2, 3 (Fit. 3) and G.

$$G = \frac{\Delta E}{\Delta S}. \tag{4}$$

4. Conclusions

Tables 3 and 4 present the results obtained from the analysis of force-displacement diagram and images of the cracked surfaces. Utilizing loading graph E, E_{spr}, E_{spr}', ΔE were evaluated. The measurements of the transcrystalline cleavage surfaces areas provide the approximate results since the interpretation of the border lines between the transcrystalline cleavage and transcrystalline ductile surfaces not always is unique. However, one may observe that, according with assumption, there exists a relation between the amount of elastic energy released on cleavage jump.

References

[1] NEIMITZ A., DZIOBA I., JANUS U., "Cleavage fracture of ultra-high-strength steels. Microscopic observations. Numerical analysis. Local fracture criterion", Key Engineering Materials, Trans Tech. Publications, (2014), pp. 168-177.

[2] NEIMITZ A., GRABA, M., GAŁKIEWICZ J. „An alternative formulation of the Ritchie-Knott-Rice local fracture criterion", Engineering Fracture Mechanics, Vol.74, No.8, (2007), pp. 1308-1322,

[3] RITCHIE, R.O., KNOTT, J.F., RICE, J.R., "On the Relationship Between Tensile Stress and Fracture Toughness in Mild Steels", Journal of the Mechanics and Physics of Solids, Vol. 21, (1973), pp. 395-410.

[4] GOŁASKI L. "Elementy doświadczalnej mechaniki pękania", (1992), Dział Wydawnictw Politechniki Świętokrzyskiej

[5] BERDIN, C., BESSON J., BUGAT S., DESMORAT R., FEYEL F., FOREST S., LORENZ E., MAIRE E., PARDOEN T., PINEAU A., TANGUY B., (2004), Edited by Besson J., "Local Approach to Fracture", Ecole des Mines de Paris, Les Presses.

[6] ANDERSON T. L. (1994) "Fracture Mechanics: Fundamentals and Applications", Second Edition, CRC Press.

TRANSCOM 2015, 22-24 June 2015
University of Žilina, Žilina, Slovak Republic

Evaluation of Initial Mechanical Properties of Surveillance Specimens for Mochovce Nuclear Power Plant Units 3 and 4

[**]Michal Kapusňák, [*]Jana Petzová, [**]Ľudovít Kupča, [*]Martin Březina
[*] VUJE, a. s., Division of Nuclear Power Plant Diagnostics, Department of Structural Analysis, Okružná 5, 918 64 Trnava, Slovakia, {Michal.Kapusnak, Jana.Petzova, Ludovit.Kupca, Martin.Brezina}@vuje.sk
[**] Slovak University of Technology in Bratislava, Faculty of Materials Science and Technology in Trnava, Institute of Materials, Bottova 23, 917 24 Trnava, Slovakia

Abstract. This paper deals with the evaluation of the experimental results of reactor pressure vessel materials which were tested in the frame of Mochovce Surveillance Specimen Program (MSSP-34) applied to Mochovce NPP units 3 and 4. More than 2000 pcs of samples have been prepared and are ready for testing and evaluation of tensile and fracture behaviour of monitored materials after their irradiation in RPVs.

Keywords: Mechanical Properties, Reactor Pressure Vessel steel (RPV), Irradiation Embrittlement, Embrittlement Monitoring, Surveillance Specimen Programme, Nuclear Power Plant, Small Punch Test,

1. Introduction

MSSP-34 is specially designed for monitoring of the neutron irradiation effects on RPV materials' mechanical properties changing due to the operational influence. During the MSSP-34 realization there are the irradiation induced changes compared with the results in as received state (zero condition) and after planned stages of radiation exposure. This paper presents the overview of the results for all types of un-irradiated materials:

- base material of reactor pressure vessel steel - 15Ch2MFA,
- weld metal - 10ChMFT steel,
- heat affected zone,
- and steel 14Ch17N2 as well.

The presented results will serve as a base for forthcoming comparison with the samples after exposure to evaluate the neutron irradiation damaging processes. The schedule of MSSP-34 irradiation program is planned to cover the operational degradation monitoring till the lifetime of individual units. This new philosophy enables not only the real prediction of irradiation degradation, but safe and reliable operation of both RPV's units Mochovce 3 and 4 too [1].

The paper and presented results herein are part of author's dissertation thesis.

2. Brief information on MSSP-34

The new Mochovce Surveillance Specimen Programme (MSSP-34) was prepared for assessment of reactor pressure vessel's materials real state. Main goal of this program is monitoring state of RPV's materials for the whole operational life-time. Within the MSSP-34 programme three different types of specimens to analyze and monitor RPV steel radiation degradation are being used. They are as follows [1, 2]:

- Small punch test specimens,
- Specimens for Charpy notched impact toughness testing,
- Pre-cracked and pre-fatigued specimens for static fracture toughness testing.

Design of chains, measuring of irradiation temperature and neutron fluence is based on experience from realized surveillance specimen programs. Innovations in this project are:

- besides the standard tests of mechanical properties there was included in the material degradation monitoring also the new testing method - Small Punch Test,
- the separation of RPV material samples into four sets by sampling through depth of the base metal and weld metal, this idea will give us the results across the RPV wall and to find which is the most sensitive part as well as to minimize results scattering.

3. Materials and Experimental Techniques

All the abovementioned specimen types are prepared from three original RPV material types such as base metal (BM), weld metal (WM) and heat affected zone (HAZ) cf. Fig. 1. Besides those mentioned experimental materials of power plant safety-related structural component, radiation damage monitoring over a period of 10 and 20 campaigns will also be monitored on special type of titanium stabilized austenitic stainless steel 08Ch18N10T used for reactor internal structures. MSSP-34 programme includes in addition to RPV material radiation damage monitoring, the measurements of irradiation temperature and neutron fluence inside of irradiation capsules as well. Irradiation capsules are filled with samples of original reactor steel with specified geometry and also melting monitors as well as neutron fluence activation monitors [1, 2].

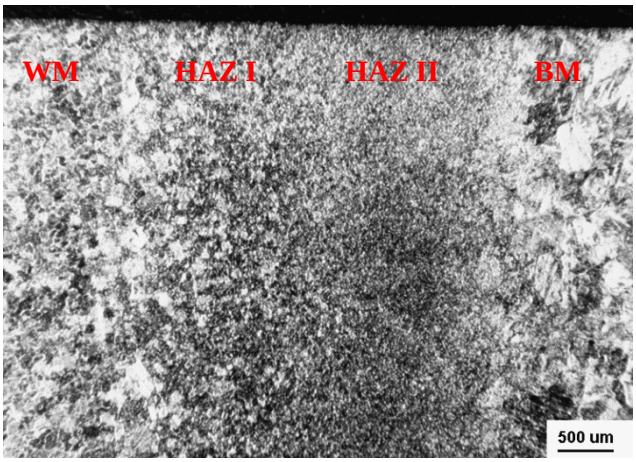

Fig. 1. The microstructure of weld metal, heat-affected zone I and II, base metal of RPV's wall [3]

The experimental technique to determine RPV materials' properties was Small Punch Test (SPT). SPT procedure in MSSP-34 is applied as the new method for estimation of base mechanical properties of the RPV materials. For MSSP-34 project there were prepared 1125 pcs of SPT samples per reactor unit totally and of that number there will be tested in an irradiated state 700 SPT pcs of different types of RPV materials. The principle of SPT testing procedure used in VUJE, a.s. is penetration of disk specimen by hemispheric rod. The small punch experimental configuration is presented in the Fig. 2 on the left, typical record of the load and deflection gained is on the right.

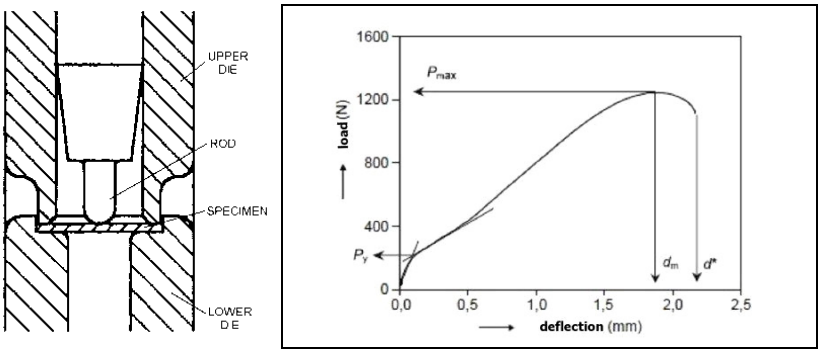

Fig. 2. Schematic of the setup for the SPT (on the left) and typical SPT load-deflection curve (on the right) [4]

4. Results of the Initial State testing

In this paper's section, there are summarized results of the SPT evaluation on the initial state of materials of MSSP-34 and the comparison between results from standard tests of the base mechanical properties and results from SPT.

The Table 1 summarizes tensile testing results obtained from SPT tests for all the evaluated materials. For base RPV's materials there are presented the results from standard tensile tests. Obtained results from both testing methods are in a good agreement. These layers represent the sampling depth and the 1st layer means a depth of 40 mm, the 2nd a depth of 55 mm, the 3rd a depth of 70 mm, the 4th layer it's a depth of 85 and 90 mm for weld metal and heat affected zone, respectively [5].

Type of material		**SPT**				**Standard**	
		Rm [MPa]	**Rm * [MPa]**	**Re [MPa]**	**Re * [MPa]**	**Rm [MPa]**	**Re [MPa]**
Base material of RPV 15Ch2MFA	1st layer	579	569	494	470.0	601	478
	2nd layer	592		497			
	3rd layer	566		452			
	4th layer	540		436			
Weld metal of RPV 10ChMFT	1st layer	611	620	477	485	606	490
	2nd layer	654		528			
	3rd layer	598		483			
	4th layer	618		450			
Heat affected zone I. (weld. No.4 of RPV)	1st layer	679	645	583	551	613	494
	2nd layer	621		548			
	3rd layer	636		559			
	4th layer	642		515			
Heat affected zone II. (weld. No.4 of RPV)	1st layer	600	607	466	471		
	2nd layer	606		473			
	3rd layer	596		445			
	4th layer	627		501			
*** Note:** the average values of SPT tests							

Tab. 1. Results of tensile properties of experimental materials in initial state for NPP unit 3 in Mochovce

The Table 2 shows the values of the fracture appearance transition temperatures (FATT) evaluated by temperature dependence of the SPT energy obtained from SPT tests at various test temperatures. Temperature dependencies of fracture energy for all the materials tested in initial state are presented in the Fig. 3 and Fig. 4. As can be seen curves' positions are very close each other. The average figures of fracture appearance transition temperature correlate very well for weld metal and rather well for a heat affected zone I. Better correlation between values of mechanical properties would have been expected at the use of the same separation for all the specimens tested by standard testing techniques.

Type of material		Transition temperature FATT [°C]		
		SPT	SPT *	Charpy V-test
Base material of RPV 15Ch2MFA	1st layer	-5.0	-15.0	-24.7
	2nd layer	-0.2		
	3rd layer	-8.4		
	4th layer	-20.2		
Weld metal of RPV 10ChMFT	1st layer	-2.1	-16.3	-16.0
	2nd layer	-18.0		
	3rd layer	-4.1		
	4th layer	-5.6		
Heat Affected Zone I. (Weld No.4 of RPV)	1st layer	7.8	+3.3	+10.8
	2nd layer	19.0		
	3rd layer	8.1		
	4th layer	-7.6		
Heat Affected Zone II. (Weld No.4 of RPV)	1st layer	-15.8	-12.5	
	2nd layer	-8.9		
	3rd layer	-33.5		
	4th layer	-1.9		
*** Note:** the average values of SPT tests				

Tab. 2. The transition temperature values for materials in initial state - NPP unit 3 in Mochovce

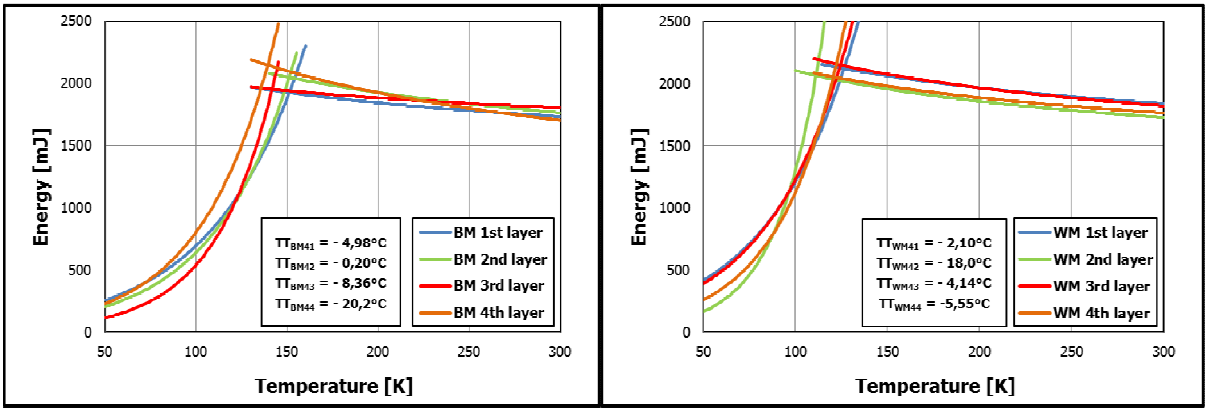

Fig. 3. The SPT energy curves in the initial state of the NPP materials unit 3 in Mochovce (left - BM, right - WM)

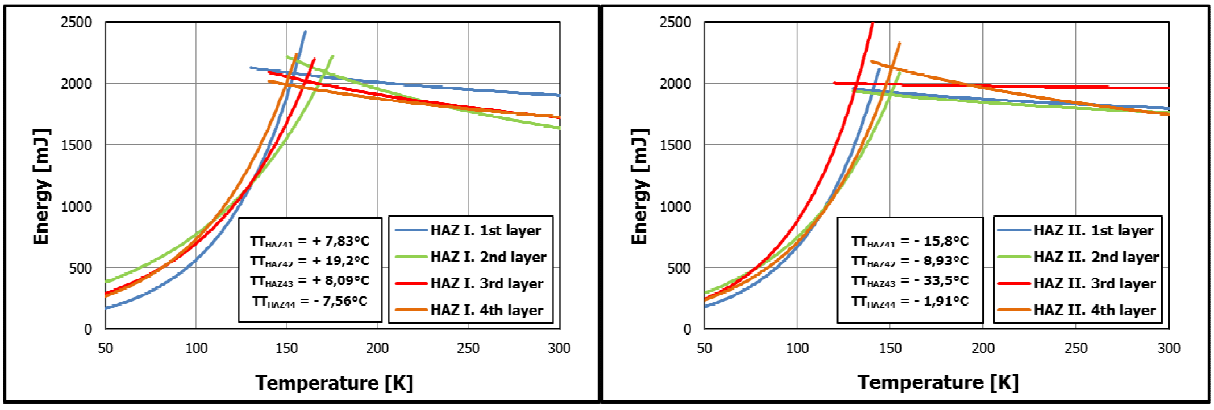

Fig. 4. The SPT energy curves in the initial state of HAZs, unit 3 in Mochovce (left - HAZ I., right - HAZ II.)

5. Conclusion

From the presented results it is possible to conclude that:

- all the values of tensile strength for base material correlate well with a value given by standard test and can be seen slight strengthening tendency towards the surface of reactor pressure vessel wall, the average values of the yield and tensile strength is very well comparable to a value given by standard testing technique,
- the weld metal strength values and average values are in good correlation with a value given by standard testing technique,
- all the values of tensile strength and yield strength for heat affected zone I are only slightly higher than that given by standard test, the same is true for the average values,
- the base material tensile strength is lower than for weld metal and heat affected zone I. and is comparable to strength values of heat affected zone II except for 4th layer,
- the average values of strength determined by SPT method are very well comparable for all kinds of materials,
- all the values of transition temperature for layers of base material are higher than a value given by standard Charpy V-test, although the difference between the 4th layer and a standardly given figure is only -4.5 °C,
- the minimal value of transition temperature for the 2nd layer within weld metal is well comparable to a value given by standard Charpy V-test,
- the transition temperature for the 4th layer within samples made of HAZ I is rather below a value defined by standard Charpy V-test,
- all the values of transition temperature for layers within samples made of HAZ II are below a value given by standard Charpy V-test,
- the transition temperature curves are very close each other for all the types of materials and the established differences seen in data are caused by microstructural inhomogeneities of tested materials that changes layer by layer and even between two close heat affected zones,
- the average values of transition temperature determined by SPT method are in a good consistency with a standardly acquired value except for material of heat affected zone II,

References

[1] KAPUSŇÁK, M., PETZOVÁ, J., KUPČA, Ľ., BŘEZINA, M. *Small punch test application for evaluation of initial mechanical properties of surveillance specimens for Mochovce nuclear power plant units 3 and 4*. in Conference Proceedings of the 3th International Conference SSTT 2014, Determination of Mechanical Properties of Materials by Small Punch and other Miniature Testing Techniques, September 23 to 25, 2014, Castle Seggau, Seggauberg (Austria), pages 212-218.

[2] KAPUSŇÁK, M., KUPČA, Ľ. *Contemporary State Of Surveillance Specimens Programme Implementation for Mochovce Nuclear Power Plant Unit 3 and 4 Reactor Pressure Vessels*, in Conference Proceedings of the 10-th European conference of young researchers and scientists Transcom 2013, Section 5 Material Engineering Mechanical Engineering Technologies, June 24-26, 2013, Žilina (Slovakia), pages 61-64.

[3] PETZOVÁ, J. *Advanced Surveillance Specimen Programme (ASSP)*, Seminar on Utilizing the Results of Tasks solved in the Department of Structural Analysis for Decision Support in the Performance of Supervision over Nuclear Safety and Reliable Operation for Slovak NPP, RZ VUJE Harmónia, Slovakia, September 19-20, 2013, Presentation (in Slovak).

[4] PETZOVÁ, J., BŘEZINA, M., KUPČA, Ľ. *Evaluation of Mechanical Properties of the Reactor Pressure Vessel Materials changes by Small Punch Test Application*, in Proceedings of the 2013 ASME Pressure vessel and Piping Conference, July 14-18, 2013, Paris, France, Paper No. PVP2013-97171, pp. V01AT01A042, 5 pages.

[5] *Reactor pressure vessel passport, document No. Ae 5688/dok*, 160 pages (in Czech-Russian).

TRANSCOM 2015, 22-24 June 2015
University of Žilina, Žilina, Slovak Republic

The Application of Optical Methods for Measuring of Roundness Profiles

*Kmiecik-Sołtysiak Urszula, *Adamczak Stanisław
*Kielce University of Technology, Faculty of Mechatronics and Mechanical Engineering, Department of Manufacturing Engineering and Metrology, 25-314 Kielce, al. Tysiąclecia Państwa Polskiego 7, Poland
* usoltysiak@tu.kielce.pl

Abstract. Continuous increase of requirements for in manufacturing engineering results in the fact that an analysis of form errors is a matter of great importance. In practice, there are two groups of methods of roundness measurement: radial methods and V-block methods. However, it is not always possible to measure roundness profiles by the contact methods. This happens when the measured object is flat and the measured hole therein has a small height, less than the radius of the measuring stylus tip. In this case, optical methods can be used. Such methods allow determination a diameter of the hole as well as deviations in shape.

Keywords: Non-contact measurement, roundness deviation

1. Introduction

A component is described as round if all points of a cross section are equidistant from a common center. Therefore, out-of-roundness or roundness error can be measured by evaluating changes in radius on a component relative to a true or perfect circle.

Roundness measurement requires rotation coupled with the ability to measure change in radius. The accepted method is to compare the profile of a component under test to a circular datum, i.e., a highly accurate spindle. After aligning the axis of the component with the axis of the spindle by means of a centering and leveling table, a gauge (transducer) is used to measure radial variations of the component with respect to the spindle axis. [1, 2, 3, 10]

Out-of-roundness is expressed as the difference between the greatest and the least distance of the profile from a center. To assist in the measurement of this distance, a reference circle (or pair of circles) is superimposed on the profile.

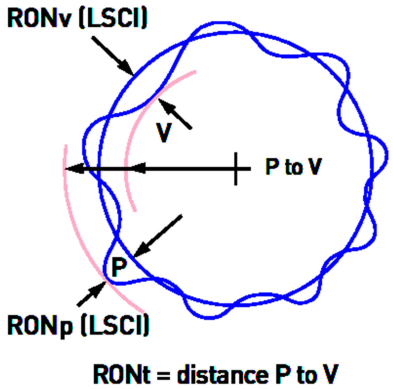

Fig. 1. Roudness deviation

Continuous increase of requirements for in manufacturing engineering results in the fact that, an analysis of form errors is a matter of great importance. Although roundness and size both play a significant role in the way things fit together, roundness is evaluated independent of size and must therefore be measured in a different manner [4, 5, 6, 7].

1.1. Methods of Measurement of Roundness

In practice, there are two groups used of methods of roundness measurement: radial methods and V-block methods. In the radial method the component is rotated on a highly accurate spindle which provides a circular datum. The workpiece axis is aligned with the axis of the spindle by means of a centering and leveling table. This method offers high accuracy; it is most commonly used in the laboratory. Devices that provide relatively high accuracy as well as satisfactory speed and flexibility of measurement tasks performed are coordinate measuring machines. They allow determination the diameter and roundness deviation of the workpiece at the same time [8, 9, 11].

However, it is not always possible to measure of profile of roundness by the contact methods. This happens when the measured object is flat and the measured hole therein has a small height, less than the radius of the measuring stylus tip. In this case, optical methods can be applied. Modern optical instruments allow determination the diameter of the hole as well as deviations in shape.

2. The Use of CMM ZEISS O-INSPECT for Measurement of Roundness

The device O-INSPECT is equipped with an optical 2D camera that features image processing functionality. As with a camera, the lens reproduces the object on the camera. Combined with the lens and the additional software, the integrated professional HD measuring camera chip achieves maximum measuring accuracy. Unlike other optical measuring devices, the CCD chip is extremely fast: it takes up to 50 images per second – the basic requirement for fast measuring and optical scanning.

Discovery zoom lens from Carl Zeiss:

- Optical 2D camera sensor with image processing functionality
- 12x zoom lens from Carl Zeiss
- Unique illumination through coaxial transmitted light and 16 segment multi-color ring light

Fig. 2. CMM Zeiss O-INSPECT machine

O-INSPECT Optical Measuring Uncertainty	
For distances	$U = 0{,}25\ \mu m + 1{,}5 * 10^{-6} * L$
For diameters	$U = 0{,}25\ \mu m + 1{,}5 * 10^{-6} * d$
For roundness deviations	$U = 0{,}4\ \mu m$
	L- length, d – diameter

Tab. 1. O-INSPECT optical measuring uncertainty

The value stated represents the expended measuring uncertainty obtained by multiplying the standard measuring uncertainty by the expansion factor k=2. The value of the measurand lies within the assigned range of values with a probability of 95% [12].

2.1. Profile of Roundness

The four holes in the workpiece of amount of 1mm were measured optically by O-INSPECT machine. The nominal diameters of the holes were 5 mm.

The reference number of measuring points was 500, the measuring speed of measurement - 0.2 mm/s. Filtering that was used is 2-15 F/O and Gaussian filter.

The measurement resulting of the roundness profiles are shown in Fig. 4.

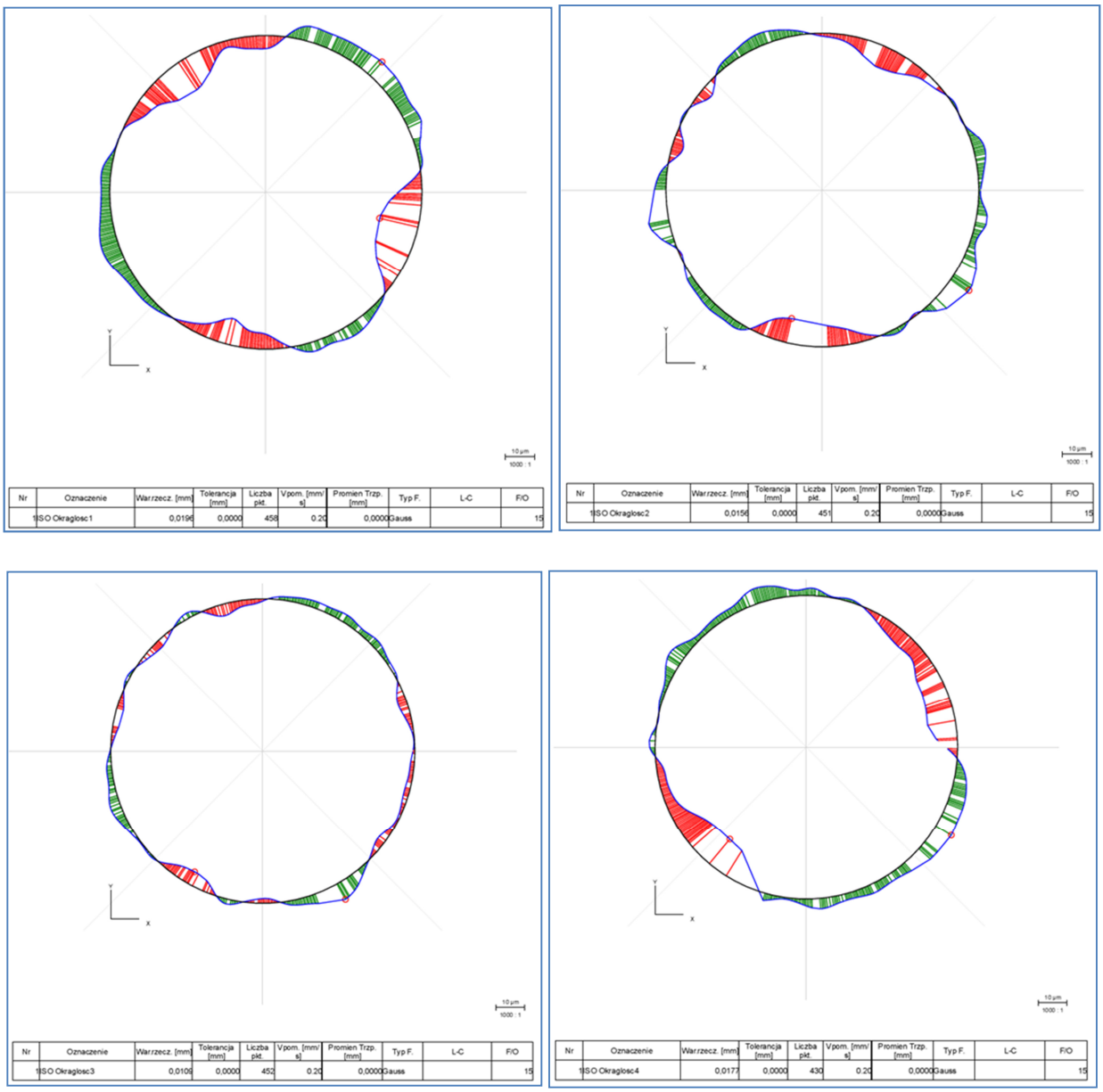

Fig. 4. Roundness profiles measured by optical method with the use of O-INSPECT Zeiss machine

Combined with the lens and the additional software CALYPSO, the integrated professional HD measuring camera chip achieves maximum measuring accuracy. Small diameter and minimal material thickness: the 12x zoom provides such high resolution of the small details that they can be measured with high point density.

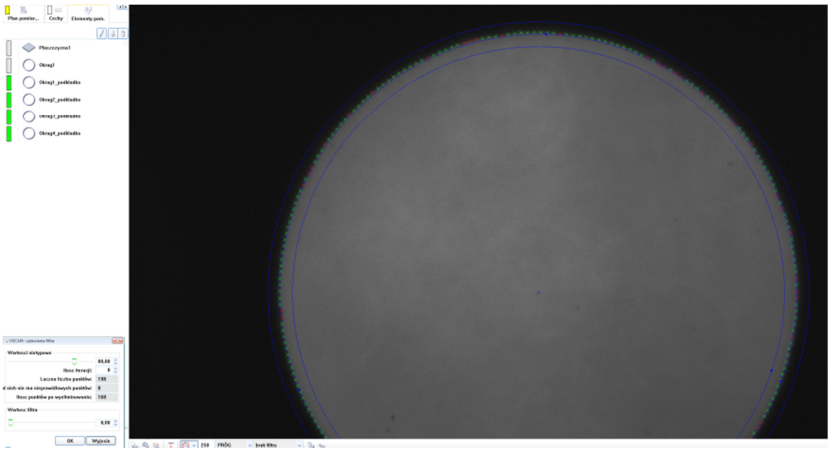

Fig. 5. Measurement of roundness profile in CALYPSO software environment

3. Conclusion

The most reliable methods for measuring roundness profiles are still radial methods and V-block methods. In the radial method, the component is rotated on a highly accurate spindle which provides a circular datum, as well as coordinate measuring technique. However, in special cases it is not possible to measure roundness by contact methods, for example if the measurement object has a small height, less than the radius of the stylus tip. Of course, this method carries with it a number of limitations and may be used only where necessary. This happens when the measured object is flat and the measured hole therein has a small height, less than the radius of the measuring stylus tip. In this case, optical methods can be used. Such methods allow determination a diameter of the hole as well as deviations in shape.

References

[1] ADAMCZAK S., JANECKI D., STEPIEŃ K.: *Qualitative and quantitative evaluation of the accuracy of the C-block method of cylindricity measurement*, Precision Engineering, vol. 34/3 (2010) pp. 619-626.

[2] ADAMCZAK S., JANUSIEWICZ A., MAKIEŁA W., STEPIEŃ K.: *Statistical validation of the method for measuring radius variations of components on the machine tool*, Metrology and Measurement systems, Val. XVIII (2011), No. 1, pp. 35-46.

[3] ADAMCZAK S., JANECKI D., STĘPIEŃ K.: Cylindricity measurement by the V-block metod – Theoretical and practical problems, Measurement, vol. 44/1 (2011), pp. 164-173

[4] JANECKI D.: *Gaussian filters with profile extrapolation.* Precision Engineering-Journal of the International Societies for Precision Engineering and Nanotechnology; 2011, No 35, pp. 602– 606

[5] JANECKI D.: *Gaussian filters with profile extrapolation*, Precision Engineering. 35, 4 (2011), pp. 602-606

[6] JANECKI D.: *A generalized L_2-spline filter*. Measurement. 42, 6 (2009), pp. 937-943

[7] WHITEHOUSE, D.J.: *Some theoretical aspects of error separation techniques in surface metrology, Journal of Physics E: Scientific Instruments*, 9 (1976), pp. 531 -536.

[8] NOZDRZYKOWSKI K. *The determination and analysis of the total measurement uncertainty of roundness deviation*, Scientific Journals Maritime University of Szczecin, 21(93) (2010), pp. 72 - 76.

[9] GAPIŃSKI B., KOŁODZIEJ A., WOŁOWIEC M., *Accuracy of diameter measurement on specialized form tester.* Mechanik 7/2013, (2013), pp. 567-570

[10] ISO/TS 12181-1:2011: Geometrical Product Specifications (GPS) – Roundness – Part 1: Vocabulary and parameters of roundness. International Organization for Standardization (2011)

[11] RATAJCZYK E., Coordinate Measuring Technique (in Polish), Warsaw University of Technology Press, Warsaw, Poland, 2005.

[12] www.zeiss.com

TRANSCOM 2015, 22-24 June 2015
University of Žilina, Žilina, Slovak Republic

Comparison of the Properties of Coatings and Coating Methods

[*]Marek Kordík, [*]Mária Čilliková,
*University of Žilina, Faculty of Mechanical Engineering, Department of Machining and Manufacturing Engineering, Univerzitná 1, 010 26 Žilina, Slovakia, {marek.kordik, maria.cillikova,}@fstroj.uniza.sk

Abstract. The article is an introduction to the topic, which deals with the analysis of certain types of coatings that are applied by various CVD and PVD technologies used in practice. The aim is to analyze the different types of coatings in terms of their characteristics and functional properties, also their impact on the life of cutting tools as well as comparison of characteristics of CVD and PVD methods associated with identifying their advantages and disadvantages in the coating process.

Keywords: Substrate, coating, drill, CVD coating, PVD coating

1. Introduction

In technical practice is currently in the process of working we can meet a wide variety of materials with different physical and chemical properties of the metal or non-metal nature, and modifications thereof. During machining are in contact the tool and the work piece. In most cases, the working process is called cutting, where the blank is obtained shape, size and surface quality of the work piece produced according to specified requirements.

Currently is placed increasing of emphasis on increasing product quality, productivity and efficiency of production. Therefore, the aim of commercial businesses in cutting materials to develop increasingly sophisticated cutting materials. Although the offer of cutting materials is very wide, "perfect" cutting material can not be real produced. Therefore, the effort of producers of the tools is mainly focuses on improving the production technology and optimal use of existing cutting materials. One such improvement is the application of CVD and PVD coatings for certain groups of cutting materials. We give through the coating of the base material (substrate) new properties as mechanical (hardness, strength, adhesion), geometric (surface roughness, shape deviations), chemical (resistance to corrosion), physical (thermal conductivity, electrical conductivity) and technological (machinability). [1]

2. Results of Experiments and their Discussion

2.1. Coatings

Coating means any substance which arises or is applied to the surface of the base material (substrate). This increases at least one dimension of the work piece or product, for example the thickness. Coating, respectively layer is characterized by the type and composition of the material, by its properties and thickness. Gradually, it was shown that it is important to respect a process for its preparation and consistency with a base material. All these properties will ultimately affect the final quality of the coating.

Coatings and layers applied to the substrate can have a thickness as required, several hundred microns or a few microns, or even nanometers.

Today there is an effort to improve the properties of coatings and methods for their preparation and methods of their control, as well as knowledge of the degradation of the coating properties under operating conditions [2]. Below are shown some examples of offered coatings and their basic properties by renowned companies currently operating in the Czech and Slovak market.

Coating	*Microhardness $HV_{0.05}$*	*Thickness (μm)*	*Friction coefficient*	*Working temperature (°C)*	*Type*
TiN	2300±200	2-4	0,6	500	TiN
TiCN	3500±500	2-4	0,2	400	TiCN
CrN	2000±200	2-6	0,3-0,4	600	CrN
CrCN	2300±200	2-6	0,2-0,3	600	CrCN
EXXTRAL	3000±300	1-3	0,7	800	AlTiN
SUPRAL	3300±300	2-4	< 0,5	800	TiAlCN

Tab. 1. Basic properties of some coatings offered by renowned Slovak company operating in the market [8]

Coating	*Microhardness (GPA)*	*Thickness (μm)*	*Roughness Ra (μm)*	*Thermal stability (°C)*	*Type*
MARWIN SI	45	2-3	0,10-0,20	> 1000	TiAlSiN
ALWIN	35	2-4,5	0,15-0,20	> 1000	CrAlSiN
DARWIN	43	1-6	0,05-0,10	> 900	AlTiN
TiN	25	2-3	0,10-0,20	~ 550	TiN+Al
TiCN MP	34	1-4	0,20-0,25	400	TiCN
CrTiN	30	1-3	0,10-0,25	600	CrTiN

Tab. 2. Basic properties of some coatings offered by renowned Czech company operating in the market [6]

Coating	*Microhardness $HV_{0.025}$*	*Thickness (μm)*	*Friction coefficient*	*Coating temperature (°C)*	*Working temperature (°C)*	*Type*
NANOCOMP	2500-3200	2-3	0,4-0,5	520	800	TiB_2
NANOCOMP ULTRA	3200-4400	1-3	0,5	520	750	TiBC
CVD HARD	4500	1-10	0,5-0,6	1000	600	TiCN
ALUCOMP	2500-3500	1-6	0,4	do 600	900	AlTiN
DLC SILLCOMP	1500-2500	1-5	0,02-0,1	160-300	450	Si-DLC
HLF COMP	2300	1-5	0,2	500	350	DLC
UNICOMP	3000	1-6	0,35	do 600	1100	AlCrN

Tab. 3. Basic properties of some coatings offered by another renowned Czech company operating in the market [7]

2.2. Coating

Coating means, that to the base material will be applied a very thin layer. The layer has high hardness and strength as compared with the substrate. A thin layer of coating forms a barrier on the backing material to chemical, physical and mechanical wear of the tool. Cutting materials are coated by two basic methods. This is a method of PVD and CVD. In addition to these basic methods in practice we can also meet with their other modifications (eg. PACVD). [4]

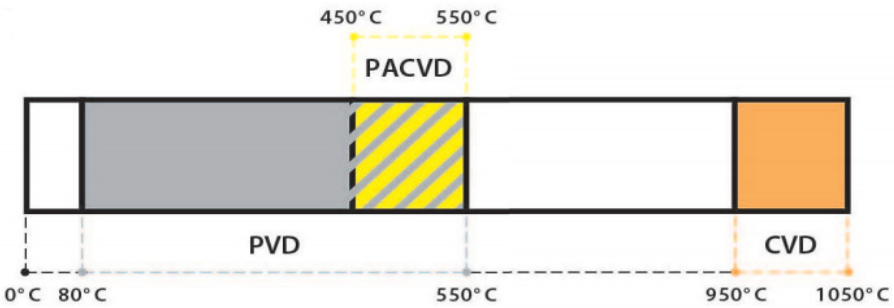

Fig. 1. An example of the temperature range of different coating. [7]

2.3. PVD Coating – Physical Vapor Deposition

PVD coating allows the production of high quality layers at about 500 ° C or less. This method was originally created for the coating of tools of high speed cutting steels to prevent the heat affecting of the instrument. It allows to create layers on work pieces of aluminum, aluminum alloys and plastics, even on very thin sheets of polypropylene, polyethylene, polyester and other materials. PVD have a high-coating results by complex shapes and sharp edges (drills, end mills, etc.).

Today it is possible to prepare the surface with such a composition, structure and useful properties that are comply fully with the application, characterized by specific working conditions. [3]

2.4. CVD coating – Chemical Vapor Deposition

In this method, the coating is applied chemically in a gaseous atmosphere from a gaseous phase at a temperature of about 700-1500 °C. The essence of the process is the reaction of gaseous chemical compounds in the immediate nearness of the base material (substrate) and the subsequent imposition of the reaction products on this surface. It is the main method of coating of cemented carbides.

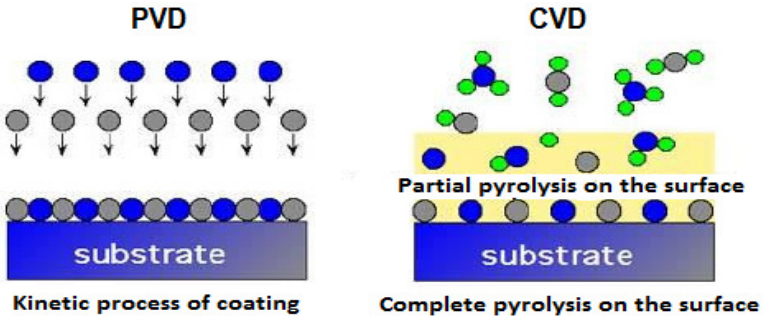

Fig. 2. An schematic representation of CVD and PVD method [9]

2.5. Comparison of the Properties of PVD a CVD Methods

The object of this article is to point out certain specific properties and parameters that characterize each coating technology. Some of these differences are shown on the Tab. 4 and Fig 2.

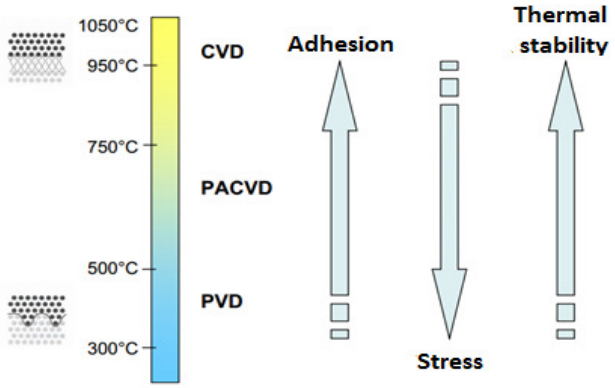

Fig. 3. Properties of the coatings regarding to the used method [9]

The factors that differ the art and methods of PVD a CVD:

- Kind of souce of deposited atoms (solid, melt, gas);
- Physical mechanisms (evaporation, precipitation), which atoms from the source entering the gas phase;
- Reduced pressure enviroment, which are gaseous particles transported.
- Overall absence of chemical reactions in the gas phase and on the substrate surface (excluding reactive PVD processes). [5]

Coating method	*Advantages*	*Disadvantages*	*Use*
PVD	Low friction	The large internal stress in coating	Machining of hard to machine materials, dies, punches, punch, drill, milling machines and other high speed cutting materials;
	High hardness	High load by temperature radial	
	Abrasion resistance	Low use of the material source	
	Coating of complex shapes and sharp edges	The formation of the shadow effect	
		Advanced vacuum systems	
	Several times longer life cycle	Complicated mechanisms guaranteeing constant movement of coated surfaces (tools)	
	Low thermal load of the substrate		
	Resistance to temperature of 550 ° C-750 ° C	For properties controlling of the coating can be used only a few process parameters	
	Corrosion and acid resistance		
	Several times longer life cycle		
CVD	High density of coating	Only for ceramics, cemented carbides, high speed cutting steels	Diamond coatings, coating of inzerts made from cemented carbides;
	The high homogenity of the coating	The negative impact on the environment	
	Economic advantage	High working temperatures and energetic difficulty	
	A good coating stoichiometry	Unable to coating sharp edges	
	The high thermal stability of the coating	Long working cycle 8-10 hours	

Tab. 4. Overview of the properties of basic coating methods [9]

3. Conclusion

Coating or spreading a film over the cutting tool is a very complex process in which there are high demands on production methodology. Coated tool even before the coating will undergo series of adjustments that include processes associated with regrinding tools, cutting edge rectification or removal of the old coating. All of these processes and modifications have a major impact on the quality of the coating and its functional properties.

This article is an introduction to the experiment which is realized in collaboration with one renowned German company focused on the production of bearings. The research will identify and verify the effect of dependence of coatings and their technological properties of the fluctuating life of coated drills during the manufacturing process. Coating of drills takes place in the renowned coating companies in the Czech and Slovak market.

The aim of my research will be also to analyze the possible link between the used type of coating and their impact on wear and durability of the drill.

References

[1] HUMÁR, A. : *Materiály pro řezné nástroje*, MM publishing, s.r.o, ISBN 978-80-254-2250-2, 2008.

[2] SEDLÁČEK, Vladimír .*Surface and coatings of metal*. Prague: Czech Techical University in Prague, 1992. 176 s. ISBN 80-01-00799-5.

[3] The layers and coatings: Proceedings. In *The layers and coatings 2003*. Trenčín: DIGITAL GRAPHIC Trenčín , 2003. s. 228. ISBN 80-968337-1-5.

[4] (http://dspace.vutbr.cz)

[5] (http://www.ateam.zcu.cz)

[6] (http://www.shm-cz.cz)

[7] (http://www.vuhz.cz)

[8] (http://www.commercservice.sk)

[9] (www.vutbr.cz)

TRANSCOM 2015, 22-24 June 2015
University of Žilina, Žilina, Slovak Republic

Testing of Welded Joints of Thin Metal Sheets Used in the Automotive Industry

[*]Jakub Kowalczyk, [*]Dariusz Ulbrich, [**]Wojciech Sawczuk
[*]Poznan University of Technology, Faculty of Machines and Transport, Division of Motor Vehicles and Road Transportation, M. Sklodowskiej-Curie sq. 5, 60-965 Poznan, Poland, {jakub.kowalczyk, dariusz.ulbrich}@put.poznan.pl
[**] Poznan University of Technology, Faculty of Machines and Transport, Division of Rail Vehicles, M. Sklodowskiej-Curie sq. 5, 60-965 Poznan, Poland, wojciech.sawczuk@put.poznan.pl

Abstract. The paper presents an assessment of the possibility of using non-destructive evaluation of welded joints of thin metal sheets that is used in car body. The study used two different ultrasonic flaw detectors USM 35 and USLT 2000.Welded joints of thin metal sheets of car body are combinations of low susceptibility flaw materials. Standards and procedures adopted works assume the ultrasonic testing is performed for plates with a minimum thickness from 6 to 8 mm. The automotive industry uses metal sheet having a thickness of less than 1 mm. Classic ultrasonic testing does not allow for the monitoring of quality of connections with small thicknesses. The study used the high frequency ultrasonic transducers - 20MHz. That transducers as research has shown can produce the correct pulses of longitudinal ultrasonic wave. Studies have confirmed that there is a possibility of non-destructive evaluation of welded joints of thin metal sheets.

Keywords: Automotive industry, Ultrasonic method, Welded joints, Metal sheets.

1. Introduction

Ultrasonic method is based on the phenomena of reflection and refraction of ultrasonic waves with a frequency above the threshold of audibility from 16 kHz to 18 kHz [1, 2]. Due to the research technique can distinguish the echoes of the ultrasonic method and the method of transmission [3]. Despite many advantages, which include, for example the possibility of study strongly damping elements and thin elements, the method of transmission is not in wide use in practice today. This is due to limitations such as the need for simultaneous use of two ultrasonic transducers which should be placed on both sides of the test piece, and they should always be placed coaxially. When testing bonding joint (adhesives) is not always possible sided access to the tested element.

Ultrasonic method is effectively used for detecting discontinuities in the studied materials. An increase in interest of this method with respect to the research, as well as broadening the scope of its industrial use and the techniques used in the method of control [4]. Besides the classical ultrasonic inspection (testing of castings, forgings, welded joints) are carried out continuously work on their wider use. Examples of potential for wider application of ultrasound in nondestructive testing of materials also in relation to the adhesive joints are presented by J. Deputat and other researchers, eg. [5]. In addition, this method leads to quality control spot-welded joints [6], measurements of stress [7] and hardness machine parts [8]. Currently performed ultrasonic testing of selected objects, allow them to control a range of 20 meters from the site of application of the ultrasonic transducer [9]. Research is also conducted in field of adhesive connections [10], including such as solder joints and connections, coating - substrate.

In the conventional ultrasonic testing, in case - welds testing, it is assumed that the tested subject splice plates of minimum thickness the range 6 to 8 mm. Observing the development trend

of automotive vehicles, there is a lot of welded steel plates with a thickness of less than 1 mm. These connections are characterized by very low flaw susceptibility. Classic ultrasound transducers can't be used to conduct of such research. This is not only the dimensions of the transducers and the possibility of application of the weld area. Example of the view of the flaw detector screen shown in Fig. 1. This view shows the signal obtained during the test. This signal is not useful for the purposes of conducting ultrasonic testing.

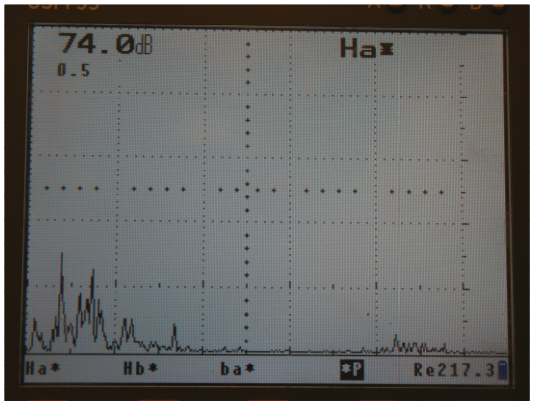

Fig. 1. The signal during the testing procedure of the welded joint in classical ultrasonic transducer obtained at USM 35 made by KRAUTKRAMER

Therefore, authors decided to use for further research high frequency ultrasonic transducer (20MHz) – Fig. 2, with water delay line (Tab. 1).

Name	f [MHz]	d [mm]	λ [mm]	N [mm]	b [mm]
DS 12 HB 1-6 KD	2,28	12	2,6	12,40	19,90
f – frequency of ultrasonic transducer, d – diameter of ultrasonic transducer, λ – wavelength (for a velocity v = 5940 m/s), N – near field, b - width of the beam, the decline rate k = 0.87 at a distance of 50 mm from the head, KD - the company Karl Deutsch					

Tab. 1. Parameters of ultrasonic transducer DS 12 HB 1-6.

a)

b)

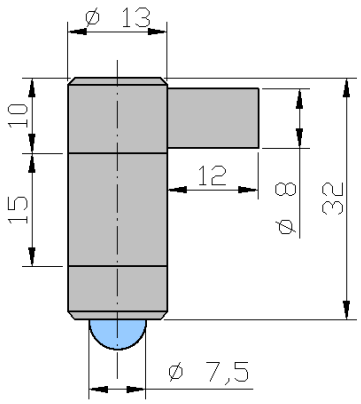

Fig. 2. Ultrasound transducer used in the study: a) view of the head, b) the main dimensions

The main aim of this work is to determine the applicability of the method of ultrasonic testing of welded joints of the small thickness of elements used in the construction of vehicle bodies. The

possibility of the research will be presented on the example of the classical and industrial flaw detector, based on PC, specialized software dedicated to perform testing of welded joints.

2. Research

The study was carried out on the welds used in the automotive industry. The thickness of the connected elements was ranged from 0.6 mm. During the study two different flaw - USLT 2000, and USM35XS shown in the Fig. 3 and 4 were used.

Fig. 3. USLT 2000 flaw detector

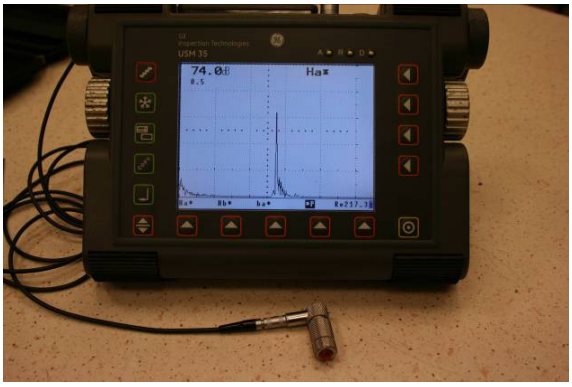

Fig. 4. USM 35XS flaw detector

Both flaw detectors made it possible to obtain correct, while the data for the study of ultrasonic pulses systems. Examples of the pulses are shown in Fig. 5 and Fig. 6. It is clear that the pulse was obtained from the bottom of the connection, which means that full penetration was achieved. Current research aims to develop a technique that allows to location of melting boundary, which is important for car manufacturers and car equipment components producers.

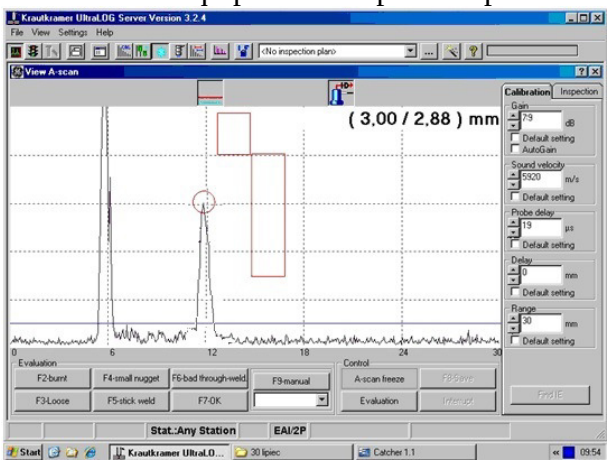

Fig. 5. View of the ultrasonic pulses obtained during the test of welded joint - visible pulse coming from the bottom of the tested weld - USLT 2000 flaw detector

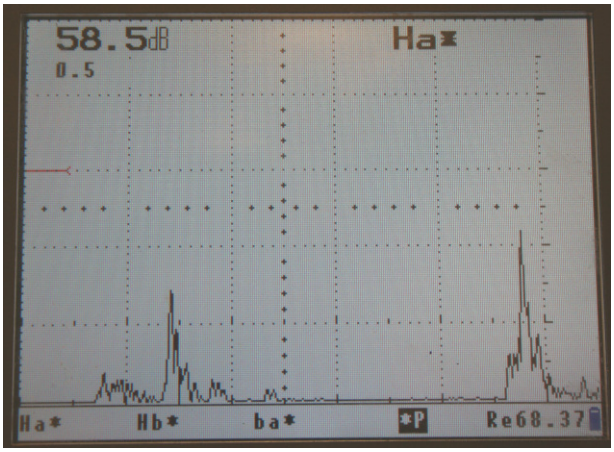

Fig. 6. The view of the ultrasonic pulses obtained during the test of welded joint - visible pulse coming from the bottom of the tested weld – USM 35XS flaw detector

3. Results and Conclusion

Under certain conditions, the classical ultrasonic flaw detector can be used to study metal welded joints with small thicknesses. Limiting the use of the classical ultrasonic flaw detector is not due to the physical possibility of obtaining useful for research pulses of ultrasonic waves, and mainly with ergonomic handling and automation capabilities of the research, affecting their time-consuming. Combination studies of welded joints conducted on a classic flaw detector require teamwork (minimum 2 person). In the case of exploratory studies and pilot projects, it is reasonable to conduct work using classic flaw detector. In the case of industrial research (during production), especially in the situation of a large number of the connections, it is strongly prefer to use ultrasonic flaw detector, dedicated to the testing of welded joints (which is often supplied for manufacturers).

Acknowledgement

The project is funded by the National Centre for Research and Development, LEADER V program, contract No. LEADER / 022/359 / L-5/13 / NRDC / 2014

References

[1] LEWINSKA-ROMICKA, A. *Badania nieniszczące. Podstawy defektoskopii*. WNT, Warszawa 2001.

[2] BROWN, B., GORDON, B. *Ultrasonic techniques in biology and medicine*. London Iliffe Books, 1967.

[3] ELPINER, I. E. *Ultradźwięki działanie fizykochemiczne i biologiczne*. Państwowe Wydawnictwa Naukowe, Warszawa 1968.

[4] CAWLEY, P., ALLIN, J.M., LOWE, M. J. S. *Adhesive disbond detection of automotive components using first mode ultrasonic resonance*. NDT&E International, Vol. 36, 7, 2003, pp. 503 - 514.

[5] DEPUTAT, J. *Postępy w ultradźwiękowych badaniach materiałów, Część I*. Przegląd mechaniczny, Zeszyt 21, 1996, s. 5 - 10

[6] AMBROZIAK, A., KORZENIOWSKI, M., KISIEL, A. *Zastosowanie badań ultradźwiękowych do oceny zgrzein punktowych w cienkościennych elementach*. Przegląd spawalnictwa, Vol. 5-7, 2004, s. 79 - 81.

[7] SZELĄŻEK, J. *Ultradźwiękowe pomiary zmian naprężeń*. Przegląd mechaniczny, Zeszyt 2, 1997, s. 5 – 13.

[8] PAKOS, R. *Pomiar twardości metodą ultradźwiękową*. Przegląd spawalnictwa, 5, 2001, s. 1 - 3.

[9] SZELĄŻEK, J. *Ultradźwiękowa defektoskopia dalekozasięgowa*. Badania Nieniszczące, 2008, nr 01, s. 1 –13

[10] BYOUNG-GEUK, K., SEKYUNG, L., TERUO, K. *Time - domain reflection field analysis for ultrasound evaluation of thin layered media*. NDT&E International, Vol. 29, 5, 1996, pp. 317 - 322.

TRANSCOM 2015, 22-24 June 2015
University of Žilina, Žilina, Slovak Republic

Stress Relaxation in SLS Additive Technology

[*]Kozior Tomasz
[*]Kielce University of Technology, Faculty of Mechatronics and Machin Design, Department of Mechanical Technology and Metrology, Al. 1000-lecia Państwa Polskiego 7, 25-314 Kielce, Poland, tkozior@tu.kielce.pl

Abstract. The paper presents the preliminary research results of the relaxation phenomena for specimens manufactured by additive technology. Specimens were printed using polyamide powder PA 2200 and subjected to a tensile test. The specimens were prepared in CAD software SolidWorks and then printed using Formiga P100, the machine working in Selective Laser Sintering technology SLS. Research was carried out on the basis of existing standards used to determine the plastic relaxation for specimens under tensile test. Based on the studies determined the effect of time and the size of the constant load the decline of the internal stress and identifies the possibility of using additive technology to build components working under constant load. Research results can be used in future to determine the possibility of apply additive technology to build a fully functional components working under constant load.

Keywords: additive technology, rapid prototyping, SLS, relaxation, PA 2200

1. Introduction

The rapid fabrication of unconventional manufacturing technology, which is largely based on materials which are plastics made that the materials produced using additive technologies are increasingly used to produce assembly parts of machines and mechanisms sometimes work under constant load. In case of models not loaded additive technology has just advantage but in case when they must work under load there is a significant problem in the form of relaxation.

Relaxation is a phenomenon that decrease stress in components exposed to long term stress, at constant deformation with time. This phenomenon is very dangerous and detrimental in the case of elements designed to maintain a constant level of stress, the best example is the combination of screw and nap, which maintain an adequate level of stress guarantees the connection. While most of screw joints are made of metal materials, snap-fit connection are over the years made of plastic and are used for a wide variety of precision parts such as mobile phone housing, dashboard components for motor vehicles and other machinery parts made of plastic. For the majority of engineering plastics relaxation process is well known, however in additive technology this phenomena is new and dependent on a large number of technological parameters of the production process and the chosen technology.

Additive technologies consist of layered construction of physical models based on the three-dimensional models prepared in CAD software. Additive technology beginning of the 80s of the twentieth century when in 1986 was awarded a patent for the first additive technology which was stereolithography. This technology was to photocuring polymer resin with UV radiation. A major problem with these technologies and particularly the technology of selective laser sintering of powders (SLS) is a shrinkage which has significant affects on the dimensional accuracy [2]. In the case of elements cooperating with one to another in different types of connections established shrinkage affects on the tolerance of the fit. At Kielce University of Technology preliminary research connected to the additive technologies relaxation was conduct.

In paper [1], the authors determined the effect of time and the type of load for elements in the form of O-rings on the value of the internal stress changes as a function of time. Specimens for testing were manufactured on the machine Connex 350 working in the PolyJet Matrix technology

for 2 base materials and their mixtures. The authors set up two types of loads for all tested samples during compression tests. Materials used in the study were VeroWhite and TangoBlack and their mixtures of different Shore hardness.

In [4] authors mixing two kinds of polyamide PA6 and PA12 and then determined suitable composition of the mix depend on the tensile strength, elastic modulus and creep.

The most important factors affecting the mechanical properties of plastic parts produced by additive technologies are: print direction and the layer thickness. Figure 1 shows an example of procedure to produce parts using most common additive technology.

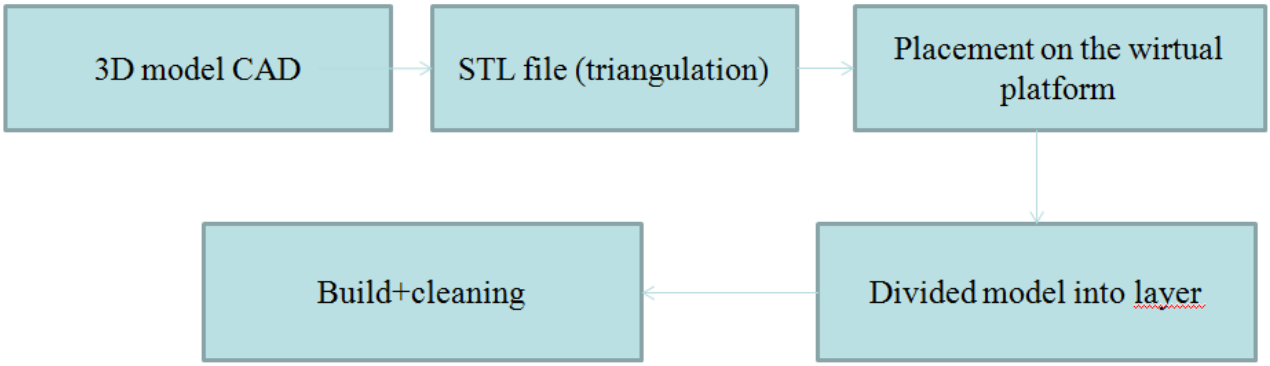

Fig. 1. Typical building process in additive technology

2. Technology

Selective laser sintering is one of the most common rapid prototyping technology. In this technology polyamide powder is distributed on a working platform on which the machine scanning laser beam selected geometry and by binding it with the previously applied layer. Then the working platform is lowered by the set thickness and the process is repeated until the completion of the construction of the model. The materials used in SLS technology are usually powders based on polyamides eg. PA2200 PA 3200, Alumide. These powders may be strengthened with glass fibers and aluminum to form a more durable material. In reported studies specimens were made using machine Formiga P100 EOS company (Figure 2) which is located in Unconventional Manufacturing Technology Laboratory KTMiM in Kielce University of Technology. The mechanical properties of polyamide PA 2200 are shown in Table 1 [7].

Mechanical properties	Value	Unit	Standard
Young modulus	1700	MPa	EN ISO 527
Udarność (23°C)	4.4	kJ/m2	ISO 180/1A
Impact strength	75	-	ISO 868
Density	930	kg/m3	EOS methods
Melting temperature	176	°C	ISO 11357-1/-3

Tab. 1. Mechanical properties of polyamide PA 2200

Fig. 2. Formiga P100 EOS company.

Polyamide PA 2200 is characterized by high resistance to aggressive chemicals and high impact resistance, which makes it a very good construction material could be use for sliding elements, or requiring high resistance to abrasion. Melting temperature of polyamide PA 2200 constructed based on PA12 is about 140 °C, which allows to use of these materials to the elements operating at temperatures ranging from -60 to about 110 °C. Wide temperature range allows the use of additive technology to build fully functional machine elements and mechanized. Selective Laser Sintering Technology is one of the most complex rapid prototyping technology. In the manufacturing process there is a lot of variables affecting the mechanical properties and dimensional accuracy [5, 6] compare to the other technologies. In the case of SLS technology significant effect has: the direction of „print", the thickness of the sintered layer, the temperature of the process chamber, the scan time, speed and power of the laser, which has a direct impact on the energy density transmitted to the sintered powder layer. Preliminary studies to determine the effect of the above factors on the mechanical properties and dimensional accuracy in SLS technology.

3. Research

Preliminary relaxation research was performed using Inspect Mini 3000N universal testing machine. The test specimens were designed according to PN-EN ISO 527. The thickness of all specimens was 4 mm and the energy density transmitted to the sintered powder layer during the manufacturing process was 0.056 J/mm^2. The direction of the print samples, and their placement on the virtual machine platform is shown in Figure 3. Table 2 and 3 shows the machine parameters and tested specimens.

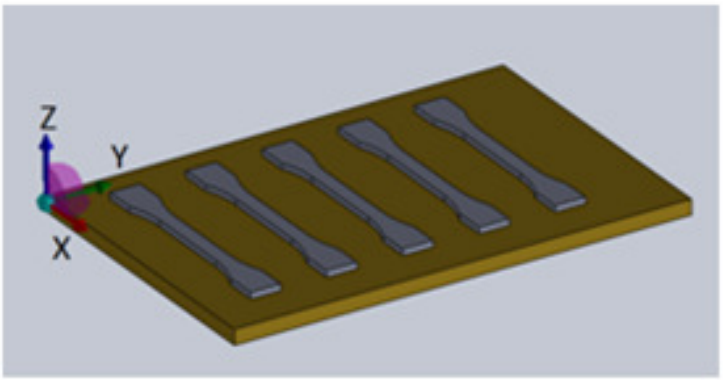

Fig. 3. Specimens on the virtual platform.

Laser setting	Value	Unit
Laser power	15	W
Hatching distance	0.25	mm
Laser speed	1500	mm/s
Focus beam diameter	0.42	mm

Tab. 2 Formiga P 100 - machine properties

The energy density transmitted to the sintered layer can be determined from equation 1 [3].

$$ED = \frac{P}{vh} x \tag{1}$$

where:

P - laser power [W], v - laser speed [mm/s], h - 0.25 [mm] hatch distance, d - 0.42 [mm] diameter of focussed beam, x - beam overlay ratio

No.	Time [s]	Loading speed [mm/min]	Energy density [J/mm^2]
1	300	25	0.056
2	600	25	0.056
3	900	35	0.056
4	1200	35	0.056

Tab. 3. Specimens properties

4. Results

Measurements of the relaxation phenomena were done for four selected time and are shown in Table 4 and Figure 4. The duration of the measurements ranged from 300 to 1200 seconds. Changes in stress measurements mainly been focused on the estimation of the percentage change this value of the stress to take into account the possibility of decline percentage change in design process.

No.	Time [s]	Beginning stress [MPa]	Stress in the end of the test [MPa]	Stress change [%]
1	300	21	18.5	12
2	600	21	18	14
3	900	18	15	17
4	1200	19	16	17

Tab. 4. Research results

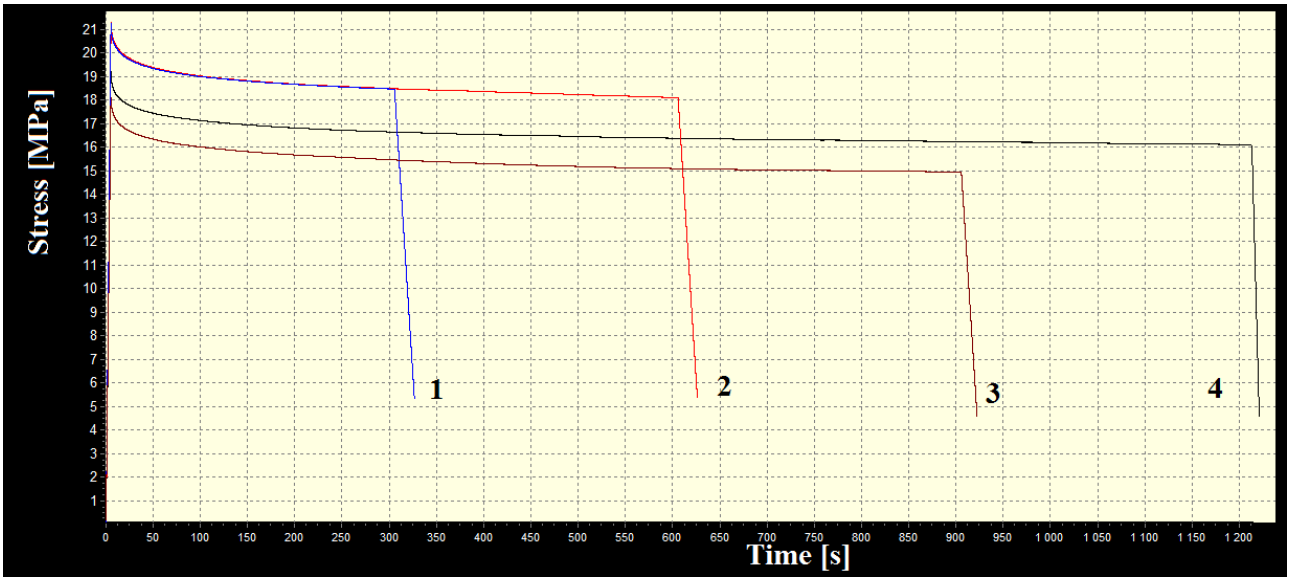

Fig. 4. Relaxation phenomena

Because of the additive character of the construction and initial stress the value of end stress are slightly different from each other. The effect of this can also be depending of loading speed.

5. Conclusion

The results of preliminary relaxation studies have shown that the problem of decrease stress with time is an important problem in most engineering plastics, in particular those produced in additive technologies due to the layered character of the construction of the specimens. Analyzing the results of previous studies which showed a significant effect of energy density delivered to the sintered powder layer on the tensile strength can be concluded that in the case of stress relaxation may be similar results. In the future it is planned to extend the relaxation studies of the impact of more parameters SLS technology and other technology.

Time after which the normalization of stress was over 1200 seconds. Below this value, the stress drop very rapidly and it was about 12% for specimens 1 to more than 17% in specimens number 4. The loading speed for the specimens 1 and 2 were slightly lower at 25 mm/min, compared to 35 mm/min for the other specimens. The value of the initial stress of samples 1 and 2 were slightly higher for the same deformation, which should also be taken into account by analyzing the relaxation process of plastics.

Acknowledgement

The study was conducted using research facilities purchased with EU funds in the framework of the 2007-2013 Development of Eastern Poland Operational Programme, LABIN Project − Support for Innovative Research Facilities of the Kielce University of Technology in Kielce. Priority 1 – Innovative Economy, Measure 1.3 – Support for R&D Projects.

References

[1] KUNDERA, Cz., Bochnia, J. *Investigating the stress relaxation of photopolymer O-ring seal models*, Rapid Prototyping Journal, Vol. 20 Iss: 6, pp.533 - 540

[2] KUNDERA, Cz., KOZIOR, T. *Assessment of technological clearance in model of sliding bearing made by SLS technology*, Mechanik 2/2015

[3] PILIPOVIĆ, A., VALENTAN, B., BRAJLIH, T., HARAMINA, T., BALIC, J., KODVANJ, J., SERCER, M., DRSTVENSEK, I. *Influence of Laser Sintering Parameters on Mechanical Properties of Polymer Product*, International Conference on Additive Technologies, Nova Gorica, Slovenia 2010.

[4] SALMORIA, G. V., LEITE, J. L., VEIRA, L. F., PIRES, A. T. N., ROESLER, C. R. M. *Mechanical properties of PA6/PA12 blend specimens prepared by selective laser sintering*, Polymer Testing 31 (2012), 411-416.

[5] SALMORIA, G. V., LEITE, J. L., PAGGI, R. A., ARHENS, C. H., POUZADA, A. S., *Microstructural characterization and mechanical properties of functionally graded PA12/HDPE parts by selective laser sintering*, Journal of Advanced Manufacturing Technology (2012), 583-591.

[6] JANECKI, D., ADAMCZAK, S., STĘPIEŃ, K. *Problem of profile matching in sphericity measurements by the radial method*, Metrology and Measurement Systems 4 (2012) 703-714.

[7] FORMIGA P100, User Manual EOS, Munich, 2008.

TRANSCOM 2015, 22-24 June 2015
University of Žilina, Žilina, Slovak Republic

Influence of Selected Water-jet Cutting Parameters on Surface Quality Aluminum Alloy

[*]Daniel Krajcarz
[*]Kielce University of Technology, Faculty of Mechatronics and Mechanical Engineering, Department of Applied Computer Science and Armament Engineering, al. Tysiąclecia Państwa Polskiego 7 25-314 Kielce, Poland, d.krajcarz@wp.pl

Abstract. This article describes the quality aspects of water jet cutting. These research studies have focused on the measurement of roughness parameters and declination angle for different traverse speeds. The relationship was carried out for the aluminum-5754 alloy. This material is an alloy in the wrought aluminium-magnesium family. Cutting abrasive jet was held on the water-jet model number APW 2010BB, with pump power of 18.5 kW, which is able to generate a maximum working pressure of 300 MPa. Abrasive materials used for water-jet machining was garnet mesh 80. Surface roughness parameters were higher for faster traverse speed. Depending on the measured profile roughness parameters was different. Each sample was measured in the three profiles. Declination angle increases with increasing traverse speed.

Keywords: Water-jet cutting, aluminum alloy, declination angle, surface roughness.

1. Introduction

Aluminum is a light-weight metal, however some of its alloys have higher strength than formable steels. Aluminum alloys are widely used in engineering structures and components, where light weight or corrosion resistance is required [2,6]. Aluminium-5754 alloy is an alloy in the wrought aluminum-magnesium family. Aluminum-magnesium alloys are both lighter than other aluminum alloys and much less flammable than alloys that contain a very high percentage of magnesium [5]. A few more interesting properties such as good formability, corrosion resistance and thermal, and electrical conductivity make aluminium-5754 alloy preferred for weight-saving potential in automotive part manufacturing industries [8].

Abrasive water-jet (AWJ) has been investigated since 1970s by many researchers in the world [5]. At present AWJ is a rapidly developing technology, which is increasingly used in industry for a number of applications. Materials commonly cut with a water-jet include ceramic, stone, metals, rubber, textiles, foam, plastics, leather, composites, tile, food, paper and much more [7]. AWJ is the method of cutting the material by the use of thin water jet under high pressure with added abrasive used to cut the target material by means of erosion [12]. Abrasive water-jet cutting is devoid of thermal effects and burr formation are very small, since a little heat generated by the water-jet is absorbed by the water. These advantages AWJ make it well suited for cutting aluminum alloys. An additional advantage of this technique is the possibility of cutting elements of different thickness which depends mainly on the amount of accumulated power in jet [10].

These research studies focus only on the measurement of roughness parameters [1] and declination angle [4] for different traverse speed.

2. Experimental Conditions

2.1. Material

The experimental tests were performed on commonly used in industry A95754 aluminum alloy, with the thickness of 20 mm. The chemical composition of materials and their properties are presented respectively in table 1 and table 2.

Si	Fe	Cu	Mn	Mg	Cr	Ni	Zn	Ti	Pb
0,4	0,4	0,1	0,5	2,6- 3,6	0,3	-	0,2	0,15	-

Tab. 1. Chemical Composition of Aluminum 5754/ H111 (%) [2].

Property	Density	Modulus of Elasticity	Thermal Conductivity	Thermal Expansion	Elongation A5	Hardness	Ultimate tensile strength
Unit	g/cm^3	GPa	W/mK	µm/mK	%	HB	MPa
Value	2.67	69	130-170	23,7	10-14	52-62	190-200

Tab. 2. Typical physical properties for aluminum alloy 5754 [2].

A95754 aluminum alloy is an alloy in the wrought aluminum-magnesium family. As a wrought alloy, it can be formed by rolling, extrusion and forging, but not casting. It can be cold worked to produce tempers with a higher strength but a lower ductility [8]. Alternate names and designations include $AlMg_3$ and 3.3535.

The material has a high resistance to corrosion in marine and industrial atmosphere. This aluminum alloy is used as a construction material in the building, railway and the maritime industry, in the construction of pressure vessels, transportation and automotive industry as a decorative material.

2.2. Equipment

The experimental equipment used to perform the tests was water-jet APW 2010BB. The process constant parameters fare are presented in table 3.

Parameter	**Unit**	**Value**
Water pressure	MPa	280
Abrasive mass flow rate	g/min	360
Stand-off distance	mm	2
Water orifice diameter	mm	0,3
Focusing tube diameter	mm	1,02
Focusing tube length	mm	76

Tab. 3. The process constant parameters for abrasive water-jet cutting.

During the experiment the traverse speed was changed and amounted successively 50, 100, 150 and 200 mm/min.

Abrasive materials used for water-jet machining was garnet mesh 80. The almandine crystal formula is $Fe_3A_{l2}(SiO_4)_3$. The density of material is 4200 kg/m^3. Average diameter of abrasive particles for mesh 80 is 0,18 mm [11]. Almandine is the ferrous iron end member of the class of garnet minerals representing an important group of rock-forming silicates, which are the main constituents of the Earth's crust, upper mantle and transition zone [3]. The appearance of garnet is visible in fig. 1a). Garnet observed in the optical microscope Nikon AZ100 (fig. 1b).

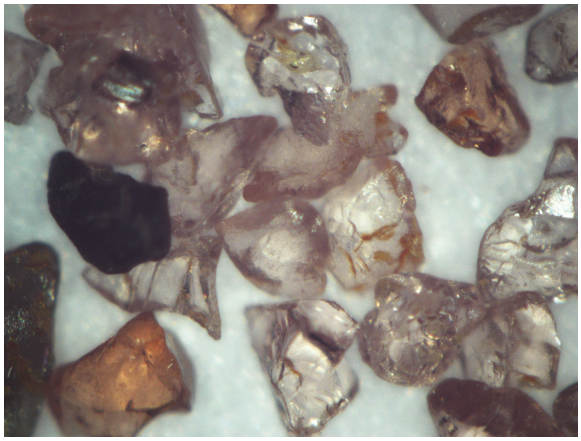


Fig. 1. a) garnet mesh 80, b) optical microscope Nikon AZ100.

Surface roughness parameters were made on the device TOPO 02 L120. All the samples were tested in 3 different sections (fig. 4). The aim was to show the differences in surface roughness depending on the measurement site.

3. Experimental Results and Discussions

The quality of surfaces processed by the abrasive water-jet cutting can be evaluated by analyzing profile roughness parameters for different traverse speeds and profile (tab. 4-6).

Parameter, µm	Description	Profile		
		P1	P2	P3
Ra	Roughness average	4,10	5,79	7,19
Rq	Root mean square roughness	5,16	7,36	8,65
Rv	Maximum profile valley depth	14,32	21,91	23,72
Rp	Maximum profile peak height	13,20	18,37	19,20
Rc	Mean height of profile irregularities	9,97	13,37	18,27

Tab. 4. Profile roughness parameters for traverse speed 50 mm/min.

Parameter, µm	Description	Profile		
		P1	P2	P3
Ra	Roughness average	5,20	7,19	15,14
Rq	Root mean square roughness	6,72	8,87	18,74
Rv	Maximum profile valley depth	21,67	24,25	39,80
Rp	Maximum profile peak height	15,34	21,29	46,69
Rc	Mean height of profile irregularities	13,83	16,34	31,55

Tab. 5. Profile roughness parameters for traverse speed 100 mm/min.

Parameter, µm	Description	Profile		
		P1	P2	P3
Ra	Roughness average	6,00	15,28	17,28
Rq	Root mean square roughness	7,40	18,90	19,94
Rv	Maximum profile valley depth	20,48	39,91	44,96
Rp	Maximum profile peak height	15,84	46,21	51,93
Rc	Mean height of profile irregularities	14,15	27,65	35,53

Tab. 6. Profile roughness parameters for traverse speed 150 mm/min.

Analyzing the profile roughness parameters, the following aspects can be remarked:

- the smallest values of surface roughness parameters were obtained in the case of the slowest traverse speed and profile P1;
- with an increase traverse speed the surface roughness parameters are highly growing. It is especially evident for the profile P3;

• for P1 profile was observed the smallest increases surface roughness parameters with an increase traverse speed. Parameter Ra increased from 4,10 µm (for traverse speed 50 mm/min) to 6,00 µm (for traverse speed 50 mm/min). In P3 profile was more than two-fold increase from 7.19 µm to 17,28 µm.

• measurements profile roughness parameters for the traverse speed of 200 mm/min were not possible in profilometer TOPO 02 L120. Cut surface quality was very low and threatened to damage the measuring instrument.

• to obtain a good cutting quality is associated with a slower traverse speed. A longer time of cutting means higher costs, since the process consumes a greater quantity of water, electricity and abrasive.

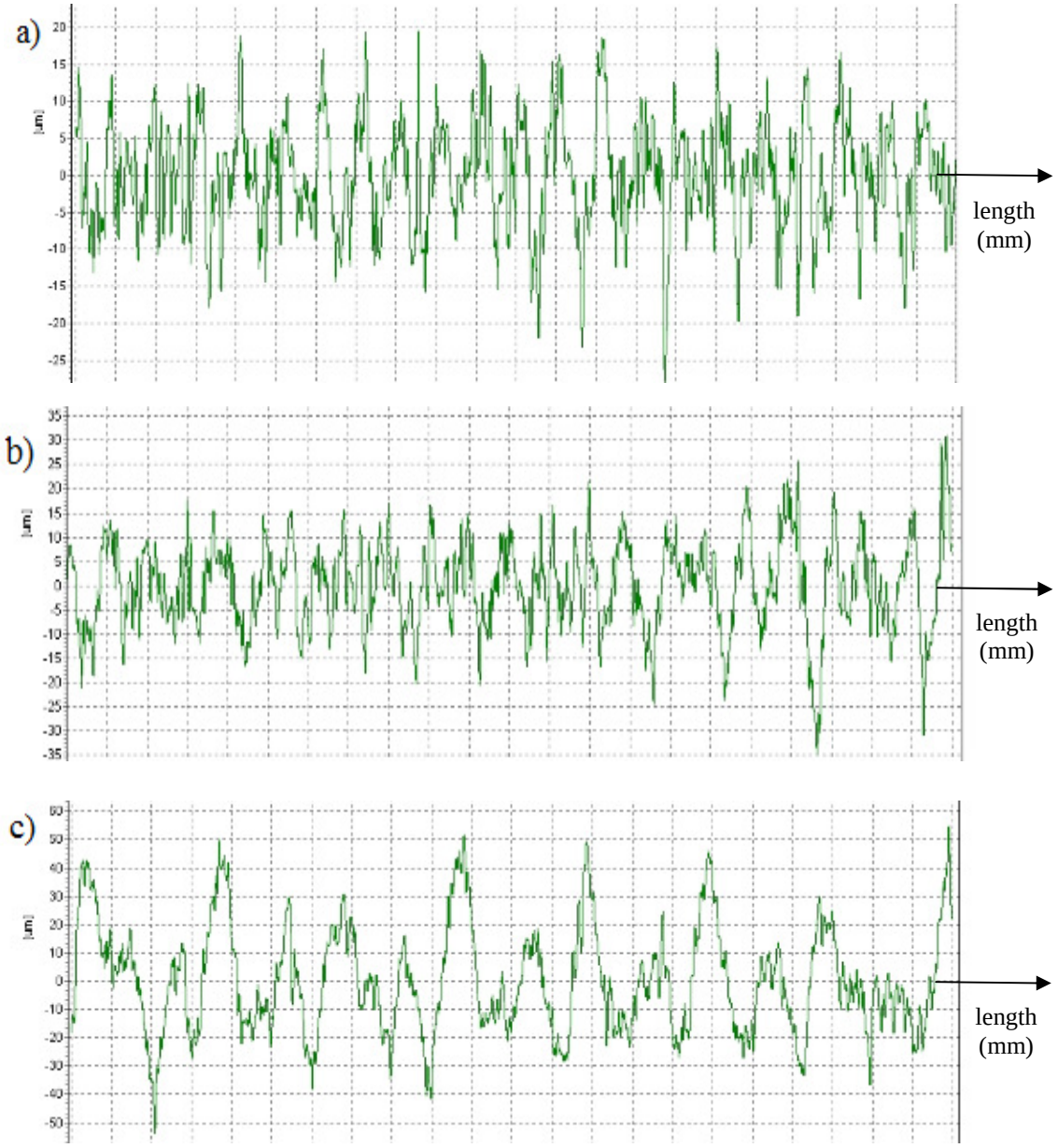

Fig. 2. Profile P2 roughness parameters for traverse speed: a) 50 mm/min, b) 100 mm/min, 150 mm/min.

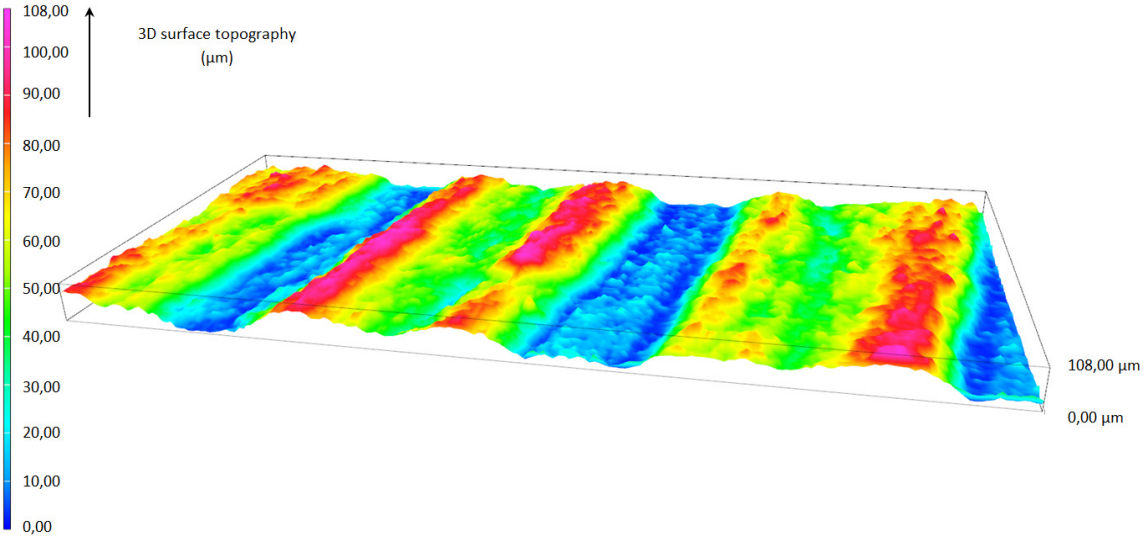

Fig. 3. 3D surface topography for traverse speed 150 mm/min.

Comparison declination angle depending on the traverse speed is shown in figure 4. The measurement of the declination angles is performed on the microscope Nikon AZ100 on the photos of the cutting walls.

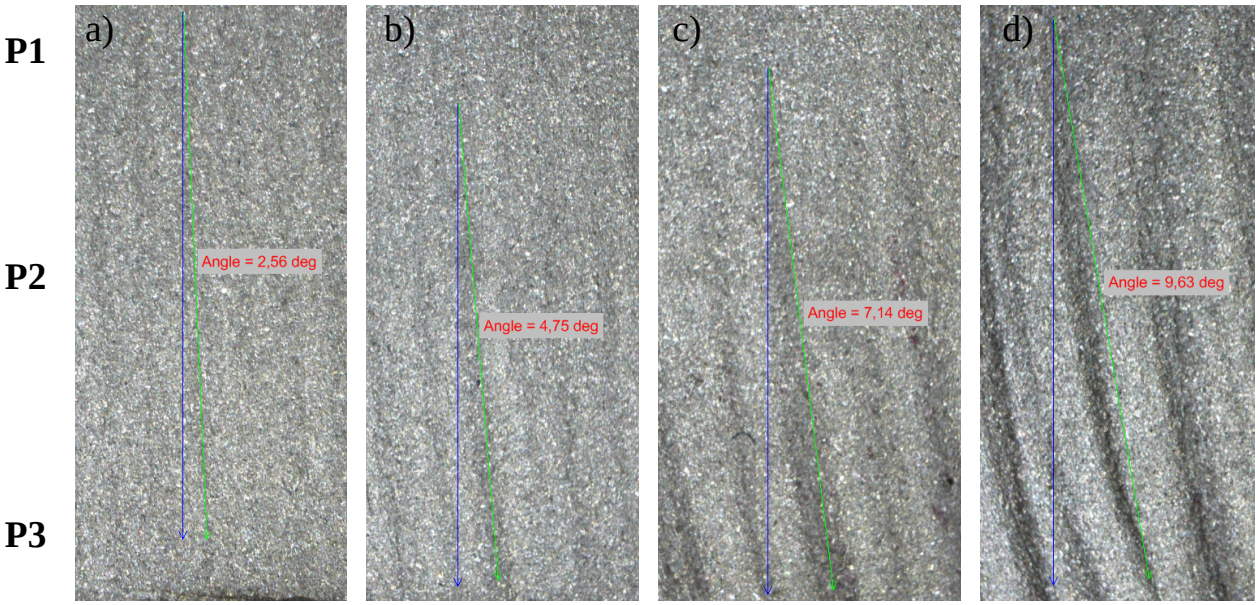

Fig. 4. The position of the measured profiles and declination angle for different traverse speed: a) 50 mm/min, b) 100 mm/min, c) 150 mm/min, d) 200 mm/min

The smallest declination angle was the slowest for traverse speed and amounted to 2.56 deg for 50 mm/min. The largest angle grooves were obtained for the fastest cutting speed. It was obtained 9.63 deg for traverse speed of 200 mm/min. When the traverse speed was increased by 50 mm/min then declination angle was increased by about 2.5 deg.

4. Conclusion

The analysis of quality of surface processed by unconventional abrasive water-jet technology shows that:

• with an increase traverse speed the surface roughness parameters are highly growing,

• the smallest values of surface roughness parameters were obtained for profile P1 (close to the upper edge cutting surface). Profile P3 was characterized by a significant increase surface roughness with an increase traverse speed,

• the smallest declination angle was for the slowest traverse speed and the largest angle grooves were obtained for the fastest cutting speed,

• to obtain a good cutting quality is always associated with a slower traverse speed. A longer time of cutting means higher costs, since the process consumes a greater quantity of water, electricity and abrasive,

• increase of declination angle was proportional to traverse speed. As the result of experiment was recorded increase of declination angle from 2.56 deg for 50 mm/min, to 9.63 deg for cutting speed 200 mm/min.

References

[1] ADAMCZAK S., MAKIEŁA W., STEPIEŃ K., *Investigating advantages and disadvantages of the analysis of a geometrical surface structure with the use of Fourier and wavelet transform*, Metrology and Measurement Systems, 2010, 12/2, 233-244.

[2] EN 573-3: 2009 Aluminium and aluminium alloys. Chemical composition and form of wrought products. Chemical composition and form of products.

[3] GEIGER C., ARMBRUSTER Th., LAGER G., JIANG K., LOTTERMOSER W., AMTHAUER G., *A combined temperature dependent57Fe Mössbauer and single crystal X-ray diffraction study of synthetic almandine: evidence for the Gol'danskii-Karyagin effect*, Physics and Chemistry of Minerals, 1992, 19, 121-126.

[4] HLAVAC L. M., HLAVACOVA I. M., GEMBALOVA L., KALICINSKY J., FABIAN S., MESTANEK J., KMEC J., MADR V., *Experimental method for investigation of the abrasive water jet cutting quality*, Journal of Materials Processing Technology, 2009, 209, 6190-6195.

[5] HLAVAC L., STRNADEL B., KALICINSKY J., GEMBALOVA L., *The model of product distortion in AWJ cutting*, International Journal of Advanced Manufacturing Technology 2012, 62, 157-166.

[6] KONIECZNY M., *Microstructural characterisation and mechanical response of laminated Ni-intermetallic composites synthesised using Ni sheets and Al foils*, Materials Characterization, 2012, 70, 117-124.

[7] KRAJCARZ D., *Comparison Metal Water Jet Cutting with Laser and Plasma Cutting*, Procedia Engineering, 2014, 69, 838–843.

[8] PATHAK N., BANDYOPADHYAY K., SARANGI M. *Microstructure and Mechanical Performance of Friction Stir Spot-Welded Aluminum-5754 Sheets*, Journal of Materials Engineering and Performance, 2013, 22(1), 131-144.

[9] POLMEAR I. J., *Light Alloys: Metallurgy of the Light Metals*, Arnold, 1995.

[10] SPADŁO S., KRAJCARZ D., MŁYNARCZYK P., *Badanie wpływu parametrów przecinania strugą wodno-ścierną stali S355 na strukturę geometryczną powierzchni*, Mechanik 2014, 9, 293-297.

[11] Technical Information GARNET Poland, data from the Internet, http://garnet.com.pl [access: 25.02.2015].

[12] WANG, J., WONG W.C.K., *A study of abrasive waterjet cutting of metallic coated sheet steels*., International Journal of Machine Tools and Manufacture, 1999, 39(6), 855-870.

TRANSCOM 2015, 22-24 June 2015
University of Žilina, Žilina, Slovak Republic

Finite Element Stress-Strain Numerical Analysis of Response of the Achilles Tendon

[*]Matej Kranjec, [*]Robert Kunc, [*]Ivan Prebil
[*]University of Ljubljana, Faculty of Mechanical Engineering, Chair of Modelling in Engineering Sciences and Medicine, Jamova cesta 12, 1000 Ljubljana, Slovenia,
{Matej.Kranjec, Robert.Kunc, Ivan.Prebil}@fs.uni-lj.si

Abstract: For the research of possibility of the Achilles tendon injury in cases of car collisions, the finite element analysis was chosen. The 3D finite element (FE) model of the Achilles tendon and assembly of a lower extremity model, including bones and muscles that are attached to the Achilles tendon, were constructed. With that model, we performed numerical analysis of the stress-strain response of the Achilles tendon for a front car collision with minimal and maximal muscle activation at the start of collision and determined the possibility of an Achilles tendon injury.
The risk for injury increases with higher muscle activation because of overloading of the Achilles tendon. In cases with minimal muscle activation, the ankle injury is more common.

Keywords: Achilles tendon, finite elements, numerical analysis, stress distribution, collisions.

1. Introduction

The Achilles tendon is the strongest tendon in human body. It is located above the calcaneus and under rear side of knee in lower extremity (Fig. 1). Previous studies of Achilles tendon have focused around the Achilles tendon material properties [1], creating material models for use in simple FE analysis using discrete or beam finite elements [2][3][4][5][6]. We wanted to analyze distribution of tensile von Mises (VM) stress in a 3D FE model of Achilles tendon. The goal of our analysis was to verify if the Achilles tendon injury starts in the area of critical i.e. smallest cross sectional area (CSA) as was discovered in previous studies [7].

In addition, our goal was to analyze the influence of minimal and maximal preloading of the Achilles tendon using calf muscles at the start of a car collision, when foot-compartment elements strike to the toe part of the foot [8]. The possibility of an Achilles tendon and ankle injury in both cases was determined. A detailed study is available in my master's degree [9].

2. Anatomy and Function

The Achilles tendon or *tendon calcanei* in Latin is a tough band of fibrous tissue that connects the calf muscles to the heel bone (Fig. 1).

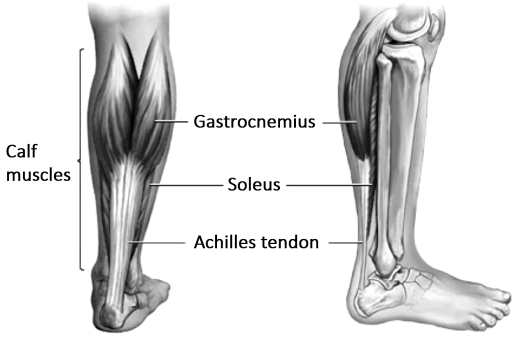

Fig. 1. Anatomy of lower part of lower extremity [10].

It is the strongest tendon in human body and is used for holding the whole bodyweight during everyday activities such as walking, running and other sport activities. Even though it is very strong, it can tear or break during excessive loading [7].

The main purpose of the Achilles tendon is transferring load from the contracting calf muscles to the heel bone and with that extending the foot around the ankle joint. The only foot action coming from calf muscles is plantar flexion of the foot i.e. extension of the foot, which means it contradicts to the dorsiflexion that comes from external loading of the toe region of the foot which turns it upwards.

2.1. Achilles Tendon Mechanical Properties

The Achilles tendon has a typical tensile stress-strain response that is similar for all human tendons. It is divided into three regions (Fig. 2). The first region is called the toe region, where tendon fibers are continuously strengthened and do not carry much load. The second one is called the linear region, where most of tendon fibers are already straightened and are carrying the load. If we stop the loading of the Achilles tendon in this region, it returns to its former state with no damage. But if we continue to stretch the tendon into the third region, microscopic ruptures of fibers occur, leading to more and more ruptures. In this region, the previously unstraightened fibers are stretched to take the load from broken fibers. Continuing loading the tendon, a critical number of fibers get ruptured, and CSA of the Achilles tendon gets too small to carry the load. At that moment, the Achilles tendon snaps.

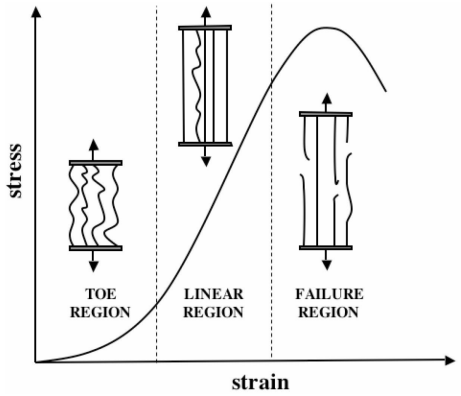

Fig. 2. Regions of Achilles tendon tensile stress-strain response [11].

2.2. Muscles and Bones

For our numerical analysis geometry of the bones of a foot and the lower part of a lower extremity were essential, because they represent fixture for muscles and the Achilles tendon and also define the axes of the ankle join. Calf muscles are used to impose load to the Achilles tendon contradicting to the external loading force on the toe region. With activating the calf muscles the Achilles tendon is preloaded during emergency braking before collision [8].

3. Construction of FE Model

For our numerical analyses we needed a meshed 3D model of a lower extremity that included bones of a foot and ankle joint, the Achilles tendon and a simple model of calf muscles. We used a 3D model of bones from the Zygote skeleton [12]. The shape of the volumetric model of the critical part of the Achilles tendon was taken from Obst [13] (Fig. 3) and modeled by SolidWorks modeling platform. For modeling the calf muscles, only the length was necessary because we used discrete elements for defining the shape of muscle in our model. Other muscle parameters were gathered from literature [14]. A complete model of lower extremity used in analyses is represented in my master's degree paper [9].

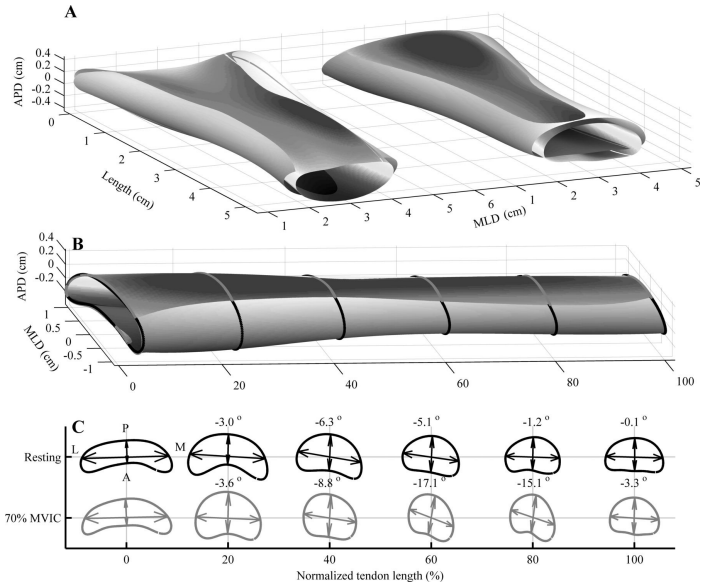

Fig. 3. Shape and size of critical part of the Achilles tendon [13].

3.1. Finite Element Types

For every part used in the FE model a different type of finite elements was used, depending on the shape and importance of results that we wanted to gather. For the calf muscles we used a discrete FE element and a muscle material model, already implemented in LS-Dyna. Bones were meshed with shell FE and a rigid material model was used to represent firm support for muscles and tendon. For the Achilles tendon, we used solid finite elements and a nonlinear material model so we could observe VM stress distribution over tendon.

3.2. Simulation Parameters

In Tab. 1, there are gathered Achilles tendon parameters used in numerical analyses which were obtained from literature [15][16][17][18] due to a lack of personal experimental data.

Maximal tensile force [N]	F_{Tmax} = 3525 ± 150
Maximal elongation [mm]	ΔL_T = 11.01 ± 1.86
Cross Sectional Area [mm²]	CSA = 153 ± 5
Resting length [mm]	L_T = 152.32 ± 11.96
Maximal tensile stress [MPa]	σ_{max} = 80.28 ± 8.62
Young modulus [MPa]	E_T = 973.4 ± 277.50
Poisson ratio [/]	ν_T= 0.4 ± 0.05
Density [g/cm³]	ρ= 1.40 ± 0.70

Tab. 1. Main Achilles tendon parameters.

The maximal and minimal angle of ankle rotation was also obtained from literature [19]. The ankle angle takes the values of 20 ± 10 degrees for dorsiflexion and 35 ± 15 degrees for plantar flexion. A flat foot standing was represented with 0 degrees of rotation.

4. Numerical Analysis

To be sure that our FE model of the Achilles tendon responds as necessary, we first had to evaluate it. Tensile stress-strain numerical analysis was performed and results were compared to the stress-strain curve of experimental data (Fig. 4). Even though the response was more linear than

experimental data [9], the relative deviation was never higher than 8 %. Furthermore, it was only 0.7 % at a critical breaking point. Analyses also confirmed that the maximal tensile stress concentrates in the area of the minimal CSA of the Achilles tendon as was experimentally discovered [7].

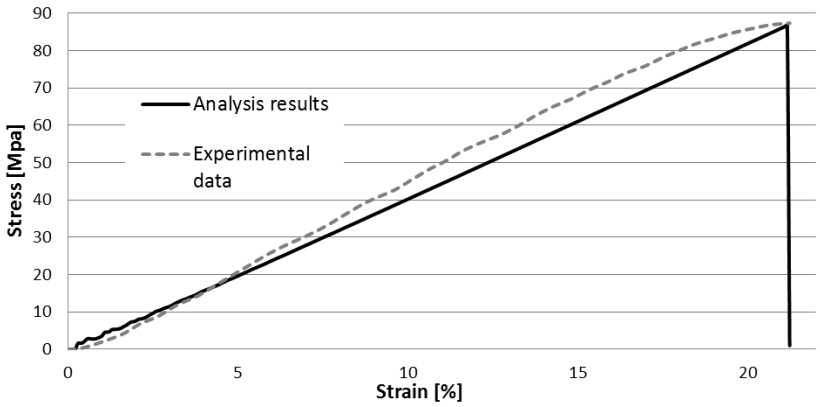

Fig. 4. Deviation of analysis results from experimental data.

Using the described model of a lower extremity, two types of collision loading of the Achilles tendon were performed. The first type was with minimal muscle activation, where muscle activates at the moment of collision, and the second type, where muscle was fully activated before collision, extending the foot and preloading the Achilles tendon. In both types of numerical analysis, the collision acceleration was defined as 10 g, 20 g and 30 g, each magnitude of acceleration for one instance of numerical analysis.

5. Results

The ankle joint angle and effective VM stress (Fig. 5) in the Achilles tendon were measured in time to determine whether ankle injury of the Achilles tendon rupture comes first. The main focus of the analysis was to compare two types of loading of the Achilles tendon and determine which one the rupture of the Achilles tendon is more likely to occur in. Results for both types of collision are shown graphically (Fig. 6). Results for the Achilles tendon evaluation and a detailed explanation of the analysis results are gathered in my master's degree paper [9].

5.1. Minimal Muscle Activation Collision Type

Calf muscles are activated at the same time as collision acceleration starts to load the toe area, which is why the foot angle only decreases from the initial neutral position. Negative foot rotation stands for dorsiflexion of the foot, i.e. foot is rotating upwards. As shown in Fig. 6, angle rotation reaches the maximal dorsiflexion angle of 30 degrees before tensile stress in the Achilles tendon reaches a critical value. That occurs in cases with accelerations of 10 and 20 g magnitude. With acceleration of 30 g magnitude, maximal tensile stress of 84 MPa in the Achilles tendon is reached very close to the maximal dorsiflexion angle of ankle rotation and takes the value of 28.6 degrees. This is the reason why we cannot surely say which injury would come first. The calculated results indicate to the Achilles tendon rupture, but maximal ankle rotation could be smaller for some people.

5.2. Maximal Muscle Activation Collision Type

In this type of collision, calf muscles are activated before the collision occurs. The reaction of muscle contraction is tension in the Achilles tendon which starts the plantar flexion of the foot as it is seen in Fig. 4 as positive foot rotation. Maximal effective VM stress at foot extension before loading takes values of 40 ± 8 MPa. At given time – the same for cases with acceleration of 20 and

30 g magnitude and a little sooner for the case with acceleration of 10 g magnitude – acceleration starts loading the toe area, increasing tensile stress in the pretensioned Achilles tendon. The angle of the foot starts to decrease while tensile VM stress quickly rises and reaches maximal value before the foot even reaches neutral position. In that moment, the Achilles tendon rupture occurs. The angle of the ankle at Achilles tendon rupture is similar for 20 and 30 g analyses and takes the value of 4 degrees of dorsiflexion. The only exception is the case with acceleration of 10 g magnitude, where load from acceleration is not strong enough to strain the Achilles tendon enough to reach maximal tensile stress. The maximal value of effective VM stress in this case reaches only 71.6 MPa. That leads to the over rotation the foot and the consequence is ankle injury because of excessive plantar flexion.

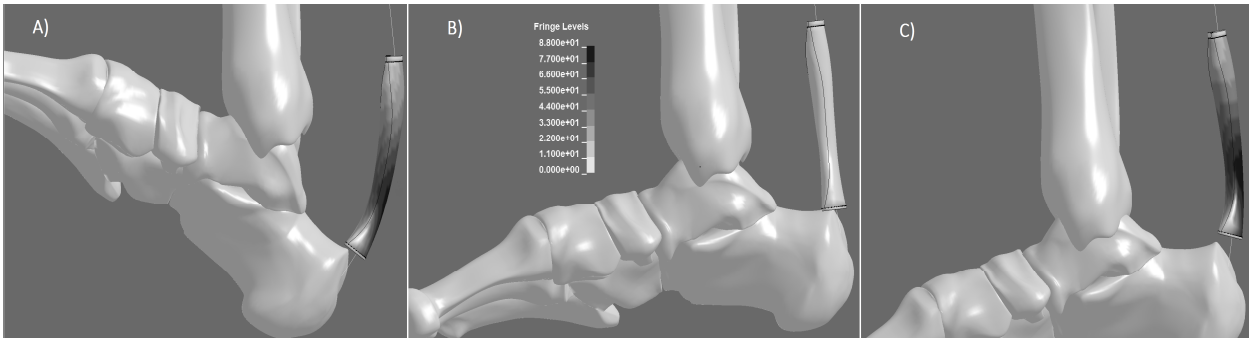

Fig. 5. Effective VM stress before injury at: A) minimal; C) maximal muscle activation. B) Position of foot before loading. Fringe levels scale is the same for all cases – range from 0 to 88 MPa.

5.3. Comparison of the Two Collision Types

If we compare the results from both types of collisions, it is obvious that in case of preloading the Achilles tendon using muscles it is more likely that the Achilles tendon will break before the ankle will reach its critical point in contrast to the other type, where ankle injury is more likely to occur because tensile stress in the Achilles tendon does not reach critical values inside the ankle's area of movement.

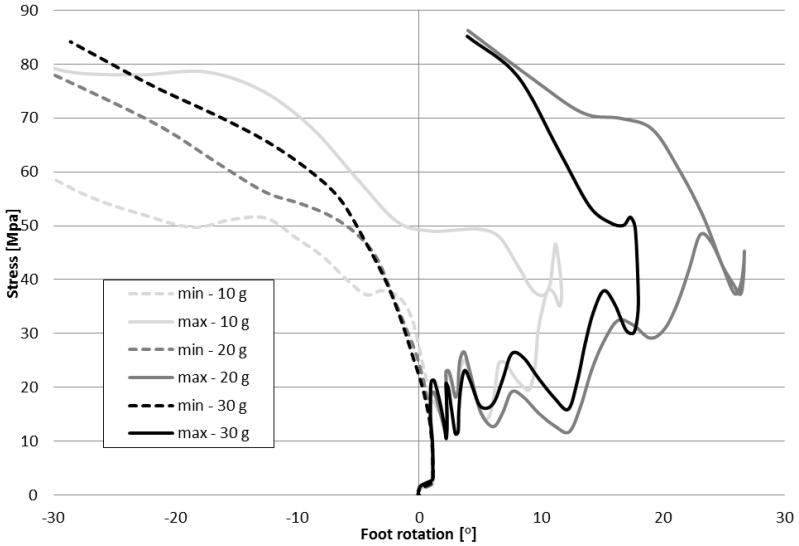

Fig. 6. Stress in Achilles tendon in dependence of foot rotation for min. and max. muscle activation collision type.

6. Conclusion

Loading of the Achilles tendon in different cases was numerically analyzed. A numerical model for use in the FE method was created and used for analyses of collision of the foot compartment in a vehicle to the toe part of a foot. The main purpose was to analyze stress distribution over the

Achilles tendon and to verify that the smallest CSA of the Achilles tendon is the place where the tendon breaks due to overloading.

Results of numerical analysis confirmed that maximal tensile stress always concentrates at the zone of minimal CSA of the Achilles tendon, which was predicted before performing analyses.

As determined based on the loading cases of collision, collisions with smaller values of acceleration/deceleration lead to a higher possibility of ankle or bone injury, while collisions with higher values of acceleration mostly lead to the Achilles tendon injury and lower the chance of ankle injury before the Achilles tendon breaks.

According to the results of the loading case analyses, it would be worth exploring injuries of ankle bones and other ankle ligaments in case of over rotation of the ankle joint.

References

[1] QUAPP, K. M. *Material characterization of human medial collateral ligament.* The University of Utah, Department of Bioengineering, 1997**.**

[2] S MUKHERJEE, S., CHAWLA, A., KARTHIKEYAN, B., SONI, A. *Finite element crash simulations of the human body: passive and active modelling*. Sadhana Vol. 32, Part 4, August 2007, pp. 409–426.

[3] SILVESTRI, C. *Development and validation of a knee-thigh-hip: Ls-Dyna model of a 50th percentile male.* International Journal of Crashworthiness. Vol. 14, Issue 2, April 2009, pp. 215-229.

[4] NAGANO, A., KOMURA, T., FAKUSHIRO, S., HIMENO, R. *Force, work and power output of lower limb muscles during human maximal-effort countermovement jumping*. J. Electromyogr. Kines., Volume 15, Issue 4, August 2005, pp. 367-376.

[5] SETH, A., SHERMAN, M., REINBOLT, J. A., DELP, S.L. *OpenSim: a musculoskeletal modelling and simulation framework for in silico investigations and exchange*. Procedia IUTAM, Vol. 2, 2011, pp. 212-232.

[6] PROKOPOW, P. *The effect of muscle strengthening on neuro-musculo-skeletal dynamics in a squat jump: a simulation study*. Human Movement. Vol. 12, Issue 4, December 2011, pp. 307–314.

[7] DORAL, M. N., ALAM, M., BOZKURT, M., TURHAN, E., ATAY, O. A., DÖNMEZ, G., MAFFULLI, N. *Functional anatomy of the Achilles tendon*. Knee Surg. Sports Traumatol. Arthrosc., Vol. 18, Issue 5, May 2010, pp. 638-643.

[8] HARDIN, E. C., SU, A., VAN DEN BOGERT, A. J. *Foot and ankle forces during an automobile collision: the influence of muscles.* J. Biomech., Vol. 37, Issue 5, May 2004, pp. 637-644.

[9] KRANJEC, M. *Finite Element Stress-Strain Numerical Analysis of Response of the Achilles Tendon.* University of Ljubljana, Faculty of mechanical engineering, 2014.

[10] BARFOD, K. W. *Achilles tendon rupture; assessment of nonoperative treatment.* Danish Medical Journal, Vol.61, No. 4, April 2014.

[11] DE VITA, R. *Structural constitutive models for knee ligaments.* University of Pittsburgh, 2005.

[12] *3D human skeleton model* – Zygote Media Group, Inc. American Fork, Utah.

[13] OBST, S. J., RENAULT, J.-B., NEWSHAM-WEST, R., BARRETT, R. S. *Three-dimensional deformation and transverse rotation of the human free Achilles tendon in vivo during isometric plantar flexion contraction*. J. Appl. Physiol., Vol. 116, No. 4, February 2014, pp. 376-384.

[14] ÖSTH, J. *Active Muscle Responses in a Finite Element Human Body Model.* Vehicle Safety Division, Department of Applied Mechanics, Chalmers University of Technology Göteborg, 2010.

[15] LEWIS, G., SHAW, KM. *Modelling the tensile behaviour of human Achilles tendon*. Department of Mechanical Engineering, The University of Memphis, 2012.

[16] HASHEMI, J., CHANDRASHEKAR, N., SLAUTERBECK, J. *The mechanical properties of the human patellar tendon are correlated to its mass density and are independent of sex.* Clinical Biomechanics, Vol. 20, Issue 6, July 2005, pp. 645-652.

[17] ARYA, S., KULIG, K. *Tendinopathy alters mechanical and material properties of the Achilles tendon.* J. Appl. Physiol., Vol. 108, No. 3, March 2010, pp. 670-675.

[18] KURIHARA, T., SASAKI, R., ISAKA, T. *Mechanical properties of Achilles tendon in relation to various sport activities of collegiate athletes.* International Symposium on Biomechanics in Sports: Conference Proceedings Archive 2012, Vol. 30, pp. 144-147.

[19] MAXWELL, D., KEER-KEER, S., BARR, N. *Functional anatomy and biomechanics project*. University of Glasgow, University of Strathclyde, Glasgow Caledonian University, University of Paisley. Gathered 17.3.2015 from world wide web: http://www.gla.ac.uk/t4/~fbls/files/fab/ .

TRANSCOM 2015, 22-24 June 2015
University of Žilina, Žilina, Slovak Republic

Multisensensory Measurements in Modern Production Techniques

*Jakub Kulpa, *Grzegorz Witkowski
* Kielce University of Technology, Department of Mechatronics and Machine Building,
Tysiąclecia Państwa Polskiego 7, 25-314 Kielce, Poland, {jakub-kulpa}@wp.pl,
{gwitkowski}@tu.kielce.pl

Abstract. The technological development of production forces the need for continuous development of measurement systems. Modern production technologies such as Rapid Prototyping require specialized measurement systems. Additive technologies allow to manufacture parts with a complex geometry. Geometry measurement of such models by traditional methods is problematic or impossible to perform.The selection of an appropriate method of measurement is influenced by many factors: required accuracy, type of the object being measured (size, material, surface) and place of measurement. Multisensory Coordinate Measuring Machine (ang.CMM) use a combination of different types of measurement sensors such as: tactile sensors, tactile-optical sensors, laser sensors, cameras processing the image, and optical sensors. Complex measurement tasks often require the use of several types of sensors to measure the same object.

Keywords: Additive technologies, cmm, sensor, tactile, coordinate

1. Introduction

Coordinate metrology as a multipurpose and efficient technology is especially important for new needs of the market.

Coordinate Measuring Machines (CMM) collect data about the measured object using sensors. CMMs can be equipped with a many different sensor such us a tactile or optical trigger probes or measurement sensors. The main task of the trigger probes is to call the trigger signal when a probe tip get a contact with the measured surface. It makes it necessary to read the data with respect to all the axes of the machine to determine the coordinates of the iterface in space. Movement against the axis is needed to determine the coordinates of the iterface. The measurement sensors have an internal measuring range of up to a few millimeters. The iterface is determined by overwriting the value read by the sensor over the coordinate values read by the measuring machine.

1.1. Multisensory of CMMs.

Typical CCMs are equipped with tactile measuring tip with the possibility of the selection of its diameter and length of the probe where the measuring tip is situated. This allows to measure the dimensions of various elements from several millimeters to several meters (Gantry CMMs). Although such measurements are the most accurate at the moment, they involve certain limitations. The first limitation are the dimensions of the measuring tips, the minimum diameter is about 0.3 mm. Another limitation is related to the physical contact of the measuring tip with the surface of the measured element; too much pressure on the element may damage its surface or cause the movement against the table.

During the last years, there is a strong emphasis on the development connected with multisensory coordinate measuring technology in order to meet the needs of the production market. There are a lot of elements that require using different measuring sensors, i.e.: micro gears, implants, delicate elements made of glass or fabric, and more. Measurements of parts with size of a few millimeters to a few micrometers or the measurements of macroscopic elements of very low uncertainty require new measurement techniques based on current machines but with improved stiffness and thermal stability. Multisensory coordinate measuring machines use a combination of

different types of measurement sensors such as: tactile measurement tips, tactile-optical tips, laser sensors, cameras processing the image, optical sensor using autofocus, sensors scanning 3D tracks [1, 2, 3, 4].

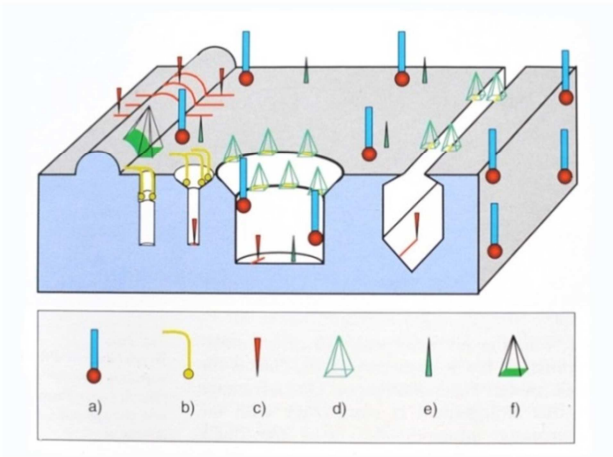

Fig. 1. Measurement sensors and their application [1]: a-tactile sensor; b- tactile-optical sensor; c- laser; d- sensor processing the image; e- autofocus; f- sensors scanning 3D tracks.

1.2. Additive Technologies.

Additive technologies known as a Rapid Prototyping (ang. RP) or „3D printing" allows to produce physical models based on a computer model developed in CAD software's or generated by reverse engineering technologies. The general principle of production of these objects involves creating layered models. The concept of "Rapid Prototyping" combines the technologies that are automated physical modeling techniques through a layered sintering, bonding, splicing, melting and curing all kinds of material, by laser or other sources and energy. RP technology is mainly used for the production of prototypes but increasingly also for the production of small series. They allow you to significantly reduce the time and cost of the launch of a new product. Although these processes are the same at end, are very different in terms of the resulting final product. One of the most popular technologies with a lot of possibilities is the POLJET Matrix technology developed by Objet company. In Polyjet technology model is created by spraying photopolymer on tray by piezo-crystal working through electronically controlled (Figure 14). Working material is fed to the nozzle with a very small pressure, then if a location is to be given the material to piezo-crystal voltage is applied to decreases a volume of the crystal. In resulting the photopolymer drop is squeezed through the nozzle. After the single layer, it is exposed to UV light that causes the immediate hardening of the material.[5,6,7]

Fig. 2. Objet Connex 350 Printer and the manufactured thin wall cube model.

2. The Use of Multisensory CMM ZEISS O-INSPECT 442 for Rapid Prototyping Models.

Applying RP technology we can produce elements of geometry impossible to perform traditional techniques. Such models require the use of a variety of sensors in order to assess the accuracy of performance. There are many different RP technologies which differ in accuracy and the principle of the prototype production. Due to the development of RP technologies they are more and more popular and they are used not only for prototyping but also for the small series production. This necessitates a proper assessment of the accuracy of these technologies and determination of their capabilities. Multisensory coordinate measuring technique is very useful for the evaluation of the models produced with the use of RP technologies. One of the most popular of Multisensory CMMs is O-INSPECT 442 produced by Zeiss Company.

O-INSPECT 442 is equipped with a three different sensors:

- Tactile sensor - passive scanning head
- Visual sensor – 2D optical CCD Camera with discovery zoom lens
- Optical sensor – white light distance sensor

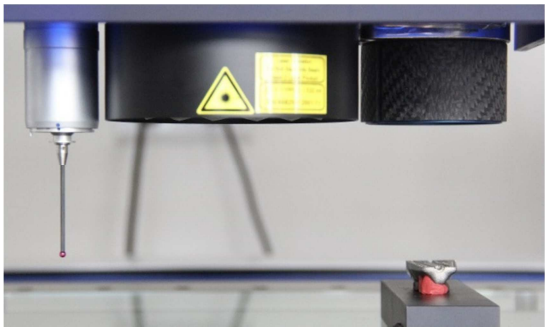

Fig. 3. O-INSPECT 442 sensors: from left side a) tactile sensor; b) 2D Camera; c) white light sensor

Figure 4 illustrates an exemplary application of multisensory CCMs for the evaluation of a prototype made of metal powders (SLM).

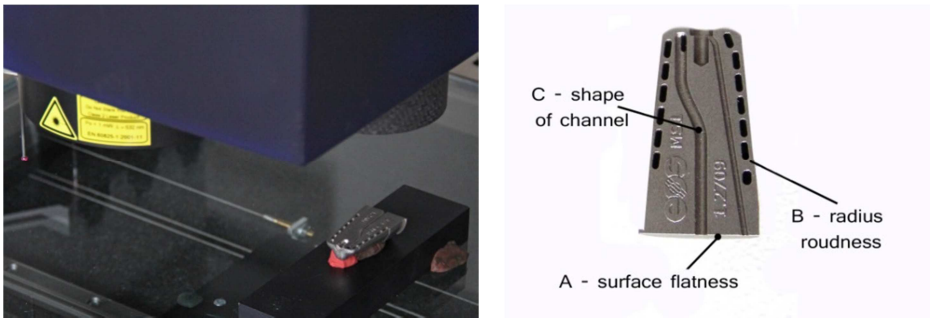

Fig. 4. Multisensory measurement of a prototype.

To measure three characteristics marked on the above prototype three different sensors were used. The evaluation of the flatness of the side wall was performed with the use of a tactile tip. The rounding radius of repeating slotted holes, due to the very small size, was determined by optical image processing method, and the shape of the channel cross-section was determined by the white light optical sensor as its dimensions did not allow for the evaluation by the tactile method. The above example illustrates well the issues and complex measurement tasks posed to us by production technology by Rapid Prototyping. At this point, multisensory measurements are necessary for the correct evaluation of a prototype.

Visual and tactile sensor were compared to check their accuracy on O-Inspect CCM using Calypso5.2 software. The diametral stencil of the value equal 49.9865 mm specified by the Central Office of Measures was used as the object of the measurement. This object was measured with a

ULM600 linear gage and its value was set to 49.9867 mm; it was accepted in further measurements as the nominal value. Both methods have been carried out in automatic mode with a fixed scan rate of 5m/s and 360 measurement points were collected. In both methods, software filtering and deleting of abnormal values were used . The measurement for each of the methods was carried out ten times. After calculations, the standard deviation obtained for the optical method was 0.0046 mm and 0.0024 mm for the tactile method. Deviation of the optical method is almost twice as large as the deviation of the tactile method, nevertheless, it is still satisfactory.

Tactile sensor was also compared to the white light sensor. The surface flatness of printed model was designated by both sensors. The result are shown on a figure 5.[8]

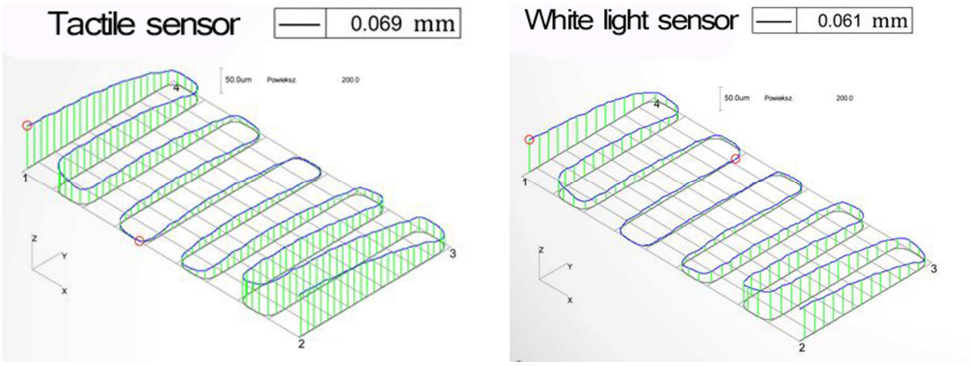

Fig. 5. Graphical evalutation of surface flatness.

The obtained results of the measurements are very similar. There are currently hard to determine which of them will be more correct. Measurement by tactile sensor could be affected by the deformation of the material caused by the contact pressure of the measuring tip. The other hand, optical measurement could be affected by the model which was made of translucent material.

3. Conclusion

Multisensor measuring technique enables a comprehensive measurement of complex parts made of RP technologies. Optical sensors can be used with a small-sized elements and easily deformable materials. Highest accuracy of measurements we achieve by tactile sensor, however due to low accuracy of RP technologies we can use optical sensor with high precision. Optical sensor are much faster than the tactile senor but not so precision. In many cases it is not possible to measure some details by contact methods, for example diameter of hole is smaller than the diameter of stylus tip. Optical method has a lot of limitations and may be used only where it is necessary.

References

[1] CHRISTOPH R., NEUMANN H.J.: *Multisensor Coordinate Metrology*. Werth Messtechnik GmbH

[2] SŁADEK J., KULPA J.: M*ultisensory coordinate measuring technology.* XI Coordinate measuring Technique 2014

[3] DE CHIFFRE L., HANSEN H. N.: *Metrological limitations of optical probing techniques for dimensional measurements.* Institute of Manufacturing Engineering, Technical University of Denmark

[4] RATAJCZYK E., Coordinate Measuring Technique (in Polish), Warsaw University of Technology Press, Warsaw, Poland, 2005.

[5] KIETZMAN J.: *Rapid prototyping polymer parts via shape deposition manufacturing* . Doctors dissertation

[6] GIBSON I., ROSEN D., STUCKER B.: *Additive Manufacturing Technologies*. Rapid Prototyping to Direct Digital Manufacturing. ISBN: 978-1-4419-1119-3

[7] ADAMCZAK S., BOCHNIA J., KACZMARSKA B.: *Estimating the uncertainty of tensile strength measurment for a photocured material produced by additive manufacturing.* Metrology and Measurement Systems book 21

ADAMCZAK S., ŚWIDERSKI J.: *Przegląd wybranych współczesnych metod pomiarów zarysów nierówności powierzchni*. Sympozjum Klubu Polskie Forum ISO 9000 "Metrologia w Systemach Zarządzania -7"

TRANSCOM 2015, 22-24 June 2015
University of Žilina, Žilina, Slovak Republic

Compare of Sliding Tribological Properties for Laser Padded Coatings Deposited onto C45 Steel Substrate

[*]Piotr Kurp
[*]Kielce University of Technology, Faculty of Mechatronics and Machine Engineering, Laser Processing Research Centre, al. Tysiąclecia Państwa Polskiego 7, 25-314 Kielce, Poland, pkurp@tu.kielce.pl

Abstract. Author of this paper presents a tribological differences between bronze B6 and Al_2O_3 coatings. Tested layers were produced onto C45 steel substrate by laser padding. Tribological properties were examined using T01 pin-on-ring tester.
A friction force of kinematics pair was examined at different loading values applied during investigation. The wear intensity was calculated for individual elements as well. Comparison of the results have been summarized in graphs and tables.

Keywords: laser padding, friction force, tribology.

1. Introduction

Laser padding is one of the surface engineering technologies in which the additional material in the form of powder, paste or wire is delivered between the focused laser beam and the base material. The surface of this material is melted by the high-power laser beam. As a result of this process, a small molten metal puddle is created. The additional material is fed continuously into a puddle and melted at high speed. A thin layer of the deposit (alloy material and filler) is generated. This leads to the creation of high-quality metallurgical surface. The whole process is carried out in an inert shielding gas with speeds up to 10^6 K/s. This provides a high purity metallurgical and fine-grained structure of the manufactured surface [1], [2], [3], [4], [6].

2. Process of laser padding and materials selection

C45 carbon steel was selected as a base material for laser padding. It is a commonly used steel intended for surface hardening and toughening. The steel include chemical elements as: C – 0,42÷0,50%, Mn – 0,50÷0,80%, Si – 0,10÷0,40%, P – max. 0,04%, S – max. 0,04% [5].

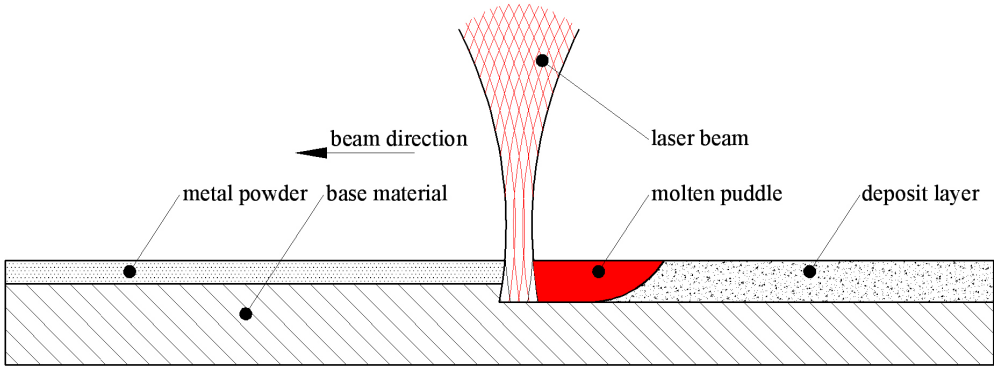

Fig. 1. Schema of the laser padding process.

Bronze B6 and ceramic Al_2O_3 coatings were produced to compare changes in properties of the surface layers. The coatings were prepared in the form of a paste made from metal powder with particle size of approx. 5μm. The paste was imposed on the 6 mm thick C45 steel ring. The

thickness of paste cover was about 0,2 mm. Trumpf TLF6000 CO_2 laser was used to execute the process. Laser operating parameters were: power – 3kW, beam speed - 1m/min. The deposition was carried out using defocused beam with 5 mm diameter. The surfaces were polished after process. Schema of the treatment is shown on Fig 1.

3. Tribological properties determination of manufactured layers

Ttribology test was prepared on T-01M tester made by Instytut Technologii Eksploatacji w Radomiu, according to DIN-50324:1992-07 standard [7]. Disc (C45 steel) with padded layers (Bronze B6 and ceramic Al_2O_3) were prepared to determine tribological properties. Ball material was 100Cr6 bearing steel, with d=6,3 mm diameter. The disc was rotated with constant speed ω=200 rpm. The ball was pressured to disc with force *F* depended on applied load. There were three different load values: 0,5 kG (F=4,91 N), 1 kG (F=9,81 N), 1,5 kG (F=14,72 N). The sliding distance (wear distance) was S=300m, and test time was t=500s. Fig. 2 demonstrate of ball-on-disc system.

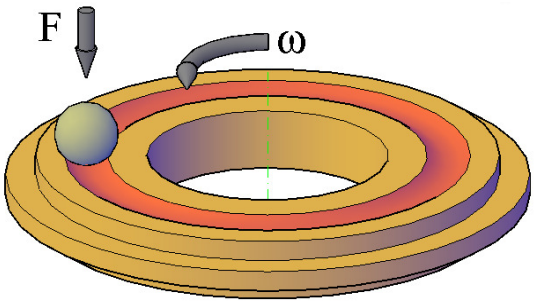

Fig. 2. Schema of ball-on-disc system.

Change in friction force as a function of time was recorded during the test. Based on the collected data, the friction coefficient was calculated. Wear intensity has been examined according to individual loads.

3.1. Friction force investigation

The frictional force is a form of motion resistance. Occurs between surfaces of two bodies which are in direct contact. The value of the friction force depends on the nature of contacting surfaces and the clamping force of one body to another. Friction force measurement is the basic tribological research. There is opportunity to determine surface properties according to obtained results.

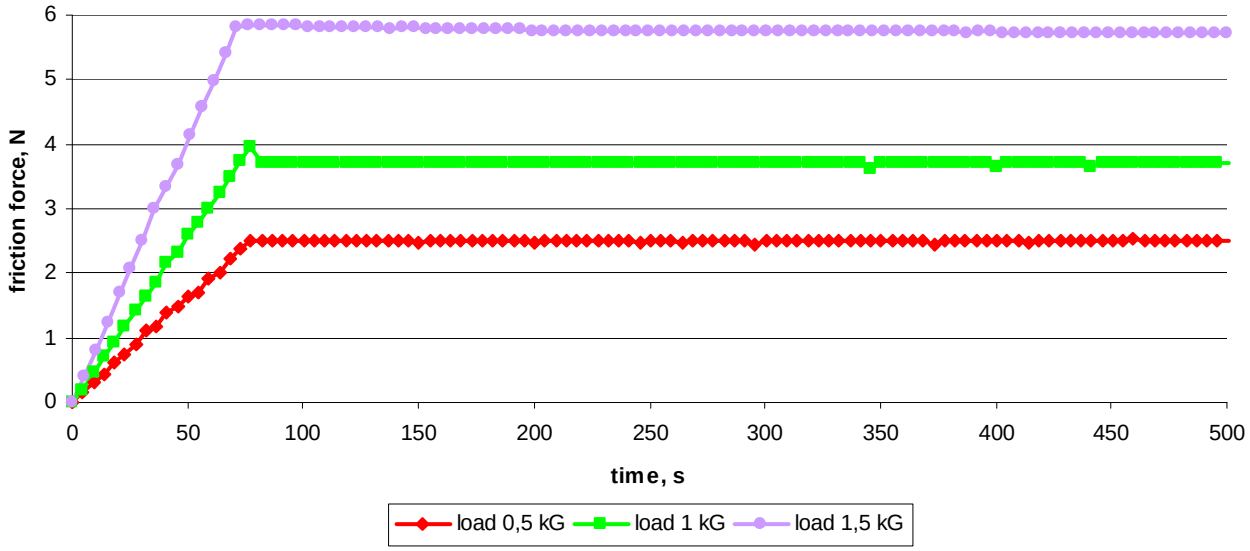

Fig. 3. Friction force measurement results under different load values for bronze B6 surface.

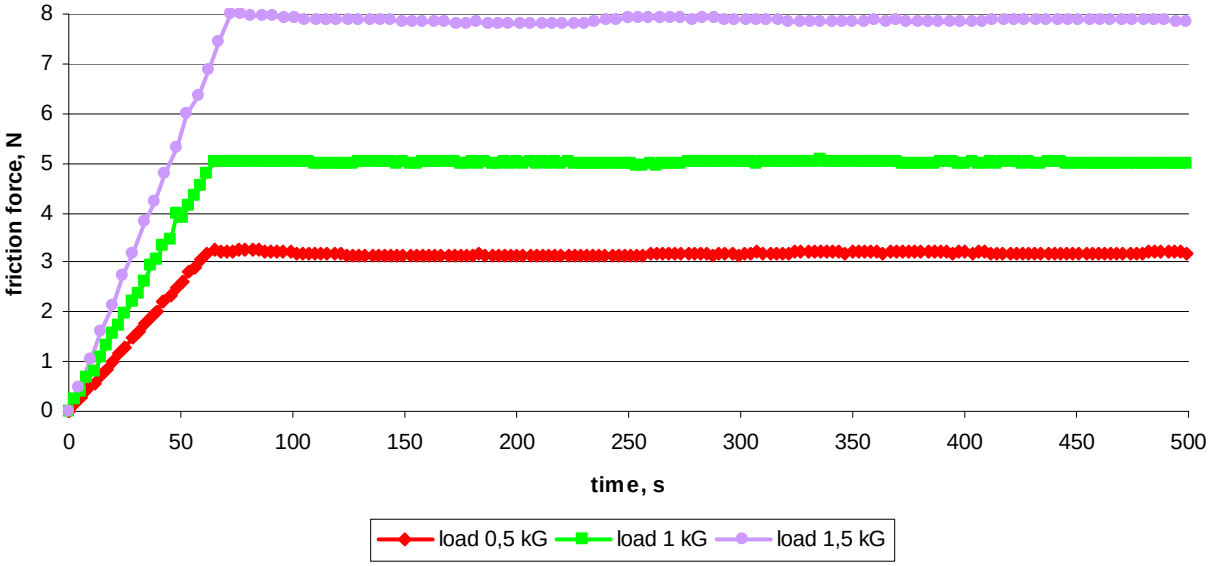

Fig. 4. Friction force measurement results under different load values for Al_2O_3 ceramic surface.

The change of friction force according to surface nature and load values are shown on charts from Fig. 3 and Fig. 4. There are two marked phases of engaged surfaces. First is the grind in phase since t=0s to approx. t=70s. Correct operation phase starts since approx. t=70s to the end of process. Friction force is the average value calculated according to results from second phase.

3.2. Friction factor determination

Friction factor is the ceoficient wchich characterize friction. For sliding friction this factor is evaluated by simple, good known formula:

$$\mu = \frac{T}{F}. \qquad (1)$$

where: μ – friction factor; T – friction force, N; F – load, N.

Evaluations of friction factor are collected in Tab. 1 and Tab. 2.

Bronze B6		
Load F, N	Average friction force T, N	Friction factor μ
4,91	2,50	0,51
9,81	3,70	0,38
14,72	5,77	0,39

Tab. 1. Friction factor for Bronze B6 surface.

Al_2O_3		
Load F, N	Average friction force T, N	Friction factor μ
4,91	3,16	0,64
9,81	5,01	0,51
14,72	7,86	0,53

Tab. 2. Friction factor for Al_2O_3 ceramic surface.

3.3. Wear intensity evaluation

Specimen weight loss during T01 test is the tribological property. Quantity weight loss estimate wear resistance of the element. Wear intensity gives opportunity to calculate this resistance. Wear intensity could be evaluate using formula:

$$I = \frac{m_1 - m_2}{SA}. \qquad (2)$$

where: m_1 – specimen mass before test, mg; m_2 – specimen mass after test, mg; $S=300m$ – sliding distance, A – specimen's cross-sectional area, m^2. Ball cross-section area is $A_b=31{,}2\ mm^2$, and disc cross-section area is: $A_d=358mm^2$. The results of calculations are summarized in Tab. 3 and Tab. 4.

Bronze B6				
	load, N	m_1, mg	m_2, mg	I, mg/m^3
Disc	4,91	44458,9	44253,6	$2{,}45\times10^{-4}$
	9,81	44452,1	43843,0	$7{,}27\times10^{-4}$
	14,72	44442,2	43229,3	$14{,}47\times10^{-4}$
Ball	4,91	1115,6	1114,4	$1{,}25\times10^{-7}$
	9,81	1115,9	1114,8	$1{,}14\times10^{-7}$
	14,72	1114,9	1113,1	$1{,}87\times10^{-7}$

Tab. 3. Wear intensity for Bronze B6 layer under different loads.

Al_2O_3				
	load, N	m_1, mg	m_2, mg	I, mg/m^3
Disc	4,91	47582,3	47566,1	$1{,}93\times10^{-5}$
	9,81	47563,3	47552,4	$1{,}30\times10^{-5}$
	14,72	47550,9	47529,2	$2{,}59\times10^{-5}$
Ball	4,91	1114,8	1092,8	$2{,}29\times10^{-6}$
	9,81	1115,1	1028,7	$8{,}99\times10^{-6}$
	14,72	1115,2	989,9	$13{,}00\times10^{-6}$

Tab. 4. Wear intensity for Al_2O_3 ceramic layer under different loads.

4. Conclusion

According to executed research and carried out calculations should be noted that B6 bronze coating has very good sliding properties. The friction factor for this layer is relatively low, 20% lower than friction factor of ceramic layer. This result could be expect because of good sliding properties of these alloys.

Bronze layer wear in relation to the ceramics layer is, however, ten times larger (wear intensity is about one order of magnitude higher for bronze). This is due to the fact that the ceramic layer has a higher hardness than the bronze layer. It means, that the greater wear of steel balls appear for ceramic layer.

To take advantage of the best properties of both layers, materials of cooperating pairs should be selected accordingly.

References

[1] KLIMPEL A. *Surfacing and thermal spraying*. Technologie WNT. 2000.

[2] KLIMPEL A., LISIECKI A., JANICKI D. *Mechanism of powder surfacing with the HPDL laser*. Przegląd Spawalnictwa, No 4, 2005, pp. 17-23.

[3] KLIMPEL A., DOBRZAŃSKI L.A., KIK T. *Mechanism of the laser surfacing process using wire*. Przegląd Spawalnictwa, No 4-5, 2005, pp. 24-31.

[4] NOWICKI B., PIERZYNOWSKI R., SPADŁO S. *The superficial layer of parts machined by brush electro-discharge mechanical machining (BEDMM)*, Proceedings of IME Part B-Journal of Engineering Manufacture, pp. 9-15, 2004

[5] PRZYBYŁOWICZ K. *Metaloznawstwo*. Warszawa WNT, 2003

[6] RADEK N., KONSTANTY J. *Cermet ESD coatings modified by laser treatment*, Archives of Metallurgy and Materials, pp. 665-670, 2012

[7] DIN-50324:1992-07. *Tribology; testing of friction and wear model test for sliding friction of solids (ball-on-disc system)*

TRANSCOM 2015, 22-24 June 2015
University of Žilina, Žilina, Slovak Republic

Possibilities of Laser Beam Using for Increasing the Fatigue Life of Welded Domex® Steel by Remelting the Weld Toe

[*]Ján Lago, [*]Otakar Bokůvka, [*]František Nový, [**]Peter Jančovič
[*] University of Žilina, Faculty of Mechanical Engineering, Department of materials engineering, Univerzitná 8215/1, 010 26 Žilina.
[**]Research Centre of University of Žilina, Univerzitná 8215/1, 010 26 Žilina

Abstract. This work deals with possibilities of using laser beam for increasing the fatigue life of welds. The Domex® 700 was used as the experimental material. The weld joint was created from two identical Domex® 700 plates. For experimental work the double V weld shape has been chosen. The welding was carried out by the MAG welding with CO_2 protective atmosphere. The solid state pulse Nd-YAG laser was used for the remelting process. The experimental work is focused on the weld toe shape after the remelting process. The incurred microstructures after the remelting process were studied the metallographic analyses. The conclusions of this work were discussed with respect to works based on the TIG dressing technology.

Keywords: Domex®, weld toe, fatigue, laser beam remelting.

1. Introduction

A Domex® is the SSAB company trademark for advanced high strength steels. The high strength of Domex® steels is ensured via the extra fine grain structure. Thanks to this structure, the Domex® steels have got higher yield strength compared to conventional steels. The Domex® steels are widely used in automotive industry, lifting equipment, trains etc. The main purpose of Domex® steels usage is saving the weight of construction (up to 40%), with keeping the same durability. The Domex® steels are also very suitable for welded constructions, which is the main field of application for this steel [1].

A weld joint is one of the most dangerous parts of a construction. A weld in construction is a local cross-section change. It is also the location of highly nonhomogeneous structure. It means that the weld is the place with the greatest probability for the initiation and propagation of the fatigue crack. The area where the crack initiation is expected is defined as a weld toe. The greatest concentration of stress is in the weld toe. It is also the location of a weld fusion zone [2, 3]. This facts decrease the fatigue life of a construction. There are several possibilities for the weld toe improvement which increase the weld joint fatigue life. The first category uses beneficial effect of compressive residual stresses at the weld hot spot (shot peening, needle peening, initial overloading etc.). The second category improve the shape of weld toe (TIG dressing, plasma dressing, burr grinding, etc.) by increasing the corner radius [4, 5].

This work deals with the possibilities of using a laser beam for the weld toe improvement. About this topic are available only limited literary sources [6]. For the weld toe remelting is used the pulse Nd-YAG laser device. The work is focused on the weld toe shape after the remelting process. It has been found out that weld toe radius is one of primary geometrical feature that controls the fatigue life. By increasing the weld toe radius the fatigue strength will probably increase due to a decrease in stress concentration at the weld toe [7]. The work discuss the conclusions with other works where TIG dressing was carried out with similar purpose [4, 5, 7]. Very important information about the incurred structures brings out the metallographic analysis realized on weld toe cross-section.

2. Experimental material

The Domex® 700 was used as an experimental material. Chemical composition and mechanical properties according to the SAAB manufacturer standard are provided in Tab.1. and Tab.2 respectively.

C % max	Si % max	Mn % max	P % max	S % max	Al % min	Nb % max	V % max	Ti % max
0.12	0.10	2.10	0.025	0.010	0.015	0.09	0.20	0.15

Tab.1. Chemical composition of Domex® 700 (wt. %)

Yield strength R_{eH} N/mm^2 min	Tensile strength R_m N/mm^2 min - max	Elongation on failure < 3 mm A80 % min	Elongation on failure > 3 mm A5 % min
700	750 - 950	10	12

Tab.2. Mechanical properties of Domex® 700

The weld joint was manufactured from two identical plates with 10 mm thickness, with weld shape as double V with 60° angle. Welding was carried out by the MAG welding method with CO_2 protective atmosphere. The OK AristoRod 69 wire with 1 mm in diameter was used as filler material. Weld wire chemical composition and mechanical properties according to manufacturer standard are provided in Tab.3. and Tab.4 respectively.

C %	Si %	Mn %	Mo %	Cr %	Ni %	V %
0.08	0.60	1.60	0.25	0.30	1.40	0.07

Tab.3. Chemical composition of OK AristoRod 69 weld (wt. %)

Yield strength R_{eH} N/mm^2	Tensile strength R_m N/mm^2	A_5 %	KV (J)/°C		
			+20	-20	-30
730	800	19	100	70	60

Tab.4. Chemical contend of OK AristoRod 69 weld

3. Experimental work

The Nd-YAG laser ALM 200 digital was used for the weld toe improvement. The German company Alpha Laser GmbH is the manufacturer of ALM 200 digital. The ALM 200 digital is the laser welding device with 1024 ηm wavelength. This device is working in the pulse mode, with maximal pulses frequency up to 20 Hz. The effective maximal laser output power is 200 W. For the experiment purpose was used 10 Hz pulse frequency. The laser beam impact zone diameter was 1.6 mm. It has been chosen 33.1 J energy output, according to the previous experimental works [8, 9]. It has been chosen 100° deflection angle between the vertical axis of laser head and the vertical axis of the weld. The 99.8% Argon gas, directly supplying to the remelting zone, was used as a protective atmosphere.

4. Results

The result before and after laser remelting can be observed on metallographic crosscut in Fig.2. On the right side of Fig. 2.(1) can be observed the base Domex® 700 material, which was not affected by laser beam. The weld toe with 0.6 mm radius Fig. 2.(5) was remelted to the shape of 1.3 mm radius. Overall width of affected area, Fig.2.(4), is 1.8 mm. The maximal depth of influence reaches 0.45 mm. It can be observed that the size of laser beam impact zone is large enough for creating the sufficient remelting zone and covers all HAZ Fig. 2.(2) and the part of the weld.

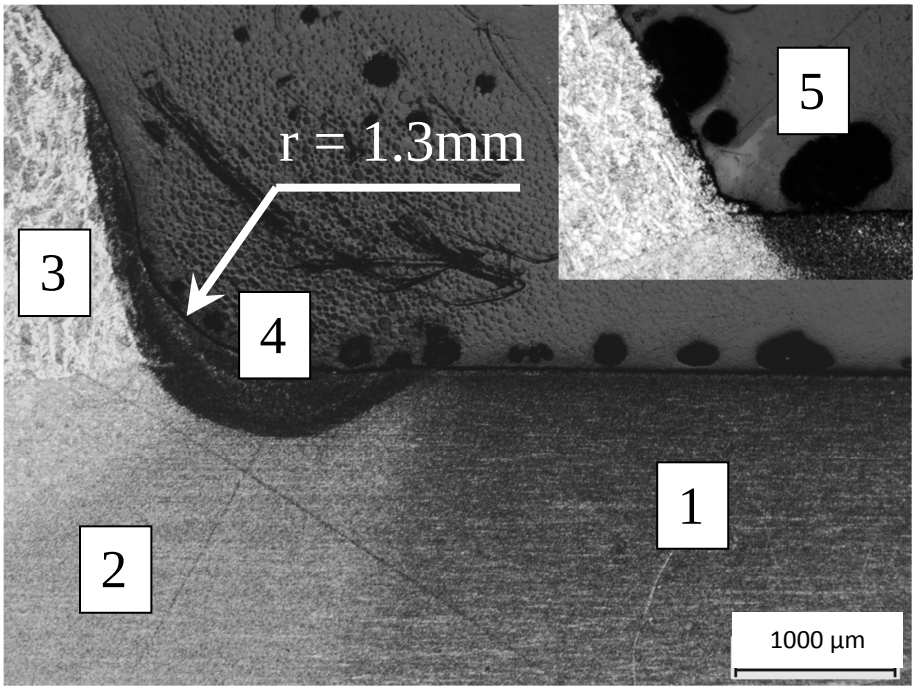

Fig.2. Weld joint after the toe treatment; metalographical crosscut; etch. Nital 2 %.

Fig. 3.(2) shows the detail of gradual coarsening of the ferrite grains in the HAZ. This coarsening is caused by the thermal cycle from the welding process. The originally polyedric ferrite grains in approximately 200 µm width area have been transformed to the acicular ferrite, Fig. 3.(W). This structure can be identified as a Widmannstetter structure. The weld, Fig. 3.(3), is created by standard casting structure with the dendrite creation in the way of heat dissipation. The detail state of the structure after the laser remelting process can be seen in Fig. 3.(4). It can be observed that all structures mentioned above have been transformed. The originally nonhomogeneous structures have become more homogenous after the remelting process. The metallographic analyses and hardness measurements have identified this structure as very fine bainite.

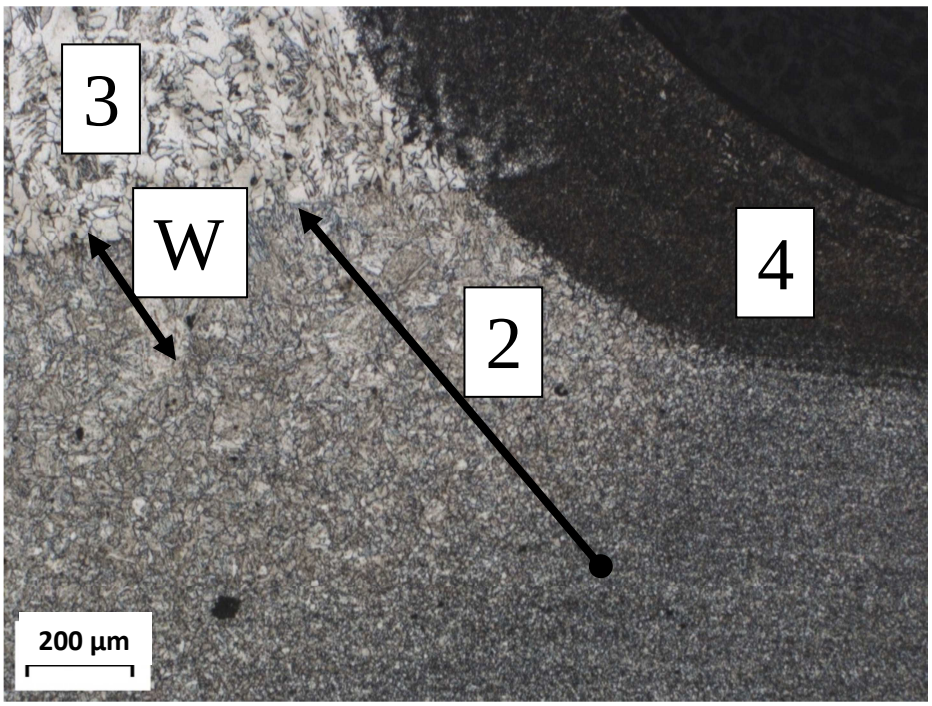

Fig.3. Remelted zone; metalographical crosscut; etch. Nital 2 %.

5. Conclusions

According to experimental works carried out on weld toe of Domex® 700 steel, remelted by laser beam can be concluded:

- Remelting process has created the better shape of the weld toe.
- Remelting process has created the fine bainite structure.
- Remelting process has increased the weld toe radius from original 0.6 mm to 1.3 mm (116 % increase).
- According to the work [7] conclusion: „A change in residual stress for about 15 % at the 300 MPa stress level had the same effect on fatigue strength as the increase of the weld toe radius by approximately 85 % from 1.4 mm to 2.6 mm.", it is necessary to make the similar experiment to test the impact of this technology on fatigue life.
- According to conclusions of other works based on the TIG dressing, [4, 5], it can be concluded that this technology has a big potential for increasing of weld fatigue strength.

Acknowledgement

The research was supported by European regional development fund and Slovak state budget by the project "Research Centre of University of Žilina", ITMS 26220220183 (90 %) and Scientific Grant Agency of the Ministry of Education, Science and Sports of the Slovak Republic and Slovak Academy of Sciences, grant No.: 1/0123/15 (10 %).

References

[1] SSAB, *http://www.ssab.com/en/Brands/Domex/Solutions1/ (10.4.2015)*
[2] LACROIX, R., KERMOUCHE, G., LENS, A., BERGHEAU, J. M., KLÖCKER, H. *Original test device for crack propagation in the weld nugget of advanced high strength steels.*, J. Engineering Fracture Mechanics
[3] ZHOU, B, THOULESS, M.D., WARD, S.M.. *Predicting the failure of ultrasonic spot welds by pull-out from sheet metal* : Int. J. Solids Struct, 43 (25–26) (2006), pp. 7482–7500
[4] HUO, L., WANG, D., ZHANG, Y. *Investigation of the fatigue behaviour of the welded joints treated by TIG dressing and ultrasonic peening under variable-amplitude load.*, International journal of fatigue.
[5] DAHLE T. *Design fatigue strength of TIG-dressed welded joints in high-strength steels subjected to spectrum loading*., J. International journal of fatigue.
[6] GERRITSEN, CH., VANROSTENBERGHE, S., DORÉ, M., *Diode Laser Weld Toe Re-melting as a Means of Fatigue Strength Improvement in High Strength Steels.*, J. International journal of fatigue.
[7] HARATI, E., KARLSSON, L., SVENNSON, L., DALAEI, K., *The relative effects of residual stresses and weld toe geometry on fatigue life of weldments.*, J. International journal of fatigue.
[8] LAGO, J., BOKŮVKA, O., *Eliminácia Praskania Laserových Návarov Ocele X153CrMoV12 Predohrevom Základného Materiálu.*, SEMDOK 2015
[9] LAGO, J., MORAVEC, J., *Laser welding of X153CrMoV12 tool steel with use of X45CrSi9-3 filler material., J. Technológ 2015*

TRANSCOM 2015, 22-24 June 2015
University of Žilina, Žilina, Slovak Republic

Optimization of Welding of the Truck's Rear Axle Semi-housing

[1]Vukić Lazić, [2]Dušan Arsić, [3]Ružica R. Nikolić, [4]Srbislav Aleksandrović,
[5]Milan Djordjević, [6]Branislav Hadzima
[1, 2, 3, 4, 5]University of Kragujevac, Faculty of Engineering, Sestre Janjić 6, 34000 Kragujevac, Serbia
[3, 6]University of Žilina, Research Center, Univerzitna 1, 010 26 Žilina, Slovakia
E-mails: [1]vlazic@kg.ac.rs; [2] dusan.arsic@fink.rs; [3] ruzicarnikolic@yahoo.com; [4]omdlab@kg.ac.rs;
[5]milan.djordjevic@fink.rs; [6] branislav.hadzima@rc.uniza.sk

Abstract. The welding technology of the truck's semi-housing is presented in this paper. Steels of different mechanical properties and chemical composition were tested and influence of welding on those base metals was monitored. Their weldability was first analyzed (semi-housing tube, ring and flange), then the welding procedure and filler metals were selected and finally the welding technological parameters were defined. The analytical (computational) methods, the TTT diagrams were applied for estimates of the base metals weldability, as well as the experimental methods based on hardness measurements in the weld's critical zones and analysis of their microstructure.

Keywords: Welding, truck, semi-hosing, cored wire, high strength steel.

1. Introduction

The semi-housing assembly with the ring and flange is manufactured by welding. All the necessary dimensions are being measured from the front of the smaller diameter of the semi-housing tube (Figure 1) [1]. The welding procedure assumes welding of a flange (3) (fillet joint 5×5) and then the ring (2) with the fillet weld of the same dimensions. After that the other side of the flange is welded by the fillet weld of dimensions 7×7 which is turned towards the ring. During the whole welding period positioning was done by the special tools. The positioner also has a role to prevent appearance of deformation on the assembly.

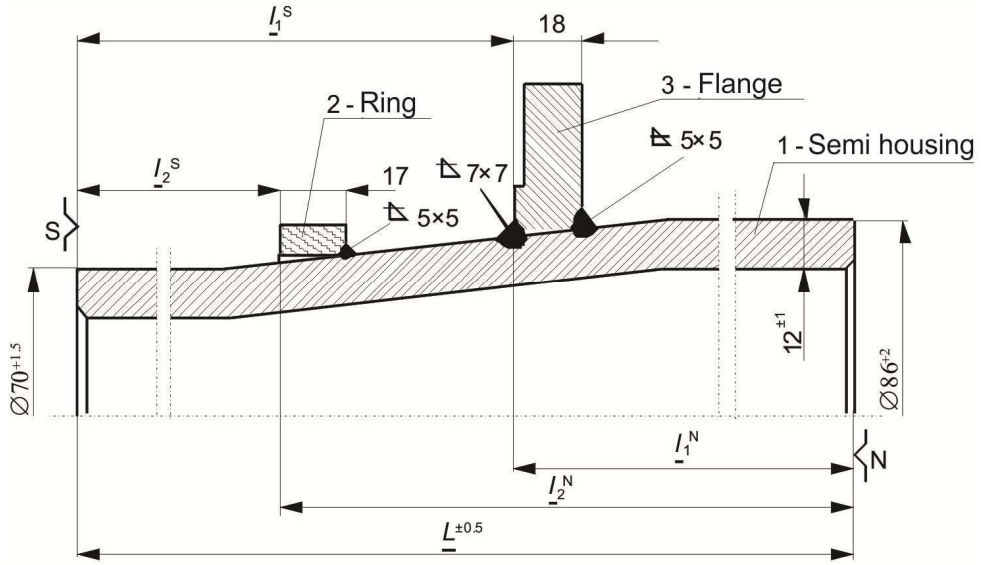

Fig. 1. Semi-housing assembly with the ring and the flange

2. Base and filler metals

In the selection of the welding procedure, the filler metal, welding parameters and protective gas, one starts from the chemical composition and thickness of the base metal (BM) and from its mechanical properties. One must primarily take into account all the requirements defined by construction drawing, which are related to required geometry and especially emphasized safety measures. Chemical composition of the steel, according to standard and analyzed in laboratory conditions is given in Table 1, while in Table 2 are presented mechanical properties, thickness and microstructure of the base metal [1, 6, 7].

Mark	Standard	Requirement	Chemical elements content, %									
			C	Mn	Si	P	S	Cr	Cu	Mo	Al	N
25MnCr6	UNI 6403 IVECO-52541	Prescribed	0.20 - 0.28	1.20 - 1.70	0.15 - 0.35	max 0.035	0.020 - 0.040	0.30 - 0.60	max 0.30	-	0.020 - 0.050	-
		Analyzed	0.26	1.28	0.15	0.012	0.020	0.40	-	-	-	-
25MnCr6	UNI 6403 IVECO-52541	Prescribed	0.22 - 0.29	0.50 - 0.80	0.15 - 0.40	max 0.035	max 0.035	0.90 - 1.20	-	0.15 - 0.30	-	-
≈ Č 4730	SRPS EN 10083-1:2011	Analyzed	0.27	0.71	0.26	0.033	0.027	1.13	-	0.21	-	-
FE 510	IVECO-52891	Prescribed	max 0.22	max 1.70	max 0.60	max 0.050	max 0.050	-	-	-	min 0.020	0.009
≈ Č 0561	SRPS EN 10025-1:2011	Analyzed	0.15	1.17	0.18	0.013	0.020	-	-	-	0.022	-

Tab. 1. Chemical composition of the base metal.

Mark	Thickness, s, *mm*	R_m, *MPa*	$R_{p0.2}$, *MPa*	A_5, %	HV	Microstructure
25MnCr6	10	875	640	14	172	Interphase tempering structure (predominantly sorbite)
(25MnCr6) ≈ Č4730	13	980	700	11	252	Interphase tempering structure (predominantly sorbite)
(FE510) ≈ Č0561	12	565	185	27	170	Lamellar ferrite-pearlite microstructure

Tab. 2. Mechanical properties of the base metal, thickness and microstructure.

Two versions are proposed for welding of the considered assembly:

1. Welding in the protective gas atmosphere with application of the cored wire VAC 60, of diameter Ø1.6 *mm* and

2. Welding with the cored wire with and without preheating with wire FLUXOFIL 42, of diameter Ø1.2 *mm*.

In table 3 are given the chemical compositions of the used wires, protective gas composition and mechanical properties of the pure weld metal [1]. By executing numerous test welds it was established that the best results are achieved by application of gas mixture of argon and carbon-dioxide in ratio $Ar/CO_2 = 80/20$ [1, 4].

3. Estimate of the base metals weldability

The semi-housing tube (position 1 in Figure 1) is made of low alloyed steel very sensitive to welding. According to computational methods for estimate of this steel's weldability, the steel should be preheated and the dried and clean welding wires should be used. Based on the corresponding

continuous cooling diagram (CCT) one can determine the cooling time between 800°C and 500°C ($t_{8/5}$), i.e., the output properties of the joint, by the adequate selection of the welding regime or the preheating temperature, [3]. In Figures 2 and 3 are presented the CCT diagrams for the two used steels.

Wire type	Chemical composition, %						Gas mixture Ar/CO_2, %	Mechanical properties of the weld metal			
	C	Si	Mn	Cr	Ni	Mo		R_m, *MPa*	R_{eH}, *MPa*	A_5, %	KV, *J*
VAC 60 cored	0.1	0.9	1.5	-	-	-	80/20	510-590	410- 490	22-30	80-125
FLUXOFIL 42 cored	0.05	0.35	1.3	0.4	2.4	0.4		730- 830	670-720	16-20	80-120

Tab. 3. Chemical composition of wires, protective gas type and mechanical properties of the pure weld metal.

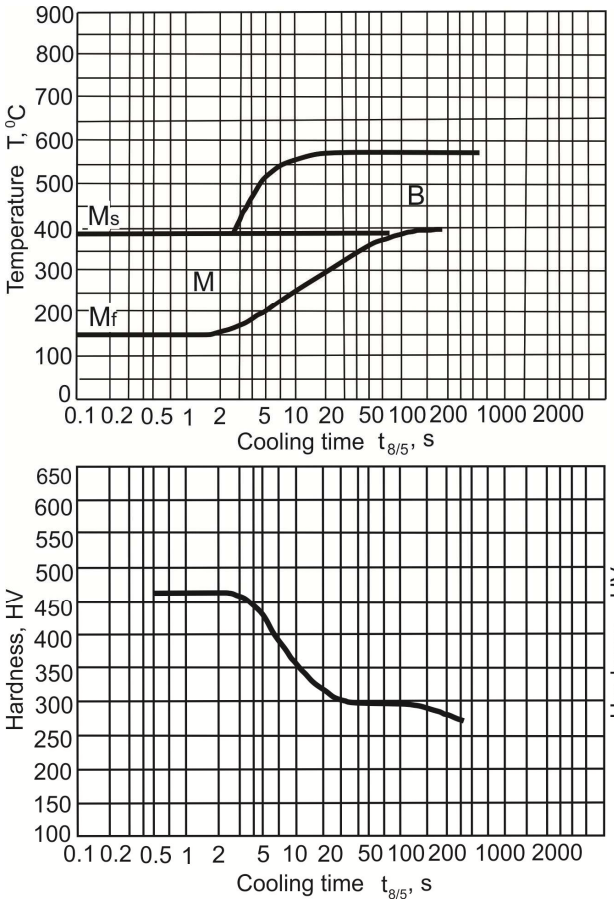

Fig. 2. KH diagram for steel 25MnCr6.

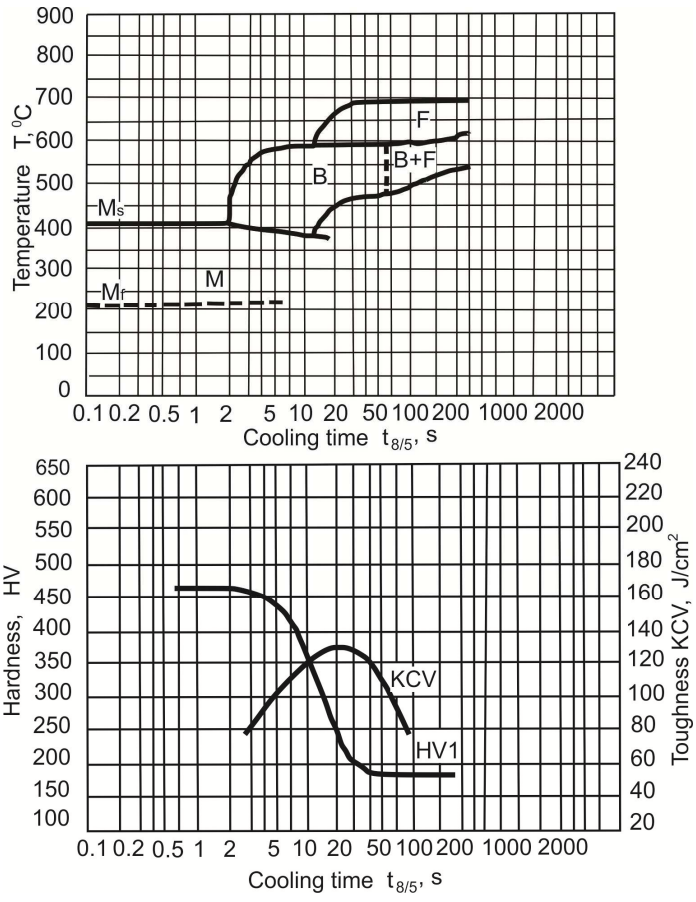

Fig. 3. KH diagram for steel FE 510.

The flange (position 3 in Figure 1) is being made of the C-Mn high strength steel, whose weldability is estimated based on the equivalent carbon formula (CE) and base metal thickness (s). Considering that in this case CE < 0.45 and s < 25 *mm*, it is assumed that this steel is well weldable and that it is not prone to appearance of cold cracks, namely the transitional brittleness. This is supported by the fact that measured hardness in the heat affected zone (HAZ) is less than 350HV. By adequate selection of the welding regime one can achieve the optimal toughness, as well.

By analyzing the CCT diagrams one can conclude that in both steels martensite appears for all the cooling times less than 3 seconds what points to necessity for the cooling time to be longer. In this case, the cooling time was controlled by the heat input, i.e., via the welding parameters – the driving energy and the welding speed.

4. Basic welding parameters

Welding parameters were adopted based on the corresponding computational methods and recommendations for selection of parameters for welding in the protective atmosphere of CO_2 (Table 4). Some earlier results were used in selecting the welding parameters [1, 2, 4, 5]. The prescribed welding parameters must be tested on several samples to establish whether the satisfactory properties of welded joints were obtained.

Weld dimensions	Basic welding parameters by the CO_2 procedure					q_l	a	δ_1, (δ_1',δ_1'')	δ_2, (δ_2',δ_2'')
Weld	I, *A*	U, *V*	v_z, *mm/s*	v_t, *m/min*	Q, *l/min*	J/*mm*	*mm*	*mm*	*mm*
5×5 Tube-ring	260-300	28-30	7.22-7.78	4.2-5.3	16-18	850-1000	6.2	2.2	3.2
5×5 Tube-flange	260-300	28-30	8.05-8.61	4.2-5.3	16-18	850-1000	6.8	6.8	3.2
7×7 Tube flange	300-350	30-32	5.5-6.1	5.3-7.2	18-20	1400-1800	8.0	3.8	2.8

Tab. 4. Basic welding parameters and penetration depth [1]

5. Results of hardness measurements and micro structure investigation

Measurements of hardness were done on specially prepared samples on the ZWICK 3812 device with indentation force of 3 N (0.3 daN). Hardness was measured only on samples welded by the full wire. In diagrams in Figures 4 and 5 are presented results of hardness measurements for joints tube-ring (5×5) and tube-flange (5×5), respectively executed by the full wire. The microstructure of the executed welded joints is given in figures 6 and 7, as well and the joints' characteristic zones are emphasized. On samples executed by the cored wire the hardness values were similar.

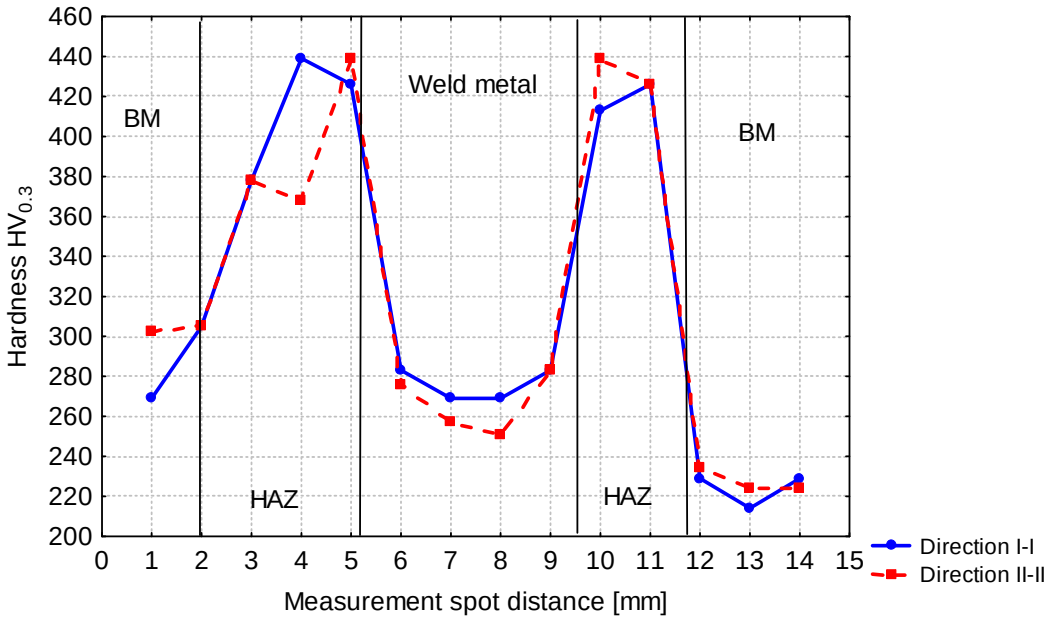

Fig. 4. Hardness distribution semi-housing tube – ring (5×5).

6. Conclusion

The truck's rear axle, as one of the most important assemblies on a vehicle requires not only prescribing the optimal welding technology for the parts of the assembly, but also that the obtained mechanical characteristics of joints and the microstructure be experimentally checked on the test samples. During the hardness measurements of the welded samples, certain zones with somewhat increased hardness were noticed, but that could be tolerated in the case when the prescribed welding technology is strictly obeyed.

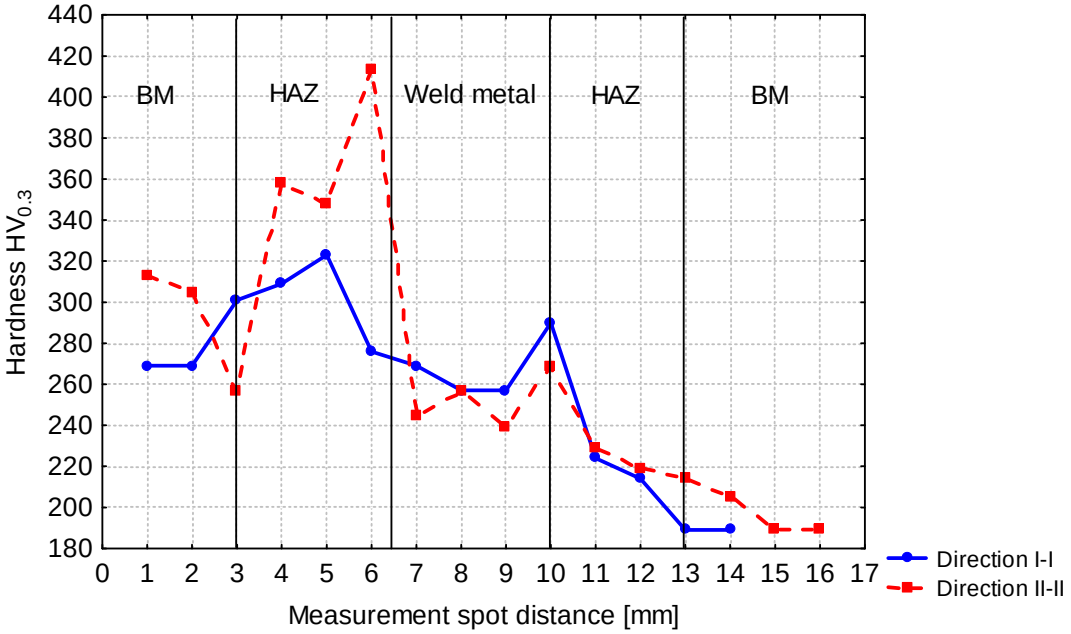

Fig. 5. Hardness distribution semi-housing tube – flange (5×5).

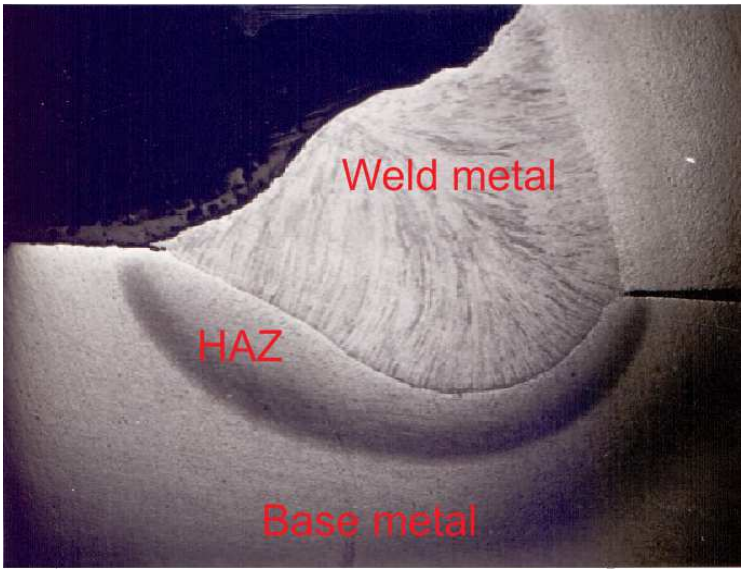

Fig. 6. Microstructure of executed welded joint

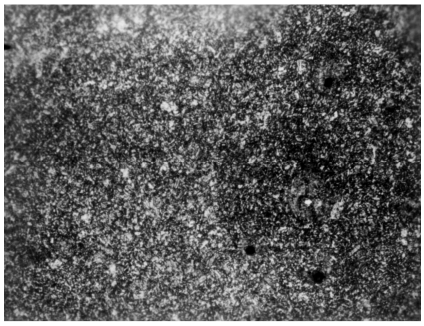

BM – tube – Interphase tempering structure – predominantly sorbite

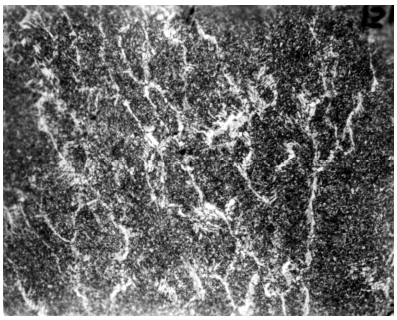

Weld metal – Vidmanstetten structure

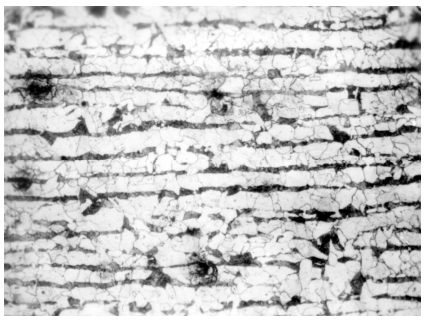

BM – flange- - Lamellar ferrite-pearilte microstructure

Fig. 7. Microstructure of individual zones of the assembly

Zones with traces of quenching structures were discovered by metallographic investigations and by measuring the hardness on the test samples. The appearance of zones with increased hardness can also be tolerated when the content of the diffused hydrogen in the weld and in the HAZ is reduced to a minimum (< 5 ml/100g of the weld metal). That is achieved by preheating, control of the content and flow of the protective gasses mixture, welding in the room without draft, maintaining the technological parameters, position of the gun during the welding, application of the clean and dry filler metals, as well as by preparation of the prescribed clean and dry groove and its vicinity.

Acknowledgement

This research was partially financially supported by European regional development fund and Slovak state budget by the project "Research Center of the University of Žilina" - ITMS 26220220183 and by the Ministry of Education, Science and Technological Development of Republic of Serbia through grants: ON174004, TR32036, TR35024 and TR33015.

References

1. LAZIĆ, V., JOVANOVIĆ, M., ADAMOVIĆ, D., RATKOVIĆ, N., *Improvement of the welding procedure of the fire truck rear axle semi housing assembly*, Mobility and Vehicle Mechanics, Vol. 30, No. 1, pp. 45-57, 2004.
2. LAZIĆ, V., JOSIFOVIĆ, D., ADAMOVIĆ, D., JOVANOVIĆ, M., *Design and application of apparatus for welding the truck body assembly in the protective gasses atmosphere*, Euromat '97, Maastricht, Nederland, 1997.
3. LAZIĆ, V., SEDMAK, A., ŽIVKOVIĆ, M., ALEKSANDROVIĆ, S., ČUKIĆ, R., JOVIČIĆ, R., IVANOVIĆ, I., Theoretical-experimental determining of cooling time ($t_{8/5}$) in hard facing of steels for forging dies, Thermal science, Vol. 14, No. 1, pp. 235-246, 2010.
4. ARSIĆ, D., LAZIĆ, V., ALEKSANDROVIĆ, S., MILOSAVLJEVIĆ, D., KRSTIĆ, B., MARINKOVIĆ, P., DJORDJEVIĆ, M., *Application of high strength steels to responsible welded structures on motor vehicles*, Mobility & vehicles mechanics, Vol. 40, No. 4, pp. 79-88, 2014.
5. ARSIĆ, D., LAZIĆ, V., NIKOLIĆ, R., ALEKSANDROVIĆ, S., HADZIMA, B., DJORDJEVIĆ, M., *Optimal welding technology of high strength steel S690QL*, Materials Engineering - Materiálové inžinierstvo, Vol. 22, No. 1, pp. 33-47, 2015.
6. SRPS EN 10083-1:2011, Steels for quenching and tempering - Part 1: General technical delivery conditions.
7. SRPS EN 10025-1:2011, Hot rolled products of structural steels - Part 3: Technical delivery conditions for normalized/normalized rolled weldable fine grain structural steels.

TRANSCOM 2015, 22-24 June 2015
University of Žilina, Žilina, Slovak Republic

Electrochemical Characteristics of Aluminum Brass

[*]Martin Lovíšek, [*]Tatiana Liptáková
[*]University of Žilina, Faculty of Mechanical Engineering, Department of Materials Engineering, Univerzitná 1, 010 26 Žilina, Slovak Republic

Abstract. Copper alloys are often used in energetic industry in cooling systems for their good corrosion resistance. But in operating conditions the life time of the same type of brasses is different. In this paper corrosion behavior of four types of Al brasses of various producers is studies. The differences of the investigated the Al brasses are observed in chemical composition and structure too. Corrosion properties were examined by potentiodynamic polarization technique in clean synthetic seawater.

Keywords: Aluminum brass, corrosion behavior, electrochemical characteristics

1. Introduction

Copper alloy tube and pipes, such as Al-brass 90-10 Cu-Ni and others are widely used in tubular heat exchangers and piping systems. The medium flowing through the tubes is in general seawater, brackish water or fresh water [1, 2]. Copper alloys are commonly used in condensers and heat exchangers due to their high thermal conductivity, mechanical workability, high corrosion resistance and relatively low cost [3, 4]. In heat exchangers the brasses are exposed not only in various water solution but they are working at elevated temperature, usually in the range from 40 to 80°C. The liquid cooling medium is flowing about 0.5 - 2 $m.s^{-1}$ [5, 6]. All mentioned factors affect reliability and lifetime of cooling systems. The purpose of the work is to fallow factors (chemical composition of brasses and cooling liquid medium, structure and selected mechanical properties of the brasses, effect of flow rate, corrosion behavior tested by several corrosion tests) influencing degradation processes [7, 8]. This paper brings first results of corrosion properties measured by potentiodynamic polarization [9].

2. Experimental material

The experimental specimens are made of four aluminum brasses CuZn20Al2As made by different producers and they are shown in Fig 1.The experimental material is in pipe shape with outer diameter 22 mm and wall thickness 1 mm.

Fig.1 The investigated aluminum brasses

Chemical composition of them is shown in Tab. 1 and as it can be seen some little disparities.

specimen	Content of elements [wg.%]								
	Zn	Al	As	Sn	Mn	Pb	Fe	Ni	Cu
M1	22.49	2.11	0.018	0.0038	<0.001	0.0097	0.0177	<0.001	75.2139
M2	23.43	2.06	0.0205	0.0225	0.0052	0.0165	0.0530	0.0492	74.0759
M3	22.65	2.10	0.0183	0.0017	<0.001	0.0052	0.0078	<0.001	75.0718
M4	22.07	2.06	0.0247	0.0143	0.0088	0.0098	0.0237	0.135	75.4696

Tab. 1 Chemical composition of the CuZn20Al2As brasses

Microstructure of the specimens M1 and M4 is formed by polyedric grains of solid solution of Zn, Al and additives in copper (grains of the solid solution λ). The twins created by plastic deformation and/or by heat treatment (annealing) during production were identified in the grains. Average grain size was determined by the quantitative metallography method in the Tab.2 (Jeffries method) [10]. In Fig. 2 it is possible to compare microstructure of the CuZn20Al2As brasses.

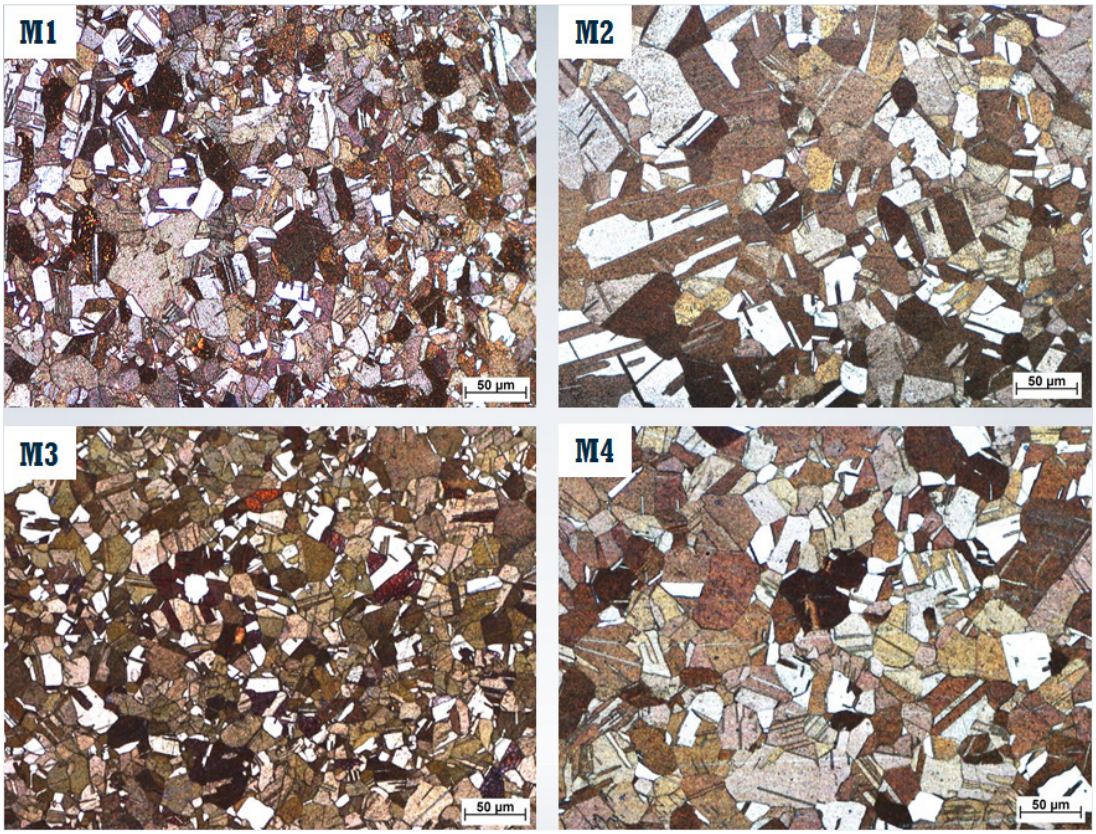

Fig. 2 Microstructure of the tested CuZn20Al2As brasses

Average grain size			
M1	M2	M3	M4
26 µm	42 µm	24 µm	38 µm

Tab. 2 Average grain size of the CuZn20Al2As brasses

3. Experiment and results

Potentiodynamic polarization investigation was carried out with a three-electrode system using a computer-controlled potentiostate/galvanostate VSP. Aluminum brasses (CuZn20Al2As) were used as working electrode (open surface 1cm^2), saturated calomel electrode (SCE) was used as a reference electrode and platinum electrode was used as a counter electrode. All experiments were performed at 25±1°C. Setting delay was 10 min. Potentiodynamic polarization measurements were made in the range -200 mV +400 mV vs. E_{oc} at the scan rate 1 mV/s.

Five specimens of all type brasses were evaluated by this experimental method and no difference in the frame work of one brass type was observed. In the Tab. 3 the representative values of electrochemical characteristics (corrosion potential; corrosion current density and corrosion rate determined using the Tafel extrapolation method) are introduced. The divergency can be seen in scale of corrosion potential which is the lowest for specimen M3 in spite of the fact that microstructure is quite homogenous and content of Cu is the highest of all tested brasses. According to the used experimental method the best corrosion properties were determined for specimen M1. Corrosion potential of the specimens M1, M2, M4 were similar, but the measured current density is for the specimen M1 the lowest and for the ones M2, M3, M4 comparable. Visually character of exposed areas was studied too, in specimens M1 only a few local traces of the white Zn corrosion products were seen. In the brasses M3 and M4 the surface was covered by light white corrosion products. The specimen M2 was attacked only locally but intensive. In Fig. 3 the course of polarization curves is shown.

Electrochemical characteristics / Specimen	E_{corr} [mV]	i_{corr} [µA/cm^2]	b_c [mV]	b_a [mV]	v_{corr} [mm/year]
M1	-47.662	0.086	102.7	39.5	0.001998
M2	-29.329	0.208	108.5	42.4	0.004834
M3	-145.486	0.206	84.6	35.1	0.004787
M4	-47.316	0.256	68.7	43.8	0.005949

Tab. 3 Corrosion characteristics of the tested aluminum brasses

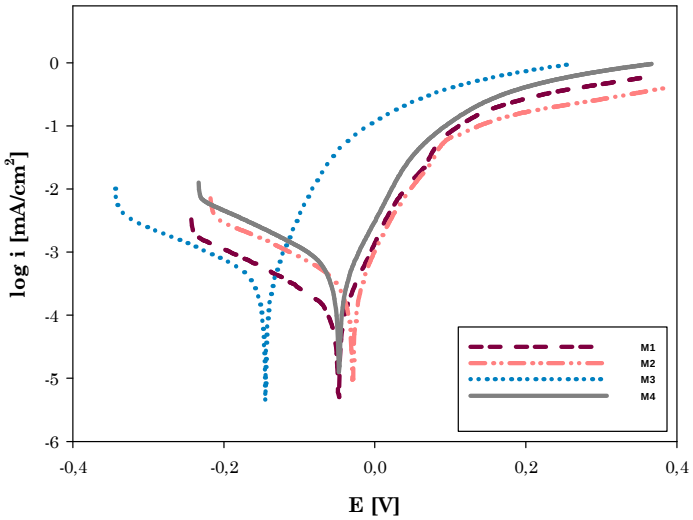

Fig. 3 Polarization curves of the tested aluminum brasses

4. Conclusions

- The first corrosion tests indicate corrosion behavior variances of the studied aluminum brasses. According to the determined corrosion characteristics it is not possible signify effect of chemical composition or microstructure. It is clear that the degradation processes are affected by many other factors (character of production, heat treatment, surface state etc.).
- The research will continue in study of corrosion behavior of the Al brasses in various environments (simulated work conditions), measuring of chosen mechanical properties and influence of flow on brass degradation. The integral of the dissertation work is design of the apparatus where the effect of different flow rate will be investigated.

Acknowledgement

The research is supported by European regional development fund and Slovak state budget by the project “Research center of University of Žilina”, ITMS 26220220183.

References

[1] CALLCUT, V. 2005. The brasses: properties & applications. Hemel Hepstead: CDA Publication, no. 117.

[2] SINHA, A. K. – Aspects of failure of condenser tubes and their remedial measures at power plants. AKS/Journal/2010

[3] TUTHILL, A.H. Guidelines for the use of copper alloys in seawater. Materials performance, vol. 26, september 1987

[4] CARVALHO, M. L.: Corrosion of copper alloys in natural seawater - Effects of hydrodynamics and pH. Dissertation, 2014.

[5] LANDOLT, D. – MISCHLER, S. – STEMP, S.: Electrochemical methods in tribocorrosion: a critical appraisal, Electrochim Acta 46, 2001, pp. 3913.

[6] LIPTÁKOVÁ,T. - FAJNOR, P. - DODEK, A.: Evaluation of the flow accelerated corrosion of copper pipes, In: Materials engineering = Materiálové inžinierstvo. - Roč. 17, č. 4, 2010, pp. 7.

[7] MCNEIL, L. S. – EDWARDS, M.: The importance of temperature in assesing iron pipe corrosion in water system distribution system, Environmental Monitoring an Assessment 77 (3), 2002, pp. 229.

[8] TAO, S. – LI, D. Y.: Investigation of corrosion- wear synergic attack on nanocrystalline Cu deposits, Wear 263, 2007, pp. 363.

[9] BABOIAN, R. ET AL.: Corrosion Test and Standards: Application and Interpretation, ASTM Manual Series, Philadelphia, PA 19103, USA 1995.

[10] FRIEL, J.J. 2000. Practical guide to image analysis. ASM International, 2000. 290 s. ISBN 978-0871706881.

TRANSCOM 2015, 22-24 June 2015
University of Žilina, Žilina, Slovak Republic

Review of Factors Affecting on the Accuracy Dimensionally-contoured Manufactured Items on Numerically Controlled Milling Machines

[*]Piotr Maj, [*]Edward Miko
[*]Kielce University of Technology, Faculty of Mechatronics and Mechanical Engineering, 25-314 Kielce, al. Tysiąclecia Państwa Polskiego 7, Poland, {pmaj, emiko}@tu.kielce.pl

Abstract. This article provides a summary discussion of the factors affecting the dimensional accuracy of the shaped objects made on CNC milling machines. These factors can be divided into several groups. The first group includes factors dependent on the workpiece. Another error is dependent on the cutting tools used during the cutting process. To the final group includes errors and inaccuracies resulting from the numerically controlled machine tool.

Keywords: CNC machine, precision dimensionally shaped, tools, workpiece errors, milling machines

1. Introduction

The continuous development of technology puts new demands related to the accuracy dimensionally-contoured manufactured items numerically controlled milling machines. To get the best accuracy objects should not be focus only on the validating machine operation, but also on the whole process. Errors man can make even during the course of the design process itself. Then there are also all the irregularities resulting from the preparation for the machining process. These can include errors resulting from the workpiece as well as the tools used for machining the material. Therefore, an important element is to check the entire machining system (machine tool, tool holder, workpiece, tool) that consists on the final object [2].

This article presents a summary and discussion of the factors affecting the dimensional accuracy of the shaped objects made on CNC milling machines. These factors can be divided into several groups. The first group includes factors dependent on the workpiece. Another error is dependent on the cutting tools used during the cutting process. To the final group includes errors and inaccuracies resulting from the numerically controlled machine tool.

2. Errors Associated with the Workpiece

There are many factors that make the error of the workpiece. They may result from the method of fixing the object as well as his measurement. Errors associated with the workpiece relate to methods of positioning and fixing of workpiece in the machine. There are many ways to fix an object: using a vise jaws (Fig. 1.), magnets and a special tool machining. Selection of the appropriate method is important because of the fact that the workpiece under different conditions is likely to vary keep. Workpieces can be taken out of the jaws of the vise with unfavorable processing, may also fall into the vibrations.

Vibration can result in: increased surface roughness, deterioration of accuracy dimensionally shaped, accelerate wear of machines and tools and to reduce the machining efficiency. Using the magnetic holder also carries some problems. Objects placed on a magnetic table can move due to the forces occurring during processing and also not all types of material can be attached in this type of holder. It should also pay attention to all the vices, jaws etc. are properly secured to the machine table. Wrongly fitted may fall into the unwanted resonance which can result in rupture of the handle of the machine table.

Fig. 1. Workpiece mounted in a vise.

Fig. 2. The workpiece settings by touch probe.

The workpiece may also be defined incorrectly in the machine. The basic errors occurring in this process step are database entry errors and machining errors to determine the dimensions of the object. These errors are incorrect interpretations indicated probes and probe damage. Figure 2 shows the orientation of the workpiece using the touch probe.

3. Errors Related with the Tool

For further factors affecting the accuracy of the dimensionally contoured objects manufactured on CNC machine tools are tools errors. Choosing the right tools for the machining process is an important element. Mismatched tool will not work well which will lead to the final accuracy of the object. Even a properly chosen tool does not guarantee the achievement of the objectives. It should be remembered mistakes of the tool itself. These can include incorrectly fitted cutting plates. Plate set incorrectly can be taken out of the tool, the tool and workpiece will be destroyed. Inserts consumption level translates to a thickness of cut during processing. It should also remember to select a suitable tool holder, which will be matched to the same tool and the cutting process. There are many types of luminaires and each depending on the machining process and chosen to keep the tools. As the workpiece cutting tool may also be wrong measured. There are many types of probes and types of measurement tools. Entered incorrectly tool dimensions translate into accurate dimensionally contoured objects.

4. Computer Numerical Control Machines Errors

Machine error can be called any difference between programmed movements of individual elements and movements carried out by the machine. It may be that a lot of reasons, external factors which affects the machine, the process of machining, assembly inaccuracy. All these factors influence the formation of errors. The most common include:

- Geometric errors
- Kinematic errors
- Thermal errors
- Errors of measurement systems
- Errors forced treatment processes
- Errors drives and controllers

An important element is appropriate to recognize the error in order to apply the correct test apparatus. General classification scheme divides it into two groups: systematic and random. Systematic errors can include geometric errors, kinematic, thermal [2]. These errors are machines which, as can easily be overcome provided quickly identify and rate of change. In addition to changes in the construction of the cause of the error can be control of machines. They can be caused

by slow processing of information by position machine sensors or an incorrect feed control. For geometric errors include errors of shape and mutual position of the surface [10].

a) b)

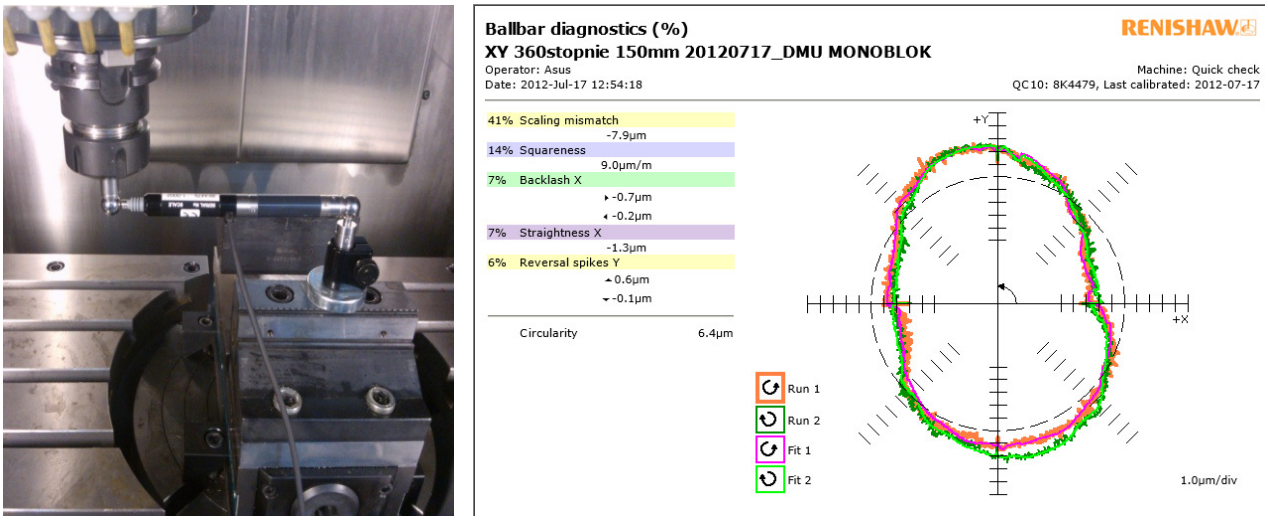

Fig. 3. Measurement of geometric errors b) Report of the machine geometric errors.

Figure 3a shows a method for measuring geometric errors of Computer numerical control machines using Ballbar QC10 device. Ballbar device is a kinematic ball wire, otherwise the telescopic linear position sensor at high accuracy. The system allows to record small changes in the radius of in the performance the machine tool programmed displacement circle [3]. In Figure 3b is shown a diagnostic measurement report of geometric machine errors. On the left side of the report is a list of the percentage impact of the five biggest errors that have a significant impact on the accuracy of the machine [6]. On the right side can be see way the report registered by the test equipment. Registered a shape other than a perfect circle indicates errors on the machine [7].

Kinematic errors relate to the movements of individual elements of the machine and in the case of high repeatability are allowing for easy compensation. The accuracy of the machine is also affected by temperature. The machine with the individual elements emits heat: engine, pumps, gears, bearings. Any increase in temperature causes expansion of the materials. The influence of external sources has also an impact on the same machine. Room temperature and humidity to a certain extent also affect the machine operation. Errors that occur during processing are associated with the drives. Servo drives operate mostly in the feedback loop and never react quickly enough to offset [1,4]. Another reason for the error is the same machining process. It causes the vibration (random errors) conditioned machining parameters.

a) b)

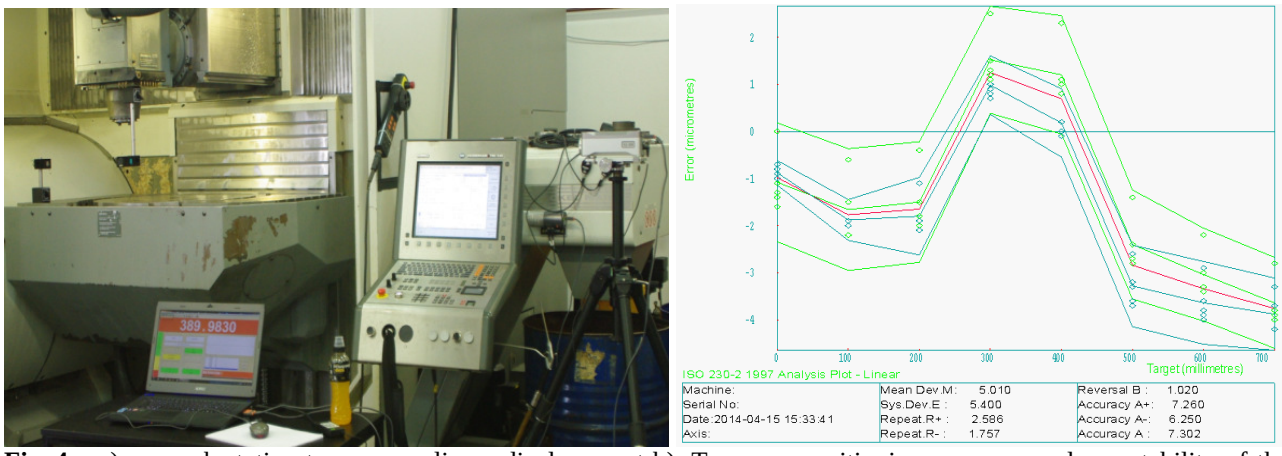

Fig. 4. a) research station to measure linear displacement b). Two-way positioning accuracy and repeatability of the X-axis CNC machine

In Figure 4a shows the method for measuring the CNC machine tool positioning accuracy with the use of a XL80 laser interferometer. Positioning accuracy test machines are intended to check the position of the individual parts and their mutual displacement [5].

Figure 4b shows a graph of the accuracy and repeatability of positioning of the X axis The generated report consists of two parts. The upper part shows a graph illustrating the positioning deviation in relation to the distance traveled by the test part of the machine. At the bottom of the graph is a table showing the numerical interpretation of the graph.

5. Conclusion

There are many factors affecting the dimensional accuracy of the final shaping of objects produced on CNC machines. These factors can be divided into several groups. The first group includes factors dependent on the workpiece. Another error is dependent on the cutting tools used during the cutting process. To the final group includes errors and inaccuracies resulting from the numerically controlled machine tool. The workpiece must be attached to the machine table. There are many ways and methods of attachment so the correct selection is important to reduce the vibrations that occur during processing. The tool should be properly matched to the type of treatment. Cutting plates and tool should be properly set. Errors resulting from machine may include errors: geometric, kinematic, and drives feeds errors and errors resulting from the machining process. Taking of frequent diagnosis of machine tools and making compensation minimize any inaccuracies resulting from their work. All of these errors influence on accuracy of the final dimensionally shaped objects are easy to diagnose. There are many methods of leveling and compensation which will result in increased accuracy of manufactured items.

References

[1] JANECKI D., CEDRO L.: *Determining of signal derivatives with the use of regressive differential filters in identification problems*, 12th International Carpathian Control Conference - ICCC, Republika Czeska, IEEE Catalog Number: CFP1142L-CDR, ISBN 978-1-61284-359-9, 2011 IEEE

[2] HONCZERENKO J., *Obrabiarki sterowane numerycznie*. W: WNT 2009

[3] *Laser measurement and ballbar diagnosis for motion system, XL-80 laser system, QC20-W wireless Ballbar system* Renishaw 2009

[4] BĄKOWSKI A., CIOSMAK J., DZIUBEK T., GRZYBEK D., HOLEWA K., IZWORSKI A., NAWROCKA A., RADZISZEWSKI L., TUREK P., WSZOŁEK W., *Wybrane zagadnienia analizy sygnałów, modelowania i sterowania w inżynierii mechanicznej i biomedycznej*, Monografie Katedry Automatyzacji Procesów AGH w Krakowie, Kraków 2014 ISBN: 978-83-64755-06-4

[5] MULLANY B., *Evaluation And Comparison Of The Different Standards Used To Define The Positional Accuracy And Repeatability Of Numerically Controlled Machining Center Axes*. University of North Carolina, Charlotte, October 2007

[6] POLSKA NORMA PN-ISO 230-4: *Badania okrągłości w obrabiarkach sterowanych numerycznie*. Marzec 1999

[7] *Renishaw Ballbar 20 System User Guide*, Renishaw 2009

[8] SZAFARCZYK M., CHRZANOWSKI J., Nowa koncepcja sprawdzania dokładności maszyn NC, materiały konferencyjne, AUTOMATION, Automatyzacja-Nowości i Perspektywy Warszawa 2005, s. 405-413

[9] www.en.dmgmori.com

[10] www.renishaw.com

TRANSCOM 2015, 22-24 June 2015
University of Žilina, Žilina, Slovak Republic

The Comparison of Surface Stereometry Using Hotelling T2 Test

[*]Włodzimierz Makieła, [*]Damian Gogolewski
[*]Kielce University of Technology, Department of Mechanical Engineering and Metrology,
Al. Tysiąclecia Państwa Polskiego 7, 25-314 Kielce
{wmakiela, dgogolewski}@tu.kielce.pl

Abstract. Comparative analysis of the surface layer of machine parts can be successfully carried out using statistical tests. The paper presents a method of comparing the surface stereometry using Hotelling's T2 test. It presents also the results of research carried out for the four types face milled steels. Steels used are: 40HM, C45, NC6 and WCL. For each type steel, it was machined four areas with the same machining parameters. Based on these results a decision was made, that the surfaces despite the same machining conditions significantly different from each other. The differences may be caused by machining errors.

Keywords: Surface roughness, Hotelling T2 test, face milling

1. Introduction

Measurement and analysis of the geometric structure of the surface is a very important step in the production process. It is not possible to obtain a homogeneous structure over the entire surface of the element. The surface layer is irregular, which may cause changes in the behavior of the mechanisms at work machine parts. There is therefore a need to monitor and assess the changes in the structure of the surface layer over the entire surface of the machine elements [3, 10]. Comparative analysis of the surface layer of machine parts can be successfully carried out using statistical tests. In the papers [1, 2] have been discussed statistical tests used for evaluating 2D profiles. There are: Pearson's correlation coefficient, Spearman correlation coefficient, method of paired comparison and the experimental method error. The authors recognize that it is appropriate to add Hotelling T2 test, which is used to assess the comparative stereometry two surfaces. The paper presents the principles of the method and procedure of comparing surface roughness, which consists in applying the Hotelling T2 test.

2. The Concept of Comparison the Surface Using Hotelling test

This test is a generalization of Student's t-statistics for the multidimensional space. The test compares the average value of the vectors in the two populations. The authors applied the test for the comparison of four 3D surface irregularities made by the same machining parameters. In the analysis, the coefficients describing the two selected surfaces are compared. Based on the results assessed that the surfaces are significantly different from each other.

It is important to consider the test assumptions. There are three assumptions underlying the Hotelling T2 test. The first is independence. The subjects from both populations are independently sampled. The next is normality. Both populations are multivariate normally distributed. The last is homogeneity of variance-covariance matrices [4,6,7]. This assumption may be assessed using Bartlett test. In this test the null hypothesis $H_0 : \Sigma_1 = \Sigma_2$ is tested against the alternative $H_1 : \Sigma_1 \neq \Sigma_2$. The Bartlett statistic is given by L and the statistic value is calculated using formula (1):

$$\mathrm{L} = c[(n_1 + n_2 - 2)\ln|S_p| - n_1 - 1)\ln|\Sigma_1| - (n_2 - 1)\ln|\Sigma_2|] \tag{1}$$

where

$$\mathrm{c} = 1 - \frac{2p^2 + 3p - 1}{6(p+1)}\left[\frac{1}{n_1 - 1} + \frac{1}{n_2 - 1} - \frac{1}{n_1 + n_2 - 2}\right] \tag{2}$$

$$\mathrm{S_p} = \frac{(n_1 - 1)\Sigma_1 - (n_2 - 1)\Sigma_2}{n_1 + n_2 - 2} \tag{3}$$

The calculated value of the statistics L is compared with the critical value χ^2 distribution on an assumed significance level α. The null hypothesis H_0 should be rejected if the resulting value is greater than the critical value.

$$L > \chi^2_{\frac{p(p+1)}{2},\alpha} \tag{4}$$

As a result of measurement of the surface layer was obtained a set of points distributed over the surface in the form of a regular grid of points (n_1 x p). The following procedure was carried out.

For each surface profile was calculated mean value.

$$\bar{x} = \frac{1}{n_1}\sum_{i=1}^{n_1} x_i \tag{5}$$

The next step is create variance-covariance matrix [5].

$$\Sigma_1 = \frac{1}{n_1 - 1}\sum_{i=1}^{n_1}(x_i - \bar{x})(x_i - \bar{x})^T = \frac{1}{n_1 - 1}\sum_{i=1}^{n_1}\left(\begin{pmatrix} x_1 - \bar{x} \\ x_2 - \bar{x} \\ \dots \\ x_{n1} - \bar{x} \end{pmatrix}(x_1 - \bar{x}, x_2 - \bar{x} \dots x_{n1} - \bar{x})\right) =$$
$$= \frac{1}{n_1 - 1}\sum_{i=1}^{n_1}\begin{pmatrix} (x_1 - \bar{x})^2 & (x_1 - \bar{x})(x_2 - \bar{x}) & \dots & (x_1 - \bar{x})(x_n - \bar{x}) \\ (x_2 - \bar{x})(x_1 - \bar{x}) & (x_2 - \bar{x})^2 & \dots & (x_2 - \bar{x})(x_n - \bar{x}) \\ \dots & \dots & \dots & \dots \\ (x_n - \bar{x})(x_1 - \bar{x}) & (x_n - \bar{x})(x_2 - \bar{x}) & \dots & (x_n - \bar{x})^2 \end{pmatrix} \tag{6}$$

Analogous calculation were performed for the second surface (n_2 x p).

$$\bar{y} = \frac{1}{n_2}\sum_{i=1}^{n_2} y_i \tag{7}$$

$$\Sigma_2 = \frac{1}{n_2 - 1}\sum_{i=1}^{n_2}(y_i - \bar{y})(y_i - \bar{y})^T \tag{8}$$

In case that the variance-covariance matrices are homogeneous Hotelling statistic is given by formula (9):

$$T^2 = (\bar{x} - \bar{y})^T V^{-1}(\bar{x} - \bar{y}) \tag{9}$$

where

$$V = \frac{\Sigma_1(n_1 - 1) + \Sigma_2(n_2 - 1)}{n_1 + n_2 - 2} \tag{10}$$

otherwise, must modify the V value

$$V = \frac{\Sigma_1}{n_1} + \frac{\Sigma_2}{n_2} \tag{11}$$

The final step is make decision that both surfaces are significantly different from each other. Hotelling statistics must be converted to Snedecor distribution using the formula (12):

$$F = \frac{n_1 + n_2 - p - 1}{p(n_1 + n_2 - 2)} T^2 \sim F_{p, n_1 + n_2 - p - 1} \tag{12}$$

The obtained value is compared with the critical value. When the calculated value is greater than the critical value at the significance level, should be noted that the surfaces are significantly different from each other [8,9].

$$F > F_{p, n_1 + n_2 - p - 1, \alpha} \tag{13}$$

3. The Results of Calculations

The analysis were performed for four types face milled steels. Each type of steel has been machined with the specified parameters:

-40HM steel (42CrMo4): cutting speed v_c = 300 m / min, axial depth of cut a_p = 0.2 mm, feed per tooth f_z = 0.16 mm / tooth,

-C45 steel: cutting speed v_c = 260 m / min, axial depth of cut a_p = 0.2 mm, feed per tooth f_z = 0.1 mm / tooth,

-NC6 steel: cutting speed v_c = 300 m / min, axial depth of cut a_p = 0.2 mm, feed per tooth f_z = 0.02 mm / tooth,

-WCL steel (X37CrMoV51): cutting speed v_c = 300 m / min, axial depth of cut a_p = 0.2 mm, feed per tooth f_z = 0.04 mm / tooth,

The surface was measured on the noncontact profilometer Talysurf CCI. In figures (1-4) is shown an isometric view of the surface.

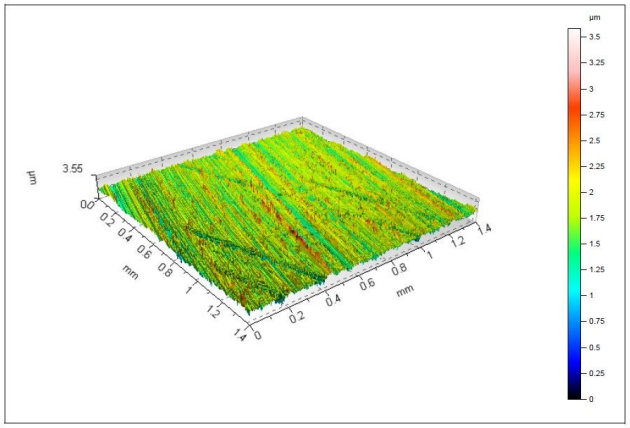

Fig. 1. The isometric view the surface - 40HM steel

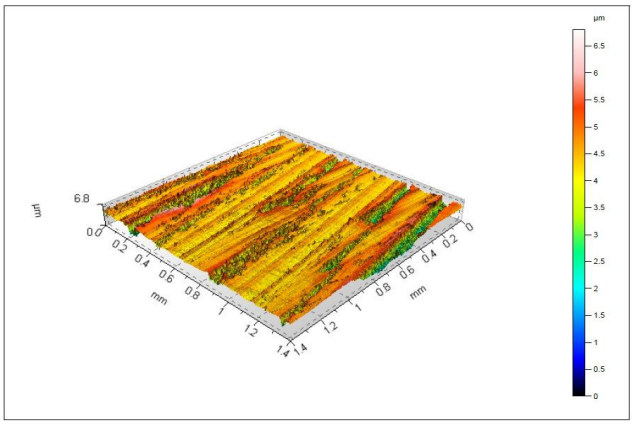

Fig. 2. The isometric view the surface - C45 steel

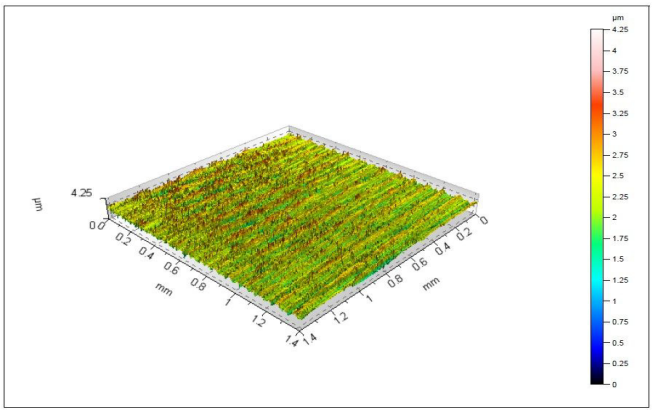

Fig. 3. The isometric view the surface - NC6 steel

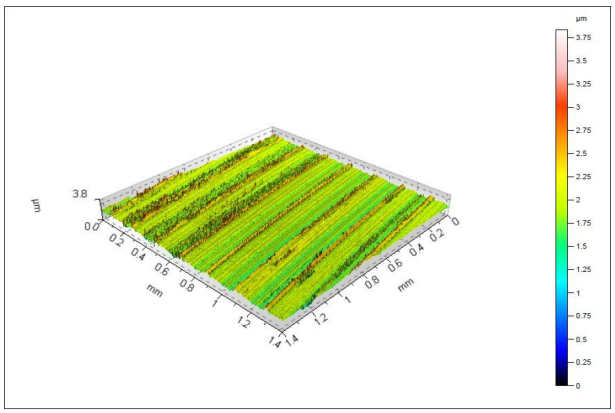

Fig. 4. The isometric view the surface - WCL steel

The calculations were performed in authorial computer procedures coded in MATLAB environment. The program by the appropriate procedures calculates the Hotelling statistics for the two surfaces.

In order to carry out Hotelling test, the measured surface was divided into four equal, independent areas. The obtained surfaces compared in pairs between each other. The results of calculations are summarized in Tables 1-4. The calculated values were compared with the critical value, with the significance level α=0,05, $F_{p,n_1+n_2-p-1,\alpha} = 1{,}1711$ according to the equation (13). On this basis, the decision was made to adopt or reject the hypothesis that the two surfaces are not significantly different from each other. The symbol "-" indicates that a pair of surface satisfies the condition (13). Otherwise, the table was placed the symbol "+".

1x2	1x3	1x4	2x3	2x4	3x4
0,108	0,2053	0,1983	0,163	0,2718	0,4145
+	+	+	+	+	+

Tab. 1. The results of calculations for 40HM steel

1x2	1x3	1x4	2x3	2x4	3x4
0,9258	1,1112	1,718	4,4183	0,9041	4,0249
+	+	-	-	+	-

Tab. 2. The results of calculations for C45 steel

1x2	1x3	1x4	2x3	2x4	3x4
2,1962	1,4516	6,5771	4,596	2,7028	1,5319
-	-	-	-	-	-

Tab. 3. The results of calculations for NC6 steel

1x2	1x3	1x4	2x3	2x4	3x4
3,2333	0,7775	0,1895	0,2869	1,1118	0,697
-	+	+	+	+	+

Tab. 4. The results of calculations for WCL steel

On the basis of the Hotelling T2 test results, at the assumed significance level should be noted that the machining parameters have a significant impact on the structure of the surface layer over the entire surface of the element. Table 1 shows the test results for 40HM steel. On the basis of the statistical tests, it was stated that the geometric structure of the surface at the measured area shows no significant difference between particular parts of surface. However, the test results for NC6 steel for each pair of significantly exceeded the critical value for the assumed significance level. According to Table 4, it must be inferred that the surface is significantly different across the element. This situation can be caused by badly selected machining parameters. The results of the calculations for the other two types of steel are presented in Table 2 and Table 4. After studying the tables should be noted that the geometric structure of surface WCL steel is characterized by high homogeneity. One pair of surfaces does not satisfy the condition (13). C45 steel reached high values of the test. These values exceed the critical value at a assumed significance level or they were a little smaller. For this kind of material and machining parameters, the test should repeated. It should be consider the larger number of surface area and their distribution over a whole element area.

4. Conclusions

Comparative analysis of the surface layer of machine parts can be successfully carried out using statistical tests. The concept of using statistical Hotelling T2 test is a new method for comparing two surfaces. The paper presents the principles on the use Hotelling test. The paper presents also the results of the possibility of adapting of this statistics in the metrology of the surface layer, for the four types of materials. For each material were determined four independent areas, which were then analyzed. Geometric structure of the surface was analyzed in pairs.

After analyzing the results it can be concluded that the best results were achieved for 40HM steel. There is no area, which is significantly different than other areas on the surface. The surface layer is homogeneous over the entire surface. Similar results were obtained for the WCL steel. Only one pair of surfaces does not satisfy the Hotelling test conditions at the assumed significance level. The C45 steel is the only material, whose the results do not satisfy the test conditions. The test results for each pair of significantly exceeded the critical value for the assumed significance level. It must be inferred that the surface is significantly different across the element. This situation can be caused by badly selected machining parameters.

Further research should be conducted during the process of wavelet analysis to determine the maximum level of approximation signal, without significant loss of character of the measured surface.

References

[1] ADAMCZAK S., KMIECIK-SOŁTYSIAK U. *The Concept Of The Method For The Comparison Of Pairs Of Roundness Profiles*. Mechanik Vol.8-9, pp 156-161, 2014 (in Polish)

[2] ADAMCZAK S., MAKIEŁA W. *The concept of statistical comparison of measuring devices.* Proceedings of the symposium "Metrology in quality management system - 4" Kielce-Ameliówka, 22-24 Sept. 2003 (in Polish)

[3] ADAMCZAK S., ZMARZŁY P., JANECKI D. T*heoretical and practical investigations of V-block waviness measurement of cylindrical parts.* Metrology and Measurement System, in press

[4] JOHNSON RA, WICHERN DW *Applied multivariate statistical analysis.* 6th ed. New York, Prentice Hall, 2007

[5] Matlab Statistic Toolbox – User's Guide

[6] PORWIK P., DROZD R., ORCZYK T. *The k-NN classifier and self-adaptive Hotelling data reduction technique in handwritten signatures recognition.* Pattern Analysis and Applications Vol. 14/3, 2014

[7] RATHBUN S., WIESNER A., BASU S. *STAT 505: Applied Multivariate Statistical Analysis*, 2007

[8] STELMACH J., KOŃCZAK G.: *On the comparison of two multidimensional population using the confidence ellipsoid volumes*. Studia ekonomiczne – Zeszyty naukowe Uniwersytetu Ekonomicznego w Katowicach pp. 146-157, 2013 (in Polish)

[9] KRZYŚKO M. *Podstawy wielowymiarowego wnioskowania statystycznego*, Wydawnictwo Naukowe Uniwersytetu im. Adama Mickiewicza w Poznaniu, 2009 (in Polish)

[10] STĘPIEŃ K. *Research on a surface texture analysis by digital signal processing method*, Tehnicki Vjesnik – Technical Gazette, Vol. 21/3, pp485-493, 2014

TRANSCOM 2015, 22-24 June 2015
University of Žilina, Žilina, Slovak Republic

The Properties of the Materials Used in the Process of Plasma Spraying of Optical Coatings

[*]Medard Makrenek, [**]Milena Pajdo, [**]Wojciech Żórawski, [***]Radosław Belka, ****Anna Góral
*Kielce University of Technology, Faculty of Management and Computer Modelling, Department of Physics, al. Tysiąclecia Państwa Polskiego 7, 25-314 Kielce, Poland, fizmm@tu.kielce.pl
**Kielce University of Technology, Faculty of Mechatronics and Mechanical Engineering, Department of Terotechnology, al. Tysiąclecia Państwa Polskiego 7, 25-314 Kielce, Poland, mpajdo@tu.kielce.pl
*** Kielce University of Technology, Faculty of Electrical Engineering and Computer Science, Department of Telecommunications, Photonics and Nanomaterials, al. Tysiąclecia Państwa Polskiego 7, 25-314 Kielce, Poland, r.belka@tu.kielce.pl
**** Polish Academy of Science, Instytute of Metalurgy and Materials Science, 25 Reymonta Street 30-059 Kraków, Poland, a.goral@imim.pl

Abstract. The purpose of the present work is to compare the structure and polymorphic phase, with respect to their potential optical properties, of titanium dioxide nanostructure and conventional powders. Morphology studies were carried out by scanning electron microscopy (SEM). Raman light scattering technique was used to investigate the phases of the titanium dioxide powders. There was observed the difference in Raman spectra of studied powders - the difference indicates that the powders are in two different phases - anatase and rutile.

Keywords: titanium dioxide, rutile, anatase, optical coatings, Raman spectroscopy, SEM.

1. Introduction

Optical coatings can be applied on many different surfaces: glass, metal and ceramics in order to change certain optical properties. They are used to enhance or reduce reflection, refraction, antireflection or conductivity. The level at which they aggravate these effects depends on many properties such as number of coating layers, the thickness of each film and crystallographic structure. Pure titanium dioxide exists in three phases: anatase, brookite and rutile. Brookite is the least common phase. The most common phase is anatase, which is metastable and reverts to rutile at temperatures higher than 915˚C. The stable phase of titania is rutile – a wide-band gap oxide with dielectric constant equal to 15-160 and with high refractive index [1]. The phase content and grain size of titanium dioxide have strong influence on properties of material and coatings.

In recent years, nanotechnologies have a wide application in science and technology because of their unique physical and chemical properties. In contrast to the materials with standard grain size, nanostructure materials have the characteristic dimensions from several nanometers to several tens of nanometers. Particles of this size are almost transparent to visible light, while absorbing ultraviolet radiation. Additionally, such fine particles possess photocatalytic properties.

Titanium dioxide (titania) is increasingly used as a coatings, including optical coatings at optical devices, antireflective coatings, solar cells. Titania dioxide coatings are applied in many ways. The most popular are: electron-beam evaporation, sputtering, pulsed laser deposition, chemical spray pyrolysis deposition (SPD), chemical vapor deposition (CVD), and the sol-gel method [2]. A special variety of chemical vapor deposition is PACVD or PECVD (Plasma Assisted or Plasma Enhanced Chemical Vapor Deposition) process – deposition of thin films using plasma [3]. The coatings are also sprayed by APS method (Atmospheric Plasma Spraying) and SPS method (Shrouded Plasma Spraying). APS method can process solid materials which exhibit a liquid phase at atmospheric pressure – ceramics, metals, cermets, semiconductors, salts.

Atmospheric Plasma Spraying (APS) can be used to gain nanostructure TiO_2 optical coatings with efficacious photocatalytic activity [4]. APS method has many advantages and disadvantages. The most important benefit is the high temperature of the plasma jet – it provides the application of coatings of materials with high melting point efficiently [5]. The most important and simultaneously the most difficult case in TiO_2 coatings sprayed by APS method is to preserve the anatase phase of the powder and ensure the lowest transformation from anatase to rutile in a spraying process. According to [6] such parameters as: the plasma arc current, the addition of secondary gas, the total plasma gas flow rate, or the ratio between the plasma power and the argon flow rate have to be very carefully adjusted in order to minimize the particle heat input.

Raman spectroscopy is an effective tool to study the local lattice structure, phase transition of a titanium dioxide materials. This method has been used in many studies of the phase transition and nanostructures of a titania. Raman spectroscopy has been utilized to characterize the composition of TiO_2 powders [7] e.g. prepared by different methods [8] or to investigate the impact of finite size, pressure and temperature on the structure and properties of TiO_2 crystals [9].

2. Experimental details

Two types of powder feedstock were applied in this study: the first was nanostructure powder TiO_2 Inframat Nanox S2201 with a grain size distribution in the range of 60 ± 20 μm. The second TiO_2 powder was Metco 102 with a grain size distribution in the range of 45 ± 11 μm.

Structure of the powders was investigated with the help of scanning electron microscope (SEM). Raman spectra measurements were performed at room temperature on NicoletAlmega XR - micro mode, excitation 532 nm, the laser output power 6mW, 10x lens (spot diameter approx. 2.5 μm) spectral range 100-4000 cm^{-1}, the resolution of ~ 6 cm^{-1}[10]. We studied two kinds of samples – nanostructure and conventional powders of titanium dioxide. Optical microscopy studies were performed using the Olympus B51 confocal microscope, under 10x magnification (NA = 0.25) and 50x (NA = 0.75).

3. Results and discussion

SEM image of titania nanopowder morphology is presented in Fig.1. Most grains have a regular spherical shape, only some of them are fractured. Imaging of the grain surface at high magnification SEM shows that each grain of powder consists of submicron grains which create sintered high porous agglomerates Fig. 2.

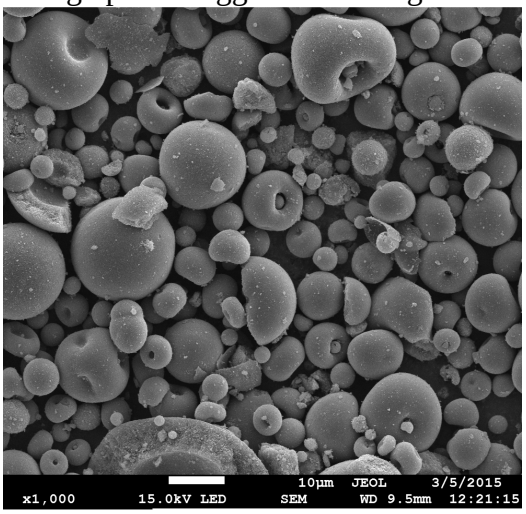

Fig. 1. Morphology of nanostructure of TiO_2 powder

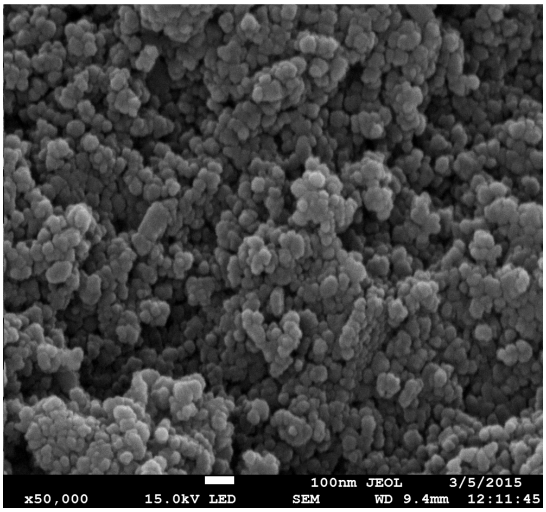

Fig. 2. The grain surface of nanostructure of TiO_2 powder

The slight necking connecting nanograins with diameter 20 ÷ 50 nm are a result of production process which allows to obtain grains in size range of 60+30 μm.

The reference spectrum of the anatase (red line) and the spectrum of the white, nanostructure TiO_2 powder (blue line) are presented in Fig.3. The spectrum is typical of the well-known anatase TiO_2 phase.

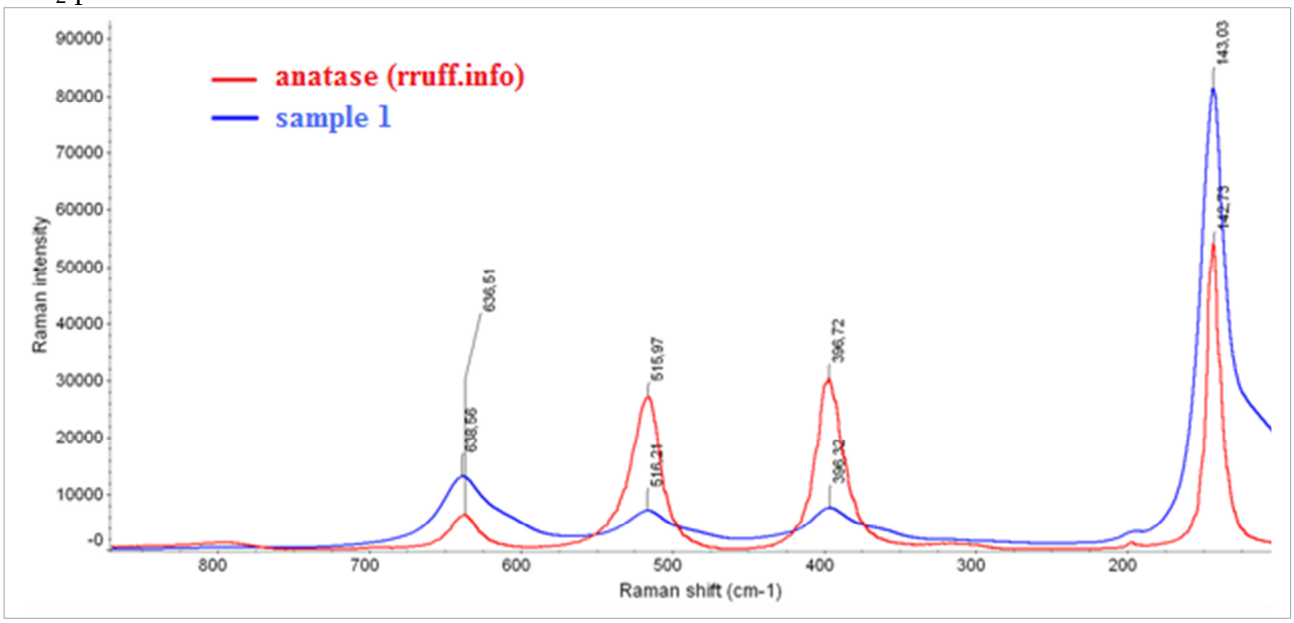

Fig. 3. The literature spectrum of anatase and spectrum of the white TiO_2 powder

Raman peaks for the measured powder are broader and slightly shifted comparing to the literature Raman peaks for anatase [11]. The Raman peak at 142,73 is shifted to 143,03, peak at 396,32 is insignificantly shifted to 396,72, peak at 516,21 is shifted to 515,97 and the last peak at 636,51 is shifted to 638,56. The lowest frequency mode at 143,03 cm^{-1} is the strongest mode in studied nanopowder. The signal intensity of the investigated sample is less than the reference sample. Raman spectrum shows that the titanium dioxide nanocrystals are well crystallized in the anatase structure.

The conventional TiO_2 powder Fig. 4 contained angular and blocky grains which are results of manufacturing process based on fusing and crushing raw material. Analysis of grains cross-section Fig. 5 showed that grains of powder are dense without any porosity.

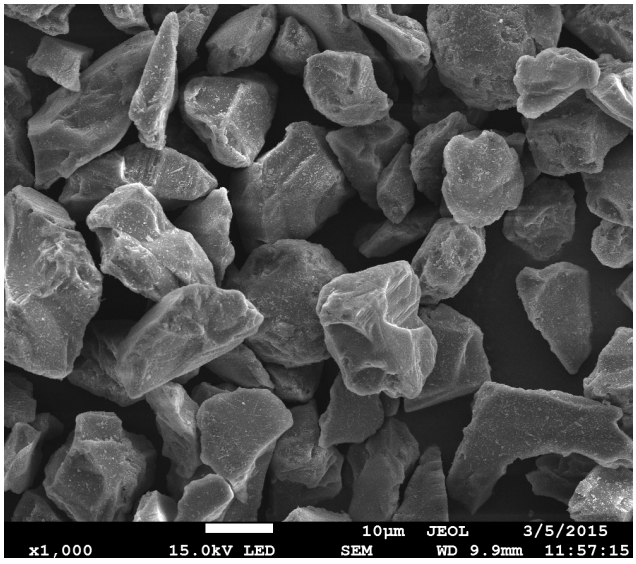

Fig. 4. Conventional TiO_2 powder – rutile

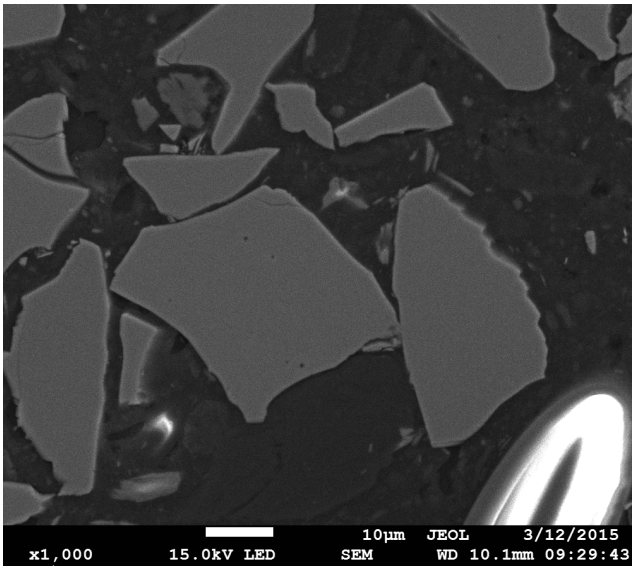

Fig. 5. Grain cross-sections - conventional TiO_2 powder

The literature spectrum of the rutile (red line) and the spectrum of the black, conventional TiO_2 powder (blue line) are presented in Fig. 6.

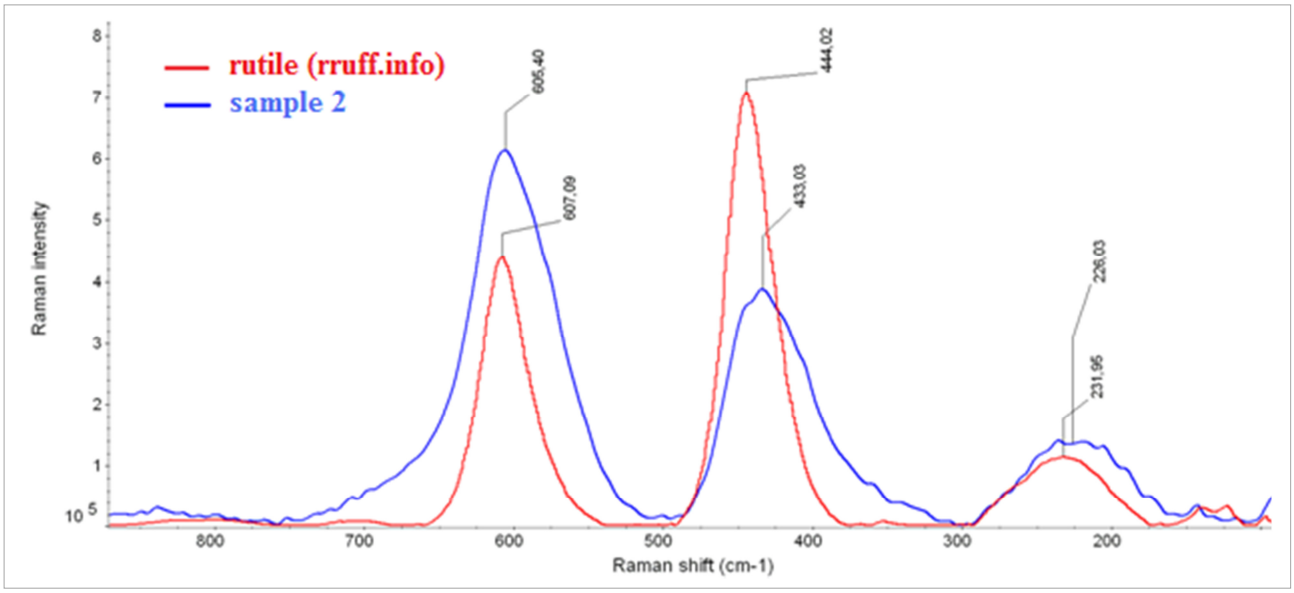

Fig. 6. The literature spectrum of rutile and spectrum of the black TiO_2 powder

The spectrum is typical of the well-known rutile TiO_2 phase. Raman peaks for this powder are broader and slightly shifted comparing to the literature Raman peaks for rutile. The Raman peak at 231,95 is shifted to 226,03, peak at 444,02 is shifted to 433,03and the last peak at 607,09 is shifted to 605,40.

4. Conclusions

In article two types of titanium dioxide powders were investigated. These powders were analyzed by Raman spectroscopy and SEM. The Raman spectra presented in Fig. 3 and Fig. 6 show typical structures with peaks in 396.32, 516.21, 638.56 cm^{-1} and 231.95, 433.03, 605,40 cm^{-1}. Literature Raman spectra of anatase and rutile compared with Raman spectra of two analyzed powders – nanostructure and conventional titania - indicate that the nanostructure powder is anatase phase and the conventional powder of titanium dioxide is rutile phase. SEM analysis of the TiO_2 powders at a magnification of 50 000 times clearly stated the presence of nanograins only in white powder (nanopowder). Morphological structure or grain size are significant parameters in terms of optical coatings because the grain size determine the light scattering behavior of the coating. Large grain size induces strong light scattering and should be avoided for optical coatings. To perform optical coatings, more favorable will be the use of the nanostructure powder in the form ofanatase phase.

Acknowledgments

This research was performed using equipment co-founded by the European Regional Development Fund within the Innovative Economy Operational Programme 2007-2013 (No POIG 02.02.00-26-023/08-00).

References

[1] ORLIANGES J.C., CRUNTEANU A., POTHIER A., MERLE-MEJEAN T., BLONDY P., CHAMPEAUX C., *Titanium dioxide thin films deposited by pulsed laser deposition and integration in radio frequency devices: Study of structure, optical and dielectric properties,* Applied Surface Science, Vol. 263, 111-114, 2012.

[2] WANG X., WU G., ZHOU B., SHEN J., *Optical Constants of Crystallized TiO_2 Coatings Prepared by Sol-Gel Process*, Materials 2013, 6(7), 2819-2830.

[3] KOWALSKI J., SOBCZYK-GUZENDA A., SZYMANOWSKI H., GAZICKI-LIPMAN M., *Optical properties and morphology of PECVD deposited titanium dioxide films*, Journal of Achievements in Materials and Manufacturing Endineering,01/2009, Vol. 37, nr 2, 298-303.

[4] YU Q., ZHOU C., WANG X., *Influence of plasma spraying parameter on microstructure and photocatalytic properties of nanostructured TiO_2-Fe_3O_4 coating*, Journal of Molecular Catalysis A: Chemical, Vol. 283, Issue 1-2, 23-28, 2008.

[5] DU Y.L., DENG Y., ZHANG M.S., *Variable-temperature Raman scattering study on anatase titanium dioxide nanocrystals*, Journal of Physics and Chemistry of Solids, Vol. 67, Issue 11, 2405-2408, 2006.

[6] MARYAMOSSADAT B., MOHAMMADREZA R., MEHDI S., MOHAMMADREZA J., *Structure and photocatalytic activity of TiO_2 coatings deposited by atmospheric plasma spraying*, Surface and Coatings Technology, Vol. 205, Supplement 2, 229-231, 2011.

[7] ZENG G., LI K.K., YANG H.G., ZHANG Y.H., *Micro-Raman mapping on an anatase TiO_2 single crystal with a large percentage of reactive (0 0 1) facets*, Vibrational Spectroscopy, Vol. 68, 279-284, 2013.

[8] ZHANG W.F., HE Y.L., ZHANG M.S., YIN Z., CHEN Q., *Raman scattering study on anatase TiO_2 nanocrystals*, Journal of Physics D: Applied Physics, Vol. 33, 2000.

[9] SWAMY V., KUZNETSOV A., DUBROVINSKY L.S., CARUSO R.A., SHCHUKIN D.G., MUDDLE B.C., *Finite-size and pressure effects on the Raman spectrum of nanocrystalline anatase TiO_2* , Physical Review B, 71, 184302, 2005.

[10] CZERWOSZA E., KOWALSKA E., BELKA R., KĘCZKOWSKA J., SUCHAŃSKA M., WRONKA H., RADOMSKA J., PŁAZA M., SCHMIDT U., *Raman and SEM studies of nanocrystalline Pd-carbonaceous films*, Proceedings of SPIE, Vol. 7502, 750223-1, 2009.

[11] ŠĆEPANOVIĆ M. J., GRUJIĆ-BROJČIN M., DOHČEVIĆ-MITROVIĆ Z. D., POPOVIĆ Z. V., *Characterization of anatase TiO_2 nanopowder by variable-temperature Raman spectroscopy*, Science of Sinterinf, Vol. 41, 67-73, 2009

TRANSCOM 2015, 22-24 June 2015
University of Žilina, Žilina, Slovak Republic

Analyze of Surface Integrity of Ausgaging Construction Parts from Nuclear Reactor Austenitic Steel

[*]Anton Martikan, [**] Vitor Luiz Sordi, [***]Jana Petru, [*]Andrej Czan, [*]Michal Sajgalik, [*]Jozef Struharnansky

[*] Department of machining and manufacturing technology, Faculty of Mechanical Engineering, University of Zilina, Univerzitna 1, 01026 Zilina, Slovakia {anton.martikan, andrej.czan, michal.sajgalik, jozef.struharnansky}@fstroj.uniza.sk

[**] Departamento de Engenharia de Materiais, Rodovia Washington Luís (SP-310), Km 235 São Carlos, São Paulo - Brasil, sordi@ufscar.br

[***] Department of Machining and Assembly, Faculty Of Mechanical Engineering, VSB-Technical University of Ostrava, 17. Listopadu 15/2172 708 33 Ostrava-Poruba, Czech Republic, jana.petru@vsb.cz

Abstract. The article deals with non-destructive detection method of residual stress and chemical properties of stainless steel after 30-years of aging of examined sample. By X-ray diffractometry, there it is possible to determine accurately the values of residual stress or austenite percentage without damage the sample and with keeping its original function. Identification of residual stress and its distribution can improve the prediction of failures and similar damage incidences due to workload over lifetime of components and also, it can be used as evaluation parameter of suitability of applied manufacturing technological operations.

Keywords: X-ray diffractometry, austenitic steel, microstructure, residual stress

1. Introduction

Residual stresses are an integral part of manufactured workpieces, whether they are introduced deliberately, as a part of the design, as a by-product of a process carried out during the manufacturing process, or are present as the product of the component's service history. Residual stresses are additive with the stresses existing in the workpieces as a result of service loads.[1,4,12] In practise, residual stress is stress which affects the entire volume of part or the majority of itself, i.e. macroscopic character. This includes the stress in infinitely thin or large area. It is important, that violation of compactness of part causes the change in macro-geometry. Methods of machining, casting, forming, etc. can cause these changes.

For full classification, it should be noted that residual stresses are called sometimes as technological stresses, because they arise from the action of technological processes during the producing of parts. Direction of residual stress (tension or compression) depends on the kind of deformation. Permanent residual stresses have the largest share on the functionality of part, and they cannot be detected by conventional methods. [2]

X-ray diffraction is specific method that can measure residual stress quantitatively in crystalline and semi-crystalline materials, which include virtually all metals and their alloys, and most ceramic materials. It is a non-destructive detection technology in many applications, and is widely accepted by the engineering community, being the subject of SAE and ASTM publications, which provide reliable sources of information on methods to ensure repeatability and reliability in the results of measurements. Because individual measurements are non-destructive, they can be replicated to demonstrate their statistical reliability [3,5,7,9].

This article is focused on determining of stress characteristics and structure properties of machined stainless steel designed for nuclear industry.

2. Residual Stress

Stress conditions are ones of demonstrations of used machining technologies. After manufacturing process, they remain in parts and constructions and they operate continuously even without load. Their impact significantly affects the functionality of machined surfaces. [2]

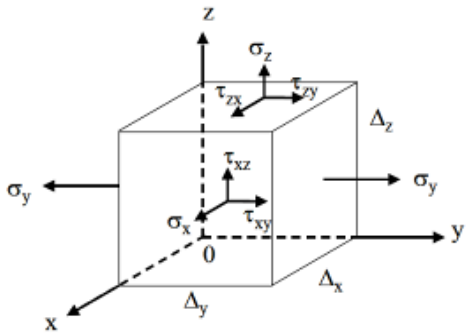

Fig. 1. Scheme of triaxial stress acting on an elemental unit cube.[6]

Normal stress is defined as the stress acting normal to the surface of a plane; the plane on which these stresses are acting is usually denoted by subscripts. For example consider the general case as shown in Figure 1, where stresses acting normal to the faces of an elemental cube are identified by the subscripts that also identify the direction in which the stress acts, e.g. σ_x is the normal stress acting in the x direction. Since σ_x is a normal stress it must act on the plane perpendicular to the x direction. The convention used is that positive values of normal stress de-note tensile stress, and negative values denote a compressive stress.[6]

A shear stress acts perpendicular to the plane on which the normal stress is acting. Two subscripts are used to define the shear stress, the first denotes the plane on which the shear-stress is acting and the second denotes the direction in which the shear stress is acting. Since a plane is most easily defined by its normal, the first subscript refers to this. For example, τ_{zx} is the shear stress on the plane perpendicular to the z-axis in the direction of the x-axis. 6,8,9,10]

3. Principles of Measurement of Residual Stress by X-Ray Diffraction

The residual stress determined using X-ray diffraction is the arithmetic average stress in a volume of material defined by the irradiated area, which may vary from square centimeters to square millimeters, and the depth of penetration of the X-ray beam. The linear absorption coefficient of the material for the radiation used governs the depth of penetration, which can vary considerably. However, in iron, nickel, and aluminium-based alloys, 50% of the radiation is diffracted from a layer approximately 0.005 mm deep for the radiations generally used for stress measurement. This shallow depth of penetration allows determination of macro and microscopic residual stresses as functions of depth, with depth resolution approximately 10 to 100 times that possible using other methods.

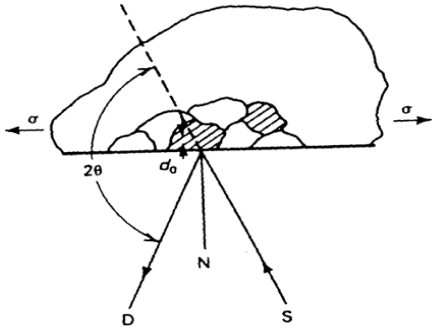

Fig. 3. Principles of X-ray diffraction stress measurement [5]

Although in principle virtually any inter-planar spacing may be used to measure strain in the crystal lattice, the availability of the wavelengths produced by commercial X-ray tubes limits the choice to a few possible planes. The choice of a diffraction peak selected for residual stress measurement impacts significantly on the precision of the method. To higher the diffraction angle, to greater the precision. Practical techniques generally require diffraction angles, 20, greater than 120° (Fig. 3)[4,13,14].

Plane-stress elastic model X-ray diffraction stress measurement is confined to the surface of the sample. Electro-polishing is used to expose new surfaces for subsurface measurement. In the exposed surface layer, a condition of plane stress is assumed to exist. That is, a stress distribution described by principal stresses σ_1 and σ_2 exists in the plane of the surface, and no stress is assumed perpendicular to the surface, $\sigma_3 = 0$. However, a strain component perpendicular to the surface ε_3 exists as a result of the Poisson's ratio contractions caused by the two principal stresses (Fig. 4) [3,16,17].

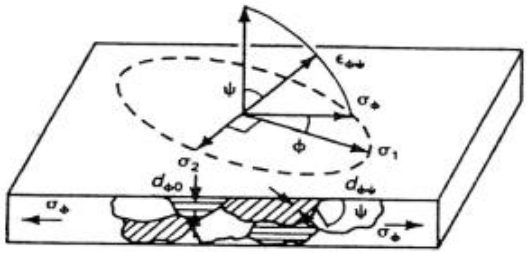

Fig. 4. Plane-stress elastic model [5]

4. Experiment Conditions

Experiment was performed on stainless steel 08CH18N10T. This steel is a typical 18Cr-10Ni austenitic stainless steel, equivalent to AISI 321 and X6CrNiTi18-10.Chemical compositions and basic material mechanical properties are shown in Tables 1 and 2.

C	Si	Mn	Ni	P	S	Cr	N
max 0.07	max 1	max 2	8 - 10.5	max 0.045	max 0.015	17.5 - 19.5	max 0.11

Tab. 1. Chemical composition of sample material (wt.%).

Rm [MPa] (+A)	Rm [MPa] (+AT)	Rm [MPa] (+AT+C)	Rp0.2 [MPa] (+AT)	Rp0.2 [MPa] (+A)	A [%] (+A)	A [%] (+AT)	Brinell hardness [HB] (+A)	Brinell hardness [HB] (+AT)
500-750	500-700	780-820	195	190-235	35-45	40	215	200

Tab. 2. Basic mechanical properties of sample material.

The measuring of residual normal and shear stress and measuring of austenite percentage was performed with Proto XRD diffractometer (Fig. 5), using WINXRD 2.0 software, on three points around the machined diameter of the sample surface.

From the theory of elasticity the relationship between residual stress (σ) and strain (ε) on the sample surface under plane stress is given by the Bragg equation, $\lambda=2d \sin \theta$, relating incident X-ray wavelength (λ), lattice inter-planar spacing (d) and diffraction angle (θ) (Fig. 6).The direction of maximum residual stress, that can be tensile or compressive, is assumed to occur in the cutting or grinding direction during most machining operations. But maximum stress often occurs at significant angles to the cutting direction.

Furthermore, the residual stress distributions produced by many cutting operations, such as turning, may be highly eccentric, producing a highly tensile maximum stress and a highly compressive minimum stress.

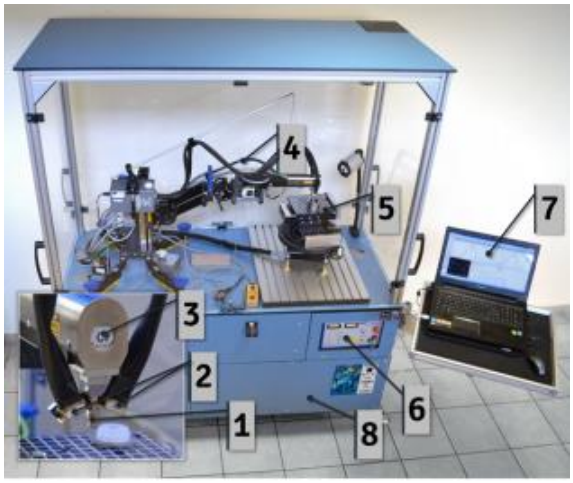

Fig. 5. X-ray diffraction residual stress measurement system (stationary):

1 - collimator; 2 – two detectors for diffraction cone; 3 - X-ray tube; 4 - Cobralink® flexible arm; 5 - positionable and rotary table; 6 – control unit; 7 – PC with software; 8 - laboratory stand

The residual stress field at a point, assuming a condition of plane stress, can be described by the minimum and maximum normal principal residual stresses, the maximum shear stress, and the orientation of the maximum stress relative to some reference direction. The minimum stress is always perpendicular to the maximum. The maximum and minimum normal residual stresses, shown as σ1 and σ2 in Fig. 4, and their orientation relative to a reference direction can be calculated along with the maximum shear stress using Mohr's circle for stress if the stress σφ is determined for three different values of φ.

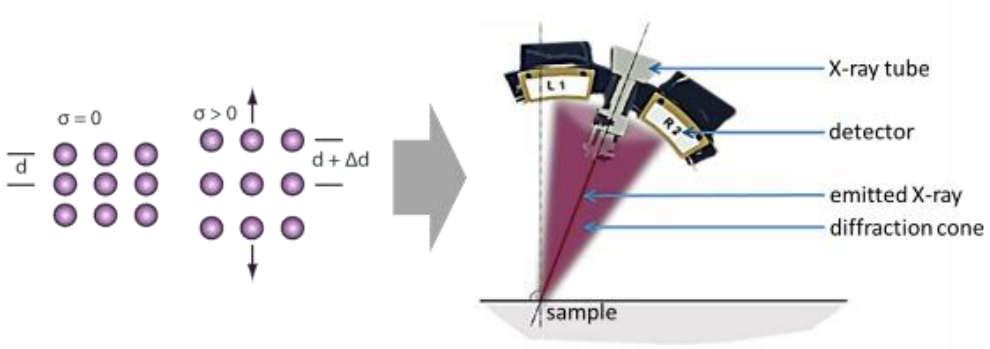

Fig. 6. Principle of measuring of residual stress by X-ray diffractometry based on Brag's Law

Measuring procedure of identifying austenite percentage using X- ray diffraction was based on average peak method. This method uses four individual peaks to determine austenite amount. For each peak is calculated *R*-value and intensity.

5. Experimental Results

With stress measuring procedure of material sample, it proceeded to metallographic analysis of machined surface to identify the structure of the sample surface and subsurface layers (Fig. 7 - 8). Graphic output and values of measured stress and austenite percentage are shown in table 4.

No.	Normal Stress [MPa]	Shear stress [MPa]	Austenite [%]
1	+109,1 ±47,3	68,11 ±25,16	95,45
2	+128 ±18,79	26,86 ±12,6	95,12
3	+93,6 ±13,8	45,56 ±24,99	96,49

Tab. 4. Surface layers stress and austenite percentage values

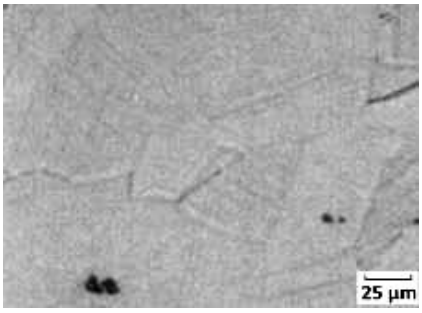

Fig. 7. Material microstructure

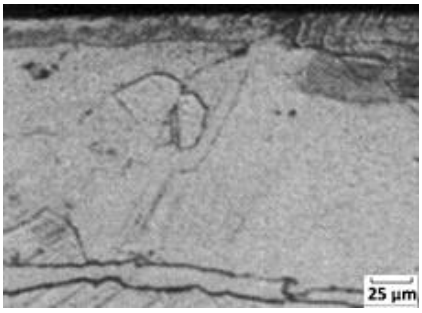

Fig. 8. Microstructure near sample surface

6. Discussion and Conclusion

Due that machining brings stress to machined material, both normal stress and shear stress, it is necessary to be able to measure its6 value and orientation. X-ray diffractometry offers the opportunity to determine these properties of machined or differently technologically treated material to predict deterioration of components. This measuring technology is non-destructive, so it can be used in wide area of applications.

Measurement on sample of machined austenitic steel determined normal stress values from +93.6 MPa to +128 MPa (Fig. 9). That means the surface of the sample is under tensile stress and there is high probability of emerging primary micro-cracks in surface layers. Metallographic evaluation of the material samples confirmed existence of micro-cracks in surface layers (Fig 10).

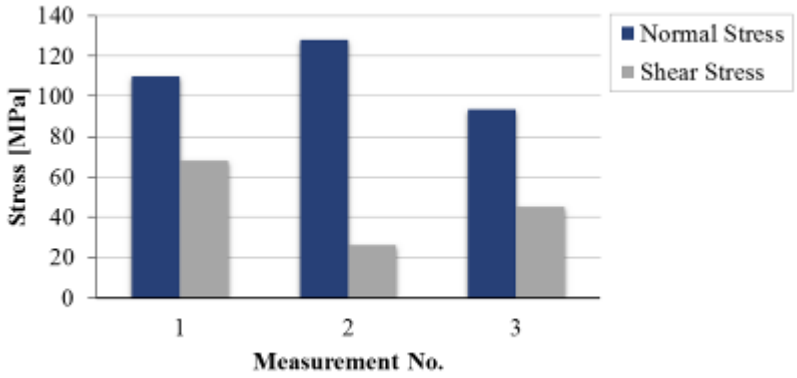

Fig. 9. Measured normal and shear stress values

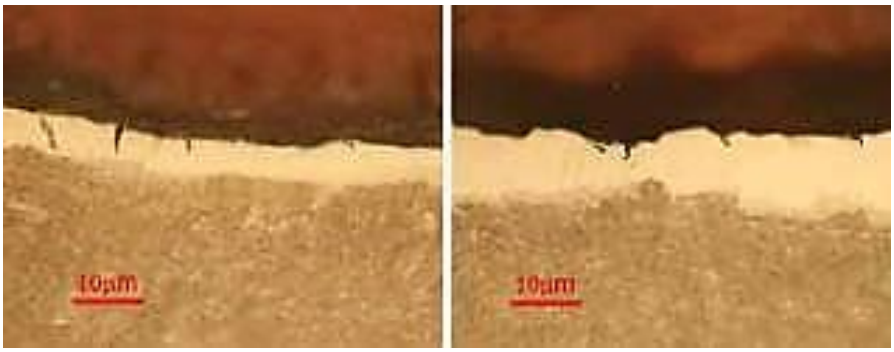

Fig. 10. Formation of micro-cracks in surface layers - light metallography

In this case, high values of shear stress supports the crack spread and can lead to secondary trans-crystal crack into subsurface layers of the material (Fig 10). Spread of micro-cracks is accelerated also by presence of working load of component and chemical influence of work environment (pitting corrosion).

Measured values of austenite percentage in surface layer (Fig. 11) ranged from 95.12% to 96.49% what means that the surface layers of material consists of small amount of another phases in addition to austenite.

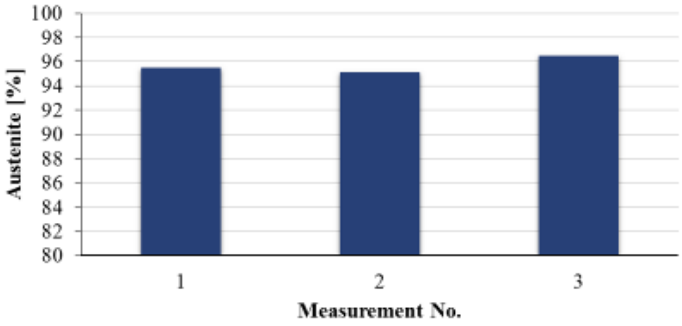

Fig. 11. Measured values of austenite percentage

The experiment proved that X-ray diffraction can be essential non-destructive method for identifying properties of used material treatment and predicting potential component deterioration. Results of the experiment identified that chosen cutting parameters are unsuitable for machining stainless steel 08CH18N10T and is necessary to continue in technological research to bring comprehensive stress into the material and to lower the shear stress.

References

[1] C. A. GRIFFITHS, C.A. Closing the Loop on Product Integrity on Bearings with Engineered Source Approval, Split Ballbearing Features, Company Newsletter, (1989).

[2] GANEV N., KRAUS I.: *X-ray diffraction measurement of residual stresses*, Material Structure, vol 9., No. 2 2002

[3] TIITTO, K. et al.: Testing Shot Peening Stresses in the Field, *The Shot Peener*, vol. 4, ISSN. 1069-2010 (1991).

[4] PREVÉY, P.S. : *X-ray Diffraction Residual Stress Techniques*, Metals Handbook 10, Metals Park: American Society for Metals, p. 380-392,. 1986.

[5] FITZPATRICK, M.E. et.al.: (2005). Determination of Residual Stresses by X-ray Diffraction. *Measurement Good Practice No. 52.* National Physical Laboratory, Teddlingtoon.

[6] BREZINA, M., KUPCA, L.: *Stress corrosion cracking of austenitic stainless steel in a nuclear power plant enviroment*. Enviroment inducted cracking of materials. Department of Structural Analysis, VUJE Inc, Trnava, p. 431 – 436, 2008

[7] SAPIETOVA, A., SAGA, M., NOVAK, P.: *Multi-software Platform for Solving of Multibody Systems Synthesis*, Comunications – Scientific Letters of the University of Zilina, vol. 14, No. 3, 43-48, 2012, ISSN 1335-4205

[8] MOHYLA, P., TOMČÍK, P., BENEŠ, L., HLAVATY, I. (2011*) Effect of post-welding heat treatment on secondary hardening of welded joints of Cr-Mo-v steel*. Metal Science and Heat Treatment 53 (7-8) , pp. 374-378. ISSN: 0026-0673.

[9] CZAN, A. , TILLOVA, E., SEMCER, J., PILC, J.: *Surface and subsurface residual stresses after machining and their analysis by x-ray diffraction*. In. Komunikacie , Volume 15, Issue 2, 2013, Pages 69-76. ISSN 1335-4205

[10]VASILKO, K., PILC, J.: New technological knowledge of the rotary turning tool, Journal Manufacturing Technology, Volume 13, Issue 4, December 2013, Pages 571-575, ISSN: 1213-2489

TRANSCOM 2015, 22-24 June 2015
University of Žilina, Žilina, Slovak Republic

Fractographic Analysis of Research on the Field of High-Cycle Fatigue Regime

[*]Magdalena Mazur, [*]Robert Ulewicz, [**]Paweł Szataniak
[*] Czestochowa University of Technology, Faculty of Management, Institute of Production Engineering, al. Armii Krajowej 19B, 42-201 Częstochowa, Poland , {mazur.m, ulewicz}@zim.pcz.pl
[**]WIELTON S.A. ul. Baranowskiego 10a, 98-300 Wieluń, Poland

Abstract. The article presents preliminary fatigue tests results of three high-strength steels used in structural elements of trailers, wagons, farm devices, etc. Paper presents an analysis of fatigue test results of high-strength steels in the range from 10^4 to 10^7 number of cycles of applied load with a frequency of 40 Hz. Wöhler curve shows the results of the fatigue properties of steels Hardox 400, Hardox 450 and Domex 700MC, which are used in the construction of vehicles. Fatigue fractures were subjected to fractographic analysis in order to determine the mechanism of fatigue crack propagation.

Keywords: fatigue crack, Wöhler curve, high-strength steels, high cycle fatigue tests.

1. Introduction

Information about the fatigue strength of the material becomes essential in solving the general problem of improving the reliability and durability of modern machines and constructions [1]. Demand for fatigue results of tested steel is reported by designers looking for new applications high strength steel. Because manufacturers are interested in optimizing operational costs and increase production therefore, they pay attention to getting the greatest durability of produced objects. This is obtained by looking for new construction solutions of theirs products and application of appropriate materials (materials with appropriate properties). Material fatigue is a process of continuous accumulation damage to form in a sufficiently long time. This process is caused by the variables mechanical stress which causes the nucleation and spreading (propagation) cracks, reserved in the end the destruction of the material [2].

Extra high strength steels are used in structures such as truck chassis, cranes and excavators. In these applications, high strength steel is used in order to reduce weight while simultaneously increasing load capacity of the structure. According to the manufacturer information, Hardox steels are defined as "high-quality abrasion-resistant steels". They are characterized by high resistance to abrasive wear, the possibility of specialized machining tools, good weldability, excellent mechanical properties and resistance to impact loads. Hardox steels are produced in six types [3]. The chemical composition of steel Domex the steel containing low levels of carbon and manganese is precisely complemented by enriching ingredients such as niobium, titanium and vanadium. Due to the low content of carbon, phosphorus and sulfur Domex 700 MC steel can be welded by all commonly used methods. The use of this material also does not require preheating [4]. There are a large number of filler metals with the same or higher strength, which can be used for welding of Domex 700MC steel, while maintaining the same filler metal strength as welded material.

2. Fatigue tests

Fatigue characteristics (dependence $\sigma = f(N)$) of steel have been determined at low testing frequency. The test was performed on Rotoflex, which one device will make it possible to load the

specimen in such a way that the bending moment, along the entire working length of the specimen, has a constant value [5]. The results obtained in a Wöhler curve are shown in Figure 1.

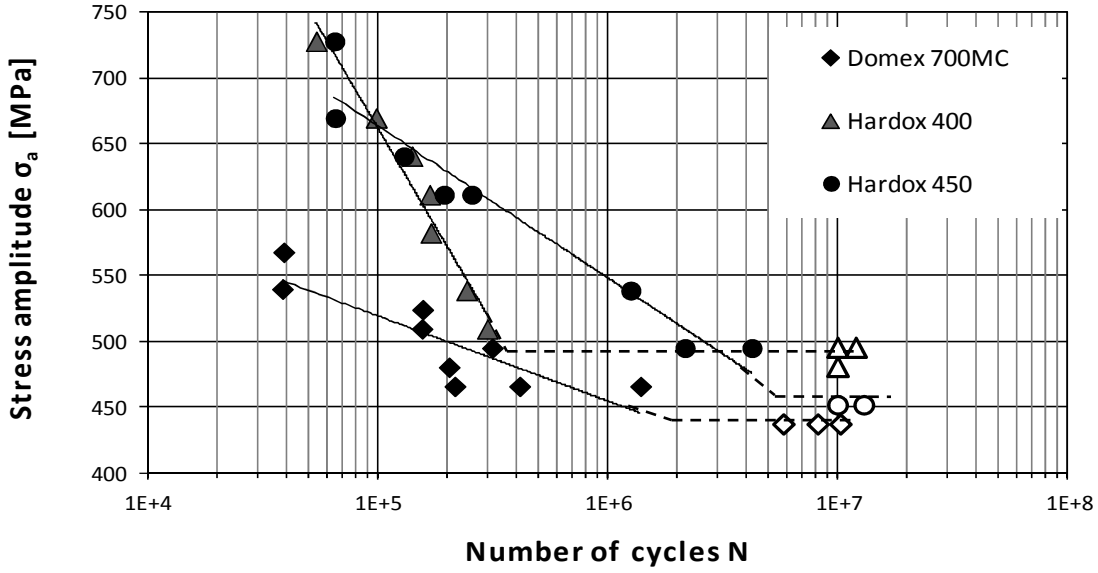

Fig. 1. Diagram of dependency between the load amplitude and number of cycles of the tested steels.

The loading system was rotating bending equipment operating at the frequency of 40 Hz. The stress ratio of R = −1 was chosen. Both experiments were performed at the ambient temperature. During the test the working part of the specimens was cooled by means of fans [6]. The tests results formed a dependency curve between the amplitude of applied load and number of cycles to the specimen crack $\sigma_a = f(N_f)$ (Fig. 1). As determined from the experimental results Wöhler curve shows a decrease in the stress values of the sample destructive with increasing number of cycles to the level of fatigue limit for steel Domex 700MC (440 MPa).

The tests results (for Hardox steels) formed a curve, which clearly shows that the stress amplitude σ_a decreases together with increase of cycles number N beyond conventional fatigue limit $N_c = 10^7$ cycles. The fatigue study showed that in the case of Hardox 400, fatigue limit was 490MPa, the amplitude difference was $\Delta\ \sigma_a = 235$ MPa. In case of Hardox 450 steel fatigue limit was 460 MPa, with the $N = 10^7$ number of cycles. The results are close to each other the difference is due to the higher strength and toughness properties of steel Hardox 450.

3. Fractography analysis for the crack areas

In order to learn about the nature of fatigue process of the tested materials fractography analysis for fatigue fractures have been performed [7]. The tests were performed on a scanning electron microscope (SEM) Tescan II.

Test results for both materials Hardox 400 and Domex 700MC (Fig. 2) confirm the occurrence of only the surface fatigue crack initiation. Only two samples of steel Hardox 450 showed fatigue crack initiation point below the surface of the sample. In these cases, the fatigue fractures showed characteristic formations known in the literature by the term "fish eyes" (Fig. 3)

On the fatigue fracture surface of Domex 700MC specimens (Fig. 4) there is transcrystalline fatigue fracture of very fine particle morphology. In the area of unstable fatigue fracture just before rupture area there are there are many degrees of radial and secondary cracks (Fig. 5).

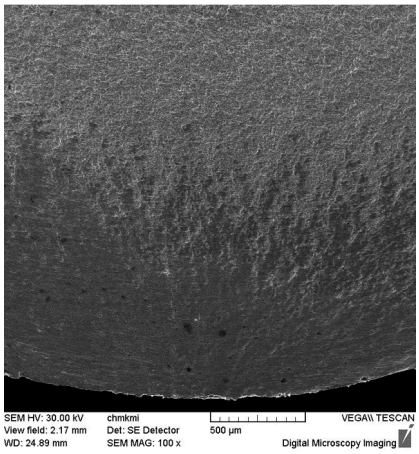

Fig. 2. *Surface fatigue crack initiation for Domex steel 700MC; σ_a = 524 MPa, N = 1,50·10^5 cycle*

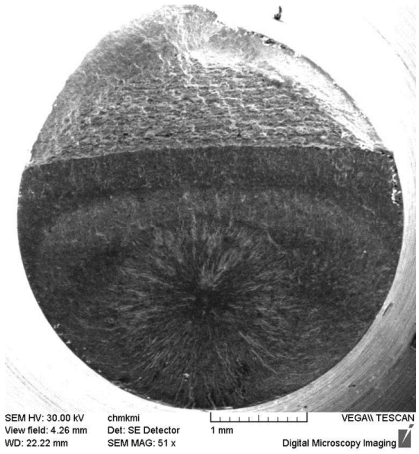

Fig. 3. *Fatigue fracture Hardox 450 steel in the macro scale; subsurface fatigue crack initiation with structure "fish-eye"; σ_a = 455 MPa, N = 6,32·10^9 cycle*

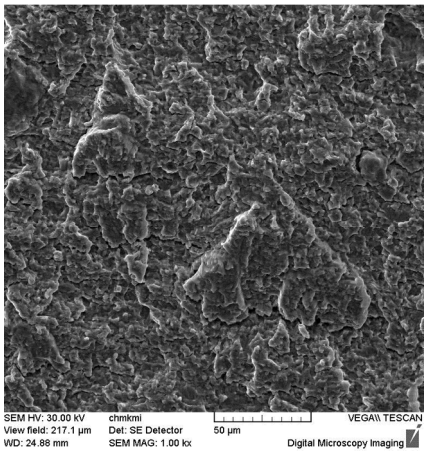

Fig. 4. *Fatigue fracture surface, area of stable crack propagation for Domex 700MC; σ_a = 524 MPa, N = 1,5·10^5 cycle*

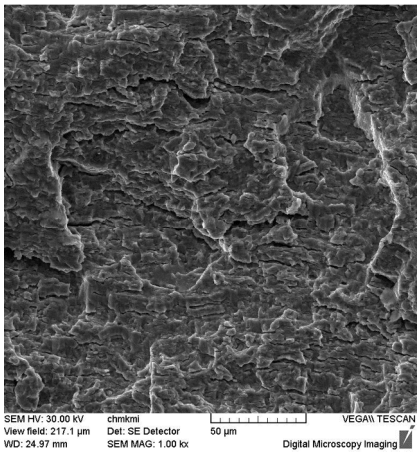

Fig. 5. Area of *unstable fatigue crack growth before rupture area with a clear prevalence large secondary cracks and striations; Domex 700MC steel σ_a = 524 MPa, N = 1,5·10^5 cycle*

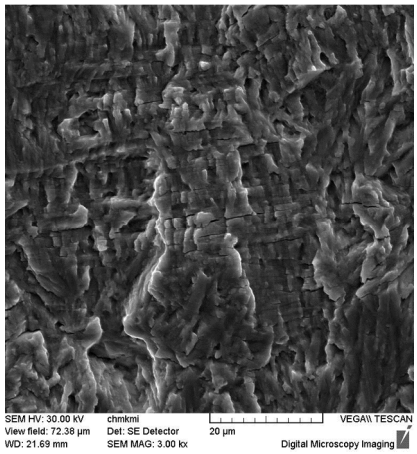

Fig. 6. *Striations in the transcrystalline fatigue fracture of specimens Hardox 450 steel; σ_a = 600 MPa, N = 1,74·10^6 cycle*

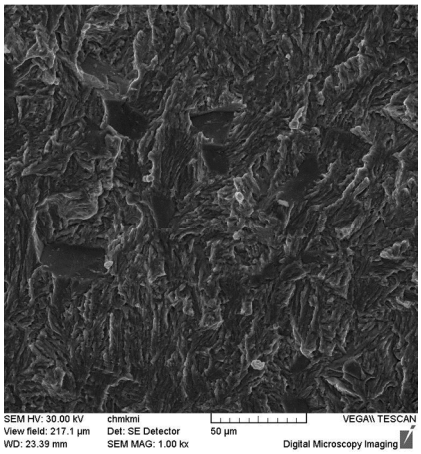

Fig. 7. *Mixed character of trans- and inter crystalline fatigue fracture in fatigue failure of Hardox 450 steel; σ_a = 480 MPa, N = 7,28·10^8 cycle*

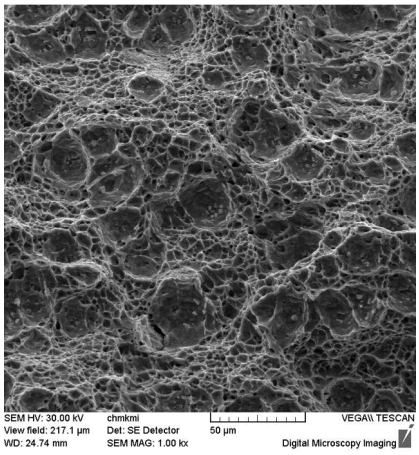

Fig. 8. *Transcrystalline ductile fracture with dimple morphology in steel Domex 700MC; σ_a = 524 MPa, N = 1,5·10^5 cycle*

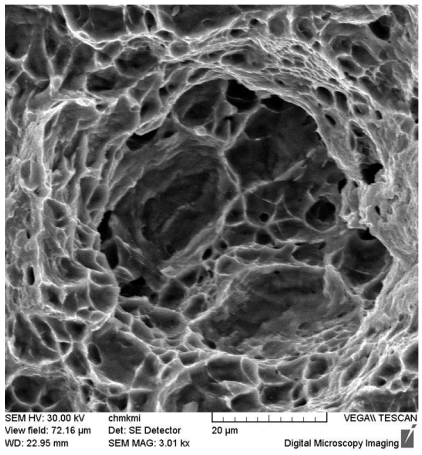

Fig. 9. *Transcrystalline ductile fracture with dimple morphology in steel Hardox 400; σ_a = 330 MPa, N = 1,55·10^9 cycle*

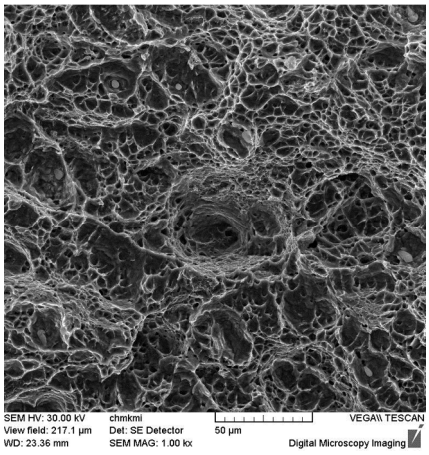

Fig. 10. *Transcrystalline ductile fracture with dimple morphology in steel Hardox 450; σ_a = 480 MPa, N = 7,24·10^8 cycle*

Transcrystalline fatigue fracture of tempering martensite is characterized for both analyzed Hardox steels. For the analysis of both steel Hardox, fatigue fractures is characterized by transcrystalline fatigue failure of tempered martensite with occurring locally in the form of intercrystalline facets present on the surface (Fig. 7). In the area of stable fatigue crack propagation was carried out according transcrystalline propagation mechanisms, which was occurrence by the presence of striations (Fig. 6).

Areas of rupture for all three tested materials are characterized by ductile fatigue fracture with dimple morphology (Fig. 8 – 10).

4. Conclusion

The research demonstrates the possibility of the use of fine-grained Hardox 400 and 450 steels in building of semi-trailers. The use of wear-resistant materials, extends the life and also reduces the weight of a trailer thanks to thinner sheets used for construction of trailers. One of the key parameters is to ensure uniformity of properties throughout the cross-section of the sheet.

Results of this study confirm the classic shape of the Wöhler curve (function of dependencies $\sigma_a = f(N)$). On the obtained graph clearly indicates the fatigue limit for all three tested materials. Fatigue tests for high cyclic fatigue, for tested high-strength steels showed a clear fatigue limit: in the case of Domex 700 MC σ_c = 440 MPa, for Hardox 400 σ_c = 490 MPa and σ_c = 460 MPa in the case of steel Hardox 450

For almost all specimens the fractographic analysis proved that initiation of fatigue cracks was present on the surface of the test specimens, which was also influenced by their loading. Only in the case of two specimens of Hardox 450 fatigue failure was observed subsurface fatigue crack initiation of the characteristic form of a "fish-eye" structure (Figure 3). However, it was impossible to determine the type of inclusions, which have an impact on the formation of "fish-eye" structure. This was due to opening and closing of a fatigue crack in a very high number of cycles, which led to total fragmentation of particles inclusions

In the case of hardox steels, the share of intercrystalline fractures in the total fatigue fracture surface generally does not exceed 1%. Fatigue crack growth area were characterized by striations that were oriented perpendicular to the direction of fatigue cracks propagation. The occurrence of fatigue striation is characteristic for the fatigue fracture of strength materials. On the fatigue fracture surface of test specimens it can be seen extending the distance between each striations running through rupture area.

References

[1] VĚCHET S., KOHOUT J., BOKŮVKA O. 2001. Únavové vlastnosti tvárné liatiny, EDIS Žilinská Univerzita.

[2] WYRZYKOWSKI J.W., PLESZAKOW E., SIENIAWSKI J. 1999. Odkształcanie i pękanie metali. Wydawnictwo Naukowo-Techniczne.

[3] SZATANIAK, P., NOVY, F., ULEWICZ, R., MAZUR, M. *Fatigue Properties Fine-Grained Steel*. SEMDOK 2013. 18th International of PhD. Student's Seminar. Terchova, Slovakia. EDIS, 2013.

[4] MAZUR, M., SZATANIAK, P., NOVY, F., ULEWICZ R. The Mechanical Properties of Domex 700 MC Steel. TRANSCOM 2013. 10th European Conference of Young Researchers and Scientists. Section 5. Material Engineering. Mechanical Engineering Technologies. Zilina Slovakia. EDIS, 2013

[5] TRŠKO, L., MIKOVÁ, K., BOKŮVKA, O. *Fatigue resistance of on shore microalloyed steels for gas transport.* In: *Toyotarity*. *Heijunka.* Yurii V. Makovetsky, Dnipropetrovsk. 2011.

[6] MAZUR, M., ULEWICZ, R., SZATANIAK, P. *Właściwości zmęczeniowe wybranych gatunków stali stosowanych w konstrukcjach naczep samochodowych*. W:Prace XL Szkoły Inżynierii Materiałowej. Wydawnictwo Naukowe AKAPIT, Kraków. 2012.

[7] ZEMANDL, M. *Fraktografie únavových lomů a její praktické využití při analýze příčin porušení strojních součástí*. In Letná škola únavy materiálov ‘2006. EDIS ŽU Žilina 2006.

TRANSCOM 2015, 22-24 June 2015
University of Žilina, Žilina, Slovak Republic

Impact on PVD Coating TiCN Increase the Operating Life of Active Parts of Cold - Moulding Tools from Steel Vanadis 4 Extra

*Borislav Melo, **Ján Moravec
*Viena international s.r.o., Kráčiny 2, 036 01 Martin, melo@viena.sk
**Žilinská univerzita Žilina, Univerzitná 1, 010 26 Žilina, jan.moravec@fstroj.uniza.sk

Abstract. Heat treatment of active components of cold – moulding tools is necessary operation for their functional guarantee. The tools made by this method loosed required quality on the durability and period of service and loss caused by their frequent of exchange are high. One way we can help it is a coating of active parts pressing tools by thin, hard and abrasion resistant deposit, which is suitable by definite method of the tool stress.

Keywords: Deposition, coating, operating life.

1. Introduction

The opportunities for quality vacuum heat treatment of high alloy tool steels in heat treatments companies with precise direction and control of the upgrading process for the producers of the moulding tools have increased after Slovakia's accession to the EU. Every year about one million tons of steel and 200 million tons of plastic are produced and processed [1]. A big part of these materials is processed by moulding tools. There are still new and higher requirements:

- Accuracy, because at ever-increasing speeds of processing and loading is required to produce flawless detail with ever tighter tolerances and thinner walls.
- Complete production on a single tool.
- Processing in dry and with minimal lubricating with the result of cost savings, reducing costs for cleaning of particles and machines and the reduction of environmental burden.
- Improved quality of product to minimize the need for additional work and the amount of scrap.

This forces us to seek more efficient methods that help to eliminate losses. One possibility is the coating of dies employed by a thin, hard and abrasion-resistant layer, which is specific for the particular type of loading tool.

2. Experimental

We have examined the effect of using of TiCN deposition coated PVD method onto a substrate - tool steel Vanadis 4 hardened on secondary hardness 58-60HRC (Figs. 1. and 2.). Selected parameters of substrate and deposition are shown in Tab. 1 and 2. Material for punching was used from sheets of material CuNi25 with strength 90HV30.

Fig. 1. Sample Nr. 1 – Cutting die

Fig.2. Sample Nr.2 – Cutting punch

Brand of Steel	Metallurgical processing	The content of chemical elements (%)						
		%C	%Si	%Mn	%Cr	%Mo	%W	%V
Vanadis 4	PM - *Powder Metallurgy*	1.50	1.00	0.50	8.00	1.50	-	4.00

Tab. 1. Description of tool steel for cold – mold working Vanadis 4 Extra

Deposition	Structure	Colour	Thikness (µm)	Microhardness (0.05HV)/1	Coeficient of friction	Process temperature	Max. service temperature
TiCN	gradient	grey	1-4	3000	0.4	<500	400

Tab. 2. The selected parameters of the deposition TiCN

2.1. Scratch test

We investigated adhesive properties of deposition with method called „scratch test“, which is one of the most basic and most frequently used methods for the detection of adhesion of coating to the substrate. The graph of the tests is shown in FIG. 3 and 4. The graph shows the loading process (left y-axis) and the coefficient of friction (right y-axis) versus time (x-axis). Vertical line represents marked critical load, which gives rise to destruction layer from the substrate. In Tab. 3 are presented the critical loads. The value of the critical loads points to satisfactory adhesion-cohesive properties of the coating.

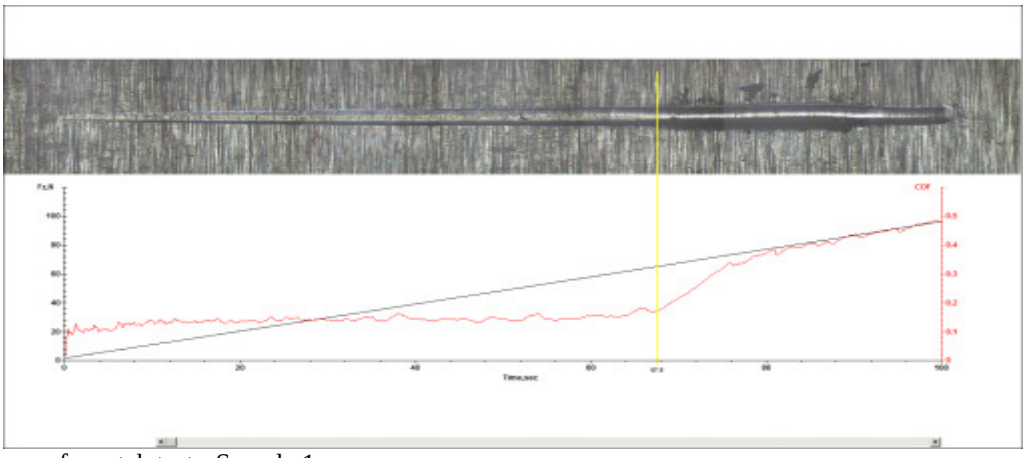

Fig. 3. Progress of scratch test - Sample 1

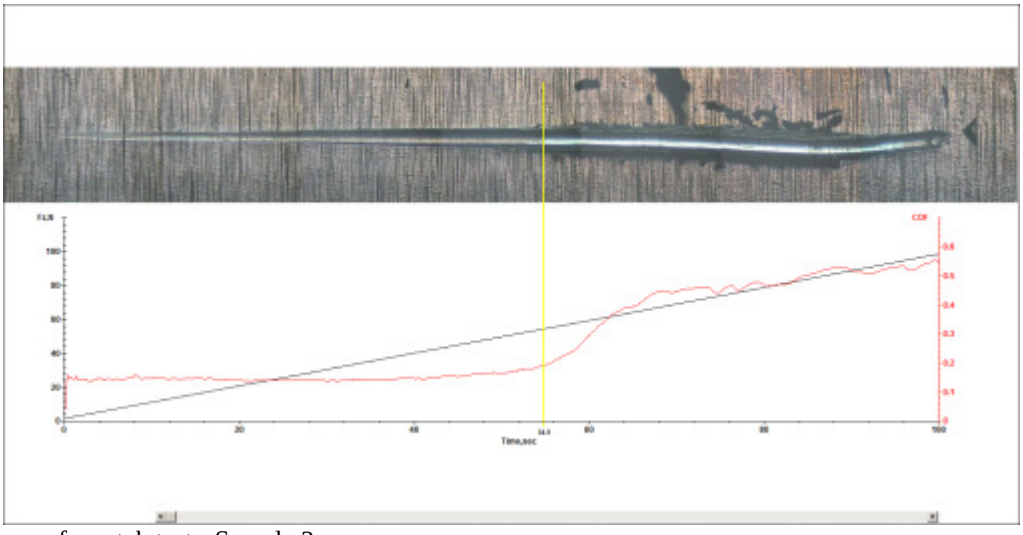

Fig. 4. Progress of scratch test - Sample 2

Sample Nr.	Critical load [N]
1	65
2	76

Tab. 3. The values of adhesive power (critical load)

2.2. Microhardness of the deposition

Measurement of microhardness of the deposition in accordance with ISO 6507-1 - both on the surface and the cross-sectional view - could not be done due to the very small thickness of the coating, because there would be a complete penetration of the layer (from surface measurements), or measuring of the overlap injection of the deposition to the substrate (measured in cross-section) [2]. For this reason it had to be done by hardness measurement method known as "Nanoindentation" using the corresponding hardness testers CSM Instruments. All positions of performed measurements of microhardness of the deposition under nanoindentation were located in the working part of samples. Measurement results are presented in Tab. 3. It represents the mean value of the 15 indentations, which have been done and the variability of the results is the coefficient of variation of the series of results.

Marking of samples	Hardness HV
Sample 1	3210±14 %
Sample 2	2992±22 %

Tab. 3. Hardness measuring of deposition - nanoindentation

2.3. Experiments results

To produce the cutting punch and die we used the substrate - cold - moulding tool steel as the base material, in the common practice it is known as Vanadis 4 - the special tool steel produced by the method of PM from Uddeholm. Active parts were hardened and tempered to secondary hardness in vacuum hardening furnace. In the first part of the experiment we produced about 75 000 strokes with prepared active components without coating on the material CuNi25 of strength 90 HV30 until the end of operating life of the active parts. In the second part of the experiment we used the active components using deposition of TiCN deposited by PVD on a substrate - the above-described tool steel hardened to secondary hardness 58-60HRC. With these modified components we have reached 1.5 million strokes until the end of their operating life, which is a 20-fold increase in service life of active components of the tool.

3. Conclusion

In the article we pointed out that the appropriate choice of coating method, layer and structure of the deposition for the mode of stress can significantly improve the properties of the active components of the cold – moulding tools, which is reflected in particular several increase of durability of tools. The forming tools are characterized by the fact that their active components are usually produced of high alloy tool steels and their profile is complicated, with strict dimensional tolerances. PVD method has been successfully used in coating technology for this type of active components of cold - moulding tool because it retains all the desired properties. With DLC or PLC layers we are improving these properties. Mainly the combinations of CVD and PVD or nanostructured coatings are becoming currently more important which imply further improvements characteristics of cold - moulding tools.

References

[1] JURČI, P.: *Obecné zásady pro volbu a zpracování nástrojových materiálú*, Medzinárodná konferencia:21.dni tepelného spracovania, Jihlava 2006
[2] *Metal Forming Handbook*, Springer Verlag Berlin, 2010, ISBN 3-540-61185-1.

TRANSCOM 2015, 22-24 June 2015
University of Žilina, Žilina, Slovak Republic

Machine Tool Verification

[*]Ing. Milan Novosad, [*]prof. Dr. Ing. Ivan Kuric
[*]University of Zilina, Faculty of Mechanical Engineering, Department of Automation and Production Systems, Univerzitna 8215/1, 01026 Zilina, Slovakia, {milan.novosad, ivan.kuric}@fstroj.uniza.sk

Abstract. The paper presents standard procedures for machine tool verification. The main objective of the machine tool verification is to know and measure all machine tool errors to understand and document its capabilities. An important purpose of verification procedures is the detection of systematic errors, providing the necessary information to compensate them. Therefore, the definition of standard procedures has been a key factor to increase precision of machines tool.

Keywords: Validation, verification, diagnostics, machine tool

1. Introduction

The manufacturing processes are important factors in establishing of geometrically correct machine tool together with continuously increasing demands for their high accuracy. The mechanical engineering industry, as other sectors where the final product is a finished part, tries to increase the quality of products.

Verification and testing procedures of machine tools can be grouped into two main categories. First category is geometric validation tests that measure and calibrate the machine tool in no-load operating conditions. Second category is the machining of test parts, which can be performed either by the machine builder or the customer to verify machine performance during its normal function.

2. Standard Procedures for Verification

Geometric validation tests measure accuracy and repeatability of machine tool with a series of simple positioning tests, generally operating under no-load conditions. Standards determine how to measure, giving admissible tolerances for linear and rotary axes. The testing procedures establish a series of target points, the accuracy and repeatability is obtained measuring several approximations to each target point. The results are the straightness, parallelism and squareness of linear axes, the concentricity errors of rotary axes, etc.

These errors are measured with high precision measurement devices like laser interferometers, collimators or calibrated rules, so measurements are quite simple to perform and information is very accurate. Many machine tool builders try to simplify the specification of the accuracy and repeatability of their machines given a numeric value, but often the user receives it without any reference about the tested conditions.

In fact this is a bad practice, because the numerical value of the accuracy can vary significantly depending on the measurement procedures. For example, the accuracy is different when fewer control points are measured, or if measurements in a forward direction instead of bi-directional measurements are done. The repeatability may also vary depending on the number of measures at each control point. The fact that the accuracy and repeatability values can differ significantly makes it very difficult to compare the performance of different machine brands. To generalize the same definition of accuracy and repeatability, some international standards have been presented. The most important ones are the ISO 230-2, JIS B6201-1993 and ASME B5.54.

These standards establish both test procedures and statistical parameters to be measured, to calculate the accuracy and repeatability for linear and rotary machine motions. The ISO 230-2 is probably the most accepted standard in the world, including some important advantages. Testing according to the ISO 230-2 has the following bases:

- Uniform temperature: All tests must be performed in a controlled environment of 20º C.
- Warm up cycle: All tests include a warm up cycle that simulates the working conditions of the machine. Other standards or procedures do not include a warm up cycle, so errors caused by the machine heat sources cannot be detected.
- UNI and BI directional approaches: All tests include uni-directional and bi-directional approaches to the target points. The accuracy of unidirectional approaches seems significantly better than bi-directional results because some errors such as mechanical backslash are not included. But machine axis works in a bi-directional way, so this is the real condition and useful value for a machine user.
- Number of target points: Linear axes require at least 5 target points per meter and rotary axes require at least 3 target points per 90 degrees.
- Number of measurements per target point: Each test requires at least 5 trials per target point and per direction of approach. Therefore, there are multiple measures for each target point which allows statistical error bands calculation. The error band used in ISO 230-2 is ±2 times the standard deviation of the measurements.

One of the most extended tests for the axes interpolation testing is the Ball-bar test. It was first developed in the mid-1980s by Jim Bryan for the Lawrence Livermore Laboratories, as a means of testing high accuracy diamond turning lathes. Since the end of the 1980s, the ASME B5 and ISO 230 committees include this in the recommended instruments for performing verification tests.

The Ball-bar system as shown in Fig. 1 is essentially a displacement transducer, held between two very accurate spheres. The spheres are set on the machine tool table and spindle nose. Once the Ball-bar is set up, the typical test is to execute a circular interpolation of the machine tool table with respect to the machine tool spindle, which is performed moving the table or head axes depending on the machine configuration. Theoretically, if a perfect circular motion is executed, the distance between the two spheres remains constant and the transducer would not detect any displacement. However, there are several deviations from the trajectory due to the lack of straightness and squareness between the two interpolated axes, the ball screws backlash, the CNC interpolation errors, the stick and slip effects on guides, etc. The bar transducer detects the relative displacement of the spheres which is represented in an easy-to-understand polar plot. Moreover, a common Ball-bar test takes about 15 minutes to check the interpolation between two axes where many sources of error can be detected.

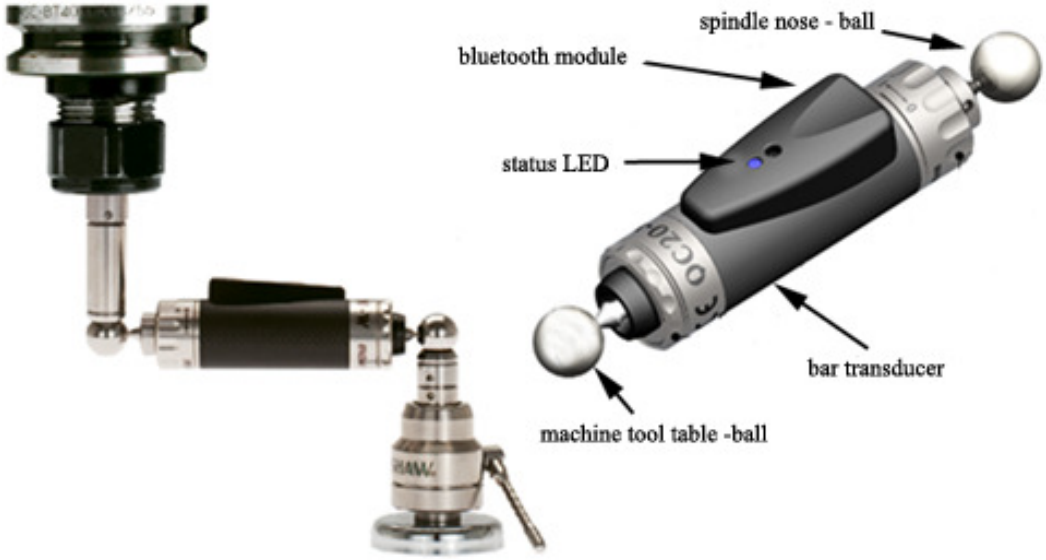

Fig. 1. Ballbar system – Renishaw [9]

3. Test Parts

As explained above, the ISO, JIS or ASME standards define no-load tests to measure the positioning error of the machines. But these tests are far from the real machining conditions. There are some operations, such as drilling or boring, which are similar to a point-to-point interpolation, but generally, machining operations involves two or more axis interpolations. Some tests, such as the circularity tests, measure the contouring errors in no-load conditions. The information of these tests includes interpolation errors between two or more axes. This information is valuable mainly for machine tool builders, because it is relevant data to compensate and fit the axis dynamics of the machine. However, all users of machine tool need the real performance during machining operations. This is why the last verification test group includes "test parts" to check the behavior of milling centres during real conditions. Milling implies the interpolation of three or five axes.

The best known is the NAS 979 test part, which was developed in 1969 and it is the basis of the workpiece described in the ISO 10791-7:1998 (Fig. 2a). The geometry of this part is a combination of a circle, a square, a diamond shape contour and a 3º angle sided quadrilateral. The standard defines two different sizes for the test part: 320 mm and 160 mm length of the external square. To obtain realistic results, the standard recommends the machining of the test part on a midpoint of the machine X, Y and Z axes. In addition, the raw material and test conditions should be arranged between the machine tool builder and the final user, but the most common material is an aluminum alloy in order to maximize the feed speed with the minimum tool wear. Once the test part is machined, the standard defines a series of feature measurements such as squareness, parallelism, circularity, etc. Measurements have to be carried out in a coordinate measuring machine. However, the ISO 10791-7 test does not include complex surfaces, while many users demand high precision in 3D contouring applications. That is why different test parts have been designed in the last years, such as the so-called Mercedes or NCG parts (the latter available at NC-Gesellschaft® association, www.ncg.de, Fig. 2b).

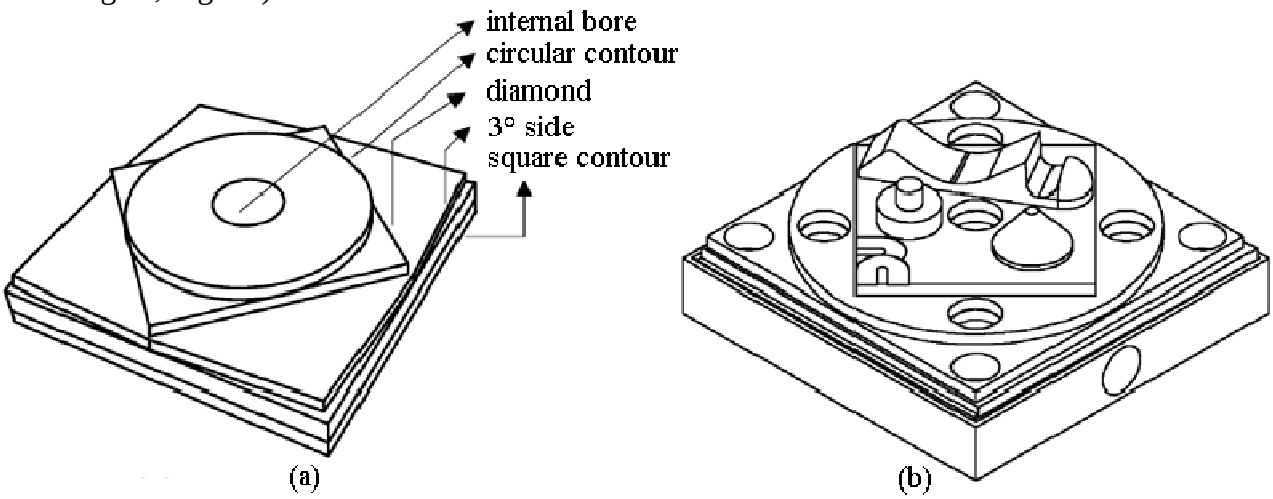

Fig. 2. a) Geometry of the ISO 10791-7 test part b) Geometry of the NC-Gesellschaft® test part

These test parts are widely spread due to customer demand and can be seen in many fairs or showrooms to demonstrate the machine tool capabilities, but none of them are as yet included in the ISO standard regulations. Most of the designed test parts are for 3-axis milling machine centres, however, the demand for 5 axis milling centres is increasing rapidly and there is a lack of specific parts and validation tests for this kind of machine. In fact, ISO 230 defines some general guides to check the rotary axis positioning accuracy, but there are no tests to evaluate the interpolation error between two rotary axes or the combination of linear–rotary axes. Therefore, some research projects have been developed to complete current standards and include specific multi-axis machine testing procedures.

For example, Fig. 3 shows the design of a specific test part for five-axis milling centres. In this part, some features helps to evaluate the position of indexed rotary axes, while others are oriented to assessing the accuracy of multi-axis milling operations, such as flank milling. The design of new test parts and testing methods and, what it is more important, the standardization and generalization thereof are the only way to evaluate machine tool performance and compare machine tools.

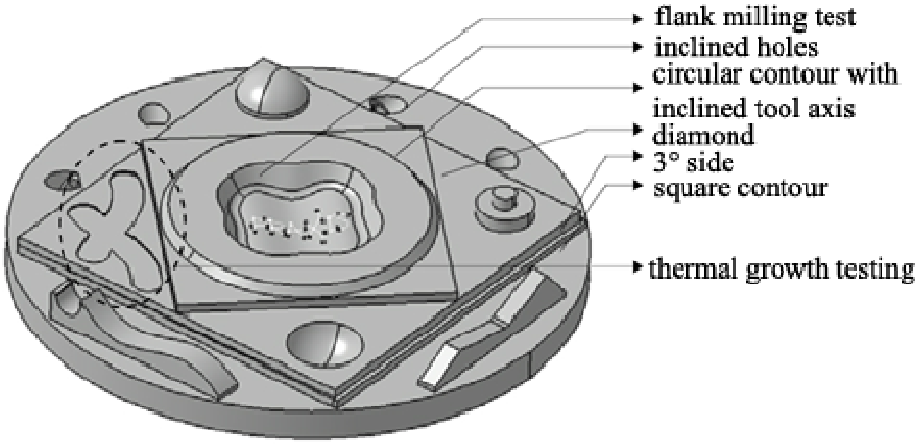

Fig. 3. New test part designed by Fatronik and the University of the Basque Country for 5 axis milling machine centres

4. Conclusion

The possibilities and basic principles of the verification procedures to estimate the accuracy and repeatability of machine tools have been presented. Machine tool verification is very complex and difficult task. There are a lot of factors which have influence on accuracy. The standard ISO 230 is a general guide for several ISO standards that define more specific tests for each type of machine tool. Hence, ISO 230-1 describes the general concepts of straightness, roundness, and squareness, defining the basic measuring methods. ISO 230-2, as previously described, specifies methods for testing and evaluating the accuracy and repeatability of the positioning of numerically controlled machine tool axes by direct measurement of individual axes on the machine. Precision is easy to define but difficult to numerically determine. The most precise machine tools are now giving errors under 1 micron but surely this value will be better in the next ten years.

References

[1] LAMIKIZ A., LÓPEZ DE LACALLE L.N., CELAYA A.: *Machine tools for high performance machining*. London, Springer, 2009, ISBN 978-1-84800-380-4.

[2] DEMEČ, P.: *Presnost obrabacich strojov a jej matematicke modelovanie*. Edicia vedeckej a odbornej literatury – SjF TU v Kosiciach, Vienala Kosice, 2001, ISBN 80-7099-620-X.

[3] BEWOOR A.K., KULKARNI V.A.: *Metrology & Measurement*. Tata McGraw-Hill education private limited, 2009, ISBN 978-0-07-014000-4.

[4] JOZWIK J., KURIC I., SAGA M., LONKWIC P.: *Diagnostics of CNC machine tools in manufacturing process with laser interferometer technology*. Manufacturing Technology, Volume 14, 2014, ISSN 12132489.

[5] SCHWENKE H., KNAPP W., HAITJEMA H., WECKENMANN A., SCHMITT R., DELBRESSINE F.: *Geometric error measurement and compensation of machines.* CIRP Annals Manufacturing Technology 57, 2008.

[6] SARTORI S., ZHANG GX.: *Geometric error measurement and compensation of machines*. CIRP Ann Manuf. Technol. 44, 1995.

[7] DORNFELD D., DAE-EUN L.: *Machine design for precision manufacturing*. In: Precision Manufacturing. Springer Verlag, USA, 2008.

[8] HSU YY., WANG SS.: *Mapping geometry errors of five-axis machine tools using decouple method*. Int Precis Technol 1, 2007.

[9] www.renishaw.com

TRANSCOM 2015, 22-24 June 2015
University of Žilina, Žilina, Slovak Republic

Effect of Extensive Recycling on High Density Polyethylene (HDPE) Mechanical Properties

[*]Pavel Oblak, [*]Joamin Gonzalez-Gutierrez, [*]Barbara Zupančič, [*]Alexandra Aulova and [*,**]Igor Emri

[*]University of Ljubljana, Faculty of mechanical engineering, Center for Experimental Mechanics, Ljubljana, Slovenia, pavel.oblak@fs.uni-lj.si
[**]Institute for Sustainable Innovative Technologies, Ljubljana, Slovenia

Abstract. In plastics industry it is a common practice to mechanically recycle waste material arising from production, however, in this process material mechanical properties change. In this study, mechanical recycling of high density polyethylene (HDPE) was simulated by one-hundred (100) consecutive extrusions cycles. Further, mechanical properties were characterized in terms of hardness and modulus, and shear creep compliance was measured to characterize the time-dependent mechanical properties. In addition, structural changes were studied through the degree of crystallinity obtained via Differential Scanning Calorimetry.

The results show that hardness and modulus significantly decrease after 10th extrusion cycle, while in case of shear creep compliance evident changes are visible in particularly after the 30th extrusion cycle. All those changes are well supported by the degree of crystallinity. It can be said that mechanical recycling causes deterioration of HDPE mechanical properties that becomes more evident after 10th reprocessing cycle.

Keywords: high density polyethylene, mechanical recycling, hardness and modulus, creep compliance, crystallinity.

1. Introduction

The plastics industry has benefited from 60 years of growth with a year expansion of 8.7% from 1950 to 2012 [1]. With continuous growth of plastic industry also amount of generated waste is increasing, not only as post-consumer waste but also as waste generated during the production process. Runners, sprues and off-specification products are common in production; they are easy to identify and are of high quality [2]. Instead of being rejected as waste they are granulated and reprocessed. This process is also called mechanical recycling, however, properties of mechanically recycled polymers do not remain the same because of degradation from heat, mechanical stresses, oxidation and ultraviolet radiation during their reprocessing.

In line with the information mentioned above, present work is focused on investigation of the mechanical properties of HDPE when exposed to extensive mechanical recycling, i.e. to one hundred (100) consecutive extrusions cycles. In this paper we focus on short-, and long-term material mechanical properties, determined through nanoindentation and creep experiments. In addition, this investigation supports changes of mechanical properties by observed structural changes presented through the changes of degree of crystallinity.

2. Material and Methodology

2.1. Material

High density polyethylene (HDPE) LANUFENE®HDI-6507UV, produced by Ras Lanuf Oil & Gas Processing Co. was used for the purposes of the investigation [3].

2.2. Simulation of mechanical recycling

The process of mechanical recycling was simulated by extensive extrusion. For this purpose, twin-screw extruder, PolyLab PTW 16/40 OS, produced by Thermo Scientific (Germany) was used. Material was extruded at screw rotation of 150min^{-1}, a processing temperature of 240 °C with a throughput between 1200 and 1300 g/h. After material was extruded, it was pelletized and a portion was removed for the purpose of afterwards characterization. The rest of material was submitted to a new extrusion cycle. 100 cycles were performed.

2.3. Nanoindentation

Measurements of hardness and modulus were performed with nanoindentation using G200 apparatus, produced by Agilent Technologies (USA). Measurements with continuous stiffness measurement technique (CSM) [4] were implemented using a Berkovich indenter tip while oscillation frequency was 45Hz and amplitude 2nm. For virgin HDPE material as well for its recyclates measurements were repeated on three samples, with 40 indentations on each. In order to obtain reliable data and exclude unstable one caused by surface effects, data from each successful indentation curve was averaged thought the depth of penetration from 1000 to 1500 nm. Further values of elastic modulus and hardness were averaged for all the indents.

2.4. Shear creep compliance

Shear creep measurements were performed on Shear Creep Torsiometer developed by research group of Center for Experimental Mechanics, Faculty of Mechanical Engineering, University of Ljubljana [5]. First, samples were heated up and annealed at 100 °C over a period 7 hrs., and then gradually cooled to 30 °C over a period of 8 h in order to remove residual stresses. After annealing, the measurement continued with loading, unloading and conditioning of the sample at 30, 50, 65, 75 and 90 °C. Loading phase lasted 3 h at a constant temperature, then the torque was removed and the temperature was increased to the next measuring temperature within 3 h. The specimen was again torque-loaded, and the procedure of exchanging the phases of loading, unloading and conditioning was repeated over the selected measuring temperature range. The stresses applied to each specimen were selected as to remain in the linear viscoelastic region for all materials and ranged from τ_0 = 9.6 x 10^4 Pa at 30 °C to 3.0 x 10^4 Pa at 90 °C. Two repetitions were performed at each condition for all materials.

2.5. Differential scanning calorimetry

Differential scanning calorimetry (DSC) analysis was performed on DSC7 instrument, produced by Perkin Elmer (USA). The measurements were carried out according to ISO 11357. Heat (enthalpy) of fusion (ΔH_f) was evaluated from a second heating run. The degree of crystallinity (X_{cr}) was calculated based on next relation:

$$X_{cr} = \frac{\Delta H_f}{\Delta H \cdot 100\%}, \qquad (2)$$

where $\Delta H \cdot 100\%$ is the heat of fusion for 100% crystalline HDPE, which has been estimated to be 293 J/g [6]. Average values of six repetitions are presented in this study.

3. Results and discussion

3.1. Hardness and modulus

Results on hardness and modulus are presented in Figs. 1 and 2. It can be seen that both, hardness and modulus, exhibit similar trend; through the first 10 extrusion cycles no significant changes are detected while further, between 10th and 20th extrusion cycle, drop is evident. Afterwards, both values are gradually decreasing up to 70th extrusion cycle where properties stabilise. When taking into account first 10 extrusion cycles, we can say that our results are in line with those reported by other authors [7, 8, 9, 10], while none of them extend their investigation above 10 reprocessing cycles. Changes of hardness and modulus can be attributed to the changes in the degree of crystallinity presented in Fig. 4.

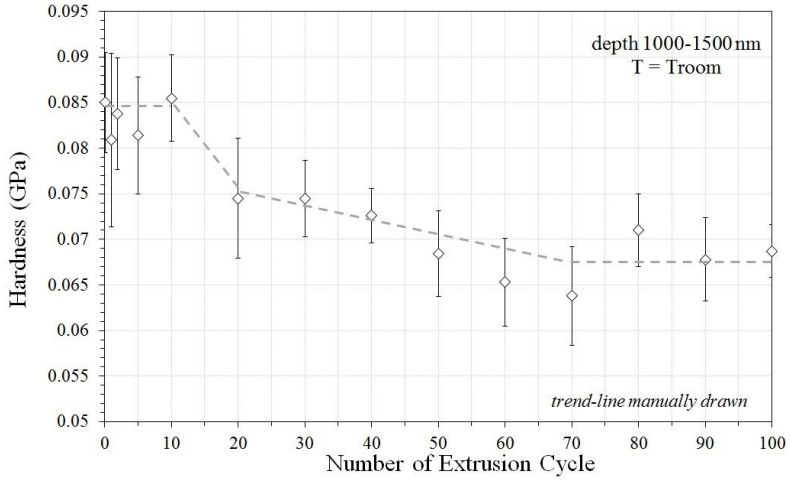

Fig. 1. Hardness in dependence of the number of extrusion cycles.

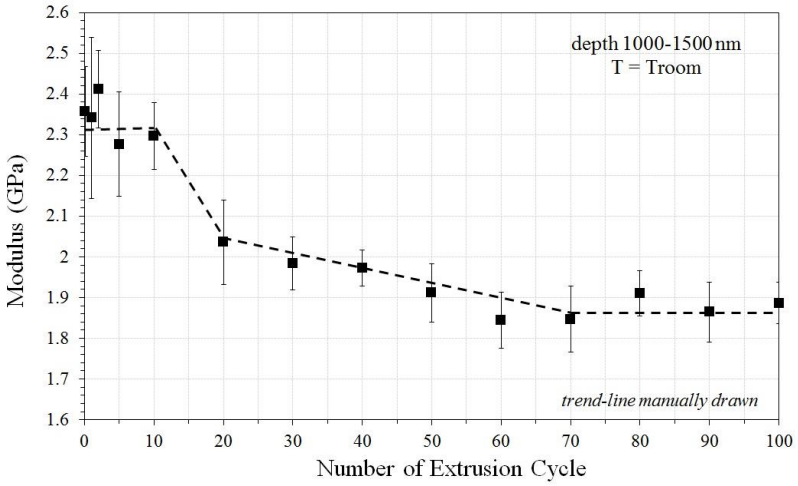

Fig. 2. Modulus in dependence of the number of extrusion cycles.

In practice, information on decreasing trend of hardness and modulus might be useful when designing products made from recycled HDPE. When using recycled material, lower performance in respect to a product made from virgin material can be expected when material recycled more than 10 times is used.

3.2. Shear creep compliance

To present long-term product mechanical stability, first, master curves of virgin HDPE and its recyclates were generated and shifted to reference temperature 30°C using the CFS methodology [11]. Further, isochronal values of creep compliance at time equal to 3 and 10 years were taken from individual master curves; results are presented in Fig. 3. It can be seen that extrusion did not significantly affect shear creep compliance through first 30 reprocessing cycles. Furthermore an increasing trend is evident in time of 3 years as well in 10 years. At 100th extrusion cycle, creep compliance rises for 16% after 3years and 20% after 10 years in comparison to virgin material. In addition we might say that difference in creep between 3 and 10 years remains more or less constant.

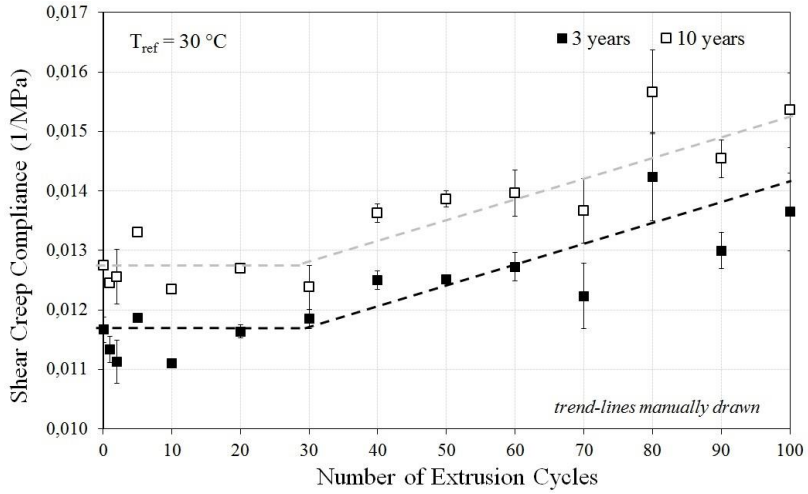

Fig. 3. Creep compliance in dependence of the number of extrusion cycles after 3 and 10 years.

Since shear creep compliance is measured in solid state we can relate increasing shear creep with extrusion cycles to the degree of crystallinity, presented in Fig. 4, which shows the opposite, decreasing trend. We may conclude that products made of HDPE recycled more than 30 times, have lower long-term mechanical stability or in other words, using those materials represent the risk that a product will have lower performance.

3.3. Degree of crystallinity

Curve, representing the degree of crystallinity is presented in Fig. 4. It shows that extrusion leads to noticeable decrease in a degree of crystallinity only after 20th reprocessing cycle. The evident leap was detected between 20th and 30th extrusion cycles while the largest drop of 18% can be observed at 90th extrusion cycle. Similarly, several authors who investigated the effect of HDPE reprocessing on degree of crystallinity [9, 10, 12, 13], did not observe any significant change on crystallinity throughout 10 reprocessing cycles. This is in line with our findings from first 20 extrusion cycles. Decreasing of the degree of crystallinity shows the reducing of molecular ability to pack and form crystal regions. This might be consequence of crosslinking or chain branching process in the material, which is one of the mechanisms present at the degradation under processing conditions [14, 15]. Moreover, changes in the degree of crystallinity may result in changes of mechanical properties, i.e. hardness, modulus and creep compliance as previously presented in Figs. 1, 2 and 3.

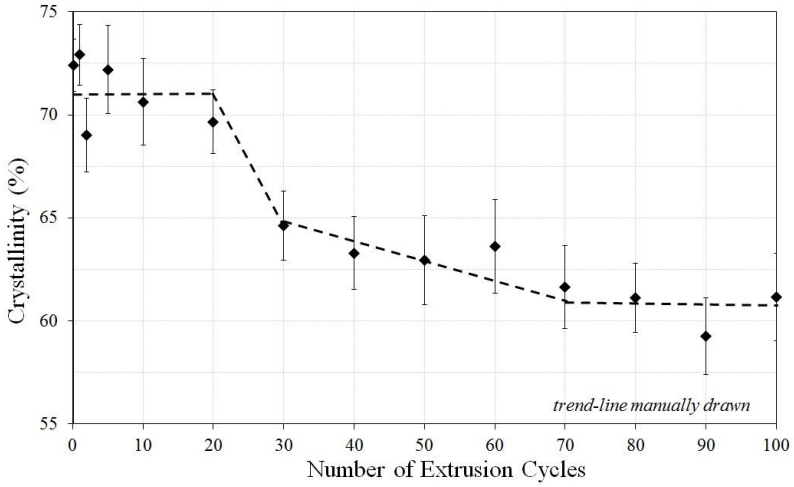

Fig. 4. Variation of crystallinity in dependence of the number of extrusion cycles.

4. Conclusion

In the current study, effect of extensive mechanical recycling on mechanical properties of HDPE was investigated. Decrease of hardness and modulus becomes increasingly evident after 10th extrusion cycle. Similarly, shear creep compliance measurements show an unfavourable effect of mechanical recycling on the time-dependent mechanical properties, while in this case, evident changes are visible in particularly after the 30th extrusion cycle. However, all those changes are well supported by the degree of crystallinity which does not show significant changes through the first 20 extrusion cycles while after, between 20th and 30th cycle, significant drop is recorded which is gradually decreasing afterwards. It can be concluded that mechanical recycling causes deterioration of HDPE mechanical properties that becomes evident after 10th reprocessing cycle. This information should be taken into account when designing products from recycled HDPE.

Acknowledgement

This work was conducted with the financial support of the Slovenian Research Agency – ARRS.

References

[1] Plastics europe, *Plastics-the facts 2013. An analysis of European latest plastics production, demand and waste data*, Plastics Europe, 2013.

[2] L. LUNDQUIST, Y. LETERRIER, P. SUNDERLAND, J. A. E. MÅNSON, *Life Cycle Engineering of Plastics: Technology, Economy and Environment*, Elsevier, 2000

[3] Ras lanuf oil & gas processing co, *LANUFENE®HDI-6507UV technical specification*, http://www.nascopolymers.com/PDF/HDPE/HDI%206507%20UV.pdf (accessed: may 2014)

[4] X. LI, B. BHUSHAN, A review of nanoindentation continious stiffness measurement technique and its applications, Material Characterization, 48, 2002.

[5] P. METLIKOVIČ, I. EMRI, Naprava za merjenje lezenja torzijsko obremenjehih polimernih preizkušancev, Strojniški vestnik, 36, 101-104, 1990.

[6] Thermal application note, *Polymer Heats of Fusion*, TA Instruments, NewCastle, USA, www.tainstruments.com/library_download.aspx?file=TN048.pdf (accessed: Jun 2014).

[7] C. N. KARTALIS, *Mechanical recycling of postused high-density polyethylene crates using the restabilization technique. I. Influence of reprocessing*, Journal of Applied Polymer Science, 73(9): 1775-1785, 1999. R. L. Blaine,

[8] E. STROMBERG, S. KARLSSON, *The Design of a Test Protocol to Model the Degradation of Polyolefins During Recycling and Service Life*, Journal of Applied Polymer Science, 112(3): 1835-1844, 2009.

[9] M. J. ABAD, *Effects of a mixture of stabilizers on the structure and mechanical properties of polyethylene during reprocessing*, Journal of Applied Polymer Science, 92(6): 3910-3916, 2004.

[10]S. APONE, *Effects of thermomechanical treatments on HDPE used for TLC ducts*, Polymer Testing, 22(3): 275-280, 2003.

[11] M. GERGESOVA, B. ZUPANČIČ, I. SAPRUNOV, I. EMRI, *The closed form t-T-P shifting (CFS) algorithm*, Journal of rheology, vol.55, no.1, p[1-16] 2011

[12]M. ALTAN, *Residual stresses determination in injection molded virgin and recycled HDPE blends: mechanical properties and morphology*, E-Polymers, 2008.

[13]S. LUZURIAGA, *Degradation of pre-aged polymers exposed to simulated recycling: Properties and thermal stability*, Polymer Degradation and Stability, 91(6): 1226-1232, 2006.

[14]E. EPACHER, Two-step degradation of high-density polyethylene during multiple extrusion, Journal of Applied Polymer Science, 74(6): 1596-1605, 1999.

[15]K. HAMAD, *Recycling of waste from polymer materials: An overview of the recent works*, Polymer Degradation and Stability, 98(12): 2801-2812, 2013.

TRANSCOM 2015, 22-24 June 2015
University of Žilina, Žilina, Slovak Republic

Electrochemical Characteristics of Elektron 21 Magnesium Alloy with Octacalcium Phosphate (OCP) Coating

[*]Miroslav Omasta,[*,**]Branislav Hadzima,
[*] Department of Materials Engineering, Faculty of Mechanical Engineering, University of Žilina, Univerzitná 1, 010 26 Žilina, Slovakia, {miroslav.omasta, branislav.hadzima}@fstroj.uniza.sk
[**]Research Centre of the University of Žilina, Univerzitná 1, 010 26 Žilina, Slovak Republic

Abstract. Electrochemical characteristics of Elektron 21 magnesium alloy surfaces after grinding and/or electrodeposition of OCP coating were investigated by potentiodynamic polarization tests in the environment simulating human body conditions (0.9 % NaCl solution, 37°C). Electrodeposition was realized in water solution of 0.167 M $CaCl_2$ + 0.1 M $NH_4H_2PO_4$. The influence of this surface treatment on corrosion potential and corrosion current density was evaluated. Basic potentiodynamic curves obtained from the voltamperometric tests were analyzed by Tafel analyses. The improvement of short-time electrochemical behaviour after OCP electrodeposition on tested alloy surface was reported.

Keywords: OCP; Magnesium alloy; Potentiodynamic tests; Light microscopy; Electrodeposition

1. Introduction

Magnesium alloys have shown desirable properties for potential application in biomaterial area, for example, high strength and Young modulus close to nature bone. However, the high dissolution rate of magnesium alloy is a problem due to its high chemical activity. Surface modification is an effective approach to solve this problem and improve the application of magnesium alloy as potential biomaterial [1].

One of the most perspective coatings for implants is calcium phosphates [2]. Calcium phosphates have extensively been studied due to their biocompatibility, chemical stability and similarity in composition with the mineral phase of teeth and bone and use as bone substitutes in biomedical industry. Among the most studied calcium phosphates are hydroxyapatite (HAP), octacalcium phosphate (OCP), brushite or dicalcium phosphate dihydrate (DCPD), monetite, monocalcium phosphate monohydrate (MCPM), tricalcium phosphate (TCP), tetratricalcium phosphate (TTCP) and amorphous calcium phosphate (ACP) [3].

For these reasons, the aim of this study is to electrodeposit OCP coating on Elektron 21 magnesium alloy surface and to improve its electrochemical corrosion properties by this way.

2. Experimental material and methods

An extruded magnesium alloy, Elektron 21, was examined. The alloy was purchased from Magnesium - Electron, Manchester, UK. The alloy's chemical composition is given in Tab. 1. The samples for metallographic observation were prepared by conventional metallographic procedures. For visualization of the magnesium alloy microstructure, etchant consisting of 0.5 % Nital was used. The microstructure of the extruded sample (Fig. 1) is formed by polyedric grains of supersaturated solution of zirconium, RE and other alloying elements in magnesium. The average grain size is 14 µm. Areas of the $Mg_{12}Nd$ intermetallic phase are visible in the microstructure [4].

Component	Nd	Gd	Zr	Fe	Cu	Ni	Zn	Mg
wt. %	2.90	1.3	0.32	0.002	0.001	<0.0005	0.32	balance

Tab. 1. Chemical composition of Elektron 21 magnesium alloy

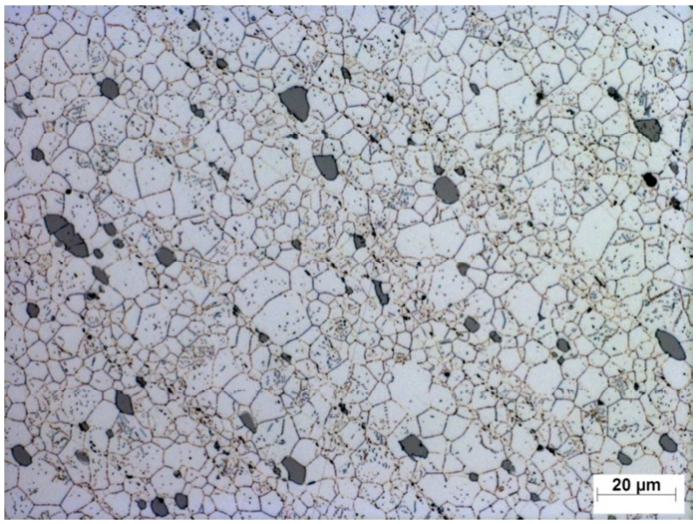

Fig. 1. Microstructure of Elektron 21 magnesium alloy, light microscopy, etch. 0.5 % Nital

2.1. Experimental material surface preparation

For the evaluation of OCP surface treatment influence on electrochemical characteristics the sample surfaces were grinded with 1000 grit SiC paper to ensure the same surface roughness, then rinsed with de-mineralized water and ethanol, and dried using a stream of air. After described pre-treating the OCP was deposed on the samples' surfaces. Treatment electrolyte solution was prepared with 0.167 M $CaCl_2$ + 0.1 M $NH_4H_2PO_4$. Solution pH was 4 and the electrodeposition was carried out at room temperature 22 ± 2 °C. Grinded Elektron 21 sample was used as the cathode, while a platinum electrode served as the anode. Electrodeposition was performed with constant potential - 2 V vs saturated calomel electrode (SCE) for 1 hour on a laboratory apparatus VSP (producer BioLogic SAS France). After electrodeposition samples were immediately rinsed with demineralized water and dried using a stream of air.

2.2. Experimental methods

The surface morphology of the treated sample was assessed by a stereomicroscope Nikon AZ100 with a digital camera using NIS Elements software. The corrosion characteristics of the untreated and OCP-coated on Elektron 21 in 0.9% NaCl were evaluated by potentiodynamic polarization using a potentiostat/galvanostat/frequency response analyser VSP from BioLogic SAS France. All the corrosion experiments were performed at 37±1 °C. A saturated calomel electrode and a platinum electrode served as the reference and auxiliary electrodes, respectively. Treated and untreated samples formed the working electrode in such a way that only 1 cm² area of the working electrode surface was exposed to the electrolyte solution in corrosion cell.

Potentiodynamic polarization tests were carried out from -200 to + 500 mV vs OCP (open circuit potential) with a scan rate of 1 $mV.s^{-1}$. Measured potentiodynamic curves were analysed using Tafel fit by EC-Lab software.

The potentiodynamic polarization measurements were repeated at least three times, so that reproducibility of the test results was ensured.

3. Results and discussion

Electrodeposition under specified conditions led to the creation of a thin layer of calcium phosphate OCP (Fig. 2). As can be seen, the continuous layer covering the entire surface is composed of irregularly branched units that overlap each other. According to [5] the chemical composition of the observed layer is $Ca_8H_2(PO_4)_6.\ 5H_2O$.

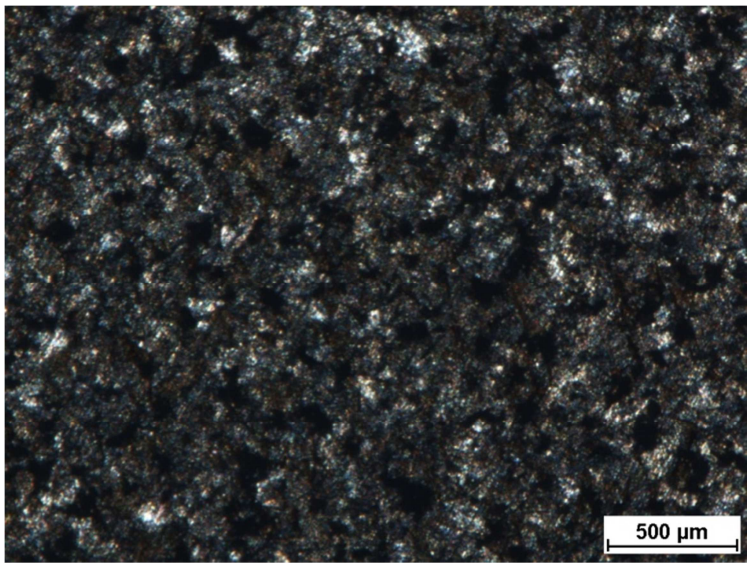

Fig. 2. Surface morphology of Elektron 21 after OCP electrodeposition

Measured potentiodynamic curves of Elektron 21 magnesium alloy samples before and after electrodeposition of calcium phosphate (OCP) are shown in Fig. 3. Based on the Tafel analysis performed by EC-Lab program V10.12 the values of corrosion potential E_{corr} and corrosion current density i_{corr} together with added values of corrosion rate r_{corr} are achieved. Particular obtained electrochemical characteristics are shown in Tab. 2. More positive corrosion potential value (-1509.6 mV) is observed on samples with the surface covered by OCP. Just grinded Elektron 21 magnesium alloy samples show the corrosion potential value E_{corr} = -1754.4 mV. These results demonstrate that the surface of tested magnesium alloy coated by OCP is electrochemically nobler and hence thermodynamically more stable. Moreover the samples coated by OCP show significantly lower values of i_{corr}. Untreated samples achieve the i_{corr} value of 154.8 $\mu A.cm^{-2}$, while samples with OCP achieve just 7.5 $\mu A.cm^{-2}$, that represents 21-fold reduction. This finding is very important for assessing the kinetics of corrosion, since corrosion current density is directly related to the corrosion rate and therefore tells us about the intensity of the ongoing corrosion process in the specific electrolyte. From this perspective, the application of OCP coating presents significant progress in terms of increasing the corrosion resistance of Elektron 21 surface layer.

Surface treatment	E_{corr} $[mV_{SCE}]$	i_{corr} $[\mu A.cm^{-2}]$	r_{corr} $[mm.y^{-1}]$
grinded surface	-1 754.4	154.8	7.08
surface with OCP coating	-1 509.6	7.5	0.34

Tab. 2. Electrochemical characteristics of Elektron 21 magnesium alloy surface after various treatments

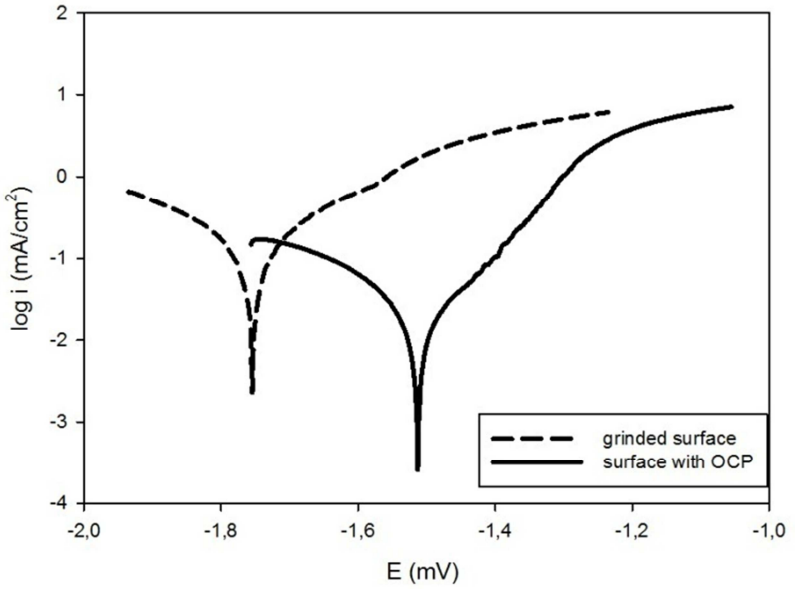

Fig. 3. Potentiodynamic curves of untreated and treated surfaces of Elektron 21 Mg alloy in 0.9% NaCl at 37±1 °C

4. Conclusions

On the basis of the measured data and analyses we concluded:

1. OCP layer created by electrodeposition continuously covers the entire surface of the substrate and is formed by irregular branched units that overlap each other.
2. Corrosion potential E_{corr} value (-1509.4 mV) of the surface covered by OCP is more positive compared to untreated samples (E_{corr} = -1754.4 mV).
3. Samples with OCP coating reach 21-fold reduction of corrosion current density i_{corr} compared to untreated samples.
4. Taking into account both electrochemical corrosion resistance criteria (thermodynamic and kinetic), the application of OCP coating presents significant progress in terms of increasing the corrosion resistance of Elektron 21 surface layer.

Acknowledgement

The research is supported by the European Regional Development Fund and the Slovak state budget by the project "Research Centre of the University of Žilina" - ITMS 26220220183. The part of the research were supported by SK-CZ cooperation project No. APVV-SK-CZ-2013-0046.

References

[1] ZHANG, X., LI, Q., LI, L., ZHANG, P., WANG, Z.,CHEN, F. *Fabrication of hydroxyapatite/stearic acid composite coating and corrosion behavior of coated magnesium alloy.* Mater. Letters. 2012, p. 76-78.

[2] ZHANG, CH. Y., ZENG, R. CH., CHEN, R.S., LIU, CH. L., GAO, J. CH. *Preparation of calcium phosphate coatings on Mg-1.0Ca alloy*. Trans. Nonferrous Met. Soc. China. 2010, p. 655-659.

[3] SÁNCHEZ-ENRÍQUEZ, J., REYES-GASGA, J. *Obtaining Ca(H2PO4)2.H2O, monocalcium phosphate monohydrate, via monetite from brushite by using sonication*. Ultrasonics Sonochemistry. 2013, p. 948-954.

[4] LORIMER, G., APPS, P., KARIMZADECH, H., KING,J. *Improving the performance of Mg- Rare Earth alloys by the use of Gd or Dy additions*, Materials Science Forum. 419-422, p. 279-284.

[5] SHADANBAZ, S. - DIAS, G. J. 2012. *Calcium phosphate coatings on magnesium alloys for biomedical applications: A review*. In Acta Biomaterialia. ISSN 1742- 7061, 2012, Vol. 8, no. 1, p. 20–30.

TRANSCOM 2015, 22-24 June 2015
University of Žilina, Žilina, Slovak Republic

The Effect of Heat Treatment on Structure Stability of AISI 316Ti

[*]Monika Oravcová, [*]Peter Palček, [*]Viera Zatkalíková, [*]Mária Chalupová
[*]University of Žilina, Faculty of Mechanical Engineering, Department of Materials Engineering, Univerzitná 1, 01026 Žilina, Slovakia, {monika.oravcova, peter.palcek, viera.zatkalikova, maria.chalupova}@fstroj.uniza.sk

Abstract. Austenitic stainless steels have been widely used in medical applications as an artificial knee and hip joint replacements, also for fracture healing aids as bone plates and screws, spinal fixation and many other usages in biomedical application. AISI 316Ti is austenitic Cr-Ni-Mo stainless steel stabilized with titanium which enables the usage in vivo medium. This steel is known due to its good corrosion resistance to most chemicals, salts and acids, because of the stabilizing element, and also due to its excellent mechanical properties. However when held on temperature 500 - 900°C sensitization occurs, chromium depletes and forms chromium carbides and the material is susceptible to intergranular corrosion. The aim of this article is to study the effect of heat treatment on structure stability of austenitic stainless steel stabilized with titanium.

Keywords: austenitic stainless steel, electrolytic etching, sensitization, chromium carbides, recrystallization.

1. Introduction

Biomaterials are materials used for making devices that can interact with biological systems. There are plenty of materials used in arthroplasty and orthopedics. It is important to choose the proper material by considering its mechanical behavior, chemical stability, biocompatibility and the corrosion resistance. Human body represents an aggressive environment, and so the implanted material can interact with this environment, which results in negative response to immune system. On the other hand, the aggressive environment can affect the properties of the implanted material as well. Some of the devices are intended to remain inside the body for a substantial period of time and some of them for long-term period [1].

Austenitic stainless steels are the most important group of corrosion-resistant metallic materials finding widespread not only in industrial but also in medical applications. Austenitic steels are characterized by their good combination of austenite and ferrite formers. They are alloyed with chromium, nickel, molybdenum and sometimes with copper, titanium, niobium and nitrogen. These steels have very good mechanical and technological properties combined with good corrosion resistance. However when a stainless steel is held at a temperature of 500 - 900°C, sensitization can occur because of chromium carbides exclusion at the grain boundaries. That means if the material is exposed to the environment containing chloride particles it might become susceptible to intergranular attack or intergranular stress corrosion cracking and to premature failure of the implanted material [2-4].

As mentioned earlier sensitization results from chromium depletion at the grain boundary and this is related to decrease in content of chromium below the level that is required for the stainless steel. Carbon normally stabilizes the austenite structure, but it has a great thermodynamic affinity to chromium. Because of this affinity, chromium carbides are formed [6]. If the carbides form a continuous network on the grain boundaries it may produce a separation or a gap at the boundary and may lead to grain loss. The loss of cross section thickness and the introduction of cracks can have severe consequences in practical applications [4].

Exclusion of chromium carbides tend to be localized at the grain boundaries because it is a high energy region and could be suggested that the increasing grain size increases susceptibility to

intergranular corrosion. So it could be assumed that in fine grained material there are more grain boundaries and therefore there is less chance for continuous network of carbides to be formed. [4]

2. Experimental procedures

The aim of this article is to evaluate the effect of the heat treatment on microstructure and structure stability.

2.1. Experimental material

As an experimental material Cr-Ni-Mo stainless austenitic steel stabilized by Ti was used. The specimens were cut from rectangular bars with dimension of 10x10x15 mm for the experiment. Quantitative chemical analysis of the steel is presented in **Tab.1**. Microstructure of the material in initial state is presented on **Fig.1**. The specimens were examined by optical microscope in longitudinal cut.

Steel/ elements	C (%)	Cr (%)	Ni (%)	Mo (%)	Mn (%)	Si (%)	S (%)	P (%)	Ti (%)
AISI 316Ti	0,03	17,83	10,62	2,36	1,54	0,44	0,03	0,06	0,14

Tab.1. Chemical composition of AISI 316Ti.

Metallographic analysis of longitudinal cross-section of the specimen in initial state after chemical etching in Kalling's (Fig.1 a-b) showed that the structure is non-homogeneous and have polyedric austenite grains with different grain sizes and occurrence of annealing twins and deformation martensite after plastic deformation as a result from the final treatment. There are a lot of black non-metallic inclusions (mainly oxides) in the line arrangement after deformation and titanium carbides of orange color. Size of the austenitic grains is between 10µm and 200µm.

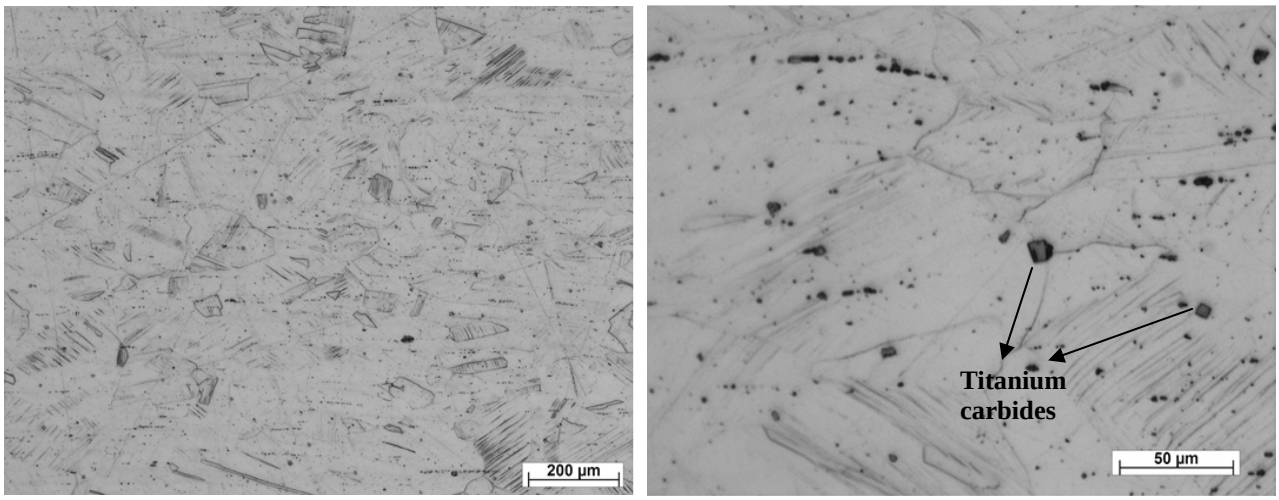

a) initial state b) detail of titanium carbides

Fig.1. Microstructure of AISI 316Ti, etched in Kalling's.

2.2. Heat treatment

Heat treatment was carried out in muffle furnace. One of the samples underwent recrystallization annealing at the temperature of 850°C for 15 minutes and followed by air cooling to reduce strength applied during cold-working as a result of plastic deformation. The other sample was sensitized at the temperature of 700°C for 10 hours followed by air cooling. The temperature and time were selected to reach the segregation of chromium carbides which are related to the phenomenon of sensitization.

2.3. Electrolytic etching

Generally it is required to evaluate austenitic stainless steel whether a fabricated component is sensitized and if it is susceptible to intergranular corrosion. For this purpose electrolytic etching is used. Electroetching involves the usage of a solution – electrolyte, an anode and a cathode (Fig. 2). In our case AISI 316Ti is the anode and is connected to the positive pole of a source of direct electric current. A piece of the same metal (austenitic stainless steel) is connected to the negative pole of the direct current source, which is our cathode. The anode and the cathode should be of the same metal to reduce unwanted electro-chemical effects. The distance between the cathode and the anode should be the smallest (app. 3 mm) as well and always the same because of the flow velocity. When the source is turned on, the metal of the anode (sample) is dissolved and converted into cations and at the same time an equal amount of cations from solution is reduced on the cathode.

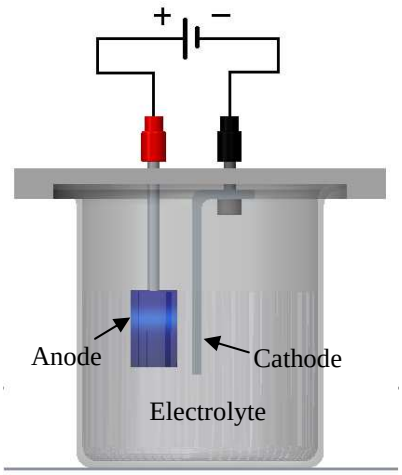

Fig.2. Scheme of electrolytic etching.

This etching test takes place in 10% oxalic acid solution (electrolyte) at room temperature at current density of 1 A/cm^2 for 90 s. Current intensity was 1.5 A according to the size of the sample's surface. The etched structures were investigated by optical and scanning electron microscope (SEM).

3. Results and discussion

Microstructures after heat treatment were metallographically prepared, chemically and electrolytically etched and examined by light and electron microscope.

Microstructures after recrystallization annealing are inhomogeneous, a presence of non-metallic inclusions and refinement of grains occurred because of the process where deformed grains were replaced by new set of grains. Microstructure after electroetching for 90 s shows that grain boundaries started to reveal, so we can assume that in the process of recrystallization chromium carbides were formed and during the etching they have dissolved (indicates the change of solution's color). Also titanium carbides started to showing off in the structure. After examination of 90 s electroetched microstructure, the sample was metalographically prepared again and electroetched first for 45 s and then for 10 s in oxalic acid and evaluated by electron microscope. It was determined that 10 s of electroetching was enough for AISI 316Ti to start revealing the grain boundaries as it is shown on the Fig. 3.

In the microstructure of AISI 316Ti after holding on temperature 700°C/ 10 hours, sensitization has occurred on grain boundaries as shown on the Fig. 4 after electroetching in oxalic acid. There are visible places (lines) of the layout after plastic deformation. Grain boundaries contain pits and the boundaries are revealed quite a lot, chromium carbides have dissolved during the etching process.

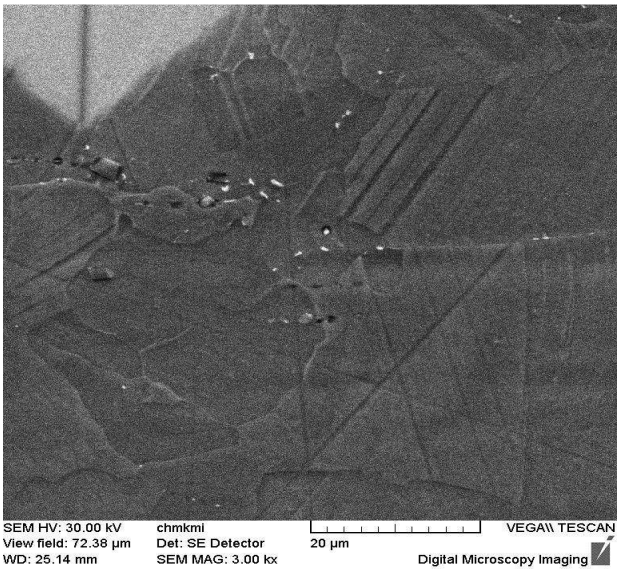

a) etched in Kalling's

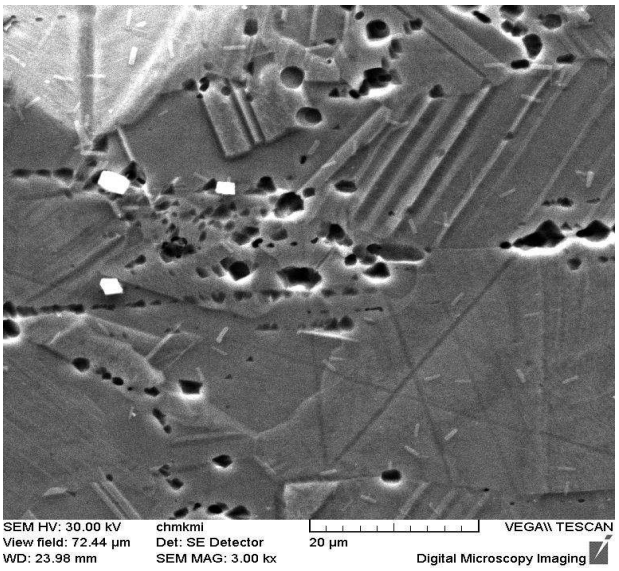

b) the same place but electroetched in oxalic acid for 45 s

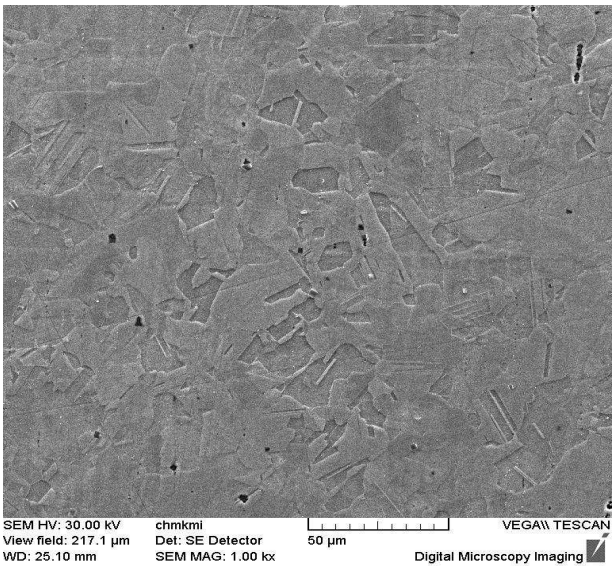

c) another place etched in Kalling's

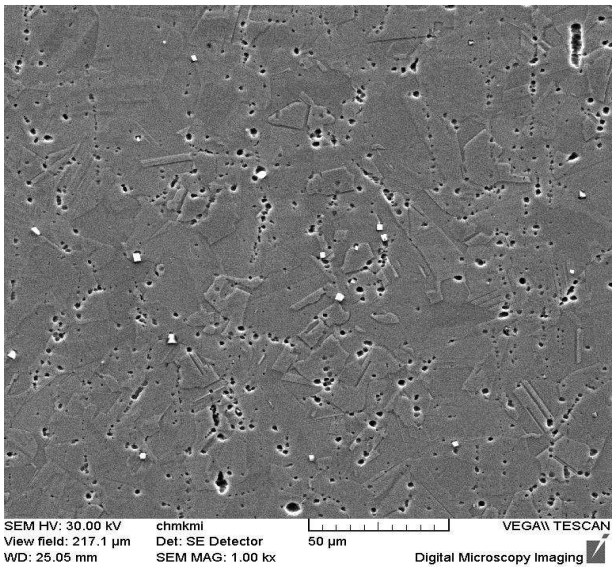

d) the same place electroetched in oxalic acid for 10s

Fig.3. Microstructures of AISI 316Ti, recrystallization annealing (SEM).

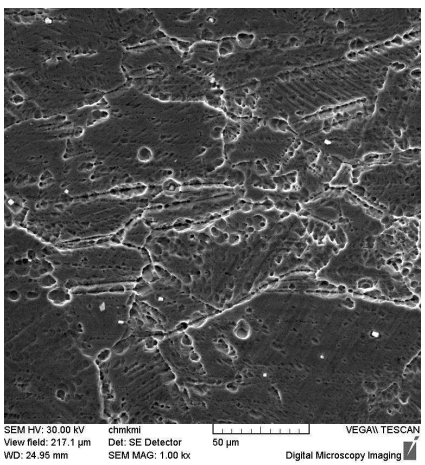

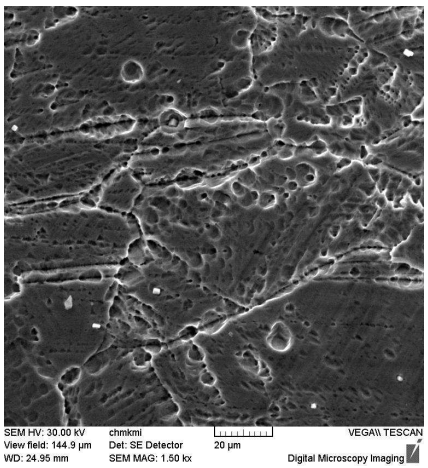

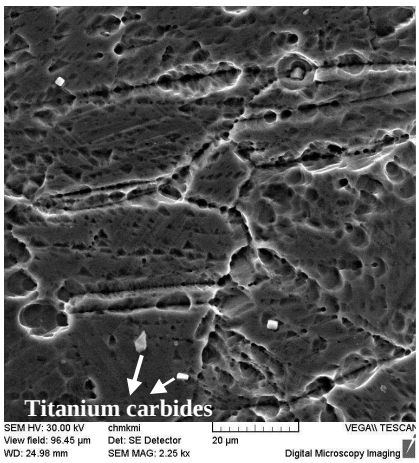

Fig.4. Microstructures of AISI 316Ti after sensitization, 700°C/10 hours, electroetched in oxalic acid for 90s, different magnification.

The addition of Ti should promote intergranular corrosion resistance of stainless steels because of the formation of titanium carbides. These carbides should reduce the formation of chromium carbides. It might be considered that titanium carbides may have fallen out from the structure during the electroetchig process and this probably may lower the corrosion resistance. This may lead to conclusion that the reduction of carbon content below 0,03wt. % improves sensitization resistance more than increasing the Ti content [4].

4. Conclusion

The results show following conclusions:

- After recrystallization annealing refinement of grains has occurred in the structure.
- After holding on temperature 700°C for 10 hours, sensitization has occurred on grain boundaries.
- With the increasing time of sensitization the more segregation appears and so grain boundaries are more revealed.
- The stabilizing element (Ti) does not suppress the segregation adequately.
- Electrolytic etching in oxalic acid started revealing grain boundaries after recrystallization annealing. That means the structure of AISI 316Ti is susceptible to sensitization more than for example steel with a low carbon content. This steel should undergo stabilizing heat treatment to avoid sensitization.
- Almost all the chromium carbides and inclusions were etched away or dissolved which means that surrounding of the carbide was depleted of chromium, thus corrosion resistance is reduced.
- Electrolytic etching revealed also titanium carbides and we can assume that etching could cause the loss of titanium carbides.

Acknowledgement

This work has been supported by Scientific Grant Agency of Ministry of Education of Slovak republic VEGA 1/0683/15 and project APVV SK-CZ-2013-0076.

References

[1] PARK, J.B., KIM, Y.K. *Biomaterials: Principles and Applications*: *Metallic Biomaterials.* CRC Press Boca Raton, 2003. ISBN 0-8493-1491-7.

[2] RASHID, M.W.A., GAKIM, M., ROSLI, Z. M., AZAM, M. A. *Formation of Cr23C6 during the sensitization of AISI 304 stainless steel and its effect to pitting corrosion*. International Journal of Electrochemical Science, volume 7, 2012. 9465-9477.

[3] LIMA, A. S., NASCIMENTO, A. M., ABREU, H. F. G., LIMA-NETO, P. *Sensitization evaluation of the stainless steel AISI 304L, 316L, 321 and 347.* Journal of Materials Science, volume 40, 2005.

[4] KHATAK, H.S. *Corrosion of austenitic stainless steels mechanism, mitigation and monitoring.* Woodhead Publishing Limited, Abington Hall, England, 2002. ISBN 1-85573-613-6.

[5] McGUIRE, M. F. *Stainless steels for design engineers.* ASM International, 2008. ISBN 978-0-87170-717-8.

[6] ČÍHAL, V. *Mezikrystalová koroze ocelí a slitin.* Praha: SNTL, 1984 (in Czech).

TRANSCOM 2015, 22-24 June 2015
University of Žilina, Žilina, Slovak Republic

Analysis of Boiling Heat Transfer on the Isothermal Surface Covered with a Single Copper Mesh

[*]Łukasz J. Orman, [**]Andrej Kapjor, [**]Jozef Hužvár
[*] Kielce University of Technology, Faculty of Environmental, Geomatic and Energy Engineering, Al.Tysiaclecia Panstwa Polskiego 7, 25314 Kielce, Poland, orman@tu.kielce.pl
[**] University of Zilina, Faculty of Mechanical Engineering, Department of Power Engineering, Univerzitna 2, 01026 Žilina, Slovakia, {andrej.kapjor, jozefhuzvar}@fstroj.uniza.sk

Abstract. Boiling heat transfer provides the opportunity to exchange considerably high heat fluxes at low temperature differences. The presented paper focuses on boiling heat transfer of distilled water and ethyl alcohol on the enhanced structure produced with the copper mesh. The nucleate boiling mode of heat transfer has been selected for analyses due to its application possibility in the design of heat exchangers. The results of experimental tests have been compared with selected models and correlations that can be found in literature. A modification of a specific correlation has been made in the paper to provide more accurate determination of the heat flux.

Keywords: boiling heat transfer, experimental correlations

1. Introduction

Boiling is a phase change phenomenon that enables to dissipate considerable heat fluxes at small temperature differences. Its practical applications are very wide and cover, among others, refrigeration systems or cooling of electronics. The following main modes can be considered depending on the heat flux: nucleate boiling (occurring at low temperature differences and characterised by the growth and departure of bubbles), film boiling (which is an unfavourable phenomenon with vapour film covering the heater and insolating it from the surroundings) and transition boiling. The nucleate boiling mode has the biggest potential for practical applications and it will be considered in this paper.

Although boiling itself is a highly efficient way of heat transfer, an increase in the values of transferred heat fluxes is still possible. It can be achieved with a number of different methods, however one of the most common is the surface modification, for instance with coatings of different design. One of the techniques to produce efficient phase change heat exchanging surfaces is the application of metal meshes on smooth surfaces. Such coatings should be durable in order to sustain mechanical vibrations and even stresses over long periods of time. They can be manufactured in the process of sintering (as the samples analysed in the present paper), which is done in the reduction atmosphere so that oxidation could be avoided.

One of the first works on boiling heat transfer on microstructural coatings is the paper by Sasin et al. [1]. The authors analysed heat transfer of water, ethyl alcohol and ether in heat pipes covered with steel and brass meshes. It was reported that for the certain number of mesh layers there exists the optimal value of aperture (distance between the wires), for which the maximal critical heat flux can be obtained. Asakavičjus et al. [2] considered R-113, ethyl alcohol and water as working fluids for heat pipes covered with steel and copper meshes of different aperture and number of layers. The microstructure proved to increase the heat transfer in relation to the smooth surface. The effect became lower as the heat flux rose. It was reported that during water boiling heat transfer coefficient was 1,8 – 3,5 larger than for ethyl alcohol. Rannenberg and Beer [3] observed enhancement of boiling heat transfer of R-11 and R-113 on mesh covered heaters. The analysed meshes were made of bronze, steel and copper. The improvement caused by the application of

meshes was especially visible for low temperature differences of a few Kelvin. What is more, the authors did not notice any impact of the height of the structure (related to the number of applied meshes). Tsay et al. [4] found out that the use of the mesh augmented heat transfer comparing to the smooth surface at the temperature difference of over 6 K. The authors investigated boiling of water on steel meshes. The meshes had aperture of 0.338 – 1.2875 mm and wire diameter of 0.17 – 0.3 mm. Li et al. [5] confirmed that the application of meshes enhances boiling heat transfer. They analysed water boiling on mesh covered copper heater under ambient pressure. 2 to 9 layers of meshes were used to produce the samples. The wire diameter was 0.056 mm and the height ranged from 0.21 to 0.82mm. Li and Peterson [6] focused on heat transfer on meshes of wire diameter from 56 to 191μm and aperture from 119.3 to 232.8 μm. The small impact of porosity of the microstructures was observed, while their application enhanced boiling as compared to the smooth surface.

2. Heat transfer analysis

The analysis of the boiling heat transfer will be conducted on the copper mesh of wire diameter 0.25mm and aperture 0.50mm. A single layer of mesh has been applied on the horizontal copper block which acts as a heating surface with heat provided by an electric cartridge resistance heater. The experimental data points have been obtained for rising heat flux. This raw data has been presented by one of the authors in [7] and is given in Fig. 1 for distilled water and ethyl alcohol as boiling curves. A boiling curve is a dependence of heat flux (q) vs. temperature difference of the heater surface and the saturation temperature (θ).

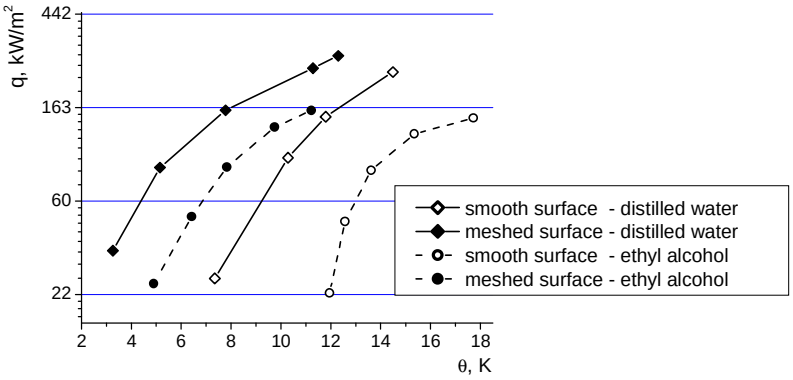

Fig. 1 The boiling curves for the meshed and smooth surfaces as in [7] for distilled water and ethyl alcohol.

The above figure indicates a considerable enhancement of heat transfer caused by the application of the mesh for both boiling agents. The analysis of the boiling curves for distilled water leads to a conclusion that the heat flux dissipated from the microstructure coated surface can be about six times higher than for the smooth surface (for low temperature differences). Consequently, heat exchangers can be much smaller and still enable to exchange the same heat flux. Moreover, boiling begins at lower temperatures, which is another advantage. This phenomenon is much more visible for ethyl alcohol. In this case the boiling curve for the mesh coated surface is shifted to the left. As a result, the same heat flux can be transferred at much lower temperature differences, which is very favourable.

Another issue to consider, which is especially vital for the design of heat exchangers, is a precise determination of heat flux as a function of the parameters of the microstructures. The data from Fig. 1 has been compared with correlations chosen from the literature. The ones provided by Smirnov et al. [8, 9, 10], Nishikava et al. [11] and Xin and Chao [12] are applied for comparison. For calculations with the model by Xin and Chao, some modifications need to be made - namely, a cell width is taken as the total of the value of wire diameter and aperture and the tunnel width as

mesh aperture. Fig. 2a and 2b present the calculation results for distilled water and ethyl alcohol, respectively.

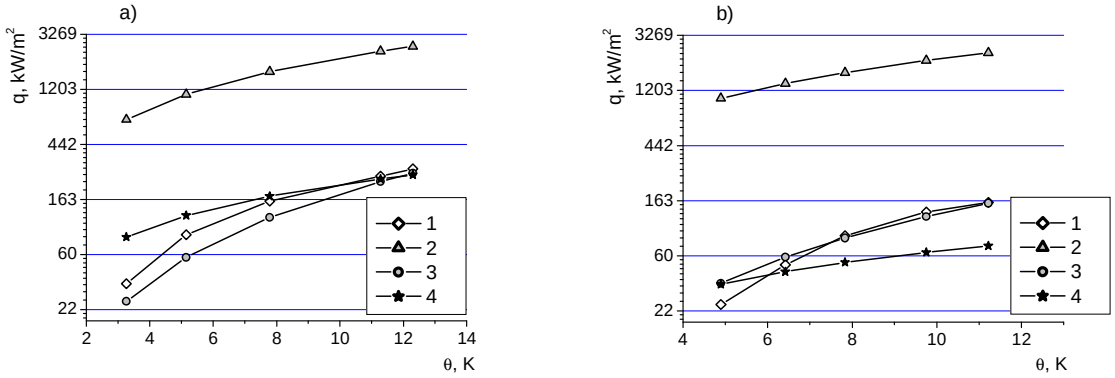

Fig. 2 Calculation results according to chosen correlations; a - distilled water, b – ethyl alcohol; where 1 - experimental results [7], 2 – calculations according to Nishikava et al. [11], 3 - calculations according to Xin and Chao [12], 4 – calculations according to Smirnov et al. [8, 9, 10].

As can be seen in the above figures, none of the correlations gives the accurate results for the analysed mesh layer for both fluids in the whole range of temperature differences. The largest discrepancies occur for the model of Nishikava et al. [11], in which heat flux is determined with the simple conduction equation. Here, the effective thermal conductivity (λ_m) takes into account porosity (ε) and thermal conductivity values of the boiling liquid (l) and solid mesh material (s) as:

$$\lambda_m = \varepsilon\lambda_l + (1-\varepsilon)\lambda_s . \quad (1)$$

The largest source of possible errors (as seen in Fig. 2) might be the value of effective thermal conductivity. As presented in [13] this value can be determined with different equations depending on the location of the solid phase in relation to the heat flow. If the solid material in a two - phase system is oriented in the heat flow direction, the conductivity is determined with (1). However, if it is in the perpendicular direction the conductivity can be determined as [13]:

$$\lambda_\perp = \frac{\lambda_l\lambda_s}{(1-\varepsilon)\lambda_l + \varepsilon\lambda_s} . \quad (2)$$

In mesh microstructures relative location of the solid material is complex. In this case the effective thermal conductivity should not be determined with (1) but rather with another formula, e.g. [13]:

$$\lambda_{eff} = \lambda_m^F \lambda_\perp^{1-F} . \quad (3)$$

Based on the research data for both water and ethyl alcohol, the value of F has been determined during calculations and equals 0.421. Fig. 3 presents the comparison of the experimental data and calculations results for the modified correlation of Nishikava et al. [11], which considers (3).

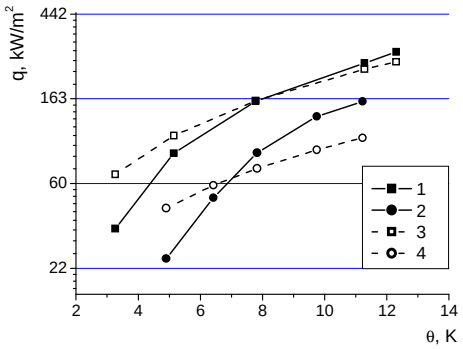

Fig. 3 The comparison of experimental data [7] for 1 - distilled water and 2 - ethyl alcohol with calculated results (3 - distilled water, 4 - ethyl alcohol).

The congruence of the data and calculation results is much better with the modified model than the original one. It is especially visible in the case of water boiling. Another issue is the inclination of the boiling curves, which cannot be adjusted with the effective conductivity value.

3. Conclusion

Boiling heat transfer is a highly efficient way of heat exchange. The use of metal coatings made from meshes enhances the transfer of heat in relation to the smooth surface. This improvement is most visible for small temperature differences and becomes less pronounced for higher ones. The comparison of experimental data with correlations leads to a conclusion that a modification should be considered. Such an alternation to a selected correlation has been proposed to enable better determination of the heat flux for the considered copper mesh.

The practical application of phase change phenomenon in the analysed mesh coatings is crucial due to their use in many areas of technology and engineering for example in heat pipes, which are highly efficient heat exchangers [14] or other systems [15, 16].

Acknowledgement

This article was elaborated within the solution of project KEGA č.026ŽU-4/2014 „The heat transfer from the heat exchange surfaces”

[1] SASIN, V.Ja., FEDOROV, V.N., SOROKIN A.Ja. *Eksperimentalnoe issledovanie teplovoj trubki na legkokipjaščich teplonositeljach*, Doklady Naučno-Techn. Konf. po Itogam Naučno-Issled. Rabot za 1968-69, MEI, pp. 79 – 84, 1969.

[2] ASAKAVIČJUS, I.P., ŽUKAUSKAS, A.A., GAJGALIS, V.A., EVA, V.K. *Teplootdača freona-113, etilovogo spirta i vody v setčatych fitiljach*, Lietuvos TSR Moksly akademijos darbai, B serija, I (104), pp. 87 – 93, 1978.

[3] RANNENBERG, M., BEER, H., *Heat transfer by evaporation in capillary porous wire mesh structures*, Letters in Heat and Mass Transfer, vol. 7, pp. 425 – 436, 1980.

[4] TSAY, J.Y., YAN, Y.Y., LIN, T.F. *Enhancement of pool boiling heat transfer in a horizontal water layer through surface roughness and screen coverage*, Heat and Mass Transfer, 32, pp. 17-26, 1996.

[5] LI, C., PETERSON, G.P., WANG, Y. *Evaporation/boiling in thin capillary wicks (I) – wick thickness effects*, Journal of Heat Transfer, vol. 128, pp. 1312 – 1319, 2006.

[6] LI, C., PETERSON, G.P. *Evaporation/boiling in thin capillary wicks (II) – effects of volumetric porosity and mesh size*, Journal of Heat Transfer, vol. 128, pp. 1320 – 1328, 2006.

[7] ORMAN, Ł.J. *Boiling heat transfer on single phosphor bronze and copper mesh microstructures*, EPJ Web of Conferences 45, Experimental Fluid Mechanics 2013 Conference Proceedings, Czech Republic, 2014.

[8] SMIRNOV, G.F. *Približennaja teorija teploobmena pri kipenii na poverchnostjach pokrytych kapilljarno – poristymi strukturami*, Teploenergetika, 9, pp. 77 – 80, 1977.

[9] SMIRNOV, G.F., COBA, A.L., AFANASIEV, B.A. *The heat transfer by boiling in splits, capillaries, wick structures*, AIAA Paper, pp. 78 – 461, 1978.

[10] SMIRNOV, G., Afanasiev, B.A. *Investigation of vaporisation in screen wick – capillary structures*, in Advances in Heat Pipe Technology, Proc. of VI Int. Heat Pipe Conference, London, pp. 405 – 413, 1982.

[11] NISHIKAWA, K., ITO, T., TANAKA K. *Enhanced heat transfer by nucleate boiling on a sintered metal layer*, Heat transfer – Japanese Research, vol. 8, pp. 65 – 81, 1979.

[12] XIN, M.-D., CHAO, Y.-D. *Analysis and experiment of boiling heat transfer on T-shaped finned surfaces*, Chem. Eng, Comm., vol. 50, pp. 185 – 199, 1987.

[13] SINGH R., KASANA, H.S. *Computational aspects of effective thermal conductivity of highly porous metal foams*, Applied Thermal Engineering, 24, pp. 1841-1849, 2004.

[14] NEMEC, P., ČAJA, A., MALCHO, M. *Testing thermal properties of the cooling device with heat pipes*, EPJ Web of Conferences 45, Experimental Fluid Mechanics 2012 Conference Proceedings, Czech Republic, 2013.

[15] PASTUSZKO, R. *Pool boiling on micro-fin array with wire mesh structures*, International Journal of Thermal Sciences, 49 (12), pp. 2289-2298, 2010

[16] PASTUSZKO, R. *Pool boiling for extended surfaces with narrow tunnels - Visualization and a simplified model*, Experimental Thermal and Fluid Science, 38, pp. 149-164, 2012

TRANSCOM 2015, 22-24 June 2015
University of Žilina, Žilina, Slovak Republic

Analysis of Weld Joints of the Split Sleeve for Branch Connections Repairs

[*]Marek Patek, [*]Miloš Mičian, [*]Augustín Sládek
[*]University of Žilina, Faculty of Mechanical Engineering, Department of Technological Engineering, Univerzitná 1, 010 26 Žilina, Slovakia, {marek.patek, milos.mician, augustin.sladek}@fstroj.uniza.sk

Abstract. Weld joints analysis belongs to the most important factors that ensures safety and reliability of the pipelines for gas transmission. Importance of non-destructive and destructive testing is even more significant when repairing methods is applied. Presented article deals with macrostructural and hardness analysis of the characteristic weld joints of the split sleeve designed for branch connections repairs. Results shows that manufacturing process of the semi-product and also final parts of the sleeve is very crucial to final quality of welds even for materials with ensured weldability.

Keywords: Split sleeve, weld joint, destructive testing, macrostructural analysis, Vickers hardness.

1. Introduction

Quality of weld joints is very important factor to ensure safety and long term lifetime of the gas transport pipelines. According to European Gas Pipeline Incident Data Group (EGIG) are construction defects (where weld joint defects also belongs) and material failures the third most frequent cause of the pipeline incidents [1]. Welding quality control is thus important and every new type of weld joint has to be analyzed by non-destructive and it also should be tested by destructive testing methods.

Numerous kinds of repair techniques are now available including the cut out and replace of the pipeline, construction of the bypass along the damaged area, grinding, weld deposition, metallic or composite sleeves [2]. Although the repairing techniques for straight parts of pipelines are well established, only a few of them is applicable for branch connections defects (for ex. defects in the area of fillet weld between header and branch pipe). Recently a new kind of split sleeve for such defects repairs has been designed [3, 4]. Relatively complicated construction together with different manufacturing processes of sleeve parts might cause weld joint problems and precise weld examination is necessary. Non-destructive examination of weld joints has been proposed by ultrasonic technique TOFD [5] but destructive testing of such welds has not been proposed yet.

The aim of presented article is to perform the destructive testing of weld joints on split sleeve for branch connection repairing. Macrostructural analysis and hardness evaluation is presented together with selected base metal properties examinations.

2. Experimental measures

Weld joint analysis has been performed on the split sleeve for branch connections repairs (Fig. 1). Split sleeve is formed by cylinder part and sphere-like parts, which has to ensure safely installation of the sleeve to the repaired branch connection. Such type of split sleeve is joined together by butt welds and to the repaired pipes it is connected by circumferential fillet welds.

Different manufacture processes and also semi-finished products were applied to parts of the sleeve. Cylindrical part was prepared by welding of end plates to thick-walled pipe (thickness of 16 mm for each part). Both end plates are made of S355J2+N steel and material of the thick-walled pipe is S355J2H steel. Sphere-like parts are made by machining of S355JR steel block to required

shape and size. Machined part was after that split to two segments. Materials used in this type of construction have ensured weldability without additional conditioning.

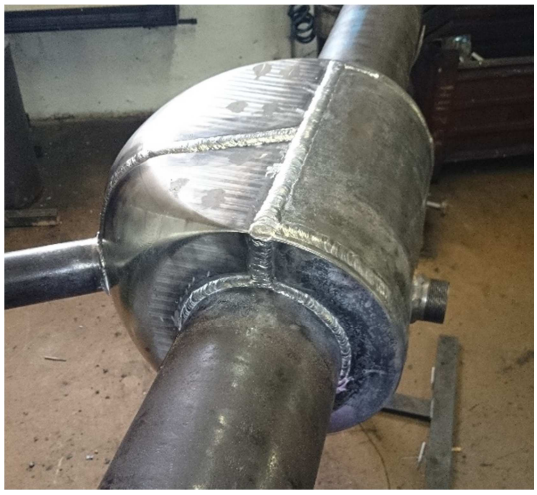

Fig. 1. Split sleeve for branch connection repairs.

2.1. Macrostructural analysis of weld joints

Macrostructural analysis of the split sleeve weld joints was performed in terms of the EN ISO 4136 standard. Four characteristic welds has been chosen to analysis. Macrographs of the butt weld joints are shown in Figs. 2 and 3. No defects has been detected neither on the macrographs of the butt joint between cylindrical and sphere-like part (Fig. 2) nor in the macrograph of weld joint between sphere-like segments of the sleeve (Fig. 3). In the lower part of the Figs. 2 and 3 a sealant carriers can be seen, which serve to carry a sealants that isolates the places of welding from places where leaking gas is present. Very large size of the root opening can be seen between the sealant carrier and wall of the sleeve in macrograph shown in Fig. 3. Weld joint between the sealant carrier and split sleeve wall are only supplementary and after the sleeve is welded onto the pipeline, it has no function. In the fig. 2, a difference between the base metal structure of cylindrical part and sphere-like part can be observed. This difference is also expressed in heat affected zone (HAZ), where a dark color of HAZ can be seen on the sphere-like part side of the weld joint. This might be a sign of ineligible microstructure and higher hardness of the HAZ, which might cause problems during the split sleeve lifetime.

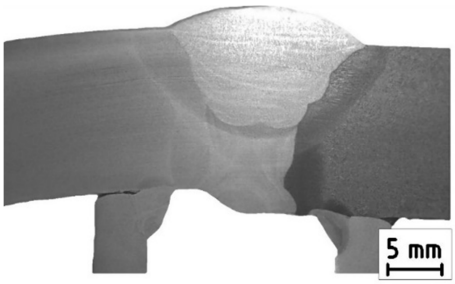

Fig. 2. Macrograph of butt weld joint between cylindrical (left) and sphere-like (right) part of the sleeve.

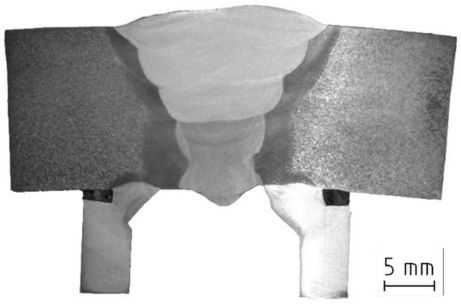

Fig. 3. Macrograph of butt weld joint between sphere-like parts of the sleeve.

Typical macrographs of the girth fillet welds are shown in Figs. 4 and 5. Fillet welds do not show the presence of unacceptable defects similarly to the butt welds. Heat affected zone on the side of the sphere-like part also pointed to darkening of this area (Fig. 4) and it might be a sign of hard and brittle microstructure.

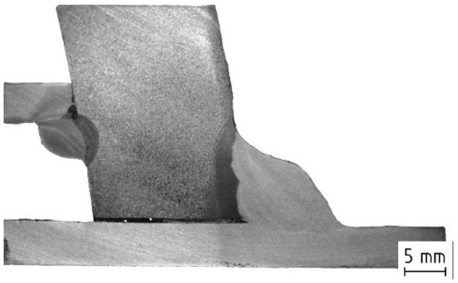

Fig. 4. Macrograph of fillet weld joint between sphere-like part of the sleeve and pipe.

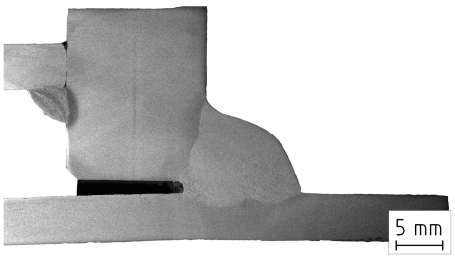

Fig. 5. Macrograph of fillet weld joint between cylindrical part of the sleeve and pipe.

2.2. Hardness measuring

Vickers hardness method was used to evaluate the weld joints hardness. Measuring was performed in terms of EN ISO 9015-1 standard. Significant increase of Vickers hardness can be seen in HAZ of the weld on the sphere-like side of weld joint (Figs. 6 to 8). In this areas hardness reaches values higher than 300 HV and in some cases it almost reached maximal allowed value for this type of material (380 HV without heat treatment according to EN ISO 15614-1 standard). Hardness of weld joint on the side of cylindrical part of the sleeve do not significantly increased in HAZ (Fig. 6, 8 and 9).

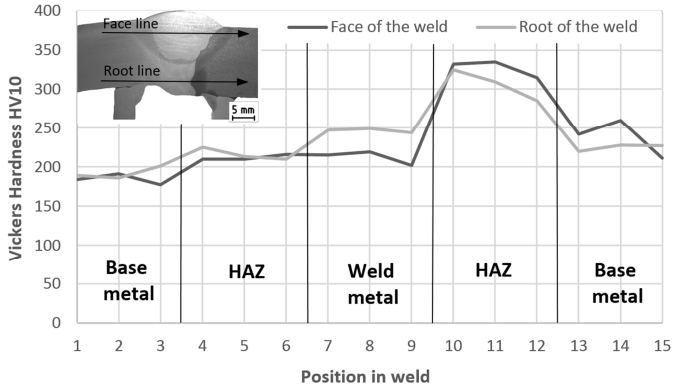

Fig. 6. Hardness of butt weld joint between cylindrical and sphere-like part of the sleeve.

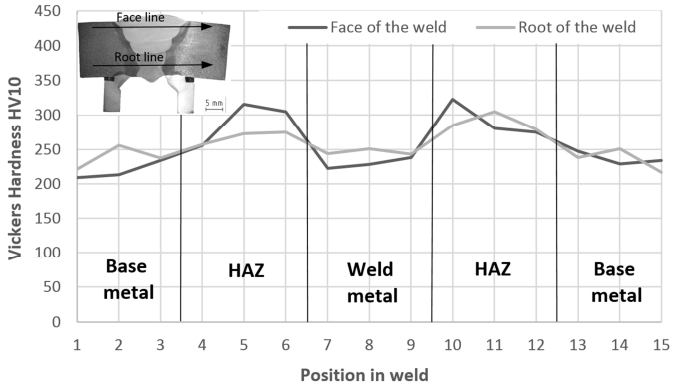

Fig. 7. Hardness of butt weld joint between sphere-like parts of the sleeve.

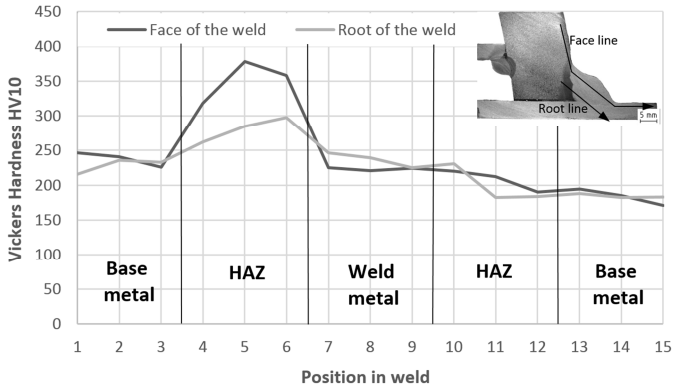

Fig. 8. Hardness of fillet weld joint between sphere-like part of the sleeve and pipe.

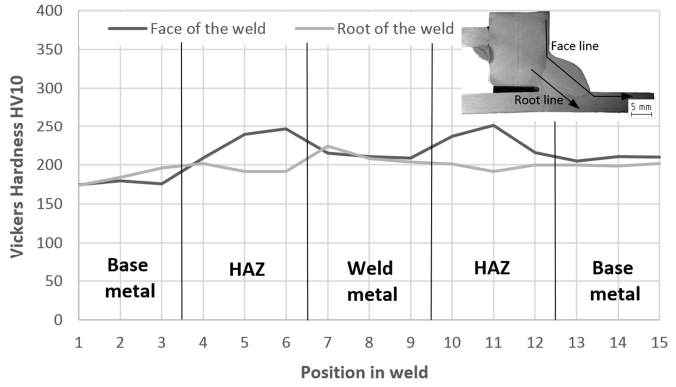

Fig. 9. Hardness of fillet weld joint between cylindrical part of the sleeve and pipe.

2.3. Approval of the sphere-like parts base metal mechanical properties

Macrostructural analysis and hardness measuring pointed out to possibility of insufficient base metal quality or to completely material interchange of sphere-like segments of the split sleeve. Tensile properties and impact toughness of base metal were analyzed to prove material quality.

Ultimate tensile strength, Yield strength and elongation was measured by tensile testing procedure according to directions of EN ISO 6892-1 standard. Three tensile specimens with diameter of 10 mm were prepared and loaded to fracture at the ambient temperature of 20 °C. Comparison of average value after measuring and values from material data sheet of S355JR steel is shown in Tab. 1.

	Yield strength R_{eH} [MPa]	Tensile strength R_m [MPa]	Elongation A_5 [MPa]
Tensile test	332	516	3
Data sheet values	275	450-630	17

Tab. 1. Comparison of tensile properties after measuring and values from material data sheet.

Tensile strength and Yield strength corresponds with data sheet requirements but elongation obtained from tensile test is evidentially insufficient.

Charpy pendulum impact test was used to determine impact toughness of the sphere-like part of the sleeve. Conditions of the testing method are defined in the international standard EN ISO 148-1. Experimental samples with V-notch, cross-section size of 10 x 10 mm and 55 mm length were used to testing. Measuring of impact energy was performed at ambient temperature -20 °C. Average value of impact energy KV obtained by three measures is 6.7 J while required value is minimum 27 J. Material thus do not satisfy impact toughness and its ductility is insufficient.

3. Discussion

Macrostructural and hardness evaluation of the weld joints of split sleeve for branch connection repairing was performed on four characteristic welds. Significant difference between material behavior after etching on cylindrical and sphere-like part was observed during macrostructural analysis. Dark color of the base metal on the sphere-like part of the sleeve is a sign of inappropriate microstructure that is in mismatch with expected microstructure for low alloyed carbon steel. Vickers hardness of sphere-like part of steel base metal shows higher values than expected and it is evidentially higher than in base metal of the cylindrical part made of similar material.

In HAZ zone of the weld on the sphere-like side is the effect of microstructure affected by the welding process and it might cause even more negative effect. It has been shown by hardness results where maximal hardness values (378 HV) almost reached maximal allowed value for such kind of material (380 HV). This effect is the most evident on the girth fillet welds between the pipe and sphere-like part of the sleeve. During the welding of fillet weld higher amount of heat is driven to sleeve because of its higher wall thickness compared to thickness of the pipe. Welding and cooling conditions then leads to increased cooling rate in HAZ of the fillet weld on the sleeve side and increasing of the Vickers hardness. This effect together with inhomogeneous material properties of welded parts might lead to exceeding of the hardness tolerance.

As the microstructure of the sphere-like part of the split sleeve seems to be inappropriate to chosen material, selected mechanical properties has been measured. Tensile and Yield strength of the base metal has been within the range of data sheet for S355JR steel. On the other hand, ductility properties of the analyzed material has been completely below expectations. Elongation reached average value of 3 % instead of minimal required 17 % and impact energy 6.7 J instead of 27 J. This results are probably influenced by manufacturing process of the semi-product used to production of sphere-like part of the sleeve. As the semi-product was large size steel block (dimensions 400 x 800 x 400 mm) from low-alloyed steel, the material properties can be after prefabrication very inhomogeneous. This might lead to different microstructure and mechanical properties in the center of the block as in its edges. To obtain homogeneous microstructure and properties across the part a full annealing is necessary.

4. Conclusions

Several conclusion can be stated from the results of the weld joint analysis performed on split sleeve for branch connections repairing as follows:

(1) Very unbalanced microstructure of the base metals and HAZ on the sides of the weld can be obtained when different manufacturing techniques of the split sleeve parts is employed.
(2) Base metal Vickers hardness of the sleeve part made of steel block can reach evidentially higher values compared to part made from thick-walled pipe.
(3) Hardness of HAZ can on the machined part reach values that are near the limits for the used material after standard welding procedure.
(4) Insufficient base metal mechanical properties might be measured when sphere-like part of the sleeve is made from steel block without heat treatment due to semi-product inhomogeneity.
(5) Sphere-like part of split sleeve should be made from homogeneous material and/or the full annealing of the machined part is necessary to obtain required material properties.

Acknowledgement

This work has been supported by Scientific Grant Agency of Ministry of Education of the Slovak Republic, grants VEGA 1/0610/12 and KEGA 034ŽU-4/2015. Authors acknowledge the grant agency for support.

References

[1] EUROPEAN GAS PIPELINE INCIDENT DATA GROUP (EGIG). *Gas pipeline Incidents. 9th Report of the European Gas Pipeline Incident Data Group (period 1970 – 2013)*, 2014.

[2] BATISSE, R. *Review of gas transmission pipeline repair methods.* Safety, Reliability and Risks Associated with Water, Oil and Gas Pipelines. Dordrecht: Springer, 2007.

[3] MIČIAN, M., PATEK, M., SLÁDEK, A. *Concept of repairing branch pipes on high-pressure pipelines by using split sleeve.* Manufacturing Technology, Vol. 14, No. 1, 2014.

[4] MEŠKO, J., FABIAN, P., HOPKO, A., KOŇÁR, R. *Shape of heat source in simulation program SYSWELD using different types of gases and welding methods*. Strojírenská technologie, č. 5, 2011.

[5] PATEK, M., KONAR, R., SLADEK, A., RADEK, R. *Non-destructive Testing of Split Sleeve Welds by the Ultrasonic TOFD Method*. Manufacturing Technology, Vol. 14, No. 3, 2014.

TRANSCOM 2015, 22-24 June 2015
University of Žilina, Žilina, Slovak Republic

Operation and Measuring the Emissions of the Fuel Cell

[*]Marek Patsch, [*]Jaroslav Čierny
[*]University of Žilina, Faculty of Mechnical Engineering, Department of Power Engeneering, Univerzitna 1, 010 26 Žilina, Slovakia, {marek.patsch, jaroslav.cierny}@fstroj.uniza.sk

Abstract. This article is addressed to describe new technologies to supply buildings with heat and electricity. We have at our department as the first in Slovakia SOFC (ceramics) type of fuel cell. The article will describe the experiments relating to the operation of fuel cell. Subsequently, the article deals with the issues of emissions compare to the conventionally available technologies.

Keywords: high temperature ceramic fuel cell, natural gas, emissions, micro-cogeneration

1. Introduction

A fuel cell is an electrochemical device, which with the assistance of a redox reaction directly converts chemical energy of fuel into electrical energy. A fuel cell consists of two electrodes (anode and cathode) separated by an electrolyte or ion-exchange membranes. All fuel cells types are different by material used for the electrodes, the working temperature and the associated fuel purity.

In a fuel cell that uses pure hydrogen as fuel and oxidant, such as oxygen from the air, to the cathode, is reduced to an oxygen anion O^{-2}. Oxygen atoms O^{-2} passes through the electrolyte to the anode, where it combines with hydrogen and simultaneously release two electrons. The cathode and anode are connected by an electrical conductor, which lead these two free electrons to the anode where the oxygen intake again. This process produces a DC electric current and at the end of the reaction water and heat are formed.

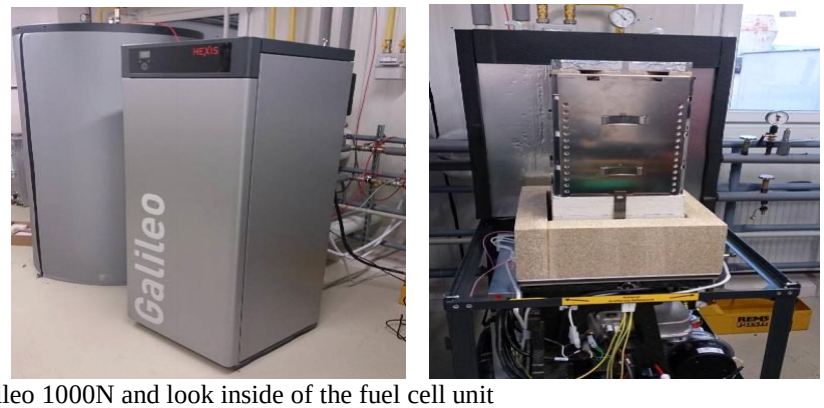

Fig. 1 SOFC Hexis Galileo 1000N and look inside of the fuel cell unit

2. Micro-cogeneration unit Hexis Galileon 1000N

Nowadays we don't have any fuel cell units in Slovakia market and therefore the first in Slovakia we can boast by ceramic fuel cell type with high operating temperature 800 – 1000°C. This unit was installed at the Department of Power engineering at University of Žilina. In experimental operation of Swiss manufacturer Hexis, type Galileo 1000N see figure 1 based on SOFC technology with following parameters:

- Operating temperature of unit 820/870°C
- Electrical power up to 1000 W

- Heat output SOFC 1,8 – 3,3 kW with auxiliary burner 7 – 20 kW
- Fuel CH4 gained by partial oxidation of natural gas

For normal operation at home in Slovakia is a unique technology, so we have undergone a fuel cell unit by series of measurements and research. We focused primarily on electric and thermal power, efficiency, fuel consumption and emissions. Measurements were performed by hookup shown in figure 2.

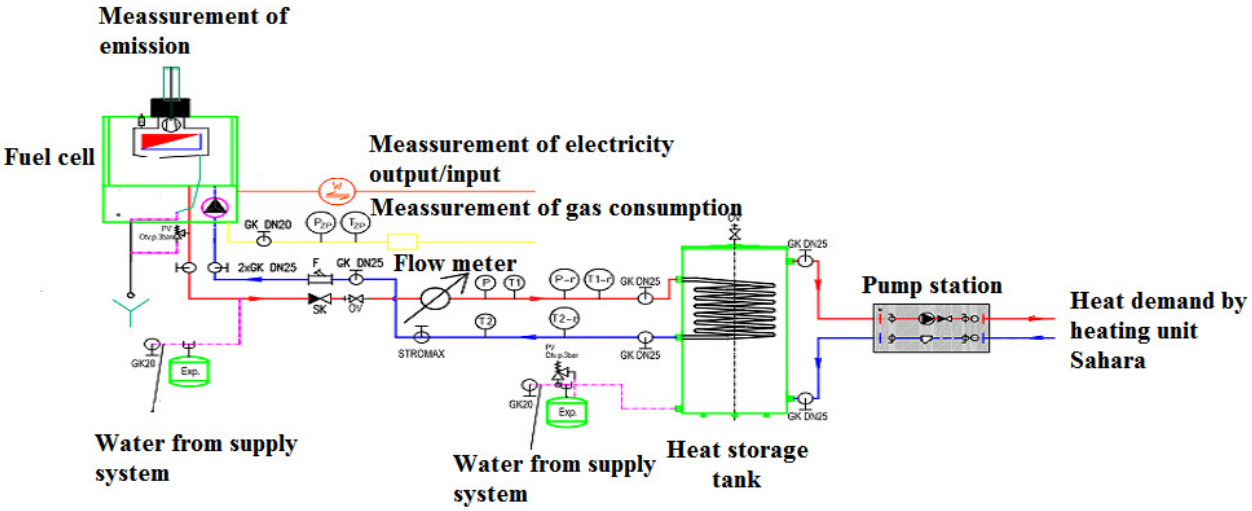

Fig. 2 Hookup of SOFC unit Hexis Galileo at University of Žilina

3. Design of house which simulates real behavior of heat demand in Slovakia

To examine the real operation of SOFC unit we have to design in the program TechCON house for 4 member family, which was located in Žilina. According to the STN we have calculated all the necessary parameters such as. heat loss (10.8 kW), the number of heating days (242), outside measurement temperature (-17 ° C), average temperature depends on the altitude (350 m), which are necessary to calculate the annual (81 GJ / year + 32 GJ / year TV), monthly and hourly heat requirement under which the measure will be implemented. We cooperated with Žilina heating plants, which gave us a real temperatures during the whole year 2014.

As we can see on figure 3 the need for heating varies during the year, depending on the outside average temperature, but demand of the heat water is constant during year.

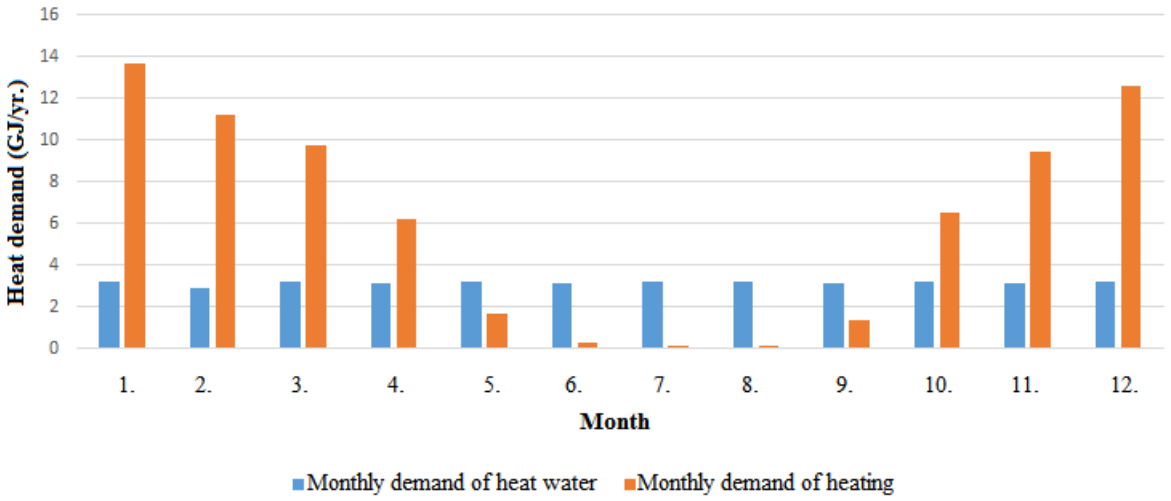

Fig. 3 Monthly demand of heat in designed house

Investigation of transients of running SOFC was provided by conventional phenomena that can occur in a family designed house, for example: power on unit, turn off unit, failure of gas supply etc. We found that achieving operational temperature of 870 ° C takes about 6 hours or more and electricity production occurs in approximately 14 hours after starts, see on figure 4. This is main disadvantage in terms of need for additional sources of electricity from an external supplier.

When we set outside temperature to -17 ° C (equithermically) in the software program of SOFC so in long-term operation were meassured values that we can see in figure 5. A fuel cell electrical performance was ranged from 900 W - 1100 W, with step-down efficiency due to worn electrode material of SOFC. Improve performance was ensured by upgrading software and by increasing operating temperature of fuel cell from 820 °C to 870 °C.

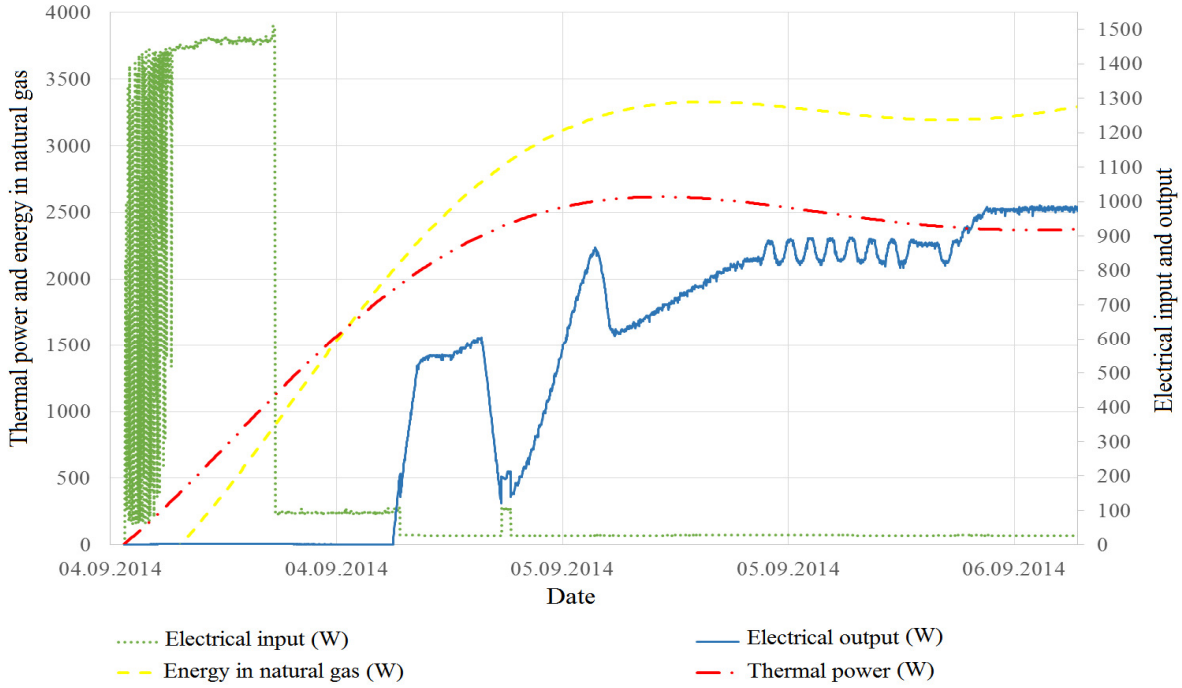

Fig. 4 Start of Hexis Galileo 1000N

Fig. 5 Long-term operation of SOFC

On the Hexis was meassured emissions (by EN 297) through a portable gas analyzer based on infrared sensors Photon II. so I briefly mentioned that emissions were lower than for operation conventionally available condensing boiler see fig. 6. When was condensing boiler powered-on we

also observed certain amount of Sirius, which when running only SOFC, fuel were processed through different filters and desulfurizator.

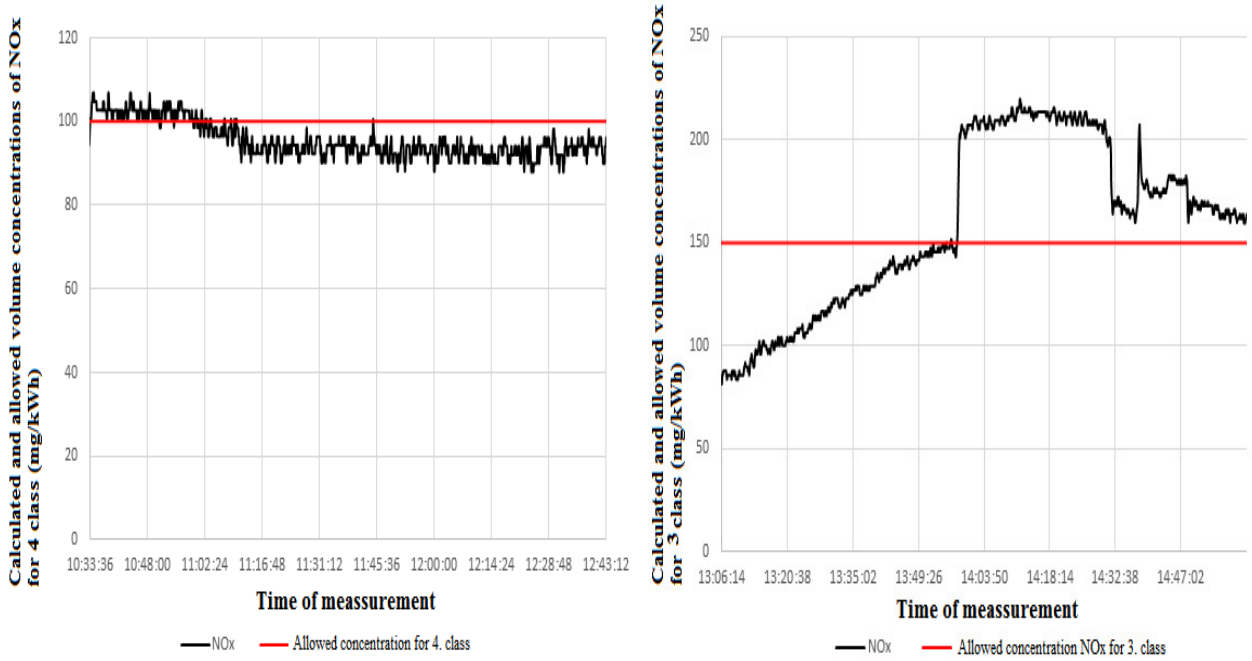

Fig. 6 Meassured and allowed emission of NOx of fuel cell and condensed boiler by EN297

4. Conclusion

Micro-cogeneration units based on fuel cell may be a revolutionary technology, but the Slovak market does not compete as an energy source. The reason is the high cost (over 50,000 €) associated with long acquisition time, high operating costs (more than € 2000 / year) and a small profit from the sale of electric energy (180 € / year), is a non-refundable technology for the ratios of the average consumer. Technologies should be attractive, if they was secured by a subsidy from the state of the technology could compete commercially available heat sources.

Acknowledgement

Project 567/PG04/2011 *"Energy efficiency comparision of natural gas in micro-cogeneration units on the principle of the fuel cell and Stirling engine"* is realized with the support of non-investment fund EkoFond, which is established by the SPP.

The task is carried out within the project „ Research Center of the University of Žilina" ITMS 26220220183.

References

[1] DVORSKÝ E., Hejtmánková P.: Kombinovaná výroba elektrické a tepelné energie, Technical literature BEN., Praha 2005

[2] WhisperGen EU 1 manufacturer literature

[3] HOLUBCIK M., HUZVAR J., JANDACKA J.: *Combined production of heat and electricity with use of micro cogeneration* / M. Holubcik, J. Huzvar and J. Jandacka. In: IN-TECH 2011 : proceedings of international conference on innovative technologies : 01.09.2011 to 03.09.2011, Bratislava, Slovakia. - [S.l.]: Jan Kudláček, 2011. - ISBN 978-80-904502-6-4. - S. 200-202.

TRANSCOM 2015, 22-24 June 2015
University of Žilina, Žilina, Slovak Republic

Influence of Relative Strain Values on Pressure Forces in Combined Extrusion of Parts Made of ENAW-1050A Alloy

[*]Piotr Thomas
[*]Department of Applied Computer Science and Armament Engineering, Faculty of Mechatronics and Machine Design, Kielce University of Technology, Al. 1000-lecia P.P. 7, 25-314 Kielce, Poland, {Piotr Thomas}thomas@tu.kielce.pl

Abstract. The paper presents the results of experimental studies of the combined extrusion of parts made of ENAW-1050A alloy. Two values of the relative strain of the material extruded in forward direction were studied: ε_1=0.77 and ε_1=0.69. For each value of the relative strain ε1, different values of relative strain of material extruded in backward direction were used, ε_2: 0.41, 0.52, 0.64. On this basis, the influence was determined of the relative strain level in the material extruded in forward and backward directions on the die pressure value. It was demonstrated that the value of die pressure increases with increasing level of relative strain of material extruded in forward and backward directions.

Keywords: Aluminum, combined extrusion,

1. Introduction

In recent years, aluminium and its alloys have become widely applied materials in a number of sectors. Their excellent mechanical properties and low specific mass are deciding factors for designers in aeronautics, aerospace and automotive industries [1,2,3]. Technological advancement of the last decade has allowed manufacturers to use these materials in car subassemblies. [4]. Extensive research is being conducted on designing aluminium-based materials with contemplated qualities and on developing new metal forming technologies or improving existing ones. The results of the research and new solutions found are becoming crucial to industry.

One of the technologies used in manufacturing products from non-ferrous metals is extrusion. Three basic techniques are used: forward, reverse and combination. The combination extrusion combines forward and backward types. The diagram of the combined extrusion is shown in Fig. 1.

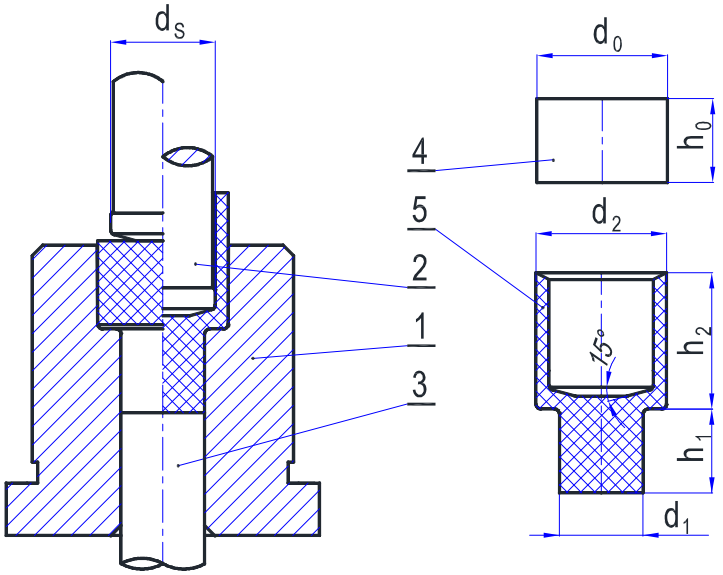

Fig.1. The scheme of combined extrusion of aluminum stampings using conical punch: 1 – die; 2 – flat-conical punch; 3 – ejector; 4 – billet; 5 – die stamping.

From among a body of literature, the most comprehensive and detailed reports on extrusion can be found in [5,6]. The available literature offers analytical solutions, experimental research findings, and recommendations for process design, all relating to forward and backward extrusion only [7,8]. As the literature on combination extrusion is scarce, it has been deemed necessary to undertake studies on the subject, focusing on the analysis of impact forces acting in the combination extrusion process.

2. Methods and test results

The objective of this study is to perform experiments relating to combination extrusion of aluminium parts for varied values of relative deformation in forward and backward directions.

The experimental studies of the combination extrusion process were conducted on the test unit composed of a ZD 100 testing machine with 1 MN impact, combination extrusion tool, and a computer station for measuring forces and displacement in plastic forming POM 16. The combination extrusion die set was developed based on the backward extrusion die. The test unit was modernized to suit the contemplated needs by designing and manufacturing punch retainers, die holders, punches, die inserts, ejectors, columns and guide sleeves. These changes allowed producing extrusions with a sleeve-cylinder shape.

As the slug for the combination extrusion process, aluminium discs A1 99.5% (ENAW-1050A) were used, softened, with external diameter d_0=24.95mm and height h_0=16mm. Table 1 shows the mechanical properties of the feedstock used in the tests. The material properties were determined based on the results of the static tensile test conducted to PN-EN 10002-1+AC1 [9].

Material	$R_{0,2}$ [MPa]	R_m [MPa]	A [%]	$A_{11,3}$ [%]	Z [%]
A1 99,5%	24	82	46	34	86

Tab.1. Aluminum A1 99.5% (ENAW-1050A) properties.

The experimental studies were carried out for flat die inserts, with punches with bullet-shaped nose and the punch front part inclination angle of 15^o.

The dimensions of the extrusions were the following:

- for the upper part of the extrusion formed in backward direction, external diameter d_2=25mm=const, while internal diameters (punch diameter) d_s=16, 18, and 20mm,
- diameters of the bottom part of the extrusion formed in forward direction are d_1=12 and 14mm, respectively.

The assumed dimensions of the input material and extrusions allowed obtaining the following degrees of relative deformations:

- consecutively for the backward extrusion

$$\varepsilon_2=d_S^2/d_0^2=0.41;\ 0.52;\ 0.64 \quad (1)$$

- for forward extrusion

$$\varepsilon_1=(d_0^2-d_1^2)/d_0^2=0.77;\ 0.69 \quad (2)$$

The increase in the relative deformation ε_2 in the backward direction reduced the thickness of the extrusion sleeve part, whereas the decrease in deformation ε_1 led to the increase in the cylindrical part of the extrusion in the forward direction. It was assumed that the maximum height of the cylindrical part of the extrusion formed in forward extrusion was h_1 = 14mm due to the design of the test die. This value restricted further movement of the material in the forward direction because of the ejector used in the tests.

The tests began for the flat insert with constant relative deformation ε_1=0.77=const (d_1=12mm) in the forward direction. The use of flat-conical punches (15^o) with varied diameters of the working parts allowed obtaining various values of relative deformations in the backward direction, ε_2=0.41;

0.52; 0.64. The tests were conducted with no lubrication applied. Figure 2 shows the plots of the impact applied by the punch as a function of displacement.

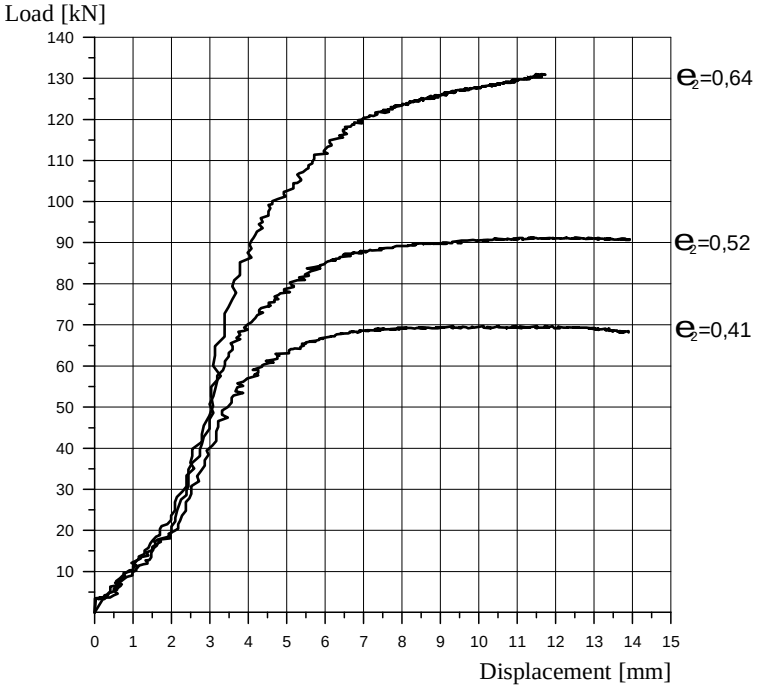

Fig. 2. The stress of the punch as a function of displacement during combined extrusion for different degrees of backward deformation ε_2 and constant value of forward extrusion ε_1 = 0,77 (d_1=12mm).

The traces of forces shown in figs. 3 were plotted for different relative deformations ε_1 in the forward direction. In fig. 3, the deformation value was taken to be ε_1=0.69 (d_1=14mm), which was possible owing to increased diameter of the die insert d_1 from ø12 mm to ø14mm, respectively.

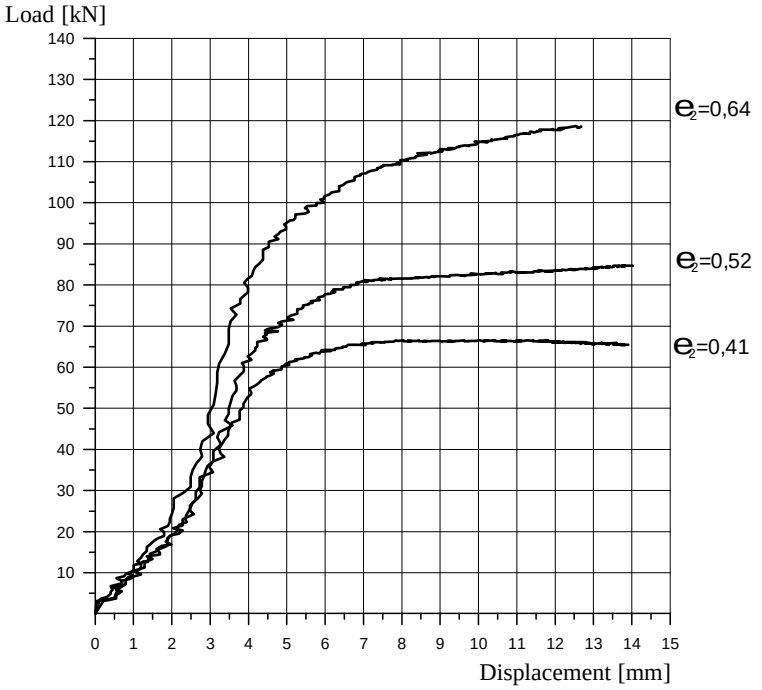

Fig. 3. The stress of the punch as a function of displacement during combined extrusion for different degrees of backward deformation ε_2 and constant value of forward extrusion ε_1 = 0,69 (d_1=14mm).

The extrusion process was conducted for the punch displacement s=14mm. The final displacement measurement was made using a dial indicator, whose plunger moved perpendicularly to the bottom surface of the upper die plate. This allowed the measurement of the end part of the punch displacement to an accuracy of 0.01mm. Ending the process earlier was associated with

reaching the ejector by the material moving in the forward direction, which caused a rapid rise in impact values. From this moment the extrusion process would be conducted as backward extrusion.

The analysis of forces presented in figs. 2 and 3 indicates that in the first stage of the combination extrusion process, a rapid gain in the values of impact occurs as a function of the punch displacement. Then, the forces become stable. For ε_2=0.41, in the final stage of the process, the forces decrease irrespective of the value of relative deformation ε_1 in the forward direction. It is also obvious that the drop in the punch impact force at the final stage is higher for lower values of relative deformations ε_1 in the forward direction (fig. 2 and fig. 3, ε_2=0.41). For ε_2=0.64 in the final stage of the extrusion process, a rise in the impact forces is observed for relative deformation ε_1=0.77 and ε_1=0.69.

In combination extrusion, the increased relative deformation ε_2 in the backward direction leads to the increase in impact force values. For ε_1=0.77 and ε_2=0.41 (fig. 2), maximum impact force value is 69kN. Increased relative deformation ε_2 in the backward direction causes the values of the forces to rise by 33% (for ε_2=0.52) and 91% (for ε_2=0.64). Increased impact force values result from greater hardening of the material.

In combination extrusion, a significant influence on the value of impact forces at the same relative deformation ε_2 in the backward direction is exerted by deformation ε_1 in the forward direction. For ε_2=0.52=const and ε_1=0.69, the maximum impact force is 84kN (fig. 3). Increasing the relative deformation ε_1 from 0.69 to 0.77 at ε_2=0.52=const results in the increase in the maximum impact force of 9% (fig. 2).

3. Conclusions

The following conclusions can be drawn based on the findings from the tests conducted on aluminium parts extruded in combination extrusion. The increase in relative deformation ε_2 in the backward direction causes higher impact forces. The increase in diameter d_1 of the die insert and thus reducing relative deformation ε_1 in the forward direction causes reduction in the impact forces for the same values of relative deformations ε_2.

Note that the results from the experimental studies presented here showed the advantages of the combination extrusion process relative to forward and backward extrusion processes, as well as expanded the knowledge of the combination extrusion process. Forming of products in combination extrusion eliminates the need to conduct two operations, where the cylindrical part of the extrusion is made in the forward extrusion process and the sleeve part of the extrusion is made in the backward extrusion process. Combination extrusion reduces the cost and effort necessary to manufacture the tools and has a significant positive influence on the durability of the tooling.

References

[1] BRANDT D. *Konstruieren mit Aluminium Schmiedestűcken*, (Designing with Aluminium Forgings), Umformtechnik, Vol. 26, No 3, 1992.

[2] DOM F.J. *Meltspun aluminium successful in racing pistons*, Aluminium, Vol. 70, Nr. 9/10, 1994.

[3] GABATHULER J.P. *Formed Components for the Car Industry*, Aluminium, Vol. 73, No. 5, 1997.

[4] *Neues Aluminiumrohr Speziell fűr KFZ-Konstruktionen*, Aluminium, t. 80, Nr 6, 2004.

[5] LANGE K. *Handbook of Metal Forming*, McGraw-Hill Book Company 1985.

[6] ERBREL S., KUCZYŃSKI K. *Selected issues of shaping geometrical bodies.* Part II. Polish Engineers and Technicians Association. Personnel Development Centre. Warsaw 1989.

[7] LEŚNIAK D., RĘKAS A., LIBURA W., ZASADZIŃSKI J. *Numerical investigations of welding conditions during extrusion of 2024 alloy through porthole dies.* Key Engineering Materials, 2012 vol. 491.

[8] ZASADZIŃSKI J., RĘKAS A., LIBURA W., RICHERTJ., LEŚNIAK D. *Numerical analysis of aluminum alloys extrusion through porthole dies.* Key Engineering Materials 2010 vol. 424.

[9] PN-EN 10002-1+AC1 *Tension Test.*

TRANSCOM 2015, 22-24 June 2015
University of Žilina, Žilina, Slovak Republic

Determining the Values of Forces in Nut Hook Bending

[*]Piotr Thomas
[*]Department of Applied Computer Science and Armament Engineering, Faculty of Mechatronics and Machine Design, Kielce University of Technology, Al. 1000-lecia P.P. 7, 25-314 Kielce, Poland, {Piotr Thomas}thomas@tu.kielce.pl

Abstract. The paper presents the results of the bending tests performed on sling hooks. Two types of nut hooks, M16 and M20, were used in testing. The hooks are produced of S235JR steel for the power industry. The tests were conducted perpedicular to the axis of the hook. The data on the force values allowed determining the capacity of the slings and the maximum values of breaking forces.

Keywords: hook, load capacity, power engineering.

1. Introduction

New regulations concerning greenhouse gas emissions force the electrical energy producers both to reduce the emission of carbon dioxide from energy production and to introduce new solutions that will allow reductions in energy transmission losses. A number of recently published works [1,2,3,4,5] are the result of the extensive research conducted to develop and implement a new generation of electric cables with increased electrical conductivity leading to more than 10% reduction in transmission loss. Some of the overhead power lines currently in service are worn out and require maintenance and repair work. Research that is being carried out is a good opportunity to implement new solutions and install modern cables and fittings.

Nut hooks are part of the equipment used for overhead lines to suspend the clamps for aerial bundled conductors as well as anchor clamps on poles or other elements of the structure supporting the transmission cables.

The purpose of the study is to determine the performance of power transmission nut hooks M16 and M20 in the bending test. The character of the test is to represent the sling work under real working conditions. Due to the design of the sling and the direction of the load, the tests were conducted perpendicularly to the axis of the hook rod.

2. Methods

The bending tests were performed on the test station, which comprises a testing machine ZD-100, a unit for measuring forces and displacements in the plastic forming processes [6] and fitting for fixing the slings. The computer station allows direct collection of measurement data during the experiments and representing these data as graphs of forces as a function of displacements [7]. The working principle of the measurement path has been described in [8].

3. Test results

The tests were performed for nut hook M16 (rod diameter ϕ16) hook-thread type and M20 (ϕ20). The shape and geometry of the element used in the tests are presented in fig. 1. The bending was carried out perpendicularly to the hook's axis. To be able to fix the hook in the working space of the testing machine, special fitting were developed and produced, as shown in fig. 2.

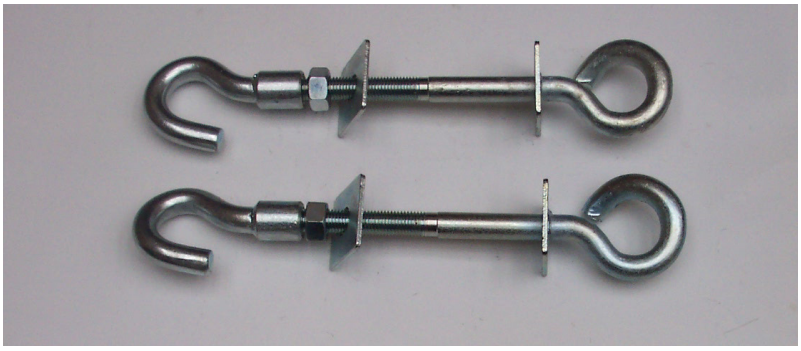

Fig. 1. Nut hook M16 before the bending tests F_Y, hook-thread type.

Fig. 2. Nut hook M16 during the bending tests F_Y, hook-thread type.

The fabricated fixing clamps corresponded fully to those used in service in real working conditions. The results form the tests in the form of graphs – force as a function of displacement – are shown in fig. 3. The tests were repeated for four elements with the same geometrical parameters. Two of these elements are shown in fig. 4.

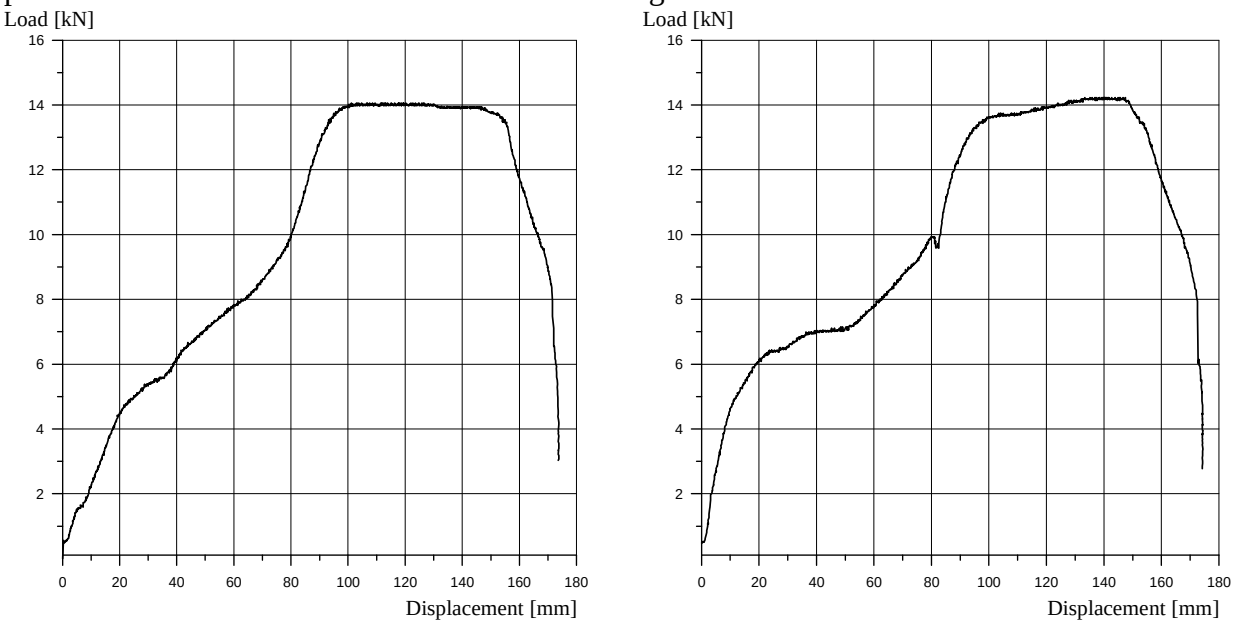

Fig. 3. Pressure force changes as a function of displacement of nut hook M16, bending tests F_Y, hook-thread type.

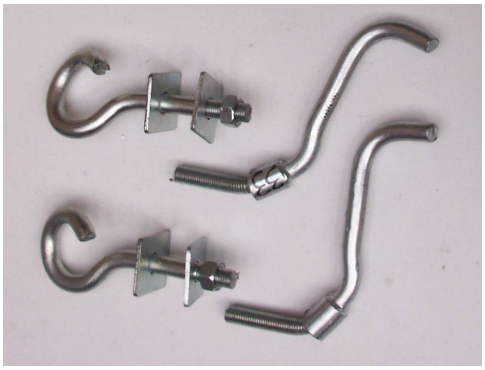

Fig. 4. Nut hook M16 after the bending tests F_Y, hook-thread type.

Maximum load for the nut hook M16 is 5kN. After exceeding this value, permanent deformation of the hook occurs. When the load exceeds 14kN, the fittings in the clamp will fail. The load of 14kN is the maximum force upon which the fittings installed in the hook M16 break thus breaking the transmission line.

The next testing step involved bending nut hook M20, hook-thread type, as shown in fig. 5. The graphs for forces in a function of displacement are shown in fig. 6.

Fig. 5. Nut hook M20 during the bending tests F_Y, hook-thread type.

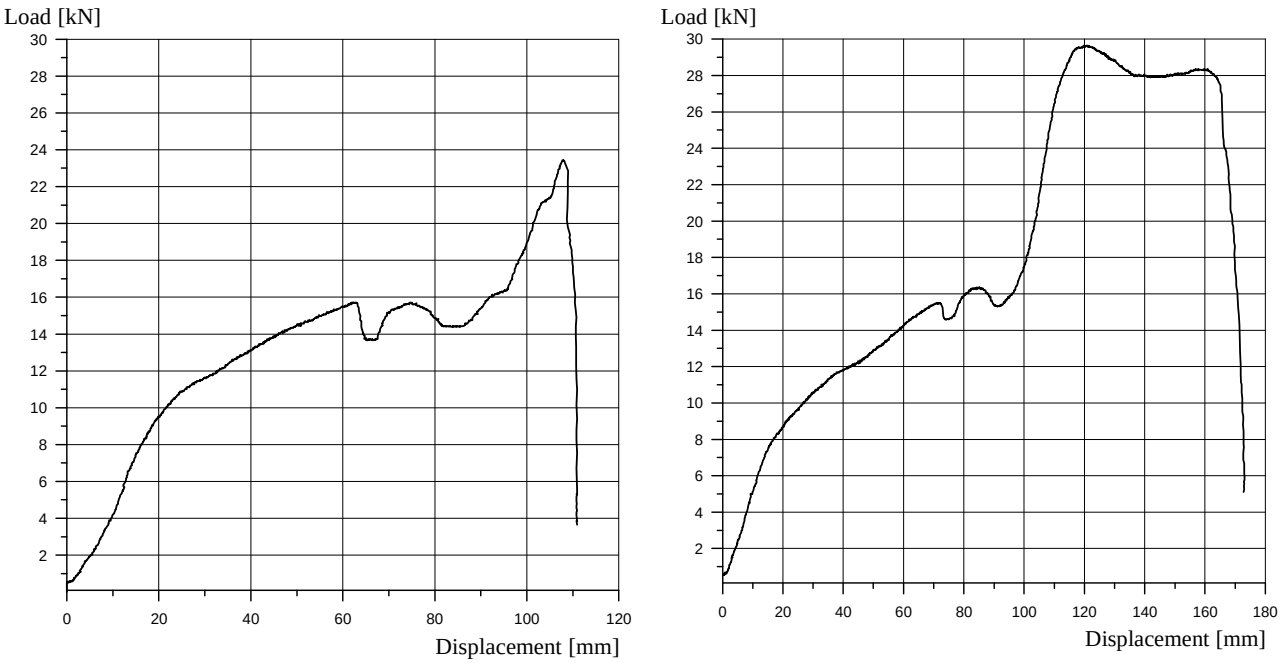

Fig. 6. Pressure force changes as a function of displacement of nut hook M20, bending tests F_Y, hook-thread type.

Figure 7 shows nut hooks M20 with deformed shanks.

Fig.7. Nut hook M20 after the bending tests F_Y, hook-thread type.

The maximum load for the nut hook M20 is 8kN. When this value is exceeded, permanent deformation occurs, and when the force reaches the value of 28 kN, the fittings break. During one of the tests, the nut hook M20 failed at the value of 23 kN. The performance of the other hooks was repeatable and the force maximum values were comparable.

4. Summary

The following conclusions can be formulated based on the bending test results:

1. Maximum load of the nut hook M16 is 5kN, with 8kN cot M20.
2. The force at which the fittings disassemble is 14kN for M16 and 28 kN for M20.

The values of pressure forces as a function of nut hook displacements will allow selecting proper sling type, depending on its load under real working conditions. The elements tested, the nut hooks, have been implemented to production.

References

[1] SMYRAK, B., KNYCH, T., MAMALA, A., ULIASZ, P., JABŁOŃSKI, M., OSUCH, P., PIWOWARSKA, M., NOWAK, A. *A study of a new generation of multi-functional aluminium alloys for the power industry*. Rudy i Metale Nieżelazne, 2010, nr 7.

[2] KNYCH T., MAMALA, A., SMYRAK, B., OSUCH, P., WALKOWICZ, M. *Evolution of structure and properties of AlMgSi alloy for wire rod during continuous casting and rolling method by Continuus-Properzi*. Rudy i Metale Nieżelazne, 2010, nr 7.

[3] JABŁOŃSKI M., KNYCH T., SMYRAK B. *Wire drawing process investigation of Al-Fe alloys for electrical purposes.* Rudy i Metale Nieżelazne, 2010, nr 7.

[4] KNYCH, T., MAMALA, A., NOWAK, A., SMYRAK, B., ULIASZ, P. *New theoretical model of high conductivity AlMgSi alloys multiwire overhead line conductors.* Rudy i Metale Nieżelazne, 2010, nr 7.

[5] KNYCH T., MAMALA, A., NOWAK, A. *Fretting research of AlMgSi alloys wire as the factor limiting the mechanical vitality of overhead lines.* Rudy i Metale Nieżelazne, 2010, nr 7.

[6] CENDROWICZ J. *Pom 16 program for the handling of research experiments*. Kielce University of Technology, Kielce 2001.

[7] THOMAS P. *Position to measurements of powers and transfers in processes of plastic working*. Kielce University of Technology, Kielce 2001.

[8] THOMAS P. *Strength development of hook bolts.* Terotechnologia 2011, Scientific booklets Kielce University of Technology, Kielce 2012.

TRANSCOM 2015, 22-24 June 2015
University of Žilina, Žilina, Slovak Republic

The Geometric Structure of the Electro-Spark Deposited WC-Cu Coatings Modified by Laser Treatment

[*]Izabela Pliszka, [*]Norbert Radek, [*]Leszek Radziszewski
[*] Technical University of Kielce, 1000-lecia Panstwa Polskiego 7, PL-25314 Kielce, Poland,
iza.pliszka@interia.pl, norrad@tu.kielce.pl, lradzisz@tu.kielce.pl

Abstract. The paper described properties of electrospark deposited coatings under influence of the laser treatment process. The properties were assessed by analyzing the coating microstructure, microhardness, porosity and surface geometric structure. The studies were conducted using WC-Cu electrodes produced by sintering nanostructural powders and molten with a laser beam. The coatings were deposited by means of an EIL-8A. The laser processing was performed with an Nd:YAG laser. The laser treatment modifies of the electrospark layer and influences on the correct it usable properties. The result of laser processing improves structure by refinement, healing of microcracks and pores of ESD coatings. Laser treated ESD coatings can be applied as anti-wear and protective coatings.

Keywords: Electro-spark deposition, laser treatment, powder metallurgy, coating properties, WC-Cu coating.

1. Introduction

Electrospark deposition (ESD) is a cheap and efficient way to improve the performance properties of the metal. Developed in the post-war period, the technology has been frequently modified. The main advantages are related to the ability of precise selection of the area to be modified and the ability of the coating thickness selection. This method makes it possible to deposit ultra thin and slightly thicker coatings made almost of any metal. The coating deposition is performed by an electrical circuit, which generates sparks between the electrode and the work-piece. Electrical pulses of high frequency and high direct current between the electrode (anode) and work-piece (cathode) release very hot micro-particles of the electrode material to form a coating on the work-piece surface. This leads to energy savings because only the micro particles are heated, while the substrate remains cool. A series of chemical and electrochemical reactions accompany ESD coating formation, which usually degrade the mechanical properties and microgeometry of the applied coatings [1, 2].

Electro-spark deposited coatings have also some disadvantages but these can be easily eliminated by laser beam machining (LBM), which can be used for polishing of the surface, sealing and modifying its topography, and chemical homogenization of coatings [3, 4].

It is envisaged that the advantages of the laser-treated electro-spark coatings will include:

- lower roughness,
- lower porosity,
- better adhesion to the substrate,
- higher wear and seizure resistance,
- higher fatigue strength due to the occurrence of compressive residual stresses in the sub-surface zone,
- higher resistance to corrosion.

2. Materials and Experimental Procedures

The work discusses the properties of electro-spark deposited WC-Cu coatings subjected to laser treatment. The properties of the coatings after laser treatment were assessed by means of scanning electron microscopy, surface geometric structure, microhardness and porosity.

The coatings were deposited on the C45 grade plain-carbon steel by the ESD method using a portable equipment shown in Figure 1.

Fig. 1. Portable EIL-8A electro-spark deposition device (TRIZ, Ukraine).

The electrodes containing 50% WC and 50% Cu were produced using the powder metallurgy hot press route [5]. The powders were mixed for 30 minutes in the chaotic motion Turbula-type mixer. The mixture was then poured into rectangular cavities of a graphite mould, each 6×40 mm in cross section, and consolidated by passing an electric current through the mould under uniaxial compressive load. A 3 minute hold at 950 °C and under a pressure of 40 MPa permitted obtaining electrodes with porosity <10% and strength sufficient to maintain integrity when installed in the electrode holder.

The equipment used for electro-spark deposition was an EIL-8A model. Basing on the results of previous research as well as instructions given by the equipment manufacturer, the following parameters were assumed to be optimal for ESD:

- voltage U = 230 V,
- capacitor volume C = 150 μF,
- current intensity I = 0.7 A.

Then, the coatings were treated with an Nd:YAG laser (impulse mode) model BLS 720. The samples with electro-spark deposited coatings were laser-modified using the following parameters: spot diameter d = 0.7 mm, power P = 60 W, laser beam velocity v = 250 mm/min, nozzle-workpiece distance Δf = 6 mm, pulse duration t_i = 0.4 ms, pulse repetition frequency f = 50 Hz, beam shift jump S = 0.4 mm and nitrogen gas shield flow Q = 25 l/min.

3. Results and Discussion

3.1. Analysis of coating morphology

A Joel JSM-5400 scanning microscope equipped with an Oxford Instruments ISIS-300 X-ray microanalyzer was used to test the coating microstructure.

In Fig. 2a the microstructure of electro-spark deposited two-layer WC-Cu coating is presented. The layer thickness is approximately 36-40 μm, and the range of the heat affected zone (HAZ) inside the (underlying) substrate material is about 20-30 μm. In the Fig. 2a, the boundary line between the two-layer coating and the substrate is clearly visible. There are microcracks running across and along the coating. A linear analysis of the elements (Figure 2b) of the WC-Cu coating shows that the distribution of elements is non-uniform; there are zones with greater concentrations

of W, Cu and Fe. Analyzing the linear distribution of elements, one can see that the adhesion of the coating to the substrate is of diffusive type.

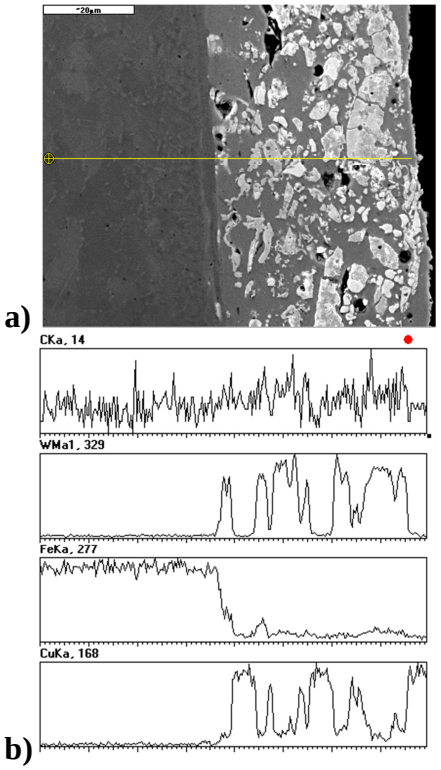

Fig. 2. Microstructure (a) and linear distribution of elements (b) in the WC-Cu coating.

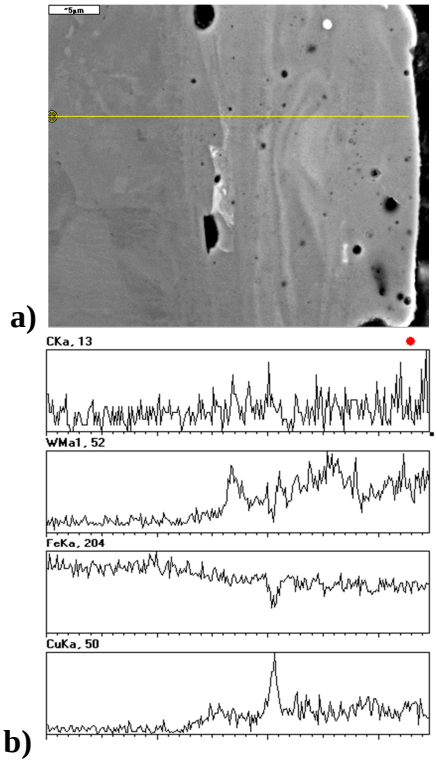

Fig. 3. Microstructure (a) and linear distribution of elements (b) in the WC-Cu coating after laser treatment.

The melting and solidifying processes during laser treatment resulted in the migration of elements across the coating-substrate interface. Laser radiation caused intensive convective flow of the liquid material in the melt pool and, in consequence, the homogenization of the chemical composition (Figure 3b). It also led to the structure refinement and highly saturated phase crystallization (Figure 3a) due to considerable gradients of temperature and high cooling rates. The technological surface layers, produced by laser alloying, were free from microcracks and pores (an effect of surface sealing), and non-continuities across the coating-substrate interface. It wasn't observed any significant change in the chemical composition of the substrate. The thickness of the fused two-layer of the WC-Cu coating was in the 40-74 μm range. In the heat affected zone (HAZ), which was 30-45 μm thick (Figure 3b)

3.2. Microgeometry measurements

The surface geometric structure (SGS) substantially influences many processes that occur in the outer layer. A lot of publications deal with the measurement methods and the assessment of surface roughness and waviness [6,7].

Measurements of surface geometric structure were carried out at the Laboratory of Computer Measurements of Geometric Quantities of the Kielce University of Technology. They were performed using Talysurf CCI optical profiler that employed a coherence correlation algorithm patented by Taylor Hobson company. The algorithm makes possible to take measurements with the resolution below 0.8 nm along the *z* axis. The result of measurements were recorded in 1024 x 1024 measurement point matrix, which yielded the 1.65 mm x 1.65 mm measured area and the horizontal resolution of 1.65 μm x 1.65 μm for the x10 lens.

Three-dimensional surfaces and their analysis with TalyMap Platinum software made it possible to precisely identify the geometric structure of the tested surfaces. Table 1 provides major parameters of the surface geometric structure of the examined specimens.

SGS parameters	Coating	
	WC- Cu	WC- Cu + laser
Sa [µm]	4.42	8.57
Sq [µm]	5.71	24.11
Ssk	0.06	0.23
Sku	3.19	3.43
Sp [µm]	40.96	95.94
Sv [µm]	20.96	83.65
Sz [µm]	61.92	179.59

Tab. 1. Parameters of the surface geometric structure.

Figure 4 present image of surface topography before and after laser treatment. A greater value of the mean arithmetic deviation of surface roughness *Sa*, a basic amplitude parameter in the quantitative assessment of the state of the surface under analysis, was recorded for the specimen after the laser treatment, for the specimen before the laser treatment the value of this parameter was by almost 50% lower.

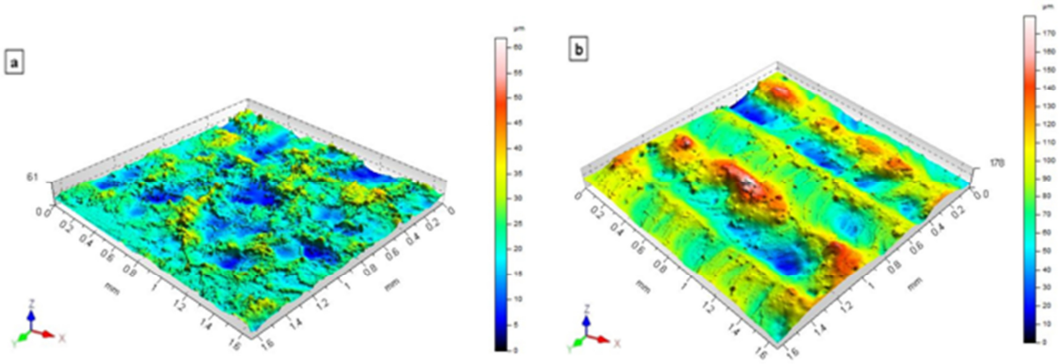

Fig. 4. Specimen surface topography: a) before laser treatment, b) after laser treatment.

A similar tendency is observed for the mean square root deviation of surface roughness *Sq*. Complementary information on how the surface of examined elements is shaped is provided by amplitude parameters, namely the coefficient of skewness (asymmetry) *Sku* and the coefficient of concentration (kurtosis) *Ssk*. Those parameters are sensitive to the occurrence of local hills or valleys, and other surface defects. The parameter *Ssk* has a positive value for both specimens, the value is close to zero for the untreated specimen, which indicates the symmetrical location of the distribution of ordinates with respect to the mean plane. The obtained values of kurtosis were close to *Sku* = 3. This indicates that the distribution of ordinates for both specimens is close to normal.

3.3. Microhardness tests

The microhardness was determined by using the Vickers method (Microtech MX3 tester). The measurements were performed under a load of 0.4 N. The indentations were made in perpendicular microsections in three zones: the white homogeneous difficult-to-etch coating, the heat affected zone (HAZ) and the substrate. The test results for the electro-spark deposited WC-Cu coating before and after laser treatment are shown in Figure 5.

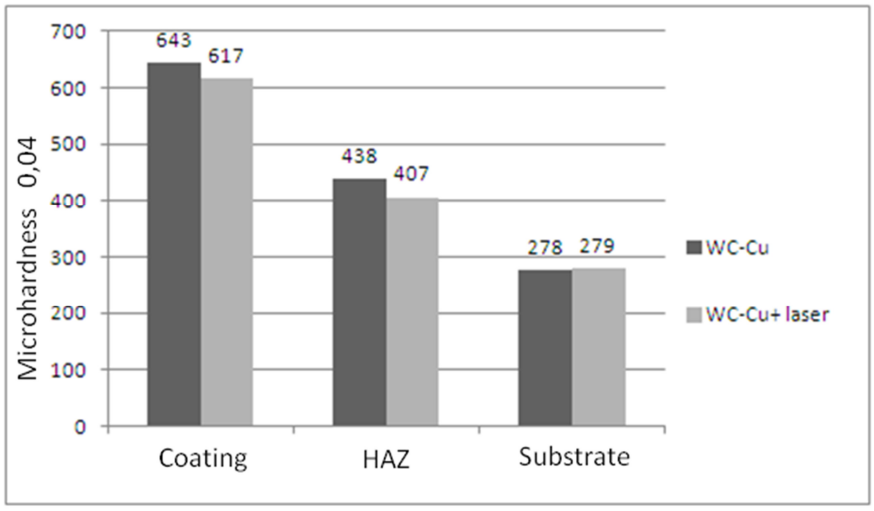

Fig. 5. Results of the microhardness tests for the WC-Cu coating before and after laser treatment.

Electro-spark deposition shows changes in the microhardness of the material. The microhardness of the substrate after electro-spark deposition was on average 278 HV0.4; the same value was reported for the substrate before the process. There was a considerable increase in microhardness after depositing the WC-Cu coating. The microhardness of the WC-Cu coating was approx. 643 HV 0.4, which gives increase of 131 %. The microhardness of the WC-Cu coating in the HAZ after electro-spark treatment was 57 % higher than that of the substrate material. Laser treatment had a favorable effect on the changes in the microhardness of the electro-spark deposited of the WC-Cu coating, however caused a decrease of 9 % in the microhardness of the WC-Cu coating.

3.4. Surface porosity

For assess the degree of porosity of the coatings tested WC-Cu before and after laser treatment, quantitative image analysis was performed using software supplied with the SIS which (SEM) Philips XL30 / LaB6. In the analysis guided by the principle of Cavalieri-Hacquerta according to which, a measure of the porosity can be shares of the pores:

- volume (the ratio of the total volume of voids to the total volume of the fragment of the coating);
- surface (the ratio of the total pore area to the total area analyzed grinding);
- the length of the control section (the ratio of the total length of the strings passing through the pores of the length of the analyzed section of the measurement plane grinding).

Coating	**Porosity [%]**			**Average value [%]**
	Number of measurement			
	1	**2**	**3**	
WC-Cu	5.7	6.3	3.5	5.2
WC-Cu +laser	0.4	0.2	0.1	0.2

Tab. 2. Results of the surface porosity for the WC-Cu coating before and after laser treatment.

Results of the surface porosity for the WC-Cu coating before and after laser treatment are shown in Table 2. Analyzing the table it can be seen that the applied coatings have a higher porosity with respect to the coating after laser treatment. Laser treatment reduced the porosity of the coatings more than 20 times. The porosity of the coatings WC-Cu was located in the range of 3.7 – 6.3%, and after laser treatment was 0.1 – 0.4%. Lower porosity of the WC-Cu coatings has positive

influence on their performance characteristics, improving their corrosion resistance, adhesion and microhardness.

4. Conclusions

1. A concentrated laser beam can effectively modify the state of the outer layer of ESD coatings thus changing their functional properties.
2. Laser irradiation of coatings assists in healing of micro-cracks and pores.
3. Parameters of surface geometric structure of ESD coatings have lower values when compared with those characterizing coatings after laser treatment.
4. Laser treatment of ESD WC-Cu coatings decreases its microhardness by 9%.
5. Coatings after laser treatment have lower porosity (more than 20 times).

References

[1] RADEK N., *The influence of laser treatment on the microstructure and properties of the tungsten carbide electrospark coatings*, Adv. Manuf. Sci. Tech., 35 (2011) 59-71.
[2] GALINOV I.V., LUBAN R.B., *Mass transfer trends during electrospark alloying*, Surf. Coat. Tech. 79 (1996) 9-18.
[3] RADEK N., KONSTANTY J., *Cermet ESD coatings modified by laser treatment*. Archives of Metallurgy and Materials, Vol. 57, 3 (2012) 665-670.
[4] RADEK, N. , ANTOSZEWSKI B., *Influence of laser treatment on the properties of electro-spark deposited coatings*, Kovove Materialy-Metallic Materials 1 (2009) 31-38.
[5] KONSTANTY J., *Powder metallurgy diamond tools*, Elsevier, Oxford 2005, 74-76
[6] ADAMCZAK S., MIKO E., CUS F., *A model of surface roughness constitution in the metal cutting process applying tools with defined stereometry*, Strojniski Vestnik-Journal of Mechanical Engineering 55 (2009) 45-54.
[7] ADAMCZAK S., MAKIEŁA W., *Analyzing Variations in Roundness Profile Parameters During the Wavelet Decomposition Process Using the Matlab Environment*, Metrology and Measurement Systems, Vol. XVIII, 1 (2011), 25-34.
[8] CHANG-BIN T., DAO-XIN L., ZHAN W., YANG G., *Electro-spark alloying using graphite electrode on titanium alloy surface for biomedical applications*, Applied Surface Science 257 (2011) 6364-6371.
[9] ZAMULAEVA E. I., LEVASHOV E. A., KUDRYASHOV A. E.: *Effect of WC–Co electrode structure on the rate of electrospark coating deposition*, Metallurgist, Vol. 55, Nos. 9–10, 2012.
[10] SCENDO M., RADEK N., TRELA J.: *Influence of laser treatment on the corrosive resistance of WC-Cu electrospark coatings*. International Journal of electrochemical science, 8 (2013), 9264 - 9277.
[11] PYACHIN S. A., NIKOLENKO S. V., BURKOV A. A., SUY N. A.: *Electrospark Coatings Based on WC-Co Alloys with Aluminium Oxide and Carbon Additives*, Materials Sciences and Applications, 4/2013, pp. 186-190.

TRANSCOM 2015, 22-24 June 2015
University of Žilina, Žilina, Slovak Republic

Safety Cooperation between Human and Robot

*Alexander Rengevič, *Darina Kumičáková
*University of Žilina, Fauclty of Mechanical Engineering, Departmet of Automation and Production Systems, Univerzitná 1, 010 26 Žilina, Slovakia
{alexander.rengevic, darina.kumicakova}@fstroj.uniza.sk

Abstract. This article talks about task of cooperation between human and robot. It analyzes cooperation related to security and think about possible solutions. At the beginning of the article is reasoned why security have a high priority in human-robot cooperation. In the following are mentioned all branches in which the robot is irreplaceable. From these broad groups are selected fields, in which the robots may be used as a device capable of direct cooperation with human. Examples of existing solutions of cooperating robots in individual industrial and non-industrial fields are there mentioned too. Current research of new technologies applied for cooperative robots is described. Of the mentioned technologies there are also selected the solutions suitable for application in laboratory of robotized assembly at the Department of Automation and Production Systems at University of Žilina.

Keywords: Human - robot cooperation, industrial application, safety cooperation.

1. Introduction

With development of a computer technology, robots find application in many fields. In addition to industrial applications, robots have irreplaceable place in medicine, military operations, space programs and research projects. Robots are increasingly used in offices, homes, and an entertainment industry. Within mentioned fields, robots are used to replace humans in carrying out certain activities. Increasingly is considering about robotization of activities, which are related with human robot cooperation. Such cooperation requires the determination of conditions ensuring a safety. It means safety of each cooperating element. The first is a human security, which is necessary to protect the human body before unwanted clashes with robot. Such clashes might cause short term, long term or persistent implications which would have a detrimental effect on the quality of life. On second place is safety of the robot, which could be damaged. Possible repair would represent increased operating costs.

You cannot set same security conditions for all types of cooperating robots. It is necessary take into consideration different dimensions, construction material, building structure, actuators and attachments of robots. Is also necessary define the field of application of the selected robot. Only then is possible to establish appropriate safety conditions.

2. Fields of Cooperating Robots Application

Based on the fields of application, robots can be divided to the next groups [5]:

- industrial robots – represent the largest group of robots designed for material handling, manufacturing, processing (welding, machining, assembling, painting), palletizing, etc.,
- exploratory robots – used to survey hard to reach places where human presence isn't possible,
- robots for medical use – used in difficult surgery, where high precision is required,
- service robots – used to automatic execution of services related to human needs,
- special robots – used to specific tasks that cannot be assigned to any particular field.

According to robot motion in environment we can talk about:

- stationary robots – which operate at one place and their movement is limited to the work area determined by their kinematic structure,
- mobile robots – which can move freely in space using undercarriage and suitable drivetrain.

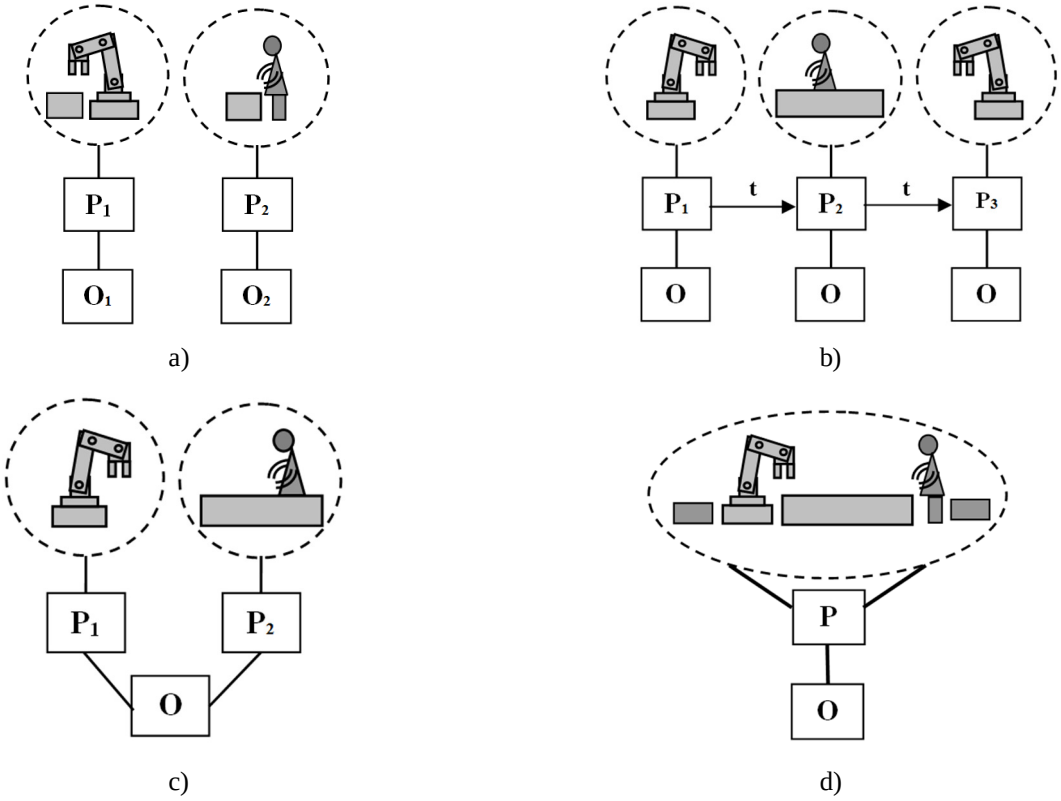

Fig. 1. The forffms of a human and robot cooperation. a) independent cooperation, b) synchronized cooperation, c) simultaneous cooperation, d)assisted cooperation

Due to different fields of application and different types, four forms of cooperation between human and robot are defined [10]:

- independent cooperation in carrying out activities on various objects – robot performs work P_1 on the first object O_1, human performs work P_2 on the second object O_2 (fig. 1a),
- cooperation during perform work at the same object O:
  - synchronized – human and robots perform various operation (P_1, P_2, P_3) on separate workplaces in particular order (fig. 1b),
  - simultaneous – human and robot perform different activities P_1 and P_2 together in one workplace (fig. 1c),
  - Assisted – human and robot work together in one process P (fig. 1d).

Within industrial robotics, cooperation between human and robot particularly applies to assembly operations. Robot performs activities quickly with high repeat accuracy. Human performs activities demanding on logical thinking and handling. This makes it possible to speed up installation and improve the working conditions of human. Currently, there are already several models of industrial robots for cooperation with human [8]. For example, industrial robot KUKA by model LBR iiwa, (see figure 2a) thanks to integrated sensor can detect force of external pressure on your own design [9]. For direct cooperation with humans is also destined UR robot from Universal Robots used for assembly applications [11]. In both cases they are single arm robots. But some assembly operations require cooperation of two robotic arms. The first robot arm provides the necessary rotation of assembled object. The second robot arm rotates with mounted part and provides its exact positioning into assembled object. An example of two armed robot is YoMi from ABB shown in fig. 2b [1].

In the industry cooperating robots are also used in interoperate transportation and material handling. Cooperation with robot can also be used in medicine. Robotic arms are used for carrying out assistance activities in operating rooms. Another example of cooperating robots is humanoid robot that cares for elderly person or the one with disabilities [5]. French company Aldebaran deal with production of this kind of robot. Robot Nao and Pepper can respond to human presence in workspace, his gestures and contact with him, they are able to communicate and teach him new knowledge. They also help improve ability of human movement through demonstrations of movements. [2]. Safety of these kinds of robot is solved by suitable design of parts, which cover skeleton of robot. Due to the fact that robot does not reach high speed of moving parts there is no need to regulate its performance. The effort in this area is to develop fully autonomous humanoid collaborative robots. This kind of robots can also be used in service robotics.

a) b)

Fig. 2. Examples of application of cooperating robots in industry. a) KUKA iiwa, b) ABB YuMi.

3. Research in Field of Cooperating Robots

It is necessary to combine different technologies in field of mechanical and electrical engineering for develop collaborative robot. Many research institutes as well as domestic and foreign universities deal with cooperating robots. They deal with suitable conditions for human robot cooperation and also with new technologies that would help improve the quality of cooperation.

The Institute of robotics and mechatronics of German Space Centre DLR has examined conditions of safe cooperation between human and robot. The research team was decided to identify real consequence of collision between human and robot. According to ISO 10218, allowed values for robot in presence of operator must be as follows: velocity $\leq 0.25 m.s^{-1}$, the maximum dynamic power $\leq 80W$, maximum static force $\leq 150N$. These values, however, according to researchers are not derived from real experiments and so far there is no analysis, which these values attest. Therefore, experiments were performed to verify truth of these values. Lightweight industrial robot KUKA LWR3 was set in motion after a defined trajectory. In range of robot motion was placed Hybrid III test dummy equipped with sensors for capture impact force in important parts of body. Using the sensors were recorded results of reaction forces in the face, neck and chest. Dummy was hit in face by aluminum impactor mounted on robotic arm, see fig. 3a. Resulting values were compared with values of standardized injury severity scales, issued by organizations AAAM – Association of the Advancement of Automotive Medicine, AMA – American Medical Association and ENCAP – European National Car Assessment Protocol.

Test results showed that values range in lower region of all comparative scales. Consequently, risk of injury is low. There is needed to take in account, that comparative scales are designed for speeds greater than10 $m.s^{-1}$. Therefore they are not fully applicable to field of robotics. From this

reason the new criteria focused on mechanisms of human-robot cooperation with should be developed.

In a follow work [6], authors were focused on reaction force detection during collision between human and robot with using five strategies of robot response:

1. Robot ignores potential danger and continues in predefined movement.
2. Robot will stop at the moment of collision arising.
3. Robot in a case of the collision switches from position control to torque control.
4. Robot in case of collision switches from position control to torque control with gravity compensation. The result is reduction of the inertial forces and the feeling of "light" robot.
5. Robot leaves the scene of the collision in case of exceeding the torque sensing caused by collision with human.

According to obtained results, strategies No. 2 and No. 3 can be considered as the best of all. After collision detecting, velocity of the robot is reduced to zero value. Consequently, it is possible to move with robot arm through torque control. Such situation gives human filling that he has control over movement of the robot.

Testing of the basic tasks of cooperation is addressed by scientists at the Institute for Robotics and Intelligent Machines in Atlanta, USA together with the Technical University of Darmstadt, Germany. [3]. Research was been based on the fact that programming of interactive skills of robot is challenging task because the robot in many cases is not ready to anticipate and to respond to behavior of human partners. The main goal of scientific experiment was to intercept behavior of two cooperating users and to infer basic algorithms of behavior for human-robot cooperation. This method was called „Interaction Primitives“. For the research was used anthropomorphic robot which has a robotic hand mounted at end of its kinematic chain. This enabled to engage a robot into standard physical activities which occurring in cooperation between two people. Activities that robot has learned at the first, were movements of human, recorded with motion capture system. This system is capable recording movement of an object and converted it to the digital model through the computer. All obtained data are used to create algorithms that specify the behavior of robot. The goal was to teach robotic arm for a realistic greeting executing of two people by lifting hand and slap with a palm of other person. The results showed that the robot can derive its path for the precisely defined target only after recognition of 60 % of whole path movement of the human arm including hand. The researchers plan is to use this method also for learning of the robot to detect human´s complex movements or series of movements.

One of technologies which begins increasingly applied in the field of cooperation between human and robot is use of intelligent camera systems and sensors of machine vision, that allow robots to recognize space around them and also various objects that are located in their working area. Authors of the work [4] deal with design of robotic assistant for operating rooms which detect human in their work space. Using sensors of Microsoft Kinect, human body moving in working space can be recorded. Sensor detected human body as points cloud, i.e. large group of points which ~~was~~ are subsequently transformed to depth maps for their further processing. The algorithm that can work with the groups of point clouds without the need to know the object overall shape was implemented to determine distance between robot and human. In the system the assisting robot is represented as another point cloud. Distances among individual point clouds are recalculated and evaluated with computer continuously. Exceeding of the minimal allowed distance causes a warning alarm which informs a human about a dangerous. In the case that a shortening of the distance is still being continued, the robot assistant is stopped in its activity.

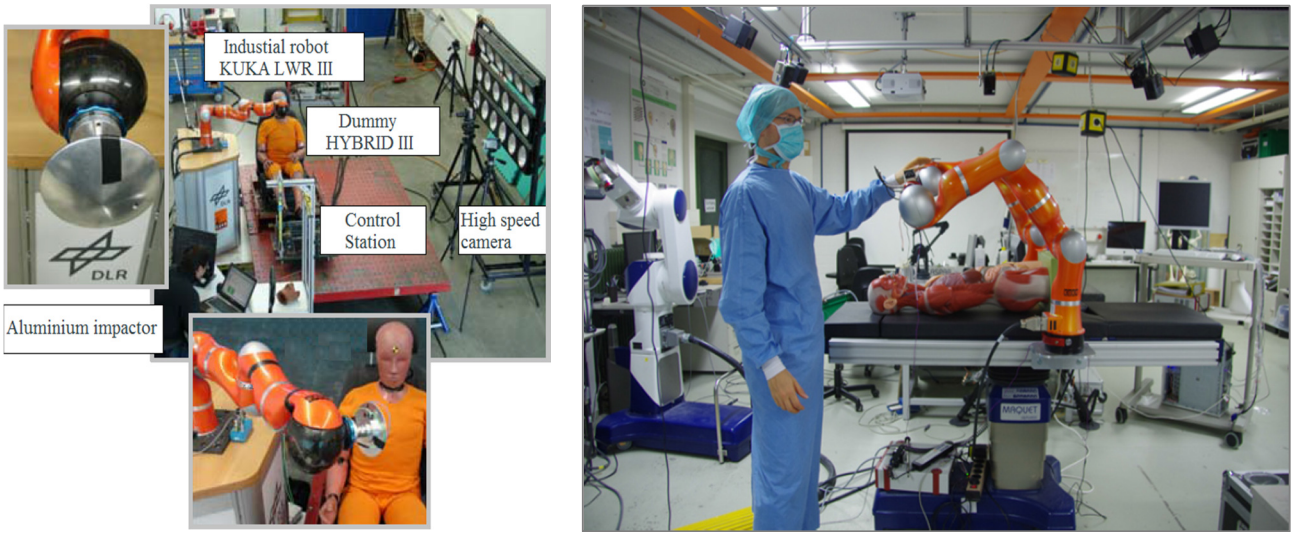

a) b)

Fig. 2. Examples of research in the field of cooperative robots problems solution. a) testing of security conditions, b) workplace with robot assistant.

The Department of automation and production systems also interests about a problem of automation of assembly process with utilization of robots. Currently, in most robotized workplaces a working space of industrial robot is protected during the execution of its activities by safety features commonly used for automated workplaces. Disruption of the robot secure workspace causes the interruption of its operating cycle and also process of assembly. An example of such workstation is the laboratory workstation of automated assembly at the Department of automation and production systems. This workstation is equipped with industrial robot Fanuc LR Mate 200iC with a control system R30iA Mate, see. Fig.4. Robot is designed primarily for realization basic handling and assembly operations as screwing, grasping, object orientation in space and palletizing. Securing the workspace is coordinated through safety light curtains Omron F3S-TFR-CL2B, which during ~~breach~~ disruption of monitored zone initialized stop of the work. This securing system is not satisfactory for planned solving of the human-robot cooperation problems in assembly process. Therefore our goal is to propose a security system that will be able to identify the presence of a human in the robot workspace, for example by means of a vision sensor, and to derive suitable behavior of robot on basis of obtained and processed data about position of human. The task will be to devise a methodology for processing scanned image of human by computer program and also to propose the algorithms for deriving the robot behavior. We plan to validate individual steps of proposed solutions for model examples and with the use of robot Fanuc LR Mate 200iC.

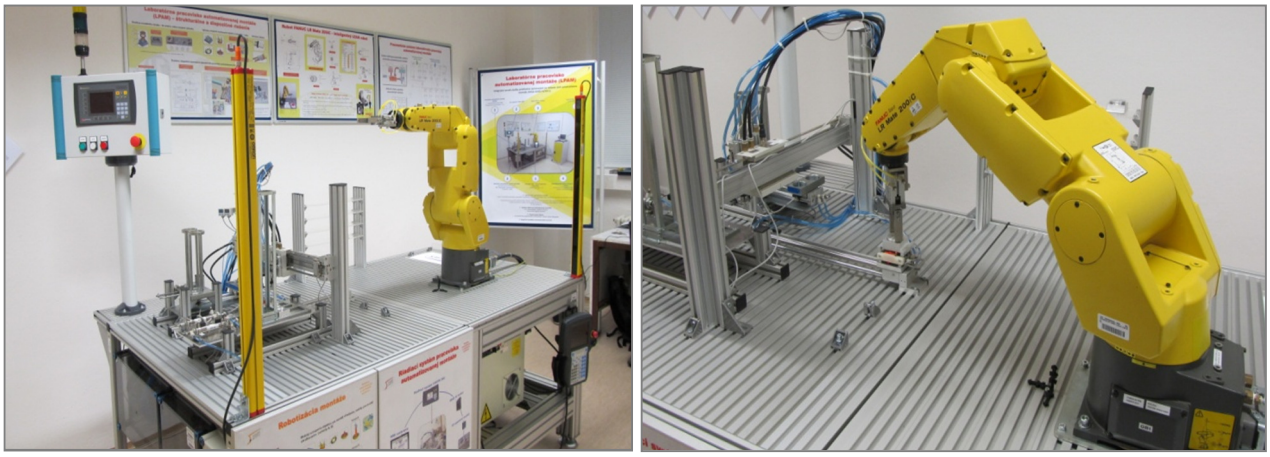

Fig. 4. Laboratory of automated assembly with utilization of industrial robot FANUC

4. Conclusion

The aim of this article was to point out that human robot cooperation has great potential for future. There were mentioned some fields, where the human-robot cooperation is currently applied. We also mentioned the research works dealing with proposals of appropriate conditions for secure human-robot collaboration and exploring new approaches to this issue. In the end of the article the planned tasks for design of system of the human-robot safe cooperation for industrial applications are also presented.

References

[1] ABB – Power and productivity for a better world. 2015.
Available on the Internet: <http://new.abb.com/products/robotics/yumi>.
[2] ALDEBARAN – Humanoid robotics & programmable robots. 2015.
Available on the Internet: <https://www.aldebaran.com/en/robots>.
[3] AMOR, H.B., NEUMANN, G., KAMTHE, S., KROEMER, O., PETERS, J., *Interaction Primitives for Human-Robot Cooperation Tasks.* International Conference on Robotics & Automation, Hong Kong, China, 2014.
[4] BEYL, T., NICOLAI, P., RACZKOWSKY, J., WÖRN. H., COMPARETTI M. D., DE MOMI, D. *Multi Kinect People Detection for Intuitive and Safe Human Robot Cooperation in the Operating Room.* International Conference onAdvenced Robotics. Montevideo, 2013.
[5] BOŽEK, P., BARBORÁK, O., NAŠČÁK, Ľ., ŠTOLLMANN, V. *Špecializované robotické systémy*. Ostrava: Ámos. 2011. ISBN 97880-904766-3-9.
[6] HADDADIN, S., ALBU-SCHÄFFER, A., DE LUCA, A., HIRZINGER, G. *Collision Detection and Reaction: A Contribution to Safe Physical Human-Robot Interaction*. IEEE/RSJ International Conference on Inteligent Robots and Systems. Nice, 2008.
[7] HADDADIN, S., ALBU-SCHÄFFER, A., HIRZINGER, G. *Safety Evaluation of Physical Human-Robot Interaction via Crash-Testing*. Conference: Robotics: Sience and Systems, 2007.
[8] HÄGELE, M., NILSSON, K., PIRES J. N., Chapter 42 Industrial Robotics, In: Handbook of Robotics. SICILIANO, B. – KHATIB, O.(Ed.) Berlin: Springer – Verlag Berlin Heidelberg, 2008. p. 963-985. ISBN 978-3-540-23957-4
[9] KUKA – Industial Robots. 2015.
Available on the Internet: <http://www.kuka-labs.com/en/service_robotics/lightweight_robotics/>.
[10] KUMIČAKOVÁ, D. *Roboty a manipulátory – významný prvok automatizácie výrobných a nevýrobných činností*. (Industrial robots - an important element of automation of production and non-production activities). Habilitation thesis. SjF ŽU Žilina, 2004.
[11] UNIVERSAL ROBOTS – Collaborative Industial Robotic Arms. 2015.
Available on the Internet: <http://www.universal-robots.com/en/>.

TRANSCOM 2015, 22-24 June 2015
University of Žilina, Žilina, Slovak Republic

Elimination of Iron in Secondary Al-Si Alloy

Ing. Lukáš Richtárech, prof. Ing. Dana Bolibruchová, PhD.
University of Žilina, Faculty of Mechanical Engineering Department of Technological Engineering,
Univerzitná 1,
010 26, Slovak Republic, Email: lukas.richtarech@fstroj.uniza.sk

Abstract. This paper deals with possibility of changing of shape of iron based phases in the secondary alloy AlSi7Mg0.3 microstructure. Iron is the most common and harmful impurity in aluminum casting alloys and has long been associated with an increase of casting defects. In generally, iron is associated with the formation of Fe-rich intermetallic phases. It is impossible to remove iron from melt by standard operations. Some elements eliminate iron by changing iron intermetallic phase morphology, decreasing its extent and by improving alloy properties.

Keywords: Secondary AlSi7Mg0.3 based alloys, iron phases, iron correctors.

1. Introduction

Due to the increasing utilization of recycled aluminium cast alloys from components such as car cylinder heads, gear boxes, window frames etc, the necessity for strict microstructural control arises to remove the deleterious impact of impurity elements; which is considered to impair the overall properties of aluminium-silicon based casting alloys. By implementing adaptable alloying- and process technology, the mechanical properties such as ductility will therefore be radically enhanced, leading to larger application fields of complex cast aluminium components such as safety details. Generally, the mechanical and microstructural properties of aluminium cast alloys are dependent on the composition; melt treatment conditions, the solidification rate, the casting process and the applied thermal treatment. The mechanical properties of Al-Si-Mg and Al-Si-Mg-Cu alloys depend, besides the Mg and Cu-content, more on the
distribution and the shape of the silicon particles. [1,2]

Alloys in which the silicon particles (eutectic or primary) are small, round and evenly distributed are usually highly ductile. Alloys in which the silicon particles are faceted and acicular are usually much less ductile but exhibit slightly higher strength. Iron is considered to be one of the most deleterious impurity elements present in aluminium. Being easily picked up from cast equipment made by steel, like ladles and inserts, iron can be added intentionally to improve the resistance to hot tearing and decreases the tendency for die sticking or soldering. The solubility of iron is very low in aluminium alloys with the result that most iron present forms intermetallic compounds. In a binary Al-Fe system, the equilibrium solid solubility of iron in aluminium is 0.03-0.05 wt. % at the eutectic temperature of 655° C and even lower at room temperature. [3,4]

Due to non-equilibrium solidification, it is not unusual to find several brittle and harmful intermetallic phases such as $FeAl_6$, $FeSiAl_3$, Fe_2SiAl_8, Al_5FeSi, and $FeSi_2Al_4$ coexist with one another and with Si in Al-Si iron containing alloys. The mechanical properties are dependent on the type and morphology of the formed intermetallic compounds, as well as on the quantities. Due to the sharp edges of the β- Al5FeSi -needles, a severe stress concentration is then introduced to the alloy's matrix. The needle-shaped Fe-bearing phase is therefore recognized as the most detrimental to the casting's mechanical properties why efforts should be dedicated to developing means of controlling the precipitation, growth and morphology of these harmful platelet-like β - Al5FeSi intermetallic phases. In order to enhance the overall properties such as tensile, fatigue and corrosion properties, the morphology of the iron rich beta-phase in a needle shape is required to be altered to a more compact, less harmful intermetallic compounds. Replacing these needles, the influence of cooling rate and iron content and also the impact of different frequently used modifiers such as Mn, Cr, Co, Sr, Be and Ca on the formation of these phases should be investigated. [5,6]

2. Experimental work

An experimental meltings were realized at laboratory for foundry experiments at Department of Technological engineering at University of Žilina. Melts was carried out in an electrical resistance furnace T15, controlled by PID regulator CAL 3200 in a graphite crucible treated by protective coating. Individual casts consisted from creating four samples poured at a temperature 760 ± 5 °C. Melts were poured into metal mold at temperature 100 ± 5 °C. As an experimental material was used AlSi7Mg0.3 cast alloy. The chemical composition of alloy is in Table 1**.**

El.	**Si**	**Fe**	**Cu**	**Mn**	**Mg**	**Ni**
[wt.%]	6.93	0.1204	0.0036	0.0037	0.3896	0.0042
El.	**Cr**	**Pb**	**Ti**	**Zn**	**Sb**	
[wt.%]	0.0011	0.0033	0.1141	0.0083	0.0001	

Tab. 1. Chemical composition of AlSi7Mg0.3 cast alloy.

Into experimental alloy was added certain amount of AlFe10 master alloy (deliberate "contaminated"), to increase the iron content. The main aim was to increase the iron content in alloy, so that amount is close to maximal allowed content by customer specification for automotive components, made from secondary alloys AlSi7Mg0.3. Added amount of AlFe10 into the basic AlSi7Mg0.3 was 70000 ppm of the total batch. The chemical composition of alloy with higher amount of iron is shown in Table 2.

El.	**Si**	**Fe**	**Cu**	**Mn**	**Mg**	**Ni**
[wt.%]	6.49	1.280	0.053	0.092	0.349	0.034
El.	**Cr**	**Pb**	**Ti**	**Zn**	**Sb**	
[wt.%]	0.087	0.006	0.113	0.027	<0.0004	

Tab. 2. Chemical composition of melts after addition of iron.

Into alloy with higher amount of iron, different amount of master alloy AlCr20 and AlNi20 had been added: 0.5 %, 1 % and 1.5 %. In Fig. 1, Fig. 2 and Fig.3 are shown microstructures of samples from melts with higher amount of iron and with addition of AlCr20 and AlNi20.

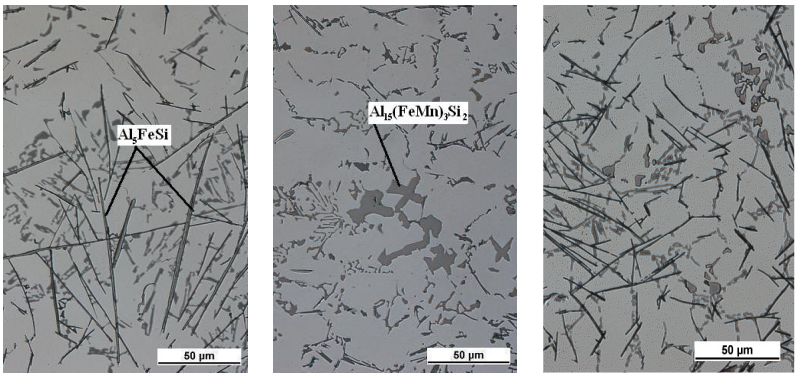

a) *b)* *c)*

Fig. 1. Microstructure from melt a) without higher amount of iron, b) 0.5 wt. % AlCr20, c) 0.5 wt. % AlNi20

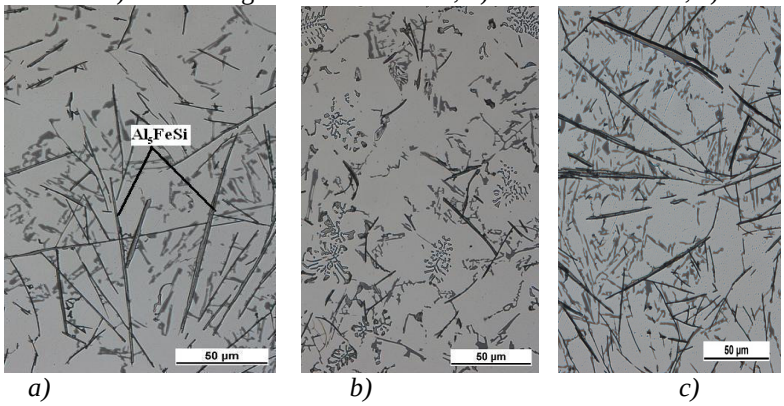

a) *b)* *c)*

Fig.2. Microstructure from melt a) without higher amount of iron, b) 1 wt. % AlCr20, c) 1 wt. % AlNi20

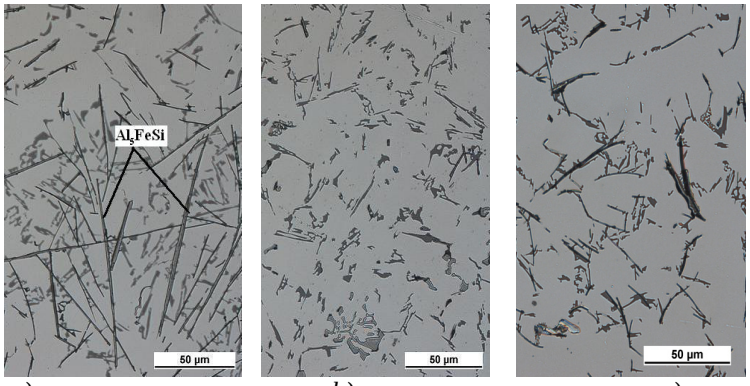

a) *b)* *c)*

Fig.3. Microstructure from melt a) without higher amount of iron, b) 1.5 wt. % AlCr20, c) 1.5 wt. % AlNi20

Influence of "iron correctors" on the microstructure and shape of intermetallic phases was studied by classic black – white contrast method. Sample preparation and execution of metallographic image was done in a standard way for evaluation of intermetallic phases in aluminum alloys. Evaluated samples were etched by 20 ml of H_2SO_4 + 100 ml of H_2O. Images of alloy microstructures were obtained by light microscope NEOPHOT 32. At Fig. 1-3a) is shown microstructure of sample from melt with higher amount of iron. The structure consists of silicon eutectic, dendrites of α – phase excreted in the form of white unites and black areas as iron based particles. On the microstructure is visible impact of the iron on iron based particles themselves. At Fig.1-3 b,c) we can see the presence of new intermetallic particles mostly in script-like form or skeletal-like form, which chemical composition has yet to be confirmed by electron microscope. Figure 2c shows presence of large intermetallic particles. On these microstructures was also measured the length of iron particles. Results of these measurements are presented in Table 3.

Amount of iron corrector	**Without iron corrector**	**AlCr20**	**AlNi20**
		Length of particles (µm)	
0.5	37.10	19.60	50.45
1	37.10	11.41	40.81
1.5	37.10	15.68	42.03

Tab. 3. Results of measurements of length of iron based particles.

For all samples were evaluated tensile strength and elongation. The tensile test was performed on a tensile machine WDW – 20 in the laboratory for mechanical tests, University of Žilina at 22 °C. Brinell hardness measurement has been performed at 22 ° C on the measuring device Innova Test, model Nexus 3002 XL with a digital output. The prints have been made by using the ball of 5 mm diameter. Compressive strength was equal to 2452 N (250 kp) and compressive strength endurance time was 15 s (HBS 5/250/15).Results of measurements of tensile strength are presented on Table 4 and Table 5.

Alloy	**Corrector AlCr20 (hm. %)**	**$R_{m\ min.}$ (MPa)**	**A_{50min} (%)**	**HBS**
Secondary AlSi7Mg0.3	**Without corrector**	167	0.93	87
	0.5	159	1.02	82
	1	173	1.26	80
	1.5	161	1.11	85

Tab. 4. Results of measurements of mechanical properties after addition of AlCr20.

Alloy	Corrector AlNi20 (hm. %)	$R_{m\ min.}$ (MPa)	A_{50min} (%)	HBS
Secondary AlSi7Mg0.3	Without corrector	167	0.93	87
	0.5	148	0.73	72
	1	160	0.7	72
	1.5	182	1.4	71

Tab. 4. Results of measurements of mechanical properties after addition of AlNi20.

3. Conclusions

The goal of the article was to evaluate the effect of iron correctors in form of master alloys in secondary alloy AlSi7Mg0.3. It is possible to conclude that iron correctors have detrimental influence on microstructure – change very long and thick phases to "chinesse-script" or "skeletal" phases. Addition of AlCr20 increases tensile strength and decreases elongation; however, even higher amount of chrome decreases tensile strength. After addition of this master alloy there has been a change in the length of intermetallic phases by almost half its original length without corrector. But the addition of AlNi20 master alloy has better results in tensile strength test, elongation test and also has a less negative effect on gas content in the secondary alloy. According to these all results and after further research and verification their effect, AlNi20 and AlCr20 can be used as an iron correctors in secondary aluminum alloys.

Acknowledgment

This work was created in framework of the grant project VEGA č. 1/0363/13. The authors would like to thank the Grant Agency for support.

References

[1] [T. Takaai, M. Koga and Y. Nakayama, *Heat treatment and mechanical properties of A356 aluminium casting alloys*, Light Metals Processing and Applications.

[2] L. Pedersen and L. Arnberg. The effect of solution heat treatment and quenching rates on mechanical properties and microstructures in AlSiMg foundry alloys, Metallurgical and Materials Transactions, volume 32A, March 2001.

[3] Z. Li, A.M. Samuel, F.H. Samuel, C. Ravindran and S. Valtierra. *Effect of alloying elements on the segregation and dissolution of CuAl2 phase in Al-Si-Cu 319 alloys*, Journal of Materials Science 38 (2003), 1203-1218.

[4] S.G. Shabestari and J.E. Gruzleski, The effect of solidification condition and chemistry on the formation and morphology of complex intermetallic compounds in aluminium-silicon alloys, Cast Metals volume 6 number 4, 1994.

[5] HURTALOVÁ, L., TILLOVÁ, E. (2013). Elimination of the negative effect of Fe-rich intermetallicphases in secondary (recycled) aluminium cast alloy. In *Manufacturing Technology*, Vol. 13, No. 1, p. 44-50, ISSN 1213-2489

[6] DINNIS, C. M. – TAYLOR, J. A. – DAHLE, A. K. 2005. As-cast morphology of iron-intermetallics in Al–Si foundry alloys. In Scripta Materialia 53, 2005, p. 955 - 958

TRANSCOM 2015, 22-24 June 2015
University of Žilina, Žilina, Slovak Republic

Chemical Analysis of Produced Prototype by Selective Laser Melting (SLM) Method Using Rapid Prototyping Technology

Róbert Sásik Author, Rudolf Madaj Co-Author, Michal Hoč Co-Author, Peter Spišák Co-Author
*University in Žilina, Faculty of Machine Engineering, Department of Design and Mechanical elements, Univerzitna 2, 01026 Žilina, Slovakia, {robert.sasik}@fstroj.uniza.sk, {robert.sasik}@fstroj.uniza.sk, {michal.hoc}@fstroj.uniza.sk, {peter.spisak}@fstroj.uniza.sk

Abstract. Additive production of the metallic prototypes in the field of Rapid Prototyping is a progressive method that will be used in many areas of the industrial production. Every product which is produced by this method is fully functional and individual. This article addresses of produced prototype by Selective Laser Melting (SLM) method using Rapid Prototyping technology.

Keywords: Rapid Prototyping, Selective Laser Melting (SLM), Chemical analysis

1. Introduction

In the recent years there is a significant growth in research and development in the field of rapid prototyping technologies and their implementation into a commercial sphere. Few years ago it was a domain of small number of big companies e.g. American company Stratasys. Nowadays there is an increasing number of either small or big competitors coming to the market. The open market environment with many competitors decreases the production costs of rapid prototyping and as a consequence many small companies and research institutes can afford the fast prototype production which causes great simplification of the work.

The rapid prototyping technologies are promising great vision for the future, since the technology can step beyond the production of prototypes into the serial mass production of working products in the field of mechanical engineering, civil engineering, biomedical technologies or even in the research and development for space applications.

1.1 Rapid Prototyping

Rapid prototyping (RP) is a general term for the technological chain which allows developing prototypes without necessity of using conventional tools or even without services that are provided by high-qualified professional modelers. [1].

Rapid Prototyping technologies are additive technologies i.e.: the material is being added during the production process (it is not removed as during the milling jobs or turning operations)

According to the next definition the rapid prototyping (RP) represents a whole scale of new technologies for the fast production of exact components directly from CAD models within few hours with minimal need for human intervention. This means that designers have a chance to produce physical models of their drawings more frequently, which enables them to control the assembly and design functions and allows them to discuss the following production process. This minimizes the number of errors and reduces development costs and thus decreases delivery times [2].

1.2 Selective laser melting (SLM) method

SLM method is a leading method for the production of very complicated metallic components that are not manufacturable by conventional technologies. This process uses high performance lases (e.g. 200W Yb) for the producing models layer by layer by sintering the metallic powders. The complete production process lasts for 2-3 days for small components and 5-8 days for big components. The building material is represented by clean metallic powder with grain size up to 20 μm. Components that are produced this way have a high resolution and usually fit the very fine tolerance criteria. The SLM products have a full density and their mechanical properties are comparable to the mechanical properties of the conventionally produced components. It is possible to apply post processes to the SLM products such as grinding, polishing and other machining methods.

SLM is a method that engages thermal processing of the metallic powder in the lower temperature then the melting temperature of the main component. This way the stiffness of the product is increased. SLM represents one of the additive techniques which uses high power laser (e.g.: carbon dioxide laser) for the fusion of small grains of metallic powder. Scanning and movement of laser is predefined by a sample pattern which has been generated according to characteristic features of the part designed in 3D CAD software or created by digital scan. After the first layer is finished the powder base is shifted in a Z-axis for the thickness of one layer and new layer of material is applied to the upper layer and the process repeats until the produced part becomes complete [3].

The metallic powder gradually melts in microscopic layer due to laser heat up which leaves low porous material. According to test results there has been estimated that the most suitable materials for the SLM are based on the nickel, iron alloys and alloys of pure titanium [4].

SLM process is applicable with two different ways. The first one is powder deposition, the second is powder base. These ways differ in the manner each layer is applied.

During the powder deposition method, the powder is stored in the cartridge, where it is melted and gradually applied in the thin layers to the building plate.

During the powder base method the piston, which is located in the lower side of the cartridge pushes the powder dosage into the working chamber where the entrancing arm removes the powder aimed for the single layer and it deposits the material on the building plate. Afterwards the laser will create one layer of the produced part.

The method of powder deposition allows the advantage of using several materials stored each in its own cartridge [5].

The powder base method is limited by the use of single material but it allows higher production speed.

Production parts are created from the metallic powder by local melting due to focused laser beam. Parts are created additively layer-by-layer, each usually 20 micrometer thin. This process allows creating very complicated geometries which can be created right out of 3D CAD data, quickly and automatically without any need for tool cultivation.

The dosage device sets the amount of powder for a single layer and the mechanic arm with ceramic cutting edge distributes the uniform powder layer onto the surface of the metallic platform according to the selected thickness of the layer. In region of the laser beam impact the metallic powder locally melts while the primer layer is “remelted” and altogether cools down to the solid state. The metallic platform also serves as a heat removal therefore the melted metal cools down very quickly. For most of the materials the working chamber is filled with nitrogen therefore the produced part is protected against the oxidation. The material for the prototyping parts is a powder in the form of metal and its alloys. The material is stored in the form of very fine powder – the

thickness of the single layer is 20-40 micrometers. This method requires the building of reinforcements.

The finishing operations are inevitable parts of production process – reinforcement's removal, classical tooling, grinding, polishing etc. (Aditivní technologie – metody Rapid Prototyping).

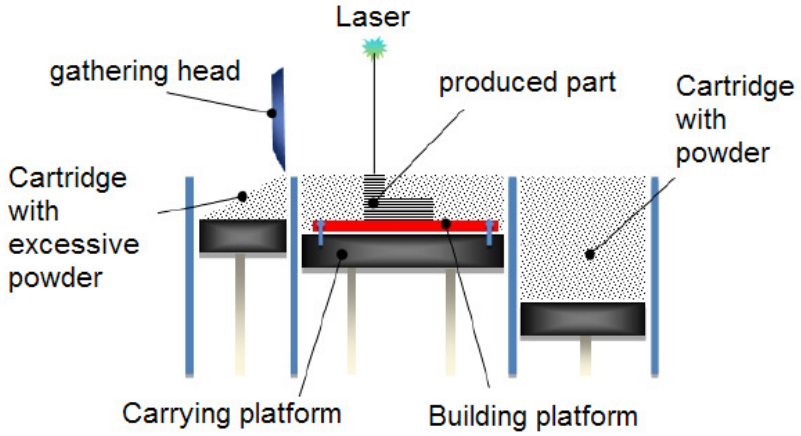

Fig. 1. Selective Laser Melting technology principle (Dadej, Hudák, Živčák, 2013, p.25)

2. Material and methods

2.1 AM250 machine for the metallic prototype production

AM250 machine, made by Renishaw Company, belongs to SLM technologies Rapid Prototyping (renishaw.com). This machine is used by University in Žilina in its laboratory of Rapid Prototyping.

Laser melting is one of the technologies of Additive manufacturing, which uses one of the strongest ytterbium filament lasers for the melting of very thin metallic powders with the goal of creating functional 3D parts.

The production process comes out from digital 3D CAD models virtually separated to layers, or 2D curves with thickness 20 µm up to 100 µm. Gradual deposition of the separate layers of metallic powder and their melting by laser in an inert atmosphere creates 3D metallic part. Argon is used as a gas for the inert atmosphere. After removal, the finished part can be post processed by surface or heat processing.

Typical applications of the laser melting technology:

- Production of the prototype parts suitable for the functional tests
- Production of implants or geometrically very complicated parts
- Unit production and small-lot production of complicated parts from the specific materials.

AM250 machine allows fast drain out of the air from the working chamber, which is afterwards filled with pure argon gas, which ensures clean environment so we can use reactive materials e.g.: titan. In this case the percentage of oxygen in a working chamber has to be very low. The argon consumption is minimized by the use of perfectly tight and professionally welded chamber which in a meanwhile supports the robustness of the process. It is also possible to treat non-reactive materials in the atmosphere from nitrogen gas.

AM250 uses external cartridge of the metallic powder with flap gate which allows refilling of the material during the production process. The cartridge with material can be removed when it is necessary to clean up the machine or replaced with cartridge with different material. The storage cartridges for the material which drops out during the production process are placed aside from the working zone and they have their own flap gates. This way it is possible to reuse the material during

the printing process. The manipulation with the powder and the produced part itself is possible by using protective glows which are placed in the door to the working zone. The filter protects the user from the emissions that originate from the printing process.

The AM250 was designed for the production industry with simple touch screen and easy user interface and robust construction. AM250 machine can produce various parts starting from mass production of implants ending up with complicated grid structures or detailed geometrical shapes for aeronautics and space industry. With the enlargement of the Z-axis it is possible to produce the parts up to 360mm high.

The whole data preparation and programming is done offline in office since whole production process is accurately controlled. The software for the preparation process allows various improvements of the process which are handy for more advanced users.

2.2 Material properties of AlSi10Mg AM250 400 W 25 micron

Mechanic properties	**Heat treatment [a]**	**Test / ISO norm according to which the test was run**
Min	Max	
Tensile strength (UTS) / MPa*	332	341	BS EN ISO 6892-1:2009
Characteristic stress (0.2%) / MPa*	173	212	BS EN ISO 6892-1:2009
Tensibility (extension) during the breakage / %*	4%	10%	BS EN ISO 6892-1:2009
Stiffness according to Vickers HV0.5*	113	125	ASTM E384-11
Surface roughness in X, Y / Ra μm[b]	3	7	JIS B 0601-2001 (ISO 97)
Surface roughness in Z / Ra μm	5	7	JIS B 0601-2001 (ISO 97)
General data		
Density	2.68 g/cm³	Generally produced materials
Heat conductivity	130 W/m·K to 190 W/m·K	Generally produced materials
Thaw point	570 °C - 590 °C	Generally produced materials
Thermal expansion coefficient [b]	21 × 10-6 K-1 to 21 × 10-6 K-1	Generally produced materials

Tab. 1. Mechanical features AlSi10Mg AM250 400 W 25 micron.

* Tested by NADCAP and UKAS accredited independent laboratory

Minimal and maximal values are stated x ± σ for the specimen of vertical and horizontal testing rods. [A] 25 um layer on AM250-400 W. All specimens were produced before the testing process. After the thermal processing at 300 ° C it cools down by the air flow. [B] In the range from 20 ° C to 100 ° C.

The chemical composition of AlSi10Mg AM250 400 W 25 micron is presented in table 2.

The powder composition / mass percentage												
Al	**Si**	**Mg**	**Fe**	**N**	**O**	**Ti**	**Zn**	**Mn**	**Ni**	**Cu**	**Pb**	**Sn**
varying	9.0 - 11.0	0.25 - 0.45	<0.25	<0.2	<0.2	<0.15	<0.1	<0.1	<0.05	<0.05	<0.02	<0.02

Tab. 2. The chemical composition of AlSi10Mg AM250 400 W 25 micron.

- Low density (suitable for light components)
- Good specific stiffness (mass stiffness)
- Good thermal conduction
- Excellent electrical conductivity
- It has got a good reactions for the post-processing modifications

2.3 Digital spectrometer ED-XRF Delta

Chemical analysis was performed by manual digital spectrometer ED-XRF Delta.

It is robust, highly efficient manual spectrometer for the analysis of metals, alloys and other materials. With the help of ED-XRF technology, which is better and faster and more flexible the high precision has been achieved.

The outcome of the measurement is represented by the name of the corresponding material norm and percentage of the concentration of corresponding elements. The device is capable to detect 21 elements (Ti, V, Cr, Fe, Co, Ni, Cu, Zn, Zr, Nb,Mo, Hf, Ta, W, Re, Pb, Ag, Sn, Bi a Sb).

3. Results

For the chemical analysis there has been used corrupted prototype made by SLM method since the test had been destructive – the specimen was cut into parts. The prototype has been produced by the sintering machine AM 250 (400 W 25 micron) by Renishaw Company using material AlSi10Mg. The chemical analysis has been performed so far from one specimen in three testing measurements. The analysis is planned to be performed from more specimens so that the obtained results are statistically provable.

	Data provided by producer /distributer Renishaw	Own chemical analysis - measurement 1,2,3			
Chemical element	Percentage of content %				Arithmetical mean
Al	Balance	90,00	89,60	89,30	89,63
Si	9-10	9,60	9,90	10,00	9,83
Mg	0.25-0.45	0,70	1,00	0,93	0,88
Fe	<0.25	0,23	0,40	0,43	0,35
N	<0.20	-	-	-	-
O	<0.20	-	-	-	-
Ti	<0.15	-	-	-	-
Zn	<0.10	-	-	-	-
Mn	<0.10	-	-	-	-
Ni	<0.05	-	-	-	-
Cu	<0.05	-	-	-	-
Pb	<0.02	-	-	-	-
Sn	<0.02	0,10	0,10	0,10	0,10
Sb	-	0,10	0,13	0,13	0,12

Tab. 3. Chemical analysis of the tested specimen producent by SLM method by sintering device AM250.

The result of the chemical analysis of tested specimen is compared with the data provided by producer. The comparison is summarized in the table 3.

Fig. 2. Specimen - ready for the chemical analysis

4. Conclusion

Additive production of the metallic prototypes in the field of Rapid Prototyping is a progressive method that will be used in many areas of the industrial production. Every product which is produced by this method is fully functional and individual. The use of this technology is also very promising in the field of biological implants where each patient can obtain its individual implant which can contribute to the better life of the individual. Automotive industry and customers industry are also interested in the implementation of this technology into their production process.

Acknowledgement

This work was created by the implementation of the "Reengineering of product portfolio VIPO a.s.", "ITMS: 26220220091" to support the Operational Programme Research and Development financed by the European Fund for Regional Development.

References

[1] KICKOVÁ, M. - HERDITZKY, A. 2008. VÝROBA MALÝCH SÉRIÍ PLASTOVÝCH SÚCIASTOK KONVENCNÝMI METÓDAMI PROTOTYPOVANIA. In Transfer inovácií [online]. 11/2008 [cit. 2015-01-07]. Dostupné na internete: <http://www.sjf.tuke.sk/transferinovacii/pages/archiv/transfer/11-2008/pdf/147-150.pdf>. ISSN 1337-70-94.

[2] PHAM, D.T. - GAULT, R.S. 1998. A comparison of rapid prototyping technologies. In International Journal of Machine Tools & Manufacture [online]. PII: S08 90- 6955(97)00137-5, 38 (1998), p.1257-1287 [cit. 2015-01-08]. Dostupné na internete: <http://www.researchgate.net/publication/222495237_A_comparison_of_rapid_prototyping_technologies/file/3deec521c7163860a5.pdf>.

[3] KOPELIOVICH , D. 2006. Sintering of metals. [online]. 2006, [cit. 2014-12-19]. Dostupné na internete: <http://www.substech.com/dokuwiki/doku.php?id=sintering_of_metals>.

[4] OSAKADA, K. - SHIOMI, M. 2006. Flexible manufacturing of metallic products by selective laser melting of powder. In International Journal of Machine Tools & Manufacture [online]. 46 (2006), p.1188-1193 [cit. 2015-01-10]. Dostupné na internete: <http://www.sciencedirect.com/science/article/pii/S0890695506000307#>.

[5] ŠARIK, M. - HUDÁK, R. - ŽIVCÁK, J. 2013. Analýza tepelných procesov pri priamom laserovom sinterovaní titánového prášku. In Transfer inovácií [online]. 25/2013 [cit. 2015-01-15]. Dostupné na internete: <http://www.sjf.tuke.sk/transferinovacii/pages/archiv/transfer/25-2013/pdf/249-254.pdf>. ISSN 1337-7094.

TRANSCOM 2015, 22-24 June 2015
University of Žilina, Žilina, Slovak Republic

Energy Parameters of Waste Generated While Vehicle Disassembly

[*]Anna Skarbek-Żabkin, [**] Marcin Szczepanek
[*] Motor Transport Institute, Centre for Material Testing, ul. Jagiellonska 80 03-301 Warszawa, tel. +48 22 43 85 138 e-mail: anna.skarbek@its.waw.pl
[**]Maritime University of Szczecin, Faculty of Mechanical Engineering, Institute of Ship Power Plant Operation, 70-500 Szczecin (Poland), ul. Waly Chrobrego1-2, e-mail: m.szczepanek@am.szczecin.pl,

Abstract. The issue of waste management is of great importance due to the constantly increasing amount of generated waste, limited storage space and hazards to the environment which waste causes. One of the waste management methods is to use the waste in the energy sector as alternative fuel. According to the Waste Framework Directive of the European Parliament and the Council, thermal waste treatment is one of the methods used for waste recovery. It complies with the waste management hierarchy included in the Directive. Applying the rules, the Member States prefer solutions which have no negative impact on human health and are the most environmentally beneficial.
In order to facilitate the recovery, waste should be segregated so that the materials having diverse properties are not mixed. The paper presents the energy properties of waste delivered by vehicles withdrawn from the operation, constituting a serious risk for human health and the environment.

Keywords: waste, recycling, vehicles withdrawn from operation, energy use of waste

1. Introduction

The applicable legal regulations create a necessity to develop mechanisms, technical solutions and new technologies whose efficiency to prevent the environment from being degraded is as high as possible.

The new Framework Directive presents the following waste management hierarchy [2]:
− prevention,
− preparing for re-use,
− recycling,
− energy recovery
− disposal (including storage).

The Directive allows departing from the hierarchy for the certain types of waste. It depends on the environmental and economical benefits. According to the Directive a “recovery” means any operation the principal result of which is waste serving a useful purpose by replacing other materials which would be otherwise have been used to fulfill a particular function, or waste being prepared to fulfill that function, in the plant or in the wider economy.

One of the main factors defining the economic viability of alternative fuel use in the energy sector is the amount of thermal energy generated during its combustion. For each type of fuel, the said property is described by two parameters: combustion heat and calorific value.

2. Alternative fuels in passenger vehicles

Taking into consideration that more than 19 million of driven vehicles is registered in Poland [3], almost one million of them should be utilized every year (5-6% of registered vehicles driven the European Union is recycled annually) which constitutes about 700,000 to 800,000 tons of waste, materials, parts and units for recycling or recovery.

70,000 to 80,000 tons per year of potential, alternative fuel may be estimated assuming that according to the requirements of the Directive and the recycle law, 10% of vehicles weight is a fraction dedicated for energy recovery in the form of incinerable waste such as maintenance fluids, plastics, rubber, fabrics, wood. An analysis of Table 1 proves that 20 to 30% of a passenger car weight refers to combustive materials.

Materials in passenger car	Share of materials [%]
Ferroalloys	55-85
Alloys of Al, Mg	1,5- 6
Alloys of Zn, Cu, Mo, Ti, Sn and other	1-2
Plastics	10-20
Rubber + tyres	5,5-6
Fabrics + wood	1-2
Glass	3-3,5
Other (maintenance fluids)	1-2

Tab. 1. Share of materials in a middle class passenger car [4].

The examples of waste generated due to a dismantling process and intended mainly for alternative fuels are presented in Table 2.

Item	Waste	Management of		
		Material	Product recovery	Energy recovery
Waste mainly intended for alternative fuels				
1.	Mats	Composite	+	+
2.	Composite	Composite	+	+
3.	Boot liner and mat	Fabrics	+	+
4.	Fuel tank	Plastics		+
5.	Door liners	Composite	+	+
6.	Door pillar liners	Plastics	+	+
7.	Seat covers	Fabrics		+
8.	Seat refill	Plastics		+
9.	Dashboard	Plastics	+	+
10.	Rear dash	Composite	+	+
11.	Steering column cover	Plastics	+	+
12.	Gauges' cover	Plastics	+	+
13.	Center console	Plastics	+	+
14.	Storage spaces	Plastics		+
15.	Sun visors	Plastics/Fe	+	+
16.	Seat belts	Fabrics		+
17.	Armrests	Plastics	+	+
18.	Steering wheel	Plastics/Fe	+	+
19.	Interior mirrors	Plastics	+	+
20.	Door seals	Rubber/Fe		+
21.	Hood seals	Rubber		+
22.	Boot seals	Rubber/Fe		+
23.	Door thresholds	Plastics		+
24.	Spoilers	Plastics	+	+
25.	Hood	Plastics		+
26.	Wheelarches	Plastics		+

Tab. 2. Waste mainly intended for alternative fuels.

Energy recovery is carried out to a lesser extent than product or material recovery and it is applicable in particular to: rubbers – including tyres, used oils, plastics, fabrics, cellulose-based materials. While oils and tyres are sourced at disassembly stations, the remaining materials create so called "light fraction" obtained from shredding [5].

2.1. Plastics [1]

Macromolecular materials – plastomers constitute 10 ÷ 15 % of the weight of passenger car with mid capacity engine, that is 100 to 150kg. The most applications of them, around 60%, occur inside vehicles. 30% of plastics are in the chassis and the remaining 10% is used under the hood and the floor plate (covers). Fragmented fractions of plastics generated during shredding constitute more than 30% of light fraction. Due to the high calorific value of plastics, they are often incinerated and the energy is recovered as a valuable complement to alternative fuel generated from municipal waste. Such fuel is co-incinerated with fuels used at power plants and heat and power generating plants.

2.2. Rubber and tyres

The production of tyres in Poland equals to around 180,000 tonnes per year. Taking into consideration the balanced export and import it was calculated that 190,000 tonnes of tyres per year is implemented on the Polish market (96% are new tyres). During the operation, the loss of the weight equals to around 20-25%. Therefore, 150,000 tons of the tyres remain for being managed. Additionally, around 10,000 tonnes of rubber is generated from disassembled seals (windshields, doors, others chassis elements), tubes, pipes, washers and suspension elements etc. The reasons for which tyres are valuable raw materials are their energy value. It exceeds energy value for the most of fuels except petroleum.

The incineration of tyres in smokeless furnaces at cement plants is safe for the environment and enables their wasteless management. Neither ash nor slag is generated in the process, because steel cord is permanently connected with produced clinker, which affects positively its strength properties. There was no evidence for an increased, in relation to coal combustion, emission of dust, nitrogen oxides, sulfur oxides and heavy metals except zinc. The temperature in cement kilns reaches up to 2000 °C. These are perfect conditions for safe incineration of tyres.

2.3. Used oils

The weight of oils and lubricants in a withdrawn vehicle equals to around 7 kg. It means approximately 0,5% of a total vehicle weight. When oils and lubricants used during the entire life-cycle of a car are added to the above, the weight will equal to 200kg. 350,000 tons of vehicle oils and lubricants are used annually.

Vehicle waste oils are mainly used engine oils and gear oils. They are one of the most hazardous threads for the environment and human and animal health. Energy recovery is carried out through incineration, as a waste disposal method, is economically viable. However, it creates the risk for the environment. Therefore, used oils should be burnt in furnaces that are properly adjusted for that type of waste.

2.4. Fabrics

Fabrics represent another group of waste which may be subjected to energy recovery process. The textiles used inside vehicles belong to technical fabrics group which amount to around 2% of a vehicle weight. It equals to 10-15 thousand tonnes of the fabrics within a year. It is a specific fabric waste group of a diversified structure of the fibrous layer and the backsheet, creating so called a textile composite. They are used as covers for car seats, various liners, safety belts, airbags. Upholstery waste from the automotive industry is considered as waste of low environmental impact. However, fibers do not decompose for hundreds of years.

3. Fuel properties

The principle of determining calorific value is based on the total incineration of a waste sample in an atmosphere of oxygen under pressure in a bomb calorimeter with a known heat capacity and the measurement of water temperature gain in a bucket. Marking: after 5-10 minutes upon starting the apparatus in which the temperature of the insulating jacket, water in the bucket and in the bomb equalizes, proper measurement is carried out consisting in three successive periods:

- initial period – lasts 5 minutes and precedes sample incineration,
- main period – occurs after the sample incineration until and lasts until the water temperature in the bucket is equalized,
- final period: lasts 5 minutes until the temperature is equalized.

The principle of the determination of combustible and non-combustible components is based on ashing the tested waste sample, and then on its calcinations to a constant weight in an electric furnace in the temperature of 800^{o} C and on determining the percent content of the components. Prior to the determination of the combustible and non-combustible components, a crucible, in which the sample will be placed, should be calcined. In order to prepare the crucible, 1-2g of dried and grinded waste should be weighted. The crucible together with the sample should be placed on a clay triangle and carefully heated with a burner until there charred particles settled on the walls of the crucible are burnt. Then, the crucible with its content should be placed in a furnace, where the temperature is 800 C, and calcined for 3 hours. Upon that time, it should be taken out and inserted into a desiccator, afterwards cooled and weighted. These activities should be repeated until the difference between the results of weighting equals to less than 0.0005 g.

Item	Waste	Waste code	Calorific value [J/g]	Non-combustible materials [%]
Rubber waste				
1.	Tyres	16.01.03	35.929	8.23
2.	Door seals	16.01.99	30.395	21.79
3.	Fuel pipe	16.01.99	37.885	3.75
Plastic waste				
4.	Seat refill PUR	16.01.19	22.671	2.12
5.	Seat belts PA	19.12.09	22.032	1.56
6.	Dashboard PP+T	16.01.19	32.709	22.69
7.	Lamp shade PMMA	19.12.09	26.502	0.00
8.	Door pillar liner PP+T	19.12.09	31.408	6.78
9.	Intake manifold PA+fiberglass	1912.09	20.174	34.87
10.	Bumber PP+EPDM	16.01.19	39.776	-
Combined waste				
11.	Rear dash: velour liner +PUR + harl	16.01.19	18.199	3.11
12.	Seat cover: velour +PUR	16.01.19	24.946	1.02
13.	Seat cover: velour +PUR+ fabrics	16.12.09	22.969	4.63
14.	Floor mat: polyester + rubber	19.12.09	40.345	0.78
15.	Headliner: velour + harl	19.12.09	25.520	1.26
16.	Door liner: PVC foil + acrylic wool + harl	19.12.09	18.884	3.29
Energy fuels				
17.	Used oil	13.02.05	41.718	0.84
18.	Fresh synthetic oil	-	44.193	0.52
19.	Pine fuel wood	-	17.879	0.66
20.	Stove coal	-	32.901	1.4

Tab.3. Calorific value and ash content in tested waste.

4. Conclusion

Combustible waste, as presented in Table 3, has high calorific value comparable to the calorific value of stove coal, and the content of non-combustible parts (ash) is only slightly higher than coal. Hence, combustible waste recovered from a vehicle withdrawn from the operation may be considered as a full substitute of solid fuels used in energy installations.

References

[1] CZOP M.: *Tests of basic fueling properties of polyolefin wastes,* Archives of Waste Management and Environmental Protection, vol. 15, issue 3 (2013), p. 71-80.

[2] Dz. U. WE L 312/3 z 22.11.2008

[3] Instytut Badań Rynku Motoryzacyjnego SAMAR

[4] MERKISZ – GURANOWSKA A.,: *Recykling samochodów w Polsce*, Poznań – Radom

[5] SKARBEK A., MICHALSKI R..: *Energy use of waste from end of life vehicles* , Archives of Waste Management and Environmental Protection, vol. 14, issue 2 (2012), p. 27-32

TRANSCOM 2015, 22-24 June 2015
University of Žilina, Žilina, Slovak Republic

Determination of Minimum Uncut Chip Thickness in Turning

[*]Michał Skrzyniarz, [*]Edward Miko, [*]Łukasz Nowakowski
[*]Kielce University of Technology, Faculty of Mechatronics and Machine Engineering, Department of Manufacturing Engineering and Metrology, Aleja Tysiąclecia Państwa Polskiego 7, 25-314 Kielce, Poland, {skrzyniarzmichal@gmail.com, e.miko@tu.kielce.pl, lnovak@poczta.fm}

Abstract. The article described the experimental method of measuring the minimum uncut chip thickness h_m during turning. The paper presents the results of measurements of impact zones the cutting edge to material, and methods of measurement of minimum uncut chip thickness by optical and stylus methods was described.

Keywords: minimum uncut chip thickness, micromachining, turning.

1. Introduction

Minimum uncut chip thickness (h_m) defines the smallest layer possible to remove in selected processing conditions. Fig. 1 depicts the chip formation with respect to chip thickness [1]. Cutting zone can be divided into three parts influence the blade cutting edge on the workpiece [1, 2]:

I - when $h < h_m$: elastic deformation and plastic kneading occurs,

II - when $h = h_m$: elastic-plastic deformation with partial machining take place,

III - when $h > h_m$: beginning removal of material as chip.

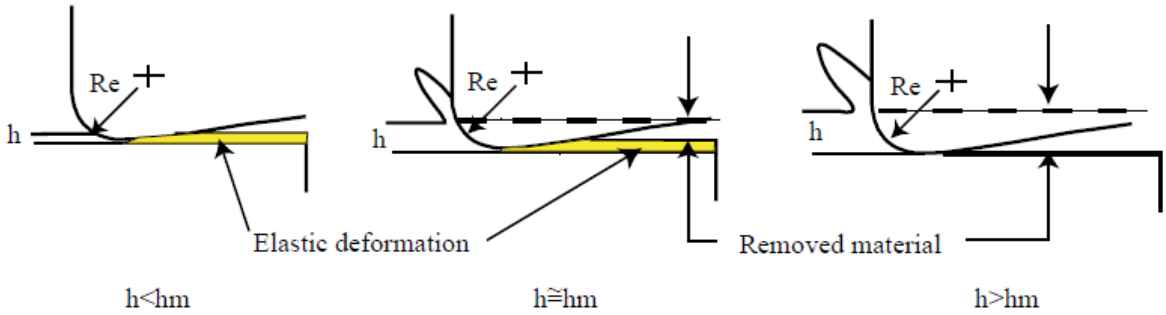

Fig. 1. Schematic of the effect of the minimum chip thickness (R_e, radius of cutting tool; h, undeformed chip thickness; h_m, minimum chip thickness) [1]

Many researchers have attempted to designation of theoretical and experimental minimum chip thickness. Currently, there are many well-known mathematical models [3, 4, 5] to predict the value of h_m. Malekian, Mostofa, Park, Jun [6] developed a model (1) to predict the minimum uncut chip thickness which is depend upon the edge radius and position the stagnation point A which is described by the angle stagnation θ. Researchers have defined the value of the parameter by formula:

$$h_m = r_e(1 - cos\theta_m) \quad (1)$$

Fig. 2. shows a schematic of material flow around a tool with a finite edge radius [6]. Cleary visible here are two zones. Material flows below the point A without forming a chip, there is phenomenon called ploughing which is elastic-plastic deformation. Above this point material is removed as a chip.

Kawalec [7] presented the equation (2) describing the minimum uncut chip thickness as the quotient of the radius of the cutting tool r_e and the coefficient of friction between the tool and the material.

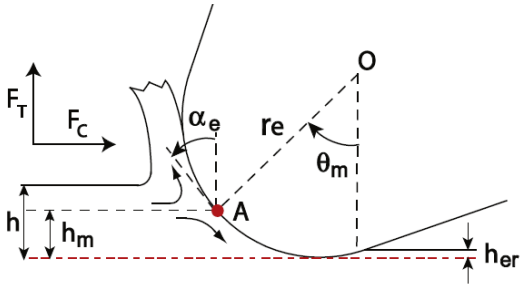

Fig. 2. Machining using an edge radius tool [6]

This factor depends on the machining conditions and it can take values from 0.1 to 1.

$$h_m = k \cdot r_e \tag{2}$$

Grzesik [8] developed a model (3) to predict the minimum uncut chip thickness using the molecular-mechanical theory of friction:

$$h_m \geq 0.5 r_e \left(1 - \frac{2\tau_a}{Y_{sh}}\right) \tag{3}$$

where: r_e is the radius of indenter or rounded cutting edge radius, τ_a is the shear strength of the adhesive junction and Y_{sh} is the yield stress of strain-hardened bulk material. Apart from mathematical model to predict the minimum uncut chip thickness also developed a practical method. Harasymowicz, Gawlik, Warziniak [9] developed a experimentally measuring a method, and they described a method of preparing a sample for measurement h_m. Sample preparation consist of cutting the transverse and subjecting it to grinding. Then it combined with each other and conduct cutting tests. Next, the sample is separated and measured using a optical microscope.

2. Methodology and Results

All set out above methods are very time-consuming and require laborious sample preparation [10]. Therefore we propose a new practical method for determining minimum uncut chip thickness.

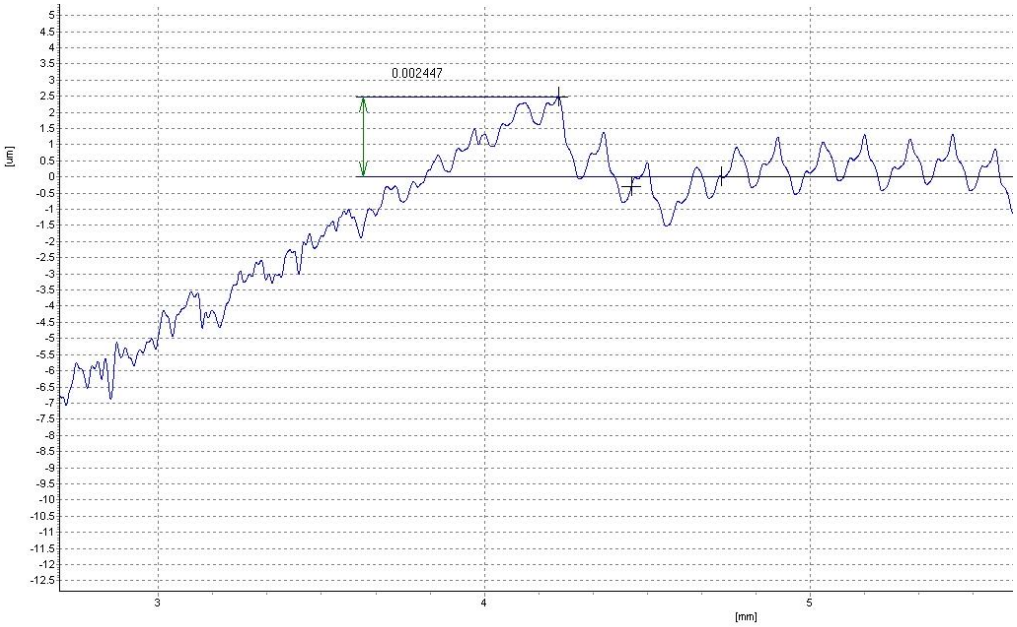

Fig. 3. Measurements of minimum uncut chip thickness using a stylus profilometer.

The new method involves preparing a ground cone with the known convergence. Then, such prepared sample is turning to determine the h_m during straight turning. Turning experiments were performed using turning center DMG ALFA 500 and the insert carbide tip was DCMT 11T308. The second step of the method consists in taking the measurements of minimum uncut chip thickness

using the stylus method. Fig. 3 shows the result of measuring the minimum uncut chip thickness using TOPO 120P stylus profilometer with head. Directly on the profile was measured minimum uncut chip thickness in this case was 2,45 µm.

The use of the contact method allows you to determine characteristic zones of influence of the tool to the material, the measurement of the angle of the sample, as well as measurement minimum uncut chip thickness with a high resolution.

a) b) c) d)

Fig. 4. Measuring instruments used in the study: a) workshop microscope, b) video device VM–2045 [8], c) optical device MarVision MM 320 QC 300 [11], d) microscope Nikon SMZ 1500 [12]

Measurements of zones interaction betweet tool and the workpiece was performed using different measuring instruments: workshop microscope (Fig. 4a), video device VM-2045 (Fig. 4b), optical device MarVision MM 320 QC 300 (Fig. 4c), and microscope Nikon SMZ 1500(Fig. 4d). By measuring the length of these zones and by knowing the angle of inclination of the sample was designated h_m parameter by trigonometric functions.

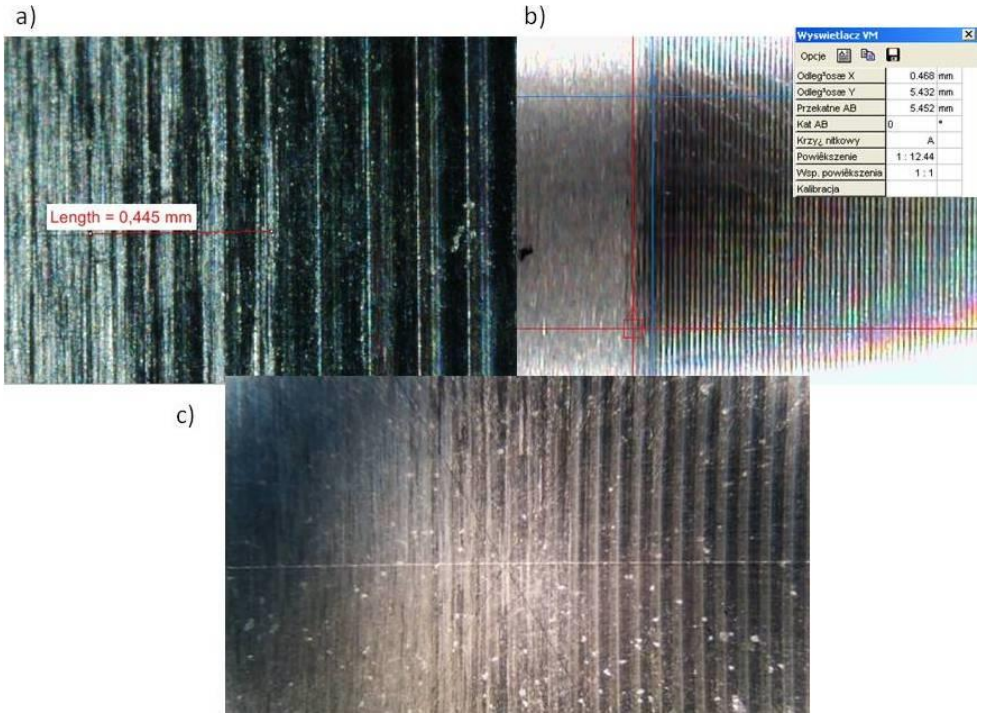

Fig. 5. Examples of measurements of the cutting zones: a) microscope Nikon SMZ 1500 b) video device VM–2045, c) workshop microscope

The results of the measurement results of minimum uncut chip thickness are summarized in table 1. In column No. 2 was placed directly results of measurement by stylus profilometer. The columns 3-6 show the measurements of the minimum uncut chip thickness by optical methods. In the last four columns was presented the experimental error method (EEM) for optical methods with respect to the contact measurements.

	hm, µm					EEM, %			
1	2	3	4	5	6	7	8	9	10
Sample	Topo 120 P	Microscope	VM-2045	MarVision	Nikon	Microscope	VM-2045	MarVision	Nikon
1	2,68	2,67	2,70	2,66	2,60	0,40	0,84	0,90	2,90
2	2,45	2,44	2,42	2,51	2,56	0,33	1,17	2,40	4,31
3	2,44	2,36	2,42	2,41	2,50	3,21	0,75	1,30	2,27
4	3,69	3,97	3,70	3,75	3,50	7,51	0,26	1,53	5,18
5	3,29	3,17	3,27	3,33	3,23	3,62	0,57	1,27	1,79
6	3,05	3,09	3,13	3,16	3,15	1,34	2,58	3,75	3,31
7	2,53	2,80	2,85	2,98	2,99	10,79	11,23	17,67	18,20
8	3,01	2,88	2,99	3,14	2,98	4,43	0,65	4,46	1,09
9	2,91	2,80	2,70	2,68	2,69	3,67	7,67	8,04	7,58
10	2,94	2,84	2,85	3,13	3,08	3,52	3,16	6,49	4,67
11	3,19	3,01	2,99	3,09	2,98	5,63	6,67	3,11	6,68
					Average	4,04	3,23	4,63	5,27

Tab. 1. Summary of the results of measurements of the minimum uncut chip thickness and experimental error method

As we see from the table disparity h_m calculated parameters in relation to the contact measurement are as follows: for microscope workshop 4,04 %, for video device VM-2045 3,23 %, for optical device MarVision 4,63 %, for microscope Nikon 5,27 %. The average value of the measurements results for optical methods is less than 10%, which indicates their accuracy.

3. Conclusion

The paper presents a new practical method for measuring minimum uncut chip thickness. Measurements by stylus profilometer are the most reliable due to the high resolution of device. Measurements using optical method require a lot of practice and attention from the operator, require knowledge the angle of inclination of the sample. In the measurements carried out show that the measurement method provided a minimum uncut chip thickness may be used alternately.

References

[1] CGAE, J., PARK, S.S., FREIHEIT, T. *Investigation of micro-cutting operations.* International Journal of Machine Tools & Manufacture 46 (2006) 313-332.

[2] GRZESIK, W. *Podstawy skrawania materiałów metalowych.* Wydawnictwo Naukowo-Techniczne, Warszawa 1988.

[3] CEDRO, L. *Identification of an electrically driven manipulator using the differential filters – input error method*, Acta Mechanica at Automatica, vol.6 no.2 (2012) p. 23-27, Oficyna Wydawnicza Politechniki Białostockiej,

[4] KEKEZ, M., RADZISZEWSKI, L. *Genetic-fuzzy model of diesel engine working cycle*, Bulletin of The Polish Academy of Sciences Technical Sciences, Vol. 58, No. 4, 2010 p. 665-671

[5] MIKO, E. *Konstytuowanie mikronierówności powierzchni metalowych obrabianych narzędziem o zdefiniowanej stereometrii ostrzy.* Monografie, studia, rozprawy 46. Kielce 2004.

[6] MALEKIAN, M., MOSTOFA, M.G., PARK, S.S., JUN, M.B.G. *Modeling of minimum uncut chip thickness in micro machining of aluminum.* Journal of Materials Processing technology 212 (2012) 533-559.

[7] KAWALEC, M. *Fizyczne i technologiczne zagadnienia przy obróbce z małymi grubościami warstwy skrawanej.* Rozprawy nr 106, Wydawnictwo Politechniki Poznańskiej 1980.

[8] GRZESIK, W. *A revised model for predicting surface roughness in turning.* Wear 194 (1996), 143-148.

[9] HARASYMOWICZ, J., GAWLIK, J., WARZINIAK, W. *Sposób określenia minimalnej grubości warstwy skrawanej*. Opis patentu tymczasowego nr. 141515, Politechnika Krakowska 1988.

[10]NOWAKOWSKI, Ł. *Wpływ wybranych czynników obróbki na strukturę geometryczną powierzchni frezowanych czołowo.* Wydawnictwo Politechniki Świętokrzyskiej 2014.

[11]http://www.mahr.com

[12] http://www.misroscopemaster.com

TRANSCOM 2015, 22-24 June 2015
University of Žilina, Žilina, Slovak Republic

Monitoring of Microstructural Changes in AZ91 Magnesium Alloy by Internal Damping Measurement

[*]Andrea Soviarová, [**]Zuzanka Trojanová, [*]Peter Palček, [*]Mária Chalupová, [**]Michal Knapek
[*] University of Žilina, Faculty of Mechanical Engineering, Department of Material Engineering, Univerzitná 8215/1, 010 26 Žilina, Slovak Republic, {andrea.soviarova, peter.palcek, maria.chalupova}@fstroj.uniza.sk
[**] Department of Physics of Materials, Faculty of Mathematics and Physics, Charles University in Prague, Ke Karlovu 5, 121 16 Praha 2, Czech Republic, {ztrojan}@met.mff.cuni.cz , {knapek}@karlov.mff.cuni.cz

Abstract. In this work is an investigated AZ91 magnesium alloy after homogenization annealing. Process of precipitation was continuously analysed by two method of internal damping measurement. Internal damping was measured as a function of temperature in AZ91 magnesium alloys by ultrasonic resonance spectroscopy and impulse excitation technique (Resonant Frequency and Damping Analysis - RFDA). The internal damping spectrum was measured in the temperature range from room temperature up-to 390 °C for both methods of measurement. Peaks of internal damping occurred in temperature range from 250 °C up-to 350 °C on AZ91 magnesium alloy. Microstructure analysis was carried out in the place of the internal damping peak maximum.

Keywords: Temperature dependence, internal damping, discontinuous precipitation, continuous precipitation, AZ91 magnesium alloy.

1. Introduction

Mg alloys with low density, high specific strength and high damping capacity are prominent materials in the control of vibration and noise. Mechanical properties of pure magnesium are low. The value of ultimate tensile strength is only about 100 MPa and the elastic modulus reaches just 45 GPa. The strength can be improved by alloying, however this decreases the damping capacity. Therefore, the crux lies in resolving the contradiction between damping capacity and mechanical properties and to create magnesium based alloys which have high damping capacity and sufficient mechanical properties [1].

Among the various magnesium alloys developed the AZ91 alloy containing 9 wt.% Al and 1 wt.% Zn is the most widely used not only for manufacturing of automotive components but also for other structural components because of its combination of excellent castability and reasonable mechanical properties at room temperature with good corrosion resistance.

During the ageing process γ ($Mg_{17}Al_{12}$) phase is formed in two modifications. At lower temperatures this phase creates discontinuous precipitates and at high temperatures continuous precipitates. Xu et. al. [2] showed that the $Mg_{12}Al_{12}$ discontious precipitation may effectively prevent the grain growth during the grain refinement process ECAP via the dynamic recrystallization. ECAP was conducted at 200 °C for 8 passes through a die with a channel angle of 90° and a curvature angle of 37°.

Internal and an elastic relaxation forms the core of the mechanical spectroscopy method, widely used in solid-state physics, physical metallurgy and materials science to study structural defects and their mobility, transport phenomena and phase transformations in solids [3].

This project focuses on measurement of the dependence of internal damping on temperature by ultrasonic resonance spectroscopy (URS) and Resonant Frequency and Damping Analysis (RFDA). In the peak maximum was performed SEM (scanning electron microscopy) analysis.

2. Method of damping measurement

The measurements of temperature dependence of internal damping were performed with use of ultrasonic resonance equipment (Fig. 1) designed on Department of Material Engineering of University of Žilina.

The measurement is based on evaluation of the resonance curve according to the loading frequency. This testing device consists of electric and mechanical part. The electric part has two separate circuits, the first one is regulating the temperature of the heating furnace and the second one is controlling and evaluating the loading process and its parameters. This second circuit consists from the computer controlled signal generator, amplifier, piezoelectric transducer and lock-in amplifier. One of influencing factors which need to be considered in this kind of measurement is that this device measures internal damping of the whole resonance system, not only of the specimen. The test specimen has an hour-glass shape and each specimen has to be adjusted individually, so it is in harmony with the resonance frequency of the ultrasonic horn. Heating rate during the measurement was 1 °C/min. The spectrum is given by internal damping associated with a particular resonance. The value of internal damping is evaluated as the quality factor Q^{-1}. From the Q^{-1} value was evaluated internal damping in half of the resonance peak maximum according to equation (1), where: f_r is the resonance frequency of the resonance peak [Hz], f_2, f_1 are frequencies in half of the peak maximum [Hz] [4-6]

$$Q^{-1} = \frac{f_2 - f_1}{f_r}\ [-]\,. \qquad (1)$$

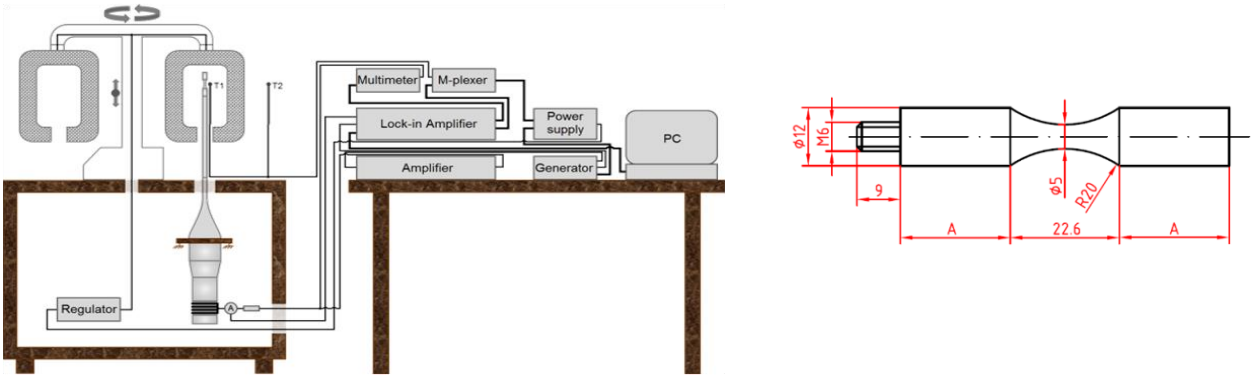

a) b)

Fig.1 Scheme of ultrasonic resonance device a); test specimen for internal damping measurement by ultrasonic resonance device b).

The Resonant Frequency and Damping Analyser (RFDA) (Fig.2) was used to determine the damping and the resonant frequency of the tested alloy. The device is situated at the Charles University in Prague on the Department of Physics of Materials. The measurements were performed in a wide temperature interval from room temperature up to 390 °C. The prism shaped specimens with dimensions of 75 x 20 x 10 mm were excited to vibrations at the resonant frequency using a small striker. Damping of the specimen's free vibrations was registered with a microphone and processed using a special programme. The resonant frequency exhibiting $f \approx 8$ kHz was evaluated with use of Fourier transformation. The heating rate was 2°C/min.

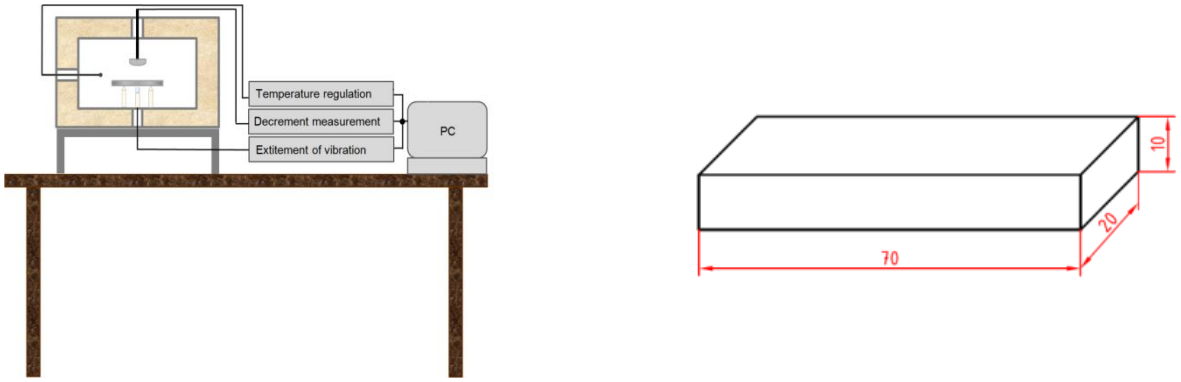

a) *b)*

Fig. 2 Scheme of the Resonant Frequency and Damping Analyser (RFDA) a); test specimen for internal damping measurement by RFDA b).

3. Material characterization

The commercially used magnesium alloy AZ91 has been studied in this work. The chemical composition is provided in Tab. 1. The alloy was manufactured by the squeeze-casting method and was delivered in as-cast state (Fig. 3a). Figure 3b shows detail of intermetallic phases, which are present, in the microstructure. The area *1* represents solid solution δ (solid solution of Al in Mg), phase γ ($Mg_{17}Al_{12}$) shows the area *2*. Discontinuous precipitate is in the area maked *3*. In the area *4* is particle based on Si and in area marked *5* are present particles on the based Mn. Before the measurement of the internal damping, the specimen was homogenization annealed for 22h at temperature of 390 °C and quenched in water (60 °C) [7, 8].

Element	**Al**	**Zn**	**Mn**	**Ca**	**Si**	**Fe**	**Mg**
AZ91 wt.%	7.280	0.554	0.202	0	0.071	0.008	Balance

Tab. 1 Chemical composition of AZ91 magnesium alloy

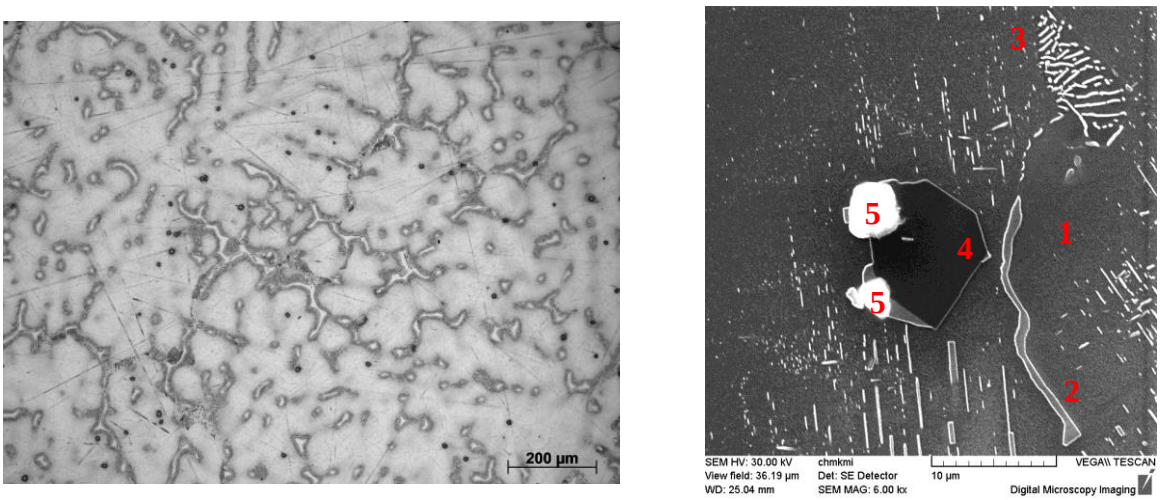

a) *b)*

Fig. 3 Microstructure of AZ91 magnesium alloy: as cast state, etch. Picral a), detail of γ phase, discontinuous precipitate and phases based on Mn and Si (SEM), etch. Picral b)

The microstructure after homogenization annealing was created by polyedric grains (Fig. 4a) with many intermetallic phases. Homogenization annealing resulted in dissolution of interdendritic areas. Detail microstructure analysis (Fig. 4b) showed that the balance of the microstructure is formed by solid solution δ (area 1) with γ phase (area 2), particles based on Mn (area 3) and particles based on Si (area 4) [9].

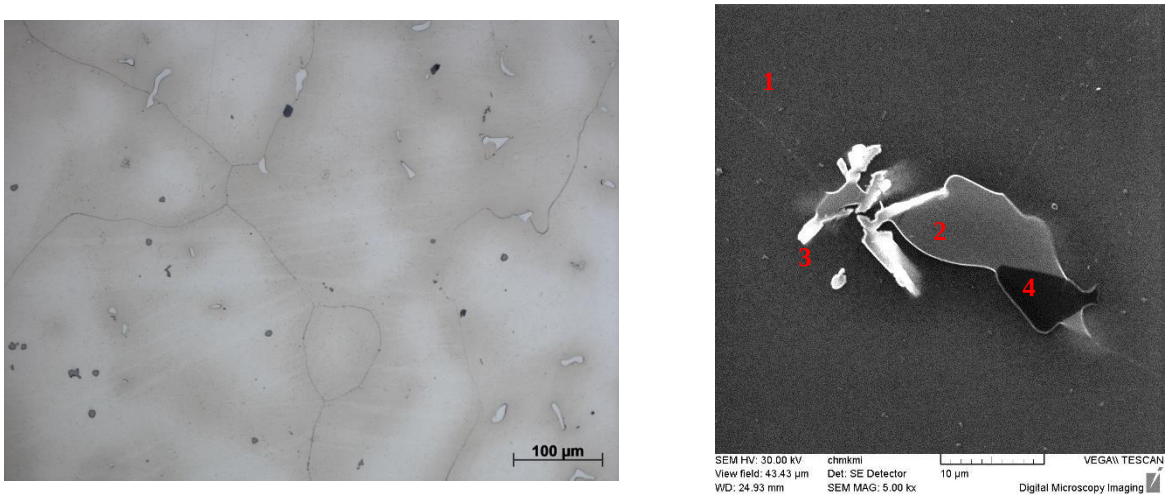

a) *b)*

Fig. 4 Microstructure of AZ91 magnesium alloy: after homogenization annealing 390°C/22h, etch. Picral a); detail of γ (area 2) phase and phase on based Mn (area3) and Si (area 4) (SEM), etch. Picral b).

4. Experimental results

During the measurement, which was carried out right after quenching, were obtained two internal damping spectras by ultrasonic resonance method (Fig.5a) and three internal damping spectras by RDFA (Fig. 5b) (two and three runs of the measurement were carried out on the same specimens for each method).

The internal damping spectrum of AZ91 magnesium alloy was measured in the temperature range from 50 °C up-to 390 °C by ultrasonic resonance method with heating rate of 1°C/min. The temperature spectra consists of athermal background, which is the part of the spectra at temperatures below 220 °C and strongly temperature dependent (temperatures higher than 200 °C), where the internal friction peak is observed. A peak of internal friction can be observed in both measured spectras (P_1 and P_2 in Fig. 5a). The top of the second measured peak P_2 damping was at temperature of 316.1 °C after 2nd run of the internal damping measurement.

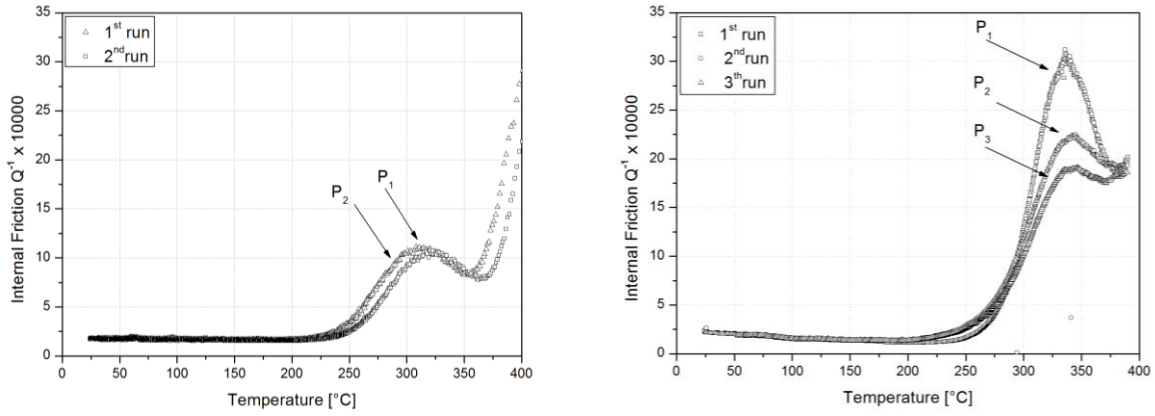

a) *b)*

Fig. 5 Temperature dependence of internal friction after homogenization annealing: spectrum of AZ91 magnesium by ultrasonic resonance method a); spectrum of AZ91 magnesium by RDFA b).

With RFDA the internal damping was measured in the temperature range from 25 °C to 390 °C with heating rate of 2 °C/min. The frequency of internal damping measurements was 8 kHz. The first peak P_1 is the most significant. Second and third run leads to reducing the size of the peak. Observed maximum position in the temperature axis is the same for all runs.

Creation of the internal damping peak is probably caused by the precipitation process. The decrease of the peak size after second and third run is probably caused by shortening of diffusion trajectories during repeated precipitation process when movement of atoms is easier than for the first run. Continuous precipitates in the microstructure caused strong pinning points for dislocations. When the temperature increases up to 320 °C the continuous precipitates are dissoluted in the matrix and the internal damping increases and dislocations are becoming movable. The average hardness after homogenization annealing was 61 HV5. The average hardness in the maximum of the peak was 82 HV5. The microstructure of AZ91magnesium alloy in the maximum of the internal damping peak was created by continuous precipitates on the grain boundaries (Fig. 6a). Detail of continuous precipitates in the volume of grain Fig. 6b).The creation of the peak is caused by absorption of energy by the process of continuous precipates nucleation and growth in the volume of material grains.

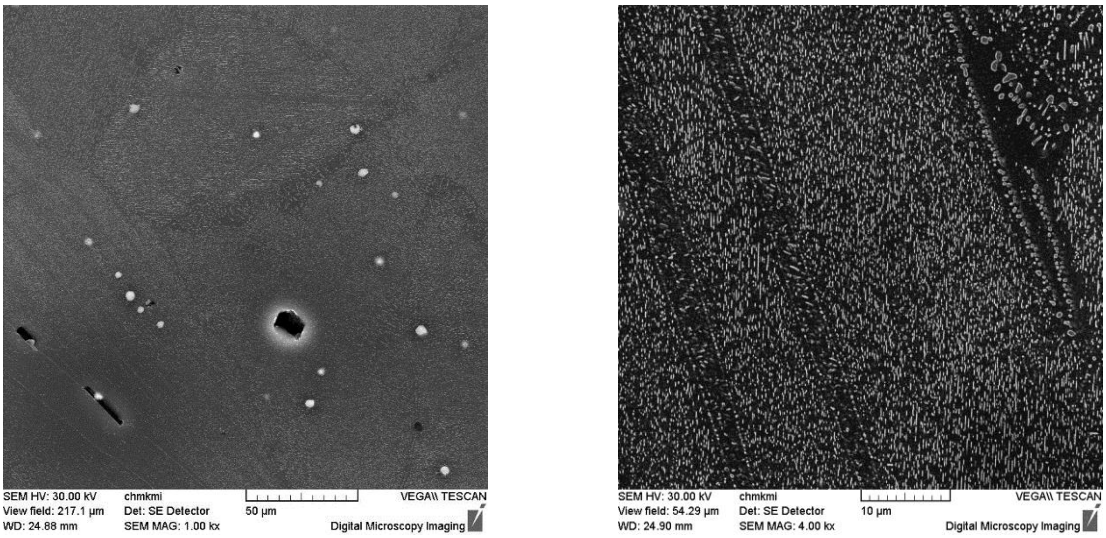

a) *b)*

Fig. 6 Microstructure of AZ91 magnesium alloy in the maximum of internal damping peak (320 °C): continuous precipitates on the grain boundary a), detail of continuous precipitates; (SEM) etch. Picral

5. Conclusions

The following conclusions can be drawn from the results of this study:

- On the temperature dependent spectra of internal damping occurred large peaks for both measurement methods.
- Creation of the internal friction peak is connected with the continuous precipitation of γ - $Mg_{17}Al_{12}$ phase in the volume of the material.
- The diffusion process necessary for precipitation of the phase in microstructure dissipates energy (both heat and mechanical) what results in increasing of the internal damping.
- At the temperature 320 °C the microstructure analysis shows continuous precipitates.
- Continuous precipitates in the microstructure create strong pinning points for dislocations what causes decrease of their mobility and decrease of the internal damping of the alloy, however further increase of the temperature causes dissolution of these precipitates and the pinning effect disappears.
- When the internal damping measurement by resonant frequency and damping analyser is repeated multiple times on the same specimen, the size of the peak decreases. This occurs because repeated precipitation process is easier than the first one (diffusion trajectories are shorter).
- The creation of continuous precipitates in the microstructure caused increase of the hardness from 61 HV5 (after homogenization annealing) to 82 HV5.

» The internal damping peak was present at lower temperatures when measured with use of the ultrasonic resonance method, when compared to impulse excitation method. This is probably connected to different deformation rate of the specimen during the loading, different heating rate and also due to significantly different mass of the specimen.

Acknowledgement

This work has been supported by Scientific Grant Agency of Ministry of Education of Slovak Republic VEGA 1/0683/15 and project APVV SK-CZ-2013-0076.

References

[1] POLMEAR I. J., Light Alloys Light Alloys Fourth edition 2006, p. 421 ISBN 0 7506 6371 5.

[2] XU, S.W., MATSUMOTO, N., KOMADO, S., HONMA, T., KOJIMA, Y.: Mater. Sci. Eng. A *517*, 2009, p. 354. doi:10.1016/j.msea.2009.04.029.

[3] BLANTER, M.S a kol. 2007. Internal Friction in Metallic Materials. Berlin Heidelberg: ©Springer -Verlag, 2007, 539 p., ISBN 3-540-68757-2.

[4] BLAŽEK D., PALČEK P. Internal friction use in monitoring the degradation processes in a material, Materials Engineering – Materiálové inžinierstvo 18 (2011) 145-150, ISSN 1335 – 0803.

[5] BLAŽEK D., Analýza spektra vnútorného tlmenia horčíkových zliatin, (Analysis of internal friction spectra of magnesium alloys) [Dissertation thesis], University of Žilina, Žilina, 2012 (in Slovak).

[6] UHRÍČIK M., PALČEK P., SOVIAROVÁ A., SNOPIŃSKI P. *Change of Internal Friction on Aluminium Alloy with 10.1 % Mg Dependence on the Temperature.* In Manufacturing Technology October 2014, Vol. 14, No. 3, pp. 467-470, ISSN 1213–2489.

[7] ZUZANA DRESSLEROVÁ, PETER PALČEK, MILAN UHRÍČIK. Zmena vnútorného tlmenia horčíkovej zliatiny AZ61 v závislosti od teploty. In: SEMDOK 2014 : 19th international seminar of Ph.D. students : Terchová, Slovakia, 29-31 January, 2014. - Žilina: University of Žilina, 2014. - ISBN 978-80-554-0832-3. - S. 108-113.

[8] DRESSLEROVÁ, Z., PALČEK, P. Temperature Dependence of the Internal Friction Measured at Different Excitation Voltages. In: Manufacturing Technology, October 2014, vol. 14, no. 3, s. 287-290. ISSN 1213-2489.

[9] SOVIAROVÁ A., PALČEK P., TROJANOVÁ Z. *Monitoring of Precipitation Process in AZ31 and AZ91 Magnesium Alloys by Internal Damping Measurement.* In Manufacturing Technology October 2014, Vol. 14, No. 3, pp. 447-451, ISSN 1213–2489.

TRANSCOM 2015, 22-24 June 2015
University of Žilina, Žilina, Slovak Republic

Implementation of the Model Trucks FTS Using 3D Printing

*Peter Spišák, *Rudolf Madaj, *Róbert Sásik
*University of Žilina, Faculty of Mechanical Engineering, Department of Mechanical parts, Univerzitna 1, 010 01 Žilina, Slovakia, {Peter.Spisak, Rudolf.Madaj, Robert.Sasik}@fstroj.uniza.sk

Abstract. Nowadays the use of new technologies such as virtual models, their analysis and simulation are a prerequisite for fast and economical prototype of a new product and its introduction into production. Of course, the use of virtual models is not confined to the simulation and analysis, but also for visualization and product promotion and may also serve as a basis for Rapid Prototyping. These options of Engineering work visualization are more accessible and with such support it is possible conduct studies even during development and in a very short time.

Keywords: Prototype, rapid prototyping, structural process, master model

1. Introduction

Technologies such as Rapid Prototyping and Rapid Tooling are primarily intended to reduce the development time of components. Their use results in cost reduction for development of new or modernization of old parts. Appropriate deployment of these technologies into design processes has brought many benefits to companies over several years. These technologies are most frequently used in the automotive and aerospace industry, but due to positive trend of the technology device prices they are beginning to spread to almost all areas of engineering production.

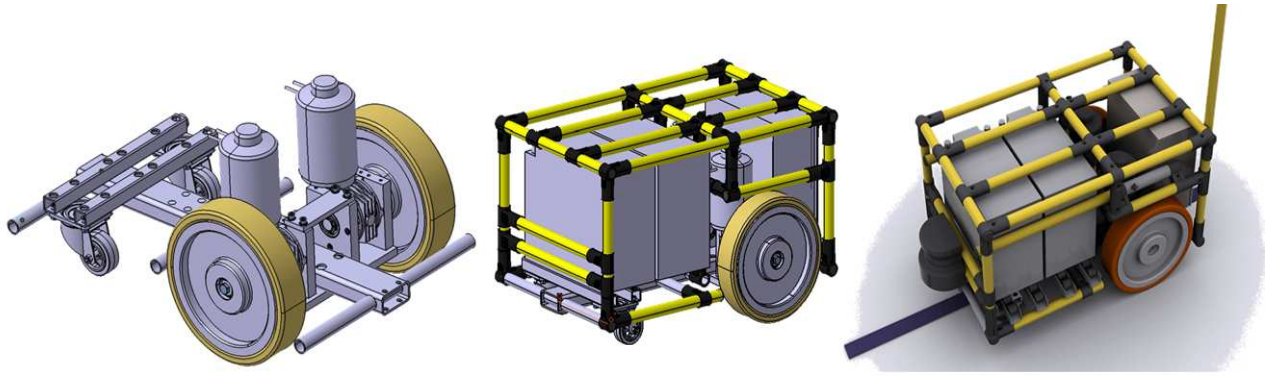

Fig. 1. 3D models of developed trucks FTS – fahrer transporting system

Technology Rapid Prototyping (RP) and Rapid Tooling (RT) are usually linked, because the master model, required for the manufacturing of instrument-mold with technology Vacuum Casting (VC) or other RT technology, is most commonly produced on RP machines. The production of prototype parts or equipment for RP follows the creation of a virtual three-dimensional model in any CAD system, which is usually stored in universal STL format, common to all RP operating software installations. Because the components produced on the RP devices have limited mechanical properties and are often made of specific materials, such as plastics, photopolymer, plaster, etc., it is possible to change properties or improve the production of components by RT technology. VC technology also allows production of a wax model for Investment Casting and subsequent production of metal parts [1].

2. 3D Printing

Considerable potential to accelerate prototyping and thus accelerate product development itself can be provided by methods of Rapid Prototyping, commercialized in the late eighties of the last century. They enable rapid production model, sample or prototype based on a three-dimensional model created in the CAD system. Compared to commercial production methods Rapid Prototyping takes significantly less time for production, days and hours instead of months.

Fig. 2. ZPrinter 650 (zcorp,2015)

A prerequisite for the full utilization of all Rapid Prototyping method benefits is their correct integration in the entire product development cycle. This way the procedures are used for example at an early stage of development or even already in the conceptual phase of the model construction. Models are then used to make the first design studio, ergonomic studies and for the presentation of the product to customers. At the same time one can obtain information for the design and construction tools necessary for mass production. In the next stage of development they are used for example for the functional testing of the product, identifying potential collisions, determining complexity of installation or the design of the assembly tools.

Use of Rapid Prototyping has a decisive influence on the philosophy of the product development process. Prototype is no longer an obstacle in the process leading to the final product, but it is its essential part. For the development of a superior product, it is preferred that the developer has a number of functional samples and prototypes. Such samples and prototypes are then verified and modified in a series of interactive activities until reaching all product requirements. An advantage of Rapid Prototyping is not only the possibility of fast prototype creation in any development stage, but mainly the possibility of creating a number of modifications and design variations of the product [3].

3. Eguipments

One such device is ZPrinter 650 3D printer that uses a technology called 3D printing. It can produce relatively thick parts quickly and cheaply. Concept Modellers are often used in the initial assessment of the product design. While prototypes made by the technologies SLA, SLS and FDM also create working models. Components manufactured by the Concept Modellers are equivalent to a three-dimensional sketch. These models help to find the right direction of product development for industrial designers.

The process starts with spreading a thin layer of powder (0,076-0,254 mm for each layer) by a cylinder on a platform mounted on the piston in the device. Numerous print nozzles pass across the surface layer and print the image of one cross-section into the powder. When the binder is printed, the powder is glued together. Loose powder around the printed area remains in place and serves as a support. When the layer is completed, the piston will lower the platform by thickness of one layer, and the process is repeated.

Some time is needed for spreading a new layer of powder between the formations of two layers. When the component is completed, the piston raises platform up and the excess powder can be removed with a brush or can be vacuumed.

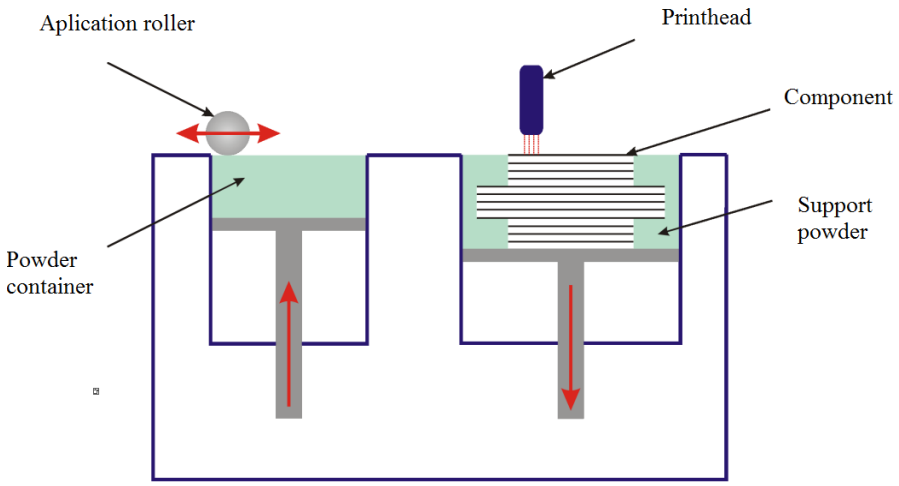

Fig. 3. Schematic of 3D printer ZPrinter 650

Because the print heads pass across the platform in a raster pattern (same as the head of an inkjet printer), 3D printing is very fast, about 40 times faster than other RP technologies. The time of printing each layer is the same regardless of layer complexity. The rate of formation is approximately 30 seconds for each layer.

Z Corporation offers two types of materials. Faster and less expensive is a powder based on starch. Components made from this material can be used as models for precision casting. Resilient components are formed from powder-based gypsum. Because the components are surrounded by the powder, no support structure is necessary. Starch parts are very fragile and need to be soaked with wax, cyanoacrylate or two-component epoxy resin to increase strength. Gypsum components are hard, but also require infiltration. Parts are porous and the infiltration is required to a depth of 6-12 mm, to form a durable shell. One can also buy an automatic system for wax infiltration of the 3D printer ZPrinter 650.

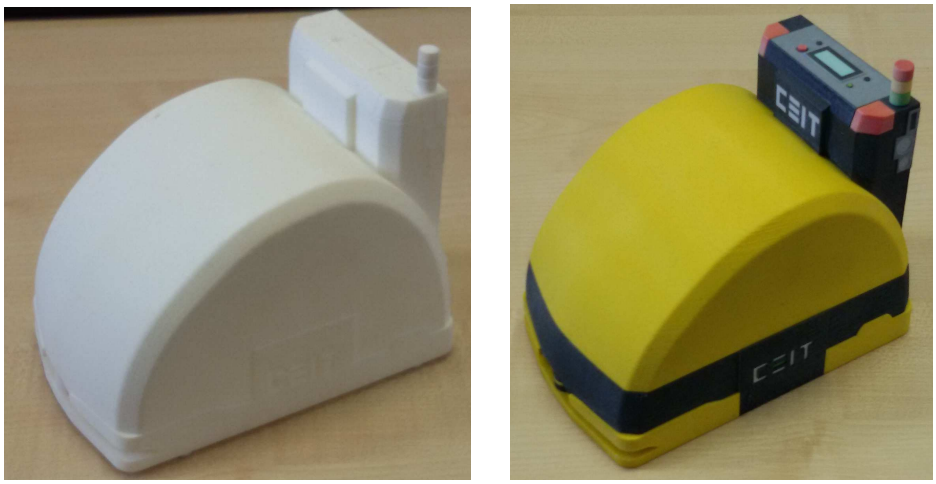

Fig. 4. Hit 3D printing using various technologies

The main advantages of 3D Printing are the speed and inexpensive materials. The accuracy and surface quality are worse than the SLA and SLS. Since the components are made of layers of powder, they have a grain structure, same as sintered parts. After infiltration can be sandblasted and so achieve a smoother surface. The unique feature of 3D Printing is the ability to produce multi-coloured parts. The colour of component is determined by colour added to the liquid binder. Each layer is basically a full colour image printed on a sheet of paper by an inkjet printer. If a decision criteria are speed and price it is best to use 3D Printing. If accuracy, surface treatment and material properties are critical then 3DP is not the most proper choice. 3DP components are most often used as a conceptual model. Parts produced from starch material can be directly used as models for accurate casting. 3DP components have relatively poor surface quality. Small elements and fine details are not properly replicated. Since all materials used in the 3DP are fragile, manufacture thin walls can be problematic.

4. Implementation Models FTS

The actual realization of prototypes begins with preparing a CAD model. The model is to be assessed in terms of manufacturability and appropriateness of the device on which the model is implemented. Bearing in mind requirements to form coloured model the only applicable execution is 3D printing technology, since this is currently the only available way. The particular scale in which the model will be formed deserves attention during preparation phase of the model to prevent model destruction due to insufficient wall thickness of the model. After model control the model can be exported to the transmission format. The most common is a format WRML or for monochromatic parts it is STL format, which can be additionally coloured in the operating software of the printer.

Each RP device has its own utility software that processes STL file, defines a way of creating a prototype and sends processed data to the concerned device. Usually defined are following parameters: the speed of prototype forming (on which the surface quality of components depends), internal structure of components (interior space filled with grid structure to save material or with filled with actual material) and finally, a way of creating a support structure (supports) if required by RP method (Stereolitography, Fused Deposition Modelling, Multijet Modelling).

In preparing the data for the RP device, utility software divides STL file into a series of horizontal cross-sections, in which the paths for creating the model and the support structure are defined. In some utility software it is possible for user to intervene into the process of creating the support structure, especially when Stereolitography method is used. After defining all the parameters the utility software sends the prepared data to the device that can start creating components.

Implementation of the model takes several hours and after its completion additional tempering is performed. After full model hardening any excess powder is removed and the model is impregnated most often by wax or fast-hardening resin. The final operation is the additional model hardening and then the model is completed to serve its purpose.

5. Conclusion

RP and RT technologies are used to accelerate and streamline the production process, resulting in costs reduction. Similar as in a case of development of FTS trucks used in transport of components to manufacturing units in various factories. Utilising the RP technology several types of trucks were printed of which after careful evaluation the best option was chosen and subsequently put into production.

Fig. 5. Functional model of FTS

Utilizing VC technology several types of FTS trucks working models were produced. They were placed on remote control chassis to be used for marketing purposes or as presents for customers.

This work was created by the implementation of the "Low-cost logistic system based on mobile robotic platforms for industrial use.", "ITMS: 26220220092" to support the Operational Programme Research and Development financed by the European Fund for Regional Development.

References

[1] MEDVECKÝ, Š., HRČEKOVÁ, A., VAJDA, R., ŠTUREK, R.: Inovácie technických systémov a technológie Rapid Prototyping. In.: Zborník z XLII. Medzinárodnej knferencie katedier častí a mechanizmov strojov. ISBN 80-7078-919-0. Str. 197-201. VŠ-TUB Ostrava, 4.-5. september 2001.

[2] HRČEK, S.: Konštrukčný návrh automobilových prevodoviek pomocou sofistikovaných metód 3D modelovania, Rapid Prototyping, Rapid Tooling a Reverse Engineering. Dizertačná práca. Žilinská univerzita, Žilina 2005.

[3] Madaj,R., Hrček,s.: Vývoj zariadení na výrobu prototypov využívajúcich moderné metódy Rapid Prototyping. In: Produktivita a Inovácie, 01/2006, ISSN 1335-5961.

[4] Zcorp 2015. Zcorp [Online] 2013. [Cit. 19. 5 2015.] Dostupné na internete: http://www.zcorpprinters.co.uk/zcorp%20650.html

TRANSCOM 2015, 22-24 June 2015
University of Žilina, Žilina, Slovak Republic

Possibilities of Renewal Energy Sources for Electric Vehicles

[*]Ján Stanček, [*]Juraj Uríček, [*]Vladimír Bulej
*University of Zilina, Faculty of Mechanical Engineering, Department of Automation and Production Systems, Univerzitna 8215/1, 01026 Žilina, Slovakia, {jan.stancek, juraj.uricek, vladimir.bulej}@fstroj.uniza.sk

Abstract. This article describes how electric vehicles and their current problems and solutions with the power source. Energy sources are usually accumulators or traction lines. Batteries have a relatively low power and problematic energy recovery. The article describes renewal of energy sources for vehicles with battery pack.

Keywords: Electric vehicle, charging battery, swaping battery

1. Introduction

The electric vehicles had made great progress within the last years. They are propelled by one or more electric motors. Nowadays their use is in all spheres of action. These vehicles are used particularly in the public transport of passengers and goods in the form of buses and commercial vehicles.

Electric motors require a continuous supply of electricity. The biggest problem is the power source and its renewal. As the energy source is usually used battery or traction line. When using traction line is the path of the vehicle is very limited. Version with battery pack has a big problem with their size and weight. Batteries currently have low power and long recharging. These problems cause a short range of the vehicle and low flexibility.

At the University of Zilina were developed two electric vehicles: EDISON and E-gokart. E-gokart is student project for ecological and economic savings vehicle (figure1).

a) b)

Fig. 1. Electric vehicles a) EDISON, b) E-gokart (both are developed at University of Zilina)[1]

2. Possibilities of Energy Recovery for Systems with Batteries

Vehicles with inside battery pack have a short range in general. Renewal electricity in batteries is important. We know some possibility of energy renewal:

- Conductive charging system
- Inductive charging system
- Battery swaping system

2.1. Conductive Charging System

Conductive charging system requires a connection between the battery inside the vehicle and the power supply. The power supply is charging device outside the vehicle.

The need for a metal-to-metal connection between the charger and the device requiring charging is one of the main drawbacks of this system. To accomplish this without the use of physical cords connected to wall outlets, special attachments are made from electronic devices which are fitted with technology that can detect when the device makes connection with the power source, often a charging base.

The power cords have a special plug at the end. These plugs are different for different types of cars and the country in which they operate. Connectors Chademo or Combo are intended for the European region (figure 2). [3]

Fig. 2. Connectors Chademo (left) and Combo (right) [2]

2.2. Inductive Charging System

Inductive charging system uses to wireless energy transfer between two objects. By this method a magnetic field transfers electricity from an external source (the charger) to a battery pack inside vehicle without the use of standard wiring. Energy is sent through an inductive coupling to an electrical device, which can use that energy to charge batteries. Electrodynamic induction does not require any contact points. This means that as long as your device is near to the source of the magnetic field, it will receive power.

The system consists of power capture resonator inside the vehicle, and power source resonator inside the charger. When the vehicle is in the right place, wireless energy transmission begins (figure 3). [4], [5]

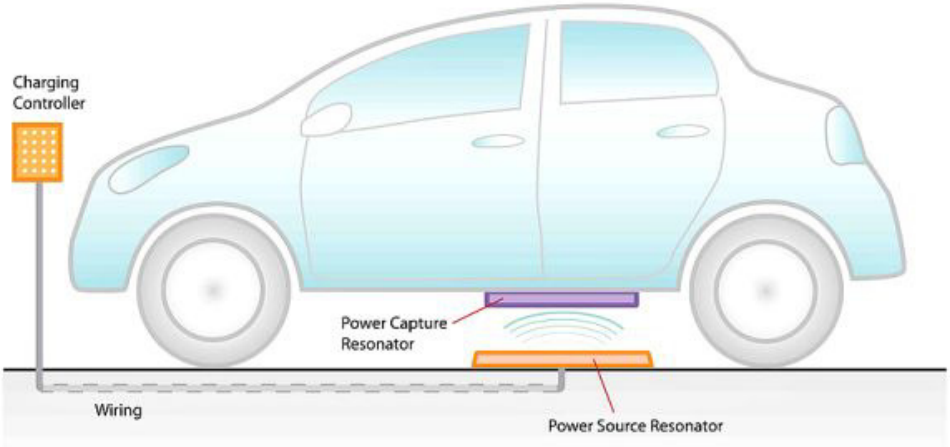

Fig. 3. Inductive charging system [6]

2.3. Battery Swaping System

Battery swapping system is based on a replacement of the fully charged battery instead of empty one. The battery is not charging in the vehicle, but in the charging station.

Unlike other possibilities of renewal energy sources which require a charging time some hours to recover the capacity for driving before the power is running out. Swaping battery require a time only few minutes. As the only way it can compete with fossil fuels.

This method is used mainly by large companies which produce electric vehicles. Some of them are Tesla, GreenWay, Betterplace. The big disadvantage is necessary to modify the design of the vehicle and battery packs. The total costs for the chain of swapping stations are very high.

Company Betterplace uses robotic shuttles that removes depleted battery for recharging and replaces it with a fresh battery. The battery shuttles can swap batteries of varied sizes. Driver needs to pilot the car up the square shaped ramp as the batteries lie on the underside of the car. Large solar photovoltaic array charge up the batteries wherein allowing zero-emission driving (figure 4). [8]

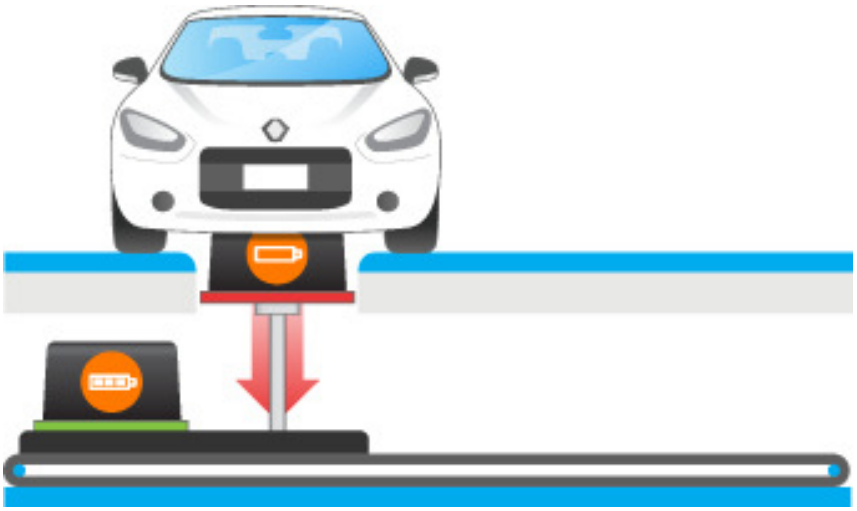

Fig. 4. Battery swaping system for company Betterplace [7]

3. Swapping Battery Stations

Nowadays we cooperate with the company KOVAL SYSTEMS to research new automatic battery swapping station. This station is intended for commercial vehicles of company Greenway.

Fig. 5. Company GreenWay and exchange of battery pack [9]

Currently, the batteries replacement is carried out by a forklift and a human operator. The target of our research is to replace the manual forklift by special automatic manipulator. This mechanism must be designed for the total weight of battery boxes up to 1 tone. The time for whole process must be less than 3 minutes (figure 5).

3.1. The conceptual design swapping battery station

According to the entire requirements for battery swapping stations we design the conceptual schema (figure 6) of automatic manipulator system for battery swapping included the storage rack for empty as well as fully charged batteries. Currently we are designing all necessary technical equipment of whole system.

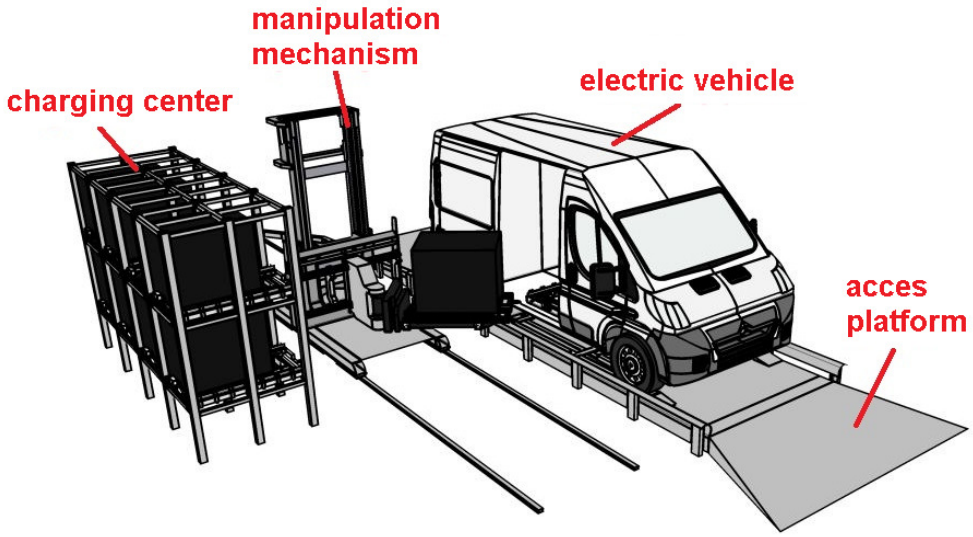

Fig. 6. The conceptual swapping battery station

4. Conclusion

Number of electric vehicles continues to grow. Their use is versatile, from industry after civilian use. The main problem of all electric vehicles is related with the power supply. This results in a short range. Therefore, it is important to research and find optimal ways how to recovery the energy sources. Standard way, charging the battery is a long process. Battery swapping system is only a temporary solution, but it is currently the fastest one. It looks as only one is able to compete with fossil fuels and standard cars with combustion engines. Therefore, we decided to further research on this system in cooperation of the company Koval Systems.

References

[1] http://www.edison.uniza.sk/edison_-_studentsky_projekt_elektromobilu_zilinska_univerzita
[2] http://www.hybrid.cz/chademo
[3] http://en.wikipedia.org/wiki/Conductive_wireless_charging
[4] http://en.wikipedia.org/wiki/Inductive_charging
[5] http://wireless-charger-review.toptenreviews.com/wireless-chargers-inductive-charging-explained.html
[6] http://techbox.dennikn.sk/temy/c8831/bezdrotove-nabijanie-je-v-plienkach-buducnost-ma-vsak-velku.html
[7] http://www.slashgear.com/tesla-battery-swap-demo-this-week-confirms-elon-musk-18286802/
[8] http://drprem.com/green/enjoy-an-uninterrupted-drive-with-automated-battery-swap-station
[9] http://www.greenway.sk/sk/blog

TRANSCOM 2015, 22-24 June 2015
University of Žilina, Žilina, Slovak Republic

FC-72 and Novec^{tm} 649 Boiling on a Mini-Fin Surface Coated with Carbon Nanotubes

[*]Ewelina Strąk, [*]Robert Pastuszko, [**]Robert Kłosowiak, [**]Rafał Urbaniak
[*]Kielce University of Technology, Al. 1000-lecia P.P. 7, 25-314 Kielce, Poland,
e-mail: enadstawna@tu.kielce.pl (Ewelina Strąk), tmprp@tu.kielce.pl (Robert Pastuszko),
[**]Poznań University of Technology, ul. Piotrowo 3, 60-965 Poznań, Poland
e-mail: robert.klosowiak@put.poznan.pl (Robert Kłosowiak),
rafal.urbaniak@put.poznan.pl (Rafał Urbaniak).

Abstract. This article describes pool boiling heat transfer on a mini-fin surface for two kinds of boiling fluid – fluorinate FC-72 and a fluorinated ketone, Novec^{TM} 649. Three types of surfaces are compared while boiling FC-72, a plain mini-fin surface (MF), a mini-fin surface coated with carbon nanotubes (MFN) and a mini-fin surface sintered with woven copper wire mesh (MF+M). Three types of surfaces are also compared for Novec^{TM} 649: a plain mini-fin surface (MF), a mini-fin surface coated with carbon nanotubes and a mini-fin surface sintered with perforated foil (MF+F). The results of the comparison, presented in the form of boiling curves, have been analyzed and discussed. The purpose of this study is to find the best heat transfer surface and fluid. The fluids can be used in the cooling of electronic devices and the best surface can be used as a heat pipe evaporator or thermosyphon. The experiments were carried out at atmospheric pressure.

Keywords: pool boiling heat transfer, carbon nanotubes, mini-fins, FC-72, Novec^{TM} 649

1. Introduction

A large number of modifications to pool boiling heat transfer surfaces have been studied and tested to increase the cooling performance. The techniques used to modify the surfaces include for example: tunnel-pore structures [1], mini-fins [2], micro-pin-fins [3, 4], rough surface [5, 6], micro-grooves [7], surface sintered with perforated foil [2], sintered with mesh [8], surface coated with carbon nanotubes [9], etc.

Ujereh et al. [9] studied the influence of coating silicon and copper substrates with carbon nanotubes on FC-72 pool boiling performance. The tested samples had dimensions of 1.27×1.27 mm. Their research showed that a substrate surface fully coated with carbon nanotubes was more effective at reducing the incipience superheat. In addition, the samples tested greatly enhanced the critical heat flux and heat transfer coefficient.

Wei and Xue [3] tested six kinds of silicon chips – five with square micro-pin-fins and one smooth surface for comparison. The fin dimensions were the following (thickness×height): 30×60, 30×120, 30×200, 50×60 and 50×120 μm. All surfaces tested exhibited higher heat transfer enhancement than the smooth surface.

Anderson and Mudawar [7] tested a surface with microstructures, 12.7×12.7 mm. They proved that the heat flux was independent not only from the surface geometry and orientation but also from surface roughness and large artificial cavities. The critical heat flux increased up to 2.5 times on the microstud and microgroove surfaces when compared with a smooth surface.

O'Connor and You et al. [10] tested a flat surface with micro-porous coating in FC-72 boiling. The reduction in incipient superheat for the surface with the micro-porous coating was about 2.0 times higher than that for the flat surface.

Vemuri and Kim [11] tested a nanoporous surface made from aluminum oxide (Al_2O_3). The data from this research were compared with those obtained from the plain aluminum surface.

The nano structure was from 50 to 250 nm in diameter. For the nanoporous surface, the reduction in the incipient superheat was approximately 30% over the plain surface.

Honda et al. [6, 4] showed on boiling FC-72 that silicon surfaces with 25–32 nm roughness yield have higher cooling performance with than micro-pin-finned silicon surfaces in the lower heat flux ranges. Critical heat flux values for the nano-roughened surface and micro-pin-finned surfaces were 1.8 to 2.2 and 2.3 times higher than those for smooth silicon surface.

Ramakrishnan [12] tested an array of 4 bars in Novec^{TM} 649 and HFE-7100 boiling. The heat flux was found to be approximately 14.6 W/cm^2 for boiling Novec^{TM} 649.

A lot of information about cooling in microchannels is included in [13]. The authors discussed some surface modifications and presented theoretical and mathematical analysis of microchannels. The article included an extensive review of the literature, which may be helpful for engineers in the current and future work.

2. Experimental setup

Table 1 summarizes the properties of the tested fluids, and the measurement system for determining heat transfer coefficients or boiling curves is presented in Fig. 1.

Properties \ Name	FC-72	Novec^{TM} 649
Normal Boiling Point, °C	56.4	49.0
Thermal Conductivity, $\frac{W}{m \cdot K}$	0.055	0.059
Liquid Specific Heat, $\frac{J}{kg \cdot K}$	1 050	1 103
Liquid Density, $\frac{kg}{m^3}$	1 602	1 610
Latent Heat, $\frac{kJ}{kg}$	94.9	88

Tab. 1. Properties of FC-72 and Novec^{TM} 649 [14, 15].

The experimental stand consisted of the main module supplied with the alternating current from the power supply, an autotransformer, a wattmeter, a dry-well calibrator, a data logger and a computer.

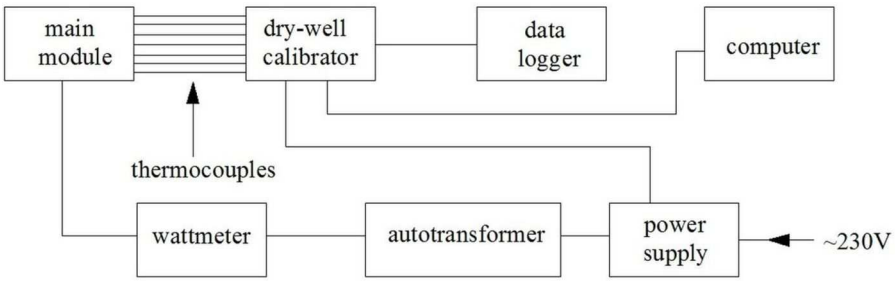

Fig. 1. The scheme of the experimental stand.

Between the main module and the dry-well calibrator, seven type *K* thermocouples (NiCr-NiAl) were installed to measure the saturation temperature (thermocouple T1 and T2), to extrapolate the temperature underneath the sample to the mini-fins base (thermocouple T3 and T4) and to determine the temperature gradient at 35, 20 and 5 mm depth in the bar (thermocouple T7, T6 and T5). All boiling experiments were carried out at atmospheric pressure. The scheme in Fig. 2 shows the main module with details explained.

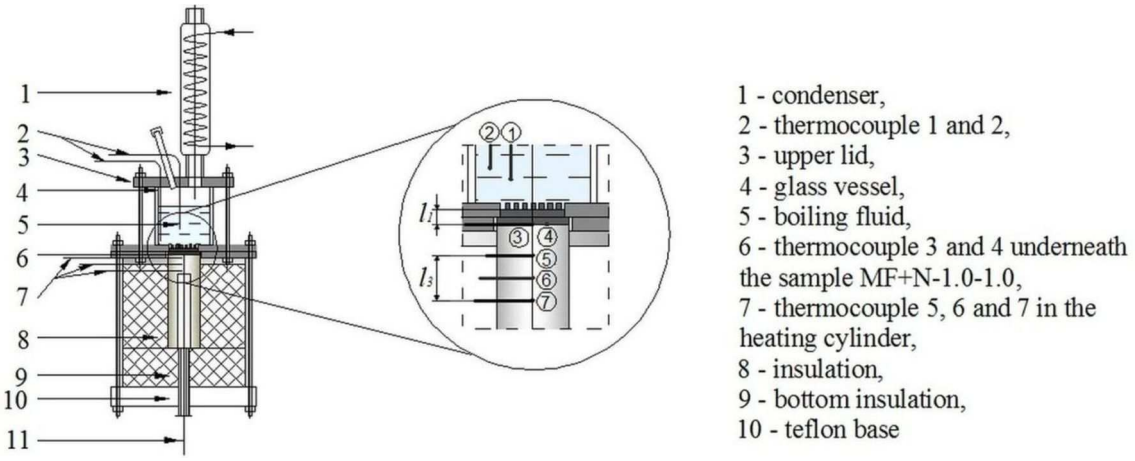

Fig. 2. The scheme of the main module.

In the above Fig. 2, the l_1 means the distance between the mini-fin base and the upper plane of the groove and l_3 means the distance between thermocouples T5 and T7.

The experimental data for the mini-fin surfaces sintered with the perforated foil come from [2] and the data for the surfaces sintered with the woven copper wire mesh to the mini-fins tips come from [8].

In this study, the following types of structural surface were used:

- 1 mm high plain mini-fins MF-1.0-0.6 and MF-1.0-1.0,
- enhanced surfaces sintered with the woven copper wire mesh to the mini-fin tips MF+M-1.0-1.0-0.3, MF+M-1.0-1.0-0.4 and MF+M-1.0-1.0-0.5,
- enhanced surfaces sintered with the perforated foil to the mini-fin tips MF+F-1.0-0.6-0.05, MF+F-1.0-0.6-0.1, MF+F-1.0-0.6-0.2 and MF+M-1.0-0.6-0.3,
- enhanced surface made by coating with carbon nanotubes to the mini-fins MF+N-1.0-1.0.

The abbreviated names of the samples were formed from the first letters of their full description. The first number after the sample name is the mini-fin height, the second number is the tunnel width in one direction, and the last number is the mesh aperture or perforated foil pore diameter.

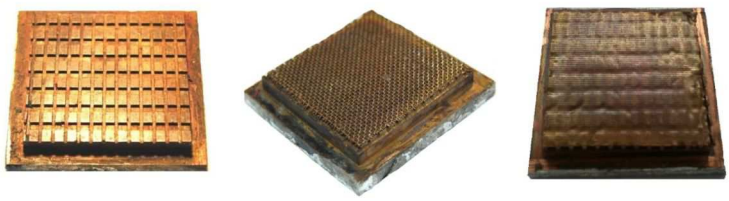

Fig. 3. Photograph of the tested surfaces.

Figure 3 shows, from the left, the plain mini-fin surface, the enhanced surface sintered with the perforated foil to the mini-fins tips and the enhanced surface sintered with the perforated foil to the mini-fin tips. Figure 4 shows the enhanced surface made by coating with carbon nanotubes to the mini-fins. The dimensions with designations of the surfaces tested are presented in Table 2.

In Fig. 4, l_2 is the thickness of the grease layer between the upper plane of the groove and thermocouple T3 or T4; w_{tun} is the tunnel width in one direction; s is the mini--fins width; h is the mini-fins height; h_{total} is the total height of sample; δ is the tunnel length in second direction, p_{tun} is the mini-fins length.

In Table 2, a means the mesh aperture and perforated foil pore diameter and p_p means the mini--fin pitch.

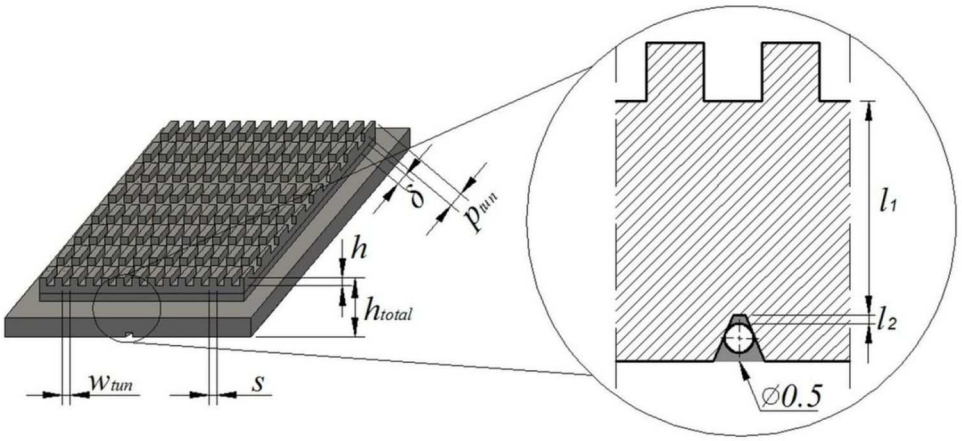

Fig. 4. Scheme of the mini-fin surface coated with carbon nanotubes.

Sample code	δ [mm]	s [mm]	p_{tun} [mm]	w_{tun} [mm]	h [mm]	h_{total} [mm]	a [mm]	p_p [mm]
MF-1.0-1.0	2.0	1.5	2.0	1.0	1.0	5.5	-	-
MF+M-1.0-1.0-0.3	2.0	1.5	2.0	1.0	1.0	6.0	0.32	0.52
MF+M-1.0-1.0-0.4	2.0	1.5	2.0	1.0	1.0	6.0	0.375/0.4	0.51/0.54
MF+M-1.0-1.0-0.5	2.0	1.5	2.0	1.0	1.0	6.0	0.5	0.82
MF+N-1.0-1.0	2.0	1.5	3.5	1.0	1.0	5.5	-	-
MF-1.0-0.6	2.0	1.4	2.0	0.6	1.0	5.5	-	-
MF+F-1.0-0.6-0.05	2.0	1.4	2.0	0.6	1.0	6.0	0.05	0.1/0.4
MF+F-1.0-0.6-0.1	2.0	1.4	2.0	0.6	1.0	6.0	0.1	0.2/0.4
MF+F-1.0-0.6-0.2	2.0	1.4	2.0	0.6	1.0	6.0	0.2	0.4/0.4
MF+F-1.0-0.6-0.3	2.0	1.4	2.0	0.6	1.0	6.0	0.3	0.6/0.4

Tab. 2. Designations and dimensions of the surfaces tested.

3. Data reduction

To create boiling curves, the heat flux, temperature superheat and heat transfer coefficient were calculated from the following equations 1, 2 and 3.

$$q = \frac{\lambda_{Cu} \Delta T_{T5\text{-}T7}}{l_3} \tag{1}$$

where:
q – heat flux [kW/m^2],
λ_{Cu} – thermal conductivity for copper [W/m K],
$\Delta T_{T5–T7}$ – temperature difference between thermocouple T5 and T7 [K],
l_3 – distance between thermocouples T5 and T7 [mm], see Fig. 2 .

$$\Delta T = \frac{T_{T3} + T_{T4}}{2} - \frac{q \cdot l_1}{\lambda_{Cu}} - \frac{q \cdot l_2}{\lambda_G} - T_{sat} \tag{2}$$

where:
T_{T3} – temperature shown by thermocouple T3, underneath the sample [K],
T_{T4} – temperature shown by thermocouple T4, underneath the sample [K],
T_{sat} – temperature saturation [K],
l_1 – distance between the mini-fin base and the upper plane of the groove, shown in Fig. 2 and Fig. 4 [mm],

l_2 – thickness of the grease layer between thermocouple T3 or T4 and the upper plane of the groove, shown in Fig. 4 [mm],
λ_G – thermal conductivity for grease [W/m K].

$$\alpha = \frac{q}{\Delta T} \tag{3}$$

where:
ΔT – superheat referred to the mini-fins base [K].

To calculate the errors, the lowest and the highest values of heat flux were taken. The heat transfer coefficient relative error for q = 23 kW/m^2 was calculated to be 56% with 1.2% for q=260 kW/m^2. The heat flux relative error for q = 23 kW/m^2 was calculated to be 18% with 0.7% for q = 260 kW/m^2. The absolute error of the temperature was calculated and referred to the base of the mini-fins. It was calculated to be 0.2 K.

4. Experimental results

4.1. FC-72 boiling

Figure 5 presents heat transfer coefficients for FC-72 at increasing heat flux for plain mini-fins, mini-fins sintered with the woven copper wire mesh and mini-fins coated with carbon nanotubes. The boiling curve for MFN-1.0-1.0 is similar to that for MF+M-1.0-1.0-0.3. The critical heat flux was observed for the heat transfer coefficient of approximately 6.15 kW/m^{2}K for both samples. Boiling incipience is different for these samples of almost 10 kW/m^2. The highest value of heat transfer coefficient was observed for plain mini-fins and the smallest – for MF+M-1.0-1.0-0.4 and MF+M-1.0-1.0-0.4. For boiling FC-72, all samples tested without the mini-fins sintered with carbon nanotubes obtained better values of heat transfer coefficient than for Novec^{TM} 649.

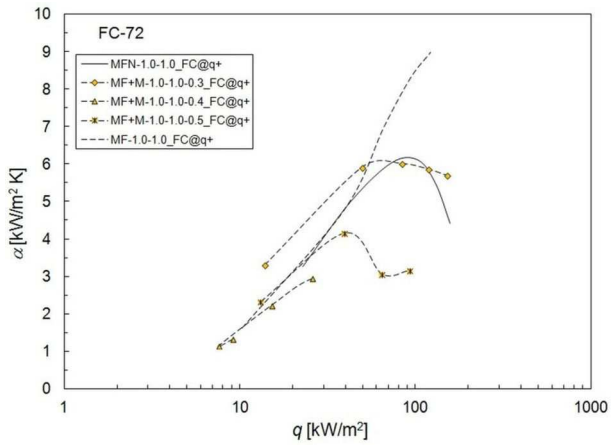

Fig. 5. Boiling heat transfer data for fluorinert FC-72.

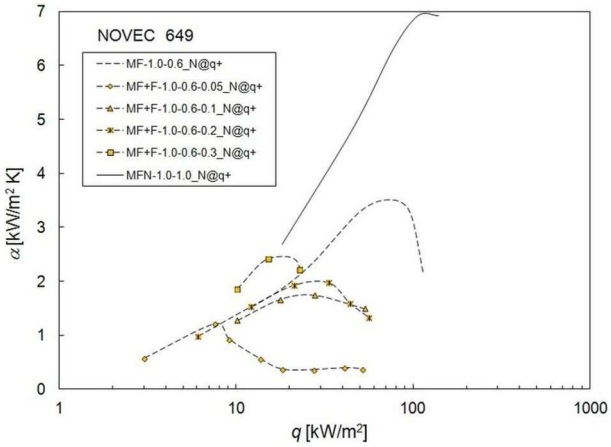

Fig. 6. Boiling heat transfer data for fluorinated ketone Novec^{TM} 649.

4.2. Novec^{TM} 649 boiling

Figure 6 presents heat transfer coefficients for Novec^{TM} 649 at increasing heat flux for plain mini-fins, mini-fins sintered with perforated foil and mini-fins coated with carbon nanotubes. For the last surface, the critical heat flux was 140 kW/m^2. This value corresponds with the highest heat transfer coefficient calculated to be almost 7 kW/m^2 K.

Maximum values of heat transfer coefficient for the mini-fin surface coated with carbon nanotubes are higher by about 50 % than those of MF-1.0-0.6 (plain mini-fins); up to 64 % than those of MF+F-1.0-0.6-0.3; up to 71 % than those MF+F-1.0-0.6-0.2; up to 74 % than those MF+F-1.0-0.6-0.1 and up to 83 % than those MF+F-1.0-0.6-0.05.

The boiling curve for Novec^{TM} 649 is similar to FC-72. For the both fluids tested from the same heat flux ranges (30÷100 kW/m^2), similar values of heat transfer coefficient were observed.

5. Conclusions

On the basis of the test results the following conclusions can be drawn:

- Additional measurements should be made for different nanostructure sizes, tunnel widths and mini-fin heights.
- The mini-fins without covering provided the most effective boiling intensification for FC-72 for the heat flux higher than 55 kW/m^2.
- The mini-fin surface coated with carbon nanotubes was the most effective surface tested for boiling Novec^{TM} 649. The proportion of the heat transfer coefficient for the mini-fin surface coated with carbon nanotubes and plain mini-fins was approximately 2.0. For the other surface this ratio is also higher.
- For both boiling fluids, FC-72 and Novec^{TM} 649, and for the mini-fin surface coated with carbon nanotubes, the boiling curves were similar.

Acknowledgement

The research reported herein was supported by the grant from the National Science Centre (No. DEC-2013/09/B/ST8/02825).

References

[1] NAKAYAMA, W., DAIKOKU, T., KUWAHARA, H., NAKAJIMA, T., *Dynamic model on enhanced boiling heat transfer on porous surfaces*, Part I: Exp. Invest., J. of Heat Transfer, 102, 445-450, 1980.

[2] NADSTAWNA, E., PASTUSZKO R., *Pool boiling heat transfer on surfaces with plain minifins and minifins with perforated foil*, MATEC Web of Conferences, 18, 0100, 2014.

[3] WEI, J., XUE, Y., *Enhanced Boiling Heat Transfer from Micro-Pin-Finned Silicon Chips*, InTech, 33-52, 2011.

[4] WEI J., HONDA H., GUO L., *Experimental study of boiling phenomena and heat transfer performances of FC-72 over micro-pin-finned silicon chips*, Int. J. Heat Mass Transfer, 41, 744–755, 2005.

[5] MCHALE, J., GARIMELLA, S., *Bubble nucleation characteristics in pool boiling of a wetting liquid on smooth and rough surfaces*, Int. J. Heat Mass Transfer, 36, 249–260, 2010.

[6] HONDA, H., TAKAMASTU, H., WEI, J., Enhanced boiling of FC-72 on silicon chips with micro-pin-fins and submicron-scale roughness, ASME J. Heat Transfer, 124, 383–389, 2002.

[7] ANDERSON, T., MUDAWAR, I., *Microelectronic cooling by enhanced pool boiling of a dielectric fluorocarbon liquid*, ASME J. Heat Transfer, 111, 752–759, 1989.

[8] PASTUSZKO, R., *Pool boiling on micro-fin array with wire mesh structures*, Int. J. Thermal Sci., 49, 2289-2298, 2010.

[9] UJEREH, S., FISHER, T., MUDAWAR, I., *Effects of carbon nanotube arrays on nucleate pool boiling*, Int. J. Heat Mass Transfer, 50, 4023–4038, 2007.

[10] O'CONNOR, J., YOU, S., *A Painting Technique to Enhance Pool Boiling Heat Transfer in Saturated FC-72*, ASME J. of Heat Transfer, 117 (2), 387, 1995.

[11] VEMURI, S., KIM, K., *Pool boiling of saturated FC-72 on nano-porous surface*, Heat and Mass Transfer, 32, 27-31, 2005.

[12] RAMAKRISHNAN, B., *Viability of server module thermal management using enhanced heat sinks and low global warming potential dielectric fluids*, Open Access Theses and Dissertations, 2014.

[13] TULLIUS, J., VAJTAI, R., BAYAZITOGLU, Y., *A Review of Cooling in Microchannels*, Heat Transfer Engineering, 32, 527-541, 2011.

[14] FORREST, E., HU, L.-W., BUONGIORNO, J., MCKRELL, T., *Pool Boiling Performance of Novec^{TM} 649 Engineered Fluid*, ECI Int. Conf. on Boiling Heat Transfer, 1-7, 2009.

[15] PASTUSZKO, R., *Boiling heat transfer in subsurface tunnels*, Kielce University of Technology, M 33, 2012.

TRANSCOM 2015, 22-24 June 2015
University of Žilina, Žilina, Slovak Republic

Evaluation of Stress Conditions in Turning with Rotating Tool

[*]Ing. Jozef Struharňanský, [*]Ing. Marianna Piešová
[*]University of Žilina, Faculty of Mechanical Engineering, Department of machining and manufacturing technology, Univerzitna 1, 01026 Žilina, Slovakia, jozef.struharnansky@fstroj.uniza.sk, marianna.piesova@fstroj.uniza.sk

Abstract. This article is focused on non-destructive method for detecting of the stress conditions in the surface and subsurface of the component, which has been machined by unconventional turning method and is dedicated to finding the optimum conditions of slope angle of the tool at the slightest load of the work piece. This tool was developed at the University of Žilina. It is an autorotary tool made of high speed cutting steel. Determination of the residual stress is realized by means of X-ray diffraction, whereby is possible to accurately determine the value of the residual normal or shear stress without breaking the sample.

Keywords: X-ray diffractometry, rotary tool, surface integrity, residual stress

1. Introduction

Residual stresses are an integral part of manufactured workpieces, whether they are introduced deliberately, as a part of the design, as a by-product of a process carried out during the manufacturing process, or are present as the product of the component's service history. Residual stresses are additive with the stresses existing in the workpieces as a result of service loads.[1,2,3] Direction of residual stress (tension or compression) depends on the kind of deformation. Permanent residual stresses have the largest share on the functionality of part, and they cannot be detected by conventional methods.[4] X-ray diffraction is specific method that can measure residual stress quantitatively in crystalline and semi-crystalline materials, which include virtually all metals and their alloys, and most ceramic materials. It is a non-destructive detection technology in many applications. [5] This article aims to determine the optimal conditions settings of unconventional tool in terms of stress load of steel 100Cr6 designed specifically for bearing production.

2. Fundamental of the Machining with the Autorotating Tool

Turning with autorotating tool can be applied in two configurations (Fig. 1).

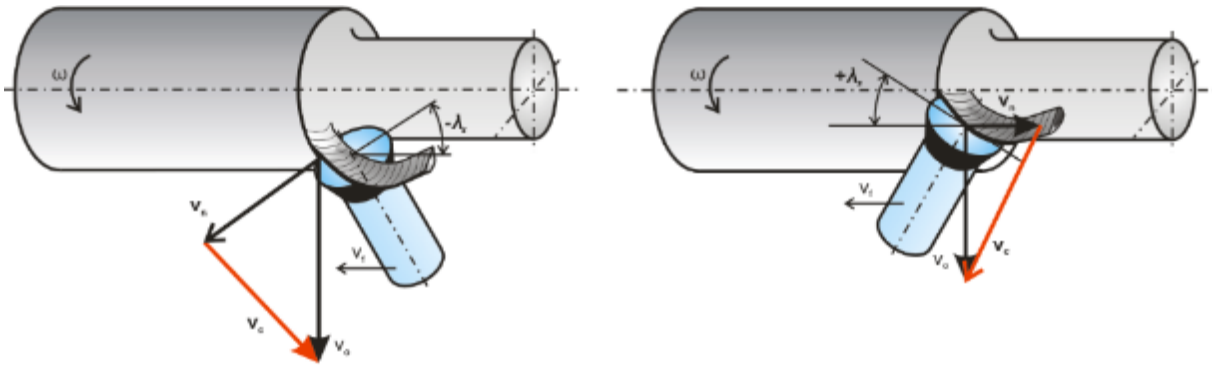

Fig. 1. Tool configuration with positive and negative slope angle (± λs)

In the first case, the tool is placed under the negative slope angle - λs. The working area of the cutting edge is below the axis of the tool. Thus all working angles along the front of this area are

negative. The configuration is suitable for machining of high strength steel, cast iron etc., therefore materials that require negative slope angle cutting edge. Right in the tool axis is the rake angle equal to zero (assuming a planar face). The actual cutting speed can be considered as relative velocity vc, which is determined as vector difference of peripheral work speed of the work piece and tool speed. Another aspect in favor of high tool life is short contact of the specific cutting edge point with the work piece. In addition, the tool edge outside the machining area is cooled by the surrounding air, so there is not intense heat. [6]

The opposite tool configuration, inclined at positive slope angle, leads to the formation of positive working angles of cutting face. It can be applied in machining of light metal, plastic, wood, etc. The tool rotates in the opposite direction, what corresponds to a different orientation and size of the cutting speed vector vc. [6]

3. Solving Tool with a Rotating Cutting Chip

Figure 2 is a photograph of the experimental tool with the chip made of high speed cutting steel. As you can see on FIG. 1, real cutting speed as the relative speed between the rotating speed of the rotating tool and work piece is substantially smaller than the peripheral speed of the work piece. Therefore, the tool can be made of high speed cutting steel.

Fig. 2. Photo of tool with the chip made of high speed cutting steel

The chip is located on the conic pin with helix groove in the circumference. Pin is placed in cone brass capsule and is supported with bullet, axially adjustable to define the bearing gap [7].

4. Measurement of Macroscopic Stresses

The stress of the sample is clearly linked to the deformation of individual areas of the sample. According to the Bragg equation is the position of the diffraction peaks given by the value of interplanar distance d_{hkl} between the lattice planes (hkl).

The determination of macroscopic stresses by X-ray diffraction – X-ray of the strain gauge – is based on the fact that during the deformation of the lattice due to application of mechanical stress there is also a change of hkl spacings. Polycrystalline materials contain a large number of different oriented crystallites. In the macroscopic stress it can be assumed that the crystals in the same area are exposed to the same deformation, and thus the change of spacings dhkl of the selected plane (hkl) will depend only on the orientation of the crystallites to main axes of tension and deformation tensors, respectively to the coordinate axes associated with the sample. Systematic scanning of a suitable diffraction (hkl) from variously turned crystallites can be used to determine the strain

tensor and consequently the stress tensor field of the samples analysed. The basic method of the X-ray strain gauges is the so called $\sin^2\psi$ method. It uses the fact that the relative change of interplanar spacings is a linear function $\sin^2\psi$ where ψ is the angle between the difracting planes normal and the normal of the sample. Factor in $\sin^2\psi$ contains planar components of the stress tensor. [8]

For the analysis of highly perfect single – crystal thin films the angular resolution of conventional diffractometers is not sufficient. The divergent bundle containing doublet Kα does not distinguish fine details of the diffraction pattern, therefore, in the primary, possibly also in the diffracted beam are included other optical elements – monochromators. This creates biaxial or three-axis diffractometers with high resolution. Bartel´s monochromator in the primary beam removes Kα2 component of the characteristic spectrum and reduces the divergence to the level of a few thousandths of a degree. Monochromator in the diffracted beam – analyzer – allows detecting the subtle changes in the direction of the diffracted beam that are caused by imperfections in the structure of the layer.[8]

In assessing the impact of technological processes on the properties of the surface layer of the work piece in its manufacture can be based on the type and intensity of energy to be involved in its implementation. That means mechanical energy, thermal and chemical. It is necessary to take into account the influence of metallurgy, physical properties and material properties. [9]

When machining is the essence of formation of residual stresses in the flexible plastic deformation in chip formation. An important factor is the time of exposure at cutting conditions and the speed of the changes in the occuring conditions. I tis significant for example at sharpening where the heating is very quick and short-term, the rate of heating and cooling time takes place under extreme conditions. [10]

In terms of conventional control methods can coating appear the same when measured hardness, roughness and dimensional deviation. While the surface layer may be different residual stress, and what the meaning as well as in size. [11]

5. Experiment

Experiment was performed on steel 100Cr6, which is a typical bearing steel. Chemical composition is shown in table 1.

Fe	C	Mn	Si	P	S	Cr
96,5 – 97,32	0,98 – 1,10	0,25 – 0,45	0,15 – 0,30	max. 0,025	max. 0,025	1,3 – 1,60

Tab. 1. Chemical composition of steel 100Cr6

Experiments were performed on a turning machine SUI 40 with using a rotating tool made of high speed cutting steel. This experiment was tasked to clarify the effect of depth of cut, feed rate and slope angle of the tool on the introduced stresses to the material by using of unconventional scheme of turning.

Measurement of residual stresses was realized on the X-ray diffractometer from the company PROTO (Fig. 3). It was used analytical software WINXRD 2.0.

Fig. 3. X-ray diffraction residual stress measurement system (stationary)

In figure 4 is shown a pearlitic-ferritic structure of the steel 100Cr6 of Pearlite – eutectoid metastable system. It has lamellar character. With increasing of cooling rate the lamellae become finer. By annealing is possible to create a globular form. Hardness of about 190HB, strenght Rm cca 700 MPa.

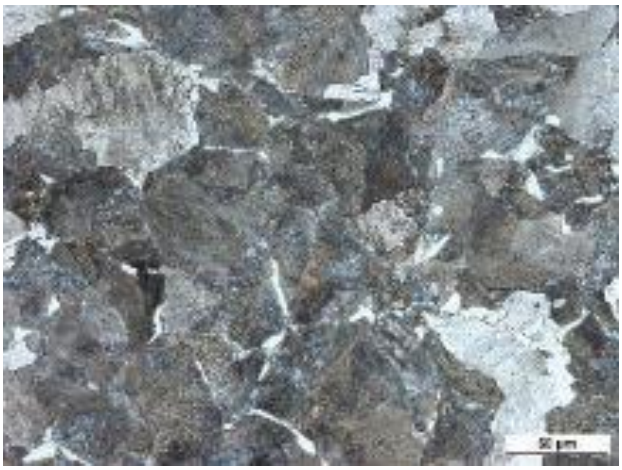

Fig. 4. Microstructure 100Cr6-500x3%Ni

6. Results of Experiment

Residual stresses in the work piece after machining by non-conventional machining method is shown in the Figures 2-3 and the graphic description of the stress progress is shown in the Figures 5-6.

a_p [mm]	**f** [mm]	**ʎs** [°]	**Residual Stress** [MPa]		
0,5	0,102	45	339,05	±	22,95
	0,3	45	751,86	±	28,98
	0,4	45	927,07	±	30,88
	0,102	50	251,83	±	20,32
	0,3	50	664,61	±	20,83
	0,4	50	685,85	±	22,42

Tab. 2. The average value of stress in a_p = 0,5mm

a_p [mm]	**f** [mm]	**ʎs** [°]	**Residual Stress** [MPa]		
1	0,102	45	118,36	±	24,45
	0,3	45	719,86	±	15,14
	0,4	45	827,89	±	18,13
	0,102	50	308,94	±	29,6
	0,3	50	851,16	±	20,94
	0,4	50	944,69	±	26,41

Tab. 3. The average value of stress in a_p = 1mm

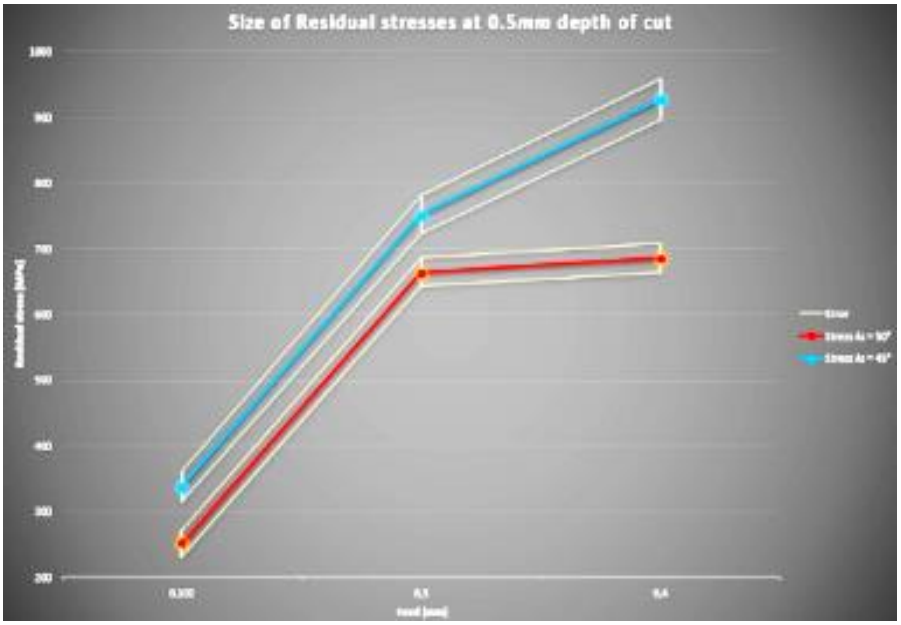

Fig. 5. Size of residual stress in a_p = 0,5mm

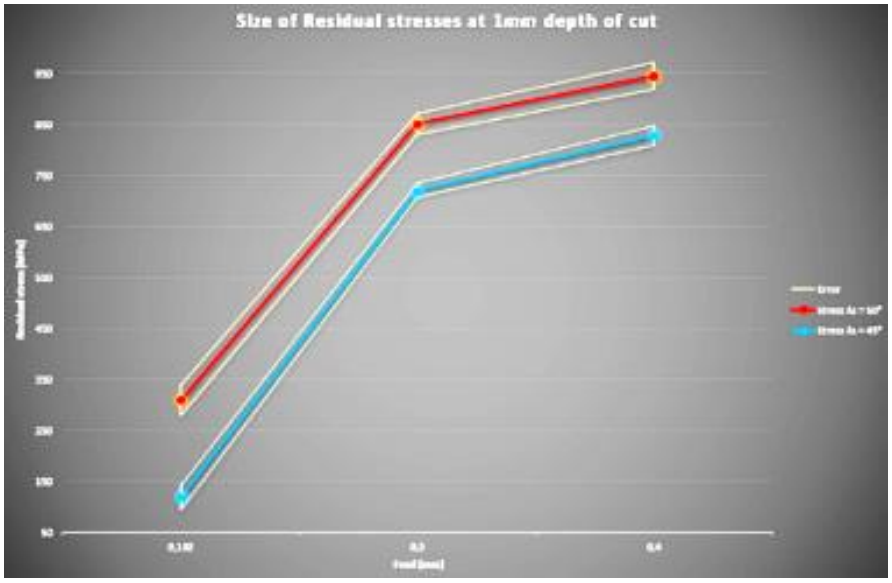

Fig. 6. Size of residual stress in a_p = 1mm

7. Conclusion

Due that machining brings stress to machined material, both normal stress and shear stress, it is necessary to be able to measure its value and orientation. X-ray diffractometry offers the opportunity to determine these properties of machined, or differently technologically treated material to predict deterioration of components. This measuring technology is non-destructive, so it can be used in wide area of applications.

The results show that the size of this stress range from +118MPa to 945 MPa, depending on the cutting conditions. That means, the cutting conditions have a significant impact on the size of this stresses introduced into the material. Therefore, the detection of these stress conditions has wide application in the future and offers a wide scope for further technological research how to improve the cutting process, that the stresses they have been introduced into the material should be the smallest.

With the increasing depth of cut should be reduced the angle of the cutting edge. The optimal slope angle is λs 30-60°. To accurately determine the optimal slope angle λs in terms of the stress and the depth of cut is needed to do even more experiments which would clarify this issue more.

References

[1] C. A. GRIFFITHS, C.A. *Closing the Loop on Product Integrity on Bearings with Engineered Source Approval, Split Ballbearing Features*, Company Newsletter, (1989).
[2] PREVÉY, P.S. : *X-ray Diffraction Residual Stress Techniques*, Metals Handbook 10, Metals Park: American Society for Metals, p. 380-392,. 1986.
[3] NÁPRSTKOVÁ, N., HOLEŠOVSKÝ, F.: *Admeasurement of Grinding Wheel Loss at FPTM*. In 24th International Colloquium (Advanced manufacturing and repair technologies,, s.159-164, 2007. ISBN 978-80-7194-962-6.
[4] GANEV N., KRAUS I.: *X-ray diffraction measurement of residual stresses*, Material Structure, vol 9., No. 2 2002
[5] TIITTO, K. et al.: Testing Shot Peening Stresses in the Field, *The Shot Peener*, vol. 4, ISSN. 1069-2010 (1991).
[6] PILC, J.-MIČIETOVÁ, A.:. 2003. *Metal machining by using of autorotary tools.* Žilina : EDIS, 2003. s. 106. ISBN 80-8070-047-8.
[7] VASILKO, K.- PILC, J.: *Slide assembly of rotating turning tool*. *Patent SR* č. 211 831, 21.3.1980
[8] http://matnet.sav.sk2F1062.ppt.
[9] http://mineralogie.sci.muni.cz/kap_5_2_metody_strukt/kap_5_2_metody_strukt.htm#5.2.1.
[10] http://gps.fme.vutbr.cz/STAH_INFO/2512_Bumbalek.pdf.
[11] BUMBÁLEK, B.-NOVÁK, Z.-VALA, P., OŠŤÁDAL, F.:. 1991. *Influence of finishing operations to change the surface layer of the work piece*. BRNO : VZ - VÚ 070, 1991.

TRANSCOM 2015, 22-24 June 2015
University of Žilina, Žilina, Slovak Republic

Fatigue Properties and Application Options of the Fine-Grained Steel of DOMEX Type

[*] Paweł Szataniak, [**]Frantisek Novy, [***]Robert Ulewicz
[*] WIELTON S.A., 98-300 Wieluń ul. Baranowskiego 10a, Poland
[**]University of Zilina, University of Žilina, Faculty of Mechanical Engineering, Department of Materials Engineering, Univerzitná 1, 01026 Žilina, Slovakia, frantisek.novy@fstroj.uniza.sk
[***] Czestochowa University of Technology, Institute of Production Engineering, 42-201 Czestochowa. Al. Armii Karajowej 19B, Poland, ulewicz@zim.pcz.pl

Abstract. The article presents the results of research of fatigue properties in the ultra-high-cycle area of ultra-high-strength fine-grained steel. In the fatigue research there were used high-frequency of sample load of the order of 20kHz. The obtained research results will be used to improve the simulation models of load of structural elements for semitrailers in Wielton SA company.

Keywords: HSLA steel, faitigue properties

1. Introduction

In the last half-century in highly industrialized countries have undergone major changes in the range of produced structural steels of mass application. Already in the 60s there was a trend to improve widely used carbon steel of normal quality, used in the raw state after prior rolling. Amendments consisted in reducing the carbon content, reducing the level of contamination of produced steel, while increasing the strength properties achieved as a result of plastic working. The next step was the use of minor amounts of alloying elements whose aim was primarily inhibiting grain growth (hence the appearance of the name "fine-grained steels"), which in turn provided a significant increase in mechanical properties. These steels in Poland were called microscopic steels with increased strength, and in Western Europe - HSLA steel. Modification of their chemical composition mainly consisted in increasing the manganese content (increase of 20% compared to carbon steel), and insignificant amounts of micro additives of alloying of niobium, titanium and vanadium (generally less than 0.1%), molybdenum (approx. 0.5%), and sometimes boron (which is also modifier) [1].

Fine-grained steels are often characterized by improved mechanical properties than the conventional steels having the same microstructure. Both the yield point and fatigue strength of steel with smaller grain proved to be significantly better, while the toughness increased dramatically. Using more durable and simultaneously lighter steels will contribute to improve efficiency of fuel consumption in cars and increase of the thermal efficiency of the power plant, as well as reduce carbon dioxide emissions [2÷7].

2. DOMEX steel

DOMEX Steel for cold forming is hot rolled steel in the thermo mechanical process where heating, rolling and cooling processes are carefully controlled. Chemical constitution of this steel consisting of low level of carbon and manganese is precisely completed by refining components such as niobium, titanium and vanadium. In conjunction with the clean structure it makes DOMEX steel the best alternative for cold formed products and welded products. DOMEX steel 700MC with

designation D and E meet and even exceeds the requirements for steel DOMEX 700 MC according to the EN-10149-2 standard [3].
Extra high-strength grades of steel are used in such structures as trucks chassis, cranes and excavators elements. In these applications, high strength of steel is used in order to reduce weight while simultaneously increasing the load capacity of the structure. These advantages in combination with good formability allow to reduce the total cost of operating. Due to the low content of carbon, phosphorus and sulphur DOMEX 700MC steel can be welded using any commonly used methods. Preheating is also not required. On the border of weld forms a narrow heat affected zone with a somewhat lower hardness. However, using normal parameters and welding methods this zone is of no practical significance. Tested samples made across the weld may show the same minimal value of the tensile strength as the welded material.
In case when the weld load will not be large, the binders may be used with less strength than the welded material. There is a large number of binders with the same or greater strength, which can be used for welding DOMEX steel 700MC, while maintaining the same strength of the weld, that the welded material. Table 1 shows the chemical composition and mechanical properties of DOMEX steel 700MC.

Chemical composition max. [% mas.]								
C	**Si**	**Mn**	**P**	**S**	**Al**	**Nb**	**V**	**Ti**
0.12	0.10	2.10	0.025	0.010	0.015	0.09	0.20	0.015
Mechanical properties								
R_e [MPa]			**R_m [MPa]**			**A5 [%]**		
700			750÷950			12		

Tab. 1. Chemical composition and selected properties of DOMEX 700MC [3]

3. Fatigue properties of DOMEX steel 700MC

DOMEX of 700MC Steels (Fig. 1) is characterized by fine-grained structure. Mirkostructure revealed sporadicaly occurring titanium nitride particles with a regular geometric shape of orange coulor. Tested steel is also characterized by the presence of a few inclusions in the form of black particles of sulfides MnS.

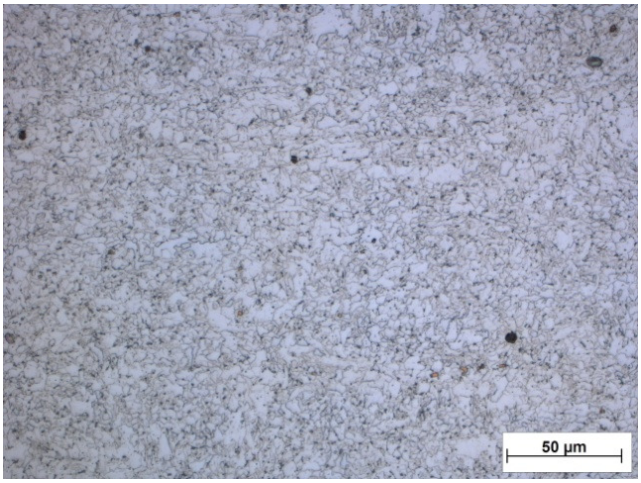

Fig. 1. Microstructure of DOMEX 700MC steel in the state of delivery, etched with 1% Nital.

Fatigue characteristic (dependence σ = f (N)) of steel DOMEX700MC was determined by low-frequency of cyclic load (VHCF). Fatigue tests in high-cycle field were carried out on the machine ROTOFLEX (Fig. 2) implementing load in the rotating bending mode. In the stress cycle asymmetry coefficient was R = -1, samples were loaded with the frequency of 30 Hz at a temperature of 20 °C ± 10 °C. To fatigue test in terms of high-cycle fatigue (using low frequencies) were used samples of the shape and dimensions shown in Figure 3.

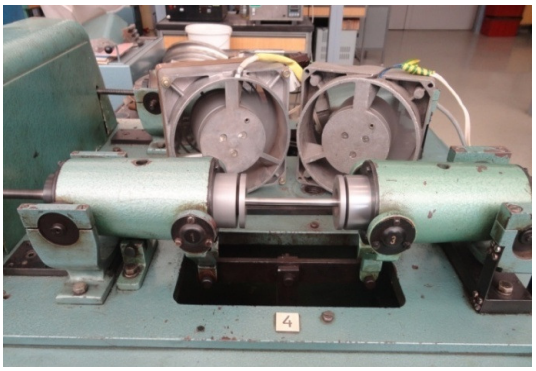

Fig. 2. ROTOFLEX machine

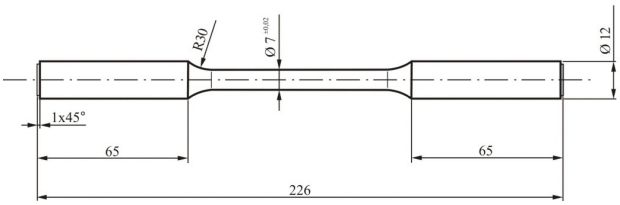

Fig. 3. Shape and dimensions of samples used in the fatigue test on the device ROTOFLEX.

Experimentally determined Whöler dependence curve shows a decrease in value of damaging stresses of the sample together with the increase of the number of cycles of load changes to the level of fatigue limit for this material (440 MPa) Fig. 4.

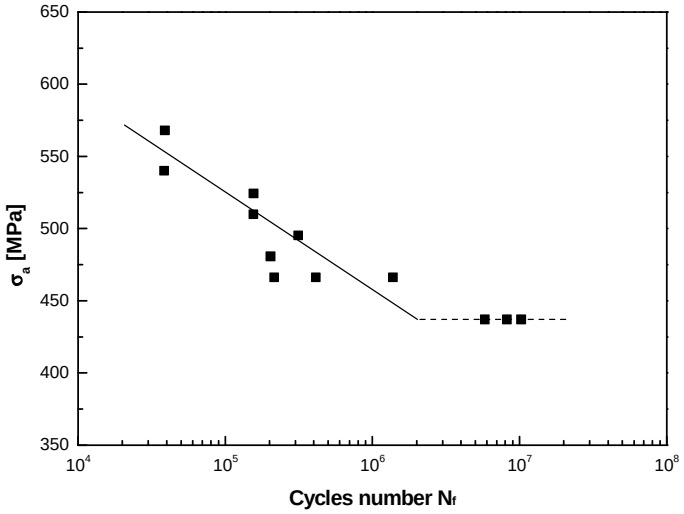

Fig. 4. Fatigue life of DOMEX 700MC steel, cantilever test, rotating bending in the field of high-cycle [f = 30 Hz, T = 20°C ± 10 °C, R = -1].

The results of fatigue tests in the field of ultra-high-cycle, conducted on high-turnout fatigue machine KAUP-ZU (Fig.5) carried out in accordance with the procedure described in works[8÷10] are shown in Fig. 6.

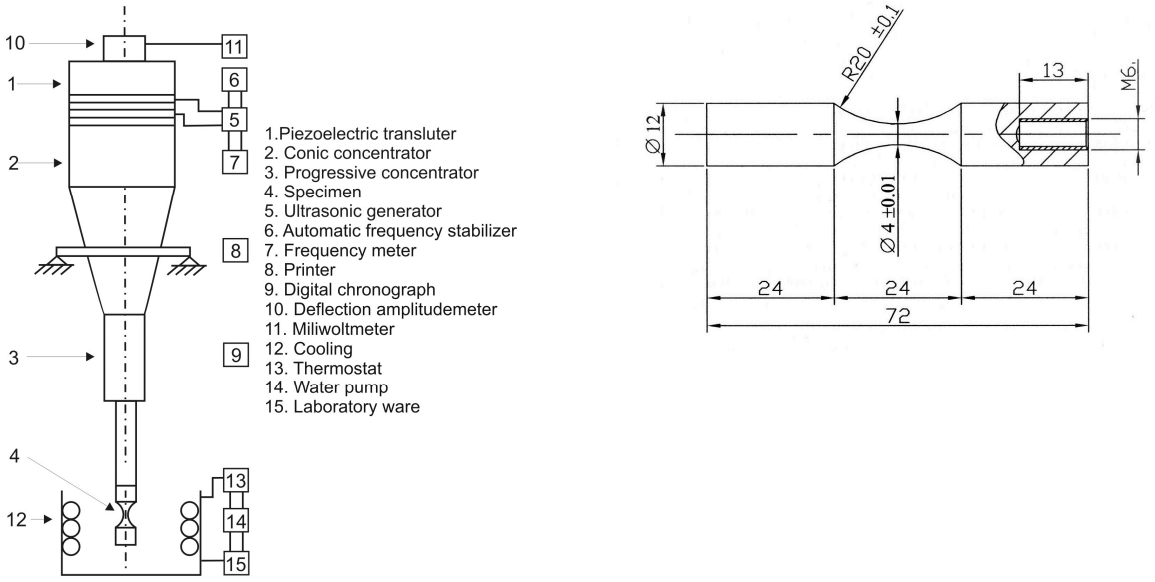

Fig. 5. Design of the resonance fatigue testing machine KAUP-ZU and geometry of the specimen used for fatigue tests at loading frequency of f ≈ 20 kHz

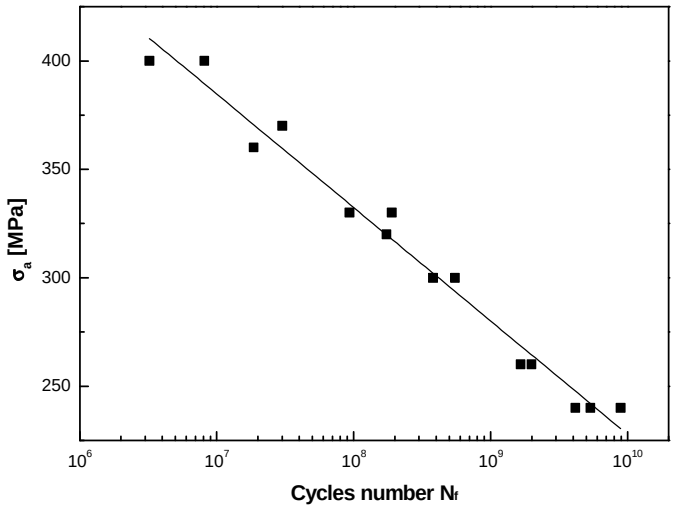

Fig. 6. Fatigue life of DOMEX 700MC steel, fatigue test using a high-frequency [f = 20 kHz, T = 20 °C ± 3 °C, R = -1].

Loading amplitude of fatigue tests of DOMEX steel 700MC decreased from σa = 400 MPa (for Nf = 3.3·106 cycles and Nf = 8.1·106 cycles) to σa = 240 MPa (for Nf = 4.1·109 cycles, Nf = 5.4·109 cycles, and Nf = 8.9·109 cycles), which gives the difference in the amplitude $\Delta\sigma a$ = 160 MPa.

4. Conclusion

Literature researches indicate [12÷16] that the material is resistant to fatigue, if it endures number of cycles N_c. Conventional number of cycles for steel, cast iron, copper is $N_c = 10^7$ cycles for light metals and their alloys $N_c = 10^8$ cycles.

Current requirements for structural elements often exceed this limit. Operating conditions of currently designed constructions require the increase of the length of the number of operating cycles and reliability. The results of carried out research work in the field of ultra-highcycle are directed at determining the fatigue characteristics of test materials and to understand the mechanism of formation of fatigue cracks above 10^7 the number of cycles. Determination of fatigue strength of new materials is of great importance in ensuring the reliability of designed devices and extending their service life. The results of all samples in the area outside the conventional fatigue limit is confirmed by further decline in stress amplitude σ_a with increasing number of cycles to fatigue failure of the sample for DOMEX steel 700MC the difference in the loading amplitude of fatigue tests at high frequencies was $\Delta\sigma_a$ = 160 MPa at low loading frequencies the load amplitude was $\Delta\sigma_a$ = 131 MPa. Fractures of all analyzed samples were created as a result of the initiation of fatigue cracks from the surface of the samples due to the formation of the intrusion and extrusion. The confrontation of the results with research of Nishijima and Kanazawa, Murakami and depending on the possible course of $\sigma_a = f(N_f)$ in the area of low cycle to the area of very high loading cycle (area giga and ultragigacycle) is possible, but further experiments are needed to verify them.

DOMEX Steel 700MC can be used to perform many components of self-dumping semi-trailers chassis, the basic requirement in relation to this material in the first place is a good weld ability. The yield point of this material for the construction of chassis longitudinal member of a frame must be not less than 600 MPa, and the tensile strength greater than 700 MPa. In case of components of the mounting plate, these requirements are at a level Re ≥ 580 MPa and Rm ≥ 650 MPa, and frame cross-beams Re ≥ 540 MPa and 650 MPa ≥ Rm. Figure 7 shows the application possibilities of DOMEX steel in the construction of semitrailers.

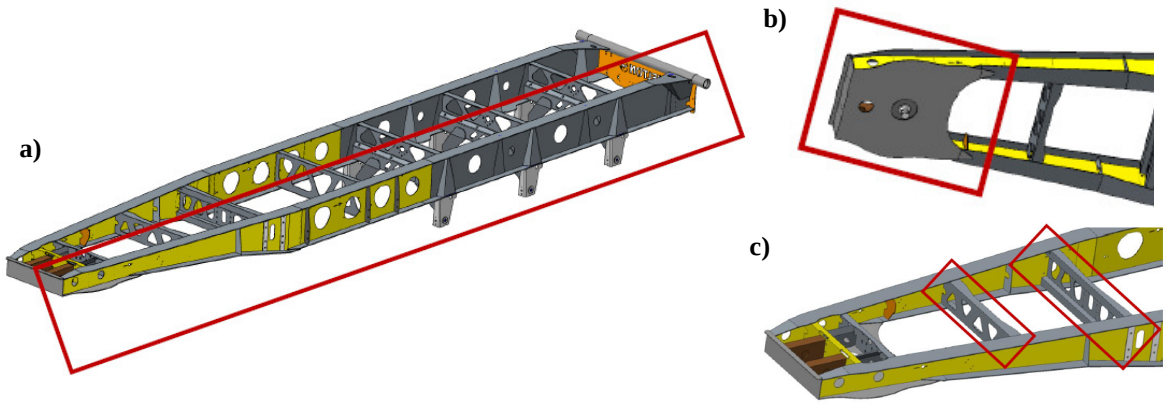

Fig. 7. Examples of the possibility of applying DOMEX steel 700MC in the construction of chassis components of semi-trailers of Company WIELTON SA: a) longitudinal members of frames, b) mounting plate, c) frame cross-beams

References

[1] GRAJCAR, A. *Struktura Stali C-Mn-Si-Al kształtowana z udziałem przemiany martenzytycznej indukowanej odkształceniem plastycznym*, Wydawnictwo Politechniki Śląskiej, Gliwice 2009.

[2] *The Steel Book. SSAB Communications. 2012* – dane producenta SSAB Oxelösund.

[3] DOBRZAŃSKI, L. A. *Materiałoznawstwo opisowe stopów żelaza*, Wydawnictwo Politechniki Śląskiej, Gliwice 2007.

[4] CISZEWSKI B., PRZETAKIEWICZ W. *Nowoczesne materiały w technice*, Wydawnictwo Bellona, Warszawa 1993.

[5] ARMIGLIATO A. *Light Weighting in Commercial Transport*, Conference "Connecting Innovations. Wielton", Warsaw 3-4 June 2014.

[6] PETERSSON, L. *Stronger Steel for Efficient and Sustainable Transport Vehicles*, Conference "Connecting Innovations. Wielton", Warsaw 3-4 June 2014.

[7] NOVÝ F., ČINČALA M., KOPAS P., BOKŮVKA O. *Mechanisms of High-Strength Structural Materials Fatigue Failure in Ultra-Wide Life Region*, "Materials Science and Engineering: A", Vol. 462, Issues 1-2, 2007, s. 189-192.

[8] ULEWICZ, R., MAZUR M., BOKUVKA O., SZATANIAK, P., NOVY, F. *HARDOX 400 Mechanical Properties*, [w:] SEMDOK 2012. 17th International of PhD. Students' Seminar. Zilina - Terchova, Slovakia 2012.

[9] BOKŮVKA, O., NICOLETTO, G., KUNZ, L., PALČEK P., CHALUPOVÁ, M. *Low & High Frequency Fatigue Testing*, EDIS University of Žilina, Žilina 2002.

[10] NOVÝ, F., MINTÁCH, R. *Únavová životnosť materiálov v oblasti nízkeho počtu cyklov zaťažovania*. In: Letná škola únavy materiálov '2010. EDIS ŽU Žilina (2010).

[11]Nishijima, S., Kanazawa K., *Step-wise-S-N curve and fish-eye failure in gigacycle fatigue*, Fatigue Fract. Eng. Mater. Struct. 22 (1999) 601-607.

[12]MURAKAMI, Y., NOMOTO, T., UEDA, T. *Factors influencing the mechanism of superlong fatigue failure in steels*, Fatigue Fract. Eng. Mater. Struct. 22 (1999).

[13]MALE, S. KIM, H.K. SALADIN, S.C. PORTER, W.J. *Effects of microstructure on fretting fatigue behavior of IN100*, Materials Science and Engineering A 527 (2010).

[14]MAZUR, M. ULEWICZ, R. NOVÝ, F. SZATANIAK, P. *The Structure and Mechanical Properties of Domex 700 MC Steel*, Communications 15/4 (2013).

[15]BARANI, A.A., PONGE, D., RAABE, D., *Strong and ductile martensitic steels for automotive applications*, Steel Research International 77/9-10 (2006)

[16]HOWE A. A. *Ultrafine grained steels: industrial prospects*. Materials Science and Technology, 16/ 11-12 (2000)

TRANSCOM 2015, 22-24 June 2015
University of Žilina, Žilina, Slovak Republic

Characterization of Solid-state Diffusion Joints between Titanium and Stainless Steel Using Nickel Interlayer

[*]Bartłomiej Szwed, [*]Marek Konieczny
[*]Kielce University of Technology, Faculty of Mechatronics and Mechanical Engineering, 25-314 Kielce, 1000-lecia P.P. av. 7, Poland, bartlomiej_szwed@o2.pl

Abstract. In the present study, solid-state diffusion bonding was performed between pure titanium (Grade 2) and stainless steel (X5CrNi 18-10) with nickel as an intermediate material. The joints were prepared in the temperature range of 850÷900 °C for 60 minutes under the compressive stress of 2 MPa in a vacuum. The bond interfaces of the diffusion joints were characterized in the optical microscope. The layers of Ni_3Ti, NiTi, $NiTi_2$ intermetallic compounds were observed in all temperature range at the nickel-titanium interface. A 0.1mm nickel interlayer prevents the diffusion of titanium to stainless steel side up to 875 °C therefore stainless steel-nickel interface is free from intermetallic compounds.

Keywords: solid-state diffusion bonding, titanium, stainless steel, nickel

1. Introduction

Rapidly developing modern industries require the use of materials which are characterized by high corrosion resistance and good mechanical properties, such materials as titanium and stainless steel. In order to meet the requirements of the aerospace, chemical and nuclear industries there is a need joining together these materials [1-4]. Diffusion bonding is one of the few joining techniques which allows to combine dissimilar materials without gross microscopic distortion and with minimum dimensional tolerance [5,6]. Direct bonding between titanium and stainless steel exhibits the formation of various types of intermetallic phases formed in the reaction zone, which cause embrittlement of the joints. In addition, the large difference of thermal expansion between these materials causes the problem of residual stresses in the joints [7-9]. The use of appropriate intermediate materials can minimize formation of the brittle intermetallic phases which in turn increases the strength of diffusion-bonded joint. Reports in the literature show that the copper layer of 0.1 mm thickness effectively blocks the diffusion of titanium to stainless steel up to 900 °C temperature if the bonding time is no longer than 30 minutes [10,11]. In previous attempt of diffusion bonding showed that copper does not form any intermetallic phase with iron, but due to the fact that the process time was 60 minutes observed the formation of the Fe-Ti phases [12]. Nickel can also be considered as a useful intermediate material due to satisfactory corrosion resistance for application at high temperature as compared to bonded joints with copper interlayer [13-14]. Kamat et al. report that a nickel-stainless (Ni-SS) steel diffusion couple is free from intermetallic [15]. However, Kundu and Chatterjee report that the Ni-SS diffusion interface is free from intermetallic compounds up to 850 °C [16, 17].

The present investigation reports solid-state diffusion bonding of titanium and stainless steel using nickel as an interlayer, with a focus on the interface microstructure of the diffusion bonded joints.

2. Experimental Procedure

The base materials used in this work were pure titanium (Grade 2) and stainless steel (X5CrNi 18-10) both received in the form of cylindrical rods having 8 mm diameter and 2000 mm length,

and nickel foil of 0.1 mm thickness. The nominal chemical composition and room temperature mechanical properties of these materials are given in Table 1.

Material	Chemical composition (wt. %)	Mechanical properties		
		YS (MPa)	UTS (MPa)	A (%)
Titanium Grade 2	Ti: 99,654; Fe: 0,171; C: 0,024; N: 0,008; O: 0,142; H: 0,001	350	420	38
Stainless steel X5CrNi 18-10	Fe: 77,99; C: 0,025; Mn: 1,460; Si: 0,390; P: 0,038; S: 0,012; Cr: 18,150 ; Ni: 8,050; Mo: 0,380	480	620	26
Nickel Ni 99,6	Ni: 99,57; Cu: 0,11; Co: 0,09; Si: 0,08; Mg: 0,07; Fe: 0,07; Al: 0,01	146	448	43

Tab. 1. Chemical compositions and mechanical properties of the base materials

From the base materials there were machined cylindrical specimens of 8 mm diameter and 10 mm length. The faces of the cylinders were prepared by conventional grinding and polishing techniques and final polishing was made with 1 μm diamond suspension. There were cut circular profiles from the nickel foil having 8 mm diameter. The samples were etched in acid solutions: titanium in an aqueous 5% solution of HF, stainless steel in an aqueous 10% solution of HCl, nickel in an aqueous 10% solution of HNO_3. The mating surface of the samples were kept in contact with steel clamp and inserted in a vacuum chamber. The compressive stress of 2 MPa along the longitudinal direction was applied at room temperature. Diffusion bonding was carried out in vacuum furnace Czylok PRC 77/1150 in the temperatures: 850, 875, 900 °C for 60 minutes with a vacuum of 10^{-3} Pa. The samples were cooling with the furnace. After diffusion bonding, the specimens were cut longitudinally and the surfaces were prepared using conventional metallographic techniques. The titanium side was etched in an aqueous solution of 95 ml H_2O and 5 ml HF. The stainless steel substrate was etched with a mixture of 90 ml C_2H_5OH, 10 ml HCl and 3 g $FeCl_3$. A solution consisting of 50 ml $C_2H_4O_2$ and 50 ml HNO_3 was used for etching nickel interlayer. The samples were observed in optical microscope Nikon Eclipse MA200 to characterize the joints.

3. Results and Discussion

To investigate the influence of bonding temperature on the titanium–stainless steel joints with nickel interlayer observations were performed with an optical microscope. The microstructures of the diffusion bonded joints are shown in Fig. 1.

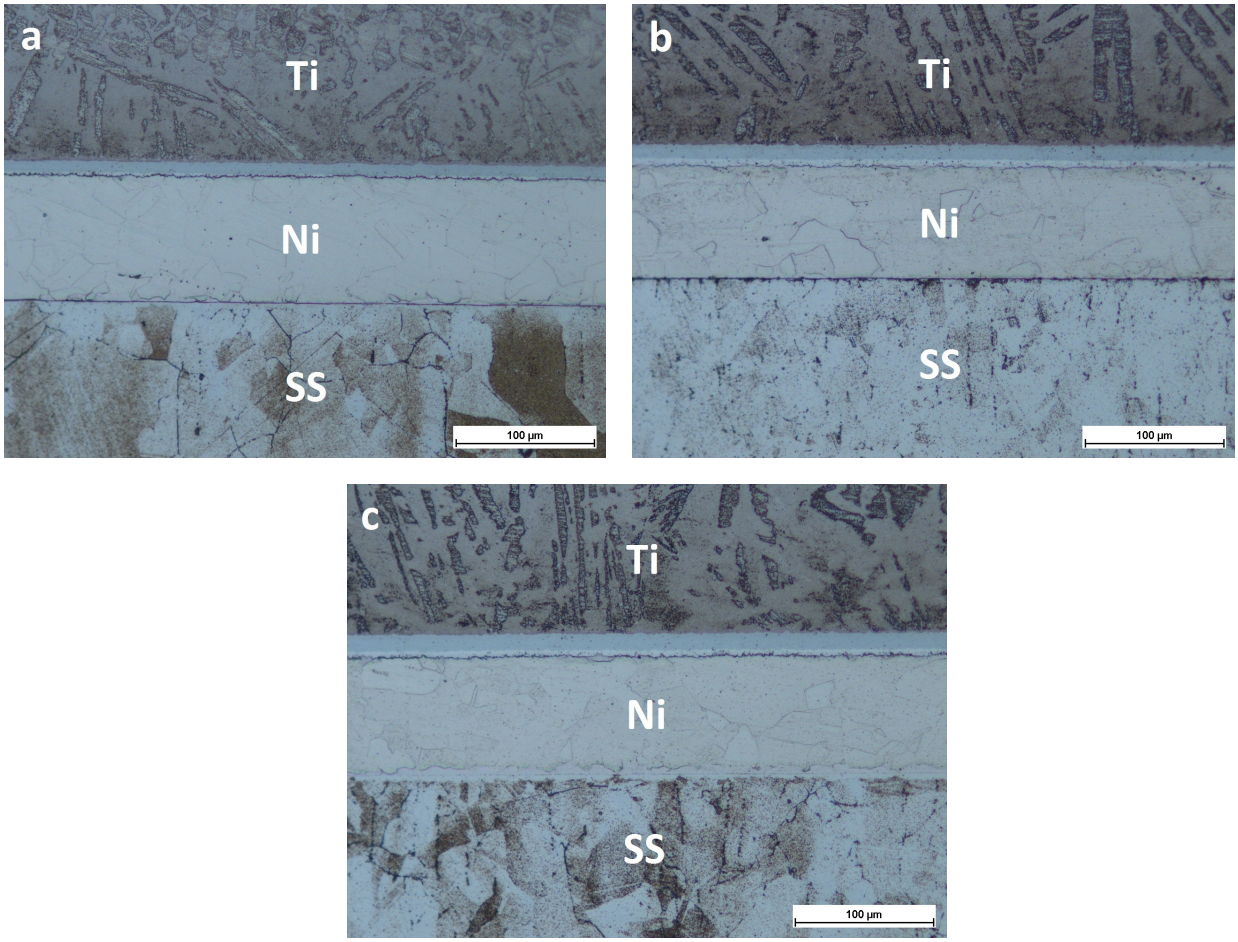

Fig. 1. Optical micrograph of the joints prepared at 850 (a), 875 (b) and 900 °C (c) for 60 minutes.

The results of the metallographical examination of the samples exhibits that diffusion occurred between the nickel interlayer and two substrates. The wide of the diffusion zone on the boundaries with joined materials grown with an increase in bonding temperature. The titanium-nickel site is characterized by the α-β Ti structure. Because nickel is a β stabilizing element it lowers the eutectoid transformation temperature of Ti [18] and the acicular α-β Ti occurs from the decomposition of β Ti during cooling with the vacuum furnace. Three distinct reaction layers have been observed at the Ni-Ti interface. According to the literature studies, the first reaction layer at the titanium base metal is Ti_2Ni intermetallic phase. The brightest layer at the nickel side is $TiNi_3$. In between those two intermetallic compounds, is present another reaction layer of TiNi phase. The thickness of the reaction products at the Ti-Ni side increases with increase in the bonding temperature. The thicknesses of the Ti_2Ni, TiNi and $TiNi_3$ layers were ~2.9; ~7.6; ~2.2 µm, respectively at 850°C and increased to the size of: ~4.1; ~11.8; ~5.2 µm, respectively at the 900°C. The diffusion zone at the stainless steel-nickel interface is smaller than that at Ti-Ni side. At the SS-Ni interface at bonding temperature from 850 to 875 °C planar and very thin diffusion layer was received. After the samples were joined at 900 °C revealed the presence of significant layer. It could be a solid solution of nickel in iron, according to binary phase diagram of Fe-Ni or it could be a intermetallic phase based on Ni-Cr phase diagram.

4. Conclusion

The solid-state diffusion bonding of titanium Grade 2 to stainless steel X5CrNi 18-10 with 0.1 mm nickel interlayer has been performed in the temperature: 850, 875, 900 °C for 60 minutes under 2 MPa uniaxial load in vacuum furnace. The conclusions are summarized as follows:

1. Diffusion bonding temperature is critical factor to control the microstructure. The diffusion zone in the titanium site of the joint becomes wider with the increase in temperature while in the stainless steel side it is planar and very thin.
2. The intermetallic layers Ni_3Ti, NiTi, Ni_2Ti, were observed at the titanium nickel side of the diffusion joint. The thicknesses of the Ti_2Ni, TiNi and $TiNi_3$ intermetallic layers were ~2.9; ~7.6; ~2.2 μm, respectively at 850°C and increased to the sizes of: ~4.1; ~11.8; ~5.2 μm, respectively at the 900°C.
3. The stainless steel nickel interface is free from any reaction layer up to 875 °C, above this temperature thin layer of reaction appears.

References

[1] *Poradnik Inżyniera. Spawalnictwo*. T. 1 i 2. WNT, Warszawa, 2005.

[2] *Brazing Handbook ed IV*, American Welding Society (AWS), Miami, 1991.

[3] *ASM Handbook Volume 6: Welding*, Brazing and Soldering, ASM International, 1993.

[4] WINIOWSKI, A., RÓŻAŃSKI M. *Przykłady zastosowania lutowania dyfuzyjnego*. Przegląd Spawalnictwa nr 4, 2010, p. 26.

[5] QINA, B., SHENGA, G.M., HUANGA, J.W., ZHOUA, B., QIUB S.Y., LIB C.: *Phase transformation diffusion bonding of titanium alloy with stainless steel*. Materials Characterization, Vol. 56, Issue 1, 2006, p. 32.

[6] KATO, H., ABE, S., TOMIZAWA, T. *Interfacial structures and mechanical properties of steel–Ni and steel–Ti diffusion bonds*, Journal of Materials Science, Vol. 32, 1997, p. 5225.

[7] ALEMAN, B., GUTIERREZ, I., URCOLA JJ. *Interface microstructures in diffusion bonding of titanium alloys to stainless and low alloy steels*. Materials Science and Technology, Vol. 9, 1993, p. 633.

[8] GHOSH, M., CHATTERJEE, S. *Effect of interface microstructure on the bond strength of the diffusion welded joints between titanium and stainless steel*. Materials Characterization, Vol. 54, 2005, p. 327.

[9] Yuan, XJ., Sheng, GM., Qin, B., Huang, WZ., Zhou, B. *Impulse pressuring diffusion bonding of titanium alloy to stainless steel*. Materials Characterization, Vol. 59, 2008, p. 930.

[10] KONIECZNY, M., MOLA, R. *Fabrication, microstructure and properties of laminated iron-intermetallic composites*. Steel Research International, Vol. 79, 2008, p. 499.

[11] KONIECZNY, M. *Mechanical properties and deformation behaviour of laminated titanium-intermetallic composites synthesised using Ti and Cu foils.* Kovove Materialy-Metallic Materials, Vol. 48, 2010, p. 47.

[12] SZWED, B., KONIECZNY, M. *Influence of diffusion bonding parameters on structure and properties of titanium and stainless steel joints with copper interlayer.* In COMAT 2014 conference: 19-2.11.2014, Pilsen, Czech Republic.

[13] SAM, S., KUNDU, S., CHATTERJEE, S. *Diffusion bonding of titanium alloy to micro-duplex stainless steel using a nickel alloy interlayer: Interface microstructure and strength properties.* Materials and Design. Vol. 40, 2012, p. 237–244.

[14] KUNDU S., CHATTERJEE, S. *Interfacial microstructure and mechanical properties of diffusion-bonded titanium–stainless steel joints using a nickel interlayer*. Materials Science and Engineering, Vol. 425, 2006, p. 107.

[15] KAMAT, GR. *Solid-state diffusion welding of nickel to stainless steel*. Welding Journal, Vol. 67, 1988, p. 44.

[16] KUNDU S., CHATTERJEE S. *Structure and properties of diffusion bonded transition joints between commercially pure titanium and type 304 stainless steel using a nickel interlayer*. Journal of Materials Science, Vol. 42, 2007, p. 7906.

[17] KUNDU S., CHATTERJEE, S. *Characterization of diffusion bonded joint between titanium and 304 stainless steel using a Ni interlayer.* Materials Characterization. Vol. 9, 2008, p. 631.

[18] OCZOŚ, KE., KAWALEC A. *Kształtowanie metali lekkich.* Wydawnictwo Naukowe PWN, 2012.

TRANSCOM 2015, 22-24 June 2015
University of Žilina, Žilina, Slovak Republic

Effect of Modifying Process on Si-Morphology and Mechanical Properties in Secondary AlSi10MgMn Cast Alloy

[*]Ivana Švecová, [*]Eva Tillová, [*]Kamil Borko, [*]Mária Chalupová
[*]University of Žilina, Faculty of Mechanical Engineering, Department of Materials Engineering, Univerzitná 1, 01026 Žilina, Slovakia, {ivana.svecova, eva.tillova}@fstroj.uniza.sk

Abstract. Recycled aluminium alloys are made out of aluminium scrap (new or old) and workable aluminium garbage by recycling. Due to the increasing production of recycled aluminium cast alloys is necessary their strict metallurgical control. Present work is focused on study of the effect of Sr-modification (0 % Sr; 0.05 % Sr; 0.1 % Sr and 0.15 % Sr) on the Si-morphology and mechanical properties (impact toughness) of recycled AlSi10MgMn cast alloy. Impact test was used to provide the impact energy. The addition of Sr to experimental alloy was effective in modifying the morphology of eutectic Si from needle (plate-like) shapes to fibrous one and improves the impact toughness. Excessive additions of Sr (> 0.10 %) will result in the formation of an Al_2SrSi_2 phase. It is also reported that at very high Sr levels (~ 0.15 %) coarsening of the eutectic silicon.

Keywords: Al-Si cast alloy, modification, mechanical properties, microstructure, Si-morphology.

1. Introduction

The Al-Si alloys are the most widely used aluminium foundry alloys today, and the control of their microstructure is one of the most important methods to improve the mechanical properties and the casting quality. Commercial Al-Si foundry alloys usually contain more than 50 vol pct of Al-Si eutectic, and extensive research to control their microstructure by eutectic modification has been carried out. The addition of alkali or alkaline earth elements changes the morphology of eutectic silicon from plate-like to branched fibres.

It is well established that modification of eutectic silicon can be achieved by several methods like faster solidification, mould vibration, melt agitation in mushy state and melt inoculation by using some elements like Na, Sr, Sb etc. Among the modifiers used, Sr and Sb are known to result in good modification in hypoeutectic Al-Si alloys. However, it has been reported that modification effect of Sr diminishes on longer melt treatment time (melt holding time), while Sb results in good modification on longer melt treatment time [1, 2].

Modification with strontium has been known since 1921 (Pacz's patent) and spread out only by W. Thiele in 1966 [3]. Thiele showed that effect of modification with strontium is similar to modification with sodium, but is more long-lasting. Comparing to sodium, strontium can be characterized by better stability - drop of its contents in modified, liquid alloy proceeds more slowly.

Strontium is the preferred modifier in current use. Addition of strontium in the near-eutectic Al-Si alloy not only results in a modification of the eutectic silicon, but also an obvious increase in the amount of α-Al dendrites and promotion of columnar growth of these dendrites, increasing both the strength and ductility of the alloy considerably.

Authors [3-5] suggested the idea "Impurity Induced Twinning" to explain the morphological changes in the presence of modifiers. Modifiers have absorbed up on the silicon growth front and these sufficiently large impurity atoms promote multiple twinning. The multiple twinning is effected by displacing a monolayer growth step to be alternative staking sequence; geometrically the ideal radius ratio r Modifier: r_{si} Silicon; would be 1.646 [4]. While atomic size seems to be a

strong factor for impurity induced twinning, it still appears as if further essential factors might have an influence on the modifying abilities such as melting point, vapour pressure or free energy of oxide formation.

Strontium is added as an AlSr or AlSiSr master alloy which also refines the Al-Si eutectic and results in castings having tensile properties comparable with those obtained when using sodium. Loss of strontium through volatilization during melting is much less and the modified microstructure can be retained if alloys are re melted. A strontium addition is that they suppress formation of primary silicon in hypereutectic compositions which may improve their ductility and toughness.

The present study is a part of larger research project, which was conducted to investigate and to provide a better understanding of the modification by Sr on the structure and mechanical properties of cast secondary Al-Si alloys. The study was confined on the most popular alloy - AlSi10MgMn that contain about 10 % Si and 0.35 % Mg.

2. Experimental

Experiments were performed on secondary (recycled - prepared by recycling of aluminium scrap) AlSi10MgMn cast alloy which chemical composition is given in the Table 1. The experimental alloy was received in the form of 12.5 kg ingots. Strontium was added in the form of AlSr10 master alloy to obtain 0.05 %; 0.10 % and 0.15 % Sr levels. The molten metal was subsequently poured with AlCu4B6. The casting was done by permanent mould casting technology into to chill. From the casted components were machined specimens for impact test (10 x 10 x 55 mm). The specimen surfaces were polished with fine sandpaper to remove any machining marks; it should be noted that the samples were used in the Charpy unnotched conditions. The impact toughness measurements were carried out on the as-cast and modified unnotched samples using a 300 J Charpy machine according to standard STN EN 10045 - 1. AlSi10MgMn cast alloy has good corrosion resistance and is suitable for high temperature applications (mechanical engineering, motor construction, textile machinery parts, etc.).

Si	Fe	Mn	Mg	Ti	Zn	Ca	Cu	Cr	Na
9.94	0.13	0.15	0.35	0.05	0.008	0.003	0.0008	0.006	0.001

Table 1. The chemical composition of the AlSi10Mg alloy (at. %)

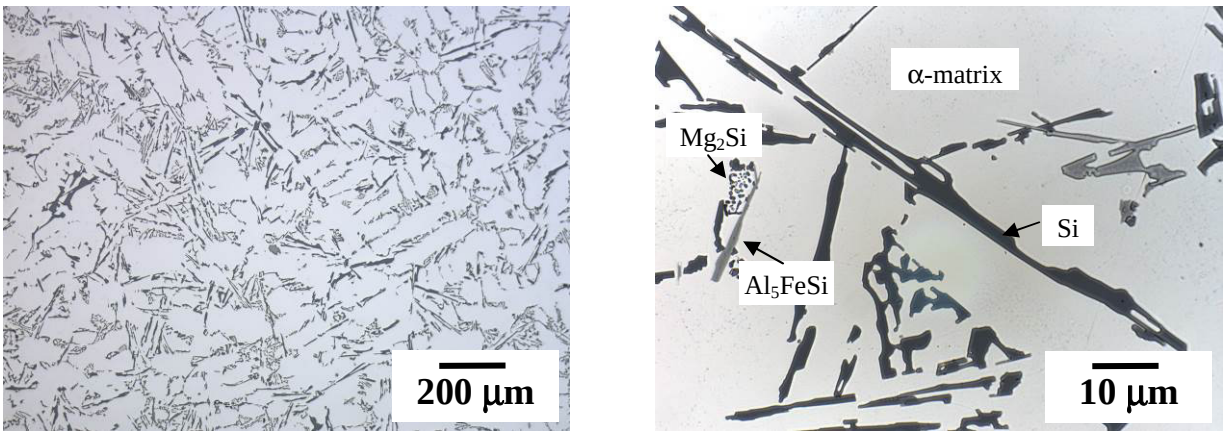

a) as cast state b) detail of Si needles

Fig. 1. Microstructure of AlSi10MgMn cast alloy, etched by 0.5 % HF, SEM.

The microstructure of experimental casts was studied using an optical microscope (Neophot 32) and scanning electron microscope (VEGA LMU II). Metallographic specimens were made from impact specimens (after testing). The specimens for microscopic analysis by optical and electron microscopy were prepared by standard metallographic procedures (preparation in bakelite, wet

ground, DP polished with diamond pastes, finally polished with commercial fine silica slurry STRUERS OP-U and etched by 0.5 % HF). Part of specimens was also deep-etched for 15 s in HCl solution in order to reveal the three-dimensional morphology of the eutectic silicon.

Microstructure of near-eutectic AlSi10MgMn cast alloy consists of dendrites α-phase (α-solid solution), eutectic (mixture of α-matrix and eutectic silicon particles) and intermetallic Fe-rich phases: $Al_{15}(MnFe)_3Si_2$ and Al_5FeSi and Mg-rich phases: Mg_2Si [6]. The α-matrix precipitates from the liquid as the primary phase in the form of dendrites and is comprised of Al and Si (Fig. 1).

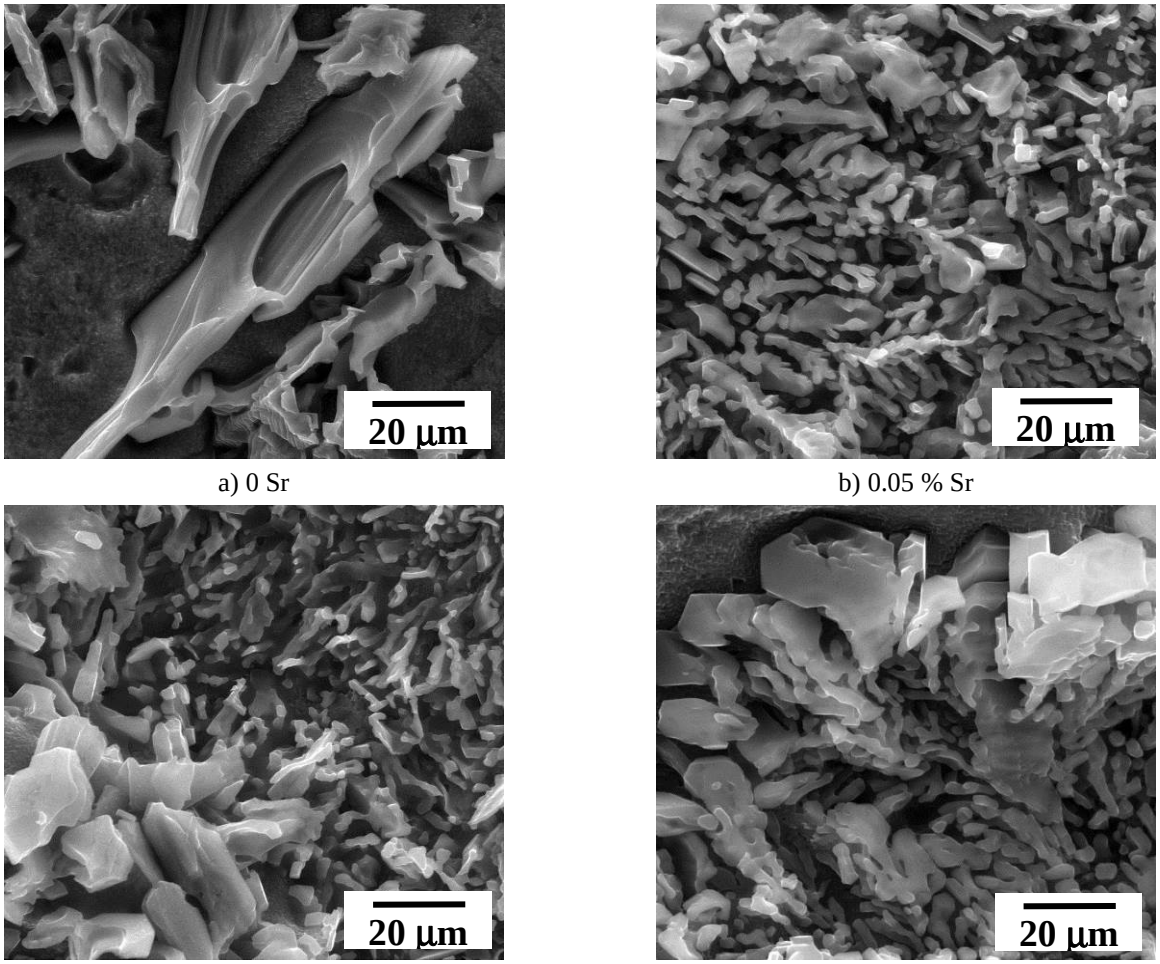

a) 0 Sr b) 0.05 % Sr

c) 0.1 % Sr d) 0.15 % Sr

Fig. 2. 3D-morphology of the eutectic silicon, deep etched by HCl, SEM.

3. Results

The mechanical properties of the Al-Si-Mg alloy are related to the size, shape and distribution of the eutectic silicon phase in the microstructure. A well-rounded silicon phase can enhance mechanical properties and can be produced by the addition of a modifier to the melt. The addition of Sr neutralizes the effect of phosphorous in forming AlP nuclei, and promotes the formation of a fibrous silicon structure by retarding the growth rate of silicon.

Three-dimensional morphology of the eutectic Si after modification shows Fig. 2. In unmodified alloy (0 % Sr), the silicon grows as platelets (Fig. 2a). Platelets are nearly parallel and thin. Structure modified by 0.05 % Sr is documented in Fig. 2b. In well modified structure Si grows in a fibrous form that looks like small individual round-shaped particles in polished surface. When the addition of Sr exceeds the amount necessary to produce a fully modified structure, it exerts a deleterious effect on the mechanical properties of the alloy. Strontium overmodification is much

more subtle. In overmodified alloys (0.1 % Sr and 0.15 % Sr) - Figures 2c and 2d, elongated Si particles that no longer grow as well as refine fibres can observed.

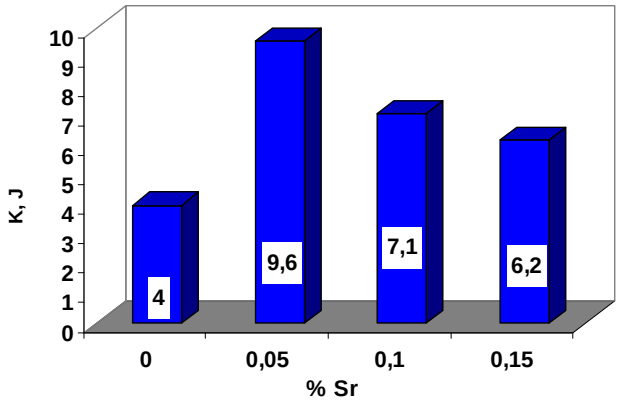

Fig. 3. Effect of Sr-modification to impact energy

The modification affects not only size and morphology of the Si particles, but also its distribution. Ideal (optimal) concentration 0.05 % Sr results in a fibrous eutectic structure, well refined and homogenous.

Fig. 3 shows the relationship between the absorbed energy (K) of the samples during impact testing and the Sr-modification (%). Values were determined by the average value of 3 test bars. The absorbed energy of the as-cast samples was 4 J. The addition of Sr to the AlSi10MgMn cast alloy improves the impact energy. The highest impact energy was observed in samples modified by 0.05 % Sr. Impact energy values of samples modified with 0.10 % and 0.15 % Sr drop to lower levels, probably as a result of increasing porosity and presence of coarsened Si particles.

4. Conclusion

The addition of Sr to experimental alloy was effective in modifying the morphology of eutectic Si from needle (plate-like) shapes to fibrous. Optimal Sr-modification (0.05 % Sr) improves impact energy. Very high Sr levels (~ 0.1 and 0.15 %) coarsening of the eutectic silicon and reduce the properties of the alloy.

Acknowledgement

The authors acknowledge the financial support of the projects VEGA N°1/0533/15 and KEGA 044ŽU-4/2014.

References

[1] KÓSA, A., GÁCSI, Z., DÚL, J. *Effect of Sr on the microstructure of Al-Si casting alloys.* Materials Science and Engineering, Vol. 37/2, 2012.

[2] TILLOVÁ, E., FARKAŠOVÁ, M., CHALUPOVÁ, M. *The role of antimony in modifying of Al-Si-Cu cast Alloy.* Manufacturing technology, Vol. 13, 1, 2013.

[3] LU, L., DAHLE ARNY K. *Effect of Sr and B interactions in hypoeutectic Al-Si foundry alloys*. Light Metals, TMS (The Minerals, Metals & Materials Society), 2006.

[4] PEZDA, J. *Effect of modifying process on mechanical properties of EN AC-43300 silumin cast into sand moulds.* Archives of Foundry Engineering. Vol. 9, 3/2009.

[5] MIRESMAEILI, S.M., CAMPBELL, J., SHABESTARI, S.G., BOUTORABI, S. M. A. *Precipitation of Sr-Rich Intermetallic Particles and Their Influence on Pore Formation in Sr-Modified A356 Alloy.* Metallurgical and Materials Transaction A. Vol. 36A, 2005.

[6] CHALUPOVÁ, M., TILLOVÁ, E., FARKAŠOVÁ, M. *Microstructure Analysis of AlSi10MgMn Aluminium Cast Alloy.* Materials Science Forum Vol. 782, 2014.

TRANSCOM 2015, 22-24 June 2015
University of Žilina, Žilina, Slovak Republic

Assessment of the Possibilities of Using Ultrasonic Method for Testing the Quality of Adhesive Joints Type Metal - Metal

[*]Dariusz Ulbrich, [*]Jakub Kowalczyk, [**]Wojciech Sawczuk
[*]Poznan University of Technology, Faculty of Machines and Transport, Division of Motor Vehicles and Road Transportation, M. Sklodowskiej-Curie sq. 5, 60-965 Poznan, Poland, {dariusz.ulbrich, jakub.kowalczyk}@put.poznan.pl
[**] Poznan University of Technology, Faculty of Machines and Transport, Division of Rail Vehicles, M. Sklodowskiej-Curie sq. 5, 60-965 Poznan, Poland, wojciech.sawczuk@put.poznan.pl

Abstract. This paper presents an assessment of the possibilities of using ultrasonic method for testing the quality of adhesive joints type metal - metal. The object of the test was motor engine part, for which a adhesive coating of brown was applied. The study was conducted on flaw detector USM 15 made by Ultrametr companies. For the preliminary study, measurements on ten samples were performed. The study involved the entire area of the adhesive connection. Due to the shape of the test piece, the ultrasonic transducer used in the tests had a small diameter and the measurements were performed from the outside of the sleeve. The results confirmed that it is possible to assess adhesive connections by ultrasonic method. Such method allow full testing of materials, in contrast to the destructive tests.

Keywords: Ultrasonic method, motor sleeve, adhesion, adhesive coating.

1. Introduction

Adhesive connections are increasingly widely used in construction of modern motor vehicles, machinery and equipment. Particularly noteworthy is the substrate-coating connections. During the research authors had encountered a problem in assessing the quality of the connection of the steel sleeve, inside of which was applied a coating of brown. The combination of these joints requires non-destructive testing [1, 2, 3]. The research method during the test was used ultrasonic echo method.

The ultrasonic method used for testing of adhesive joints is the nondestructive method, because it does not cause any changes in studied adhesive joints and in examined elements. The ultrasonic method is based on the elementary ultrasonic waves phenomena, i.e. on the reflection and passage of ultrasonic wave through boundary of two solids [5,6]. The ultrasonic wave is generated during an investigation and it is directed to glue joint. A part of wave energy passes through the glue joint, and a residue part of wave energy is reflected from adhesive joint and bath element.

One of the main problems during the test of this type of connection is to match the ultrasonic transducer to tested element resulting from the difference in shape of the test sleeve and the transducer. Due to the shape of the test piece the ultrasonic transducer was applied from the outside of the sleeve. At the time the study was conducted sliding movement of the head. This enabled the study throughout the adhesive connection (Fig. 1).

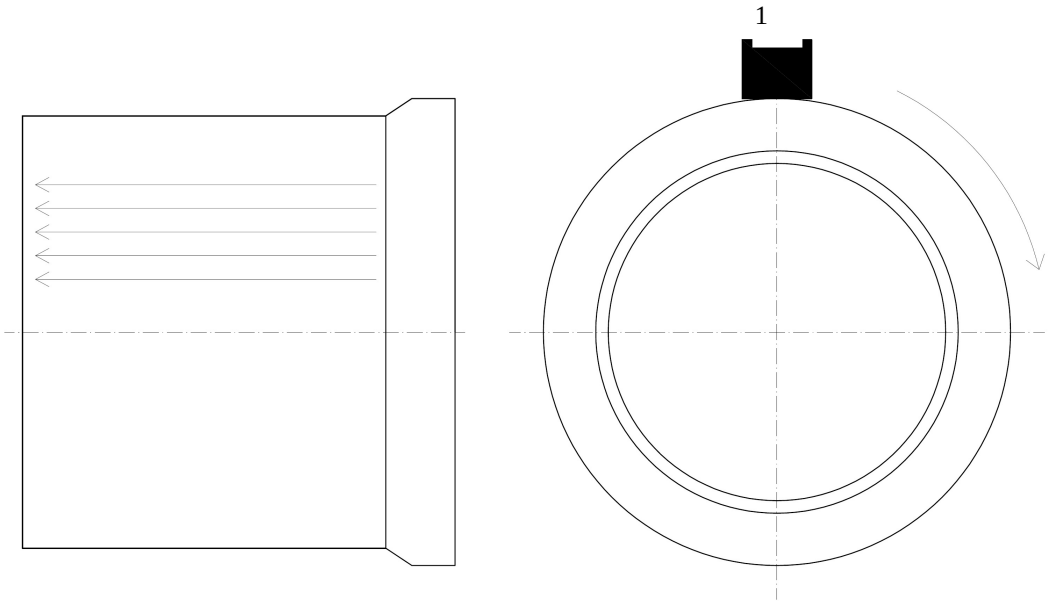

Fig. 1. A scheme of the head direction during the tests of the element; 1 - ultrasonic transducer

Depending on the quality of the connection and the suppression of tested materials, it is assumed to achieve different longitudinal wave pulses of ultrasonic flaw detector screen. The image of the expected pulses is shown in Fig. 2.

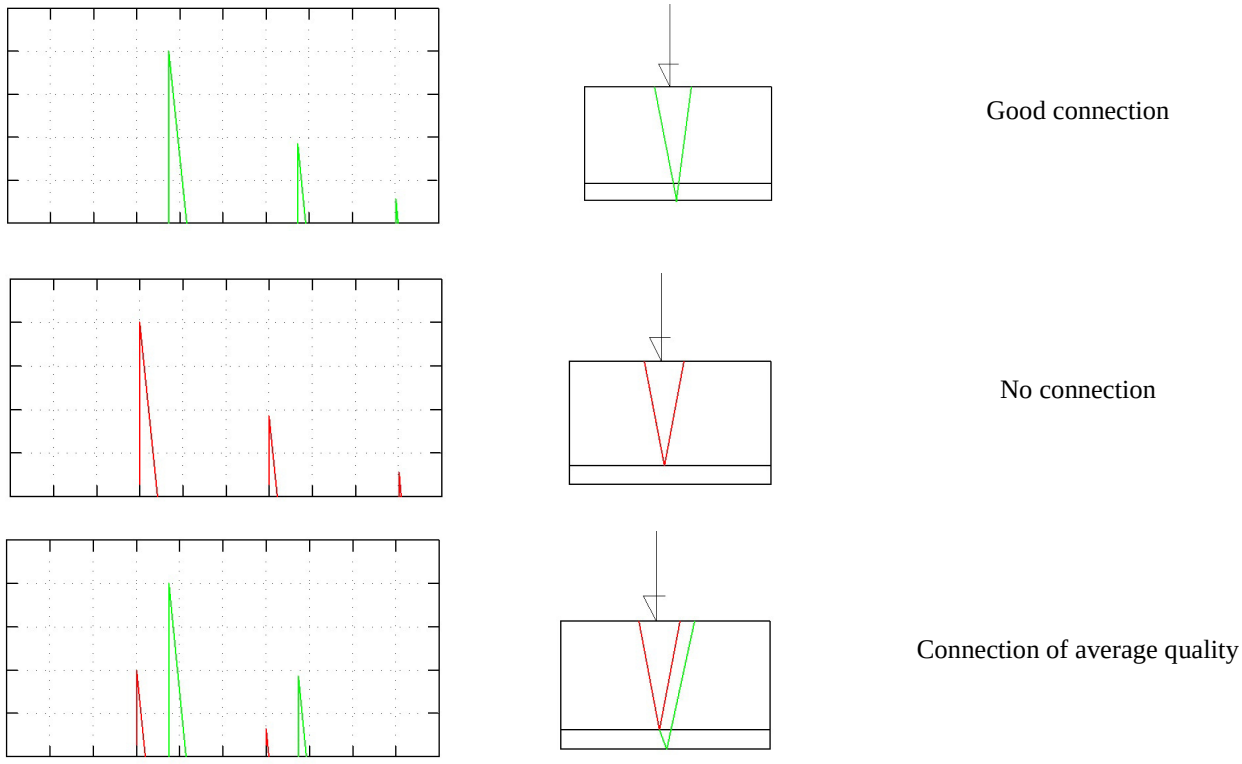

Fig. 2. Theoretical waveforms during the examination of the adhesive connection

After the analysis of theoretical course of the ultrasonic pulses of longitudinal wave investigation on the sample was performed. In the study ultrasonic flaw detector UMT made by company Ultramet was used. Due to the acoustic properties of tested materials in the study broadband ultrasound transducer DS 12 HB 1-6 made by Karl Deutsch was used. This transducer has parameters shown in Tab. 1.

Name	f [MHz]	d [mm]	λ [mm]	N [mm]	b [mm]
DS 12 HB 1-6 KD	2,28	12	2,6	12,40	19,90
f – frequency of ultrasonic transducer, d – diameter of ultrasonic transducer, λ – wavelength (for a velocity v = 5940 m/s), N – near field, b - width of the beam, the decline rate k = 0.87 at a distance of 50 mm from the head, KD - the company Karl Deutsch					

Tab. 1. Parameters of ultrasonic transducer DS 12 HB 1-6.

2. Test

The study was conducted in the NDT laboratory of Poznan University of Technology. View of an ultrasonic transducer and sample during the test is shown in Fig. 3.

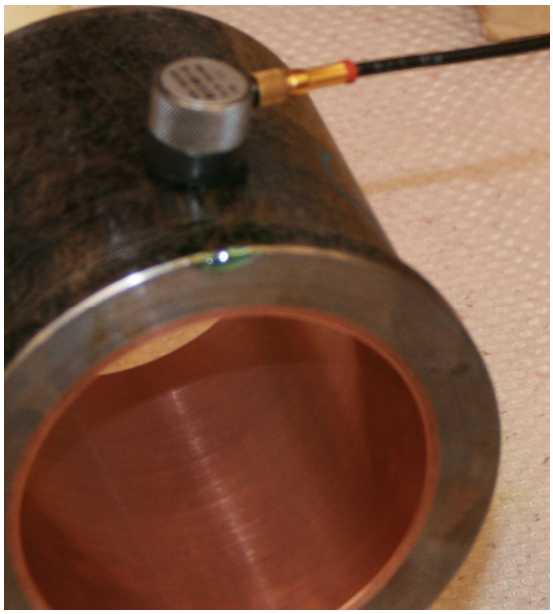

Fig. 3. View of the ultrasonic transducer with the test sleeve

In the present stage of the research, test carried out on 10 samples. All measurements confirmed the possibility of carrying out the assessment of the quality of adhesive joints. A sample view of the ultrasonic pulses configuration obtained on the screen of flaw detector is shown in Fig. 4.

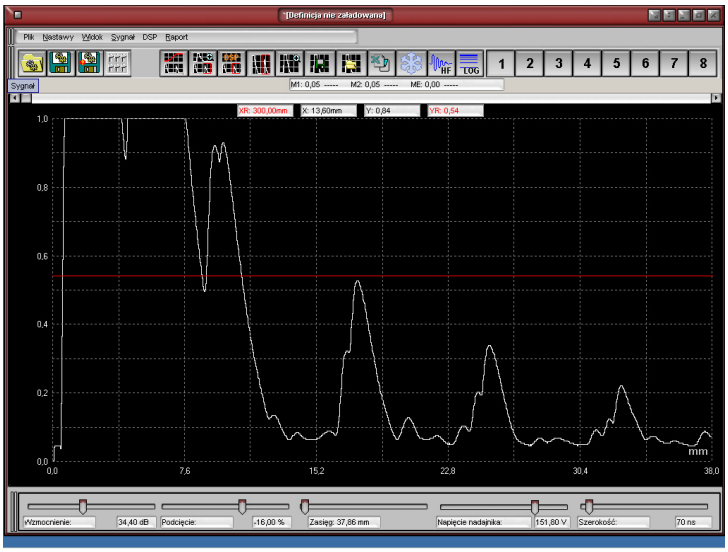

Fig. 4. View of the ultrasonic flaw detector screen during the test

On the screen of the flaw detector (Fig. 4) can be observed pulse configuration coming from the bottom of the tested element. No pulses from the border of the adhesive connection means that the test joints had high quality.

3. Conclusion

Based on extensive investigations can be concluded that:

- Ultrasonic method allows full control of studied connections and after the tests sleeve can be exploited.
- During the test of the adhesive connection is necessary to correctly fit the ultrasonic transducer to tested element.
- During the ultrasonic test of the adhesive joint is possible to obtain a useful configuration of ultrasonic pulses for assessing the quality of connection.

Acknowledgement

The project is funded by the National Centre for Research and Development, LEADER V program, contract No. LEADER / 022/359 / L-5/13 / NRDC / 2014

References

[1] JÓSKO, M., JARMUŻEK, M. *Evaluation of adhesive joint between coating and substrate using ultrasonic spectroscopy*. Communications, 4, 2001, pp. 65 – 70.

[2] DEPUTAT, J. *Postępy w ultradźwiękowych badaniach materiałów. Część I.* Przegląd mechaniczny, Zeszyt 21, 1996, s. 5 - 10

[3] GOGLI, L., ROSSETTO, M. *Ultrasonic testing of adhesive bonds of thin metal sheets*. NDT&E international, Vol. 32, 6, 1999, pp. 323 – 331.

[4] OBRAZ, J., PILARSKI, A. *Ultradźwięki w technice pomiarowej*. WNT, Warszawa 1983.

[5] LEWINSKA–ROMICKA, A. *Badania nieniszczące. Podstawy defektoskopii*. WNT, Warszawa 2001.

TRANSCOM 2015, 22-24 June 2015
University of Žilina, Žilina, Slovak Republic

Machinability of Steel S690 after Laser and Plasma Beam Cutting

*Alena Vajdová, *Anna Mičietová
*University of Žilina, Faculty of Mechanical Engineering, Department of Machining and Manufacturing Engineering, Univerzitná 1, 010 26 Žilina, Slovakia, {alena_vajdova, anna_micietova,}@fstroj.uniza.sk

Abstract. This paper deals with non-conventional methods of machining such as laser beam and plasma beam cutting. These techniques were employed for cutting of high strength steel S690. Machinability of the steel was evaluated through thickness of heat affected zone due to intensive thermal load of produced surface. Results of this study demonstrate that machinability during the following milling cycle is sensitive to the thickness of plasma and laser cut samples.

Keywords: Plasma beam, laser beam, heat affected zone

1. Introduction

Automotive industry is very fast developed and new components of complicated geometry are more and more employed. Production of such components requires integration of new techniques for production with the possible economy benefits.

Plasma beam and especially laser beam techniques becomes more and more employed for such purpose. Especially laser beam machining enable to obtain components of relative satisfactory accuracy and limited heat affected zone in the near surface regions. However, in some cases the machined surface has to be finished via the milling or grinding cycles to improve accuracy, decrease surface roughness or remove heat affected zone (HAZ) [4]. It is well known that milling operations are sensitive to the microstructure features. Being so, thermally softened or re-hardened layer can significantly contribute to the cutting forces, thus heat generation as well as intensity of tool wear. Moreover, such layers can negatively affect joints welds or other consecutive operations and the following functionality of machines, which in turns can contributes to the early cracks initiation and premature failures [3].

1.1. Laser beam machining

Laser beam machining (LBM) is one of the variety of laser applications in the real industrial production. Mechanism of chip separation is based on high energy beam of photons produced by a laser device. LBM is a thermal process in which the high concentrated light energy is concentrated onto small area. [5] This energy is converted to the heat and material in the loaded area is evaporated. This way the required shape of the components can be obtained [1]. On the other hand, the main disadvantage of LBM can be viewed in limited sample thickness as opposed to the PBM or other conventional or non conventional methods.

1.2. Plasma beam machining

Plasma beam machining (PBM) is a process during which the neutral gas of high speed (for instance air) flows through the nozzle to the electric arc. Ionization of the gas is produced by the high voltage spark. Plasma arc is due to creation of electric circuit between the gas and metal surface. Surface melting is due to high temperature of plasma beam.[2] The melted metal is removed from the cutting zone by the high speed gas through the cutting gap. The main disadvantage can be viewed in a quite thick HAZ. On the other hand, much thicker samples can be machine via PBM.

2. Cutting and Other Conditions

The main goal of this study is evaluation of machinability of high strength steel S690 based on dynamic machinability (measurement of cutting forces) during milling cycles. The samples of various thicknesses were cut via PBM and LBM cycles as well as conventional non thermal method (saw cutting).

First series of samples were cut on laser cutter TRUMPF TRUMATIC L3030. The samples were cut at different cutting conditions as those indicated in tab.1.

	S690 thickness 3 mm		S690 thickness 6 mm	
Sample n.	h3v1L	h3v2L	h6v1L	h6v2L
Cutting speed	1800 $mm.min^{-1}$	2520 $mm.min^{-1}$	1320 $mm.min^{-1}$	1760 $mm.min^{-1}$

Tab. 1. Cutting speeds for LBM

Cutting width	Focus distance of lens	Nozzle diameter	Laser power	Adjustment distance	Gas
0,15 mm	5 mm	0,8 mm	2000 W	0	oxygen

Tab. 2. Other cutting conditions for LBM

The second series of samples were cut by plasma cutter MAX 70. The samples were cut at different cutting conditions as those indicated in tab.3.

	S690 thickness 3 mm		S690 thickness 6 mm	
Sample n.	h3v1P	h3v2P	h6v1P	h6v2P
Cutting speed	0.99 $m.min^{-1}$	1.55 $m.min^{-1}$	0.5 $m.min^{-1}$	0.99 $m.min^{-1}$

Tab. 3. Cutting speeds for PBM

current	gas	Gas pressure	Distance of nozzle from surface	Nozzle diameter
60 A	air	100 MPa	5 mm	2 mm

Tab. 4. Other cutting conditions for PBM

The cutting conditions, as those indicated in the previous tables, were modified due to higher strength of steel S690. For this reason, cutting conditions usually employed for conventional steel were adapted for this specific purpose. Step by step method the optimal cutting conditions were suggested, especially cutting speeds, for machining samples of variable thickness cut via the different methods (LBM and PBM). Such samples were routinely prepared for metallographic observations and Nital etched (3%) to reveal structure transformation in near surface (HAZ). Thickness of HAZ was evaluated as a thickness of the zone appearing dark in the micrographs. Each thickness of HAZ was obtained by averaging of 5 different measurements at different positions, see figures 1, 2, 3 and 4.

3. Results of Experiments and their Discussion

3.1. Measurement of HAZ Thickness

The results of metallographic observations show that thickness of HAZ after LBM is significantly lower that that found after PBM. Thermally softened (or rehardened) HAZ appears dark; its boundary can be easily recognized and measured. Higher thickness of HAZ after PBM indicates much higher temperatures in the cutting zone as well as the corresponding time during which the high temperatures penetrates deeper beneath the free surface. The higher thermal load also indicates thin while layer (WL) occurring after PBM whereas surfaces after LBM are WL free. Furthermore, as the thickness of samples increase the thickness of HAZ also increases. Thickness of HAZ is also sensitive to cutting conditions (especially cutting speed). Lower cutting speed produces thicker HAZ a vice versa. Such behavior is also connected with slowed motion of thermal source and longer interval during which a certain cutting area is exposed to elevated temperatures.

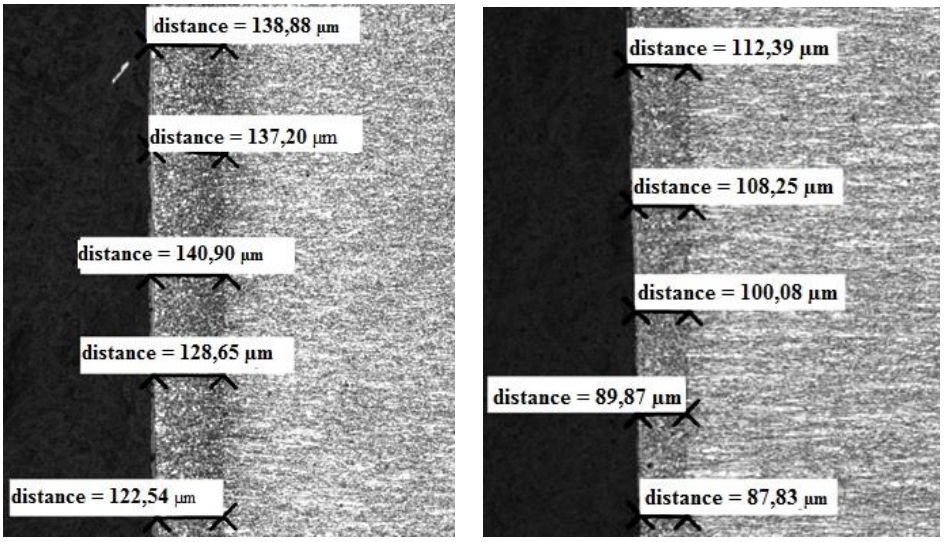

a) HAZ h3v1L b) HAZ h3v2L

Fig. 1. Thickness of HAZ after LBM, sample thickness 3 mm

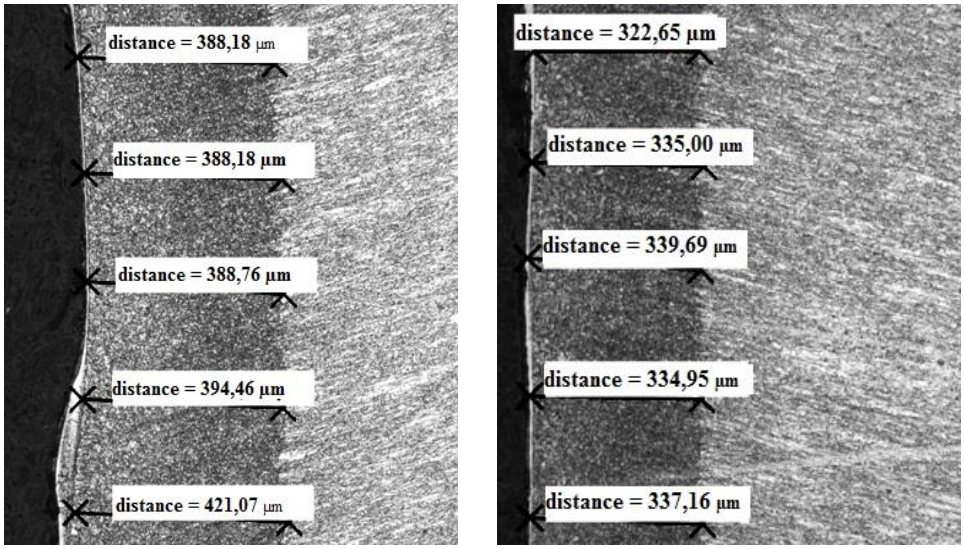

a) HAZ h3v1P b) HAZ h3v2P

Fig. 2. Thickness of HAZ after PBM, sample thickness 3 mm

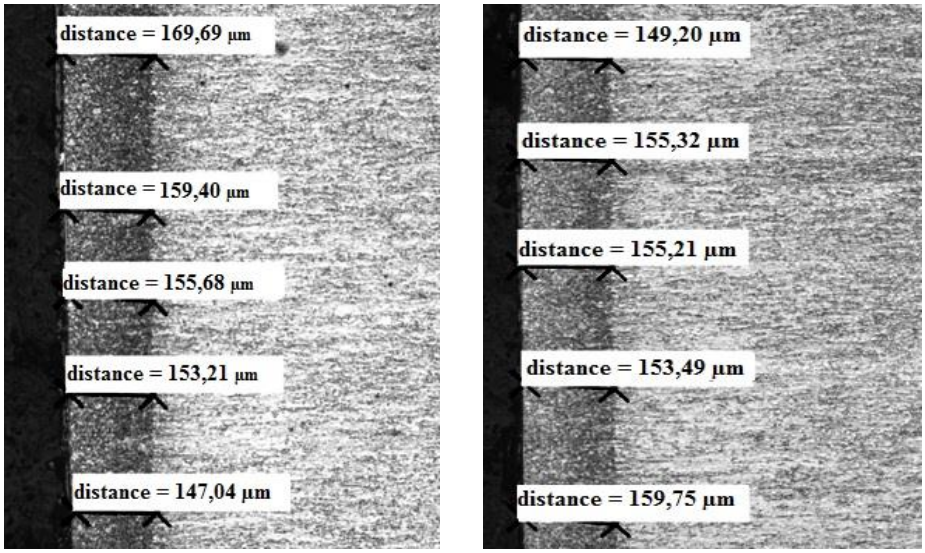

a) HAZ h6v1L b) HAZ h6v2L

Fig. 3. Thickness of HAZ after LBM, sample thickness 6 mm

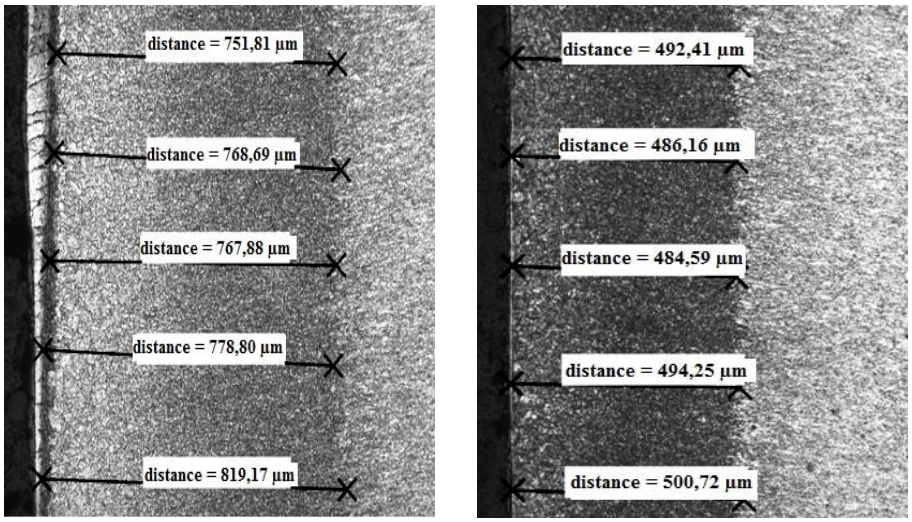

a) HAZ h6v1P b) HAZ h6v2P

Fig. 4. Thickness of HAZ after PBM, sample thickness 6 mm

Measurement of HAZ as well as WL is important since strongly affect the following machining cycles such as grinding or milling from the point of view of allowances for these operations. The higher thickness of HAZ is the higher corresponding volume of near surface region should be removed via grinding or/and milling.

3.2. Milling Cycles

Machinability of the structures after LBM and PBM was evaluated via measurement of cutting forces during milling cycle. The reference state of cutting forces was given by milling of nearly untouched surface produces by conventional saw cutting. Measurement of cutting forces was carried out via application of dynamometer KISTLER 9255A on milling machine FA4AV at the following cutting and other conditions: n = 500 min^{-1}, f = 112 $mm.min^{-1}$, a_p = 0,25 mm, tool – face milling cutter of diameter 16 mm, cutting inserts APRX 1505 PDER – M. The raw signals were recorded and analyzed in software package DasyLab. Example of index of machinability indicates equation (1).

$$k_v = \frac{h3v1L}{h3} = \frac{1180,07}{1034,08} = 1,14 \qquad (1)$$

method	sample	force	index of machinability
		F (N)	Kv
LBM	h3v1L	1180.07	1.14
	h3v2L	1146.21	1.11
	h6v1L	1229.09	1.02
	h6v2L	1041.4	0.86
PBM	h3v1P	962.06	0.93
	h3v2P	840.17	0.81
	h6v1P	988.62	0.82
	h6v2 h6vP	845.06	0.70
SAW cutting	h3	1034.08	
	h6	1210.58	

Tab. 5. Cutting forces and the corresponding indexes of machinability

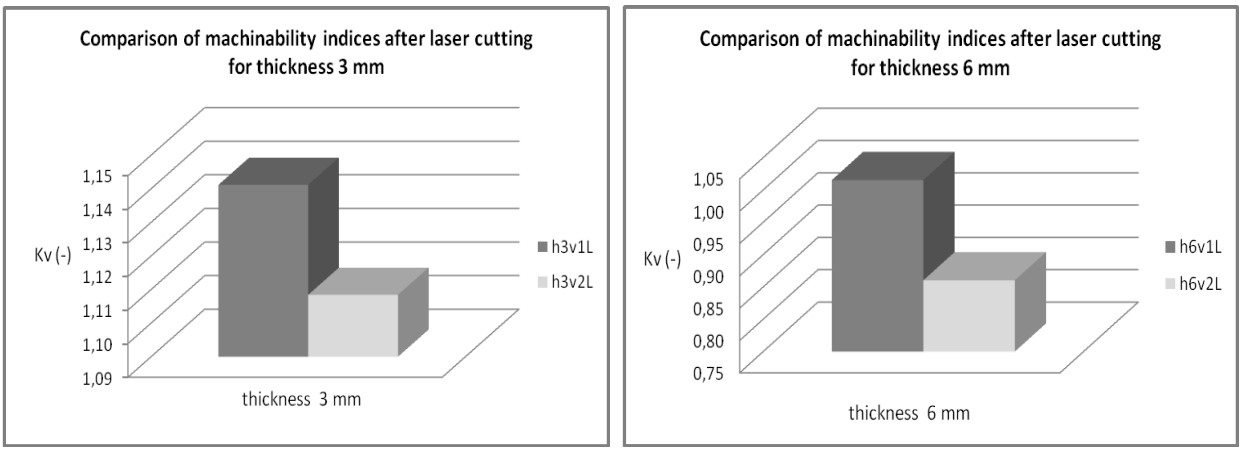

Fig. 5. Indexes of dynamic machinability versus cutting speed after LBM for samples of variable thickness

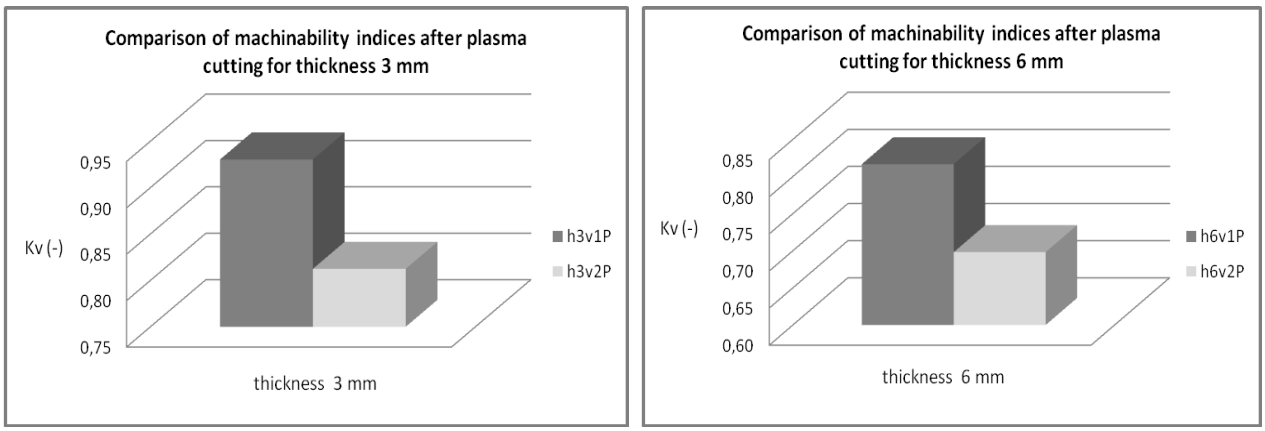

Fig. 6. Indexes of dynamic machinability versus cutting speed after PBM for samples of variable thickness

It should be noticed that milling of samples after LBM were carried (and evaluated) as a first pass of tool over the sample surface since the thickness of HAZ is always below cutting depth (0,25 mm). Moreover, higher precision of a cut and the corresponding low skew of the samples takes only minor role during the consecutive milling process. On the other land, PBM machined samples exhibit quite high skew as well as high HAZ thickness exceeding cutting depth. Being so, cutting forces were analyzed from the raw records of cutting forces after second pass of the tool over the surface.

Fig. 5 and 6 as well as tab.5 show that index of dynamic machinability after LBM and application of higher cutting speed gives lower cutting forces and so the corresponding dynamic machinability below 1. Expressed in other words, structure after LBM becomes thermally softened in the case of steel S690. On the other hand, PBM produces surface in which effect of structure rehardening dominates, thus higher cutting forces during milling gives lower indexes of machinability. It is well known that cutting forces represent the energy needed for chip separation which in turns converts to heat. Mechanical and thermal load of tool represent two major aspects affecting intensity of tool wear. Being so, it is believed that milling of surface after PBM accelerates tool wear whereas LBM does not.

4. Conclusions

Except tool wear, thickness of cut samples strongly affect accuracy of produced components (especially after PBM due to attainable much higher thickness of components). As it was mentioned, thickness of HAZ together with skew of obtained profile strongly influence allowances for further operation. Industrial experience indicates that application of PBM for thick parts make longer further milling, drilling or grinding cycles. These cycles should improve accuracy of produced parts as well as remove the HAZ. Being so, nowadays skew of a profile is reduced via compensation of position of nozzle (its angular positioning). Such approach enables intensification of production which in turns corresponds with the possible economy benefits.

Acknowledgement

This project is solved under the financial support of KEGA agency (projects n. 005ŽU and n. 009ŽU - 4/2014).

References

[1] BEŇO, J. - MAŇKOVÁ, I.: *Technologické a materiálové činitele obrábania*. Vienala – vydavateľstvo Košice 2004, ISBN 80 - 7099- 701-X, 418 s.

[2] MIČIETOVÁ, A. - MAŇKOVÁ, I. – VELÍŠEK, K.: Top trendy v obrábaní, V. časť – Fyzikálne technológie obrábania. MEDIA/ST, s.r.o., Žilina, 2007,ISBN 80-968954-7-2, 225 s.

[3] NESLUŠAN, M.- CZÁN, A.: *Obrábanie titánových a niklových zliatin.* EDIS -vydavateľstvo ŽU, 2001, ISBN 80-7100-933-4.

[4] NESLUŠAN, M. – ČILLIKOVÁ, M. (2008): *Teória obrábania,* EDIS - vydavateľstvo ŽU, Žilina , ISBN 978-80-8070-790-3.

[5] ZRAK, A, MEŠKO, J. : Technology of laser cutting .*In: TRANSCOM 2013* : 10-th European conference of young research and scientific workers : Žilina, June 24-26, 2013, Slovak Republic. - Žilina: University of Žilina, 2013. - ISBN 978-80-554-0694-7. - S. 219-222.

TRANSCOM 2015, 22-24 June 2015
University of Žilina, Žilina, Slovak Republic

Alternative Uses of NDT-leak Testing Method of Pressure Changes in the Gas Industry.

[*]Ing.Peter Vrzgula, author, [**]Ing. Miroslav Buchaco-author of,
[***]doc. Ing.Miloš Mičian, PhD. co-author of

[*]SPP-Distribution, a.s., Mlynské nivy Cap-44/B, Bratislava, workplace, Local Centre, Závodská road 26, Zilina, Slovakia,010 22 peter.vrzgula@spp-distribucia.sk
[**]SPP-Distribution, a.s., Mlynské nivy Cap-44/B, Bratislava, workplace, Local Centre, Levice road 26, Nitra, Slovakia, 95 054 miroslav.bucha@spp-distribucia.sk
[***]University of Žilina, Faculty of Engineering, Department of technology engineering, University road 1, Zilina, Slovakia, 01026, milos.mician@fstroj.uniza.sk

Abstract. As in a number of industries, as well as in the gas industry we have confronted the issue of controls, which are constantly exposed to large differences in the pressure containment. Due to the fact that gas is a natural gas - a distribution medium, which is a highly flammable medium and explosive under certain conditions, it is necessary to make every effort to identify leaks in the pipelines and technological objects, in order to prevent undesirable effects of possible leaks. In addition to the traditional methods based on the location of the main component of natural gas, i.e. methane (CH_4) using highly sensitive instruments with extremely high sensitivity to moisture we would like to offer the use of an alternative test method i.e., methane leakage test by a method of pressure changes.

Keywords: leakage test, NDT, calibrated leak, test specification, test equipment, piping, GIS node

1. Theoretical research

For the determination of the speed of an object subjected to the influence of the different pressures in enclosed wall leaks penetration a number of methods are used, which are based on the evaluation of the changes in quantity of gas in the tested object. Equation for an ideal gas is the ratio between the amount of pressure, temperature, and volume of the gas contained in the free internal volume of the test object. Under certain circumstances, it may be that one or more of the variables considered to be constant, and so may be considered a change in weight, for example tracking changes in pressure or changes in pressure-temperature inside the test object [1].

The volume changes of the tested object (based on variations in pressure and temperature during the tests) are recommended to be take into account. In most industrial applications, this change is so small that it can be neglected. For our experimental use we can consider the volume to beconstant.

Deformation of the test object is typically considered when the test specifications are set and due to the fact that the precision of the test may be influenced by the changes in the volume, you can use alternative procedures or methods, which maintains a constant pressure (flow measurement) [6].

2. Design of experiment

The tightness of an object is determined by testing the measurment of the pressure drop of the test gas. The test object is connected to the valve V1 with pressure ZT (compressor, cylinder) (Fig. 1). The test object is connected with:

ZT-pressure source
V1 – filling valve
V2-valve for discharge of the test gas
V3 – shut-off valve for the calibrated leak
V4 – connecting valve
M-pressure gauge
CN – calibrated leak
VP1-relief valve for pressure source
VP2-relief valve, which pressure sure test object
(increase in pressure as a result of an increase in the temperature of the test gas, object)
N – auxiliary vessel
MD – differential pressure gauge

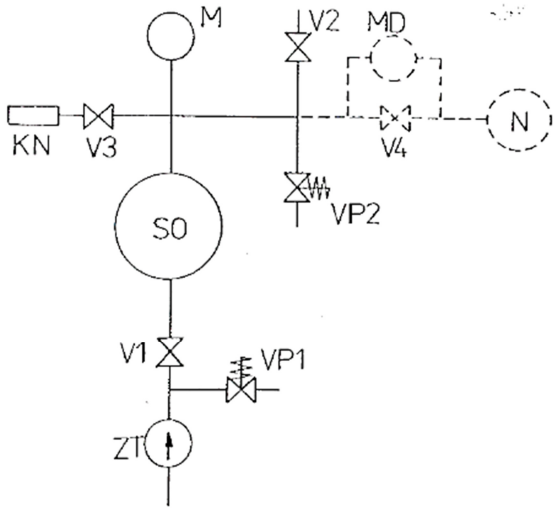

Fig. 1. Diagram of the arrangement of test equipment for pressurized gas leak test

Testing procedure:

-test gas (most often air, or nitrogen) over is pressured in through the ZT source (compressor, or cylinder) into the test object with the valves V1 and V3 opened.
- We monitor the pressure vale in a gas monitor M on an ongoing basis
- In excess of the permitted pressure in the feed pipe the safety valve opens VP1.
- When the prescribed test pressure is reached, close the filling valve V1 and a source of pressure to turn the ZT.
- During the test the tightness of the gas pressure we allow agas leakage by a way of calibrated leakage. The we calculate the volume of gas that escaped by the calibrated leakage during a time $t_1$whencauses the pressure drop in the value of the object tested Δp.

- Then, the valve closes, the V3 is separated from the tested object CN leak with calibrated object ZT.
- Then we pressurize the test object on the prescribed test pressure again.
- After pressurizing we measure the time t_1, in which the pressure falls in within the same value as the pressure Δp of the same object tested by calibrated pressure leakage CN attached.
- After the test, the test object tested with pressure by opening the valve gets rid of leaks V2. [4]

The evaluation of the tests:
Escape from the tested object shall be calculated according to the relation (1):

$$q_n = \frac{V_{KN}}{t_2 - t_1} - q_2 \qquad [\ Pam^3s^{-1}\ ] \qquad (1)$$

In the volume (amount) of the test-$_{CN}$ gas, which escaped calibrated leak problems for time t_1
t_1 – time in which dropped the pressure in the revolving facility with a calibrated leak problems on the value of the attachedΔp.
t_2 – time for which decreased pressure in the revolving object without an attached graduated about the value of Δp leaks.
q_2 – leak of the test gas through the leaks in the test equipment. (Value of q is necessary to measure in any possible way)

The conclusion of the test:

The test is considered satisfactory if the object is estimated to be less than the allowable leakage (2), i.e.

$$q_n < q_{dov} \qquad (2)$$

(If the pressure dropof the value of Δp is in real time, is less than the object being tested is a range of methods of leak.)[2][3]

2.1 Safety experiment

To ensure the inviolability of the difference in pressure at the test temperature shall be tested and approved for the construction of an object with respect to the effects of the increase in temperature due to possible changes in the surroundings (heating by the Sun, etc.). In addition, it is necessary to ensure compliance with local safety conditions, as well as to provide facilities to prevent unplanned increase in pressure to ensure that under no circumstances will design limits not be exceeded[5].

2.2 The feasibility of the experiment

The speed is determined by the change in the overall presure in the leaks at the intersection of period of time. For this reason, there must be a resolution so high, measuring devices so that they can be accurately determined by pressure changes. The sensitivity of the measurement instruments

should be 5 to 10 times higher than the expected pressure. Resolution of the device must be defined in the criteria for admissibility[1].

3. Use of the experimental findings to identify leaks in the gas distribution network

The test method can be used on all operating systems, so that the method of testing to the pipe pressure pipeline gas is also considered as an alternative to the standard methods of checking for leaks. Its use is necessary to meet the conditions set out below:

- For the purpose of measuring the pressure of the gas leakage of a particular section of the pipeline is a natural gas pipeline compared to its node respectively and tightness insulation from the operating pipeline system.
- It is necessary to provide for the possibility of alignment of all components needed to test the tightness of the existing fittings within the test leg of the pipeline or pipeline node (under the scheme in Fig. 2)

On the basis of the fulfilment of these conditions, it is possible to proceed to the test. tightness gas pressure test NDT-LT with calibrated leak problems according to available information on gas installations was applied, so you'll need VTZ carried out an experiment in practice to a similar procedure as for laboratory testing. Suitable locations for testing tightness on the facilitate identifying to gas pipelines can serve a geographic information system (GIS), which provides mapping coverage of all distribution pipelines and technological objects in the Slovak Republic with a large information potential (fig. 2).

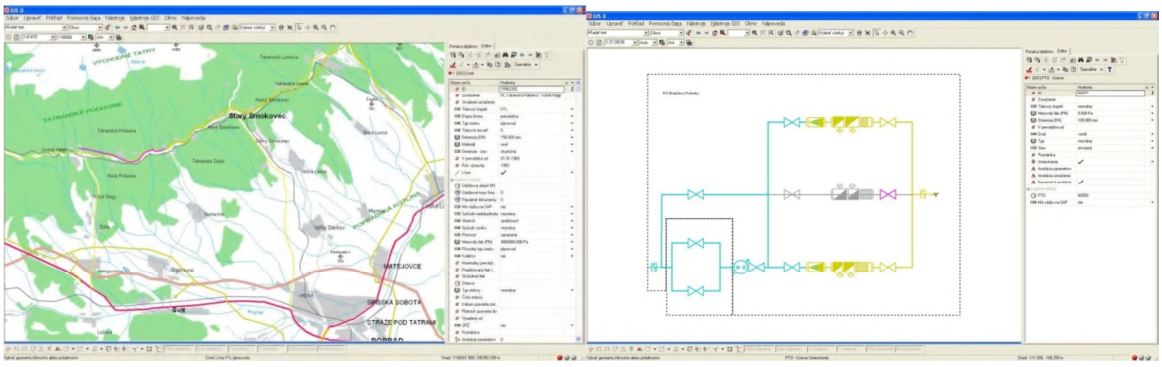

Fig. 2. Geographic information system GIS in CAP-D

4. Conclusion

Gas distribution network in the Slovak Republic, as well as distribution networks in other countries are due to the nature of the distributed chanel very prone to leaks. Since it is the responsibility of the operator of such equipment to deliver the required chanel – natural gas from the source to the final consumer, it is necessary to safely and reliably up to the highest possible degree of localization of any leaks and their subsequent removal. This effort is closely linked to the economic efficiency of the distribution system operator and its pipeline. I am convinced that the methods of NDT LT

reviewed and tested within the framework of this project have a much greater potential for indoor use in the gas sector thenhas been completed before.

References

[1] The CSN EN 13184 *Nodestruction testing. Testing for leaks*. The method of pressure variation

[2] ŽÚBOR. P.: *an overview of the standards (CSN) associated with the tests for leaks (leakproofness) objects containing dangerous substances*, NDT-LT and entry into the EU Seminar. The requirements and realities, Piešťany 2004

[3] ŽÚBOR. P.: *determination of leak test (tightness) objects containing dangerous substances,-LT and a new technique*, Piešťany NDT Seminar 2007

[4] www.netesnosti.informacie.sk

[5] KOPEC, B. et al.: *non-destructive testing of materials and structures*, CERM, s.r.o. Brno, 2008, 573, ISBN 978-80-7204-591-4.

[6] SKRBEK, b. (2014): *Advances in the field of non-destructive testing*. TUL: Liberec. 56 s. ISBN 978-80-7494-165-8

TRANSCOM 2015, 22-24 June 2015
University of Žilina, Žilina, Slovak Republic

The Impact of Supplementing Motor Oil with Carbon Nanotubes on Improving the Tribological Piston – Cylinder System's Performance

[*]Emil Wróblewski, [*]Antoni Iskra,[*]Maciej Babiak
[*]Poznan University of Technology, Institute of Internal Combustion Engines and Transport, Piotrowo 3, 60 – 965 Poznan. {Emil.z.wroblewski}@doctorate.put.poznan.pl,{Antoni.Iskra,Maciej.Babiak}@put.poznan.pl

Abstract. This article presents the results of motion resistance measurements of an engine equipped with pistons coated with carbon nanotubes and using carbon nanotube additions to the engine's oil as the active additive. Covering the side surface of the piston with carbon nanotubes results in significant reduction in friction loss of the piston-cylinder system, and reduction in fuel consumption. Supplementing the lubricating oil working in the piston-cylinder liner area with nanotubes could also result in a further reduction of frictional resistance. Nanotubes in the lubricating oil can create structures able to significantly change oil properties, however, suspension creation processes are radically different. It should be also noted that modifications of lubricating oils by creating CNT suspensions does not exhaust the possibilities of obtaining different oil properties.

Keywords: Carbon nanotubes, friction losses, engine oil

1. Introduction

The combustion engine's durability strongly depends on the dimensional and geometric surfaces unchangeability in interdependent systems. An example of such system is a piston-cylinder group. For the above reason all acting surfaces are treated accordingly to some extent by manufacturers. Most treatments are done by using surface hardening or by applying a layer of chromium or other materials that have good frictional properties to the surface. Currently, surface treatment methods based on applying nanomaterials, such as carbon nanotubes, become a fast developing domain.

The use of carbon nanotubes to coat the lateral bearing surface of the piston introduces three main improvements:
- reduction of friction,
- an increase in the surface abrasion resistance,
- vibration reduction in piston combustion engine,

however, these effects do not necessarily occur simultaneously, actually they can be mutually exclusive.

Reduction of friction losses has also an effect on reducing fuel consumption. One method of reducing friction losses is to use the lubricating oils with reduced viscosity or with additives. Such a method, however, has limitations. Using oils with too low viscosity would result in a reduction of lubricating properties and too rapid wear of the interdependent components. In the extreme case too low viscosity might even cause engine damage due to abrasion.

This paper will present the results of resistance friction losses for engine oils with carbon nanotube additives.

2. Changes to the friction resistance of the piston coated with CNT

The measured results of the research show that applying layer of carbon nanotubes to the bearing surface of the piston can lead to significant reduction of combustion engine's internal friction loss, hence to reduce fuel consumption.

Reduction of friction losses for CNT coated pistons can be observed for all engine coolant temperatures, loads and engine speeds.

Table 1 shows summary of friction losses expressed as torque changes of the combustion engine equipped with default pistons and then the pistons coated with layer of carbon nanotubes.

The research was conducted under the following conditions:

- the engine oil temperatures of 50, 80 and 110 °C,
- the average compression resistance of the working fluid in the combustion chamber of the engine: 0, 1 and 1.5 bar,
- the engine revolution speed in the range of 1500 - 3000 rpm.

Oil temperature		50°C			80°C			110°C		
Pressure [bar]		0	1	1,5	0	1	1,5	0	1	1,5
		The engine torque [Nm]								
Engine speed [rpm]	1500	5,042	6,338	7,751	3,961	5,071	6,516	3,513	4,777	6,302
		4,839	6,296	7,747	3,701	4,985	6,53	3,131	4,719	6,015
	1750	5,421	6,728	7,892	4,178	5,239	6,606	3,766	4,956	6,336
		5,104	6,491	8,02	3,837	5,249	6,652	3,258	4,765	6,03
	2000	5,732	6,926	8,056	4,447	5,542	6,675	3,996	5,225	6,413
		5,325	6,691	8,035	4,029	5,488	6,718	3,514	5,134	6,088
	2250	5,984	7,186	8,337	4,705	5,622	7,157	4,174	5,481	6,643
		5,734	6,956	8,047	4,326	5,607	6,757	3,697	4,868	6,109
	2500	6,415	7,571	8,496	5,207	6,231	6,95	4,676	5,704	6,698
		5,948	7,208	8,063	4,604	5,923	6,822	3,774	4,959	6,322
	2750	6,524	7,639	8,589	5,318	6,411	7,638	4,923	5,849	6,731
		6,161	7,11	8,546	4,861	5,828	6,799	4,001	5,478	6,479
	3000	6,907	7,953	-	5,527	6,641	7,485	4,902	6,151	7,122
		6,418	7,474		4,951	5,989	7,028	4,269	5,333	6,527

Tab.1. Resistance in petrol engine equipped with a factory pistons - upper value; resistance in petrol engine equipped with a pistons coated with nanotubes - lower value

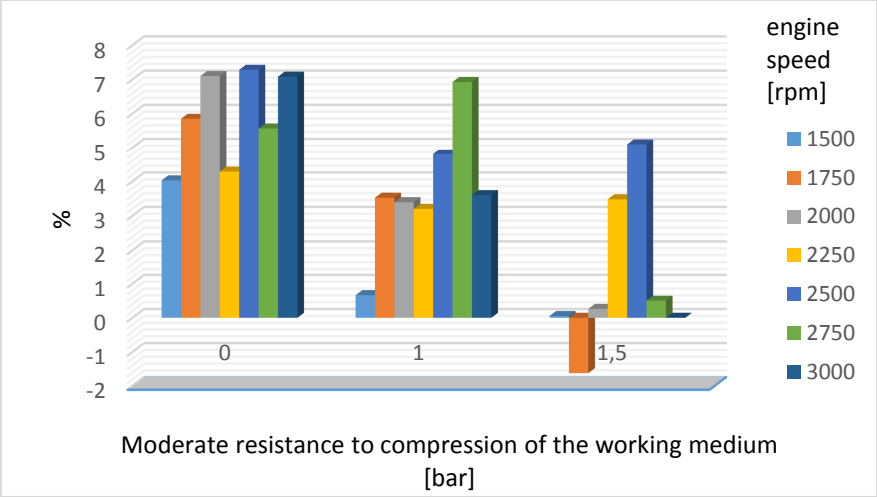

Fig. 1. Reduction of the loss of friction at different engine's revolutions speeds, temp of 50 °C

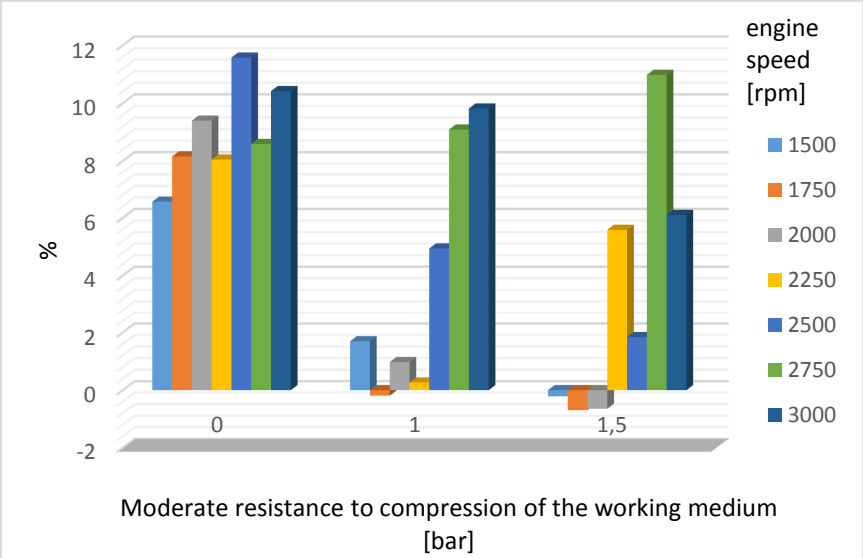

Fig. 2. Reduction of the loss of friction at different engine's revolution speed, temp of 80 °C

Fig. 3. Reduction of the loss of friction at different engine's revolutions speed, temp of 110 °C

Changes in frictional resistance as a result of the pistons' bearing surface coated with the CNT layer are shown in Figures 1-3.

Graphs show trends in the change rate of resistance due to coating with the CNT. As engine's revolution speed gets higher the frictional resistance reduction increases accordingly. This is an important observation, because along with higher engine speed the friction losses also get higher, so if better friction resistance reduction is possible it may result in additional fuel savings.

The analysis of combustion engine's internal frictional resistance levels indicates higher average reductions at higher temperatures, along with the lower viscosity of lubricating oil. The temperature range used in the study includes temperatures lower than the temperature of the oil on the cylinder liner, so it can be assumed that the internal resistance reduction levels under average usage conditions may be even more significant than those shown above.

3. Changes to the friction resistance in the spark and compression ignition engines by using CNT with additives

Supplementing of the piston cylinder liner's working area with the creation of nanotube structures with MoS2 particles may lead to a further reduction of frictional resistance. However, the

audit of both engines (spark and compression ignition), proved the use of MoS2 to reduce friction losses and fuel consumption unprofitable.

Analysis of internal frictions of spark-ignition engine shows that supporting the oil film formation's environment using conventional additives does not produce the expected reduction in motion's resistance of the motor. A slight increase in the internal friction resistance at a speed of 2500 rpm can be observed from the audit. 2500 rpms is the most common speed at which combustion engine is driven in the cars. The use of the MoS2 additive in various configurations of the CNT at 80 °C leads in each case to a slight increase in the internal friction as shown in Fig. 5. As it can be seen engine's operation within temperatures range of 50-110 °C results in both positive and negative changes in frictional resistance. It can be therefore concluded that frictional resistance changes fall into measurements error category. Much more likely, however, both the CNT and MoS2 additives affect the conglomerate's structure that is not a subject to the Newtonian fluid motion law, where the only internal resistance force is viscosity.

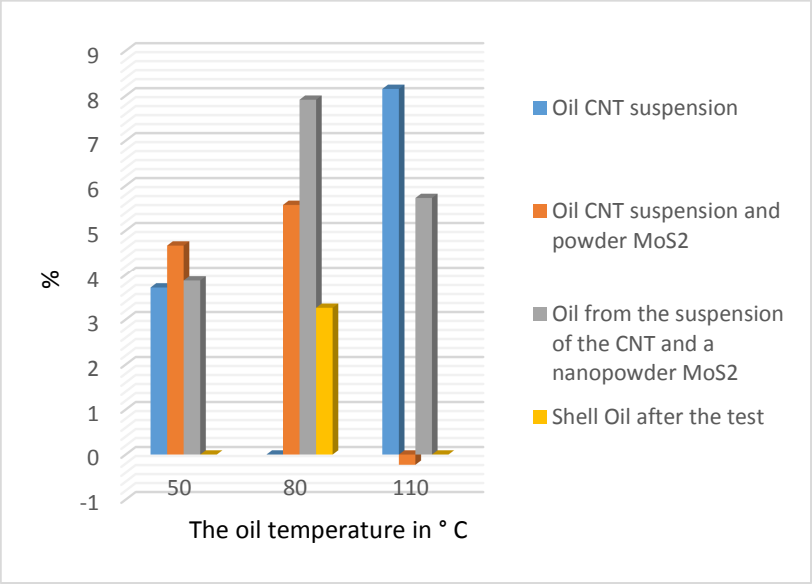

Fig. 4. Percentage of internal friction of the engine with spark ignition at the speed of 2000 rpm

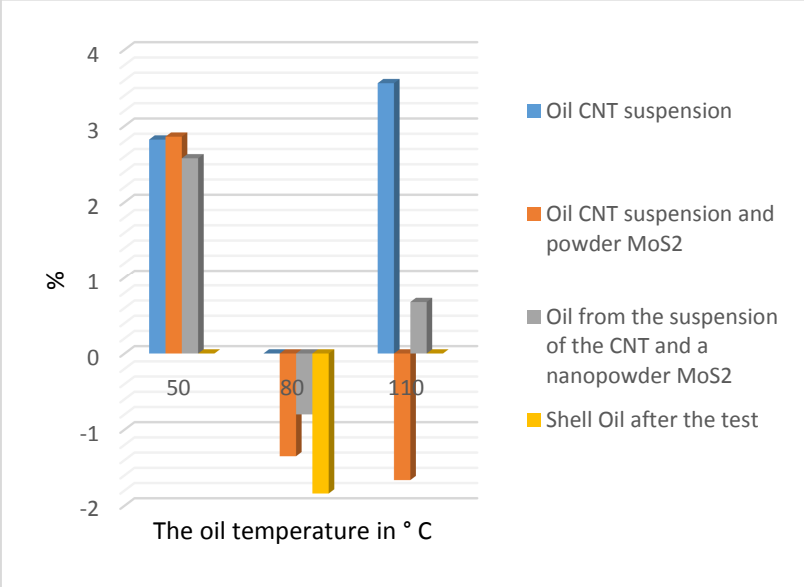

Fig. 5. Percentage of internal friction of the engine with spark ignition at the speed of 2500 rpm

The analysis of the friction resistance measurements showed that the only effective method of reducing internal friction losses is to cover the piston's side surface with CNT layer. However the results got for spark-ignition engine do not apply to the diesel one. The oil's film in diesel engine

undergoes heavier conditions such as higher loads and higher temperatures. Therefore, the research was performed for a diesel engine separately. The average revolution speed of the engine is 2500, and this was engine speed assumed in the study.

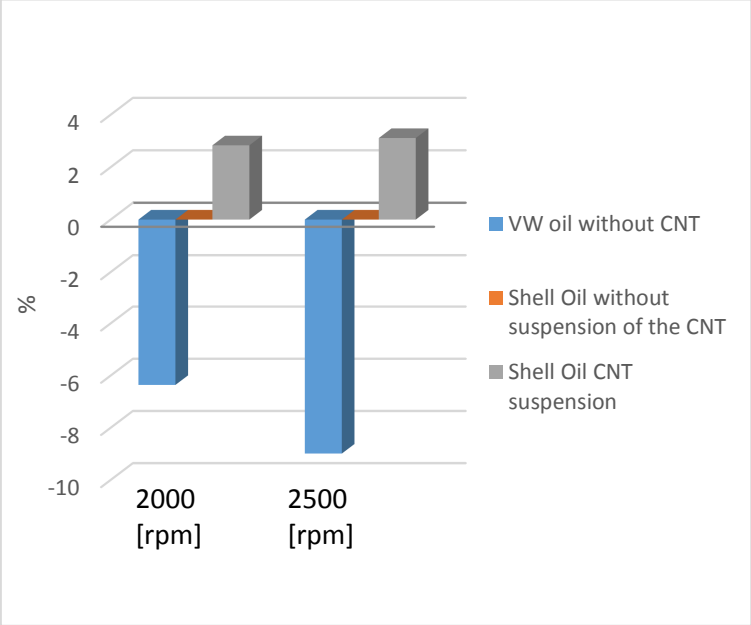

Fig. 6. Percentage of internal friction of the diesel engine series A, 2500 rpm

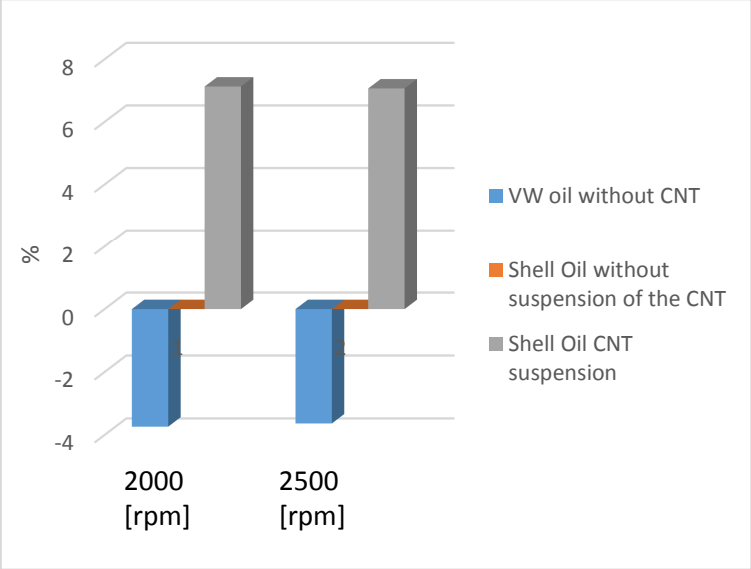

Fig. 7. Percentage of internal friction of the diesel engine series B, 2500 rpm

Because of the ambiguous lubricating oil additives impact on friction resistance, the measurements were repeated for constant operating conditions, The analysis of the results obtained in few days intervals was performed by selecting the measured points within the one test cycle. The tests were performed for motor temperatures fixed at 90 °C. To ensure fixed temperature the default cooling circuit was modified by using separate cooling systems in order to allow controlling the temperature of the coolant at selected points, as well as the temperature of the cooling oil.

4. Summary

The research results show that small both positive and negative changes in engine's internal friction are possible after CNT additives in the engine oil are used. It demonstrates the ambiguity of

CNT additives' impact on such resistances. The overall conclusion is that previously developed criteria to show CNT oil additives' efficacy are not well founded. It should be also noted that CNT suspension creation does not exhaust number of possibilities to obtain the lubricating oil with modified properties. Nanotubes used in lubricating oil environments can create structures able to significantly change oil features. However, processes to create such suspensions are radically different from the existing methods used to change oil properties.

The more promising way of applying CNT is to create coating layers on piston bearing surface. In such application friction losses reduction were observed for all engine operating conditions, which give a chance to mass production application.

References

[1] DEUSS T., EHNIS H., ROSE R., K KÜNZEL R., Reibleistungsmessungen am Befeuerten Dieselmotor –Einfluss von Kolbenschaftbeschichtungen MTZ 4/2011

[2] FAHR M., HANKE W., KLIMESCH CH., REHL A., Reibungsreduzierung bei Kolbensystemen im Ottomotor, MTZ 07-08/2011

[3] GOLLOCH R., Untersuchungen zur Tribologie eines Dieselmotors im Bereich Kolbenring/Zylinderlaufbuchse, VDI Verlag GmbH, Reihe 12, Nr. 473, Düsseldorf 2001

[4] JUNKER H., K., Pistons and engine testing, Springer Fachmedien Wiesbaden GmbH 2012

[5] KAŁUŻNY J., Eksperymentalne zastosowanie nanorurek węglowych w konstrukcji tłokowego silnika spalinowego. WPP, seria Rozprawy, nr 503, Poznań 2013

[6] MERKER G. P., SCHWARZ C., TEICHMANN R., Grundlagen Verbrennungsmotoren, ATZ/MTAZ-Fachbuch, Springer Fachmedien Wiesbaden GmbH 2012

[7] ZIMA S., Kurbeltriebe, Vieweg Verlag, Braunschweig-Wiesbaden, 1999

TRANSCOM 2015, 22-24 June 2015
University of Žilina, Žilina, Slovak Republic

The Adaptation of Unconventional Manufacturing Technology in Casting

[*]Zmarzły Paweł, [*]Gogolewski Damian
[*]Kielce University of Technology, Faculty of Mechatronics and Mechanical Engineering, Department of Manufacturing Engineering and Metrology, al. Tysiąclecia Państwa Polskiego 7, 25-314 Kielce, Poland, pzmarzly@tu.kielce.pl, dgogolewski@tu.kielce.pl

Abstract. An analysis of the state-of-the-art related with additive technology in casting was presented in the article. Describes the main types of non-conventional generation technologies, ie. Selective Laser Sintering, PolyJet Matrix, Fused Deposition Modeling and 3DP. Moreover summarizes selected mechanical properties and dimensional accuracy of these technologies based on their own research results and the literature. The analysis proposes the use of the above mentioned technologies for specific applications manufacturing casting pattern for sand form and lost material methods. This proposal could be a base to create standards for the manufacturing models using additive technologies.

Keywords: Additive technology, rapid prototyping, casting, cast pattern, CAD

1. Introduction

Casting is a technology that involves the flooding of the previously prepared mold a liquid material, usually a metal alloy, but also plaster, wax, [1,2] or plastics and control the solidification process or chemical reaction to obtain a product with the appropriate structures and mechanical properties, dimension-shape accuracy and quality of the surface layer. Casting also includes techniques for preparing the molds, which mainly consist of providing an adequate model to achieve a casting mold. Models quality has significant impact on the obtained dimensionally-shaped accuracy of casting models and any costs associated with the aftertreatment. Number of elements included in the casting model depends on the shape of the cast object, its size and the number of forms that must be manufactured. For many complex models is necessary to produce core box, which was made in the same way as molds. Patterns are made of wood, metal, ceramics and plastics. Patterns wear depends on the material used to make the model and the way of use and store the model, as well as the number of molds.

The conventional method of casting is manufactured a model and optionally core boxes, and then the process of the casting mold, the flooding of a suitable liquid metal mold, then casting solidification process and cleaning. In some cases there is a need for removal of the gating system and riser which limiting the shrinkage effects of the contraction of some metals. The traditional method of building models based on the manufacture of wood, metal or plastic models.

There are several main casting process which depend on the technology. These methods are presented in the classic foundry guides book [1] and in a readily available domestic and foreign literature [2]. The most common methods are casting method using: sand, pressure and gravity die castings molds.

Pattern manufacturing in above-mentioned techniques using conventional methods is a well known method and widely used throughout the world. Despite the high prevalence these methods there is no technology that would allow to immediate manufacture of durable cast models and forms, and thus increased productivity and reduced time. This problem can be eliminated by introducing into the casting process a new method of preparation of the models and molds, ie. additive technology. The choice of additive technology depends on the type of production, the

estimated number of molds, cast material, the complexity of the casting, the casting technology used, storage conditions, and financial capabilities of foundry

2. Unconventional manufacturing technology

The beginning of additive technology dates back to the 80s of the twentieth century, when it was invented technology of photo-curable liquid polymer resins - stereolithography. Despite the passage of more than thirty years only last years additive technologies are increasingly used in many fields, ie. the industry, medicine, architecture.

Additive technologies are layered structure technique based on previously prepared CAD solid models which is saved in .stl file (stereolitography language). This file are use to triangulation process where solid model is divided into triangle. This is also necessary to divide model into layer. These technologies, however, may differ because of layer join process, the strength of models, further treatment, the cost of construction and the accuracy of a model. Materials applications used in the construction of the elements may be in form of: solids, liquids and powders.

Most of these materials are plastics based on polyamide and polymers, but more often in modern machines are used in metal-based powders with high mechanical properties and high accuracy. Additive technologies in many cases allow a significant reduction of the machinery needed to build a prototype (Rapid Prototyping), the fully functional parts (Rapid Manufacturing), and even tools (Rapid Tooling), for example. cast patterns, molds.

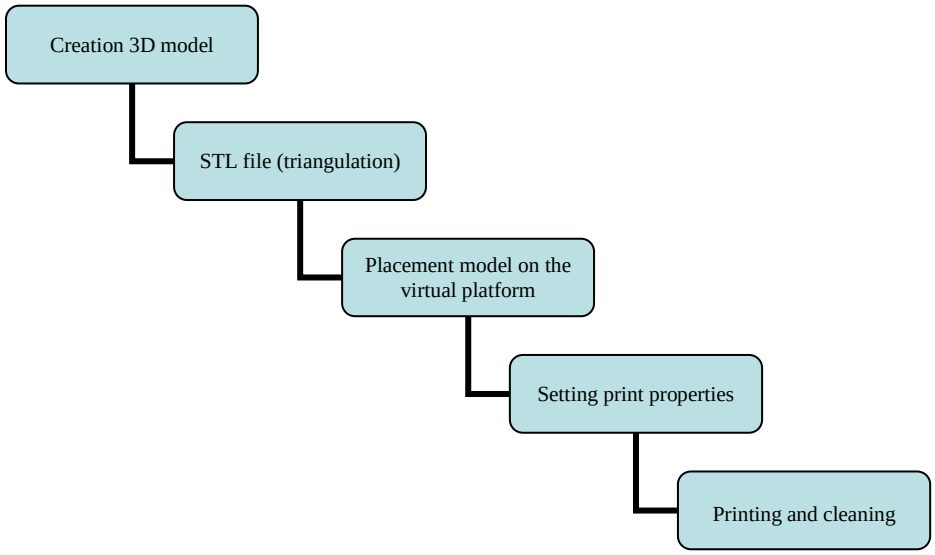

Fig. 1. The creating models of additive technologies process

2.1. Selective Laser Sintering

SLS - Selective laser sintering. On the platform is distributed very thin layer of powder, which is scanned by laser beam CO2 or Nd: YAG laser (λ = 1.06 microns). As a result of this activity, the powder are sintered or melted. Next, the platform is lowered by a setting value and on the next layer is distributed powder. The process is repeated until the completion of the model. The advantage of this technology is the possibility to build highly accurate models [3] with high mechanical properties [4,5], limited only by the dimensions of the working chamber. Previously research carried out at Kielce University of Technology [11, 12, 13] confirm the possibility to used

these technologies to build a foundry pattern with high mechanical properties and high dimensional accuracy. Moreover, models made in this technology can be further machined, paint, metalize and cover with protective coatings. Another very important advantage of technological is not necessary to create support structures. In the article [4], the authors determine the effect of the basic parameters of selective laser sintering technology, ie. laser power, printing direction, the speed of the laser beam, the thickness and the chamber temperature and the amount of energy density which has directly affects the accuracy of polyamide specimens. The mechanical properties of the specimens in the SLS technology were also described in [5], where have been describe many tests, ie. uniaxial tensile test according to PN EN ISO 527, bending test according to PN EN ISO 178 and measured hardness Shore 'a on scale D.

After analyzing the literature and based on the own previous results it can be stated that the additive selective laser sintering technology successfully can be used to build pattern for foundry to sand molds, as well as in the case of selected materials to build patterns for the lost material casting technology.

2.2. PolyJet Matrix

PolyJet Matrix is the additive technology where liquid photocuring polymer resins comprises spraying the liquid resin through a dispensing nozzle to the working platform, and then cured by irradiating with light in the infrared. This technology is an extension of stereolithography technology, which is the oldest additive technology [7]. This technology is necessary to use supporting structures, which adversely affects the technological capabilities of the products. The advantage of this technology is the ability to mix different types of resins, which results in a product with a specific mechanical properties in different areas [8] and high accuracy. There are a wide range of materials which can be used in the printing process.

In [7], the authors presented the results of the basic process parameters ie. printing direction, time scanning and layer thickness and their impact on the accuracy of stereolithography resin specimens. The authors have set the basic shape and position deviation as a function of the print direction and other parameters. Therefore confirmed that the important issue is the selection of appropriate process parameters. The mechanical properties of the specimens made by PolyJet technology described also in article [8]. A strength tests were carried out inter alia uniaxial tensile test in accordance with ASTM D638-10. The authors designated tensile strength and modulus of elasticity depending on the direction of printing.

Following an analysis of the literature it can be concluded that they were carried out research of adaptation of additive techniques in casting.

In article [9] authors applied technologies of photocuring polymer resins to build a complex pattern of the coin. Then they used this patter to made finally product by lost material technology. The disadvantage of this method is, however, a plurality of error associated with the manufacture of the finished casting. It is now possible to reduce the steps performed by the authors which will minimize the cumulative error. The authors no conducted any metrology research and strength this pattern and castings.

2.3. Fused Deposition Modelling

FDM technology is modeling liquid thermoplastic. FDM technology actually is one of the most popular and cheapest technology of rapid prototyping methods. It involves imposing on the platform layered molten plastic, occurring most commonly in the form of fiber located on a spool arranged vertically supplied to the printheads. The head heat the material above its melting point so that cause the material to form a semi liquid. When the head is moving, material is extruded through a nozzle, and following its deposition on the platform in the form of a thin thread. In that case the new layer is manufacture. The material solidifies after left the nozzle as a result of lowering the temperature and becoming solid, which is bind with the platform and becomes the basis for

subsequent layers. In order to produce the entire model platform lowered after deposition of the layer of setting layer thickness. Layering process is repeated until the model is done. This method requires the creation of supporting structures, which has some restrictions on the ability of models. Significant impact on the accuracy of the obtained prints is the type of material, its contraction, the print nozzle diameter and model position on the platform. The mechanical properties of components manufactured by this technology are presented in [6].

2.4. 3DP

3DP technology involves bonding a layer of gypsum-based powder appropriate binder. This technology is widely used, particularly in architecture and rapid prototyping due to the possibility of obtaining products in wide range color. This technology is possible to use powder ZCast enabling the performance of molds ready in short time without any other treatment. This material allows the casting alloy to a melting temperature of 1100 ° C. The research on the use of additive technology 3DP in casting to build a mold used for the implementation of the prototype turbine blade were carried out in paper [10]. The authors have done mold and finishing cast, stating that it is possible to adapt the additive manufacturing technology for the construction of casting models.

3. Technology comparing

For comparative studies were selected four most important additive technologies SLS, PolyJet Matrix, FDM, 3DP that are used in Laboratory of Unconventional Manufacturing Technology at Kielce University of Technology. These technologies differ in the way the lamination and a number of properties, however, each of them can successfully be used to build patterns or molds.

Table 1 presents a summary of selected mechanical properties of additive technology for a few selected materials based on the manufacturer's data and our own results [2, 3, 11]. Mechanical properties for all additive technologies do not depend only on kind of technology but also it depend on type of use material.

Technology	SLS PA 2200	PolyJet FullCure 720	FDM ABS	3DP Zp150	Unit	Standard
Young's Modulus	1500	2870	1385	1068	MPa	ISO 527
Tensile Strength	40	60	22	26	MPa	ISO 527
Impact Strength	4	20-30	5-20	-	kJ/m^2	ISO 180
Shore'a Hardness	75	83-86	80	87	Scale D	ISO 868
Density	930	1092	1,05	-	g/cm^3	-

Tab. 1. Selected mechanical parameters

Accuracy and mechanical properties of produced parts for all additive technologies are depend not only on the material, but also on the technological parameters. Technologist affects the placement of the model on the working machine platform and on the thickness of the layer. In some technologies can be also controlled more parameters in the manufacturing process.

In the SLS technology tensile strength presented in the table 1 is about 40 MPa. This value is the maximum obtainable only for specific parameters of the laser power and speed and print direction. In the case of print in other directions, and with reduce energy density transmitted to the sintered powder layer tensile strength drastically reduced by up to several MPa.

The keys parameters are the additive technology are strength and accuracy. Accuracy in most additive technology in Z axis is equal to the layer thickness. In other directions, it depends on many technological parameters. Analyzing the data in Table 1 it can be stated that the greatest tensile

strength presents SLS and PolyJet Matrix technology but the SLS technology based on polyamide powders are characterized by high wear resistance, for which are exposed patterns in casting process. FDM and 3DP technology despite the low tensile strength is characterized by high hardness. Furthermore, due to the relatively complicated construction of this technology it can be use direct for casting mold.

4. Conclusion

Analyzing the research results and an analysis of the state-of-the-art related with additive technology it can be stated that the best mechanical properties eligible additive technologies to build models foundry molds of sand has a technology SLS, FDM and PolyJet. In the case of 3DP technology, it is possible to apply it directly to the metal casting mold having a melting point to 1100 ° C, which can not be obtained for other technologies. This technology is the most similar to the conventional casting molds production that rely on manual or mechanical hardening sand mold. In the case of precision casting methods such as the method of lose material only PolyJet technology with a low melting point allows for easy removal of material from the mold.

Acknowledgement

The study was conducted using research facilities purchased with EU funds in the framework of the 2007-2013 Development of Eastern Poland Operational Programme, LABIN Project − Support for Innovative Research Facilities of the Kielce University of Technology in Kielce. Priority 1 – Innovative Economy, Measure 1.3 – Support for R&D Projects.

References

[1] SOBCZYK J., *Odlewnictwo współczesne – Poradnik odlewnika*, I, Stowarzyszenie Techniczne Odlewników Polskich 2014

[2] PERZYK M., WASZKIEWICZ S., KACZOROWSKI M., JOPKIEWICZ A.: *Odlewnictwo*. Warszawa, WNT 2004

[3] WANG X. C., LAOUI T., BONSE J., KRUTH J. P., LAUWERS B., FROYEN L.: *Direct selective laser sintering of hard metal powders: experimental study and simulation.* Advanced Manufacturing Technology 2002, 19, s.351-357

[4] SALMORIA G.V., LEITE J.L., VIEIRA L.F. PIRES A.T.N., ROESLER C.R.M.: *Mechanical properties of PA6/PA12 blend specimens prepared by selective laser sintering.* Polymer Testing, 2012, 31, s. 411-416

[5] PILIPOVIC A., VALENTAN B., BRAJLIH T., HARAMINA T., BALIC J., KODVANJ J., SERCER M., DRSTVENSEK.,: *Influence of laser sintering parameters on mechanical properties of polymer products*. iCAT 2010

[6] BAGSIK A.: *Mechanical properties of fused deposition modelling parts manufactured with ULTEM 9085*. ANTEC 2011, Boston

[7] ZHOU J. G., HERSCOVICI D., CHEN C.C., *Parametric process optimization to improve the accuracy of rapid prototyped stereolithography parts*. Machine Tool and Manufacture 2000, 40, s. 363-379

[8] BARCLIFT M.W., WILLIAMS C. B.: *Examining variability in the mechanical properties of parts manufactured via PolyJet direct 3D Printing. International Solid Freeform Fabrication Symposium*, Austin, TX, s. 876-890

[9] JARCO A., RZADKOSZ S., KROKOSZ J., PABIŚ R., GIL A., CZEKAJ E., MŁODNICKI S., ĆWIKLAK R.: *Studium technologiczno-konstrukcyjne wykorzystania szybkiego prototypowania do wykonania odlewu artystycznego – medalu 65-lecia instytutu odlewnictwa w Krakowie*. Prace Instytutu Odlewnictwa 2012, LII (1), s. 55-70

[10]BUDZIK G., BUDZIK W., CYGNAR M., JANISZ K.: *Możliwości zastosowania szybkiego prototypowania w procesie projektowania i wytwarzania elementów pojazdów samochodowych*. Problemy eksploatacji 2009, I, s.7-16

[11]KUNDERA CZ., KOZIOR T.: *Badanie wpływu ilości energii dostarczanej do spiekanej warstwy poliamidu w technologii SLS na właściwości mechaniczne*. Logistyka 2014,6, s. 6374-6380

[12]KUNDERA CZ., BOCHNIA J. *Investigating the stress relaxation of photopolymer O-ring seal models*, Rapid Prototyping Journal, Vol. 20 Iss: 6, pp.533 - 540

[13]ADAMCZAK S., BOCHNIA J., KACZMARSKA B. *An analysis of tensile test results to assess the innovation risk for an additive manufacturing technology*, Metrology and Measurement System, Vol. XXII No:1, pp.127-138

TRANSCOM 2015, 22-24 June 2015
University of Žilina, Žilina, Slovak Republic

Computer Analysis of Three-point References Method Parameters to Waviness Measurement of Cylindrical Surfaces

[*]Paweł Zmarzły
[*]Kielce University of Technology, Faculty of Mechatronics and Machinery Design, Department of Manufacturing Engineering and Metrology, Al. 1000-lecia P. P. 7, 25-314 Kielce, Poland, pzmarzly@tu.kielce.pl

Abstract. In many branches of industry there are large and heavy cylindrical elements. The most popular methods applied to measure roundness and waviness of cylindrical parts are radial method. This method can be used mainly for objects with small dimension and lower weight. Radial method is useless for large-size cylinders. For this reason researchers developed V-block method knows as references method to measure roundness of large cylindrical surfaces. At the Kielce University of Technology research is carried out to extend applicability of the V-block method to waviness measurements of large cylindrical mechanical parts. The paper presents fundaments of V-block method and mathematical model. The four types of three-point references method was characterized. In order to determine the most appropriate type of three-point method to waviness measurements the computer simulation was carried out. The simulation was performed in range 16-50 UPR (undulation per revolution) which correspond to surface waviness.

Keywords: Three-point references, waviness measurement, cylindrical surfaces

1. Introduction

Dynamic development of modern machine-building industry dictates high requirements to manufactured mechanical parts. Nowadays produced parts should be reliable and high quality. Additionally modern industry aims at increasing of production efficiency and reduction of manufacturing costs. Application of suitable measuring technology substantially allows to meet these requirements.

Geometrical structure of mechanical parts includes proportion, accuracy to shape, accuracy to size, alignment and surface topography. All these parameters are dependence at technology, manufacturing parameters, material properties, but also at human [1].

One of the most important error form is roundness and waviness of cylindrical surfaces, because plenty of all cylindrical engineering components perform responsible functions [2]. Roundness and waviness measurement is essential in mechanical production control. Roundness and especially waviness error of rotating parts generates vibrations. This phenomenon is very dangerous, because reduces service cycles of mechanical components, generates excessive noise and causes serious malfunction.

The development of proper measurement methodologies for large cylindrical shapes is a critical issue to manufacturers since their customers are increasingly demanding to new product developments and product quality [3]. Accuracy to shape play an important role in product quality, but its characterization is still limited. In many times only roundness deviation measurments is insufficient. For this reason shape deviation should be measured in wide range which cover waviness of cylindrical surfaces.

1.1. Roundness and Waviness of Cylindrical Surfaces

Roundness expresses a particular geometric form of a three-dimensional figure, most frequently that of a body of revolution. Circular contour is the characteristic form of the entire or partial periphery of a plane figure [3].

Considering error form of cylindrical surfaces roundness profiles should be filtered according with ISO/TS 1281-2. Roundness measurements always contain imperfections at a number of different UPR (undulations per revolution). Filters can be arranged to remove undesirable information of profile above or below a certain frequency [4]. Roundness or waviness deviations values are also dependent on the types of reference circle [5]. Performing measurments of cylindrical profiles is assumed that roundness is in range 2-15 UPR and waviness is range 15-500 UPR [6]. Using V-block method waviness should be measured in range 16-50 UPR, because evaluation waviness deviation above 50 UPR is inaccurate. Figure 1 shows profile filtered in two ranges: (a) 2-15 UPR, (b) 16-50 UPR.

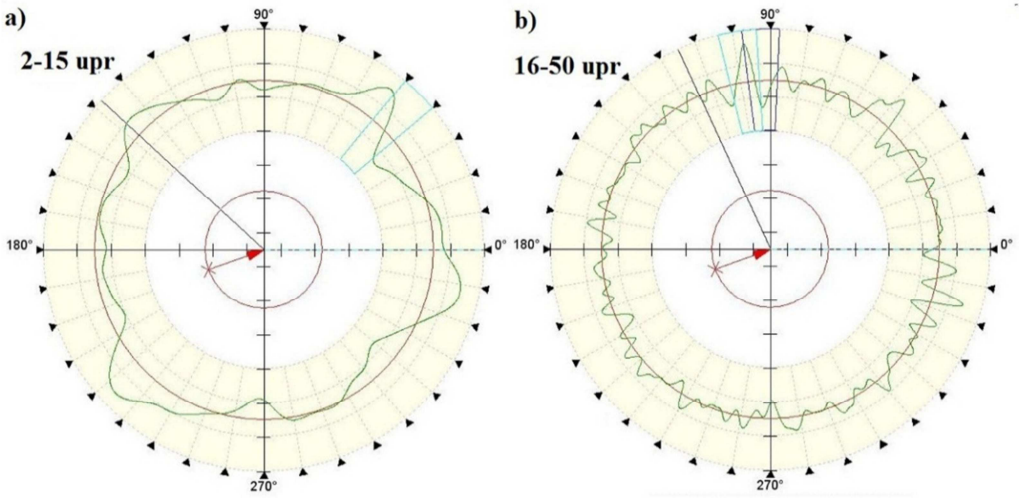

Fig. 1. Filtered profile: a) roundness profile – 2-15 upr, b) waviness profile 16-50 upr.

1.2. Characteristic of V-block Method to Waviness Measurments

V-block methods can be divided into: two-point, three point and n-point methods. In this method, one can distinguish points of supports that are base points (B,C) and point of measurement – A. Their position with regard to assumed co-ordinate system is determined by the angles α and β (see fig. 2). The value of α and β are the angular parameters, which are responsible for detecting particular harmonic components of measured profile.

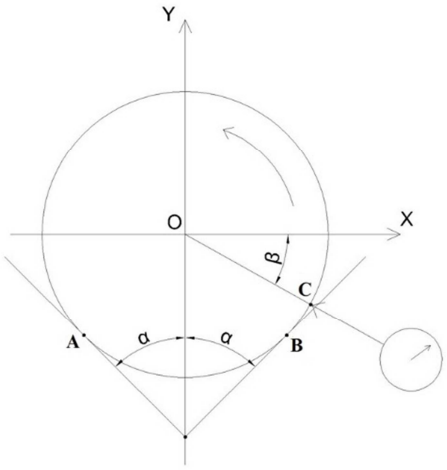

Fig. 2. The principle of measurments of roundness and waviness profile by three-point references method.

Characteristic feature of V-block method is that the measured roundness deviation ΔF does not coincide with roundness deviation ΔZ, because values of signal read by the sensor depends on deviations in the point of measurement C and base points B,C (see Fig. 2). That is why the basic problem of V-block method application is the necessity to obtain information on the dominant type

of form error, for which, by means of an appropriate coefficient, called the coefficient of detectability, it is possible to estimate the roundness or waviness deviation ΔZ.

$$\Delta Z \cong \frac{1}{K_n}\Delta F \tag{1}$$

where ΔF – measured deviation, K_n – coefficient of detectability for n-th harmonic.

To sum up, the coefficient of detectability K_n is the function of the method parameters i.e. the angles α and β, as well as the number "n" determining for regular profiles, the so-called n-lobbing.

At the beginning V-block method had low accuracy and were applied to the approximate roundness measurements. For this reason mathematical models were developed to increase accuracy of V-block method (see ref. [7,8]).

2. Computer Simulation

In order to obtain appropriate types of three-point references method to waviness measurements of cylindrical parts computer simulation was carried out. The procedures used to simulation were written in Matlab software. The simulation was performed for four types of three-point references method:

a) three-point, symmetrical, simple reference method (summit): α=36°, β=90°,
b) three-point, symmetrical, inverted reference method (rider): α=60°, β=-90°,
c) three-point, unsymmetrical, simple reference method (summit): α=60°, β=80°,
d) three-point, unsymmetrical, inverted reference method (rider): α=60°, β=-33°.

First of all real profile R(φ) and profile measured by sensor F(φ) was generated. A real profile R(φ) described by Eq. (2) consist 19, 21, 37, 41, 47, 50 harmonic components, which covers waviness deviation.

$$R(\varphi) = R0 + 0.001 * (\cos(19\varphi) + 3 * sin(21\varphi) + \cos(37\varphi) + \sin(41\varphi) + 2\sin(47\varphi) + \cos(50\varphi)) \tag{2}$$

where: R0 – the nominal cylinder radius, φ – angle of rotation.

In next step we calculated the profile F(φ) measured by the sensor. This calculation was based on mathematical model presented in [9,10].

$$F(\varphi) = R(\varphi+\beta) - \frac{1}{2}R(\varphi+\alpha)\left[\frac{cos\beta}{cos\alpha} + \frac{sin\beta}{sin\alpha}\right] - \frac{1}{2}R(\varphi+\pi-\alpha)\left[-\frac{cos\beta}{cos\alpha} + \frac{sin\beta}{sin\alpha}\right] \tag{3}$$

where: φ – angle of rotation, α,β – angular parameters.

In order to obtain high accuracy of V-block waviness measurements we need transform, measured profile F(φ) into reconstructed profile R_p(φ). As we can see in Eq. 3 only the profile R(φ) is unknown. Thus, the equation should be solved in relation to R(φ). This problem, however, can be simplified when the measured and real profiles are presented in the form a complex Fourier series. Then we get from Eq. (3):

$$\hat{F}_n = \widehat{R_n} \cdot \widehat{K_n} \tag{4}$$

where: $\widehat{R_n}$ - real profile, $\widehat{K_n}$ – coefficient of detectability for the n-harmonic of profile defined by Eq. (5).

$$\hat{K}_n = e^{in\beta} - \frac{1}{2}e^{in\alpha}\left[\frac{cos\beta}{cos\alpha} + \frac{sin\beta}{sin\alpha}\right] - \frac{1}{2}(-1)^n e^{-in\alpha}\left[-\frac{cos\beta}{cos\alpha} + \frac{sin\beta}{sin\alpha}\right] \stackrel{\text{def}}{=} \frac{\hat{R}_n}{\hat{F}_n} \quad (5)$$

As we can see in Eq. (1) above relationships permits computer transformation of the measured profile into the reconstructed profile.

The results of computer simulation for four types of three-point references method to waviness measurments of cylindrical surfaces were plotted to show profiles in Cartesian coordinates and harmonic components of profiles in the form of bar charts.

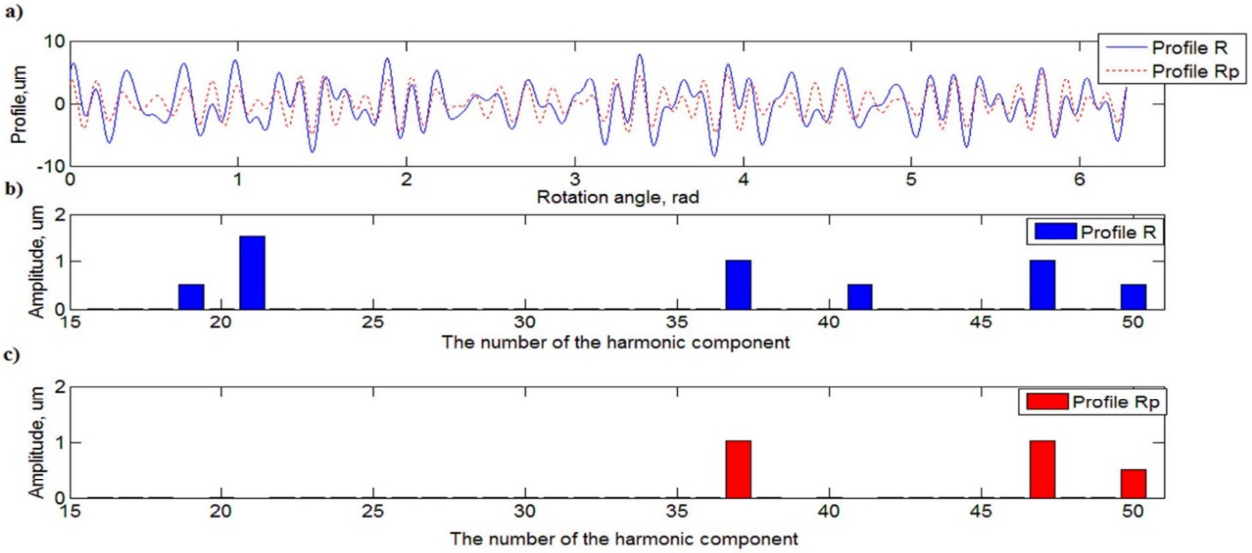

Fig. 3. Three-point, symmetrical, simple reference method (summit) - α=36°, β=90°:
a) real profile R(φ) – blue continuous line, reconstructed profile $R_p(\varphi)$ – red dotted line
b) bar chart of harmonic components (from 16-50) for real profile R(φ),
c) bar chart of harmonic components (from 16-50) for reconstructed profile $R_p(\varphi)$.

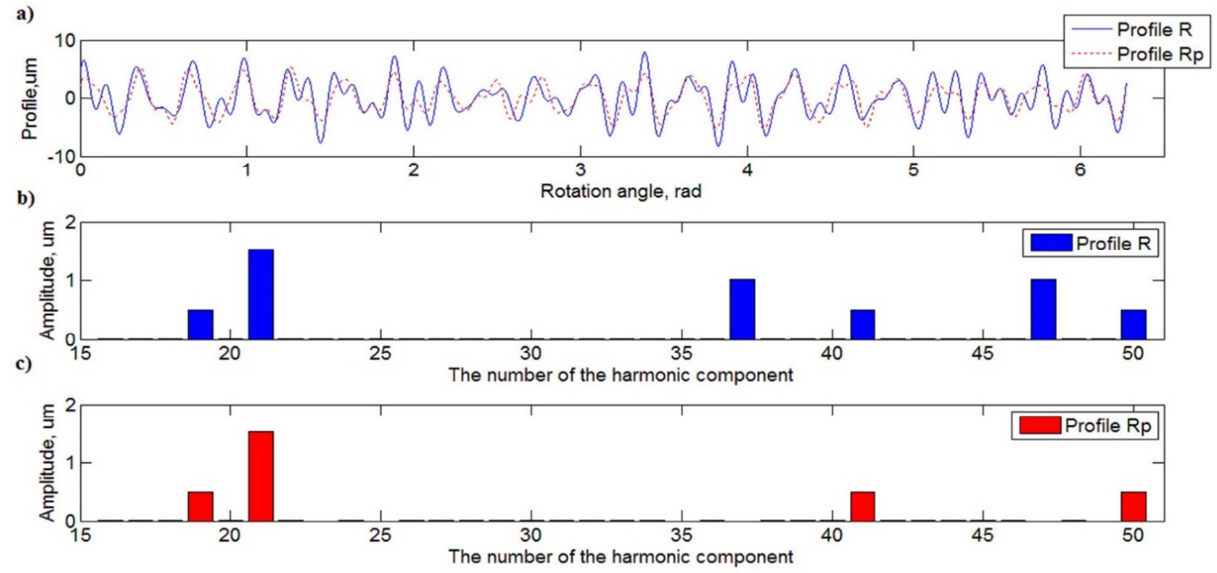

Fig. 4. Three-point, symmetrical, inverted reference method (rider): α=60°, β=-90°:
a) real profile R(φ) – blue continuous line, reconstructed profile $R_p(\varphi)$ – red dotted line
b) bar chart of harmonic components (from 16-50) for real profile R(φ),
c) bar chart of harmonic components (from 16-50) for reconstructed profile $R_p(\varphi)$.

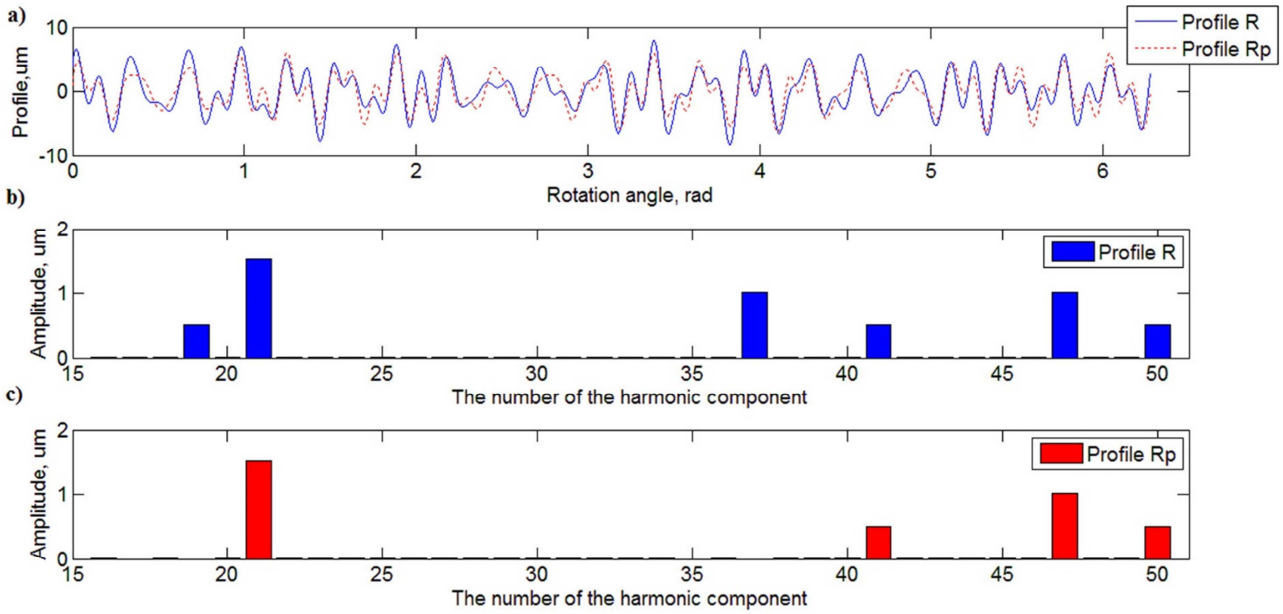

Fig. 5. Three-point, unsymmetrical, simple reference method (summit):α=60°, β=80°,
a) real profile R(φ) – blue continuous line, reconstructed profile $R_p(\varphi)$ – red dotted line
b) bar chart of harmonic components (from 16-50) for real profile R(φ),
c) bar chart of harmonic components (from 16-50) for reconstructed profile $R_p(\varphi)$.

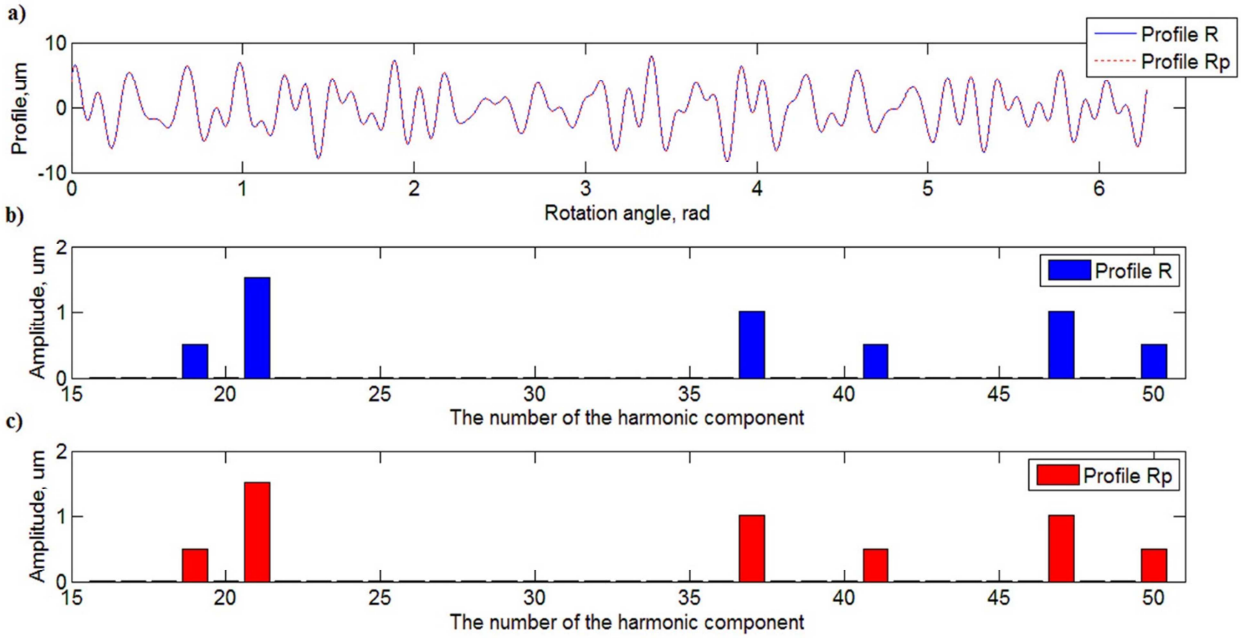

Fig. 6. Three-point, unsymmetrical, inverted reference method (rider): α=60°, β=-33°,
a) real profile R(φ) – blue continuous line, reconstructed profile $R_p(\varphi)$ – red dotted line
b) bar chart of harmonic components (from 16-50) for real profile R(φ),
c) bar chart of harmonic components (from 16-50) for reconstructed profile $R_p(\varphi)$.

3. Summary and Conclusion

Computer simulation was carried out to determine optimal type of V-block method to waviness measurments of cylindrical surfaces. Analyzing result of simulation we can conclude that accuracy of V-block waviness measurments depends on values of angle α and β.

As we can see in Fig. 3 visual comparison of real profiles R(φ) and reconstructed profile $R_p(\varphi)$ for three-point, symmetrical, simple reference method showed that profile obtained by computer simulation differs from real profile. This deference is caused by the facts that the values of angles α=36° and β=-90° do not allowed detection the 19th, 21th and 42th in the generated profile (see Fig. 3c). Similar is for three-point, symmetrical, inverted reference method (Fig. 4) and three-point, unsymmetrical, simple reference method (Fig. 5). For this method we cannot detection all harmonic components in range $n\epsilon<16,50>$.

However as we can see in Fig. 6 for three-point, unsymmetrical, inverted reference method reconstructed profile $R_p(\varphi)$ is overlap with real profile R(φ). In this case compatibility of compared profile is very high, because all harmonic components in range $n\epsilon<16,50>$ for angles α=60° and β= -33° are detected.

Summarize the three-point, unsymmetrical, inverted reference method for angular parameters α=60° and β= -33° can be use waviness measurments of cylindrical surfaces. Measuring device based on this method could be used to measure waviness deviation of large cylinder directly on machine tool in industrial conditions (see ref. [11]).

References

[1] OCENASOVA L., GAPINSKI B., CEP R., GREGOVA L., BARISIC B., NOVAKOVA J., PETRKOVSKA L. *Roundness Deviation Measuring Strategy at Coordination Measuring Machines and Conventional Machines.* World Academy of Science, Engineering and Technology, vol. 32, 2009, pp. 523-526

[2] NOZDRZYKOWSKI K, JANECKI D. *Comparative studies of reference measurements of cylindrical profiles of large machine components.* Metrology and Measurement Systems, Vol. 21, No. 1, 2014, pp. 67-76,

[3] FARGO F.T.,. CURTIS M.A, *Handbook of dimensional measurement*. 3th ed., Industrial Press Inc., New York, 1994, p. 371.

[4] SEEWING J., EIFLER M. *Periodic Gaussian filter according to ISO 16610-21 for closed profiles*. Precision Engineering. Vol. 38, 2014, pp. 439–442.

[5] XIUMING L., ZHAOYAO S. Evaluation of roundness error from coordinate data using curvature technique. Measurement vol. 43, 2010, pp. 164–168.

[6] ADAMCZAK S., JANECKI D., DOMAGALSKI R., *Eksperymentalna istotność wyznaczania harmonicznych zarysów okrągłości i falistości powierzchni*, Pomiary Automatyka Kontrola, vol. 5, 2000, 17-20, (in Polish).

[7] ZMARZŁY P., ADAMCZAK S., *Badanie modeli matematycznych odniesieniowych metod pomiaru zarysów okrągłości w aspekcie ich zastosowania do pomiarów falistości powierzchni*, Inżynieria Wytwarzania, (2012), Kalisz, Poland, 2012 (in Polish).

[8] STEPIEŃ K., JANECKI D., ADAMCZAK S., *Investigating the influence of selected factors on results of V-block cylindricity measurements,* Measurement, vol. 44, 2011, pp. 767–777.

[9] ADAMCZAK S., JANECKI D., STĘPIEŃ K., *Qualitative and quantitative evaluation of the accuracy of the V-block method of cylindricity measurements,* Precision Engineering, vol. 34/3, 2010, pp. 619-626.

[10]ADAMCZAK S., JANECKI D., STEPIEŃ K., *Cylindricity measurement by the V-block method – Theoretical and practical problems,* Measurement, vol. 44, 2011, pp. 164–173.

[11] ADAMCZAK S., ZMARZŁY P., JANECKI D., *Theoretical and practical investigations of V-block waviness measurement of cylindrical parts.* Metrology and Measurement Systems. 2015, (in press).

TRANSCOM 2015, 22-24 June 2015
University of Žilina, Žilina, Slovak Republic

Heat Transfer Analysis by Using Finite Element Method

[*]Andrej Zrak , [*]Jozef Meško
[*]University of Žilina, Faculty of Mechanical Engineering, Department of Technological Engineering,
Univerzitná 1, 01026 Žilina, Slovakia, {jozef.mesko, andrej.zrak}@fstroj.uniza.sk

Abstract. The paper deals with the temperature field during process of laser cutting based on the finite element method (FEM). The article describes the principle of laser cutting machine and formation the laser beam and the procedure for establishing simulation model for thermal analysis for laser cutting. The analysis includes two modes, as determined by the defined conditions. For modelling of simulation model was the software Comsol Multyphysics using.

Keywords: Finite element modelling. Heat flux. Heat transfer in the solid. Laser beam heat source.

1. Introduction

Among the most commonly used laser in cutting is the carbon dioxide laser (CO_2 laser). It is capable of emitting a maximum of 100 kW at 9.6 μm and 10.6 μm, of cutting 20-30 m/min of one millimeter-thick material.

The laser used in technical practice for cutting a large variety of materials. Laser cutting is a complex process that heat affects the material being cut. The heat may cause changes in the structure of materials, components may be deformed or increase the hardness of the material. To prevent adverse effects, it is necessary to know the principle of heat transfer in the cut material and its size.

2. Laser cutting

Laser cutting is a technology that uses a laser to cut materials, and is typically used for industrial manufacturing applications. Laser cutting works by directing the output of a high-power laser, by computer, at the material to be cut. The material then either melts, burns, vaporizes away, or is blown away by a jet of gas, leaving an edge with a high-quality surface finish. Industrial laser cutters are used to cut flat-sheet material as well as structural and piping materials.

Generation of the laser beam involves stimulating a lasing material by electrical discharges or lamps within a closed container. As the lasing material is stimulated, the beam is reflected internally by means of a partial mirror, until it achieves sufficient energy to escape as a stream of monochromatic coherent light. Mirrors or fiber optics are typically used to direct the coherent light to a lens, which focuses the light at the work zone. The narrowest part of the focused beam is generally less than 0.32 mm in diameter. Depending upon material thickness, kerf widths as small as 0.10 mm are possible. In order to be able to start cutting from somewhere else than the edge, a pierce is done before every cut. Piercing usually involves a high-power pulsed laser beam which slowly makes a hole in the material, taking around 5–15 seconds for 13 mm stainless steel, for example.

The parallel rays of coherent light from the laser source often fall in the range between 1.5–2.0 mm in diameter. This beam is normally focused and intensified by a lens or a mirror to a very small spot of about 0.025 mm to create a very intense laser beam. In order to achieve the smoothest possible finish during contour cutting, the direction of beam polarization must be rotated as it goes

around the periphery of a contoured workpiece. For sheet metal cutting, the focal length is usually 38–76 mm.

There are many different methods in cutting using lasers, with different types used to cut different material. Some of the methods are vaporization, melt and blow, melt blow and burn, thermal stress cracking, scribing, cold cutting and burning stabilized laser cutting.

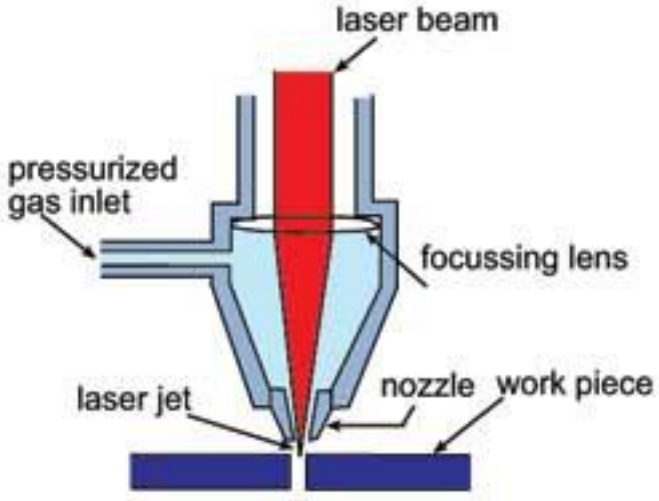

Fig.1. Laser cutting process

3. Laser cutting theory

By enhancing the fundamental governing equation for heat transfer problems the equation for heat transfer in laser cutting problems, the body heat load will have the form:

$$Q(x,y,z) = Q_0(1-R_0)\frac{A_c}{\pi\sigma_x\sigma_y}e^{-\left[\frac{(x-x_0)}{2\sigma_x^2}+\frac{(y-y_0)}{2\sigma_y^2}\right]}e^{-A_c z} \quad (1)$$

where:

Q_0 - total power input of the source,
R_0 - reflection coefficient,
A_c - absorption coefficient,
x_0, y_0 - pulse center for the x and y coordinates,
σ_x, σ_y - pulse standard deviation in the x and y direction.

4. Finite element model of laser cutting

The paper presents the problem of laser cutting by using the finite element method. The finite element model consists of two parts, the laser beam and the plate (Fig. 2). In such case the beam is modelled only as an input parameter. The plate was meshed by using triangular elements. The maximum element size was 0.2 mm (Fig. 3). The smallest elements were used on the laser boundary where the heat beam came in contact with the plate.

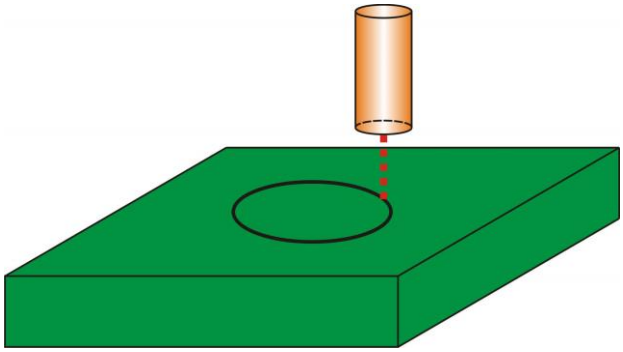

Fig. 2. The model of the plate and laser beam

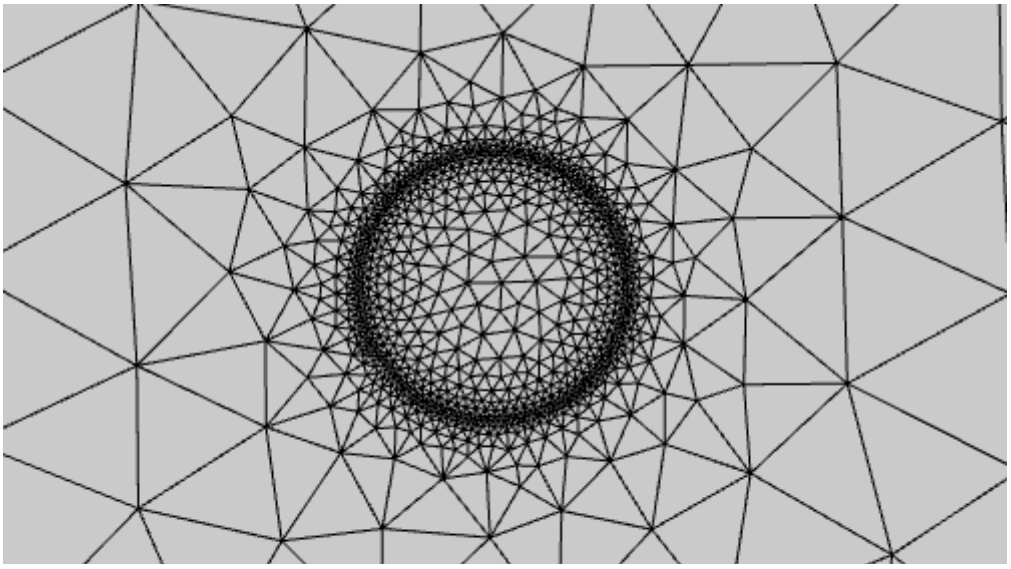

Fig. 3. Meshing of model plate

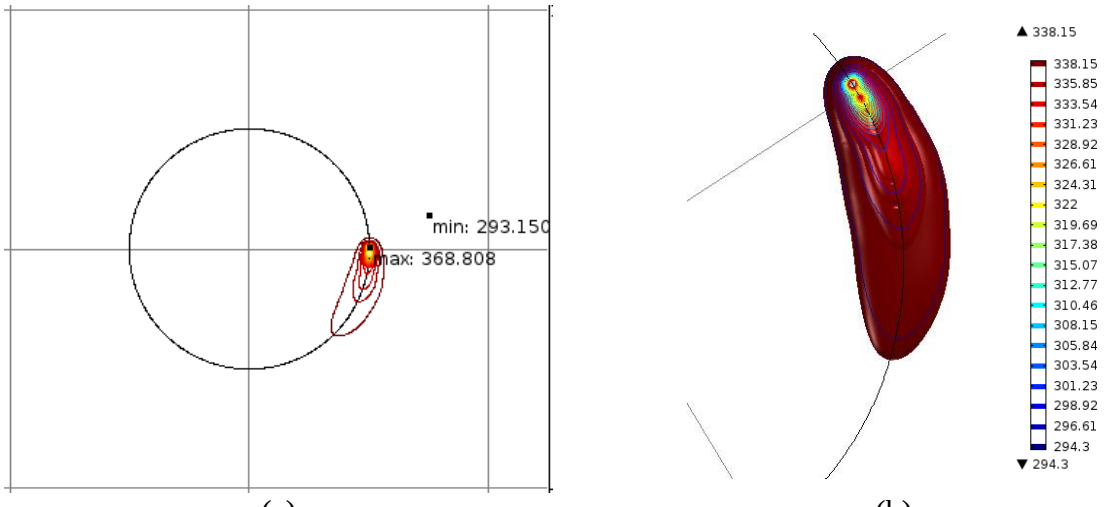

(a) (b)

Fig. 4. (a) 2d isosurface plot of the heat threated domain (b) 3D detailed plot of the heat distribution of the whole affected domain

5. Conclusions

The simulation module in the COMSOL program uses the extended heat transfer equation. On the basis of the simulation it is possible to determine the heat transfer and it is possible to determine the material temperature in the coordinate system x, y, z, t, where x, y, z are the coordinates of the point and his temperature at time t. As computational results in fig. 4 shown, the direct distribution of the heat in the material can be also shown. Model of heat transfer can be used to solve problems of laser cutting if need of defining the temperature and the need for knowing of the principle of heat transfer.

Acknowledgement

The article has been developed during the solution of project: VEGA V-13-013-00. Principal investigator: prof. Ing. Jozef Meško, PhD.

References

[1] NOVÁK, P., ŽMINDÁK, M., PELAGIĆ, Z. High-Pressure Pipelines Repaired by Steel Sleeve and Epoxy Composition. In: Experimental Stress Analysis 2013, 51st international conference : conference proceedings, June 11-13 2013, Litomeřice, Czech republic, 2013, ISBN 978-80-7414-579-7

[2] KOŇÁR, R., MIČIAN, M. Numerical simulation of residual stresses and distortions in butt weld in simulation program Sysweld. In: Comunications: scientific letters of the University of Žilina. Vol. 14, No. 3. pp. 49-54. ISSN 1335-4205. Žilina.

[3] KOŇÁR, R., MIČIAN, M., STRAŠKO, J. *Numerical simulation of temperature fields in sysweld simulation programme*. In: International journal of applied mechanics and engineering, Vol. 15, No. 2, pp. 423-431. ISSN 1425-1655

[4] RADEK, N., ANTOSZEWSKI, B. *Influence of laser treatment on the properties of electro-spark deposited coatings.* In: Kovove Materialy - Metallic Materials 47, pp. 31-38, 2009

[5] ŽMINDÁK, M. et all. *Numerical simulation of contact stresses analysis with crack*. In: Machine modelling and simulations 2012. pp. 321-330, Poznan, ISBN 978-83-923315-2-0

[6] KOVANDA, K., HOLUB, L., KOLAŘÍK, L., KOLAŘÍKOVÁ, M., VONDROUŠ, P. *Experimental verification of FEM Simulation of GMAW bead on plate welding*. Manufacturing Technology Vol.12, No. 12, pp. 30-33.

TRANSCOM 2015, 22-24 June 2015
University of Žilina, Žilina, Slovak Republic

Vanadium and Combined Vanadium and Chromium Influence to Mechanical Properties of AlSi10MgMn Alloy with Elevated Iron Level

[*]Maria Žihalová, [*]Dana Bolibruchová
[*] University of Žilina, Faculty of Mechanical Engineering, Department of Technological Engineering, Univerzitná 1, 010 26 Žilina, Slovakia, {maria.zihalova, danka.bolibruchova}@fstroj.uniza.sk

Abstract. Recent trends in aluminum castings leads to application of higher amount of recycled materials. Recycled (secondary) Al-Si alloys are characterized by increased content of impurities, mainly iron that is thought to be detrimental to mechanical and foundry properties of final castings. Manganese addition is mostly used to reduce iron effect but its application is sometimes limited. Other elements, or they combinations, can be also added to improve mechanic properties of Al-Si alloys containing higher iron level such as Cr, V, Co, Mo, Be, etc. Influence of V and combined V and Cr addition to mechanical properties is described in the presented article.

Keywords: AlSi10MgMn alloy, iron-based intermetallics, tensile properties, hardness, fracture surface.

1. Introduction

Cast Al–Si–Mg alloys are dispersion hardened by the eutectic Si particles reinforcing the aluminum matrix. It is well known that ductility and fracture of these alloys are strongly affected by the size, distribution, and morphology of the Si particles [1]. Significant influence to properties of Al-Si alloys have also iron intermetallic phases present in the alloy. Iron effect is more important in secondary aluminum alloys made of recycled materials.

Iron, as one of the main impurities in aluminum, is always present in alloys made from commercially pure base material. The solid solubility of iron in aluminum is very low with the result that most iron present forms intermetallic compounds, the nature of which depends strongly on other impurities or alloying elements present [2]. Even with an extremely low amount of Fe in the melt, the monoclinic particles of β-Al_5FeSi crystallize during solidification. The sharp tips of these needles act as stress raisers with a general reduction of the ductility and ultimate tensile strength. The formation and amount of porosity is also dependent on iron content. It was suggested that the formation of coarse β-Al_5FeSi intermetallic platelets restricts the liquid metal-feeding during the casting process [3].

The harmful effects of Fe can be minimized by various techniques such as the melt superheating or addition of Co, Mn, Cr, Ni, V, Be and K elements. All of these methods modify the platelet shape of intermetallics with platelet morphology. Addition of Mn to the melt will change β-Al_5FeSi platelets to α-$Al_{15}(Fe,Mn)_3Si_2$ in the form of Chinese script or polyhedral morphologies [4].

The influence of V occurs by amount 0.05 – 0.15 % of the melt weight. V reduces the length of β-phase platelets Al_5FeSi and with Ni and Ti has significant influence on improving the mechanical properties (R_m and A_5). Similarly to Fe and Co, vanadium has the negative influence to fluidity of Al-Si alloys [5]. There is also significant beneficial influence of vanadium on hardness [6].

It has been shown that small Cr addition can strongly influence the morphology of the Fe-containing phases or enhance the precipitation of compounds less harmful than β-Al_5FeSi phase, i.e. with a Chinese script or polyhedral morphology. A Fe to Cr ratio of 3 is required in order to promote the formation of a Chinese script α-$Al_{13}(Fe,Cr)_4Si_4$ phase [7].

Presented article deals with influence of vanadium and combined V and Cr influence to mechanical properties of AlSi10MgMn alloy with increased iron level. Fracture surfaces after tensile test are also analyzed.

2. Methodology of experiments

Aluminum AlSi10MgMn alloy was used to performing experiments. Aluminum alloy was polluted by iron in form of AlFe10 master alloy to obtain alloy with approximately 1 wt. % of Fe (AlSi10MgMnFe1). Higher iron level was chosen to obtain secondary alloy characteristic by high level of impurities, mainly iron. Such prepared alloy was in next step of experiments alloyed by vanadium in amount of 0.2 wt. %. Alloys with combined V and Cr addition were prepared by chromium additions in amount of 0.5 and 1.0 wt. % of Cr, respectively. Vanadium and chromium additions was obtained by additions of AlV10 and AlCr20 master alloys. Prepared alloys was poured into permanent mould preheated to 200 ± 5 °C. Pouring temperature was for each alloy the same, 760 ± 5 °C. Chemical compositions of the prepared alloys are shown in Tab. 1. Poured castings were then machined to form of tensile strength samples with diameter of 10 mm and samples for hardness measuring. After tensile test was performed, fracture surfaces were cutted off and observed on SEM microscope.

Alloy	Si	Mg	Mn	Fe	Ti	Zn	Cu	V	Cr	Al
AlSi10MgMn	10.220	0.277	0.108	0.448	0.046	0.029	0.047	0.010	0.006	rest
AlSi10MgMnFe1	9.73	0.313	0.118	0.980	0.041	0.026	0.048	0.009	0.037	rest
AlSi10MgMnFe1 + 0.2 wt. % V	9.133	0.265	0.116	1.588	0.034	0.026	0.046	0.216	0.166	rest
AlSi10MgMnFe1 + 0.2 wt. % V + 1.0 wt. % Cr	8.996	0.291	0.119	1.446	0.033	0.029	0.047	0.139	>0.480	rest
AlSi10MgMnFe1 + 0.2 wt. % V + 0.5 wt. % Cr	8.539	0.290	0.098	1.182	0.031	0.028	0.053	0.135	>0.480	rest

Tab. 1. Chemical compositions of the alloys with iron, vanadium and chromium additions.

3. Results

3.1. Mechanical properties

Average value of the commercial alloy tensile strength (Fig. 1) decreased after iron addition probably due to higher amount of iron intermetallics in alloy microstructure. After addition of V, tensile properties of the alloy increased and almost reached properties of commercial alloy strength. The opposite behavior has been observed after combined V and Cr addition that caused significant decrease of tensile strength. Values of tensile strength after V and Cr addition were even lower than in iron treated alloy.

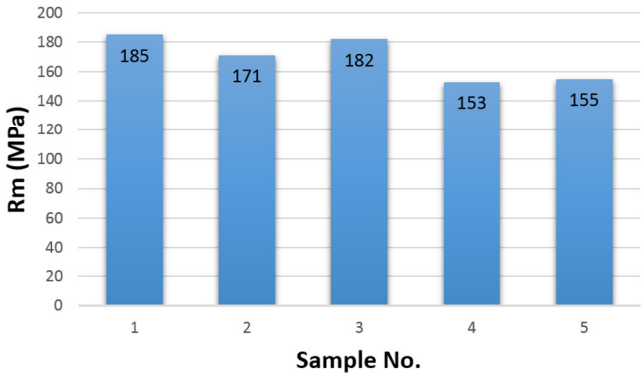

Fig. 1. Tensile strength of AlSi10MgMn alloy: 1 – commercial AlSi10MgMn alloy, 2 –AlSi10MgMnFe1, 3 - AlSi10MgMnFe1 + 0.2 wt. % V, 4 - AlSi10MgMnFe1 + 0.2 wt. % V + 0.5 wt. % Cr and 5 - AlSi10MgMnFe1 + 0.2 wt. % V + 1.0 wt. % Cr.

Elongation behavior (Fig. 2) were similar to ultimate tensile strength. The highest value has been measured in commercial alloy. Vanadium caused increasing elongation of alloy with increased iron level but after mutual V and Cr addition elongation decreased again. After Cr addition in amount of 1 wt. % elongation raised again.

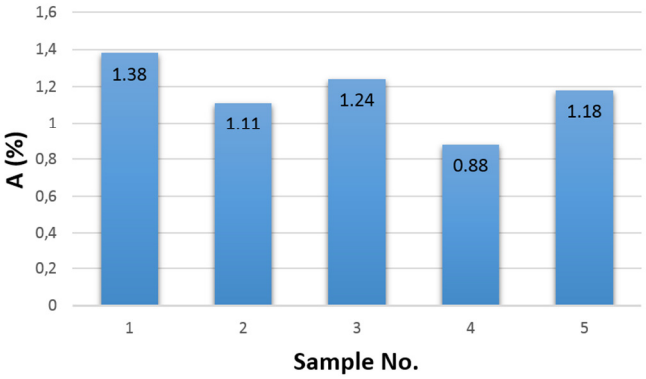

Fig. 2. Elongation of AlSi10MgMn alloy: 1 – commercial AlSi10MgMn alloy, 2 –AlSi10MgMnFe1, 3 - AlSi10MgMnFe1 + 0.2 wt. % V, 4 - AlSi10MgMnFe1 + 0.2 wt. % V + 0.5 wt. % Cr and 5 - AlSi10MgMnFe1 + 0.2 wt. % V + 1.0 wt. % Cr.

Measuring of the Brinell hardness (Fig. 3) shows increase of its values compared to untreated alloy after addition of each analyzed elements. Maximal hardness was measured after V addition with value of 91 HB. Hardness of samples with combined V and Cr additions reached almost the same values as alloy with increased iron level.

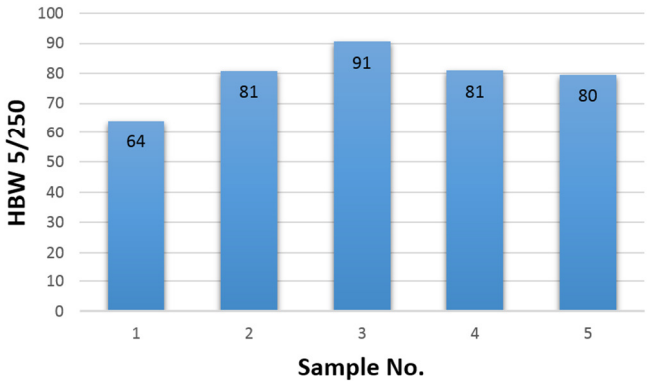

Fig. 3. Brinell hardness of AlSi10MgMn alloy: 1 – commercial AlSi10MgMn alloy, 2 –AlSi10MgMnFe1, 3 - AlSi10MgMnFe1 + 0.2 wt. % V, 4 - AlSi10MgMnFe1 + 0.2 wt. % V + 0.5 wt. % Cr and 5 - AlSi10MgMnFe1 + 0.2 wt. % V + 1.0 wt. % Cr.

3.2. Fracture surfaces observations

Observations of fracture surfaces were performed on the static tensile test samples. Sample with maximal and minimal values of both tensile strength and elongation were analyzed.

Maximal tensile strength has been measured on the sample after addition of 0.2 wt. % of V to the alloy with increased iron level. Fracture surface of the sample is highly developed with transcrystaline fracture. Fracture areas of cleavage and cellular morphology are visible on the surface (Fig. 4a). Large cleavage facets are probably caused by fracture of iron-based intermetallic phases with platelet morphology. Detail of fracture surface with cellular morphology (Fig. 4b) shows presence of eutectic Si particles and ductile fracture of α-aluminum.

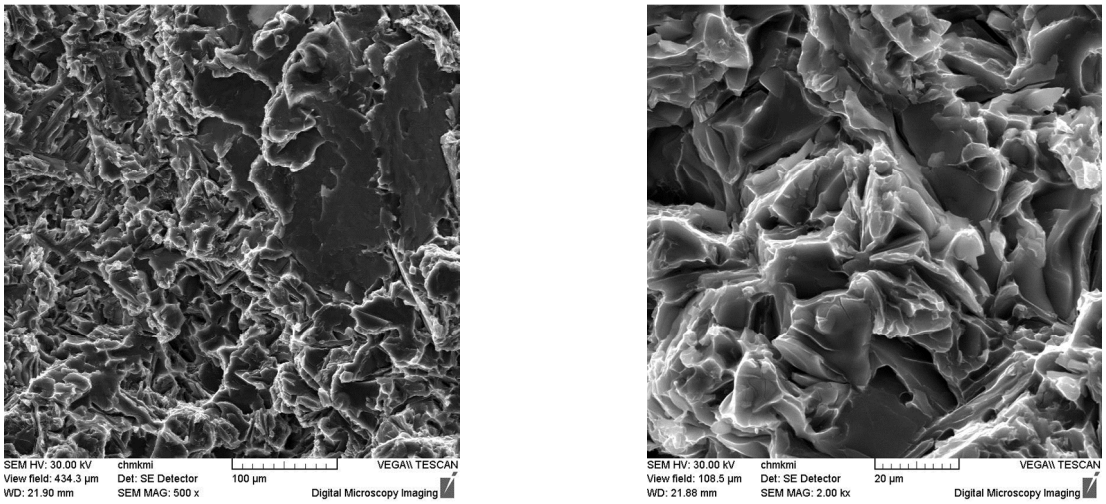

a) 500x magnification b) 2,000x magnification

Fig. 4. The fracture surface of sample with maximal tensile strength (AlSi10MgMnFe1 alloy with 0.2 wt. % of V).

Maximal elongation was measured on the sample of alloy with addition of 0.2 wt. % of V and 1.0 wt. % of Cr. Fracture surface (Fig. 5) of the sample is medium developed and compared to sample with maximal tensile strength there is no visible such large cleavage facets. Cellular morphology is mostly present on the surface but cleavages are also present. Higher number of shrinkage pores was observed (Fig. 5a in the middle) that might cause decrease of tensile strength but has not such significant effect to elongation. Detail of area with cellular morphology (Fig. 5b) have similar morphology as sample with maximal strength. Larger secondary cracks are visible in silicon particles.

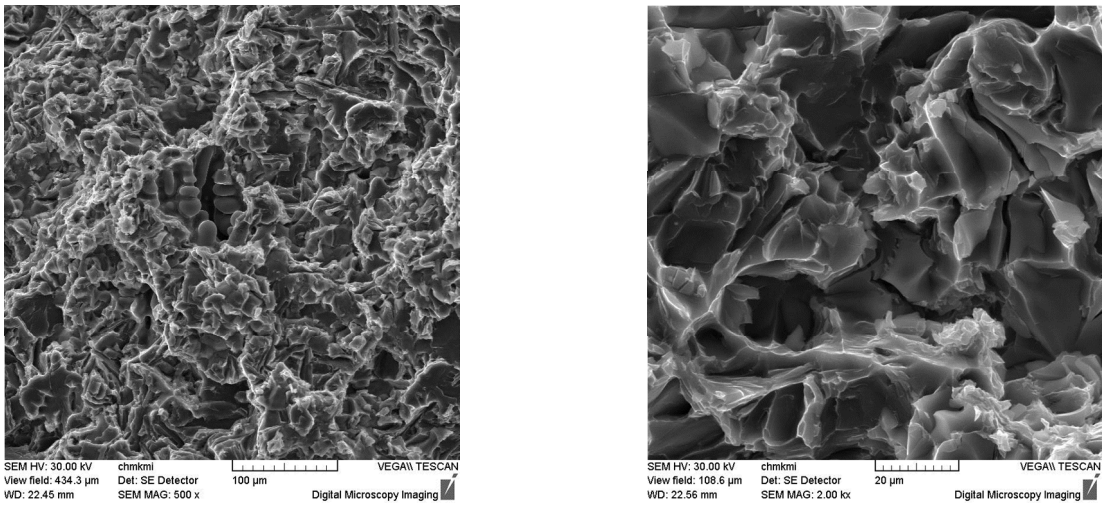

a) 500x magnification b) 2,000x magnification

Fig. 5. The fracture surface of sample with maximal elongation (AlSi10MgMnFe1 alloy with 0.2 wt. % of V and 1.0 wt. % of Cr).

Sample of AlSi10MgMnFe1 with addition of 0.2 wt. % of V and 0.5 wt. % of Cr reached minimal value of both tensile strength and elongation. Highly developed fracture surface with cleavage and cellular morphology were observed (Fig. 6a). Transcrystaline crack crossed through iron based intermetallic phases with script-like morphology (Fig. 6b), where secondary cracks can be also visible.

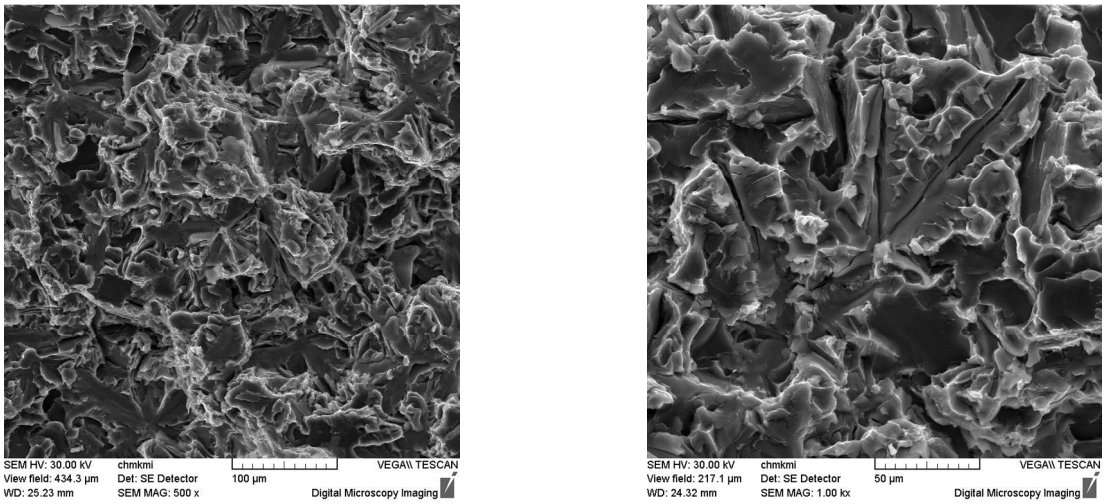

a) 500x magnification b) 1,000x magnification

Fig. 6. The fracture surface of sample with minimal tensile strength and elongation (AlSi10MgMnFe1 alloy with 0.2 wt. % of V and 0.5 wt. % of Cr).

4. Discussion

Each alloying element has a significant influence to mechanical properties of AlSi10MgMn alloy. Iron addition in amount of 1 wt. % caused decrease of tensile strength and elongation but Brinell hardness increased. Decreasing of tensile properties is commonly connected with formation of iron-based intermetallic particles with platelet morphology. The same particles has an influence to hardness of the alloy. Addition of V to alloy with elevated iron level leads to improving its tensile strength and also elongation. Fracture surface still shows presence of large cleavage areas probably due to presence of iron intermetallics. Measures shows that vanadium decreased such detrimental iron effect. It is still not clear in which way vanadium improves mechanical properties of the alloy. The reason can be that vanadium decreases length of iron particles and/or improves strength of α-Al matrix. Tensile strength and elongation of AlSi10MgMn alloy after combined V and Cr addition decreased and minimal values were measured after addition of 0.2 wt. % of V and 0.5 wt. % of Cr. Chromium addition might lead to formation of so-called “sludge” phases [8]. Presence of such phases can be also detrimental to tensile properties of the alloy. Surprisingly, maximal elongation has been measured on the sample with addition of 0.2 wt. % of V and 1.0 wt. % of Cr. Average value of tensile strength and elongation has also increased compared to alloy containing 0.5 wt. % of Cr. Slightly increase of mechanical properties can be caused by higher number of “sludge” with polyhedral morphology and smaller size than large platelet-like particles of β-Al_5FeSi. Although tensile properties of the alloy with higher Cr level slightly increased it still do not reached values of alloy with only iron addition. It might be influenced by higher amount of porosity observed on fracture surface. Presence of “sludge” can be more detrimental to alloy properties due to reduction of molten metal feeding to interdendritic space and thus increasing of porosity [9].

5. Conclusions

Several conclusions can be stated from measuring of tensile strength, elongation and Brinell hardness in conjunction with fracture surface observations of AlSi10MgMn alloy with increased iron level and additions of V and Cr, as follows:

(1) Vanadium addition in amount of 0.2 wt. % leads to improving of tensile strength, elongation and Brinell hardness of the alloy with elevated iron level.

(2) Combined addition of V and Cr caused tensile properties decrease but hardness increase probably due to formation of so called "sludge" phases.
(3) Maximal tensile strength has been measured on the sample with V addition even with presence of large cleavage facets on the fracture surface.
(4) Elongation reached maximal value on the sample with addition of V and 1.0 wt. % of Cr. This might be a result of formation of smaller "sludge" compared to large β-platelets.
(5) Porosity of the alloy increased after combined V and Cr addition probably due to "sludge" phases formation.

Acknowledgement

This work was created in the framework of the grant project VEGA N° 1/0363/13. The authors acknowledge the grant agency for support.

References

[1] ALEXOPOULOS, N.D., STYLIANOS, A., CAMPBELL, J. *Dynamic fracture toughness of Al–7Si–Mg (A357) aluminum alloy*. Mechanics of Materials 58, pp. 55–68, 2013.

[2] SHABESTARI, S.G. *The effect of iron and manganese on the formation of intermetallic compounds in aluminum–silicon alloys.* Materials Science and Engineering A 383, pp. 289–298, 2004.

[3] TIMELLI, G., BONOLLO, F. *The influence of Cr content on the microstructure and mechanical properties of $AlSi_9Cu_3$(Fe) die-casting alloys.* Materials Science and Engineering A 528, pp. 273–282, 2010.

[4] SHABESTARI, S.G., KESHAVARZ, M., HEJAZI, M.M. *Effect of strontium on the kinetics of formation and segregation of intermetallic compounds in A380 aluminum alloy*. Journal of Alloys and Compounds 477, pp. 892–899, 2009.

[5] PETRÍK, J., HORVATH, M. *The iron correctors in Al-Si alloys. Annals of Faculty Engineering Hunedoara – International Journal of Engineering*, pp. 401-405, 2011.

[6] SZARVASY, P., PETRÍK, J., ŠPEŤUCH, V. *Use of iron correctors for improving properties of silumin castings.* Foundry Industry Journal, 11-12, pp. 521-524, 2005. (in Slovak)

[7] TIMELLI, G. et al. *The role of Cr additions and Fe-rich compounds on microstructural features and impact toughness of AlSi9Cu3(Fe) die casting alloys*. Materials Science & Engineering A 603, pp. 58–68, 2014.

[8] TILLOVÁ, E., CHALUPOVÁ, M. *Structural Analysis of Al-Si Alloys*. 1st ed. EDIS ŽU: Žilina, 2009. (in Slovak)

[9] BRUNA, M., KUCHARCIK, L., SLADEK, A. *Complex Evaluation of Porosity in A356 Aluminium Alloy using Advanced Porosity Module*. Manufacturing Technology, vol. 13, No.1, 26–30, 2013.

TRANSCOM 2015

Proceedings, Section 5

Published by University of Žilina
First Editions
Printed by EDIS - Žilina University publisher
Printed in 500 copies

ISBN 978-80-554-1047-0
ISSN of Transcom Proceedings CD-Rom version: 1339-9799
ISSN of Transcom Proceedings online version: 1339-9829
(http://www.transcom-conference.com/transcom-archive)


9 788055 410470